NASA/CP-1999-209704/VOL1/PT2

1999 NASA High-Speed Research Program Aerodynamic Performance Workshop

Volume I—Configuration Aerodynamics

Edited by
David E. Hahne
Langley Research Center, Hampton, Virginia

December 1999

The NASA STI Program Office . . . in Profile

Since its founding, NASA has been dedicated to the advancement of aeronautics and space science. The NASA Scientific and Technical Information (STI) Program Office plays a key part in helping NASA maintain this important role.

The NASA STI Program Office is operated by Langley Research Center, the lead center for NASA's scientific and technical information. The NASA STI Program Office provides access to the NASA STI Database, the largest collection of aeronautical and space science STI in the world. The Program Office is also NASA's institutional mechanism for disseminating the results of its research and development activities. These results are published by NASA in the NASA STI Report Series, which includes the following report types:

- TECHNICAL PUBLICATION. Reports of completed research or a major significant phase of research that present the results of NASA programs and include extensive data or theoretical analysis. Includes compilations of significant scientific and technical data and information deemed to be of continuing reference value. NASA counterpart of peer-reviewed formal professional papers, but having less stringent limitations on manuscript length and extent of graphic presentations.
- TECHNICAL MEMORANDUM. Scientific and technical findings that are preliminary or of specialized interest, e.g., quick release reports, working papers, and bibliographies that contain minimal annotation. Does not contain extensive analysis.
- CONTRACTOR REPORT. Scientific and technical findings by NASA-sponsored contractors and grantees.
- CONFERENCE PUBLICATION. Collected papers from scientific and technical conferences, symposia, seminars, or other meetings sponsored or co-sponsored by NASA.
- SPECIAL PUBLICATION. Scientific, technical, or historical information from NASA programs, projects, and missions, often concerned with subjects having substantial public interest.
- TECHNICAL TRANSLATION. English-language translations of foreign scientific and technical material pertinent to NASA's mission.

Specialized services that complement the STI Program Office's diverse offerings include creating custom thesauri, building customized databases, organizing and publishing research results . . . even providing videos.

For more information about the NASA STI Program Office, see the following:

- Access the NASA STI Program Home Page at ***http://www.sti.nasa.gov***
- Email your question via the Internet to help@sti.nasa.gov
- Fax your question to the NASA STI Help Desk at (301) 621-0134
- Telephone the NASA STI Help Desk at (301) 621-0390
- Write to:
  NASA STI Help Desk
  NASA Center for AeroSpace Information
  7121 Standard Drive
  Hanover, MD 21076-1320

NASA/CP-1999-209704/VOL1/PT2

1999 NASA High-Speed Research Program Aerodynamic Performance Workshop

Volume I—Configuration Aerodynamics

Edited by
David E. Hahne
Langley Research Center, Hampton, Virginia

Proceedings of a workshop sponsored by
the National Aeronautics and Space
Administration, Washington D.C., and
held in Anaheim, California
February 8–12, 1999

National Aeronautics and
Space Administration

Langley Research Center
Hampton, Virginia 23681-2199

December 1999

Available from:

NASA Center for AeroSpace Information (CASI)
7121 Standard Drive
Hanover, MD 21076-1320
(301) 621-0390

National Technical Information Service (NTIS)
5285 Port Royal Road
Springfield, VA 22161-2171
(703) 605-6000

PREFACE

The High-Speed Research Program sponsored the NASA High-Speed Research Program Aerodynamic Performance Review on February 8-12, 1999 in Anaheim, California. The review was designed to bring together NASA and industry High-Speed Civil Transport (HSCT) Aerodynamic Performance technology development participants in areas of: Configuration Aerodynamics (transonic and supersonic cruise drag prediction and minimization) and High-Lift. The review objectives were to: (1) report the progress and status of HSCT aerodynamic performance technology development; (2) disseminate this technology within the appropriate technical communities; and (3) promote synergy among the scientist and engineers working HSCT aerodynamics. The HSR AP Technical Review was held simultaneously with the annual review of the following airframe technology areas: Materials and Structures, Environmental Impact, Flight Deck, and Technology Integration. Thus, a fourth objective of the Review was to promote synergy between the Aerodynamic Performance technology area and the other technology areas within the airframe element of the HSR Program.

The work performed in the Configuration Aerodynamics (CA) element of the High-Speed Research Program during 1998 was presented in the following sessions:

Propulsion Integration
Analysis Methods
Design Optimization
Testing

The work performed in the High Lift (HL) element of the High-Speed Research Program during 1998 was presented in the following sessions:

High-Lift Configuration Development
Tools and Methods Development

The proceedings for the Aerodynamic Performance Annual Review are published in three volumes:

Volume I, Parts 1 and 2	Configuration Aerodynamics
Volume II, Parts 1 and 2	High Lift

AP Review Chairperson: David Hahne
NASA Langley Research Center

CONTENTS

---

*Part 1 is presented under separate cover.

Design Optimization Session

Part 2

Testing Session

Geometry–Driven Mesh Deformation

James Reuther, *MCAT*

Mark J. Rimlinger, *Raytheon*

David Saunders, *Raytheon*

HSR Airframe Technical Review
Anaheim, Ca
February 8–12, 1999

Outline

An outline of the material to be presented. Note that the examples section consisted of a video presentation that is not included in this documentation.

Outline

- Motivation
- General Strategy
- Details of Methodology
- Examples
- Future Work

Motivation

At each design step during the application of an aerodynamic shape optimization method, it must be possible to obtain a mesh representing the current design changes and the gradients of the cost function. In an adjoint based method, the determination of changes in the cost function require that the variation in the mesh metrics be computed. Since it would be difficult to obtain an explicit relationship between arbitrary surface changes and variations in mesh metrics for complex configurations, these quantities are calculated through finite differences. This requires the mesh to be regenerated a number of times proportional to the number of design variables. The use of hyperbolic or elliptic iterative mesh generation techniques to construct a mesh for a single design variable perturbation becomes computationally prohibitive and may approach the cost of a flow solution. Additionally, no automated method exists for generating multiblock meshes about complex three–dimensional configurations.

Here, these difficulties are overcome through the use of a mesh perturbation technique. In this approach, a high quality mesh appropriate for the flow solver is first generated by any available procedure prior to the start of the design. This initial mesh becomes the basis for all subsequent meshes which are obtained by analytic perturbations.

Applications for a mesh perturbation scheme can be found in any area which wishes to take advantage of an existing mesh in order to avoid the laborious and time intensive process of regenerating a grid system. Rapid mesh morphing permits the reuse of existing mesh topologies on similar configurations as well as analysis and design accounting for static aeroelastics.

Motivation

- **Demands Arise From:**
  - Aerodynamic Shape Optimization of Complex Configurations
  - Reuse of Existing Mesh Topologies on New Configurations
  - Analysis and Design Accounting for Static Aeroelastics

- **Limitations of Manual Approach:**
  - **Geometry Treatment**
    * Lofting
    * Intersections/Trimming
    * Constraints
  - **Grid Generation**
    * Calendar–Intensive
    * User–Intensive
    * Difficult to Automate

Structured Multi–Block Volume Mesh

The surface and symmetry planes of a typical multiblock volume mesh are illustrated in this slide. In practice, a multiblock volume mesh for a complex configuration requires a skilled grid generator one to three weeks to complete as well as related CAD support. In the event of design changes, the mesh perturbation scheme allows one to circumvent this labor–intensive grid generation process by recycling the previous multiblock mesh through an automated procedure of surface and volume mesh warping.

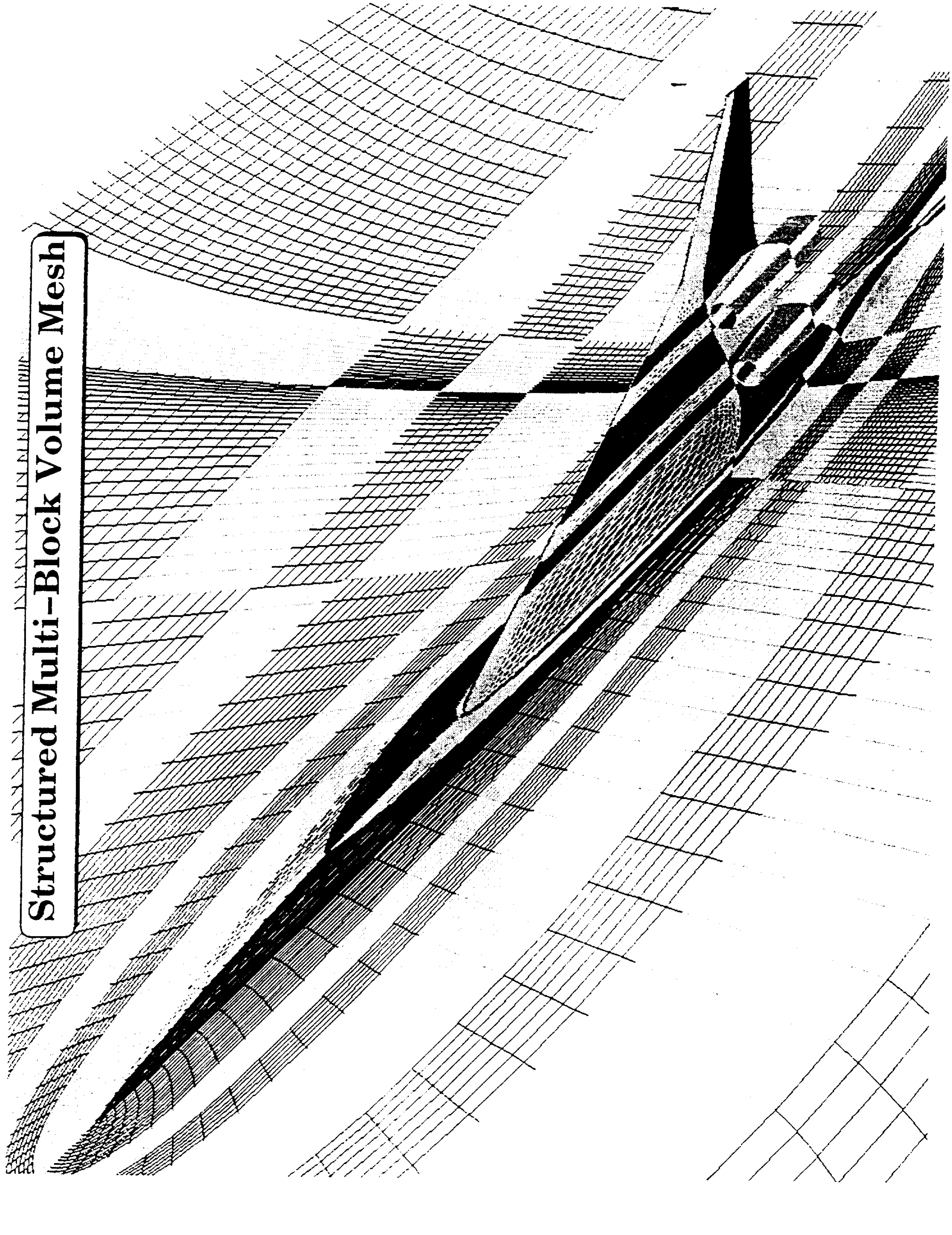
Structured Multi-Block Volume Mesh

Direct Mesh Perturbation Approach

The necessity of having an underlying representation of the individual geometry components can be seen in the context of applying design variables and constraints to the geometry illustrated in this slide. Without an underlying geometry definition, a vertical translation of the wing relative to the fuselage proves to be problematic in that the original surface mesh cannot be resplined to reflect the previously hidden lower fuselage features. In general, when perturbations affect the intersections of geometry components, such as the wing–fuselage root in this example, the motion of mesh points lying directly on these intersections is ill–defined.

The imposition of constraints directly on the mesh point locations creates difficulties in implementing generalized routines. Consider, for example, the imposition of wing fuel volume or cabin polygon constraints on a system of surface meshes which cannot precisely differentiate between wing and fuselage components.

An advantage, however, of using the mesh points as design variables is that, when combined with an analytical mesh mapping transformation, the calculation of the gradient can be performed without explicitly computing the variations in the mesh metrics. Unfortunately, obtaining such a general mapping transformation increases in difficulty with added geometric complexity.

Direct Mesh Perturbation Approach

- **Wing Vertical Translation Relative to Body**

  Deform fuselage shape?

  Re–spline fuselage shape?

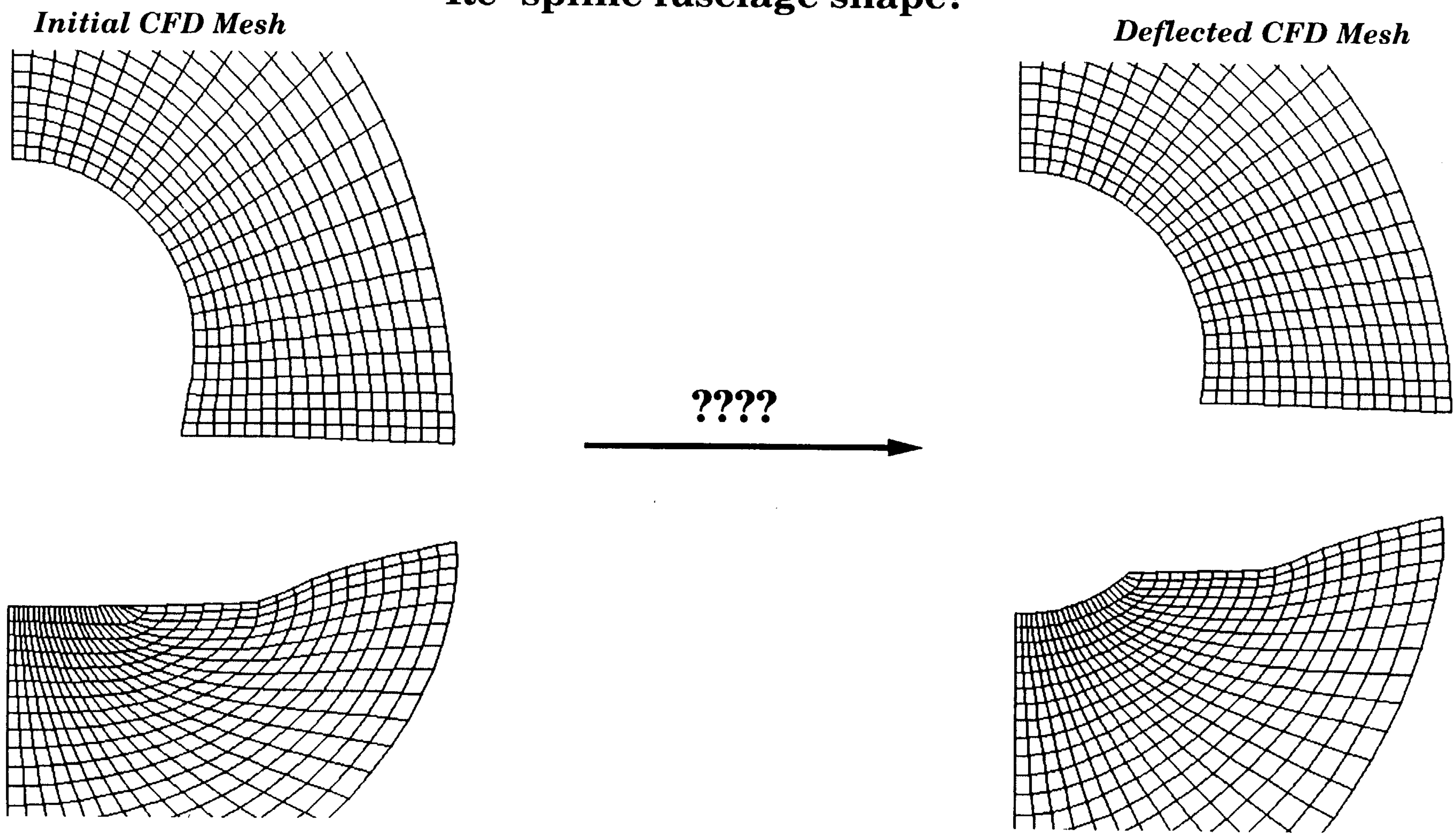

Geometry Kernel Approach

The alternative to applying design variables to the surface mesh points is to develop an underlying geometry kernel which represents the configuration's components as unintersected entities distinct from the CFD mesh. In this approach, design changes are applied directly to the individual components, such as the wing or fuselage, through design variables or, in the case of an analytic surface definition, through a modification of coefficients. Since the raw unintersected geometries are available, constraints and design changes affecting intersections are easily treated without regard to the actual mesh that is used for the flow and adjoint calculation.

At any particular point in the design process, changes in the underlying geometry are relayed to the mesh surfaces by first intersecting all of the geometric entities to construct a set of parametric surfaces, or panels, representing the modified complete configuration. Using a predetermined parametric mapping of the surface mesh points to the paneling of the initial configuration, changes between the modified and initial panelings at the CFD mesh points are evaluated and the surface mesh perturbed.

The important feature of this approach is that a set of simple geometric entities lies at the core of the entire design process. This technique retains the typical way in which aerodynamic vehicles are defined and provides strict control over how the surface intersections are treated. Furthermore, since the chosen design variables act directly on the geometric entities, these entities may be output for future analysis at the end of the design process.

Geometry Kernel

- Use geometry components
- Apply design changes to components
- Impose constraints on components
- Intersect components and panel the surfaces
- Map changes to CFD mesh

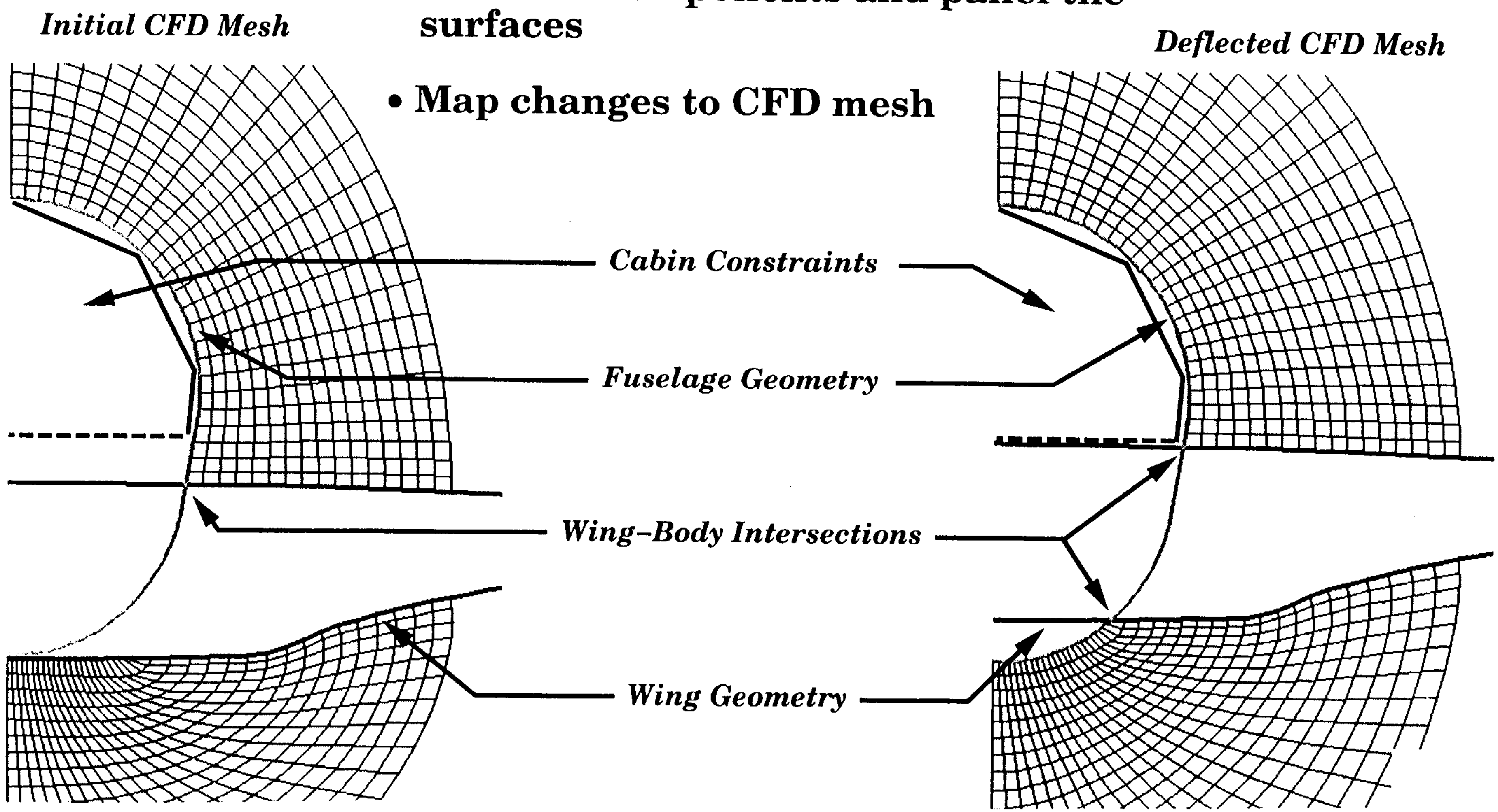

General Strategy

In the method developed in this research, an underlying geometry database consisting of a set of simple geometric entities, such as wings and bodies, is input to the design algorithm along with the multiblock mesh used for the flow and adjoint calculations. An additional pre–processed input consists of the location of each surface mesh point in the initial mesh determined in relation to the parametric patch representation of the initial geometry and is termed the (u,v) map.

Within the design code, the PERTURB routine applies the design variables, which are defined as a set of analytic shape functions, directly to the geometric entities. PERTURB then evaluates the linear and nonlinear constraints on these primary entities.

Next, an automated paneling method, AEROSURF, intersects the geometry components and constructs parametric patches for the exterior geometry. AEROSURF is a generalized paneling engine able to handle variable topologies of wings, fuselages, nacelles, pylons, and diverters in an automated and efficient manner.

Having constructed the parametric patches representing the modified geometry, the MAPXYZ procedure updates the CFD surface meshes. The perturbed surface mesh point locations are determined by evaluating the modified parametric geometry patches at the pre–determined (u,v) locations.

Finally, the WARP–MB procedure is used to morph the CFD volume mesh to follow the updated surface meshes producing a volume grid to be used in calculating the adjoint and flow solutions.

General Strategy

- **Starting Point:**
  - Initial **3D Structured** Mesh (**GRIDGEN**)
  - **Basic Geometry Components** as Defining Sections
- **PERTURB:**
  - Apply **Shape Changes** and **Constraints** to **Geometry Components**
- **AEROSURF:**
  - **Intersect** All **Geometry Components**
  - **Panel** Exterior Geometry Surfaces into **Parametric Patches**
- **MAPXYZ:**
  - Use **Parametric Patches** to Update **CFD Surface Mesh**
- **WARP–MB:**
  - Morph **CFD Volume Mesh** to Follow **Surface Mesh**

Mesh Deformation Flow Chart

In this slide, the mesh deformation scheme implemented in the SYN107–MB design code is represented as a flow diagram illustrating the functionality and sequential relation of the individual modules as well as the module dependency upon the input data. The four internal SYN107–MB procedures comprising the geometry engine and mesh perturbation scheme are shown along the centerline of the diagram and are invoked sequentially from left to right: PERTURB, AEROSURF, MAPXYZ, and WARP–MB. Additionally, the three pre–defined inputs and their entry points to the procedures are indicated: an initial set of geometry components, a multiblock volume mesh, and the (u,v) map relating the surface mesh points to the parametric paneling of the initial geometry.

Given a set of geometry components, the PERTURB module applies the design variables to affect changes in the geometry. AEROSURF then intersects the modified geometry entities and produces a parametric paneling of the new configuration. The (u,v) map is then used by MAPXYZ to propagate changes in the paneled geometry to CFD surface mesh. Finally, WARP–MB completes the method by warping the volume mesh to follow the modified surfaces.

Mesh Deformation Flow Chart

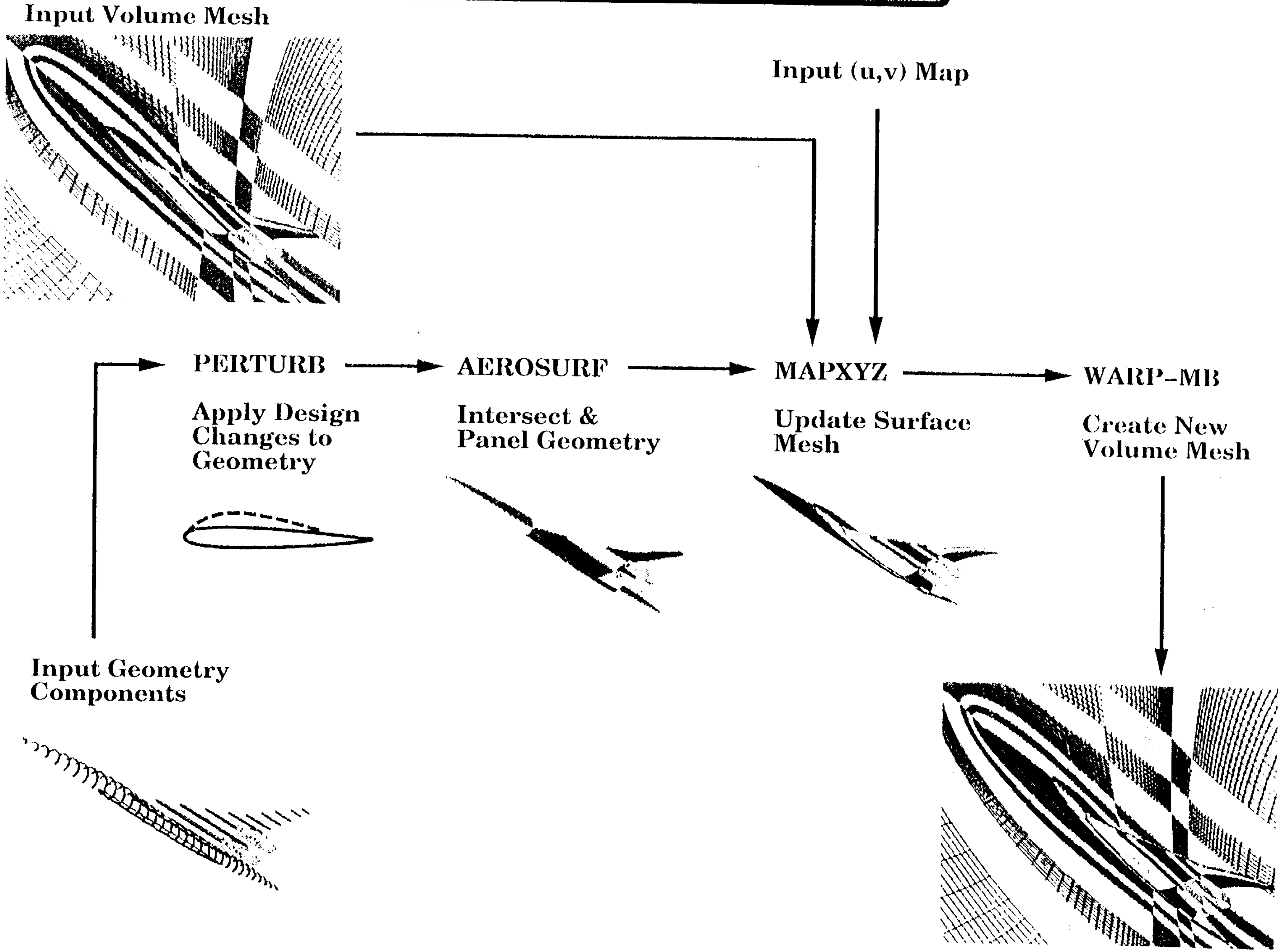

Basic Geometry Component Representation

The current implementation of the geometry kernel requires that the configuration components be expressed as sectional cuts at constant wing span or fuselage station locations. The sectional cuts are themselves composed of strings of discrete points which are usually extracted from the NURBS representation of the surface definition through a CAD utility. Each component represents the unintersected form of the entity hence a wing, for example, would be defined to the symmetry plane.

A typical set of geometry components for the TCA–6 wing, fuselage, nacelles, and diverters configuration is shown in the figure. The wing contains 41 sectional cuts with 100 points per section while the fuselage has 200 sections of 100 points per section and the nacelles have 178 sections of 101 points per section.

Basic Geometry Component Representation

- Sectional Cuts
- Unintersected
- Point Definitions

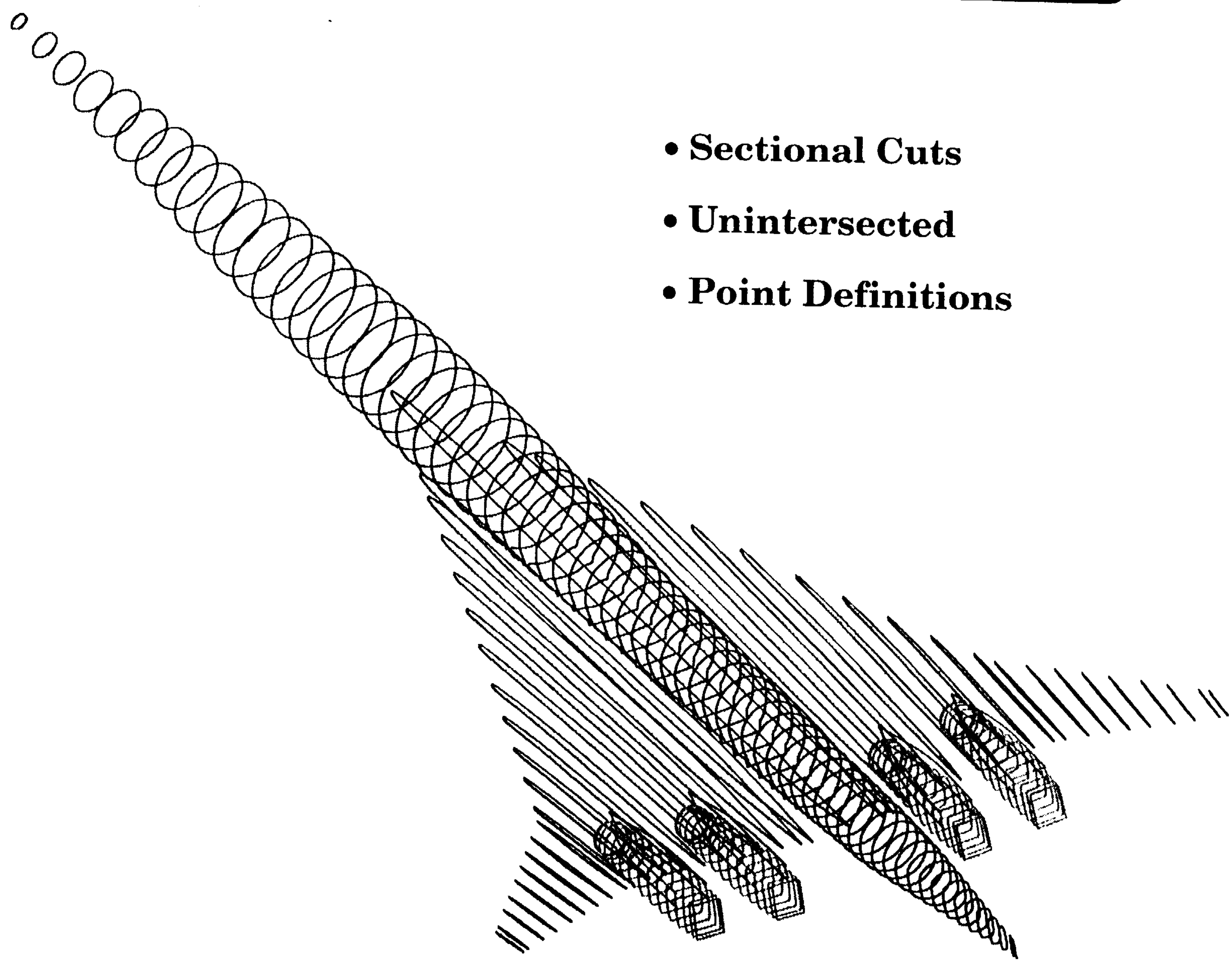

Design Variables and Constraints

The PERTURB module is responsible for the application of design variables to the unintersected geometry components. The design variables consist of analytic shape functions including Hickes–Henne sine bumps, Wagner functions, and various polynomial and exponential functions. These functions allow the designer to make changes in wing planform and sectional shapes such as: taper, dihedral, sweep, span, camber, and thickness. Additionally, some of the specialized functions allow control of flaps, slats, leading edge droop and trailing edge angle. Design variables applied to the body allow for changes in length, camber, sectional area, radius, and, through the application of sine bumps, local surface shape.

Additionally, PERTURB is responsible for the imposition of constraints to the geometry entities. Examples of implemented constraints include the thickness for spars of hinges, cabin radius, fuel volume, spar carry–through, and spar straightness.

Design Variables and Constraints

- **PERTURB:**
  - **Wing–Type Changes**
    - Twist, Taper, Dihedral, Sweep, Span
    - Camber
    - Thickness
  - **Body–Type Changes**
    - Radius, Length
    - Camber
    - Surface Shape
  - **Constraints Imposed on Geometry Components**
    - Thickness for Spars or Hinges
    - Cabin Radius
    - Fuel Volume
    - Spar Carry–Through and Spar Straightness

Geometry Intersecting and Paneling

After PERTURB has completed applying design changes to the underlying geometry entities, the AEROSURF module first intersects the components then panels the exterior surfaces with a set of parametric patches. AEROSURF is a robust and automated tool which has been designed to handle general aircraft topologies containing features such as fuselage, wings, canards, empennage, nacelles, pylons, and diverters. AEROSURF is able to panel diverse topologies as the HSCT configurations, business jets, high–, mid–, and low– mounted wings, multiple nacelles, and multiple lifting surfaces. In order to panel the HSCT geometry correctly, AEROSURF has been modified to handle cases where the wing drops below the fuselage lower surface and the nacelles touch the wing trailing edge.

Since the paneling procedure is repeated once for each design variable at each design cycle, special attention has been paid to developing an efficient routine. The paneling of the HSCT wing/body/nacelles/ diverters configuration requires 1.1 CPU seconds on an 195 MHz Origin2000 processor while a full configuration business jet requires 0.4 CPU seconds on a similar processor.

Geometry Intersecting and Paneling

- **AEROSURF:**
  - **Intersects Geometry Components** (Simple Connectivity Scheme)
  - **Panels** Exterior Surfaces with **Parametric Patches**
  - **Variable Topology**
    - * Multiple Lifting Surfaces
    - * Multiple Nacelles
  - **Capabilities**
    - * Handles Wing Dropping Below Body
    - * Handles Nacelle Touching Wing
  - **Automated**
  - **Efficient**
    - * HSCT wing/body/nacelles/diverters: 1.1 O2K CPU sec.
    - * Business Jet wing/body/nacelle/plyon: 0.4 O2K CPU sec.

AEROSURF Parametric Surface Paneling

The AEROSURF parametric surface paneling for the TCA–6 wing, body, nacelles, and diverters configuration shown in the slide consists of 39 panels with approximately 120,000 points. Since AEROSURF is an automated procedure, the paneling topology will remain consistent for reasonable design changes. It is this topological consistency which allows one to treat the panels as a parametric space and map changes in the parametric surfaces to changes in the CFD surface mesh.

AEROSURF Parametric Surface Paneling

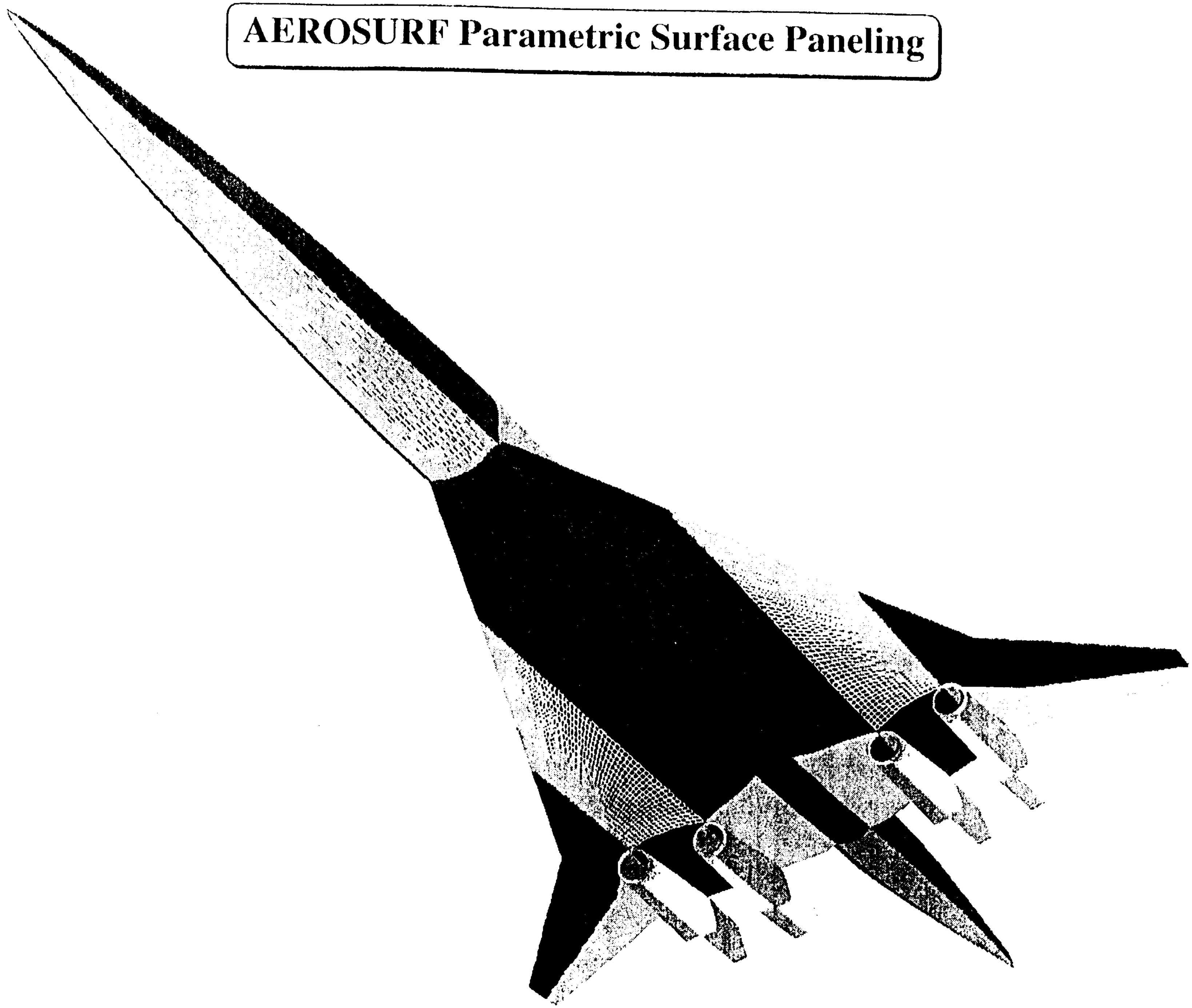

Surface Preprocessing and Mesh Updating

In order to map changes in the parametric panels to the CFD surface mesh point locations, one must have knowledge of where the surface points lie in the parametric space. Since the AEROSURF panelings are toplogically consistent, the determination of this (u,v) parametric map can be done once as a preprocessing step. A utility, UVMAP, has been developed which finds the locations of the initial CFD surface mesh points on the initial AEROSURF geometry paneling using a shortest distance projection method.

Within the design code, the MAPXYZ module is responsible for updating the surface meshes to reflect the changes in the parametric geometry paneling. By evaluating the original and modified geometry panelings at the predetermined (u,v) values, one can determine the required motion of each surface point and create an updated set of CFD surface meshes.

Surface Preprocessing and Mesh Updating

- **UVMAP:**
  - Run **AEROSURF** on **Initial Geometry**
  - Prepare a CFD **Surface Mesh** (**GRIDGEN** or Equivalent)
  - For Each **CFD Surface Mesh Point**, Calculate a **(u,v)** Pair Within Some Patch (Shortest Distance Projection Method)

- **MAPXYZ:**
  - **Perturb** the **Geometry Components**
  - **Reintersect** and **Repanel** via **AEROSURF**
  - Apply **(u,v)** Map to Evaluate **New CFD Surface Mesh** Points

Updated CFD Surface Mesh

The result of transforming a set of surface meshes from the TCA–6 baseline geometry into the NCV geometry is shown in the figure and may be compared with an earlier slide depicting the baseline mesh.

Updated CFD Surface Mesh

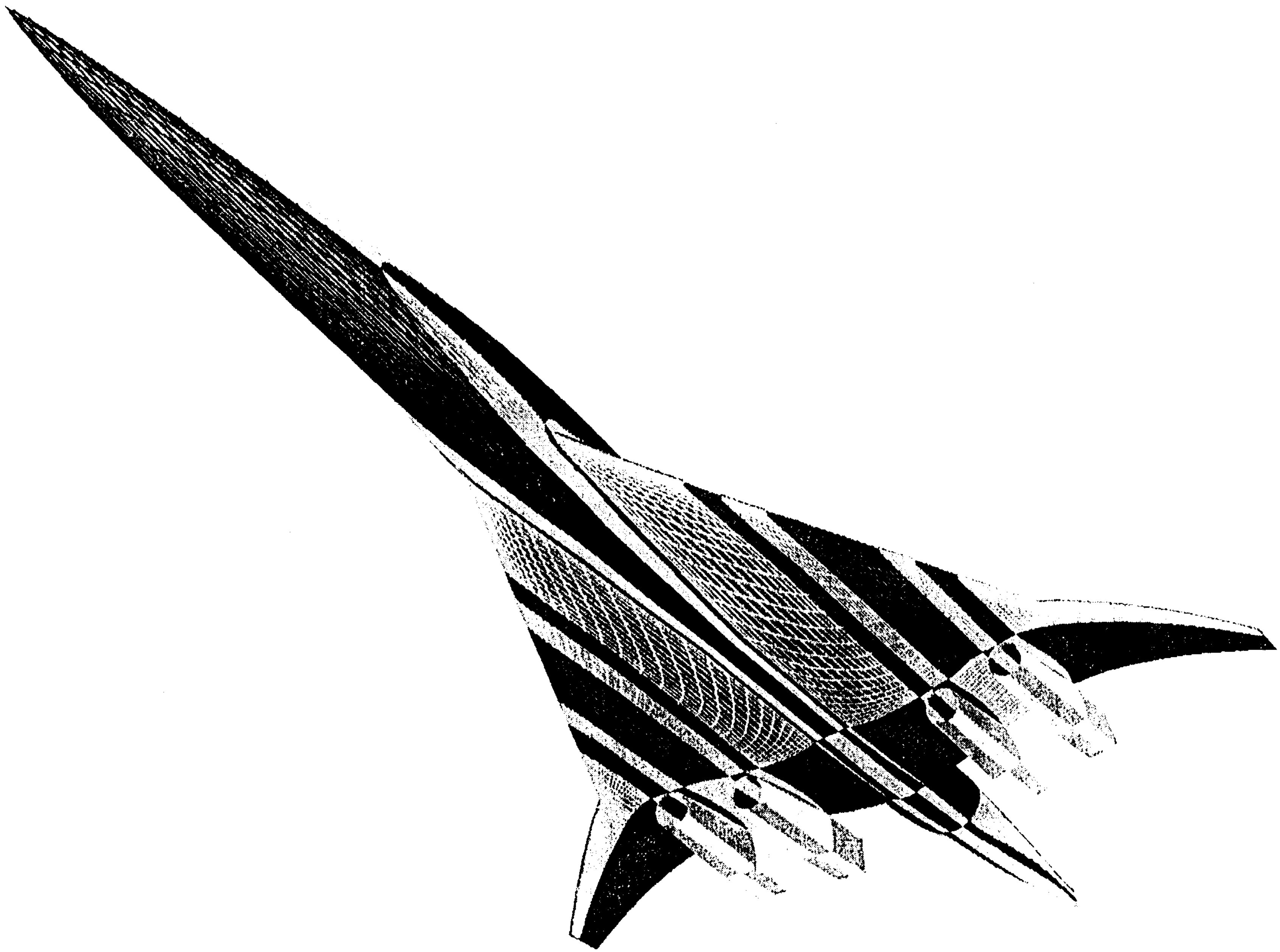

Volume Mesh Deformation

Once the surface meshes have been modified to follow the desired geometry changes, WARP–MB perturbs the remaining portion of the mesh. In order to perturb the multiblock mesh, two capabilities are required. First, the block corners, edges, and faces must be moved in a manner that follows the desired surface changes and simultaneously retains mesh continuity throughout the domain. The second requirement is to move all the points interior to each block such that the spacing distributions and smoothness of the original mesh are retained.

The methodology used to achieve the requirement of maintaining continuity in the blocking structure is given as follows:

1. All faces that are directly affected by the design variables (active faces) are explicitly perturbed.

2. In order to maintain mesh quality, internal faces that have been flagged by the user to move in conjunction with the active faces are perturbed using weighted contributions from the active faces.

3–4. All corners and edges that touch an active face, either in the same block or in an adjacent block, are implicitly perturbed by a simple arc–length–based algorithm.

5–6. All inactive edges and faces that either include an implicitly perturbed corner or edge or abut an active face are implicitly perturbed by an arc length based method.

7. The internal points of each block that has one or more explicitly or implicitly perturbed faces are adjusted using a TFI/Arc length based algorithm.

Volume Mesh Deformation (cont.)

Note that much of the mesh, especially away from the surfaces, will not require mesh perturbations and thus may remain fixed through the entire design process. Close to the surfaces, any blocks will either contain an active face or touch a block which contains an active face, either by an edge or by a corner. As the design variations affect the active faces, the above scheme ensures that the entire mesh will remain attached along block boundaries. Added complexity is required to accomplish steps 3 and 4 since the connectivity at the various edges and corners must be indicated somehow. Currently, pointers to and from a set of master edges and master corners are determined as a pre–processing step. During the design calculation, perturbations to any edges and corners are fed to these master edges and master corners which in turn communicate these to all connected edges and corners.

Since four of the required steps (1,5–7) during the warping procedure are independent of operations on other blocks, WARP–MB has been highly parallelized. This, combined with the algebraic nature of the deformations, results in a scheme able to process 500,000 mesh points per second on an Origin2000 processor.

Volume Mesh Deformation

- **WARP–MB:**

Steps	Operation	Parallelization	Type of Deformation
1	Active Surface Face	Independent	Explicit
2	Active Internal Face	Message Passing	Weight Contribution
3	Master Corners	Message Passing	Explicit
4	Master Edges	Message Passing	Explicit
5	Implicit Edges	Independent	Arc Length–Based
6	Implicit Faces	Independent	Arc Length–Based
7	Internal Volume	Independent	TFI/Arc Length–Based

- **Algebraic Mesh Deformation + Parallelization = Extreme Speed**
  - ≈ 500,000 Mesh Points / Second / O2K Processor

Updated 3–D Mesh

The result of transforming the TCA–6 baseline mesh into the NCV geometry through the use of the geometry–driven multiblock mesh deformation scheme is shown and may be compared with the earlier slide depicting the baseline volume mesh.

Updated 3-D Mesh

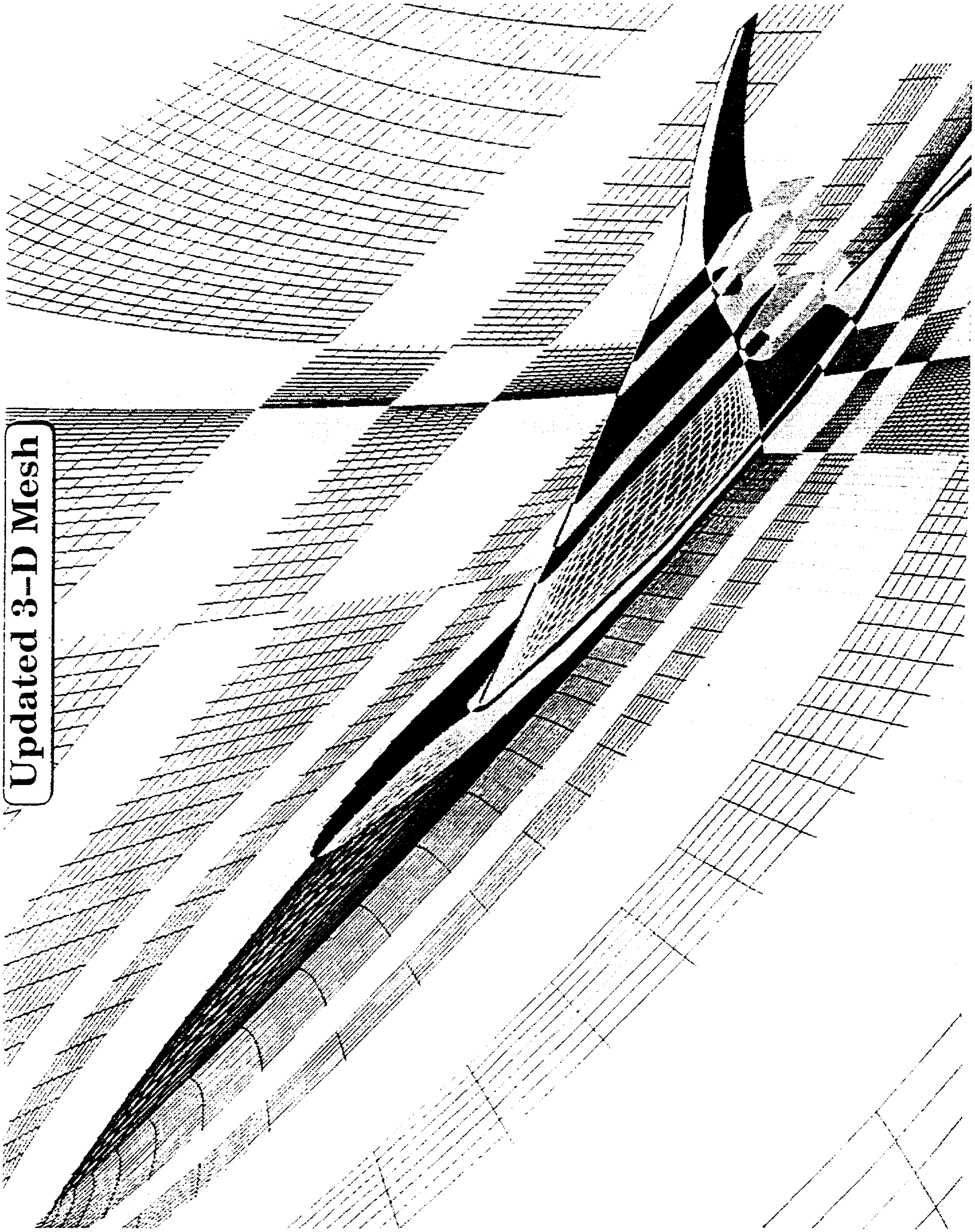

Future Work

The mesh deformation scheme and geometry kernel implemented in the SYN107–MB design code have proven to be a robust and efficient method of applying design variables and constraints to a configuration and communicating those design changes to an existing volume mesh. In an effort to reduce required user input, the specification of active internal faces for the WARP–MB procedure is being internalized through a method based on monitoring several grid quality metrics. Additionally, the ability to specify active faces as a subset of a block face is being implemented in an effort to reduce the overall number of blocks required in a given multiblock mesh topology.

Currently, the procedures controlling the mesh morphing method are only implemented as an internal part of the SYN107–MB design code. Work is underway to combine the PERTURB, AEROSURF, MAPXYZ, and WARP–MB modules into a stand–alone utility enabling designers to test hand perturbations or morph between two pre–existing geometries without requiring recourse to the design code.

In the current implementation, input geometric entities are restricted to those defined by sets of points. However, in the future, CAD entities such as NURBS surfaces will also serve this role, thereby allowing both the input and the output from the aerodynamic surface optimization method to interface directly with a CAD database.

Future Work

- **Enhance Current Capabilities**
  - Automatic Interior Boundary Control
  - Subfacing
- **Adapt** as a **Stand–Alone Structured Mesh Utility**
- **Develop Unstructured Mesh Deformation Capability**
- **Upgrade AEROSURF** as a **CAD–Based Geometry Kernel**

WBS 4.3.1.2

Aerodynamic Design Optimization Capability

Progress Toward Single and Multi–Point Optimization Tool Realization

R. S. Conner

February 10, 1999
Anaheim, CA

Configuration Aerodynamics Technology Development

This presentation covers the progress made during the last year on single and multi–point optimization at BCAG. Subtask 2, Aerodynamic Design Optimization Capability, WBS 4.3.1.2, is a continuation of previous years' efforts on constrained full configuration optimization. In contract year 1999, the completion of this work will occur under subtask 2, WBS 4.3.1.2, Aerodynamic Design Optimization Process.

This figure is the Configuration Aerodynamics Program on a Page. As shown, the work reported here falls under both Cruise Point and Multi–Point Optimization.

Configuration Aerodynamics Technology Development

Program Selects Best Analysis / Design Optimization Methods

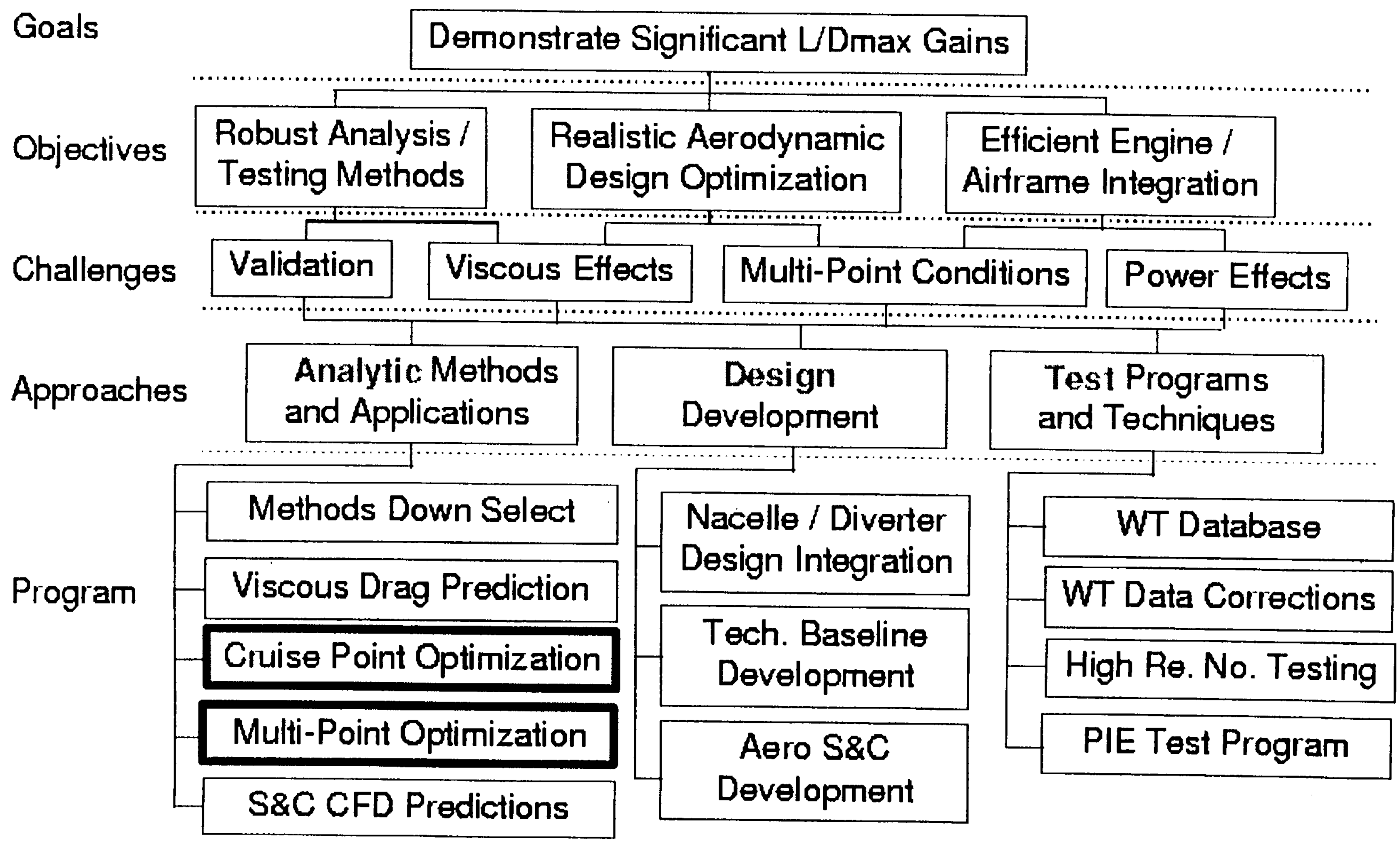

This Is the Outline

The presentation is organized as shown on this figure. After some brief background information, the past year's progress in the three main areas: Methods Refinements, Point Design, and Multi–Point Design, are discussed. The presentation is then concluded with a brief overview of the remaining work in 1999.

This Is the Outline

- Background
  - Goals
  - Objectives
  - Personnel
- Progress
  - Methods Refinements (WBS 4.3.1.2.1)
  - Point Design (WBS 4.3.1.2.2)
  - Multi–Point Design (WBS 4.3.1.2.3)
- Plans

The Goal is Multi–Point Optimization

The highest level goal guiding this work is to accomplish an evaluation of the benefits of nonlinear multi–point optimization. This is not seen as a final answer to the question, but rather just the start. There are many variations on the application of multi–point techniques to the HSCT design problem. The efforts represented here are aimed at the completion of the basic problem that has evolved from many years of linear design efforts. More details of the target evaluation are given in the conclusion of the presentation.

Point design technology is not fully mature. As the enabling technology upon which multi–point is built, improved point design is the next highest goal of this work.

The Goal Is Multi–Point Optimization

- Evaluate multi–point optimization
- Continue development of underlying point design

Multi–Point Models the Mission

The particular multi–point optimization problem being pursued by these efforts is illustrated on this figure. The single TCA design mission is shown as a trace of altitude verses time. Spotted on the mission are the three flight conditions that years of HSCT configuration development at BCAG have shown to quantify the total system efficiency based on multi–disciplinary (MDO) trade studies. From left to right, the points are first, a transonic acceleration condition which represents an evaluation of the initial climb through the least favorable thrust to drag segment, commonly referred to as the transonic pinch point. The second point is a representative midpoint of the supersonic cruise segment, and the final point is the corresponding representative midpoint of the terminal subsonic cruise segment.

Multi–Point Models the Mission

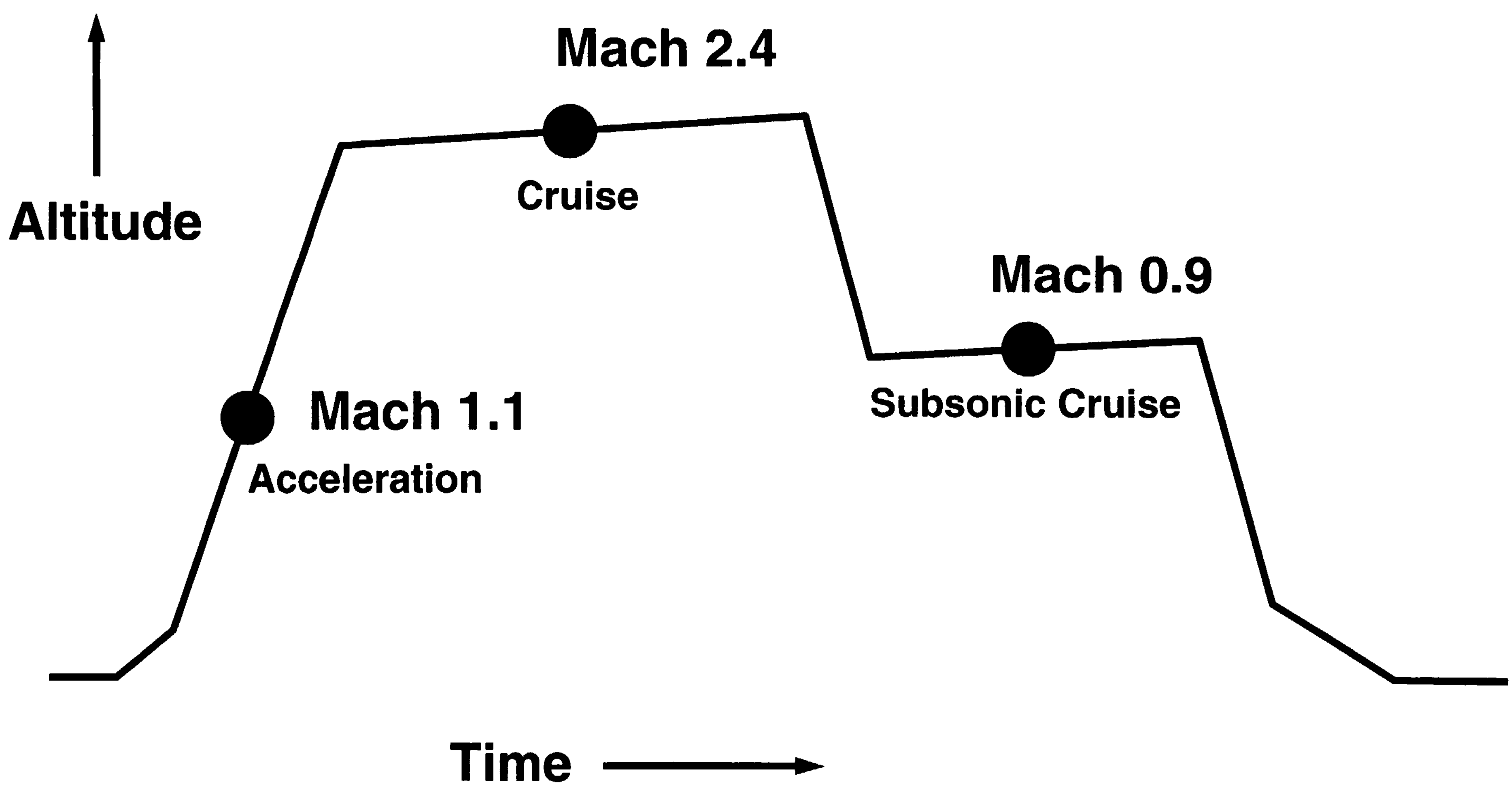

Multi–Point Concludes Years of Effort

The coordinated, multi–year effort that will culminate in an evaluation of multi–point optimization in 1999 is illustrated by this figure. Efforts can be divided into a major inviscid part and a smaller viscous effort.

The inviscid, TRANAIR–based work began with initial exploratory efforts in 1994, characterized by few constraints, but which established the viability of the basic point design capability. Building on this, 1995 was dedicated to constructing a process which attempted to incorporate a wide variety of project constraints that would be necessary to support the MDO considerations inherent in the HSCT preliminary design process. These efforts, based on the Reference H configuration, were very successful, and lead naturally to the formalized, multi–site efforts on the TCA configuration in 1996. A single set of extensive constraints were developed and provided by Technology Integration (TI) for this exercise. Two complete rounds of point design optimization were accomplished, and the final BCAG design was chosen for wind tunnel evaluation in 1997. The resulting wind tunnel model was designated the Nonlinear Cruise Point Validation model, NCV.

Based on lessons learned during the TCA optimization exercise, process and technology upgrades were pursued during 1997. Additional guidance in these upgrades was gained from the results of the multi–site, optimized TCA cross check analysis exercise.

Starting in 1998, work began on further extending the method to incorporate a three surface configuration and the target multi–point optimization problem. This presentation covers much of that work.

Viscous HSR optimization efforts began in 1997 with a demonstration of an inlet flow quality design on the NCV using OVERFLOW and a process developed under IR&D in 1996. The 1997 work showed that inlet flow quality could be improved without degrading the improvements produced by the inviscid TRANAIR process. Given the current process, and computational resource limitations, this capability is considered to be a viscous tune–up to a larger inviscid optimization in areas where a small number of variables can work a viscous issue.

Based on this success, the viscous OVERFLOW optimization capability was directed at multi–point optimization of the TCA wing leading edge in 1998. That work is described in this presentation.

Multi–Point Concludes Years of Effort

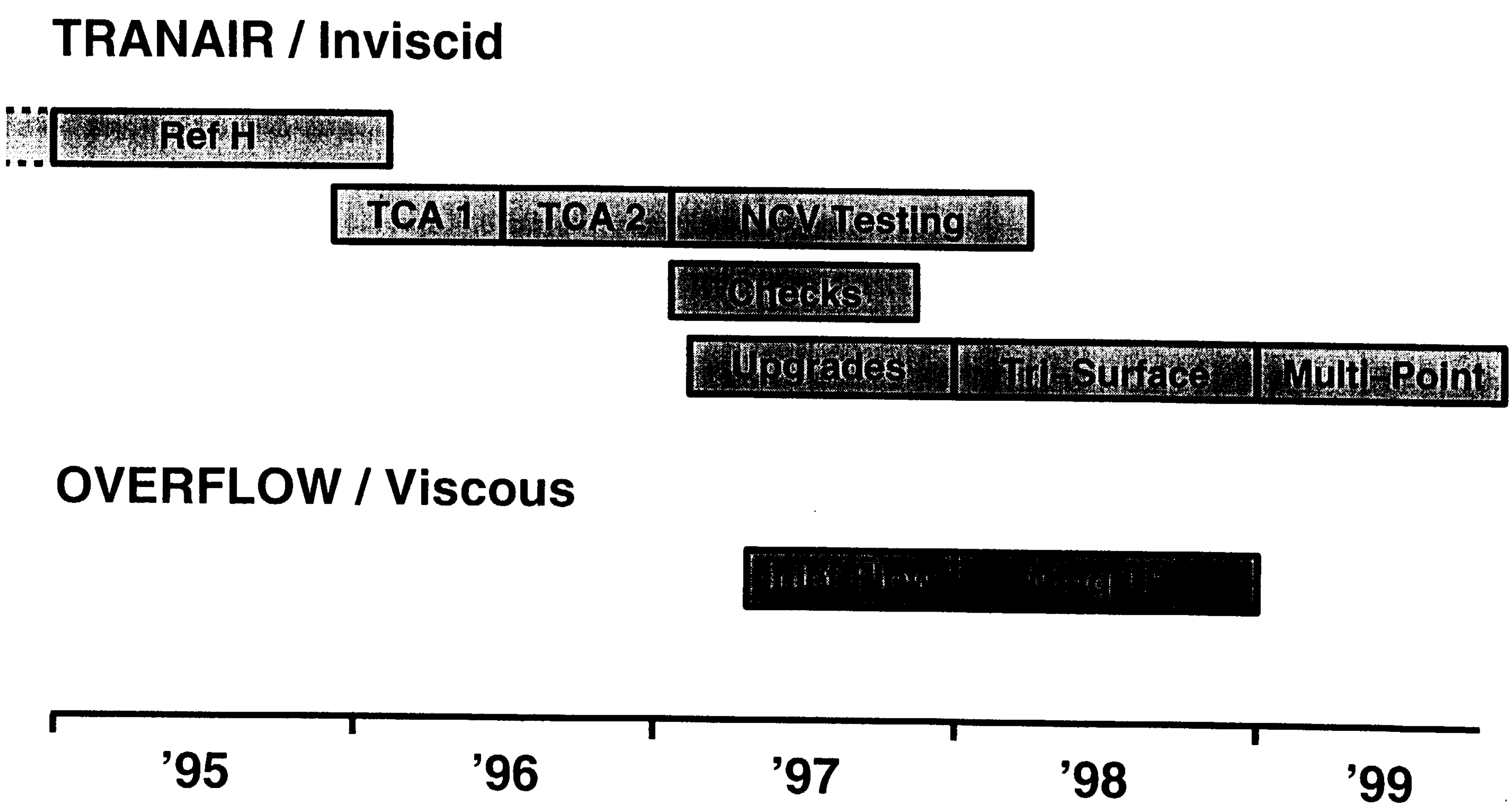

There Are Multiple Objectives

The six objectives which support the goals are shown in this figure. They represent the simple steps required for the target multi–point evaluation and the complementary viscous efforts.

The three TI–prescribed conditions must be realized as stand alone point design capabilities. With these three point design capabilities, a baseline sequential design can be created. This baseline, against which the multi–point optimization will be compared, is composed of a full point design optimization at the supersonic cruise condition, followed by flap deflection optimizations at the two other conditions.

The three stand alone point design capabilities must be integrated into the existing TRANAIR multi–point capability. The principle characteristic of this step is an extension to allow for different outer mold line (OML) geometries at the three conditions. Following this step, the final simultaneous multi–point optimization can be produced. The final step in this exercise is to perform the comparison with the sequential baseline.

Concurrent with this inviscid effort, is the complementary viscous multi–point work. It is assumed that a viscous tune–up of an inviscid multi–point optimization should most likely also be multi–point.

There Are Multiple Objectives

- Develop the 3 conditions as point designs
- Produce a baseline sequential optimization result
- Develop the 3 condition multi–point capability
- Produce a multi–point optimization result
- Compare the sequential and multi–point results
- Explore N–S multi–point capabilities

Many People Contribute

This presentation represents the work of many people. The full list of contributors are shown on this figure. The results which follow are primarily the work of a subset of this group, and are described here in the order shown on the figure.

The two viscous multi–point optimization cases and the work on collarless OVERFLOW grids are the work of Gordon Blom.

Flap effects correlation analysis with wind tunnel data for Mach number 1.2 and the initial efforts at flap deflection optimization at Mach number 1.1 were performed by Rusty Conner.

Josh Elliott produced the Mach number 0.90 spillage calculations, the work on transpiration modeling improvement, and the initial Mach number 0.90 point design.

Chris Vegter is responsible for much of the work reported here. Specifically, he produced the flap correlation and optimization work at Mach number 0.90, the development of spilling inlet modeling, the initial trimmed supersonic cruise point design, and the initial two condition TRANAIR multi–point optimization. He also has picked up the remaining optimization work at Mach number 1.1 and has been preparing to begin the initial three condition TRANAIR multi–point optimization.

The OVERFLOW reference viscous solution for TRANAIR boundary layer calibration and the implementation of enthalpy damping in viscous OVERFLOW are the work of Anutosh Moitra.

Again, everyone listed on this figure has contributed to the work that is being reported. The specific progress described below is directly or indirectly the result of the efforts of everyone shown.

Many People Contribute

Gordon Blom	N–S optimization
Rusty Conner	Optimization focal & TRANAIR optimization
Josh Elliott	TRANAIR optimization & optimization technology
Bill Huffman	Optimization technology
Chris Vegter	TRANAIR optimization
Robyn Wittenberg	TRANAIR optimization consultation
Eric Adamson	Configuration design (TI)
Chet Nelson	Configuration design (TI) lead
Steve Chaney	N–S verification
Anutosh Moitra	N–S verification
Kevin Mejia	Wind tunnel verification
Bob Patton	Technology development lead & CA ITD leader
Bob Kulfan	CA ITD member & Boeing TF

Progress

The progress of the past year can be divided into the three reporting categories: Methods Refinements, Point Design, and Multi–Point Design. Descriptions of progress in these three areas follow in that order.

The inviscid optimization efforts have narrowed to a specific problem characterized by a single configuration, a single variable set, and a single process. All evaluations are made with longitudinally trimmed configurations which include the fundamental propulsion forces and prescribed full scale viscous drag terms. When appropriate, inlet spillage is also included in the aerodynamic model. The cases and results presented here are based on this focused approach, whether explicitly noted or not.

Progress

Point Design Refinement Continues

Progress on Methods Refinement can be divided into the five categories shown on this figure. The first three are components of the efforts to develop and evaluate multi–point optimization. Flap deflection optimization is required off–design for both point designs of sequential optimization and to support multi–point optimization. Similarly, inlet spillage effects are present during off design and have been added to the flow modeling at the two specified conditions. Finally, trimmed baseline configurations, necessary as starting conditions for optimization and as baselines for sequential optimizations, were developed.

The fourth category shown here, transpiration modeling, was the primary effort to reduce the cycle time of the current preferred process.

Work on viscous modeling, the final area shown here, continued a complementary effort to explore and develop techniques to add viscous elements to the principle inviscid TRANAIR optimization process.

Point Design Refinement Continues

- Flap deflection optimization
- Spilling inlet modeling
- Trimmed baselines
- Improved transpiration modeling
- Viscous modeling

Flap Deflections Are Optimized

Optimization of flap deflections is an important enabling capability for multi–point optimization. The most important aspect, however, is the effect on drag, both as an increment and as an absolute. Drag is the aspect of flap deflection optimization that appears in the objective function. Flap deflection values that result from drag optimization are of secondary interest.

The last year's efforts can be divided into two main areas. The first was establishing the correlation between the wind tunnel results produced during LaRC 16' test 484 and inviscid TRANAIR analysis. For both Mach number 0.90 and 1.20, the effects of leading and trailing edge flap deflections on drag showed good correlation. When further quantified with the weighting factors used for multi–point evaluation and optimization, the correlation is sufficiently accurate to support multi–point design.

It is interesting to note that the correlation of flap deflection angles was also encouraging. Agreement on implied optimum leading edge flap deflections was very good. Predictions of optimum trailing edge flaps were less accurate, as should be expected for inviscid analysis, although as noted above, the drag increments for optimum trailing edge flaps were sufficiently accurate.

All the correlation work was and the subsequent optimization efforts are limited to the flaps of the outboard wing only.

Once the validity of flap deflection optimization was established with the correlation exercise, the capability was applied to all the appropriate cases. As shown here, that included the trimmed baselines at Mach number 0.90 and 1.10, point design demonstrations at these two off–design conditions, and an initial two condition multi–point optimization.

Flap Deflections Are Optimized

- (Inviscid) Correlations with LaRC 16' 484
- Outboard flaps only
- Used in ...
  - Trimmed baselines, Mach 0.9 & 1.1
  - Mach 0.9 point design
  - Mach 1.1 point design
  - 2 condition multi–point (Mach 2.4 & 0.9)

Inlet Spillage is Modeled

The computational technique used in TRANAIR to model the off design inlet spillage is illustrated by this figure. Shown are Mach number color contours on a streamwise cut, approximately through the centerline of the outboard nacelle for the Mach number 0.90 condition. Two changes were required to the standard flow through nacelle model, first, the inlet spike was added. The spike location is the same for both Mach number 0.90 and 1.10.

The second change was to the nozzle exit condition. The standard flow through model uses internal transpiration to account for nozzle trailing edge thickness. This is significant on the sidewalls which have been truncated to match the upper and lower surface flaps. The transpiration modeling allows the effective nozzle exit area to be smaller than the nozzle OML without introducing the difficulties associated with base areas. For inlet spilling, the effective nozzle exit area is further reduced to that which provides the specified spillage. This new effective internal contour appears as green lines on this image. In general, cuts through surface geometry appear as green. The survey network used to measure the inlet spillage also appears as a green annular surface between the spike and nacelle, near the inlet.

The resulting internal solution is a well–behaved subsonic flow. Inlet lip acceleration due to spilling is apparent on the lower lip.

Inlet Spillage is Modeled

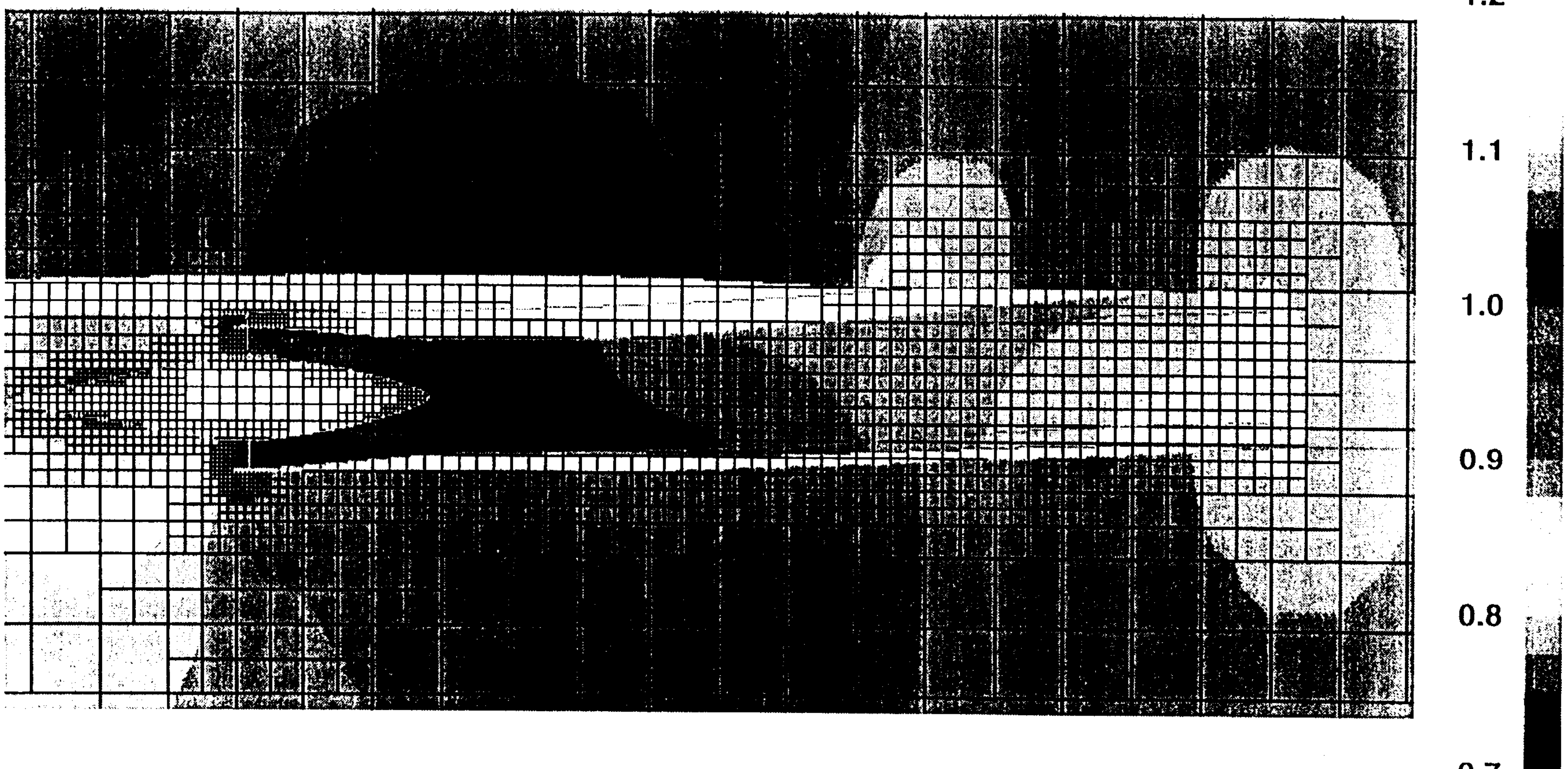

Outboard Nacelle Mach=0.9 Spillage=39.7%

Mach 0.9 Spillage

The effects of inlet spillage on the external flow at Mach number 0.90 are shown on this figure. Lower wing surface Mach number contours with and without spillage are compared. The two solutions were obtained at the same angle of attack, that of the spilling model at the design condition shown.

Inlet spilling has a substantial effect on the flow fields under the wing and about the nacelles. Both the compressions and expansions are stronger in the presense of inlet spilling. Increased inlet lip expansion is also very evident.

The force and moment increments between the two cases (spilling minus not) are

delta lift coefficient	=	0.0023
delta drag coefficient	=	−0.00028
delta pitching moment coefficient	=	0.0016

The moment is taken about the aft C.G. limit , station 2281.92 and waterline 218.

The flap deflections shown do not represent optimally trimmed configurations. They are, however, representative of optimally trimmed states and should not invalidate these increments.

Mach 0.9 Spillage

~Zero spillage (no spike)

CL=0.18, Flaps=+8.0/–2.0

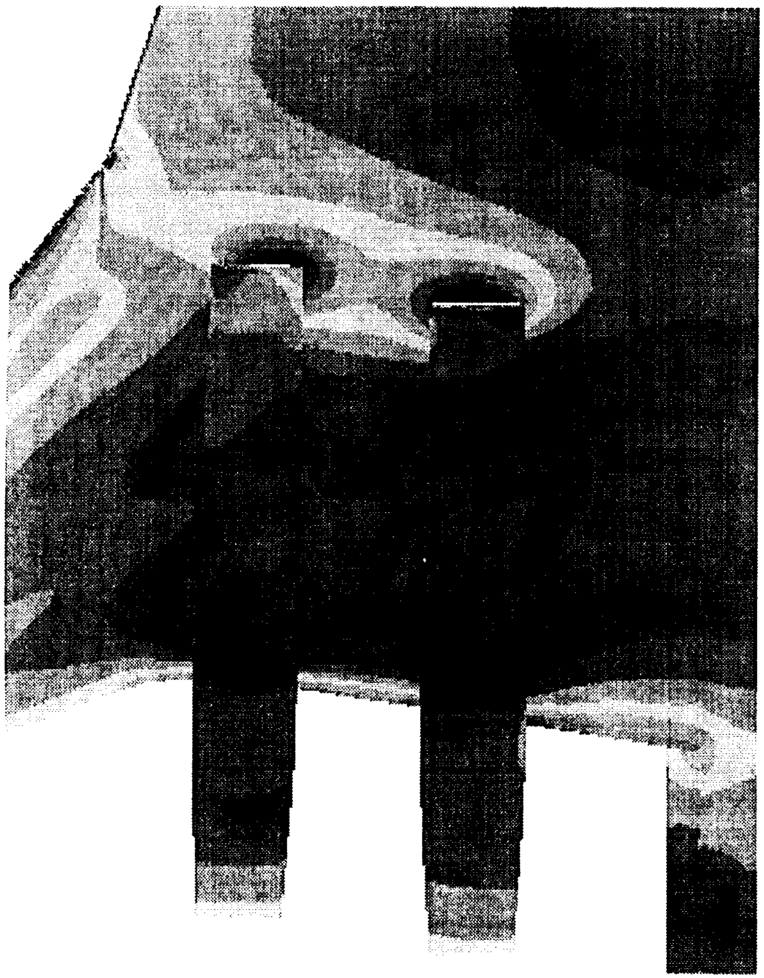

39.7% spillage

CL=0.18, Flaps=+8.0/–2.0

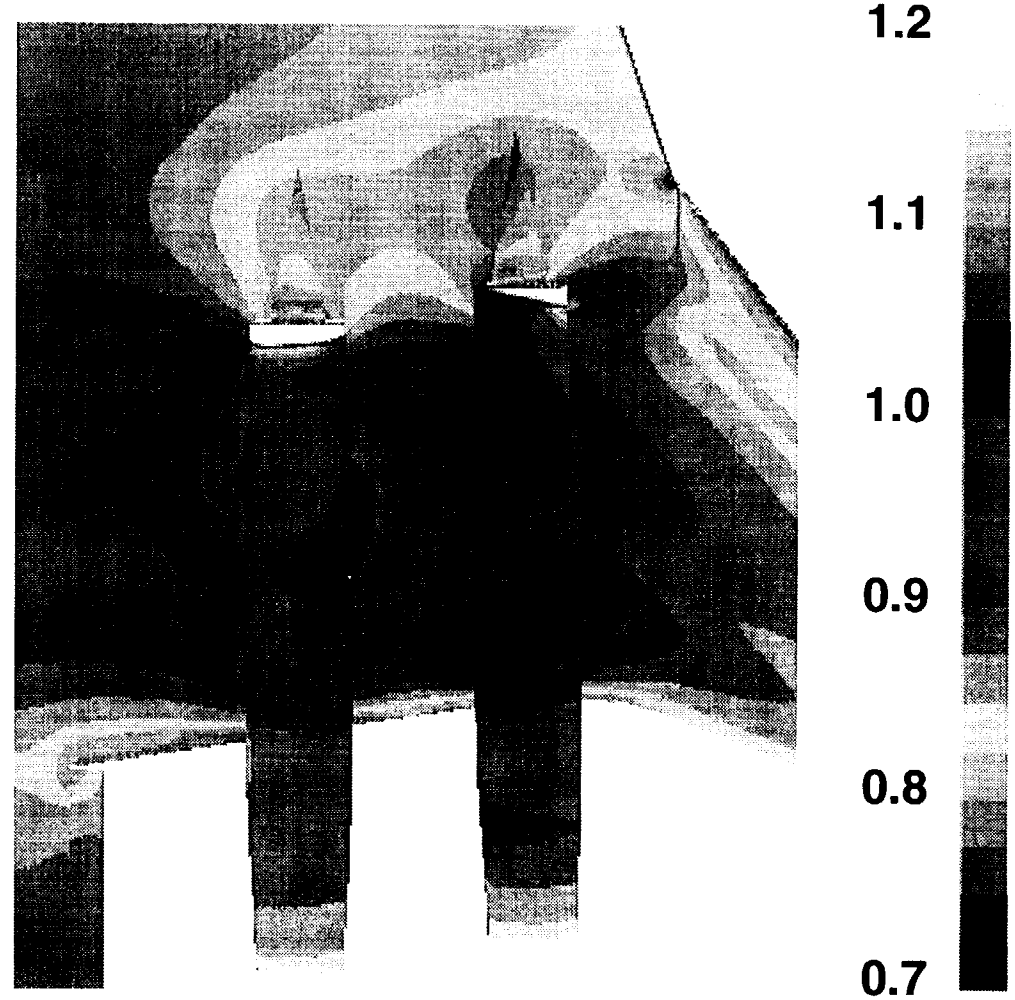

Mach 1.1 Spillage

Similarly, the effects of inlet spillage on the external flow at Mach number 1.10 are shown on this figure. Lower wing surface Mach number contours with and without spillage are compared. The two solutions were again obtained at the same angle of attack, that of the spilling model at the design condition shown.

Inlet spilling appears to have an even more substantial effect on the flow fields under the wing and about the nacelles at this Mach number. Again, both the compressions and expansions are stronger in the presense of inlet spilling. The compression field ahead of the nacelles actually starts with a full span, almost unswept shock. Significant changes to the outboard wing are also indicated. Increased inlet lip expansion is also very evident.

The force and moment increments between the two cases (spilling minus not) are

delta lift coefficient	=	0.0036
delta drag coefficient	=	–0.00032
delta pitching moment coefficient	=	0.0026

The moment is taken about the aft C.G. limit , station 2281.92 and waterline 218.

The flap deflections shown represent the optimally trimmed spilling configuration.

Mach 1.1 Spillage

Optimum Flaps −10.10/+0.66

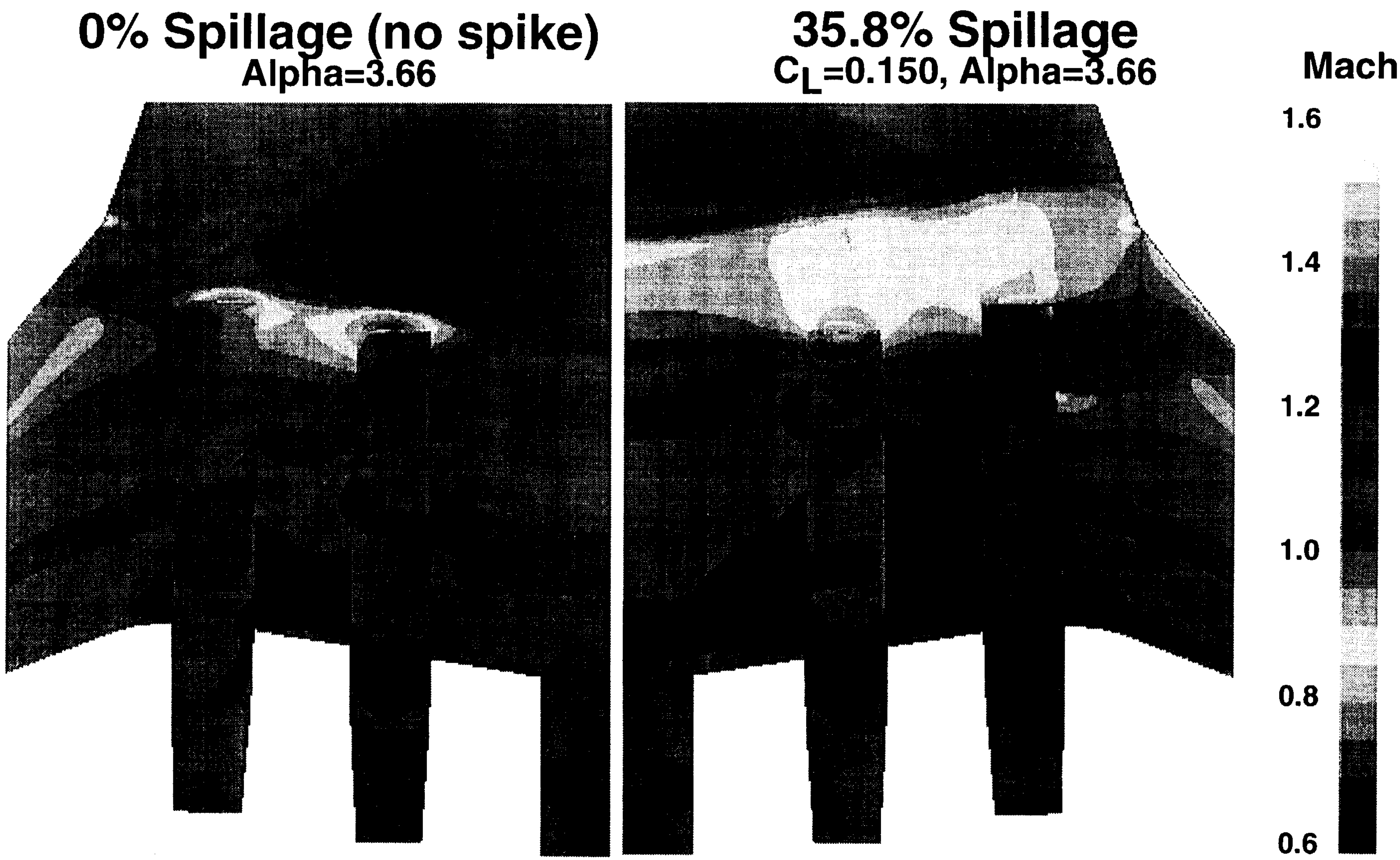

Baselines Are Trimmed

Trimmed baselines are the result of a small constrained drag optimization which is outlined on this figure. The variables are canard and horizontal tail incidences, C.G. longitudinal location, and configuration angle of attack. For the two off–design conditions, leading and trailing edge flaps become active variables. The cases are constrained to the design lift coefficient and zero net pitching moment. Reasonable approximations of the propulsion forces are also included in the force and moment balance. The optimization problem solves for the minimum gross thrust configuration, subject to the constraints.

To date, every case using the TI–specified tri–surface limits has driven the C.G. to the aft limit.

An image of the trim problem, both the force and moment balance, and the variables, is shown on the next figure.

Baselines Are Trimmed

- 4 (or 6) variable drag optimization
  - Canard incidence
  - Horizontal tail incidence
  - C. G. location
  - Angle of attack
  - Leading edge flap deflection (Mach 0.9 & 1.1)
  - Trailing edge flap deflection (Mach 0.9 & 1.1)
- At specified C_L & C_M
- Propulsion forces included
- Gross thrust as objective function

Trimmed Tri–Surface Design Force Balancing

An illustration of the configuration force balance for longitudinal trim with propulsion forces is shown on this figure. Propulsion forces are divided into the two parts shown. Propulsion drag is defined to be the difference between gross thrust and net thrust. The total is equally divided among the engines. It is applied in the flight direction at the centroids of the nacelle inlet faces. Gross thrust, the other propulsion force, is set to that value which produces zero net longitudinal force. That is, the flight direction component of gross thrust equals the total drag of the configuration. The specified viscous drag term and the propulsion drag are treated as constants.

The propulsion forces are also included in the lift and pitching moment balances.

An additional variable shown here is nozzle pitch angle. The current implementation assumes that this is a single value for all engines. An additional simplifying assumption is that the thrust vector can change without changing the nozzle exterior contours. The nozzle pitch angle variable is active during general optimization, but not when calculating the trimmed baseline starting configurations.

Trimmed Tri–Surface Design Force Balancing

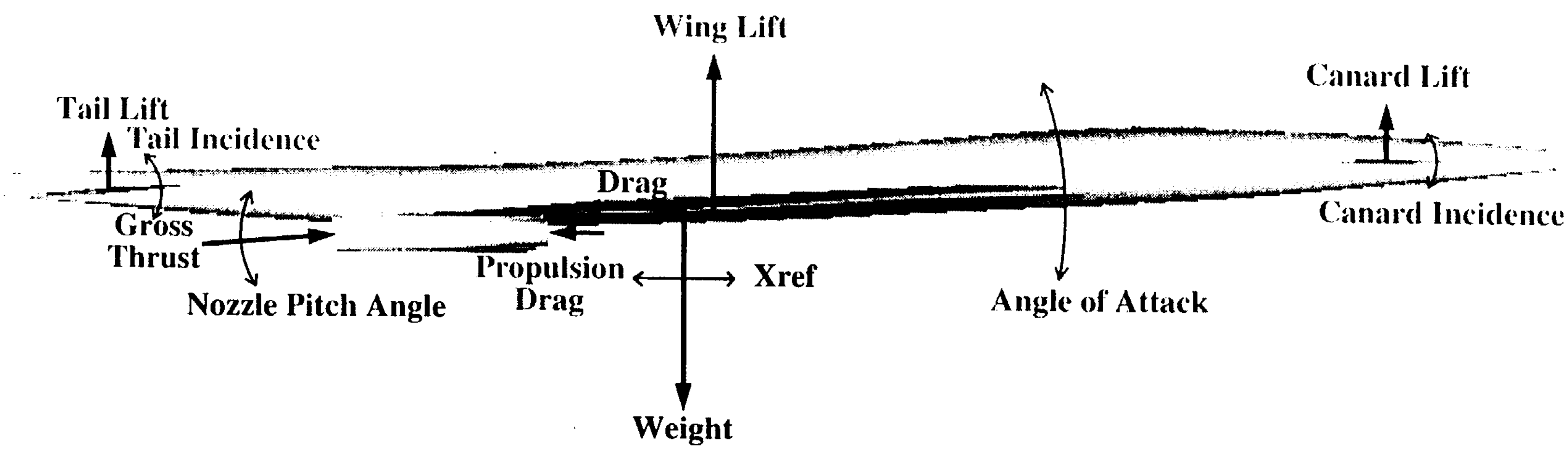

Trim Variables:

- Alpha
- Tail Incidence Angle
- Canard Incidence Angle
- Nozzle Pitch Angle
- Xref (variable c.g.)
- Outboard LE and TE Flaps

<u>Thrust is the objective function:</u>

Drag Component of Thrust = $C_{D_{Pressure}} + C_{D_{visc}} + C_{D_{propulsion}}$

$C_{D_{visc}}$ and $C_{D_{propulsion}}$ are constants

Lift (fixed) = $C_{L_{Pressure}}$ + Lift Component of Thrust

$C_M = 0.0 = C_{M_{Pressure}} + C_{M_{Thrust}} + C_{M_{propulsion}}$

Transpiration Modeling Was Improved

The principle effort on cycle time reduction was to improve the transpiration modeling used to calculate optimization sensitivities by TRANAIR. Two transpiration models are currently used. Most of the design process uses two–term transpiration modeling, the most accurate, but limited to small movements. A separate optimization problem is posed for wing twist and shear using one–term transpiration modeling to efficiently allow the large movements characteristic of those variables starting from linearly designed HSCT configurations. The current standard process is to start with a two–term cycle with all variables active, and follow with the one–term cycle, just for wing twist and shear. The process then uses three additional full variable set, two–term cycles. Some of the benefit of these subsequent two–term cycles appears to be recovering from the inaccuracies of the one–term cycle.

One way to improve the efficiency of the TRANAIR design process would be to develop a new mixed transpiration model which matches the modeling to the variable movements, so that dedicated one–term cycles are unnecessary. This is the approach that was taken this year. The specific implementation uses one–term modeling for wing twist and shear movements and two–term modeling for wing camber and thickness. The new model has been shown to be an improvement on the 3–dimensional test cases checked. An example is shown on the next figure.

Eliminating the one–term cycle, and perhaps one of the subsequent two–term cycles, would reduce the flow time required for the current process by twenty to forty percent.

Transpiration Modeling Was Improved

- Mixed transpiration model developed
- Modeling matched to movement
  - 1–term –> wing twist & shear
  - 2–term –> wing camber & thickness
- Could eliminate 1 or 2 TRANAIR cycles
  - 20 – 40 % flow time reduction

Mixed Transpiration Model Is Superior

This figure compares the new mixed transpiration model with both the one– and two–term models, and with the actual solution. The case is a simple untapered, low aspect ratio, swept wing at Mach number 0.1 and 1.5 degrees angle of attack. Onto this is imposed a one percent camber bump on the upper surface near the leading edge and a half a degree twist increase. The streamwise data shown here is taken at the 0.25 semi–span location. These movements are larger than allowed in the current process when using two–term transpiration, but are representative of one–term movements.

The upper plots show local surface pressure coefficient and the lower plots show the corresponding airfoil geometry. The plots on right are an expanded view of the first twenty percent of the airfoil.

The upper right plot shows how the new mixed transpiration model matches the exact solution everywhere but a localized region about the pressure peak. The one–term model over–predicts the velocities on the region shown, while the two–term model appears to under–predict, and is also unacceptably unstable.

Mixed Transpiration Model Is Superior

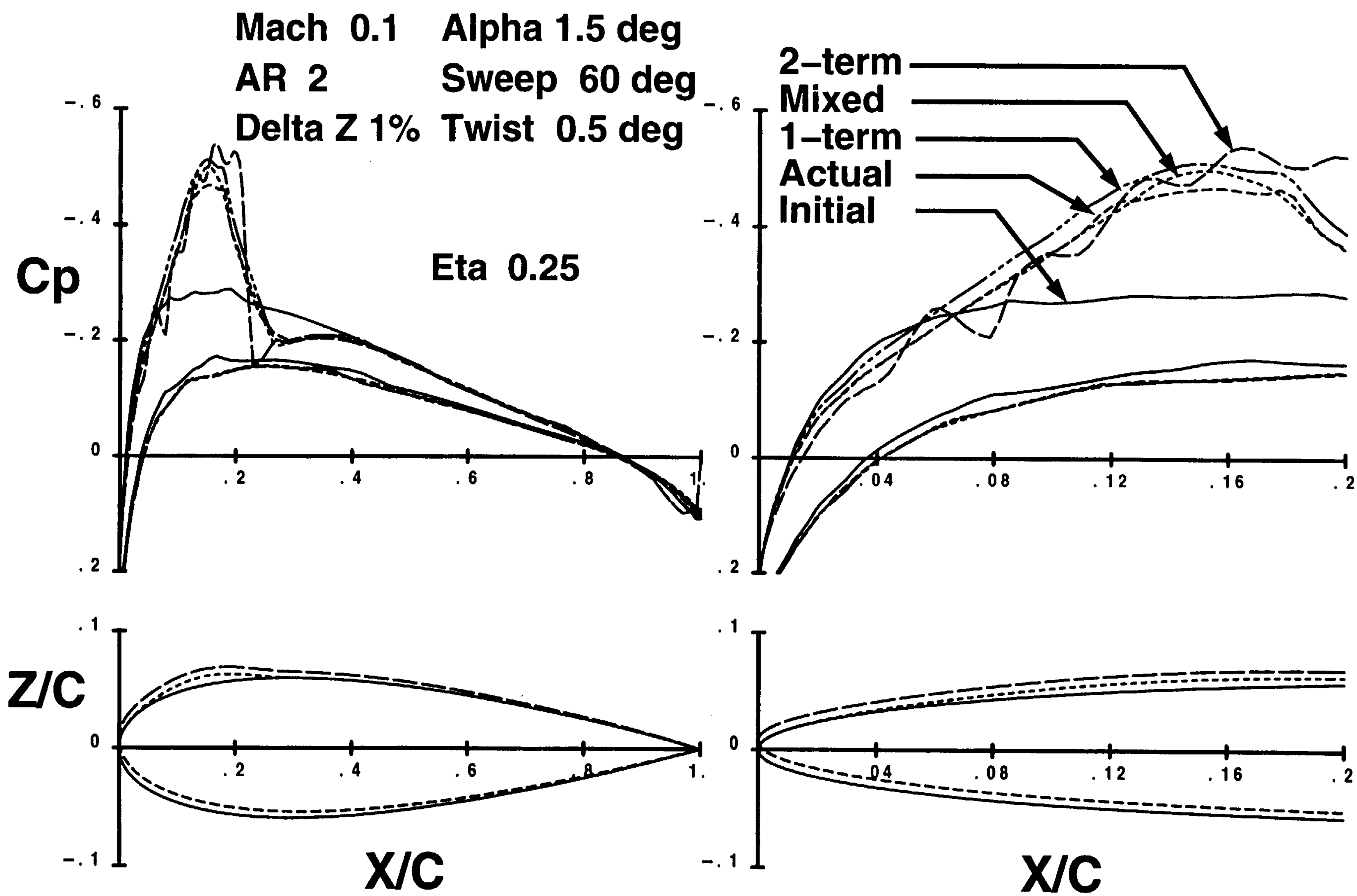

Viscous Modeling Was Addressed

The three efforts to increase the impact of viscous modeling in optimization are listed on this figure. The first effort is to calibrate the existing TRANAIR coupled boundary layer for the shock strengths and patterns characteristic of the nacelle/diverter region at the cruise condition. This year a reference viscous solution for a simplified problem was created. The simplified problem is an inboard TCA nacelle/diverter installed on a flat plate at zero angle of attack. A viscous OVERFLOW solution for this case was produced and then boundary layer parameters were extracted from the OVERFLOW viscous layer. This reference boundary layer data is currently being used to calibrate the TRANAIR coupled boundary layer on the same simplified problem.

The second effort was aimed at the development of a collarless OVERFLOW grid approach. This technique would allow OVERFLOW–based optimization to design regions of component intersections. This is currently prevented by the need to use collar grids and the accompanying interactive Pegsus step. A collarless TCA wing/body grid was developed with featured matched overlapping grid cells. An OVERFLOW solution was obtained for this grid, but it was found that there were small differences in overall forces and moments, relative to the standard grid solution, and that the flow details in the wing/body intersection region were also different. It was concluded that this particular approach was not sufficiently accurate to produce the finite difference sensitivities needed to support optimization.

The third effort was to increase the efficiency of OVERFLOW analysis through the implementation of an enthalpy damping technique. Building up to increasingly complex configurations, the work concluded this year with a demonstration of a two to three improvement in the convergence rate of a TCA wing/body/nacelle/diverter configuration case at the cruise condition.

Viscous Modeling Was Addressed

- OVERFLOW data for calibration of TRANAIR coupled boundary layer
- Collarless OVERFLOW grid
    - Not successful
- OVERFLOW implementation of enthalpy damping
    - 2–3 convergence improvement, w/b/n/d, Mach 2.4

Point Design(s) Have Continued

Work has continued on point design technology, to address lessons learned during the previous round of TCA cruise point design, and to extent the capability to the additional conditions specified for the multi–point optimization exercise. Some common aspects of this work and the flight conditions of interest are listed on this figure.

A single basic configuration has been used for essentially all this work. It is the same configuration that the multi–point exercise will be based on. It is referred to as the three–surface, or tri–surface TCA, being the result of adding the PTC canard and empennage to the TCA configuration. This provides some ties to the previous cruise point design work and allows the continued use of the effort invested in the TCA constraints.

All this year's point design work has been based on longitudinally trimmed conditions, using the same approach described above in reference to trimmed baseline efforts. Like optimally deflected flaps, longitudinal trim is assumed for all work at all conditions.

The specific flight conditions addressed as point designs are the TI–specified multi–point conditions listed here. Some features common to the cases and this past year's progress are described next.

Point Design(s) Have Continued

- "Tri–surface TCA" configuration
  - TCA wing/body/nacelles/diverters
  - PTC canard/empennage
- Longitudinally trimmed
  - Same as baselines
- 3 conditions
  - Supersonic cruise
  - Subsonic cruise
  - Transonic acceleration

3–Pt Multi–Point Design Variable Layout

A single variable set has been developed, building on previous work on cruise point design, and specifically tailored and sized for the multi–point exercise. The set is shown on this figure. As with previous work, this variables definition has been and will continue to be common to all cases.

There are general shape variables for all the wing and most of the body. As with previous work, there are the three cabin floor kink angles and nacelle/diverter yaw variables. With the extension to trimmed multi–point cases, incidence angles for the canard and horizontal tail were added, along with leading and trailing edge flap deflections, and the previously noted nozzle pitch angle and C.G. location. A single deflection angle is assumed for an entire flap, one for the leading edge and one for the trailing edge flap.

For the supersonic cruise point design, there's a total of 439 variables. The total grows to 441 for the other two flight conditions due to the addition of flaps. The full three condition multi–point case will have a total of 451 variables. These totals represent the largest three condition multi–point case that will fit in the eight hour vn queue using the current process. Sensitivities calculation for the Mach number 0.90 case is the limiting job.

3–Pt Multi–Point Design Variable Layout

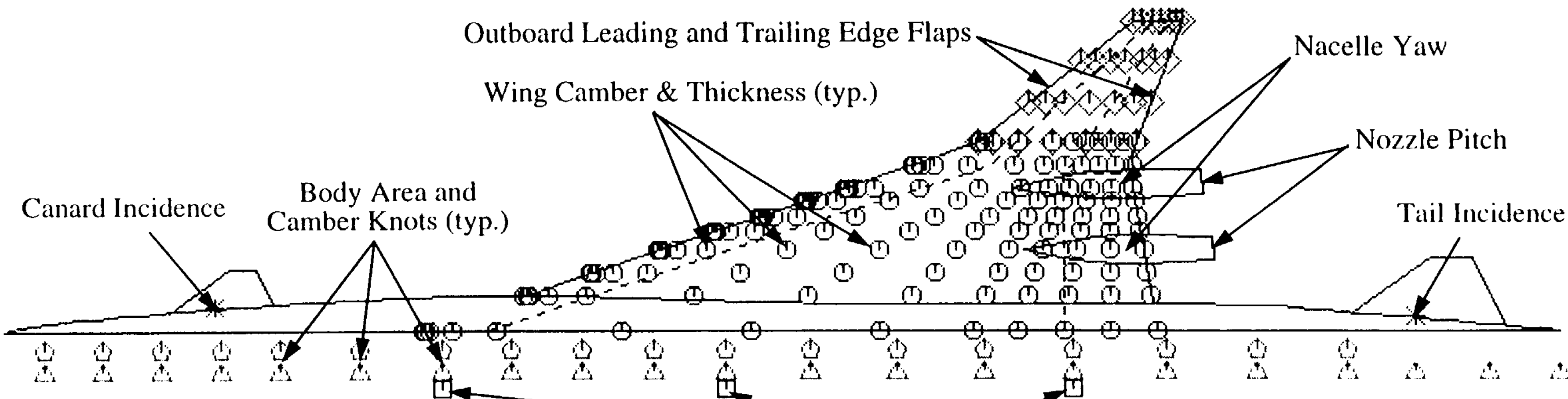

<u>10 Inboard Wing Sections:</u>

12	Camber
13	Thickness
1	Twist
1	Shear
270	Total

<u>4 Outboard Wing Sections:</u>

6	Camber
7	Thickness
1	Twist
1	Shear
60	Total

<u>Body Variables:</u>

80	Body Area (5x16)
19	Body Camber
3	Floor Angle
102	Total

<u>Trim Variables:</u>

3	Alpha	(1x3)
1	Nozzle Pitch	
3	Xref	(1x3)
3	Tail Incidence	(1x3)
3	Canard Incidence	(1x3)
4	LE and TE Flaps	(2x2)
17	Total	

<u>Total Variables</u>

270	**Inboard Wing**
60	**Outboard Wing**
102	**Body**
2	**Nacelle Yaw**
17	**Trim**
451	**Total**

Initial Cruise Point Design Is Complete

The initial tri–surface trimmed cruise point design was completed this year. Several aspects of the case are listed on this figure.

Several observations can be made. First, less than half of the total variable set was free at the conclusion, 237 variables were lost to active constraints and 19 were on their bounds. Next, the case was not taken to full completion since the purpose was to demonstrate the elements of trimmed cruise point optimization. Only four TRANAIR cycles were used, rather than the standard five. Note that the drag improvement is based on inviscid TRANAIR analysis, is relative to a trimmed baseline configuration, and is actually quantified in terms of gross thrust reduction. Finally, the resulting shapes were very similar to the previous TCA point design results, suggesting that trim has little effect at this condition. This is actually to be expected since the C.G. variable was not against either of the rather liberal bounds specified for this case.

Initial Cruise Point Design Is Complete

- Mach = 2.4, $C_L = 0.092$
- 437 variables, 19 on bounds
- 34k constraints, 237 active
- 4 TRANAIR cycles
- 7.6 counts of thrust improvement
    - Inviscid analysis
    - Relative to trimmed baseline
- Shape changes similar to TCA optimization

Trimmed Cruise Point Design Drag Reduction

The drag reduction of the initial trimmed cruise point design is compared to previous untrimmed cruise point designs on this figure. All increments are based on inviscid TRANAIR analyses. The third bar from the left is the result of analysis of this latest design, without the canard and empennage, and is at the design lift coefficient for that version of the configuration. Compared to the second bar from the left, the NCV, about one count of additional drag improvement is shown. This most likely represents process and technology improvements that have been made since the TCA cruise point design, rather than an effect of including trim.

The first bar from the left is the Ames 103 design. Of interest are both the total and the nacelle/diverter increment. Both are comparable to that achieved with this latest design. The larger nacelle/diverter increment, relative to the NCV, is one of the features of the Ames 103 which was addressed by the process and technology improvements mentioned above.

Trimmed Cruise Point Design Drag Reduction

Tri–surface TCA   Mach=2.40 C_L=0.08556

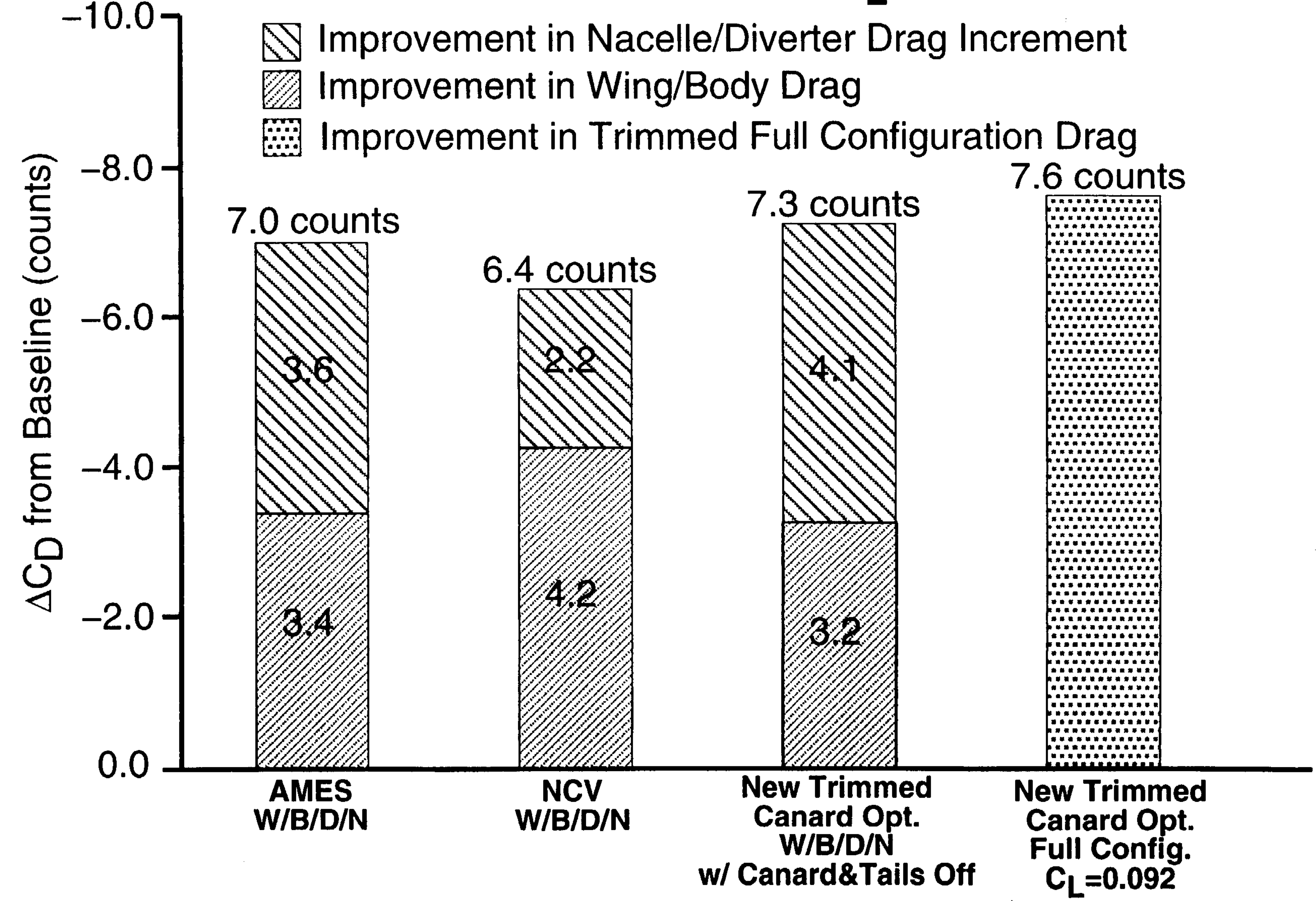

Trimmed Tri–Surface Cruise Point Design

An upper surface view of the resulting geometry is shown on this figure. Apparent are the familiar bump features on the inboard wing and the out–of–plane outboard wing shape. The inboard wing bumps are different from the NCV in that there are three rather than two. This suggests that there may be some effect of the spanwise distribution of variables on the wing. The distribution was changed from that used for the TCA cruise point design. The new distribution is very near uniform, whereas the old variable layout was more clustered about the nacelle/diverter locations.

The canard and horizontal tail incidences shown indicate that both surfaces are lifting. The C.G. location noted is not on its limits, further indicating that trim was achieved with no aerodynamic penalty. The C.G. location just fell out. This may be one reason that the resulting shapes are similar to the previous untrimmed cruise point designs.

Finally, the nozzle pitch angle shown seems to indicate that some thrust deflection beyond that inherent in the nacelles is beneficial.

Trimmed Tri–Surface Cruise Point Design

Mach=2.40 C_L=0.092

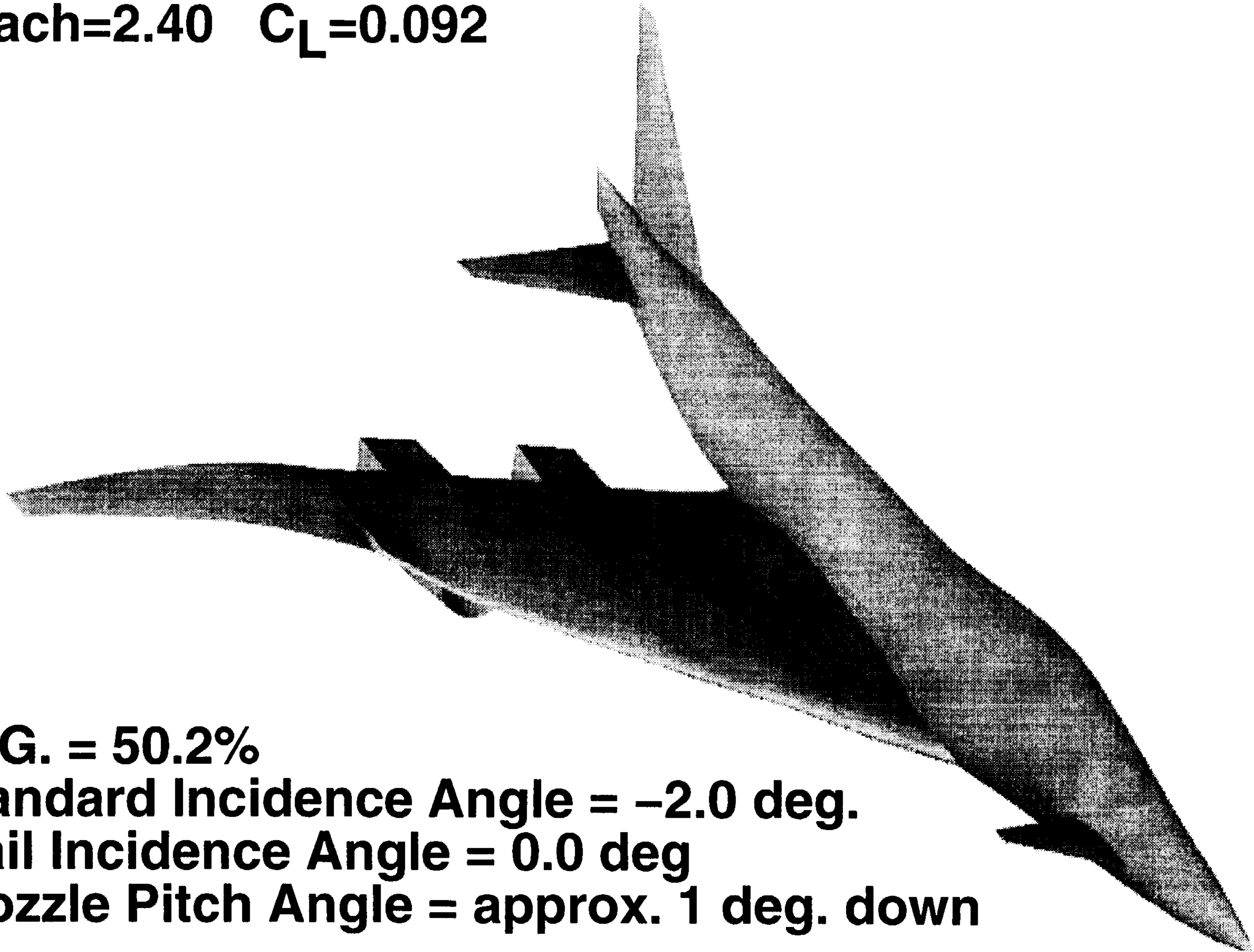

C.G. = 50.2%
Candard Incidence Angle = –2.0 deg.
Tail Incidence Angle = 0.0 deg
Nozzle Pitch Angle = approx. 1 deg. down

Trimmed Tri–Surface Cruise Point Design

The corresponding lower surface view of the trimmed cruise point design is shown on this figure. The most apparent features in this view are the wing lower surface troughs associated with the nacelles and the bump between the troughs. These features are also present on the NCV. The sculpting present around the nacelle/diverters is not well resolved by this image.

Trimmed Tri–Surface Cruise Point Design
Mach=2.40, C_L=0.092

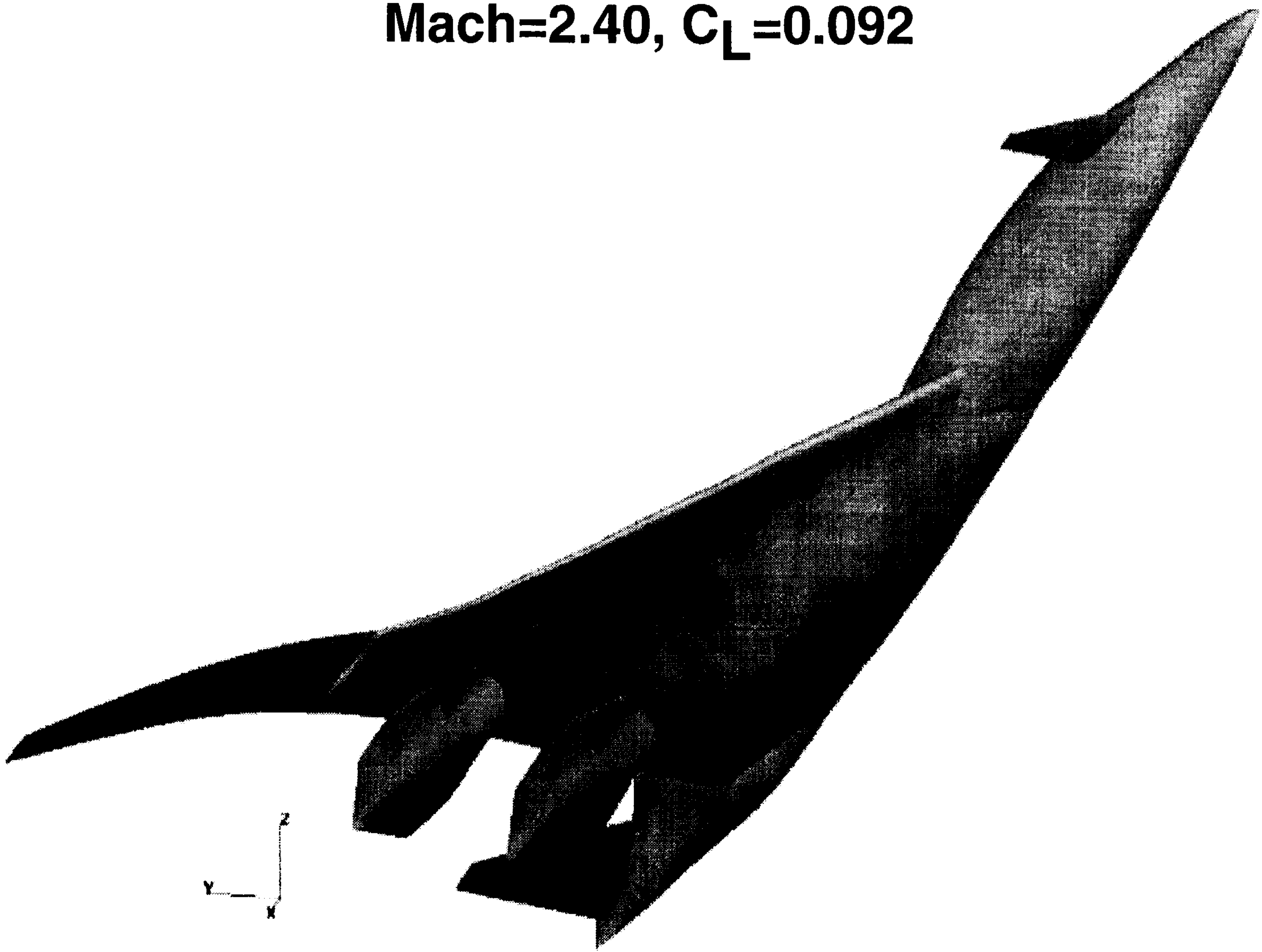

Initial Subsonic Cruise Point Design Is Almost Complete

A full variable set trimmed optimization of the tri–surface TCA at the subsonic cruise condition was started this past year, and the case is almost complete. Some characteristics and intermediate results are shown on this figure. The condition is that specified by TI for the multi–point problem except that the lift coefficient has been reduced so that the configuration angle of attack is closer to that of the supersonic cruise condition. This consistency in flight attitude at the two cruise points would be a characteristic of a design, more well balanced than the TCA. Maintaining this geometric relationship between the two flight conditions was judged to be more important than strict adherence to the design mission lift coefficient at the subsonic cruise condition. Note that inlet spillage is included in the flow model. As indicated previously, the case uses the common variable set and constraints.

The results shown here and on the following figures are after the first design grid of the third TRANAIR cycle. Most cycles use three design grids. This case will be finished with the completion of the third cycle. The purpose of this case is to verify the mechanics of this condition, and to provide an indication of where this flight condition will attempt to steer the multi–point case.

As with the cruise point design, the thrust improvement shown is relative to the trimmed baseline, and based on inviscid TRANAIR analysis. As expected, the shapes produced by this case are not similar to those found in the cruise point case.

Initial Subsonic Cruise Point Design Is Almost Complete

- Mach = 0.9, $C_L = 0.18$, 39.7% spillage
- 441 variables
- 34k constraints
- 2.3 TRANAIR cycles
- 4.1 counts of thrust improvement
    - Inviscid analysis
    - Relative to trimmed baseline
- Shape changes dissimilar to cruise point designs

Trimmed Tri–Surface Subsonic Point Design

An upper surface view of the intermediate result is shown on this figure. No apparent shape changes are visible in this view. The transition from inboard leading edge to outboard leading edge flap is shown, and illustrates that this is modeled without the unporting of the actual system. The same modeling approximation is used for the trailing edge flap also.

Two geometric results of the optimization thus far are, one, an increase in leading edge camber on the inboard wing, and two, a general thickening of the outboard wing. The latter occurs primarily in the inspar region, and appears to be reducing the flap hinge turning angles.

There is very little change to the body, or the wing twist and shear.

Trimmed Tri–Surface Subsonic Point Design

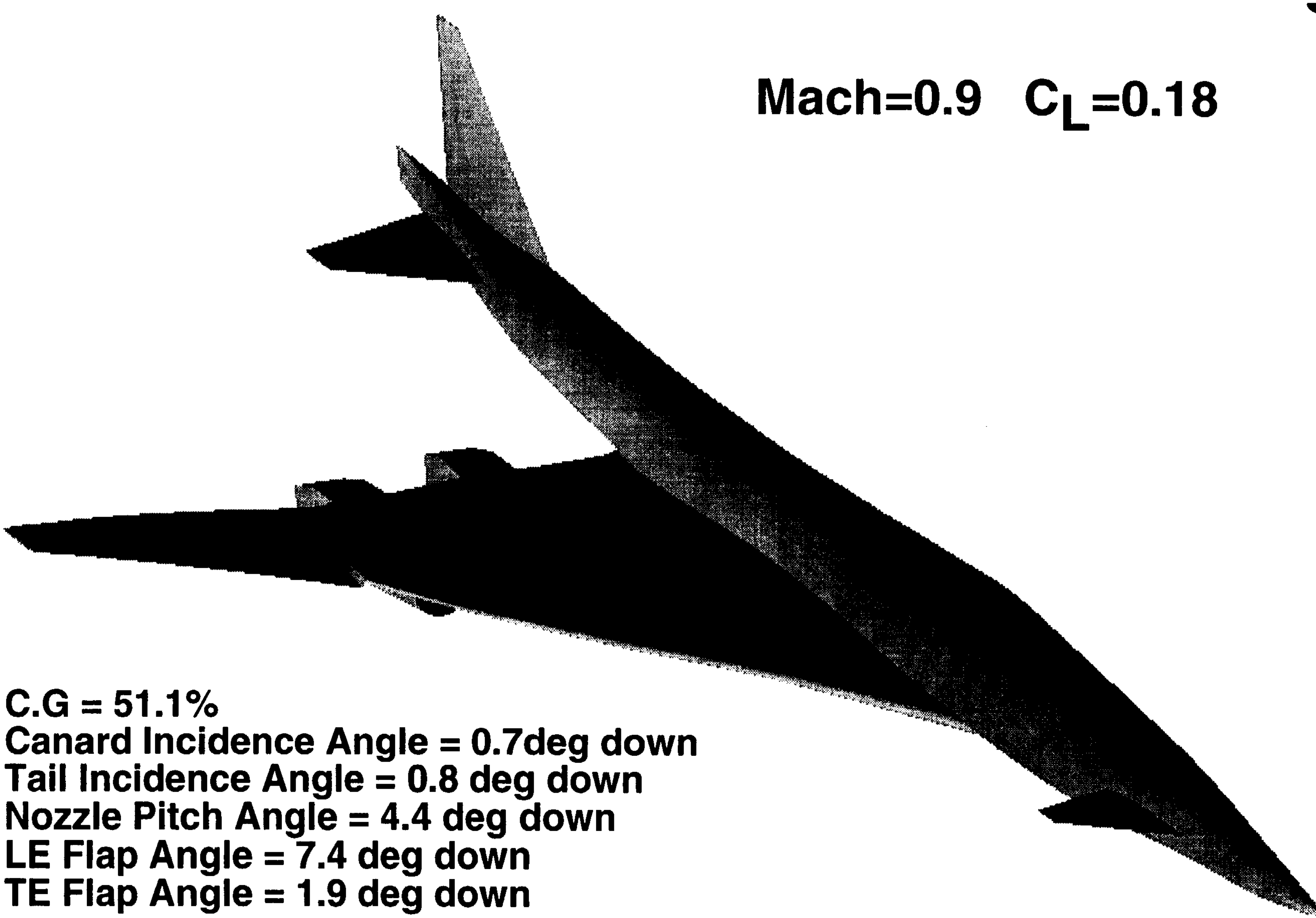

Mach=0.9 C_L=0.18

C.G = 51.1%
Canard Incidence Angle = 0.7deg down
Tail Incidence Angle = 0.8 deg down
Nozzle Pitch Angle = 4.4 deg down
LE Flap Angle = 7.4 deg down
TE Flap Angle = 1.9 deg down

Trimmed Tri–Surface Subsonic Point Design

This figure is the corresponding lower surface view of the intermediate subsonic point design geometry. As with the upper surface, little change is apparent. There are, however, small changes occurring about the nacelle/diverter regions in apparent response to the pressure fields of those components and the spilling inlets. The changes appear to be similar to what occurs at the supersonic cruise condition in terms of cause and effect, but are at different locations since the compressions and expansions driving the features are at different locations.

Trimmed Tri–surface Subsonic Point Design

Mach=0.9 C_L=0.18

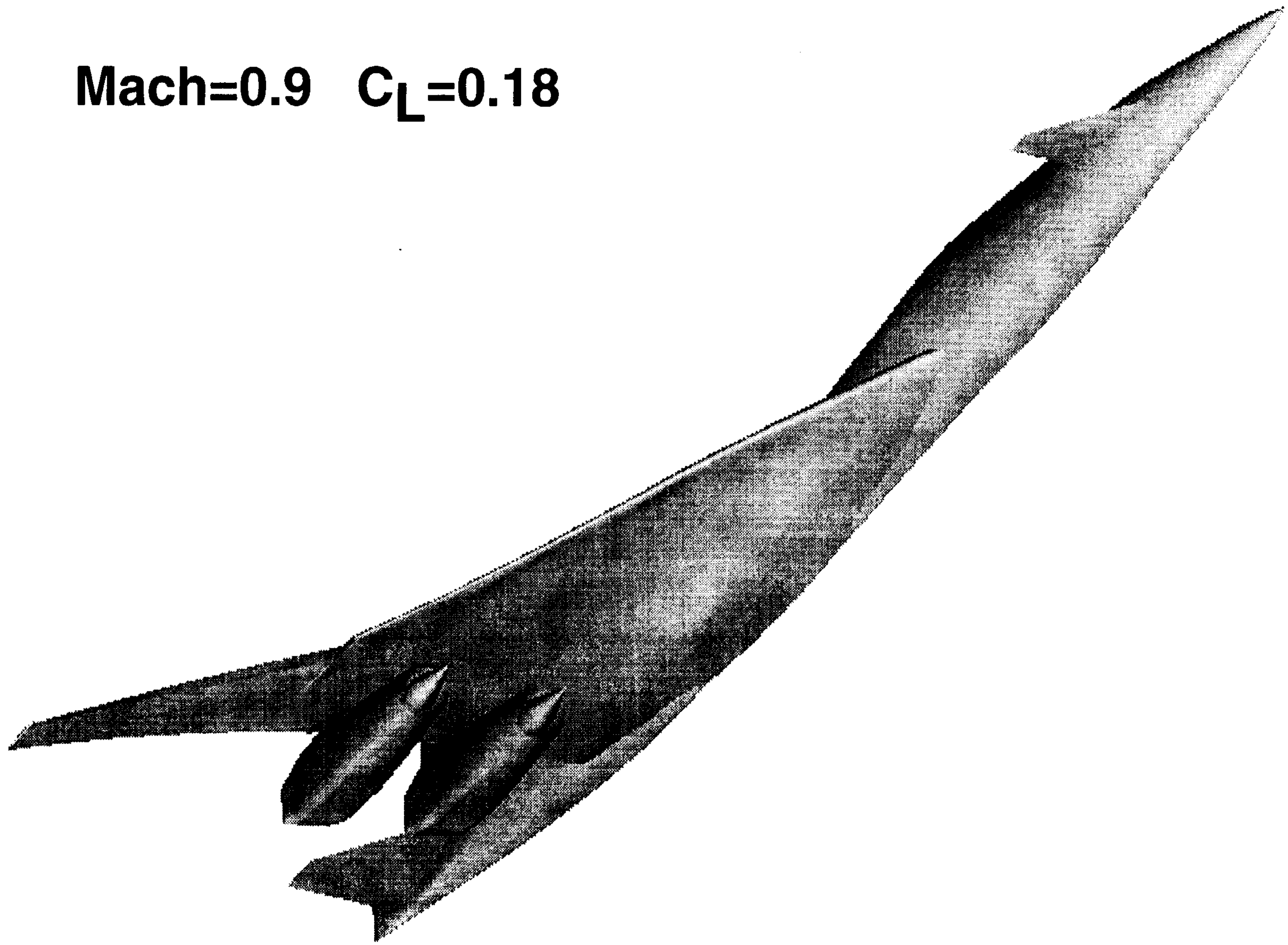

Initial Transonic Acceleration Point Design Has Almost Started

The third and final multi–point optimization flight condition is the transonic acceleration point outlined on this figure. This TI–specified condition represents the transonic pinch point of the initial climb out and, like the subsonic cruise condition, has significant inlet spillage.

The variable and constraint sets are the same as with the other cases.

This case is ready except for the trimmed baseline starting point, which is currently in work.

Initial Transonic Acceleration Point Design Has Almost Started

- Mach = 1.1, $C_L = 0.15$, 35.8 % spillage
- 441 variables
- 35k constraints
- Waiting for trimmed baseline starting point

Multi–Point Design Has Started

Initial efforts on multi–point optimization were started and/or completed this past year, and are outlined on this figure. Two cases of viscous multi–point design using OVERFLOW were accomplished. The cases demonstrated the feasibility and potential benefits of, and resources necessary for this viscous multi–point technology.

The initial TRANAIR HSCT multi–point optimization was also completed. This two condition developmental case exercised and demonstrated the process which will be employed for the upcoming three condition case.

Finally, preparations for the culminating three condition TRANAIR multi–point optimization exercise were started.

These three area of progress are next discussed in greater detail.

Multi–Point Design Has Started

- 2 viscous demonstrations (N–S OVERFLOW)
- 2 condition TRANAIR shakedown problem
- Initial 3 condition TRANAIR problem

Viscous Multi–Point Was Demonstrated

Two closely related viscous multi–point optimization cases were accomplished this past year and are outlined on this figure. The cases used viscous OVERFLOW as the analysis tool. The optimization technique is the same hybrid genetic approach used in previous work on inlet flow quality. The configuration used for both cases is the TCA wing /body, and the designs were limited to the leading edge region of the inboard wing.

The initial case is a three condition subsonic cruise design. The multiple conditions are used to optimize the wing leading edge over a wide range of lift coefficients.

The second case is a two condition optimization based on flight conditions in the both the supersonic and subsonic cruise regimes. This case is closer to the type of multi–point problem being pursued with the inviscid TRANAIR process.

Viscous Multi–Point Was Demonstrated

- N–S OVERFLOW based
- TCA wing/body configuration
- Inboard wing leading edge designs
- First case
  - 3 conditions (C_L's) at Mach 0.9
- Second case
  - 2 conditions : Mach 2.4 & 0.9

Region of Grid Manipulation

Case 1

Viscous multi–point numerical optimization was tested by using a hybrid genetic optimization driver connected to the OVERFLOW CFD solver. The TCA wing/body inboard wing leading edge was modified to minimize an objective function that required three CFD solutions at Mach number 0.90 for different angles of attack.

The figure shows the wing leading edge surrounded by a grid of boxes in red. These boxes define a region where free–form deformation (FFD) methods were used to modify the geometry. Four design variables controlled the movement of FFD control points within each box. The inboard wing between WBL 98.74 and WBL 471.56 forward of 2 percent of chord was modified. In order to avoid a large drag penalty at Mach number 2.40 that might be produced by an expected increase in leading edge camber, the leading edge point was held fixed and only the shape modified.

Region of Grid Manipulation

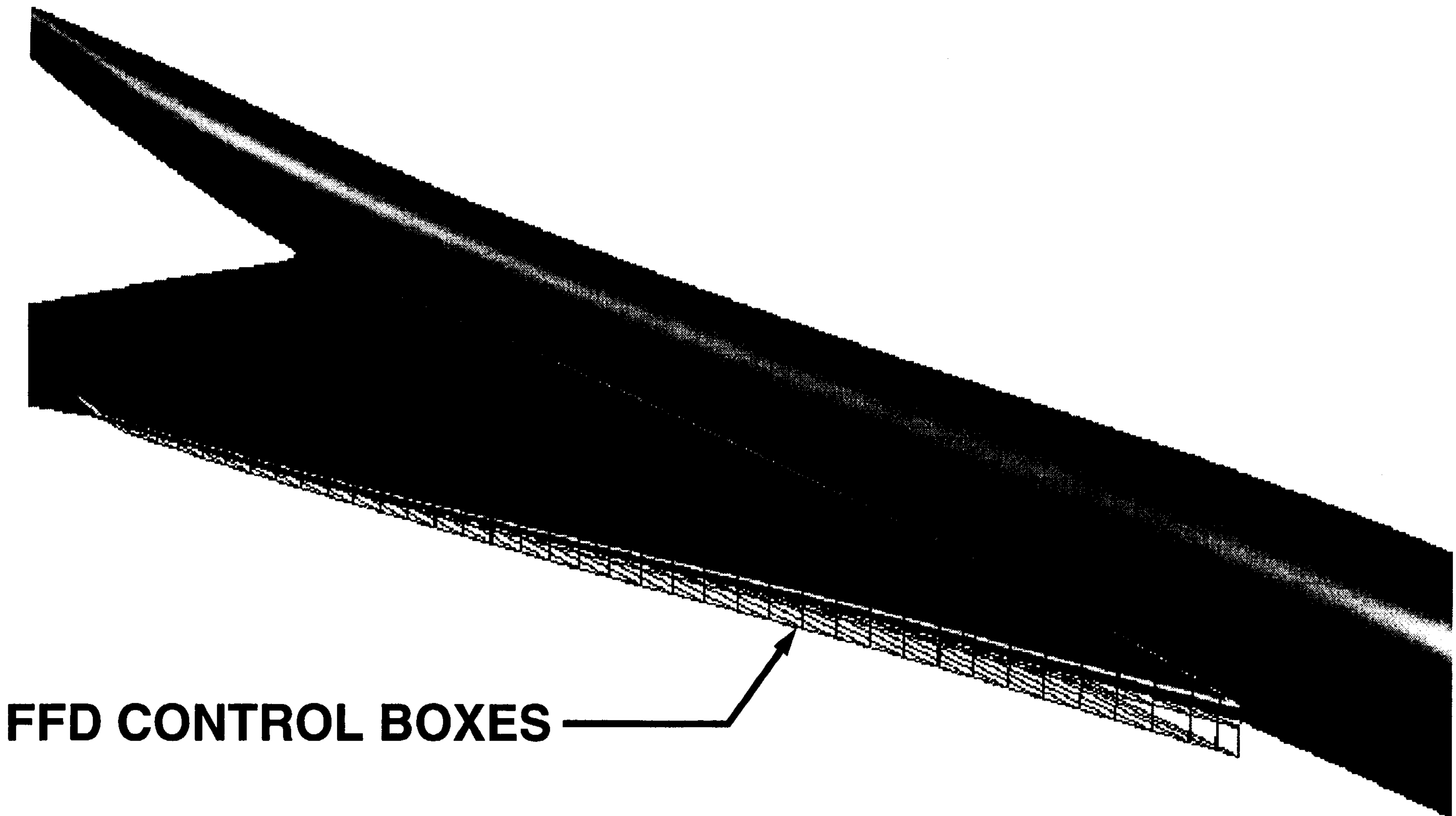

Multi–Point Objective Function

The figure graphically depicts the function being minimized. An objective function is formed from the integral shown by using three OVERFLOW solutions and fitting a cubic spline to the resultant lift and drag. The OVERFLOW solutions were for angles of attack of two, five, and eight degrees at Mach number 0.90.

Multi–Point Objective Function

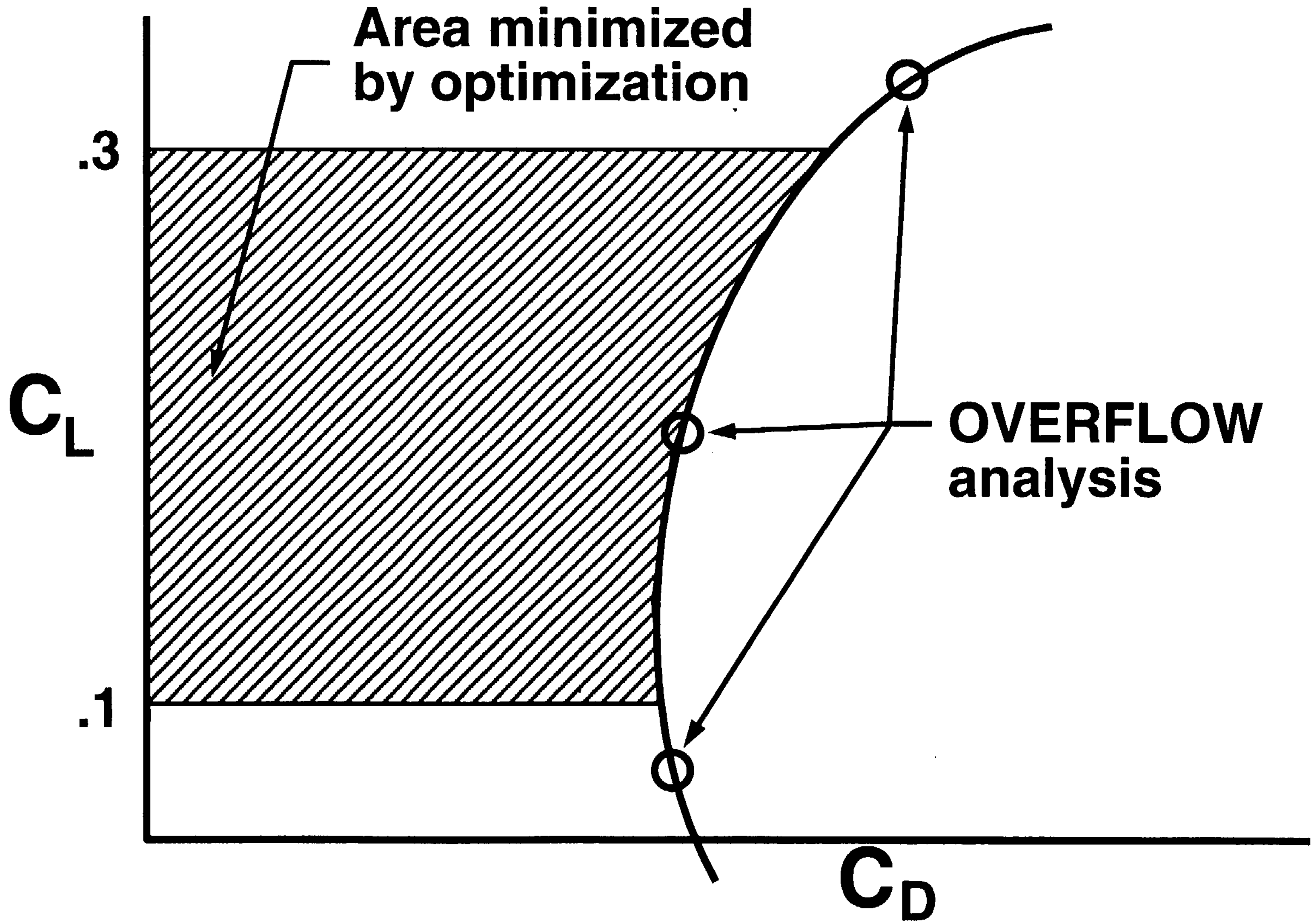

Objective Function History

The figure shows a history of the optimization process. The objective function value is shown for each evaluation in sequence. The TCA baseline value is 0.004191 and the optimum value is 0.004176 for a reduction of 0.000015. The optimization required 99 function evaluations each using three OVERFLOW solutions. Each OVERFLOW solution was a restart from a TCA baseline solution and required approximately 55 minutes of NAS C90 CPU time.

Objective Function History

3 condition, viscous multi–point subsonic cruise optimization
TCA wing/body inboard leading edge shape

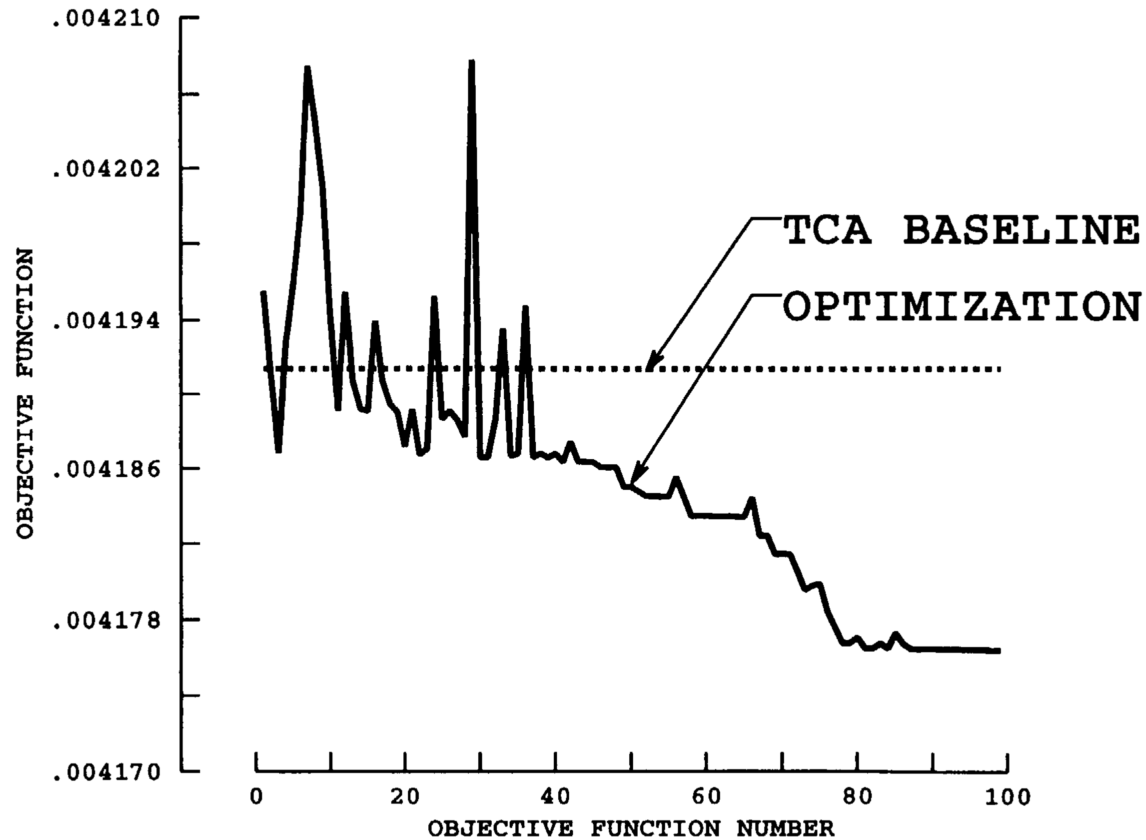

Mach 0.9

C_L 0.1–0.3

Drag Increment Due to Optimization

The figure shows the drag increments as a function of lift coefficient for the optimized wing leading edge at Mach number 0.90, the optimization Mach number, and at Mach number 2.40, the cruise Mach number. Note that there is a drag penalty of 0.00004 at the cruise Mach number.

Drag Increments Due to Optimization

3 condition, viscous, multi–point, subsonic cruise optimization
TCA wing/body inboard leading edge shape

Viscous analysis RN = 6.1 million/MAC

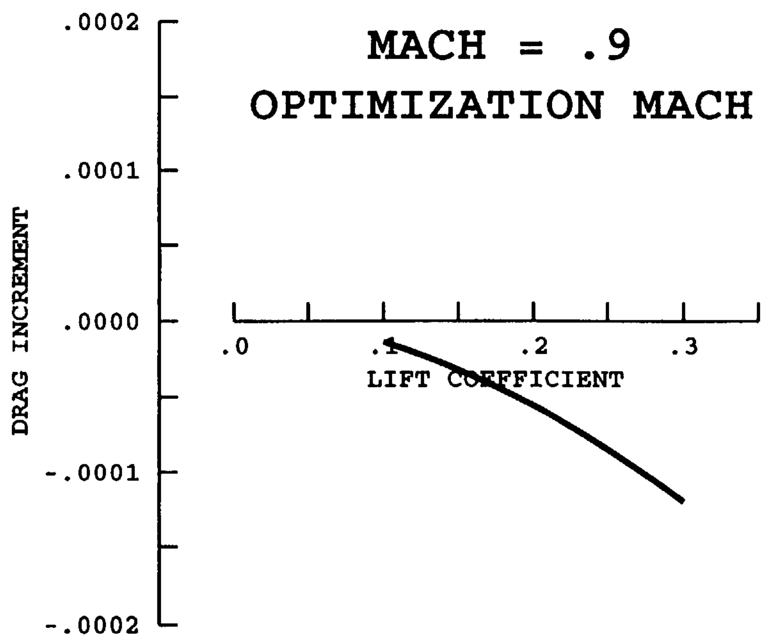

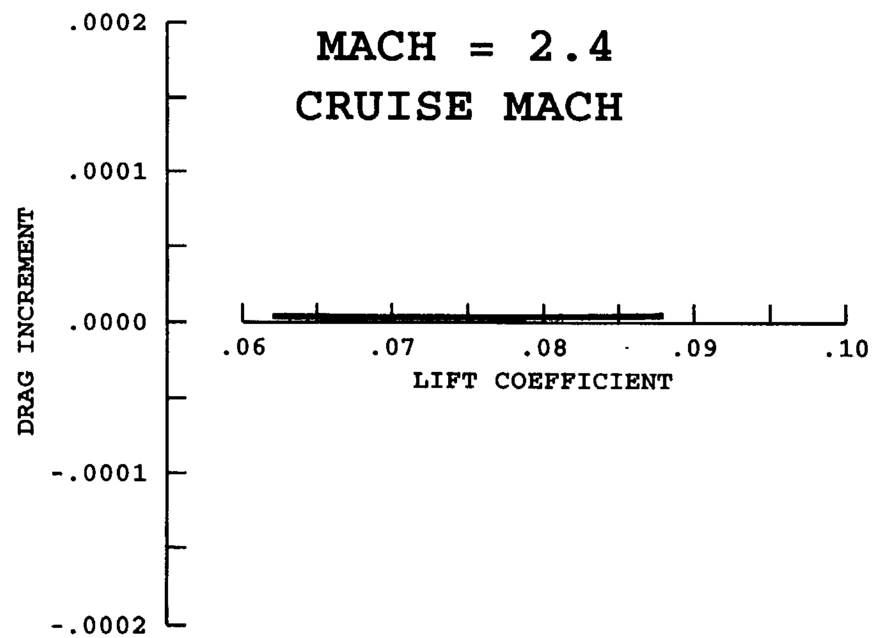

Geometry Changes Due to Optimization

The figure shows the wing leading edge airfoil section geometry for the TCA and for the optimized configuration at several representative spanwise locations. Note that the leading edge points were not moved and the upper and lower surfaces aft of the leading edge were recontoured in minimizing the objective function.

Geometry Changes Due to Optimization

3 condition, viscous multi–point
Flaps up, TCA wing/body

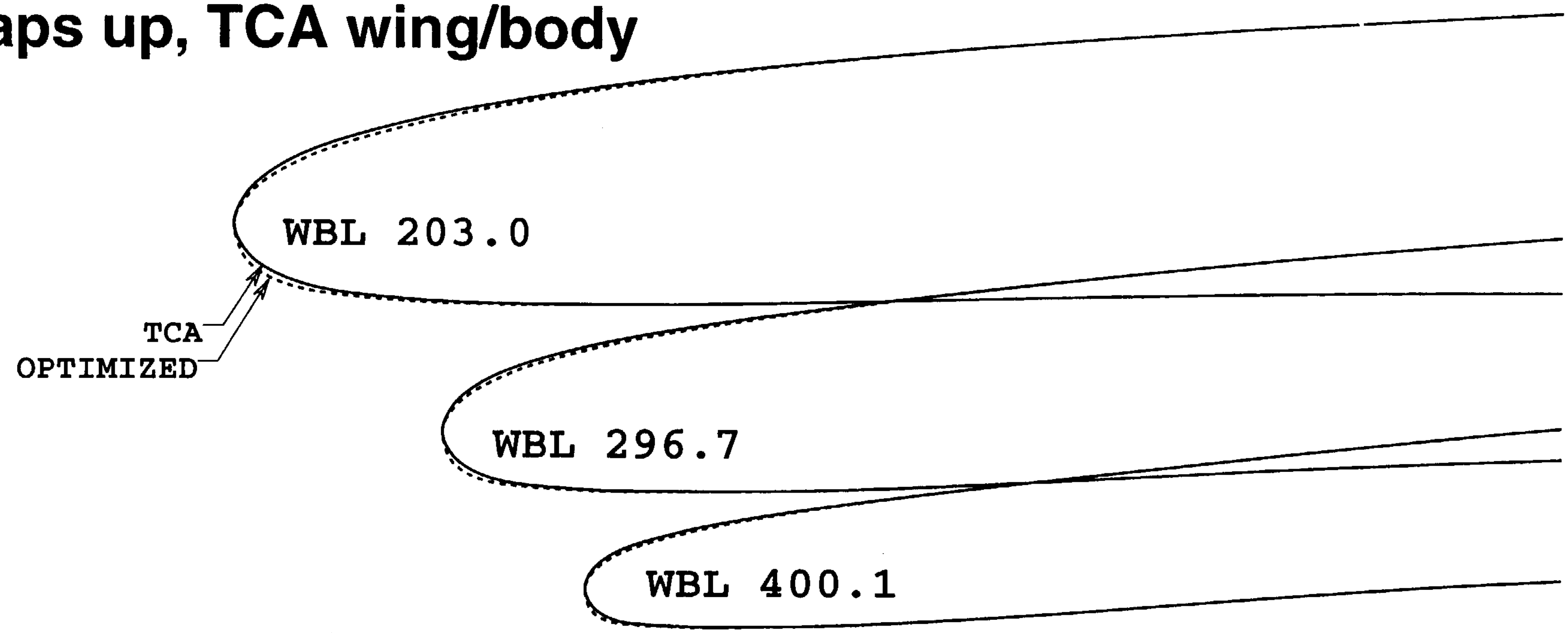

Mach 0.9

C_L 0.1–0.3

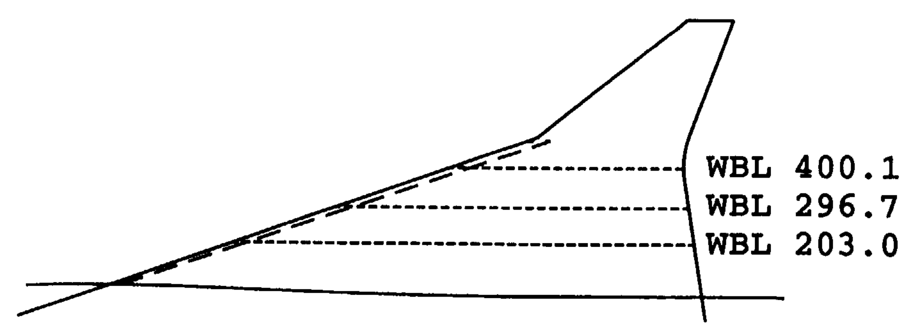

Inboard Leading Edge Design Region

Case 2

The TCA wing/body was used to demonstrate viscous multi–point numerical optimization. The inboard wing leading edge was modified while using the OVERFLOW CFD program to provide lift and drag for the optimization process. The objective function minimized was the sum of the change in drag coefficient at Mach number 0.90 and angle of attack of six degrees plus six times the change in drag at Mach number 2.40 and angle of attack of three degrees. Lift variations were accounted for by calculating the drag increments at the resultant lift coefficient by cubic spline interpolation of the TCA baseline polar. Trivariate Bernstein polynomials, sometimes called free–form deformation (FFD), were used to modify the leading edge geometry.

The figure shows the region of the inboard wing that was redesigned. Six design variables were used to modify the leading edge geometry. The design variables provided for leading edge shape variation as well as leading edge camber variation by moving the control point locations of each of the FFD boxes.

Inboard Leading Edge Design Region

Two condition viscous multi–point optimization
TCA wing/body – flaps up

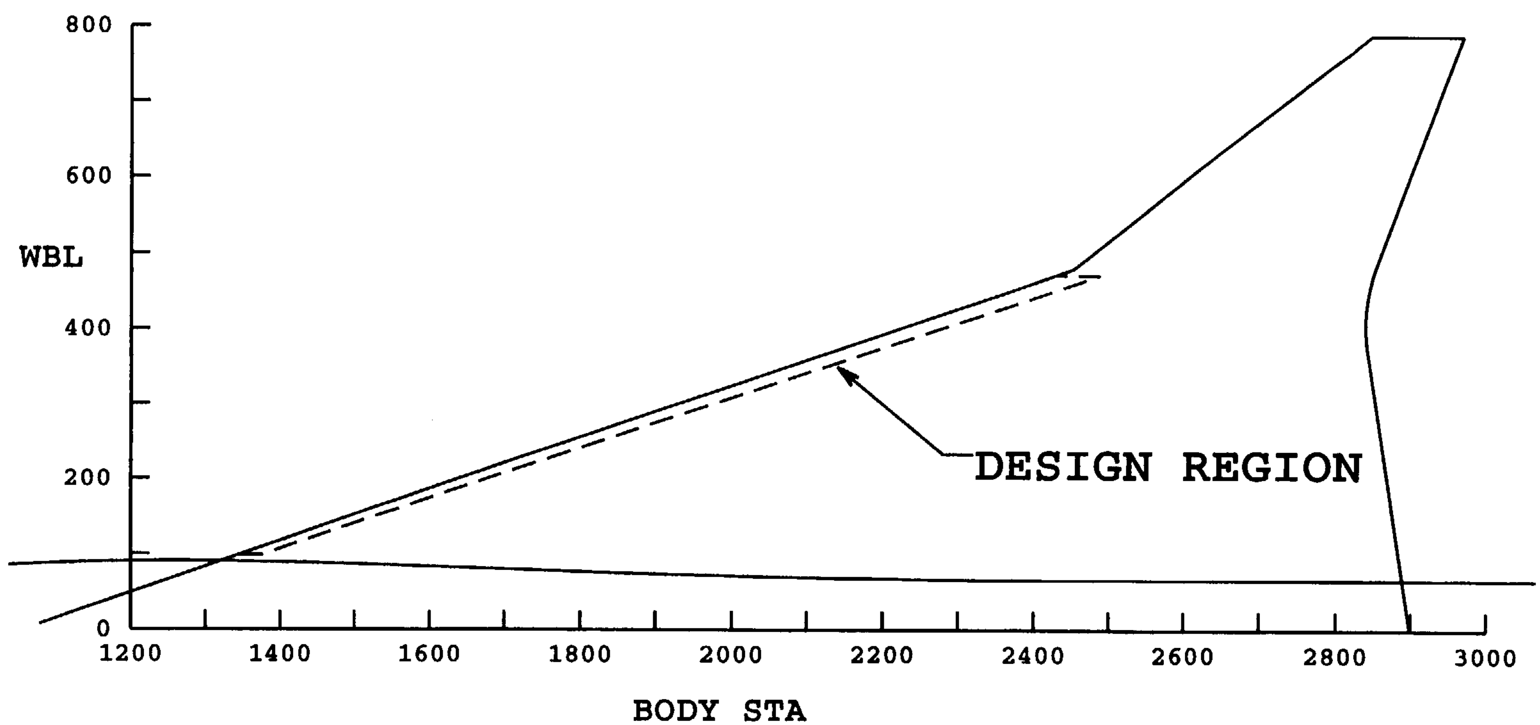

Two Condition Objective Function History

A hybrid genetic optimizer driver was used in the optimization process. This method begins with a standard genetic optimization algorithm to locate the vicinity of the global optimum point in design space and then switches to a simple hill–climbing technique to find the best design. Design sensitivities are not required in this process nor are any smoothness assumptions made concerning the nature of design space.

The figure shows the optimization history. The process began with eighteen randomly selected points in design space. These points were evaluated using OVERFLOW followed by operation of the genetic algorithm. After the genetic algorithm demonstrated a tendency to cluster around a point in design space the optimization process was completed by using the genetic population best point as a starting point for the hill–climbing method. The hill–climbing method then arrived at a point in design space where no perturbation of any design variable produced a better design. This point was taken as the global optimum.

Two Condition Objective Function History

Two condition viscous multi-point optimization TCA wing/body – flaps up

Objective Function = $\text{Delta CD}_{M=0.9} + 6(\text{Delta CD}_{M=2.4})$

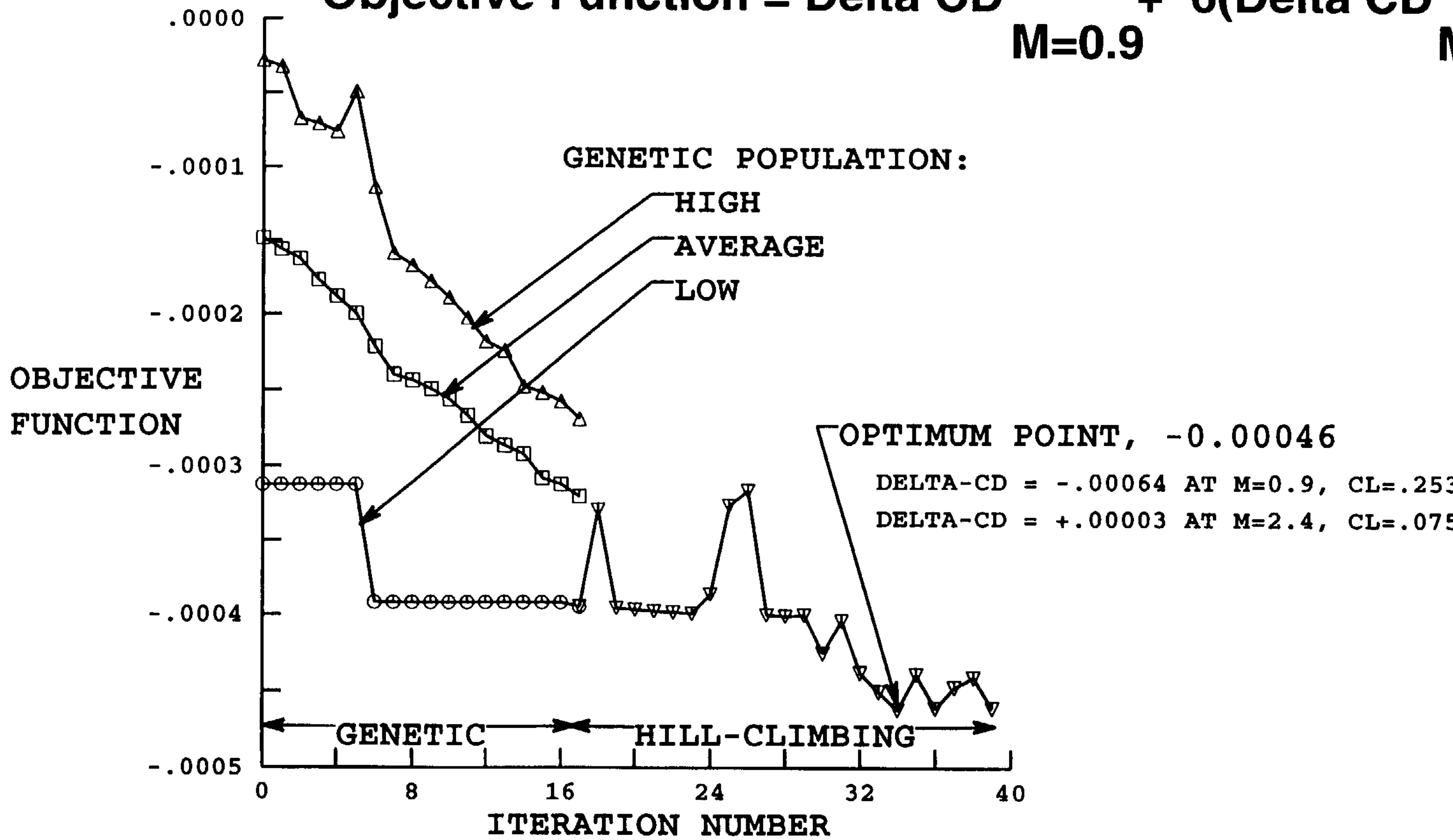

Geometry Changes Due to Optimization

The figure shows the resultant leading edge geometry at three representative spanwise locations. The TCA starting geometry is shown along with the geometry after optimization. Note that the leading edge camber is increased and the leading edge shape altered to provide less curvature for the upper surface near the leading edge.

Geometry Changes Due to Optimization

Two condition viscous multi–point optimization
TCA wing/body – flaps up

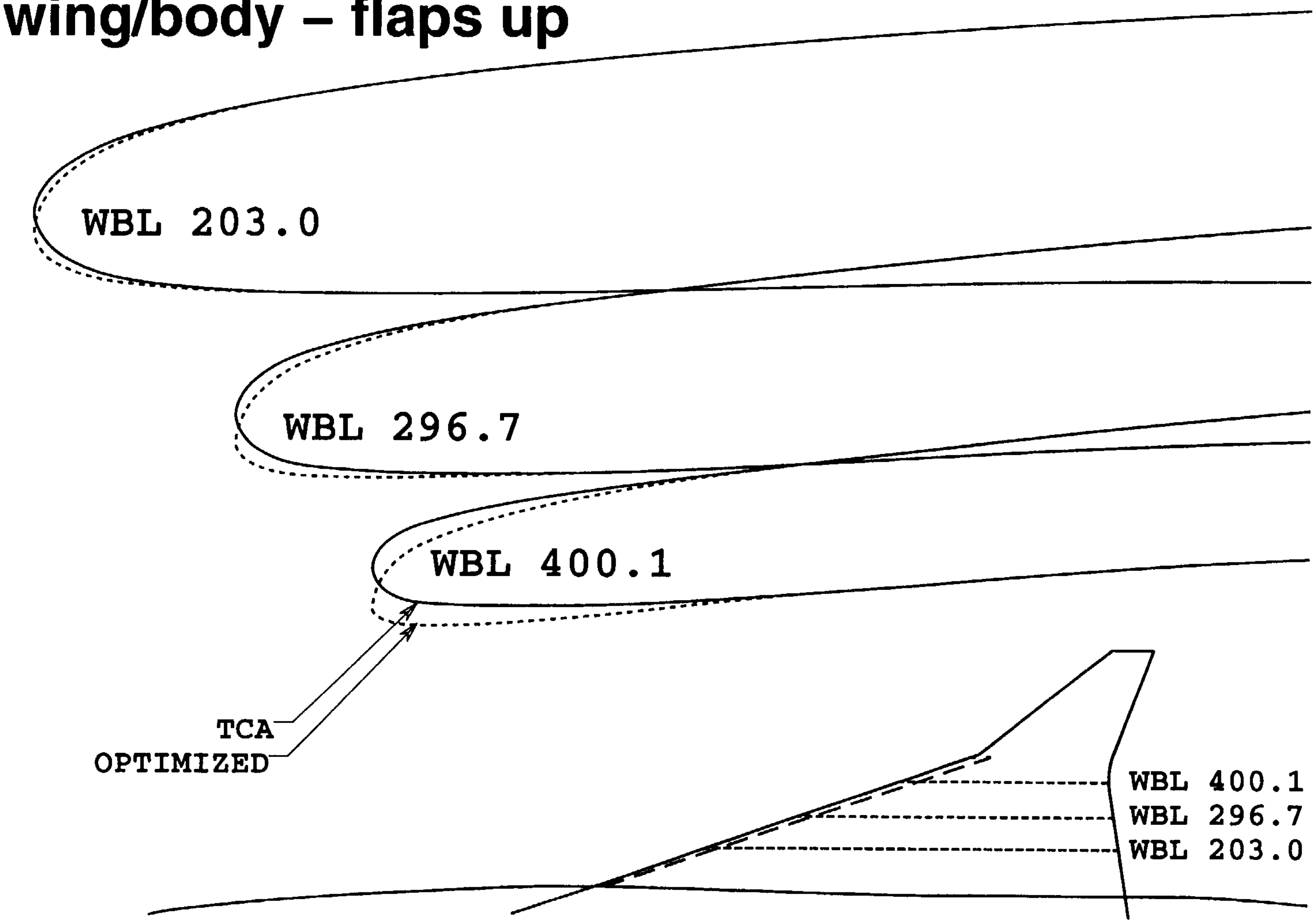

Drag Changes Due to Multi–Point Optimization

The figure shows the drag polars for the TCA and the optimized points for Mach number 0.90 and Mach number 2.40. The drag reduction is 0.00064 at Mach number 0.90 and an increase of 0.00006 at Mach number 2.40.

Drag Changes Due to Multi–Point Optimization

Two condition viscous multi–point optimization

Flaps up TCA wing/body

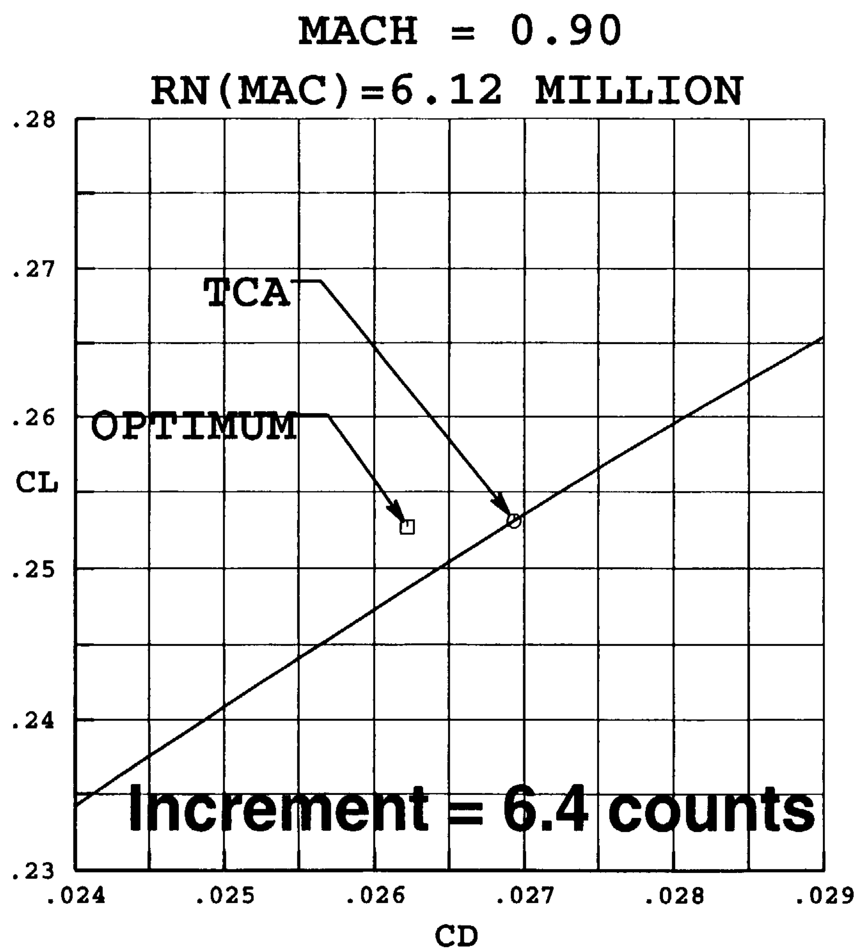

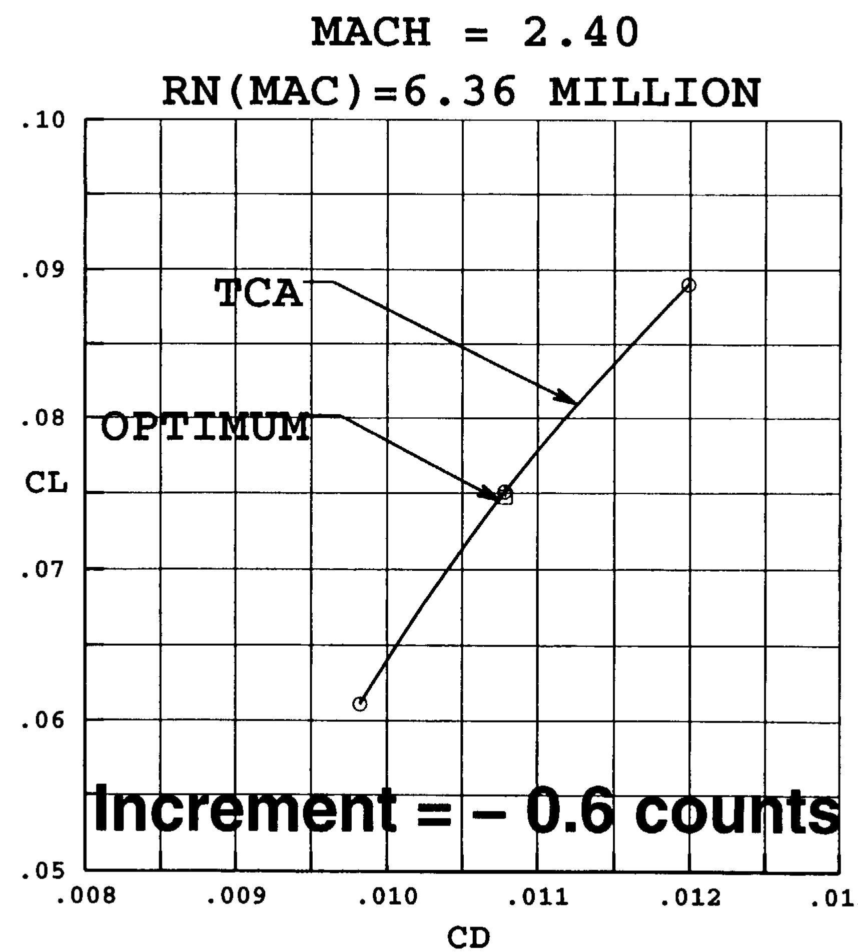

Optimization Effects on Surface Pressures

The figure shows the surface pressure distribution at three representative spanwise locations on the inboard wing. The TCA baseline is shown as well as the optimized wing at Mach number 0.90. Note that at WBL 296.6 there is evidence in the upper surface leading region of suppression of a leading edge vortex by the optimization process.

Optimization Effects on Surface Pressures

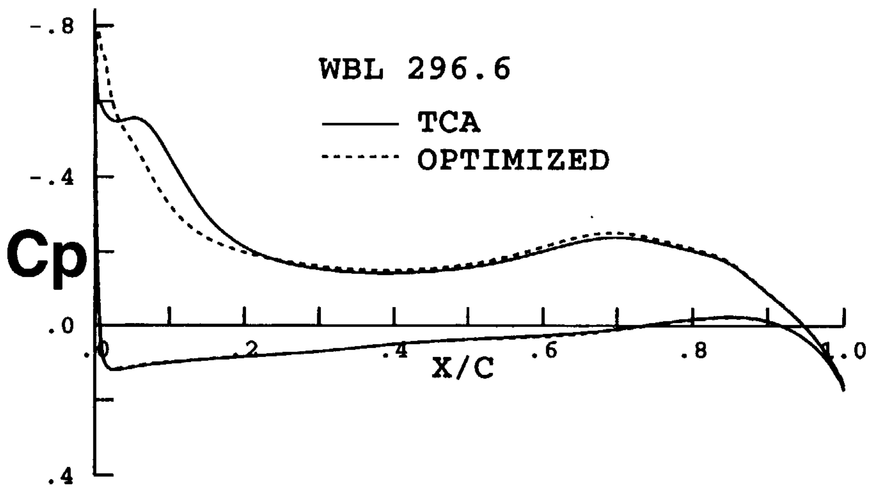

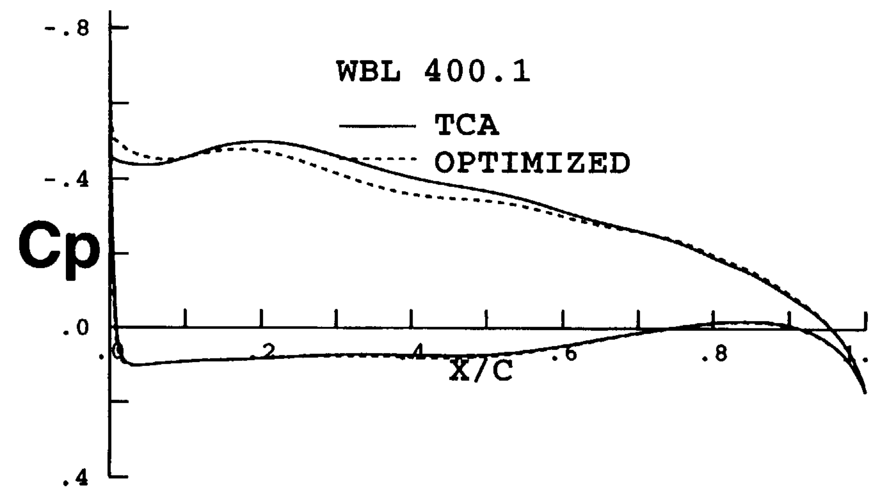

Two condition viscous multi–point optimization

Flaps up TCA wing/body   Mach 0.9 Alpha 6.0 deg

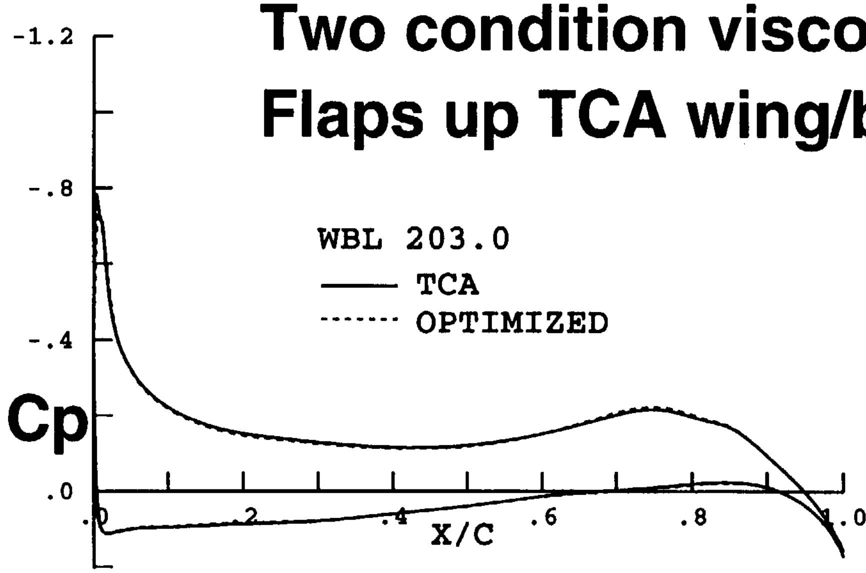

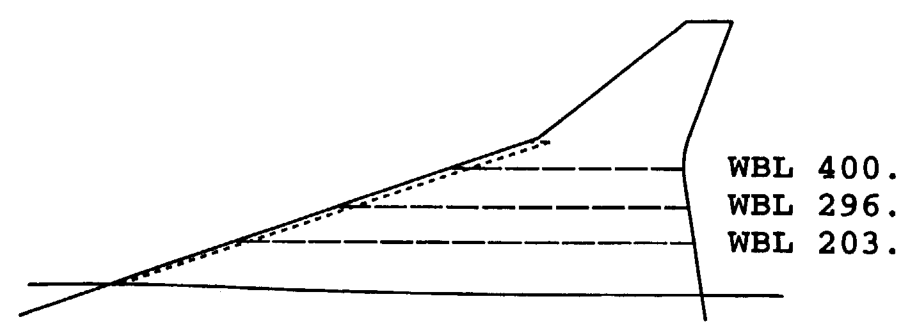

Two Condition TRANAIR Case Is Complete

The initial TRANAIR multi–point HSCT optimization was completed this year and is outlined on this figure. As noted previously, this case was also based on the common tri–surface TCA configuration, and used the same variable and constraint sets as the point design work. The supersonic cruise condition is that of the TCA, although close to the tri–surface TCA condition, and the subsonic cruise condition is the tri–surface TCA condition. The objective function weighting factors were based on preliminary recommendations, rather than the final TI–specified values, 6:1 rather than 1:0.3.

As was the case with the cruise point design, over half of the 445 variables were lost due to active constraints and variable bounds. Only three TRANAIR cycles were completed, which was sufficient to verify the mechanics of the process. As a result, the slight decrease in thrust reduction relative to the cruise point design is inconclusive. This effect of multi–point will be evaluated with this coming year's three condition exercise.

It is encouraging that a drag improvement was found at the subsonic cruise condition. The magnitude of the improvement is not a final result, however. As noted above, this was a process development case, and is only representative. A more valid evaluation will be made with the three condition multi–point optimization exercise.

Relative to cruise point designs, no new geometric effects of optimization were observed on this case.

Two Condition TRANAIR Case Is Complete

- Tri–surface TCA configuration
- Mach 2.4/C_L 0.092 & Mach 0.9/C_L 0.18
- 6:1 weighting in objective function
- 445 variables (29 on bounds) & 34k constraints (214 active)
- 3 TRANAIR cycles
- 7.45 counts of thrust improvement
    - 7.4 counts at Mach 2.4
    - 0.3 counts at Mach 0.9
- Shape changes similar to cruise point design

Two Condition Multi–Point Design

An example of the result of the two condition multi–point optimization is shown on this figure. Lower surface Mach number contours in the nacelle/diverter region before and after optimization are compared. Typical cruise point design effects are apparent in the reduction of both compression and expansion fields. These type of changes suggest that the larger nacelle/diverter increment, characteristic of the Ames 103 and the subsequent TRANAIR cruise point design described earlier in this presentation, is still occurring.

Two Condition Multi–Point Design

Mach=2.40, C_L=0.092

After 3 Design Cycles | Trimmed Baseline

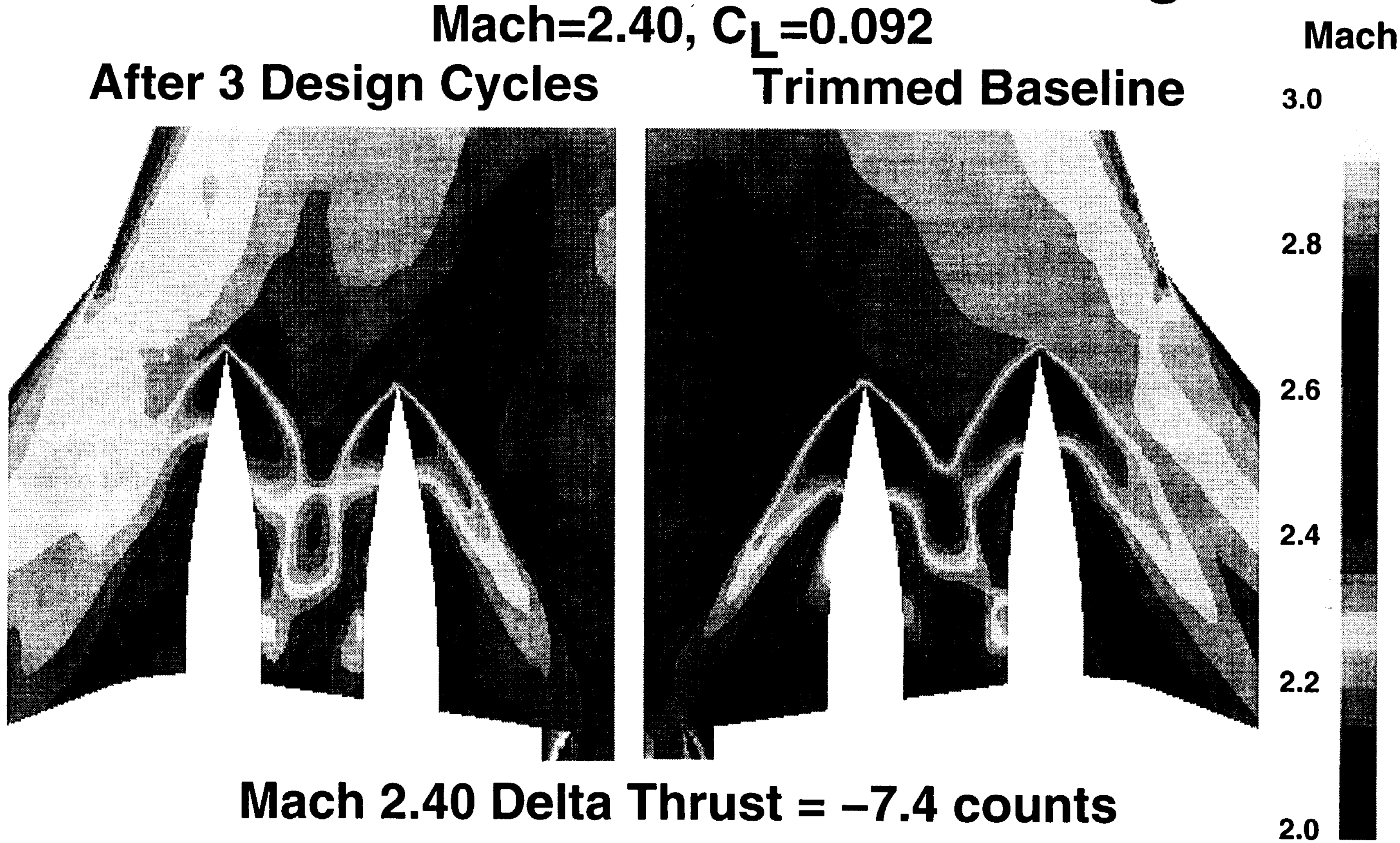

Mach 2.40 Delta Thrust = –7.4 counts
Mach 0.90 Delta Thrust = –0.3 counts

Three Condition TRANAIR Shakedown Case Has Almost Started

The initial three condition TRANAIR multi–point optimization case, outlined on this figure, is essentially ready except for the trimmed baseline starting points. The common configuration, TI–specified design points and weighting factors, and variable and constraint sets are ready, as are the optimization routines.

Once fully underway, this problem will represent the multi–point case on which the final evaluation will be made. More details about the evaluation process, and how this case fits in the process, are outlined in the concluding section of this presentation.

Three Condition TRANAIR Shakedown Case Has Almost Started

- Tri–surface TCA configuration
- Mach 2.4/C_L 0.089, Mach 0.9/C_L 0.18 & Mach 1.1/C_L 0.15
- 1:0.3:0.15 weighting in objective function
- 451 variables & 35k constraints
- Waiting for trimmed baseline starting points
- Will begin with initial Mach 1.1 sensitivities

Plans

The remaining activities of this subtask are described on the following figures. The work is divided into the completion of the multi–point evaluation and the other remaining activities.

Plans

Multi–Point Exercise Will Be Completed

The remaining work required to complete the evaluation of multi–point optimization is outlined on this figure. The basic evaluation requires three main pieces. First, there are the common starting points, referred to as the trimmed baseline configurations. These are not the baselines against which the results of multi–point optimization will be compared, but will be used as baselines for the sequential optimizations. They are also the common starting points for both the sequential and multi–point optimizations. The second main part is the sequential optimization. This is composed of first, a full variable set, cruise point optimization. The result of this point design then passes through a trim drag optimization with flaps at the two other flight conditions. These three results, combined in the weighted multi–point objective function, constitute the sequential baseline against which multi–point will be evaluated. The third main part is the simultaneous multi–point optimization. It also starts from the trimmed baseline configuration and the three flight conditions are inherently combined in the weighted objective function.

Through coordination with the other CA organization participating in the multi–point evaluation exercise, NASA Ames, the task has been expanded to two separate, but related, multi–point problems. The problem described in this presentation is referred to as the extended problem in this context. A slightly simpler problem, representing the common capabilities and/or obtainable capabilities of both sites, is referred to as the core problem. The extended problem will allow each site to demonstrate local strengths and the largest possible optimization increment. The core problem will provide a more rigorous comparison of the two optimization processes.

As with past cruise point design exercises, the final evaluation of the multi–point optimization results will be viscous analysis. As a minimum, this will require N–S analyses of nine configurations, the three trimmed baseline configurations, the three sequential results and the three simultaneous results. Resource issues limit this step to only one of the two problems. The current plan is to provide viscous verification of the extended problem.

There are two obvious open issues with viscous verification of inviscid, trimmed, multi–point results. First, optimum inviscid flap deflections are not optimum viscous flap settings, particularly for the trailing edge flap. Second, a trimmed inviscid configuration will not be trimmed in viscous analysis. Resolution of these issues will be made as data is obtained. Additional viscous analyses may be required.

The final scheduled element of the multi–point exercise is a design review leading to the milestone deliverable.

Multi–Point Exercise Will Be Completed

- 3 main parts
  - Baselines
  - Sequential optimizations
  - Simultaneous optimization
- 2 main problems
  - Core
  - Extended
- Viscous verifications
  - Extended problem only
  - Open issues
    - Flap deflections
    - Trim
- Design review

Other Activities Are Planned

Beyond completing the basic multi–point evaluation, three other activities are planned and shown on this figure. First, is exercising and validating a capability to provide objective function sensitivities to active constraints. The sensitivities produced will represent linear evaluations about the final configuration. Validation is envisioned as a repeat optimization with the previously active constraint relaxed.

The second activity is continuing the efforts to calibrate the coupled TRANAIR boundary layer with the viscous reference data created this past year. Completion of this step will lead to an evaluation of the coupled viscous capability in optimization.

The final planned activity is an exploration of another version of the multi–point problem. One candidate problem is an all supersonic multi–point case, substituting an intermediate Mach number in place of the subsonic cruise condition. Another case of interest is a modification of the sequential optimization process where an all supersonic body area ruling tune up case is added prior to the off design trim drag with flaps optimizations

Other Activities Are Planned

- Sensitivities to active constraints
- Coupled viscous TRANAIR optimization
- Other TRANAIR multi–point problems

Design Cycle-Time Reduction using TLNS3D-Adjoint

Geojoe Kuruvila
Robert P. Narducci

The Boeing Company
Phantom Works, Long Beach

NASA / Industry HSR Airframe Review
Anaheim, California
February 8-11, 1999

Design Cycle-Time Reduction using TLNS3D-Adjoint

Significant cycle-time reduction has been achieved by using the TLNS3D-Adjoint code for the aerodynamic shape optimization of High Speed Civil Transport (HSCT) configurations. Using the adjoint of TLNS3D (Euler) flow analysis code, aerodynamic gradients are computed, both accurately and efficiently, for hundreds of design variables. Results obtained by using TLNS3D-Adjoint in the aerodynamic shape optimization of HSCT Technology Concept Airplane (TCA) configurations are presented.

Outline

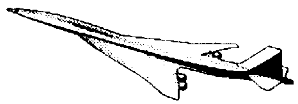

- Objective
- TLNS3D-Adjoint
- TCA Optimizations
  - Wing/body, M_∞=2.4
  - Wing/body/nacelle/diverter, M_∞=2.4
  - Leading-edge/flaps, M_∞=0.9
  - Leading-edge/flaps multipoint, M_∞=0.9, 2.4
- Summary

Objective

Nonlinear aerodynamic shape optimization is essential in designing an economically viable High Speed Civil Transport (HSCT). Aerodynamic optimization of complete airplane configurations, using hundreds of design variables, at low overall cost and low cycle-time remains a challenge. In a typical optimization, significant cost is incurred in obtaining the gradient of the cost function, especially when finite-differences or sensitivity equations are used.

It is well known that, by using the adjoint method, the gradients of hundreds of design variables can be computed accurately and efficiently. With design cycle-time reduction as a goal, an adjoint code was developed for TLNS3D (Euler), a versatile flow analysis code. Results of the aerodynamic shape optimization of HSCT Technology Concept Airplane (TCA) configurations, performed using this code, are presented in this paper.

Objective

- Reduce the cycle-time for HSCT aerodynamic shape optimization

- Develop an adjoint code for TLNS3D (Euler)
  - Compute aerodynamic gradients accurately and efficiently
  - Use hundreds of design variables

TLNS3D-Adjoint

TLNS3D-Adjoint is a suite of three codes which, computes the aerodynamic gradients of design variables, both accurately and efficiently, using the adjoint method.

The first code, TLNS3D, is the standard version of the NASA developed flow analysis code. Although it can analyze fully turbulent viscous flows, the adjoint of only its inviscid (Euler) component has been created. Given the grid, X, around an airplane configuration and the freestream conditions, the Euler equations along with the boundary conditions, $R(Q,X)=0$, are solved, using TLNS3D, to obtain the flow solution Q and consequently the cost function $F(Q,X)=0$. The drag, lift, moments, etc. are examples of the cost function.

The second code, ATLNS3D, solves the adjoint of the Euler equations and the corresponding boundary conditions for the user-specified cost function, F. In addition to the grid, X, and the freestream conditions, ATLNS3D requires the flow solution, Q, to obtain the adjoint solution, λ.

The third code, GTLNS3D, uses the flow and adjoint solutions along with the grid sensitivity, $\partial X / \partial b_i$ to compute the gradient of the cost function, $\partial F / \partial b_i$, with respect to each design variable. GTLNS3D is executed as many times as the number of design variables.

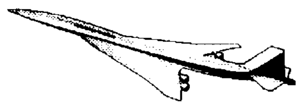

TLNS3D - Adjoint

High Speed Aerodynamics, Long Beach

TLNS3D (Analysis Module):

$R(Q, X) = 0$: (Euler Eqns. + Boundary Conds.)

$F(Q, X)$: (Cost Function)

ATLNS3D (Adjoint Module):

$$\left[\frac{\partial R}{\partial Q}\right]^T \lambda = -\frac{\partial F}{\partial Q}$$

GTLNS3D (Gradient Module):

$$\frac{\partial F}{\partial b_i} = \left\{\left[\frac{\partial R}{\partial X}\right]^T \lambda + \frac{\partial F}{\partial X}\right\}\frac{\partial X}{\partial b_i}; \quad i = 1, 2, \ldots N$$

BOEING

TLNS3D / ATLNS3D

In ATLNS3D, the discretization of the adjoint equations together with the dissipation terms is consistent with that of TLNS3D (Euler). Both TLNS3D and ATLNS3D use central-difference discretization and blended 2^{nd} and 4^{th}-order dissipation. They use Runge-Kutta time-stepping to advance the solution and multigrid to accelerate the convergence to steady state. Both support structured multiblock patched grids and they can be executed on either a serial or a parallel machine.

TLNS3D / ATLNS3D

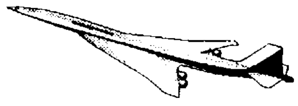

High Speed Aerodynamics, Long Beach

- Central-difference discretization
- Blended 2nd and 4th-order dissipation
- Runge-Kutta time-stepping
- Multigrid acceleration
- Multiblock patched grids
- Serial and Parallel (MPI) versions

AEROSHOP Framework

AEROSHOP (*AERO*dynamic *SH*ape *OP*timization) is a Boeing – Long Beach developed shape optimization system. It features a modular structure and runs on many platforms including the Cray C-90, J90, T3E, the SGI Origin 2000, and clusters of Hewlett Packard workstations. In a top-level viewpoint, the design problem definition is input to the *AEROSHOP* core executable. The optimizer within the core is MDOPT, a Boeing proprietary version of NPSOL. When the optimizer needs to perform a search direction or a line search calculation, the core relinquishes control to *AEROSHOP* scripts. The scripts are UNIX shell commands designed to perform a function. At the end of a script's execution, control of the optimization is returned to the core. The scripts can be custom-built to incorporate well established, heritage technologies or new, state-of-the-art technologies. The modularity of the *AEROSHOP* scripts also allows codes to take advantage of parallel environments.

In the adjoint approach, any time the flow solution is required, the evaluation script is called to execute TLNS3D. When *AEROSHOP* needs the gradients, the gradient script first calls the evaluation script to execute TLNS3D and then calls auxiliary scripts to execute the adjoint module, ATLNS3D and the gradient module, GTLNS3D.

AEROSHOP Framework

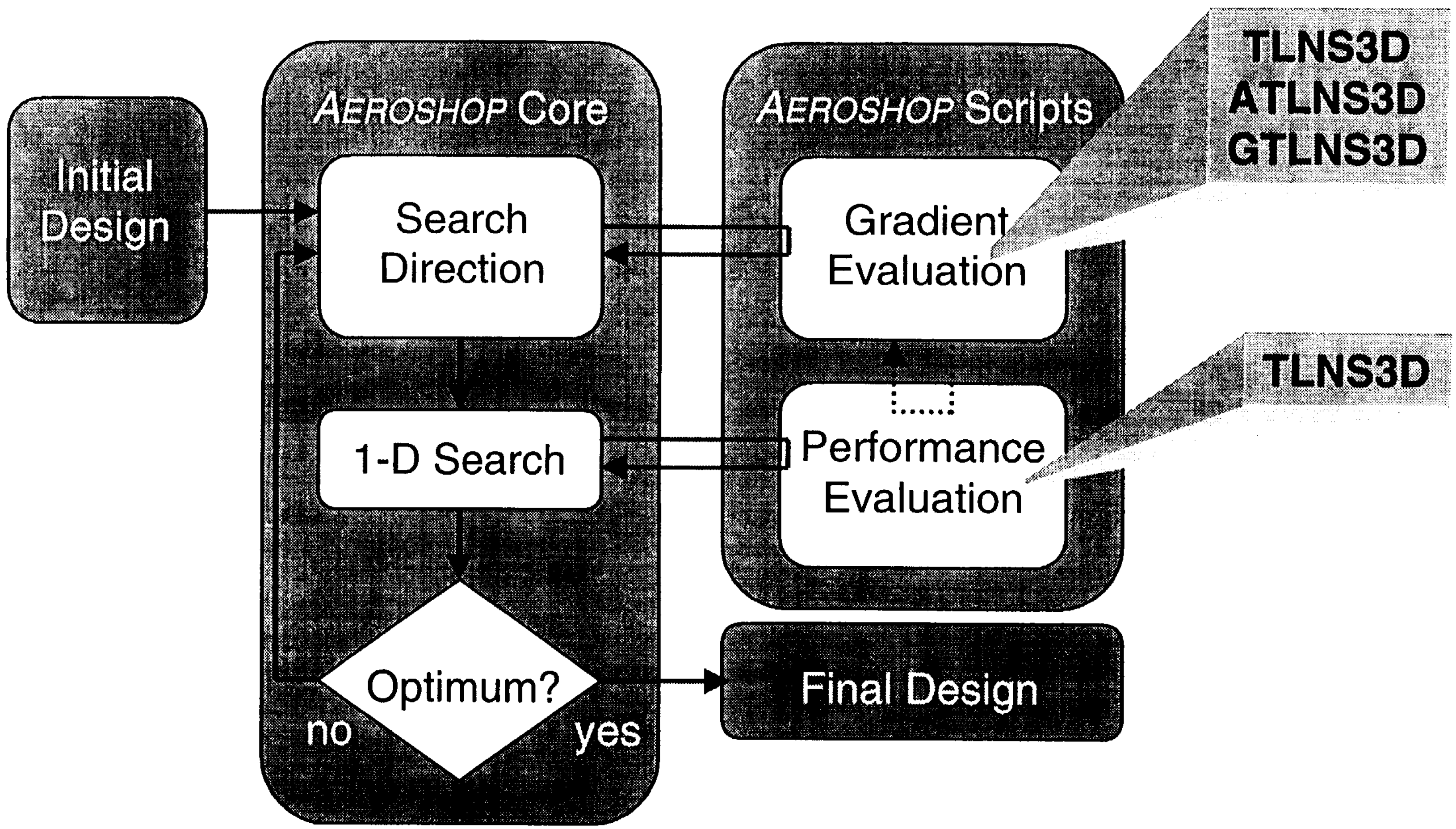

TLNS3D

TLNS3D is the standard version of the NASA developed flow analysis code. It is efficient, versatile and easy-to-use and is widely used in the aerospace industry in a production environment.

For grid topologies where all the blocks are point-matched, TLNS3D reads the grid-file and the map-file where the boundary conditions are specified. The flow solver parameters, like the freestream conditions, number of iterations, the CFL number, the Runge-Kutta coefficients and the dissipation coefficients are read from a third file. For grid topologies where there are patched interfaces, two additional files that specify the interpolation coefficients are also read. When the specified number of iterations are completed, the flow solution is output into a file.

TLNS3D

High Speed Aerodynamics, Long Beach

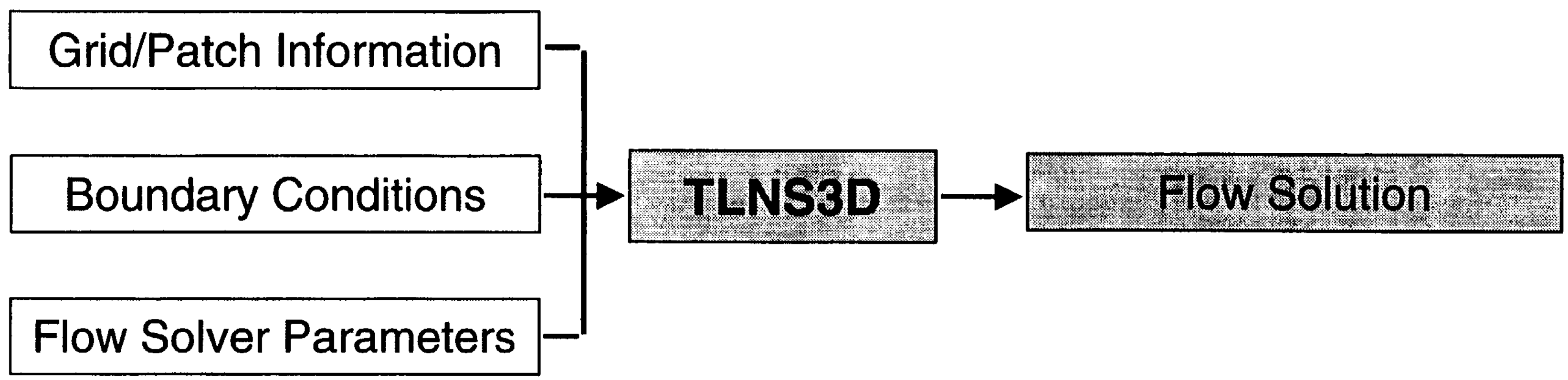

ATLNS3D

ATLNS3D is similar to TLNS3D in structure, versatility and ease-of-use. Its performance and computer resource requirements are similar to that of TLNS3D.

In addition to all the input that TLNS3D reads, ATLNS3D needs the flow solution obtained from TLNS3D. The cost function, for which the adjoint solution is sought, is also specified via an input file. Note that, the CFL number, the Runge-Kutta coefficients and the dissipation coefficients used are identical for both TLNS3D and ATLNS3D.

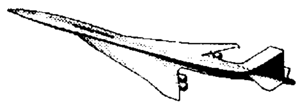

ATLNS3D

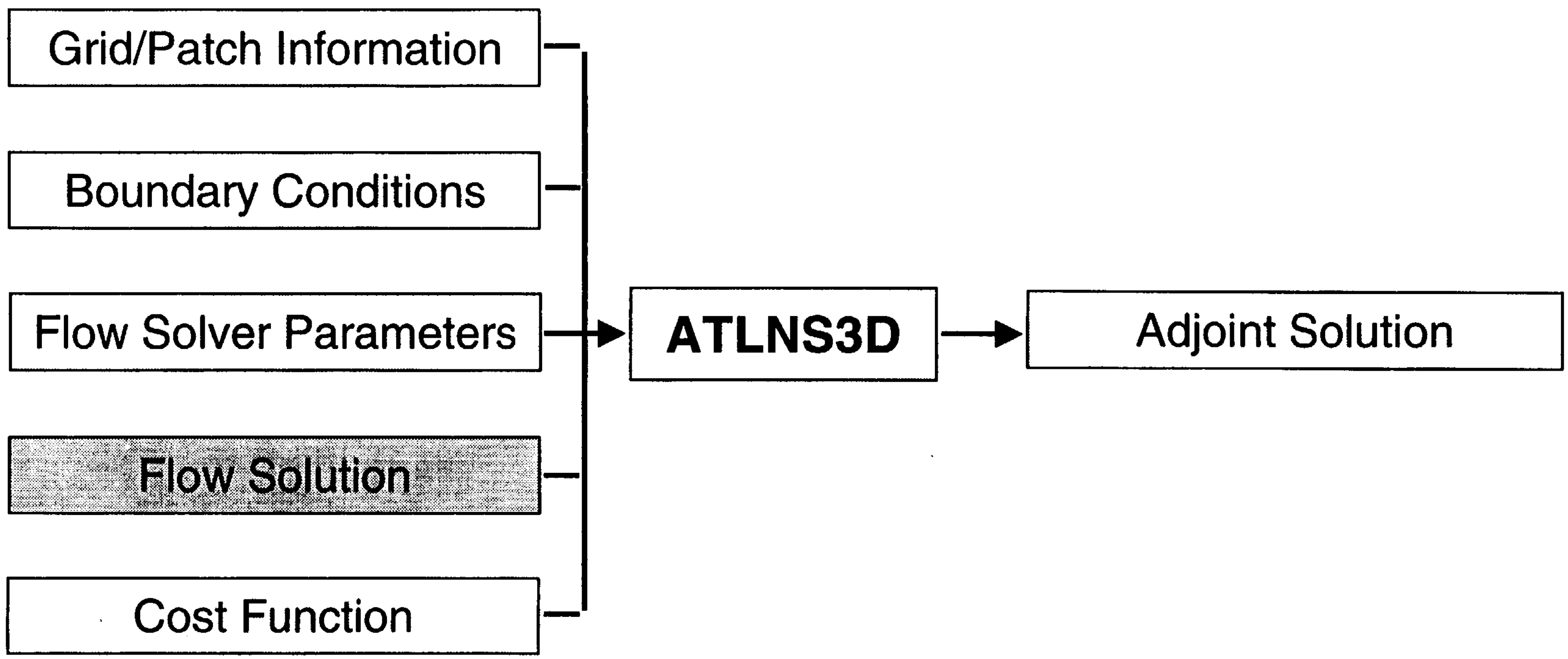
Grid/Patch Information
Boundary Conditions
Flow Solver Parameters
Flow Solution
Cost Function
ATLNS3D
Adjoint Solution

GTLNS3D

GTLNS3D computes the gradients of the cost function with respect to each of the design variables. It is executed as many times as the number of design variables.

In addition to all the input that ATLNS3D reads, GTLNS3D needs the adjoint solution obtained from ATLNS3D and the grid sensitivities corresponding to each of the design variables.

GTLNS3D

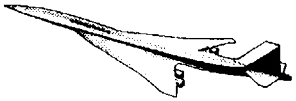

High Speed Aerodynamics, Long Beach

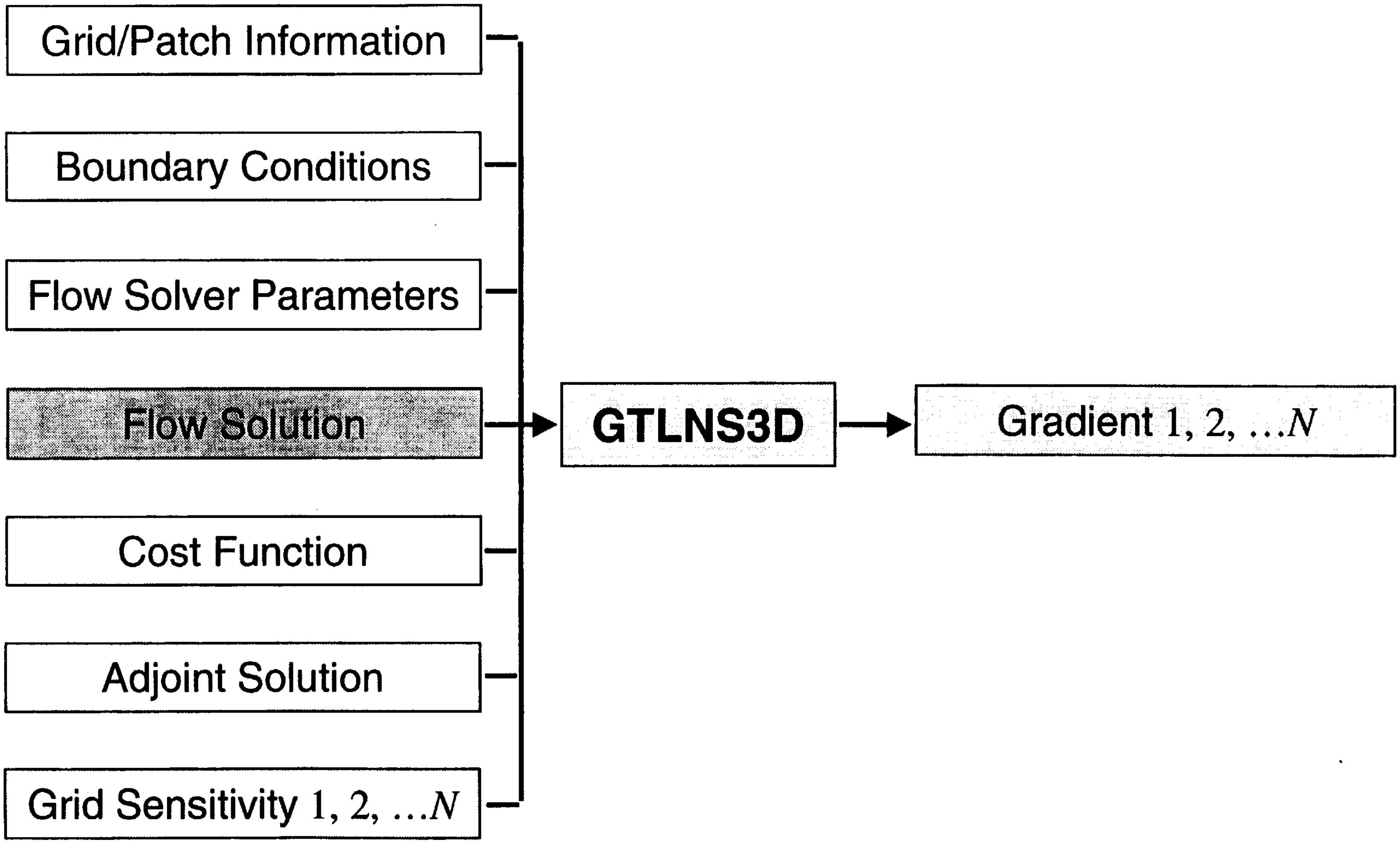

Grid Sensitivity Options

The sensitivity of the grid to each design variable can be obtained using finite-differences or computed analytically. Generally, it is tedious to differentiate the grid generation process by hand. Therefore, an automatic differentiation tool like ADIFOR (Automatic Differentiation for FORTRAN) is used to obtain analytical sensitivities. Although analytical grid sensitivities are accurate, they are more expensive to compute than finite-difference sensitivities.

Since the aerodynamic shape optimization seeks to find the best OML (Outer Mold Line) of an airplane, it maybe sufficient to use only the sensitivity of the grid representing the airplane surface. Some evidence supporting this is discussed later in the paper. The CPU time saved, by using surface sensitivities, can be significant when hundreds of design variables are used.

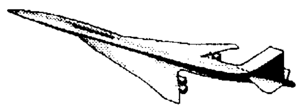

Grid Sensitivity Options

High Speed Aerodynamics, Long Beach

	Finite-difference	Analytical
Volume grid sensitivity	Need step-size	Using ADIFOR
Surface grid sensitivity	Need step-size	Using ADIFOR

Cost, Accuracy →

Cost, Accuracy ↑

Cost Functions

TLNS3D-Adjoint currently supports the following cost functions. In addition to finding the gradients of drag, D, lift, L, and moments, it can also find the gradient of D/L or that of $D + w(L - L^*)^2$, where L^* is the desired lift and w is a weighting factor. Note that for each cost function, a separate adjoint solution has to be obtained using ATLNS3D.

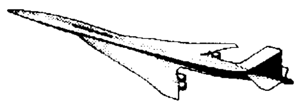

Cost Functions

- Drag, D
- Lift, L
- D/L
- $D + w(L - L^*)^2$
- Moments, M_x, M_y, M_z

Computer Platforms

TLNS3D-Adjoint has been tested on Cray C-90 serial, SGI Origin 2000 parallel, and HP Exemplar parallel computers. In the parallel mode, it uses the Message Passing Interface (MPI) protocols to communicate among processors. The MPI version of TLNS3D-Adjoint has also been successfully executed on a cluster of HP workstations.

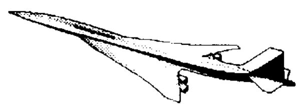

Computer Platforms

High Speed Aerodynamics, Long Beach

- Serial Machines
  - Cray C-90
- Parallel Machines
  - SGI Origin 2000
  - HP Exemplar
- Workstations
  - HP Cluster

Gradients of Drag/Lift

Gradients of D/L obtained using TLNS3D-Adjoint, for 26 typical design variables used in the shape optimization of an HSCT, are compared with those obtained using finite-differences. The first 18 design variables were located on the wing and the rest on the fuselage. These design variables included twist, camber and thickness of the wing, cross-sectional shape and camber of the fuselage and position of the wing on the fuselage. The finite-difference gradients were computed, using CFL3D flow analysis code, with carefully selected step-sizes and converged solutions. The grids, corresponding to the change in each design variable, were obtained using the grid perturbation code, FlexMesh.

For the adjoint gradient, both TLNS3D and ATLNS3D solutions were converged by over six orders of magnitude. The grid sensitivities corresponding to the change in each design variable were obtained by finite-differences. The perturbed grids were obtained using CSCMDO.

In spite of the many differences, from flow solvers to grid perturbation schemes, the gradients computed using the adjoint and the finite-difference methods agree well.

Gradients of Drag/Lift

High Speed Aerodynamics, Long Beach

TCA Wing/Body, Grid: 193x33x73, $M_\infty = 2.4$, $\alpha = 3.5°$

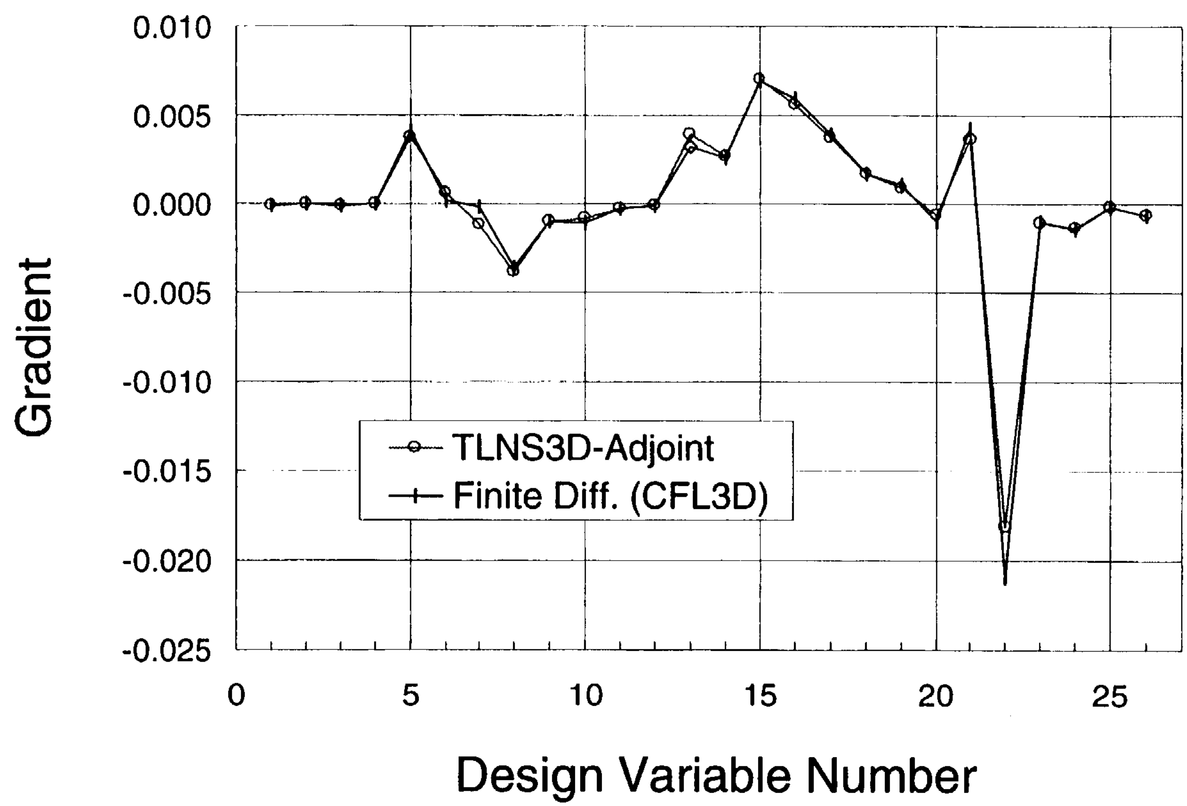

TCA Wing/Body Optimization

The first application presented is the optimization of the TCA wing/body configuration at $M = 2.4$. The objective was to minimize the ratio of drag-to-lift (D/L) at a specified lift. The design-space was made up of 400 geometric functions and the angle-of-attack. These geometric functions included twist, camber, thickness, etc., of the wing, cross-sectional shape, camber, etc., of the fuselage, and position of the wing on the fuselage. In addition to the lift, 54 geometric parameters of the configuration were constrained. These constraints were obtained from the TCA Configuration Description Document.

TCA Wing/Body Optimization

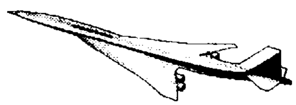

High Speed Aerodynamics, Long Beach

- Wing/body at $M_\infty = 2.4$
- Minimize D/L
- Design variables
  - 400 geometric functions
  - Angle-of-attack
- Constraints
  - 54 geometric constraints
  - Lift

BOEING

Convergence History

The convergence of the analysis (Euler) and the adjoint equations, for the TCA wing/body configuration at M=2.4, are shown. For a grid that has 193x33x73 points in the chordwise, normal, and spanwise directions, respectively, the residuals of both the systems decreased by over six orders of magnitude in about 200 iterations. The convergence rates of the analysis and adjoint equations are comparable. Note that, the solver parameters like the CFL number, the Runge-Kutta coefficients, and the dissipation coefficients, used for the solution of both these systems, are identical.

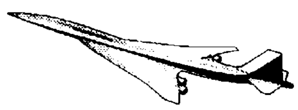

Convergence History

High Speed Aerodynamics, Long Beach

TCA Wing/Body, Grid: 193x33x73, $M_\infty = 2.4$, $\alpha = 3.5°$

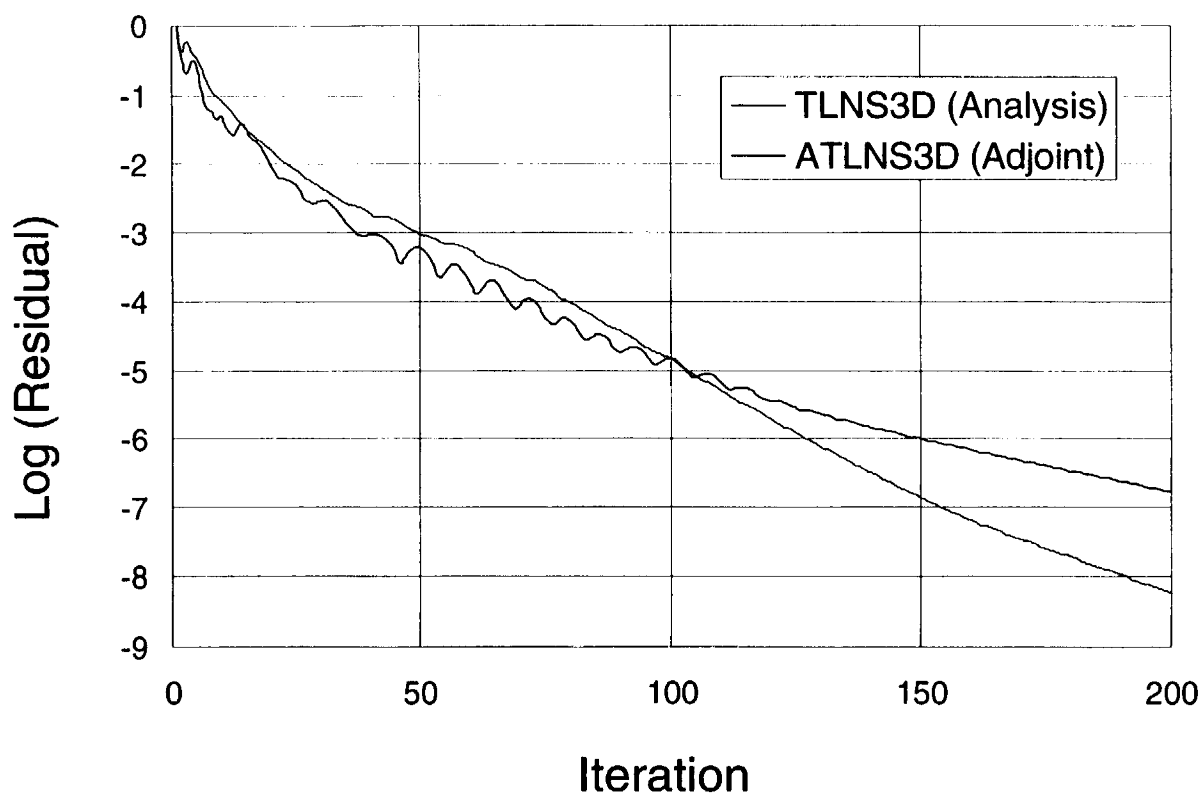

Optimization History

The optimization history shows that the objective function decreased by about 5% in 24 design iteration. The drag decreased by about 5 counts and the lift constraint was satisfied. Note that the drag shown is only the pressure drag. In this optimization, only the surface grid sensitivities were used to compute the gradients. These sensitivities were computed analytically by differentiating the tools for surface grid perturbation using ADIFOR (Automatic Differentiation of FORTRAN)

An identical optimization exercise was performed, using the sensitivity equations method*. The sensitivity equations were obtained by automatically differentiating the CFL3D analysis code using ADIFOR. In this study, the analytical volume grid sensitivities were used to compute the gradients. In spite of these differences, the final design was similar in shape and performance to the one obtained using TLNS3D-Adjoint with surface grid sensitivities. This indicates that, in shape optimization problems, surface grid sensitivities are sufficient to improve the performance of configurations. Whether this argument holds true for more complex wing/body/nacelle/diverter configurations is yet to be demonstrated.

Computing only surface grid sensitivities requires considerably less CPU hours than computing volume grid sensitivities, especially for large number of design variables. Typically, the cost of computing volume grid sensitivities, using the geometry and grid perturbation tools at Boeing, Long Beach, is about twice that of computing only the surface grid sensitivities.

* Technology Development for a Multipoint Optimization Process for an HSCT, Robert Narducci, et al., The Boeing Company, Phantom Works - Long Beach, NASA / Industry HSR Airframe Review, Anaheim, CA, Feb 8-11, 1999.

Optimization History

High Speed Aerodynamics, Long Beach

TCA Wing/Body, Grid: 193x33x73, $M_\infty = 2.4$
401 Design Variables, 55 Constraints

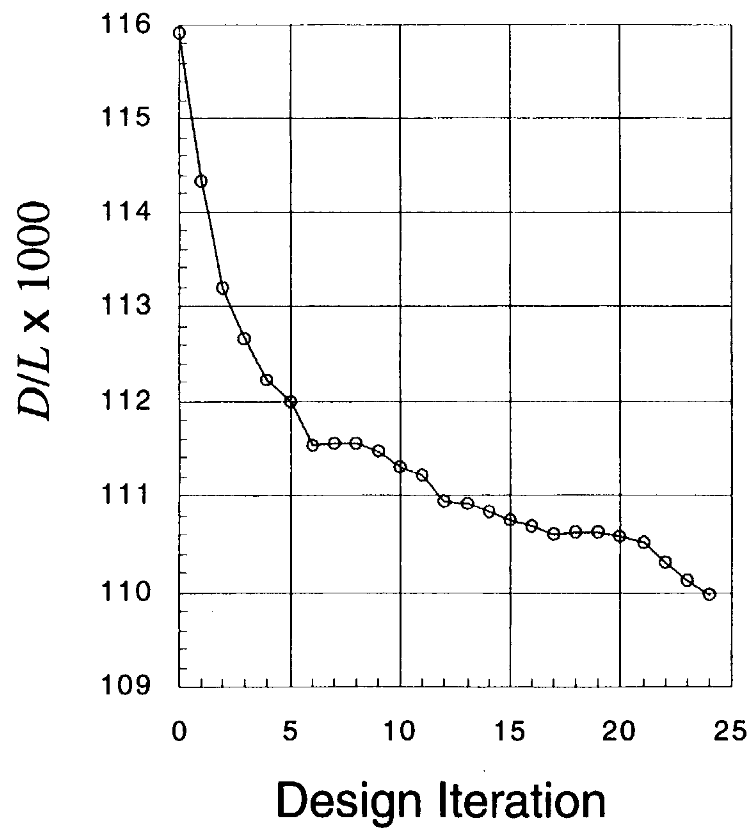

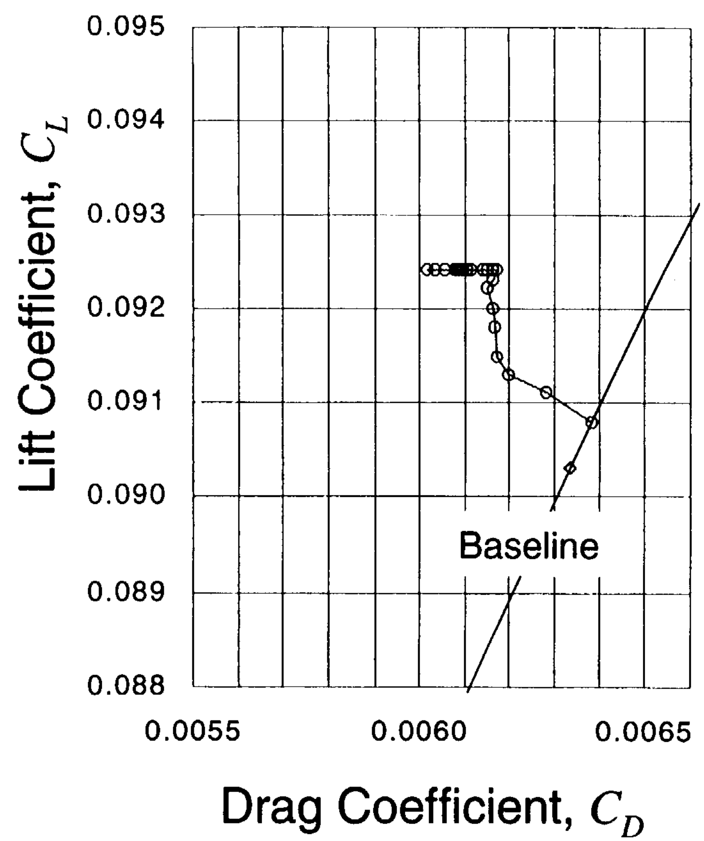

CPU Time / Memory on Cray C-90

This wing/body optimization was performed on von Neumann, the Cray C-90 at NAS. The CPU time and the memory, required to obtain a converged solution, for both TLNS3D (analysis) and ATLNS3D (adjoint) codes, are comparable. The gradient module, GTLNS3D, required about 30 seconds to compute the gradient of each design variable. Therefore, the CPU time for computing the gradients of all the design variables exceeded 3 hours. Yet, the total cost of 24 design iterations was only 136 hours, about 15 times less than an optimization using the finite-difference method.

Of the 30 seconds used by GTLNS3D, 28 were spent in computing the analytical surface grid sensitivity of each design variable. If the volume grid sensitivities were used, the computational cost would have doubled.

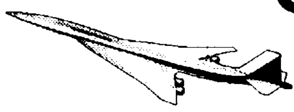

CPU Time / Memory on Cray C-90

High Speed Aerodynamics, Long Beach

TCA Wing/Body, Grid: 193x33x73, $M_\infty = 2.4$

TLNS3D	: 22 minutes / 35 mw
ATLNS3D	: 25 minutes / 39 mw
GTLNS3D	: 30 seconds per DV / 33 mw
1 Design Iteration	: 5 hours and 40 minutes
24 Design Iterations	: 136 hours*

* Estimated CPU time for finite-difference method > 2000 hours

TCA Wing/Body/Nacelle/Diverter Optimization

The second application presented is the optimization of the TCA wing/body/nacelle/diverter configuration at $M = 2.4$. The objective was to minimize the pressure drag at a specified lift. The design variables were 319 geometric functions and the angle-of-attack. These geometric functions included twist, camber, thickness, etc., of the wing, cross-sectional shape, camber, etc., of the fuselage, and nacelle shear variables. In addition to the lift, 84 geometric parameters of the configuration were constrained. These constraints were obtained from the TCA Configuration Description Document.

TCA Wing/Body/Nacelle/Diverter Optimization

High Speed Aerodynamics, Long Beach

- Wing/body/nacelle/diverter at $M_\infty = 2.4$
- Minimize pressure drag
- Design variables
  - 319 geometric functions including nacelle shear
  - Angle-of-attack
- Constraints
  - 84 geometric constraints
  - Lift

Optimization History

This TCA wing/body/nacelle/diverter configuration was modeled using a 19-block patched grid. The starting point of the optimization was a previously optimized configuration called TCA Cycle 3. Starting with the TCA baseline, the Cycle 3 configuration was obtained by a sequence of optimizations that included both finite-difference and adjoint methods*. The optimization history shows that, the decrease in drag from Cycle 3 is about 2 counts and the lift constraint is satisfied. Overall, this configuration has about 7.3 counts less drag than the baseline. Note that the drag shown is only the pressure drag. In this optimization, volume grid sensitivities were obtained using finite-differences.

* Technology Development for a Multipoint Optimization Process for an HSCT, Robert Narducci and et al., The Boeing Company, Phantom Works - Long Beach, NASA / Industry HSR Airframe Review, Anaheim, CA, Feb 8-11, 1999.

Optimization History

High Speed Aerodynamics, Long Beach

TCA W/B/N/D, 19 blocks, 400K points, $M_\infty = 2.4$
320 Design Variables, 85 Constraints

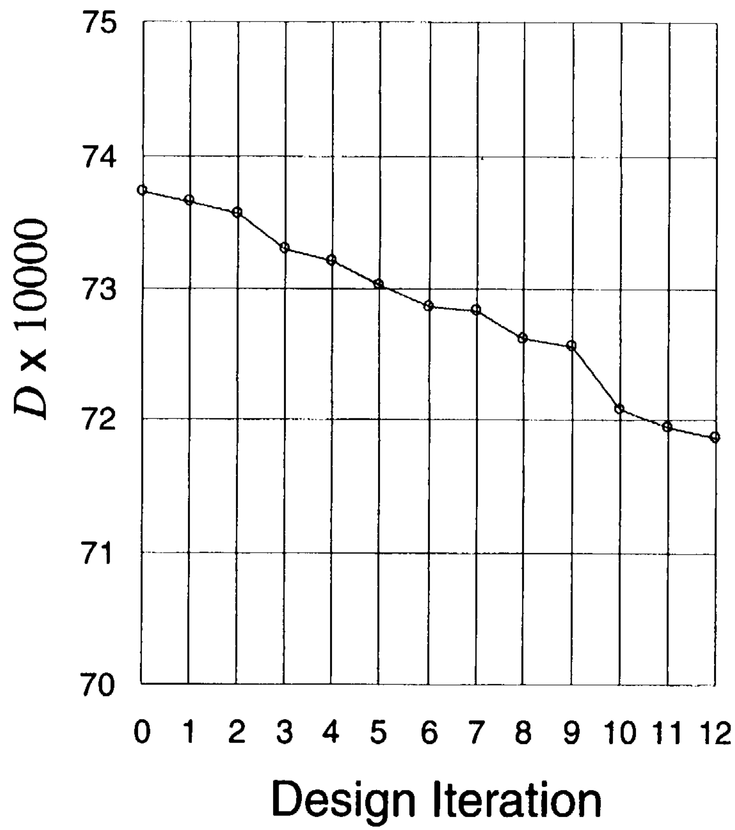

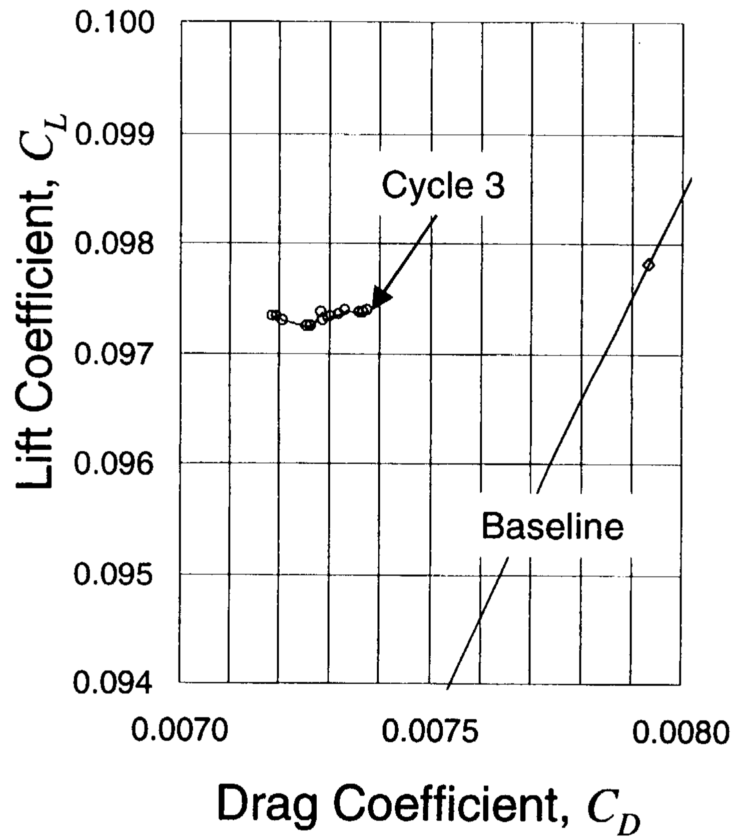

TCA Leading-Edge/Flaps Optimization

In the third application shown here, the TCA wing/body/flaps configuration at M=0.9 is optimized for minimum pressure drag at the cruise lift. The design variables included 22 leading-edge thickness and droop function, 5 leading and trailing-edge flaps, and the angle-of-attack. In addition to the lift, 55 leading-edge spar-thickness constraints were also imposed.

TCA Leading-Edge/Flaps Optimization

High Speed Aerodynamics, Long Beach

- Wing/body/flaps at $M_\infty = 0.9$
- Minimize pressure drag
- Design variables
  - 22 Leading-edge shape functions
  - 5 Leading- and trailing-edge flaps
  - Angle-of-attack
- Constraints
  - 55 Leading-edge spar thickness
  - Lift

Convergence History

The convergence of the analysis (Euler) and the adjoint equations, for the TCA wing/body/flaps configuration at M=0.9, are shown. For a single-block grid with 113x33x89 points in the chordwise, normal, and spanwise directions, respectively, the residuals of both the systems decreased by over 4 orders of magnitude in about 500 iterations. The convergence rates of the analysis and adjoint equations are comparable. Note that, the solver parameters like the CFL number, the Runge-Kutta coefficients, and the dissipation coefficients, used for the solution of for both these systems, are identical.

Convergence History

High Speed Aerodynamics, Long Beach

Wing/Body/Flaps, Grid: 113x33x89, $M_\infty = 0.9$, $\alpha = 4.5°$

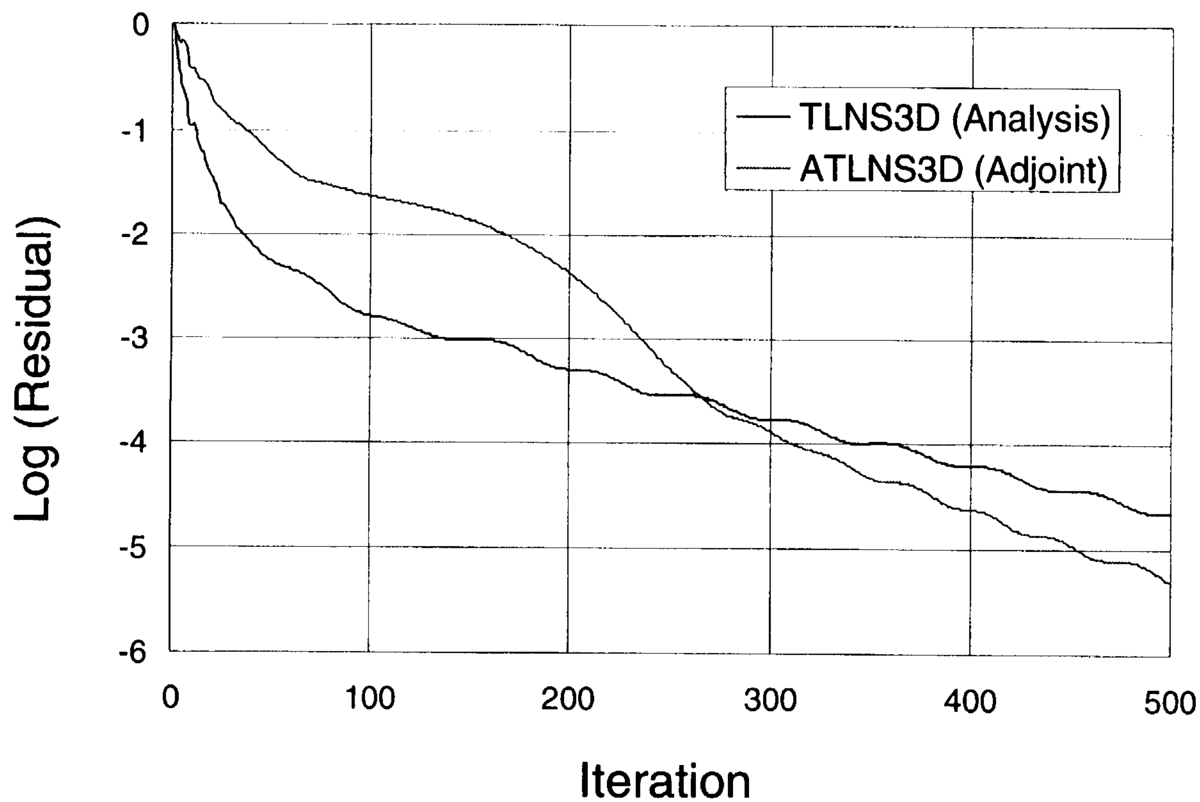

Optimization History

The starting point of this optimization was the TCA baseline with optimized flaps. The optimization history shows that the decrease in drag from the starting point is about 2.5 counts and the lift constraint is satisfied. Note that the drag shown is only the pressure drag. Volume grid sensitivities obtained using finite-differences were used in this optimization.

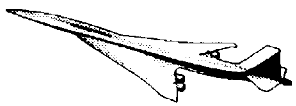

Optimization History

High Speed Aerodynamics, Long Beach

Wing/Body/Flaps, Grid: 113x33x89, $M_\infty = 0.9$
27 Design Variables, 56 Constraints

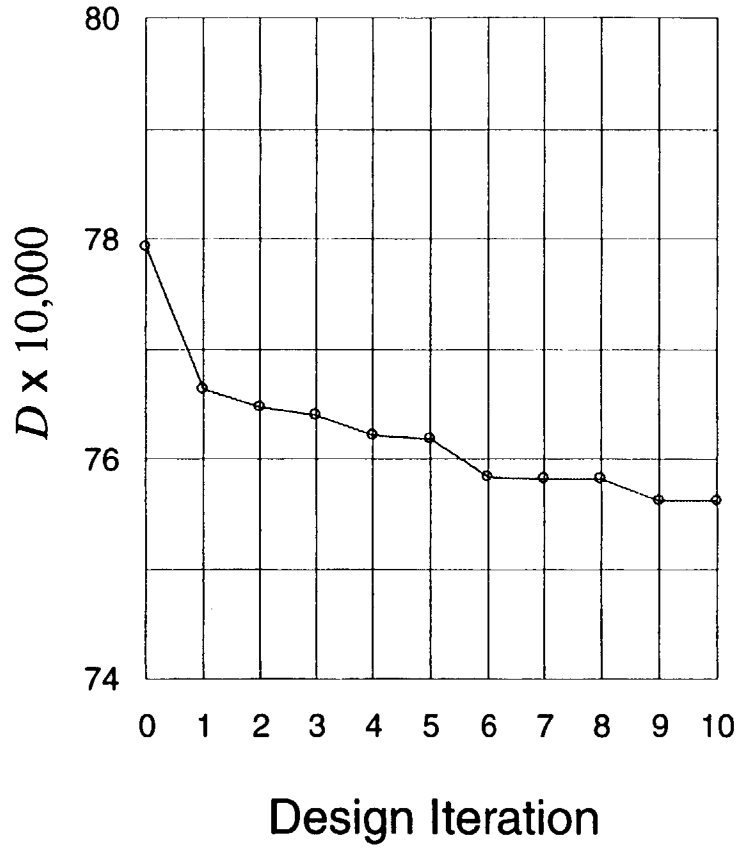

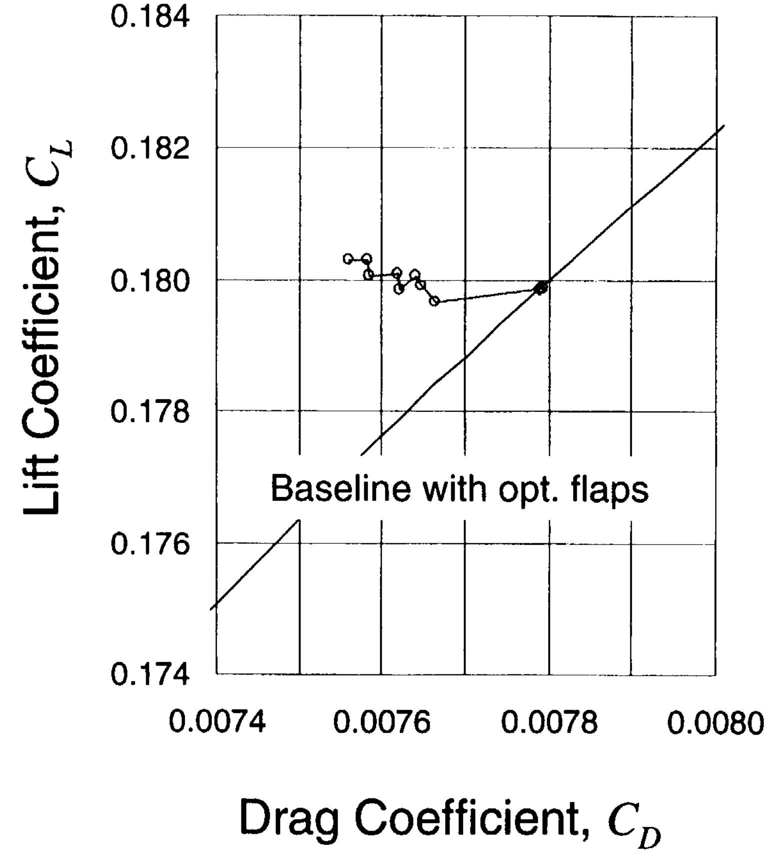

Wall Clock Time / Memory on SGI Origin 2000

The leading-edge/flaps optimization was performed on Turing, the SGI Origin-2000 at NAS, using 14 processors with the parallel versions of TLNS3D (analysis) and ATLNS3D (adjoint) codes. The CPU time and the memory required to obtain a converged solution, for both TLNS3D and ATLNS3D codes, are comparable. GTLNS3D was executed on all 14 processors to obtain the gradients of 14 design variables at a time. The total cost of the 10 design iterations was only 30 hours, about 2.5 times less than an optimization using the finite-difference method. This factor is not as large as the previous wing/body optimization, since the number of design variables is considerably fewer in this case.

Wall Clock Time / Memory on SGI Origin 2000

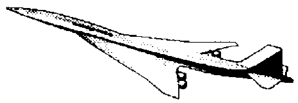

High Speed Aerodynamics, Long Beach

Wing/Body/Flaps, Grid: 113x33x89, $M_\infty = 0.9$

No. of Processors	: 14
TLNS3D	: 27 minutes / 29 mbytes
ATLNS3D	: 30 minutes / 31 mbytes
GTLNS3D	: 1 minute for 27 DVs / 23 mbytes
1 Design Iteration	: 3 hours
10 Design Iterations	: 30 hours*

* Estimated time for finite-difference method > 80 hours

TCA Multipoint Optimization

The final application shown here, is a multipoint optimization of the TCA wing/body/flaps configuration at Mach 0.9 and Mach 2.4. The objective was to minimize the weighted sum of the pressure drags at the two Mach numbers. The design variables included 22 leading-edge thickness and droop function, the 5 leading and trailing-edge flaps and the angle-of-attack. While the flaps were optimized only at Mach 0.9, the leading-edge thickness and droop functions, and the angle-of-attack were optimized at both the Mach numbers. Lift and 55 leading-edge spar thickness were constrained.

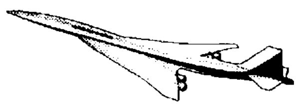

TCA Multipoint Optimization

- Wing/body/flaps at $M_\infty = 0.9$
- Wing/body at $M_\infty = 2.4$
- Minimize $C_{Dp\_2.4} + 0.3\, C_{Dp\_0.9}$
- Design variables
  - 22 Leading-edge shape functions ($M_\infty = 0.9, 2.4$)
  - 5 Leading- and trailing-edge flaps ($M_\infty = 0.9$)
  - Angle-of-attack
- Constraints
  - 55 Leading-edge spar thickness
  - Lift

TCA Multipoint Optimization

The analysis of the wing/body configurations of the baseline TCA is compared with the ones obtained from the single point optimization at Mach 0.9 and the multipoint optimization at Mach 0.9 and 2.4. While the single point optimization reduced the drag at Mach 0.9 by about 2.5 counts, the drag at Mach 2.4 went up by about 1.5 counts. In the multipoint optimization, the drag at Mach 0.9 was reduced by about 1.5 counts, without any penalty at Mach 2.4.

TCA Multipoint Optimization

High Speed Aerodynamics, Long Beach

Drag Polars of W/B Configurations Resulting from Single and Multipoint Optimizations

M_∞=2.4

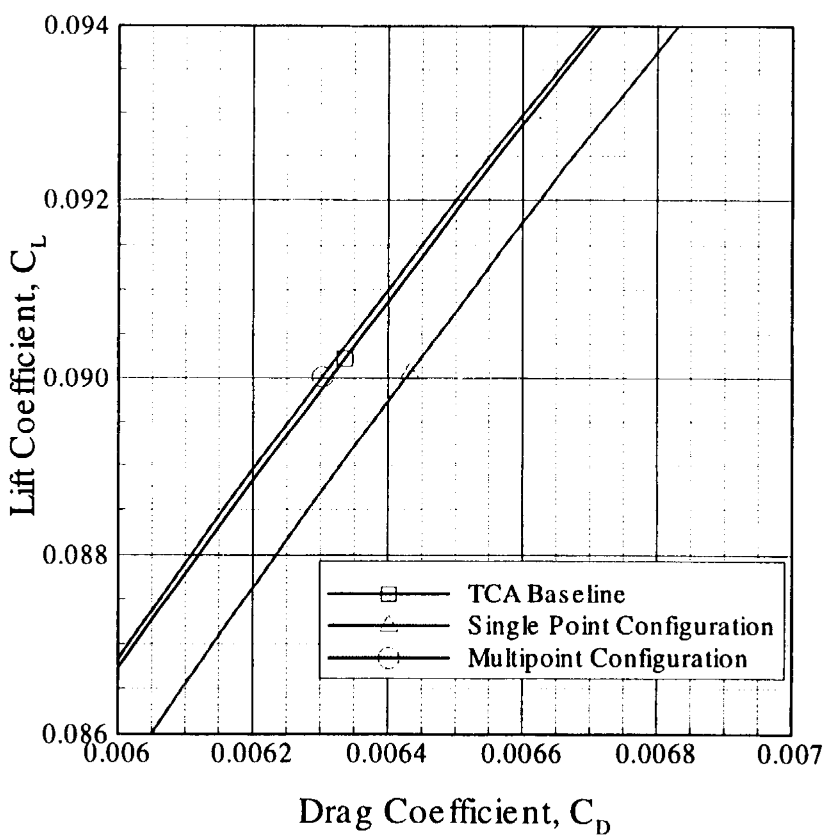

M_∞=0.9

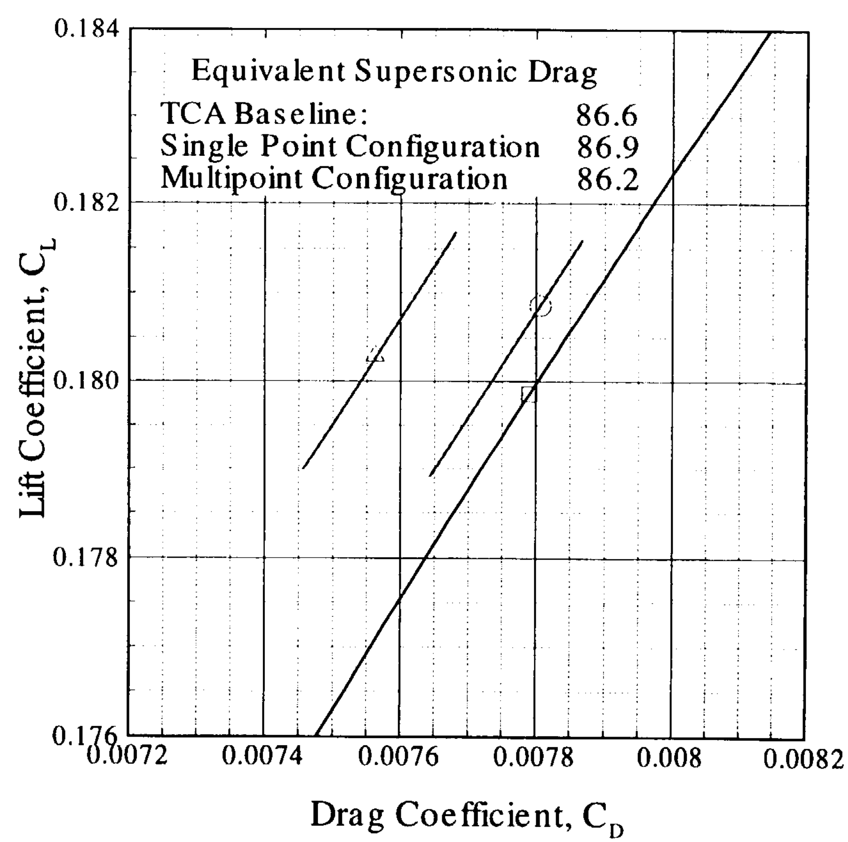

Technology Transfer

Due to the efficiency and versatility of TLNS3D-Adjoint in computing aerodynamic gradients, it is being used in other Boeing programs. It has been successfully used to improve the performance of a space vehicle. This lifting-body type configuration was optimized at Mach 1.2. The cost function was a function of the pitching moment.

Technology Transfer

High Speed Aerodynamics, Long Beach

- This technology being used in other Boeing programs
- TLNS3D-Adjoint successfully used to improve performance of a space vehicle
  - Wing/body/tail at $M_\infty = 1.2$
  - Cost function: Function of pitching moment

Summary

The development of TLNS3D-Adjoint (Euler) is complete. It computes the aerodynamic gradients for large number of design variables, both accurately and efficiently. The memory requirements of the adjoint (ATLNS3D) and the gradient (GTLNS3D) modules are comparable to that of the analysis (TLNS3D) module. By using TLNS3D-Adjoint in AEROSHOP, significant reduction in design cycle-time has been realized.

TLNS3D-Adjoint has been applied to several aerodynamic shape optimization problems at supersonic and subsonic Mach numbers. It has been applied to HSR as well as non-HSR problems.

Summary

- Completed development of TLNS3D-Adjoint (Euler)
  - Computes aerodynamic gradients accurately and efficiently
  - Can use large no. of design variables (~400)
  - Memory requirement comparable to analysis problem
  - Significantly reduced design cycle-time
- Successfully applied TLNS3D-Adjoint to several HSR aerodynamic shape optimization problems
- Successfully applied this code to a non-HSR problem

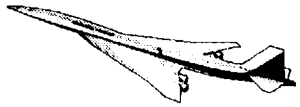

Progress Towards Viscous Design Optimization Using Automatic Differentiation

P. Sundaram and Shreekant Agrawal
Configuration Aerodynamics
Phantom Works, The Boeing Company
Long Beach, CA

High Speed Research Airframe Review
Anaheim, California
February 8-11, 1999

BOEING

Acknowledgment

Several people helped during the course of this investigation. Arthur Taylor of Old Dominion University was stationed at Boeing Long Beach from January to June 1998 under a subcontract through Eagle Aeronautics, a small disadvantaged business located at Hampton, Virginia. He was primarily assisting in the development of the ADIFOR versions of the BPW-LB grid tools. Alan Carle of Rice University was instrumental in developing the ADJIFOR version of CFL3D code as part of a subcontract to Rice University.

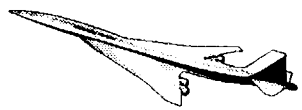

Acknowledgment

High Speed Aerodynamics, Long Beach

- James Hager, BPW-Long Beach
  - Assistance in ADIFOR-ing grid tools and linking with optimizer
- Alan Carle, Rice University
  - Expert help and developing the ADJIFOR-ed CFL3D code
- Arthur Taylor, Old Dominion University
  - CFL3Dhp.ADII code and ADIFOR-ed grid tools
- Larry Green, MDO Branch, NASA Langley
  - Training in ADIFOR and encouraging us in this area

BOEING

Terminology

ADIFOR and ADJIFOR are preprocessors used to obtain the computer generated derivative versions of FORTRAN function codes. ADIFOR was originally developed by a team of researchers from Argonne National Laboratory and Rice University. They include Chris Bischof, and Paul Hovland of Argonne National Laboratory and Alan Carle of Rice University. More recently, the ADJIFOR development is actively pursued by Alan Carle and Mike Fagan of Rice University. Although ADJIFOR and reverse mode ADIFOR are interchangeably used in the present context, it is important to note the difference that ADJIFOR is specifically developed for iterative solvers while reverse mode ADIFOR is applicable for a more general class of problems.

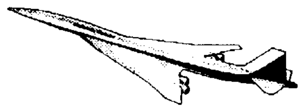

Terminology

High Speed Aerodynamics, Long Beach

- ADIFOR
  - Preprocessor - when applied to <u>any</u> FORTRAN function code outputs a <u>computer generated</u> function+derivative FORTRAN code
- ADJIFOR
  - Reverse mode ADIFOR preprocessor that generates the <u>adjoint</u> code for iterative function code in FORTRAN

BOEING

Background

Design cycle time in a nonlinear shape optimization process is mainly dependent on the time taken for the objective function sensitivity calculation. Considerable effort has been spent in the past few years to develop efficient techniques for calculating the sensitivities. Primary among them is the method of deriving the adjoints by posing the original continuous form of the problem as a calculus of variation problem. This requires long and tedious analytical derivations and hand-differentiation of the underlying partial differential equations. The adjoint variables for the Euler equations already derived and codes based on this are available. For Navier-Stokes equations, the theory of adjoints is much more complicated and becomes almost intractable. More so, for different turbulence models the hand-differentiation method of adjoints is impractical.

The ADIFOR-based methods, on the other hand, are straight-forward and are applied directly to the differential form of the equations of motion already available in the form of FORTRAN codes. The resulting computer-generated differentiated form of the existing function computer codes provide accurate analytical sensitivities. Also, the ADIFOR and ADJIFOR application procedures are the same for both the Euler and Navier-Stokes codes. This, it can be seen that the automated procedure for generating adjoint codes using ADJIFOR has several advantages over the hand-differentiated adjoint codes.

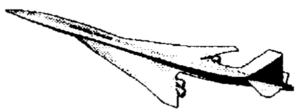

Background

High Speed Aerodynamics, Long Beach

- Fast and accurate sensitivities calculation is vital for cycle time reduction in nonlinear shape optimization
- Hand-differentiated adjoint code for N-S codes takes too long
- ADIFOR 2.0 from Argonne National Lab. and Rice University can provide accurate sensitivities of any FORTRAN code
- Alliance between LaRC, BPW-Long Beach, and Rice to advance the ADIFOR technology for shape optimizations

BOEING

Motivation

The TCA Cycle 2 supersonic cruise-point optimization for the wing/body/nacelle/diverter configuration performed under the 1997 HSR Configuration Aerodynamics task has provided the best possible Euler design at that time. Several wind-tunnel tests to validate the optimum design have since yielded significant confidence and as much confusion about the discrepancies between the predicted nonlinear optimized geometry performance predictions and wind-tunnel test data. Also, the Technology Readiness Level (TRL) obtained from these designs is not adequate and more nonlinear optimization benefits have to be realized and the issues such as the off-design performance penalties must be evaluated. Further, the technology benefits assumed by the TI team for the linear design for the full aircraft configuration must be realized. These questions can only be answered by performing a full configuration multipoint optimization.

The details of the flow-field in these Euler designs did not include viscous effects and particularly the viscous interactions that are prevalent in the region between the nacelles. It is expected that the inclusion of these details will produce a more realistic representation of the local flow at the correct flight conditions. Although it is understood that it is an expensive proposition to perform Navier-Stokes optimization of the full configuration, it is also necessary to obtain all the available performance benefits in a realistic flow-field. Also, the Navier-Stokes design might produce a more desirable smoother geometry compared to the earlier Euler designs. The application of several technology advancements in the area of gradient calculations combined with the parallel processing might render this ambitious undertaking realizable. With this motivation, several new technologies are used in this task.

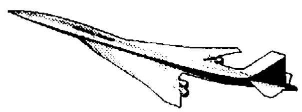

Motivation

- Viscous effects in shape optimization is expected to:
  - Provide more accurate wing/nacelle interference; enable design of wing and nacelles with less installation drag
  - Correctly model the leading-edge and hinge-line flow separation for transonic cruise configurations with flaps
  - Account for the boundary layer growth on the aft-body that might provide an aft-body shape with lower drag
  - Enable designs at the appropriate Reynolds number

Outline

The outline of the presentation is given in this chart.

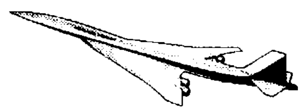

Outline

- Objective
- Approach
- Automatic differentiation using ADIFOR and ADJIFOR
- Parallel processing in ADIFOR applications
- Shape optimization using ADIFOR/ADJIFOR sensitivities
- Results
  - TCA W/B Euler design-ADIFOR technology demonstrator
  - N-S flow sensitivities using ADJIFOR-ed CFL3D
- Conclusion and Future Work

BOEING

Objective

This chart outlines the objectives of the present task

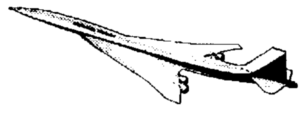

Objective

High Speed Aerodynamics, Long Beach

- Develop technology and tools required for efficient nonlinear viscous optimization using Navier-Stokes solver
- Apply the technology to full configuration design

BOEING

Approach

The nonlinear shape optimization scheme used at BPW-LB requires flow sensitivities of an objective function to drive the optimizer. The approach chosen by the BPW-LB team is to obtain the viscous flow sensitivities using the automatic differentiation (AD) approach. The CFL3D Navier-Stokes equations solver is the chosen flow solver. Parallel processing is needed not only to yield the large computer resources required, but also for achieving fast turn-around time of the design cycles.

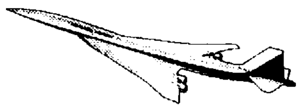

Approach

- Apply ADIFOR to obtain computer generated sensitivity codes used in nonlinear shape optimization at BPW-LB
- Validate ADIFOR / ADJIFOR-based codes for calculating accurate grid and flow sensitivities
- Perform HSCT shape optimization with large number of design variables using CFL3D Euler and N-S sensitivities
- Utilize parallel processing for fast turn-around time

BOEING

Automatic Differentiation Using ADIFOR

One of the major accomplishments in the area of application software technology that has happened in the last few years is the development of automatic differentiation tools. Automatic differentiation has a large spectrum of applications for problems arising in numerical weather prediction, nuclear engineering, and numerical optimization. Several tools have been developed for automatic differentiation, but only a very few have sustained the times and gone farther to render them usable. The Automatic DIfferentiation of FORtran (ADIFOR) software has been under development since the early 90's jointly at Argonne National Laboratory and Rice University with the support of DOE and NASA.

The ADIFOR preprocessor augments a FORTRAN function code and generates another FORTRAN program that can compute both the original function and gradients. The preprocessor generates analytical chain-rule differentiation based on the user-specified independent and dependent variables. Since the differentiation is analytical, no step-size is required which is a major advantage compared to the divided-difference method of calculating gradients. Since ADIFOR performs analytical differentiation, it can use single-precision arithmetic to reduce the memory requirement on some computers. Because ADIFOR is memory-intensive, this property is very attractive. Also, ADIFOR can be easily applied to most FORTRAN code of any size. Last, but not the least, it is a software available open to public.

Several codes have been ADIFOR-processed to obtain sensitivities. These codes have varied sizes and applications. The ADIFOR software does not require large user intervention from function code to derivative code.

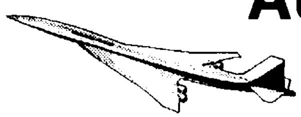

Automatic Differentiation Using ADIFOR

High Speed Aerodynamics, Long Beach

- Augments FORTRAN code to generate a derivative code
- Accurate analytical sensitivity calculations
  - Uses chain-rule differentiation
  - No step-size (an issue in finite-difference approach)
  - Can use single-precision to reduce memory requirement
- Easily applied to any FORTRAN code
- ADIFOR is available in public domain

BOEING

Forward Mode ADIFOR

In the forward mode ADIFOR, or simply ADIFOR, the program flow maintains the function program flow direction and calculates the directional derivative of the dependent variables w.r.t. the independent variables.

The main drawback of the ADIFOR software is the large computer resource requirement compared to some of the state-of-the-art sensitivity calculation methods such as the hand-differentiated adjoint codes for sensitivity determination. The memory and CPU time for ADIFOR-processed code are directly proportional to the number of design variables used. As a result, the computer resource requirements for ADIFOR derivative code can quickly become staggering for large problems with hundreds of design variables. However, significant developments are taking place to allay these concerns. The reverse-mode ADIFOR is becoming practical for large problems. These discussions will be alluded to later in the presentation.

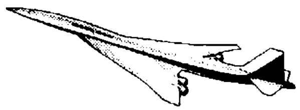

Forward Mode ADIFOR

High Speed Aerodynamics, Long Beach

- Given the shape function *X*, and seed matrix, ***R*** = d*X*/dv, with *p* columns (indep. var.) and *q* rows (dep. var.)

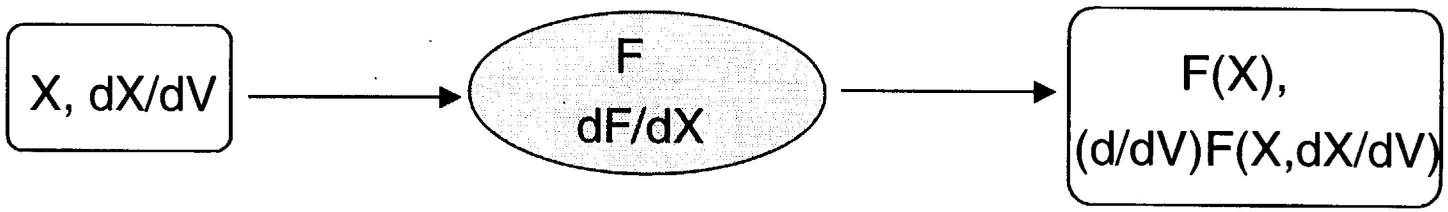

<u>Issues</u>

- Program memory requirement increases with number of DV
- CPU time for derivatives-at best (*nDV*+1) times CPU for function evaluation

Forward Mode ADIFOR in Shape Optimization

The application of ADIFOR for a sequence of function codes is shown in this chart. Since gradient calculation is a linear operation, it can be mathematically represented by matrix multiplication. The gradient information is passed between codes through a sequence of matrix multiplication of a Seed Matrix (SM). The SM consists of p rows and q columns where p and q are the independent and dependent variables, respectively. The BPW-LB grid tools have several components. They all have been ADIFOR-ed. As the seed matrix passes through each code, it gets accumulated with the gradient information for that segment of the function.

Forward Mode ADIFOR in Shape Optimization

High Speed Aerodynamics, Long Beach

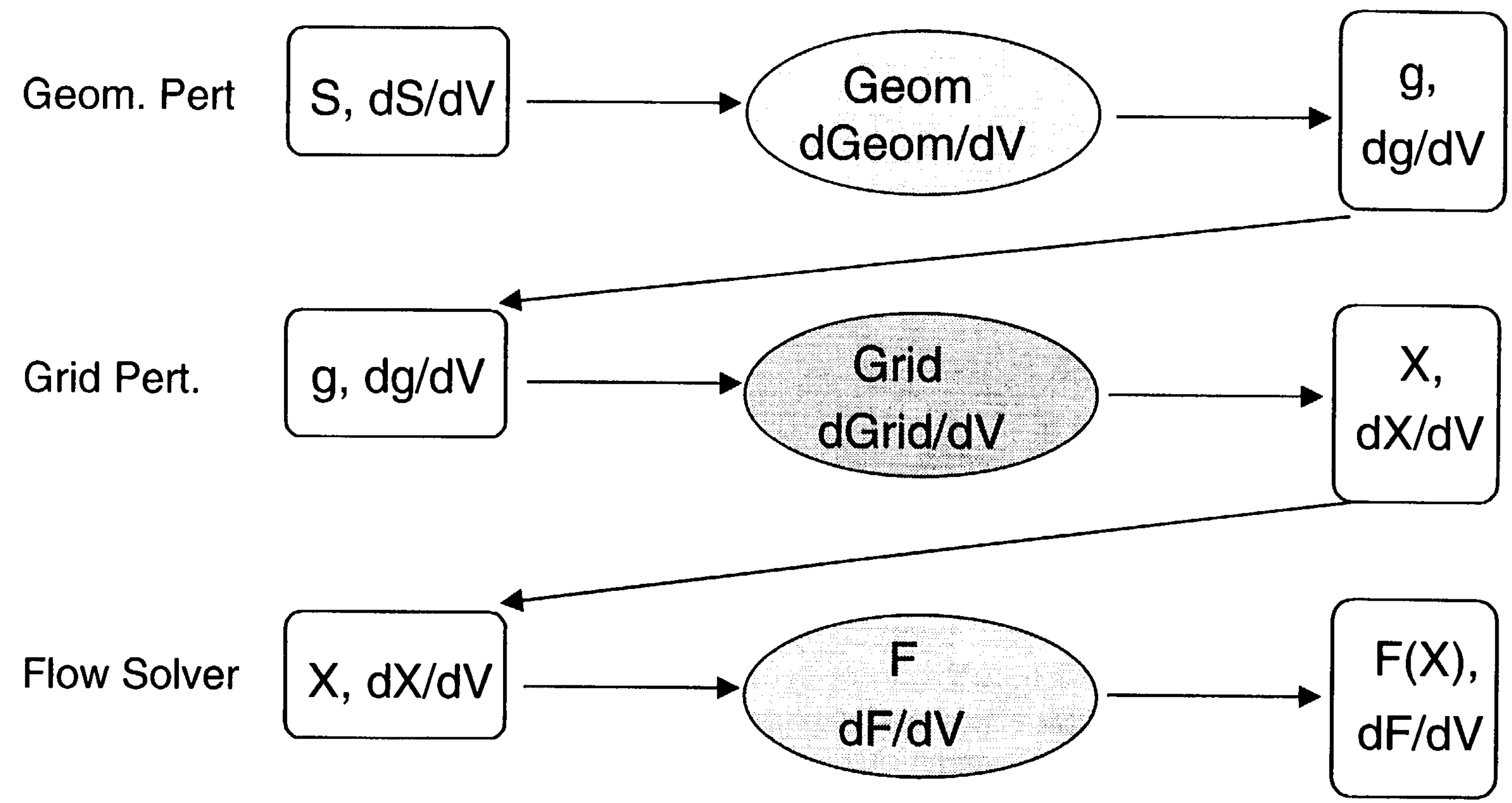

$$F' = J_s\, J_{gr}\, J_{ge} V$$

BOEING

ADIFOR and F-D Objective-Function (D/L) Sensitivity

This chart shows the comparison of the ADIFOR sensitivities of the TCA baseline for the (D/L) objective function with the finite-difference sensitivities. The finite-difference sensitivities have been computed with a careful control of step size and a detailed step-size convergence study. The finite-difference study was done on the CRAY C90 system in double precision. In contrast, the ADIFOR sensitivities have been obtained on the SGI Origin 2000 system in single precision. The comparison between the two is very good. When double precision was used for ADIFOR sensitivity calculation, the minor discrepancies that are seen had completely disappeared.

ADIFOR and F-D Objective-Function (D/L) Sensitivity

High Speed Aerodynamics, Long Beach

TCA Wing/Body, FlexMesh, CFL3D, Euler, M_∞=2.4, α=3.518°, C_{Dv}=41.35 cts.

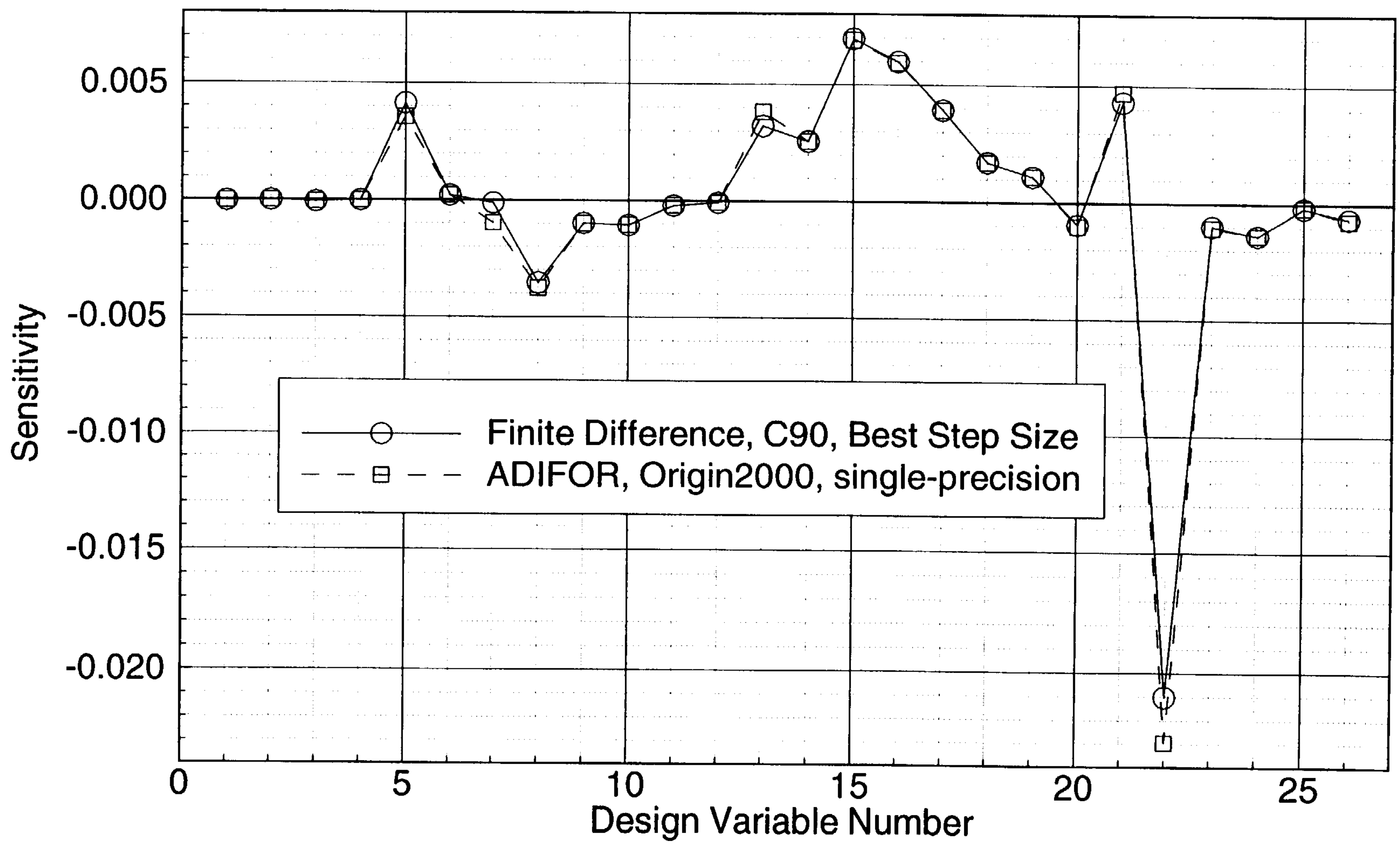

BOEING

Reverse Mode ADIFOR

The reverse mode ADIFOR uses adjoint principles to compute the gradients. The function and gradient calculation steps are reversed and the derivatives are accumulated from the output to the input. In this mode, the gradient of the output for unit value of the input is computed. For iterative solution processes, the intermediate steps have to be stored to generate the adjoints. As a result, large storage space is required for adjoint solutions of iterated solvers. If the number of dependent variables is much smaller than the independent variables, the reverse mode is significantly faster. In CFL3D, if $p > 25$, the reverse mode is faster. For shape design problems with large number of design variables, the reverse mode method of calculating the gradients is the best choice.

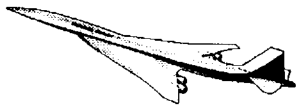

Reverse Mode ADIFOR

High Speed Aerodynamics, Long Beach

- Uses Adjoint principles to compute gradients
- Accumulates derivatives from the output to the input
- Reverses the program flow and stores intermediate values that nonlinearly impact final result
  - Need huge storage space for large codes
- If $q << p$, reverse mode is significantly faster
- In CFL3D,
  - If $p < 25$, use forward mode

CPU Time for Forward and Reverse Mode ADIFOR

Geom1, QGRID, and FlexMesh are the standard BPW-LB grid tools used in the design process. Geom1 is the geometry kernel that modifies the baseline surface points based on a set of design variables; QGRID uses surface point distribution and generates the surface grid; and FlexMesh perturbs the baseline volume grid for a given surface grid modifications.

The chart below shows the CPU time comparison for computing the gradients using forward and reverse mode ADIFOR. Note that the reverse mode ADIFOR CPU times are for 401 DVs. The advantage of using the reverse mode ADIFOR is very clear.

CPU Time for Forward and Reverse Mode ADIFOR

High Speed Aerodynamics, Long Beach

	CPU Time (seconds)	
	Reverse-mode (401 DV)	Forward-mode (1 DV)
Geom1	17.2	6.1
QGRID	135	5.4
FlexMesh	423	143

ADJIFOR for Iterative Solvers

The mathematical theory of the application of reverse mode ADIFOR approach for iterated solvers is described elsewhere in the literature. However, it is important to point out here that the adjoints for the iterated solution schemes can use a simpler approach, denoted as ADJIFOR, of avoiding the storage of all the forward mode iterations to evaluate the adjoint gradients typically used in reverse mode ADIFOR. In the ADJIFOR appraoch, the converged solution to the problem at a given point is first obtained and the logged iterated information for the last few cycles is used to construct the adjoint variable derivatives. This derivative information is used for all the adjoint iterations to calculate the objective function gradient information. Since the number of iterations for which the arithmetic operations have to be logged is only the last three or four cycles, the information to be stored is manageable. This ADJIFOR procedure for iterated solvers is very attractive for calculating the gradients.

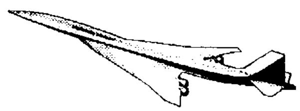

ADJIFOR for Iterative Solvers

High Speed Aerodynamics, Long Beach

- Reverse-mode ADIFOR is too expensive for iterative solvers
- Careful algorithm reversal is required
  - Generate ADJIFOR code that only affects the derivatives
- Use function solution at the start of the iterative process
- Iterate to ensure only the derivative convergence
  - Mathematical similarity to discrete adjoint derivatives
- Contraction mapping theorem states, for $\|J_{S_{Qn}}\| < 1$,
  - Need to store only 4 reverse-mode steps for $J_{S_{Qn}}$
- Derivative of objective function can be written as:

$$V' = L\, J_F\, J_{S_{Qn}} \ldots\ldots J_{S_{Qn}}\, J_G\, R$$

BOEING

ADIFOR/ADJIFOR Euler Sensitivities Comparison

This chart compares the objective function (D/L) sensitivities of the TCA W/B configuration. Both ADIFOR and ADJIFOR-processed CFL3D code is used for calculating the sensitivities. The design variable set chosen is a representative subset of the usual design variables used for shape optimization. Excellent comparison between the forward mode and reverse mode adjoint sensitivities is observed for all design variables except a few fuselage shape variables. This difference is attributed to the inadequate convergence of the incremental iterative (II) version of the CFL3D forward mode ADIFOR iterations. The sensitivities calculated using the black-box differentiated version of CFL3D showed identical results as the ADJIFOR adjoint results.

ADIFOR/ADJIFOR Euler Sensitivities Comparison

High Speed Aerodynamics, Long Beach

TCA W/B, ADIFOR and ADJIFOR Processed CFL3D, Euler, $M_\infty = 2.4$, $C_{Dv} = 41.35$ cts

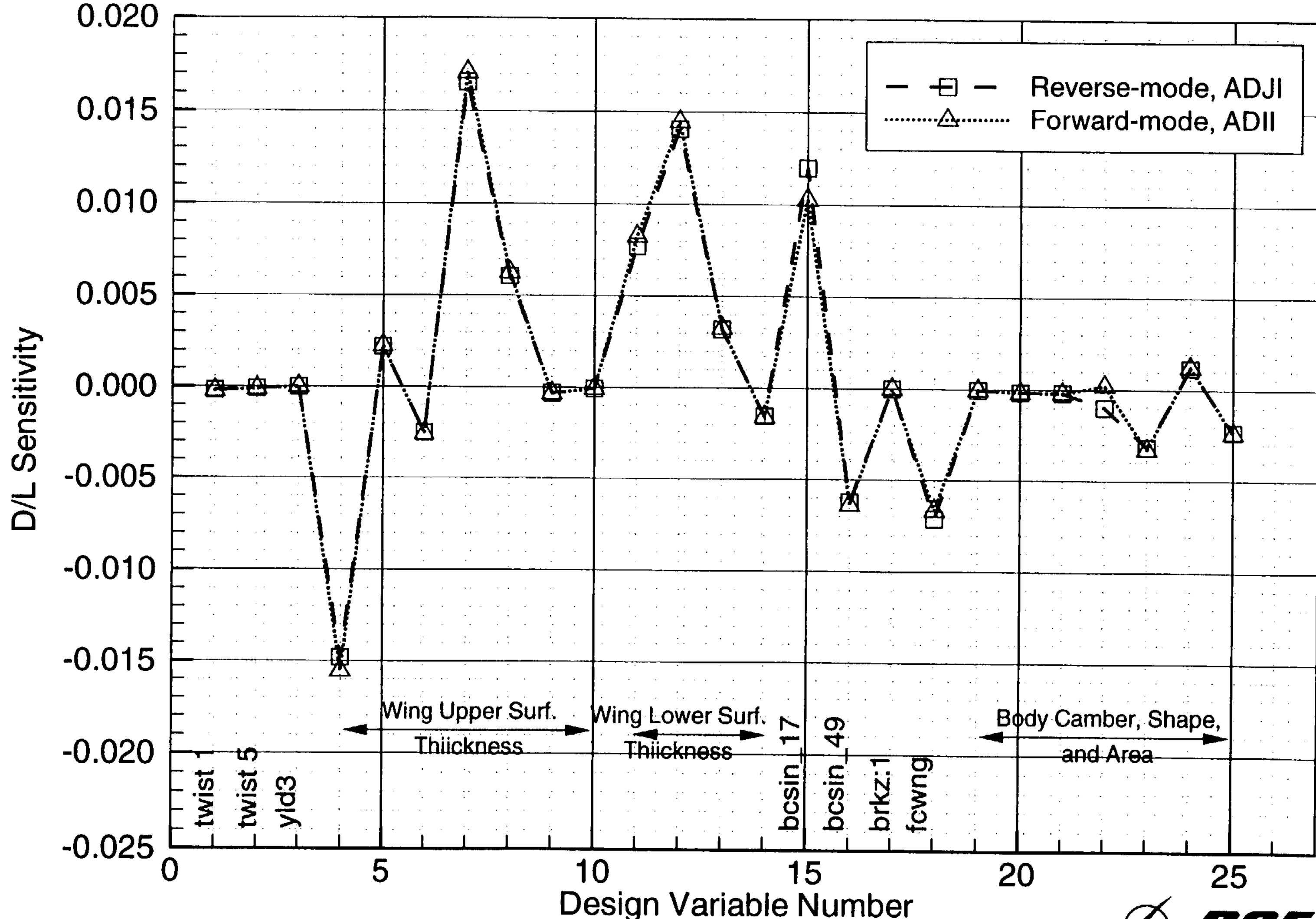

BOEING

Comparison of Sensitivity Calculation Methods

The table below compares the various sensitivity calculation methods. Although the method of divided difference is the simplest, its main problem is the need for knowing the proper step-size to calculate the correct gradient values. The choice of improper step-size may yield a very erroneous gradient value. ADIFOR does not suffer from this inaccuracy; but its computer resource requirement increases in direct proportion with the number of independent variables. The adjoint methods have the power of providing the derivatives with very little memory as well as execution time. However, the determination of the adjoint variables for the problem as well as mathematically deriving the expressions for Navier-Stokes equations is a very time consuming, labor intensive, and tedious task. ADJIFOR, on the other hand, has the advantage of the adjoint-based approach so that the CPU time for derivative calculations is independent of the number of design variables. Also, the adjoint code can be quickly generated. However, the memory and disc storage requirements for ADJIFOR are large due to the data logging requirement of iterative solvers. This is not a major concern for large parallel platforms.

Comparison of Sensitivity Calculation Methods

High Speed Aerodynamics, Long Beach

	Finite-Difference	ADIFOR	ADJIFOR	Hand-Derived Adjoint
Development Cost	Negligible	Very Low	Low	High
Step-Size	Required	Not Required	Not Required	Not Required
Accuracy	Depends on Step-size & Convergence	Depends on Convergence	Depends on Convergence	Depends on Convergence
No. of Solutions	N+1 Analyses	1 Analysis & N gradients	1 Analysis 1 Adjoint	1 Analysis 1 Adjoint
CPU Cost	$(N+1)\alpha C$	$(N+1)\beta C$	$C + \sigma C$	$2C + N\gamma$
Memory	λM	$(N+1)\lambda M$	λM	λM

N: No. of DVs; C: CPU time for 1 analysis; M: No. of Grid points, λ: words/grid point

α, β: Savings factor due to the use of previous solution as initial guess

γ: Cost of evaluating one gradient; σ: for CFL3D, approx.= 20 to 25

BOEING

Importance of Parallel Processing in ADIFOR

The nonlinear shape optimization performs better with increasing number of design variables. Since the ADIFOR-processed derivative codes require memory and CPU time proportional to the number of design variables, there is a major bottleneck in using this sensitivity calculation approach for large problems using sequential computers. However, distributed parallel processing using large number of processors is a good source of large amount of memory and CPU. For example, the 256-processor SGI Origin 2000 system at NAS has a total memory of 64 gigabytes and terabytes of disc storage. Hence using parallel systems for ADIFOR, the large memory requirement is not a major concern.

The ADIFOR-processed CFL3D requires 2.5 times the function evaluation CPU time to compute the Euler gradients of each design variable for a 0.48×10^6 point Euler grid. However, when 50 design variable sensitivities are computed simultaneously, the CPU time required is only 63 times the function evaluation time. This is due to the fact that when the grids are split and mapped on to the processors, several design variable gradients can be computed in each processor simultaneously. This reduces the number of function evaluations in each processor that results in significant CPU savings. The use of large number of processors can also result in fast turn-around time.

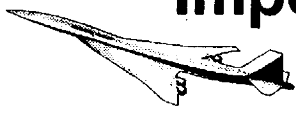

Importance of Parallel Processing in ADIFOR

High Speed Aerodynamics, Long Beach

- Typically, nonlinear optimization shows more benefits with larger number of design variables (DV)
- In ADIFOR, memory and CPU time increases with DVs
- Forward mode ADIFOR-ed CFL3D Euler with 0.5×10^6 grid
  - CPU time for 1 DV gradient~2.5 x CPU for function
  - CPU time for 50 DVs gradients ~ 63 x CPU for function
- Memory increase with DV requires parallel processing
- Parallel processing enables fast turn-around time

BOEING

Parallel Flow Sensitivities

The importance of utilizing parallel processing for ADIFOR sensitivity calculations was highlighted earlier. As a result, all the grid sensitivity codes have been parallelized in a strip-mined fashion. In this approach, each processor computes the grid sensitivities of a design variable.

To compute the flow sensitivities, this approach is a very poor choice since it requires the function evaluation for each design variable. Instead, an alternate way is used for the forward mode ADIFOR sensitivity calculation. First, the parallel version of CFL3D is utilized so that the split volume grid can be mapped onto each processor. This code is black-box ADIFOR differentiated to obtain the forward mode ADIFOR version of the CFL3D code. Next, the back-box differentiated ADIFOR code is modified to include the incremental iterative (II) enhancement of Arthur Taylor. This served as the workhorse ADIFOR-ed CFL3D code for the design iterations during the TCA wing/body design.

The seed matrix that contains the grid sensitivities of all the design variables is also split along the same way as the original grid is split and fed to the ADIFOR-processed CFL3D code. Since the grid is split, the sensitivity calculations of a group of design variables can fit into each processor. Several such groups were created to span the full set of design variables. Each of these groups is mapped to a set of processors. This method enables a fast turn-around time of the gradient computation.

For the ADJIFOR adjoint gradient computation, the grid is split and mapped on to a set of processors similar to function evaluation. However, the increased memory requirement for ADJIFOR requires the grid to be split further to accommodate the increase in the memory requirement of the ADJIFOR-processed code compared to the function code. Since the gradients are computed based on the last four iterations of the converged function solution, large log files are stored. However, since log files are written and read by each processor in parallel, the per-processor load is reasonable.

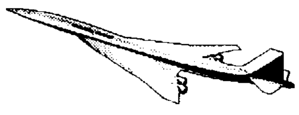

Parallel Flow Sensitivities

High Speed Aerodynamics, Long Beach

- Black-box ADIFOR-differentiated CFL3D parallel code
- Incremental iterative approach of Arthur Taylor
  - Residual terms tending to zero are not ADIFOR-ed
- 3-levels of parallelism for efficiency and fast turn-around
  - Grid split and mapped to PEs for best load-balance
  - Gradient calculation for a group of DVs that fits in a PE
  - Multiple DV groups mapped on as many sets of PEs
- Each PE solves the flow and gradients of *its* split grid for *its* group of DVs

BOEING

ADIFOR/ADJIFOR Euler Design Resource Needs

The resource requirements of the ADIFOR and ADJIFOR-processed CFL3D sensitivity code for a 0.48×10^6-point Euler grid is shown in this chart. It can be seen that the total memory requirement of the ADIFOR sensitivity calculation is nearly 40 gigabytes using single precision. Also, the CPU time for obtaining the Euler flow sensitivities of the 401 design variables is nearly 450 single-processor hours on the SGI Origin 2000 system. This is significantly large compared to the grid sensitivity calculation. However, making use of large pool of processors, the wall-time to obtain the gradients can be reduced.

The table also highlights that the resource requirements of the ADJIFOR adjoint sensitivity calculation approach are very small compared to the ADIFOR approach. First, the memory requirement for ADJIFOR is an order-of-magnitude smaller. Second, the CPU hours required for ADJIFOR gradients is nearly 25 times lower than that is required for ADIFOR. The wall time for adjoint gradient calculations performed for this grid using a 24-processor Origin 2000 system is only 0.6 hour. This is a major advantage of using the ADJIFOR approach. Although the disc space requirement for logging the intermediate steps during the adjoint calculation in ADJIFOR is nearly 16 gigabytes, it is not a concern.

ADIFOR/ADJIFOR Euler Design Resource Needs

High Speed Aerodynamics, Long Beach

- ADIFOR and ADJIFOR-processed CFL3D Euler code
- 401 DV TCA W/B Euler design with ~480,000 grid points
- DVs mapped onto PEs for parallel grid sensitivities
- Split grid mapped onto PEs for parallel flow sensitivities

Task	Proc. Memory (MW)		Single Processor CPU (Hours)	
	ADIFOR	ADJIFOR	ADIFOR	ADJIFOR
Grid Sensitivity	15	20	10	1
Flow Sensitivity	10,000	1,000	450	16
Line Search	24	24	5	5

BOEING

Shape Optimization Using ADJIFOR Sensitivities

The flow chart shown below outlines the various shape optimization modules for the ADJIFOR sensitivity calculation. All the grid tool modules, Geom1, QGRID, and FlexMesh, as well as Constraints module have been ADIFOR-processed while Objective function, CFL3D, and Grid Splitter have been ADJIFOR processed. The grid and flow sensitivities are glued together at the interface for the entire volume grid to obtain the objective function gradients. The computed gradients are fed to the optimizer to determine the optimum direction.

Shape Optimization Using ADJIFOR Sensitivities

High Speed Aerodynamics, Long Beach

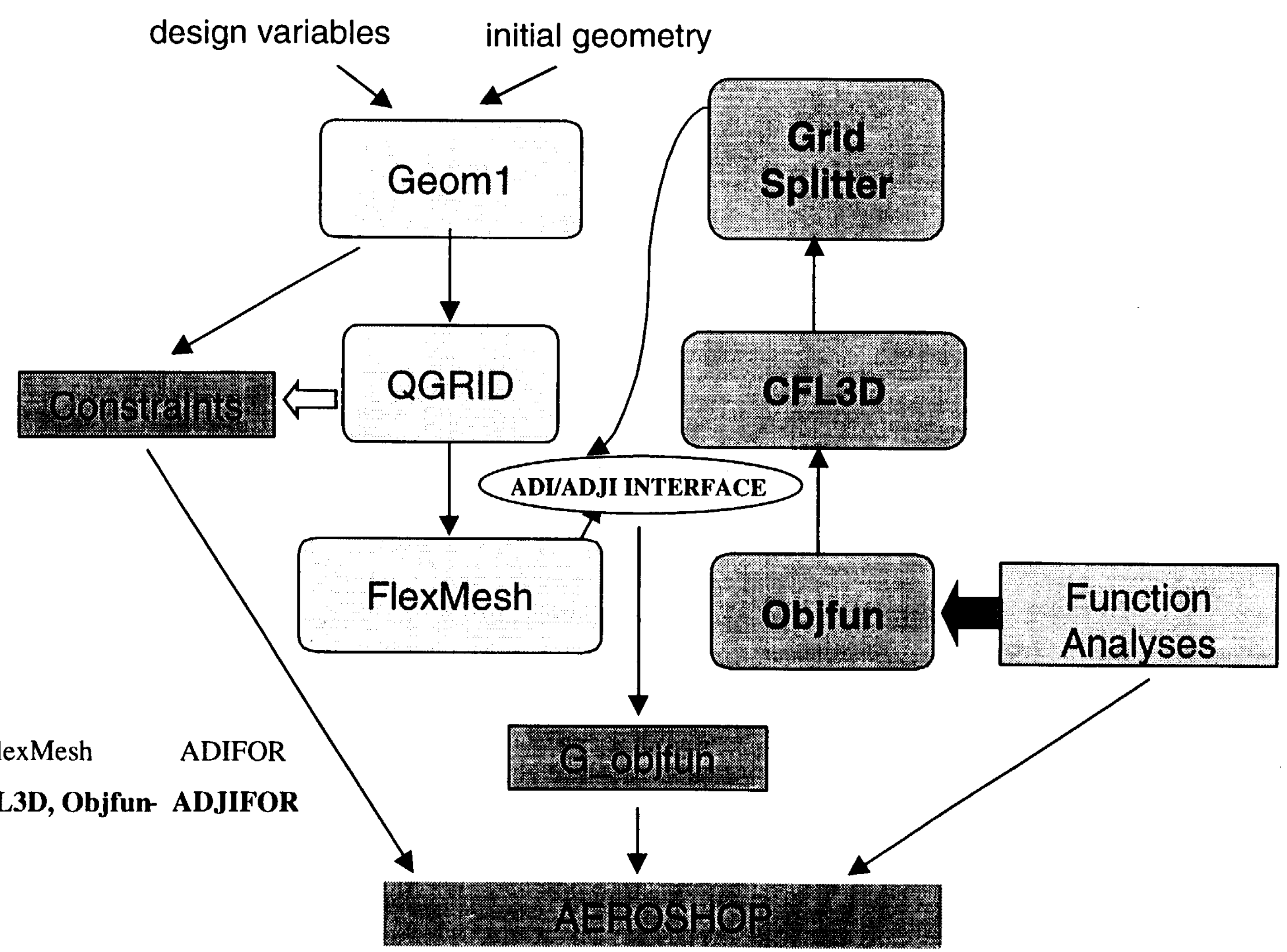

Geom1, QGRID, FlexMesh ADIFOR

Grid Splitter, CFL3D, Objfun- ADJIFOR

AEROSHOP Framework

AEROSHOP is a Unix script-driven optimization environment. The heart of the *AEROSHOP* optimizer environment is the NPSOL optimizer. The other segments of *AEROSHOP* are the gradient generation and performance evaluation. The gradient-generation module built inside *AEROSHOP* is based on finite difference. However, interfaces are provided to replace this with the customer-preferred gradient modules such as ADIFOR or ADJIFOR and hand-differentiated adjoint.

AEROSHOP Framework

High Speed Aerodynamics, Long Beach

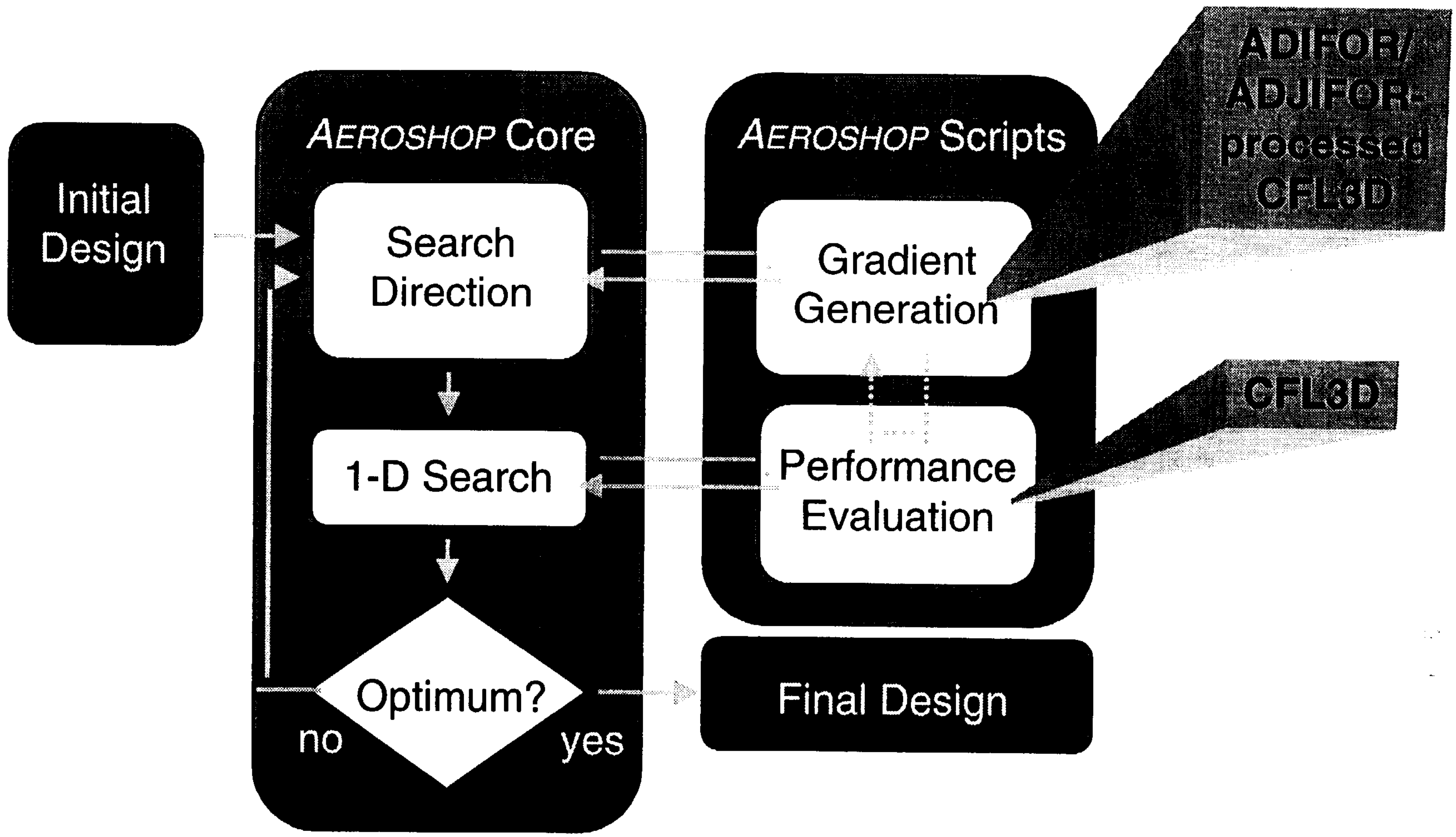

ADJIFOR-Based N-S Design

The next step in the grand scale of activity is to extend the ADJIFOR methodology to perform viscous optimization. At this stage, the advantage of using ADJIFOR approach in contrast to the hand-differentiated method of calculating the gradients is evident. The ADJIFOR adjoint code for Navier-Stokes sensitivities was obtained in a quick and direct way by simply passing the CFL3D Navier-Stokes code through the ADJIFOR preprocessor instead of the CFL3D Euler code used for the Euler sensitivities.

To perform the Navier-Stokes wing/body design, the TCA baseline Euler wing/body design grid was reclustered for the flight $Re_c = 212 \times 10^6$ with $y^+ = 5$ near the wall. Care was taken to ensure that the viscous drag results of this design grid matches closely with the TCA baseline Navier-Stokes analysis grid values. The resulting Navier-Stokes design grid had 0.89×10^6 points. The same set of design variables and constraints used for the earlier Euler design were chosen for the Navier-Stokes design as well.

Since this is the first time that the ADJIFOR technology is used to perform Navier-Stokes design, a systematic study is warranted at the early stages to address the issues related to the iterative adjoint procedure to calculate the derivatives. Also, the number of adjoint iterations required for the Navier-Stokes gradient convergence should be established, prior to the beginning of design cycles. To this effect, many adjoint gradient runs were made. From these evaluations, it was concluded that a large number of adjoint iterations, comparable to the number of iterations required for function convergence, is also required for gradient convergence. Another observation was that although accurate sensitivities are obtained with single precision in ADJIFOR, due to the very tight spacing of the grid close to the wall, double-precision arithmetic is required.

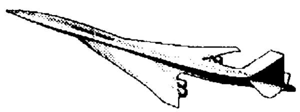

ADJIFOR-Based N-S Design

High Speed Aerodynamics, Long Beach

- ADJIFOR-processed CFL3D N-S code
- N-S (Baldwin-Lomax) 0.89×10^6-point W/B grid, $y^+ = 5$
- 401 DVs and 55 constraints
- ~ 600 adjoint iterations are required for gradient convergence
- Need double-precision arithmetic
  - Converged single-precision gradients resemble unconverged double-precision sensitivities

BOEING

N-S Design Resource Requirements

The large size grid combined with the requirement of double precision arithmetic pose a burden on the computer memory requirement for Navier-Stokes ADJIFOR sensitivities. In addition, the hundreds of adjoint iterations needed for gradient convergence implies large CPU time for sensitivity calculations during the optimization. However, on parallel systems this is not a major concern. Using 72 processors of the SGI Origin parallel system, it is possible to obtain the converged adjoint gradients for the wing/body design grid in less than 2.3 hours of wall time. The ratio of CPU time for adjoint to analysis for the Navier-Stokes ADJIFOR sensitivities remained to be 20 to 25 as in the case of Euler ADJIFOR sensitivities. Indeed, very large log files (~57 gigabytes) are created during the iterative adjoint calculation process. It is anticipated that the available CPU and memory resources on the NAS Origin 2000 parallel system can easily handle up to 3×10^6 grid points. It is expected that the full configuration viscous multipoint design grid could fit within the available resources at NAS.

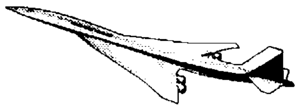

N-S Design Resource Requirements

High Speed Aerodynamics, Long Beach

- ADJIFOR sensitivities computed using 72 processors
- Wall time for adjoint gradients is 2.3 hours
- Double-precision computations with minimal CPU overhead
- Adjoint to analysis ratio is approx. 20 to 25
- Large log-files (~57 Gbytes) are created
- Available NAS resources can handle up to 3×10^6 grid points

BOEING

Results

The presentation so far discussed the ADIFOR and ADJIFOR-related details and computer resources, etc. At this time, the design results are presented. To reiterate as a reminder, it was shown earlier that the ADJIFOR-based Euler design can be performed with quick turn-around time and it is possible that a complete design with 25 iterations can be completed within a week for a reasonably large grid with almost unlimited number of design variables and constraints. The Navier-Stokes designs are most CPU intensive, but full configuration designs could be completed within the available NAS computer resources.

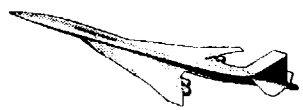

Results

High Speed Aerodynamics, Long Beach

- TCA wing/body Euler design
  - 401 DV $0.5x10^6$ grid CFL3D Euler ADIFOR gradients
- Large parallel ADIFOR Euler design completed with reasonable turn-around time
- ADJIFOR adjoint sensitivities enables rapid designs
- CFL3D N-S ADJIFOR sensitivities
- Current status of TCA wing/body Navier-Stokes design

BOEING

Design with ADIFOR-Based Euler Sensitivities

The design iteration history for various aerodynamic and optimization parameters for the TCA wing/body design with 401 design variables and 55 constraints are shown below. The chosen objective function for the minimization problem is drag/lift. The G_{vio} shown is the ratio of the constraint violation with over the constraint value. The first 20 design iterations were performed without any design parameter modification. As can be seen, the design progressed smoothly. At that time, these iterations were performed using the forward mode ADIFOR sensitivities that required more than a couple of month's time since the ADJIFOR adjoint technology was not available. It is interesting to see that switching to the ADJIFOR sensitivities, these steps can be completed within a couple of days. The ADJIFOR-processed CFL3D adjoint code became available when this design was completed. The last couple of design cycles were the only ones performed using the ADJIFOR Euler sensitivities. The comparison of the ADIFOR and ADJIFOR gradients were already shown in an earlier chart. Since the constraints were not being satisfied, the design variables were scaled after 20 iterations which significantly increased the weight of the constraints in the merit function in the optimization. Finally, all the constraints were satisfied. This Euler design yielded an L/D improvement of nearly 5% over the TCA baseline.

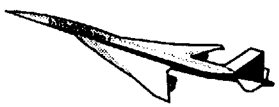

Design with ADIFOR-Based Euler Sensitivities

Baseline TCA W/B, 401 Design Variables, 55 Constraints
AEROSHOP, CFL3D Euler, $M_\infty = 2.4$, $Re_c=212\times10^6$ (C_{Dv} = 41.35 cts.)

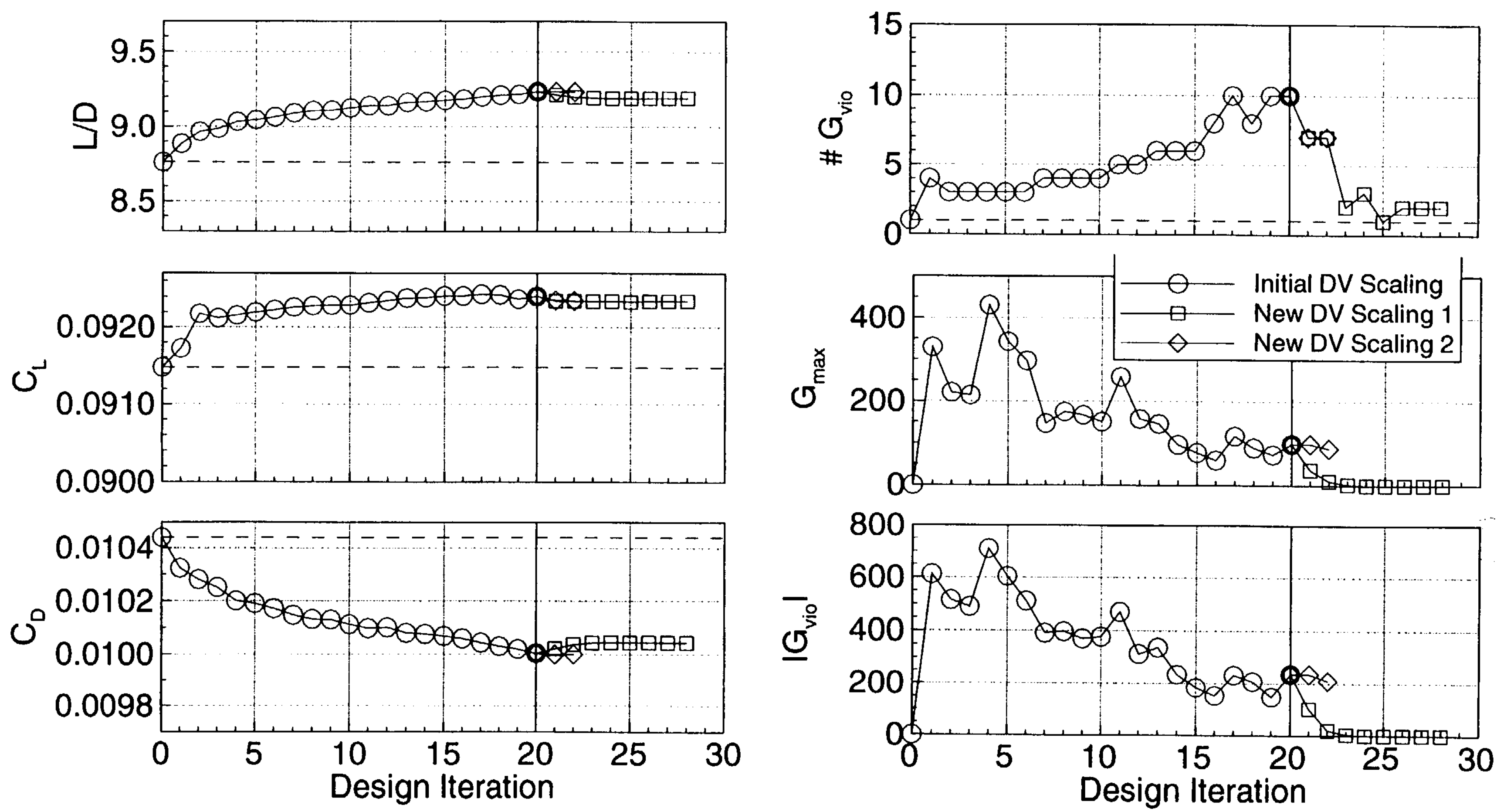

PS - 12/10/98

Design with ADIFOR-Based Euler Sensitivities

The variations of aerodynamic quantities with respect to the design iterations are shown in the typical lift curve and drag polar form. The lift constraint is also shown as the dotted line.

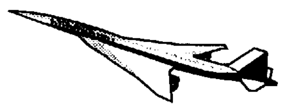

Design with ADIFOR-Based Euler Sensitivities

High Speed Aerodynamics, Long Beach

Baseline TCA W/B, 401 Design Variables, 55 Constraints, New DV Scaling 1
AEROSHOP, CFL3D Euler, $M_\infty = 2.4$, $Re_c=212\times10^6$ (C_{Dv} = 41.35 cts.)

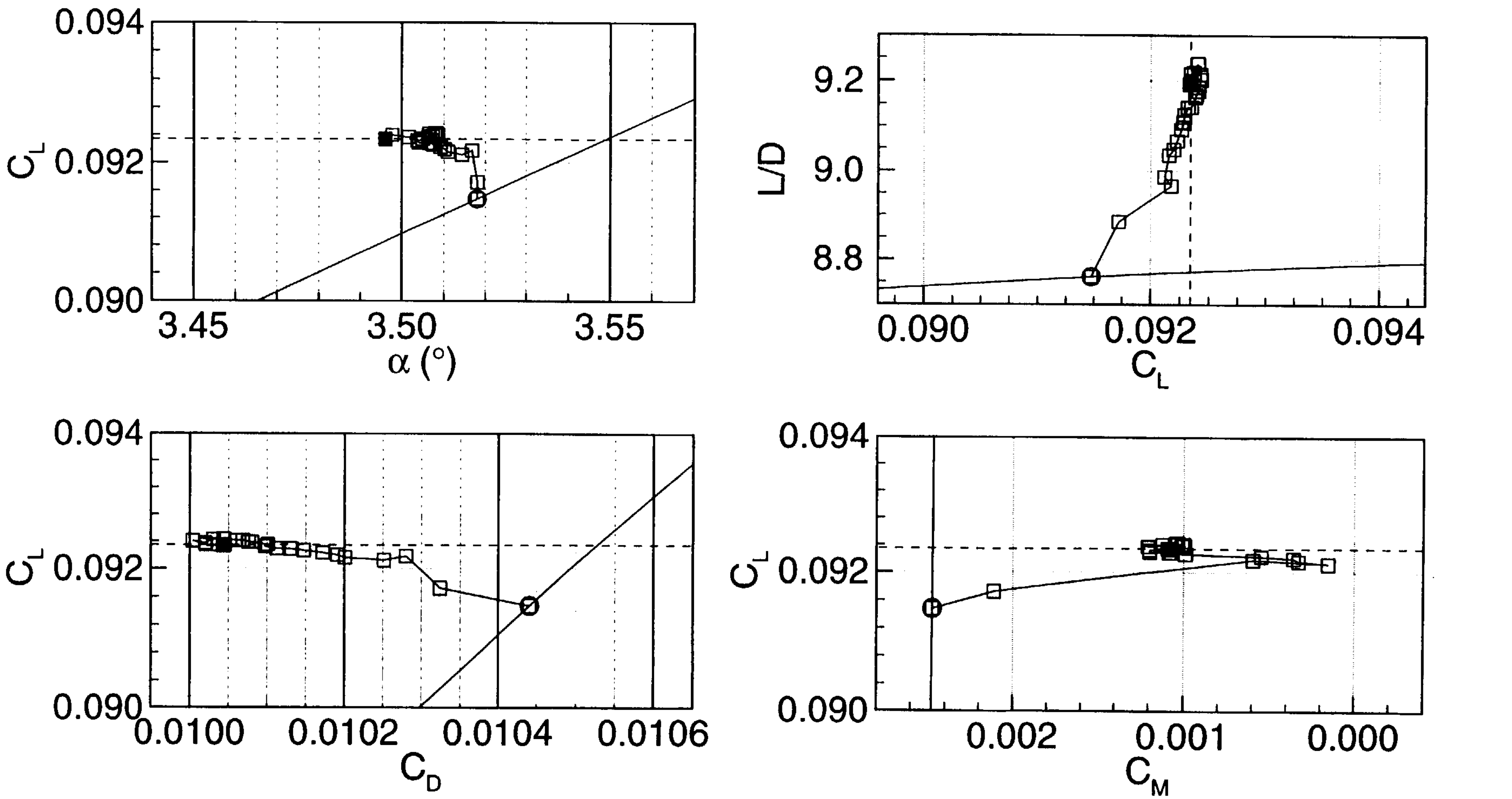

BOEING

ADIFOR/ADJIFOR Optimized TCA W/B Configuration

The ADIFOR/ADIFOR optimized wing/body configuration is shown in this perspective view. A significant spanwise waviness is seen that was absent in the TCA baseline linear design. A similar waviness has also been obtained in other similar nonlinear Euler designs. Another observation to be made is the nose droop. This was also absent in the baseline TCA configuration.

ADIFOR Euler Optimized TCA W/B Configuration

High Speed Aerodynamics, Long Beach

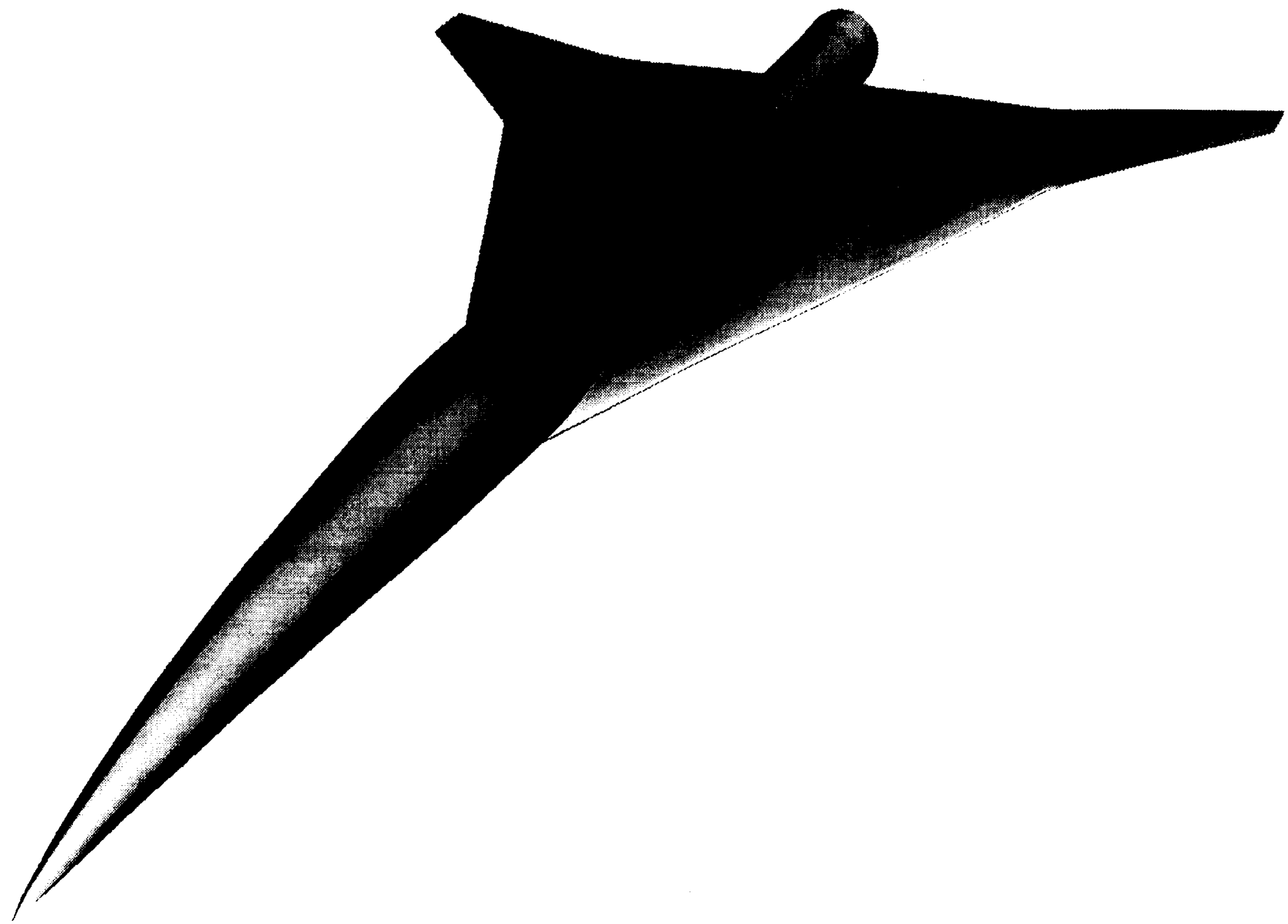

ADJIFOR-Processed CFL3D Navier-Stokes (B-L) Sensitivities

The comparison of the sensitivities of the drag/lift objective function for the 401 design variable problem using the ADJIFOR-processed CFL3D Euler and Navier-Stokes adjoint codes are shown here. Important to observe are the large gradients of the *fcwing* design variable and the large fluctuations in the fuselage camber sensitivities for different number of Navier-Stokes adjoint iterations. The insets show that acceptable gradient convergence has been reached for around 600 adjoint iterations. As a result, all the wing/body design iterations based on the Navier-Stokes sensitivities use 700 adjoint iterations. Other design variables do not show a major change between Euler and Navier-Stokes sensitivities in this scale.

ADJIFOR-Processed CFL3D Navier-Stokes (B-L) Sensitivities (D/L)

High Speed Aerodynamics, Long Beach

TCA Wing/Body, 193x57x73 N-S Grid, 72-blocks, $Re_c = 212\times10^6$, $y^+ = 5$, $M_\infty = 2.4$

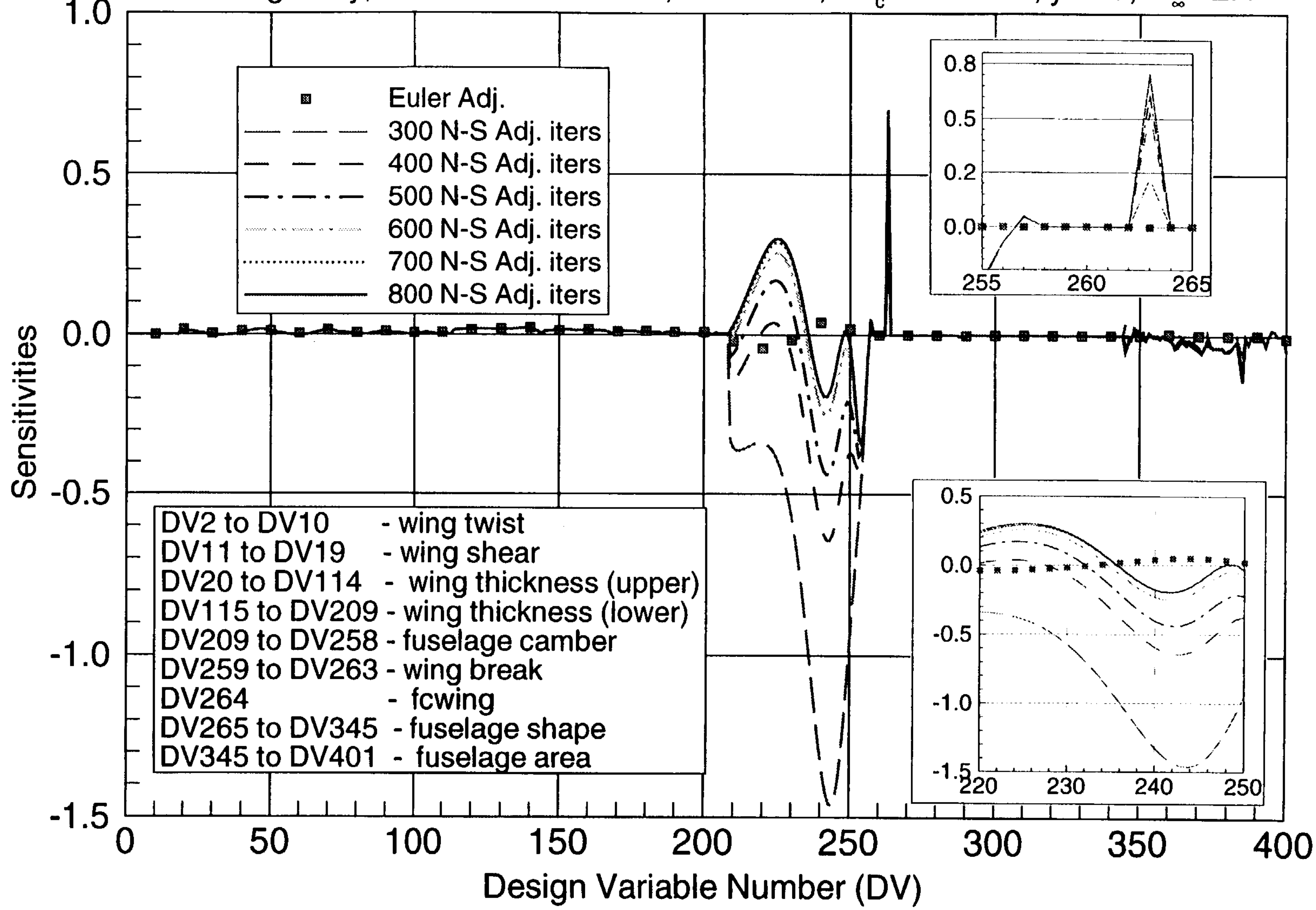

BOEING

ADJIFOR-Processed CFL3D Navier-Stokes (B-L) Sensitivities

This chart shows the close-up view of the wing design variables shown in the previous chart. It is seen that, the Euler wing design variable sensitivities show a slightly different trend compared to the Navier-Stokes sensitivities. Also, the number of Navier-Stokes adjoint iterations required for gradient convergence of the wing design variables is not as large as the fuselage camber design variables. It is noted that a mixed ADIFOR and ADJIFOR gradient calculation scheme is probably more economical.

ADJIFOR-Processed CFL3D Navier-Stokes (B-L) Sensitivities (D/L)

High Speed Aerodynamics, Long Beach

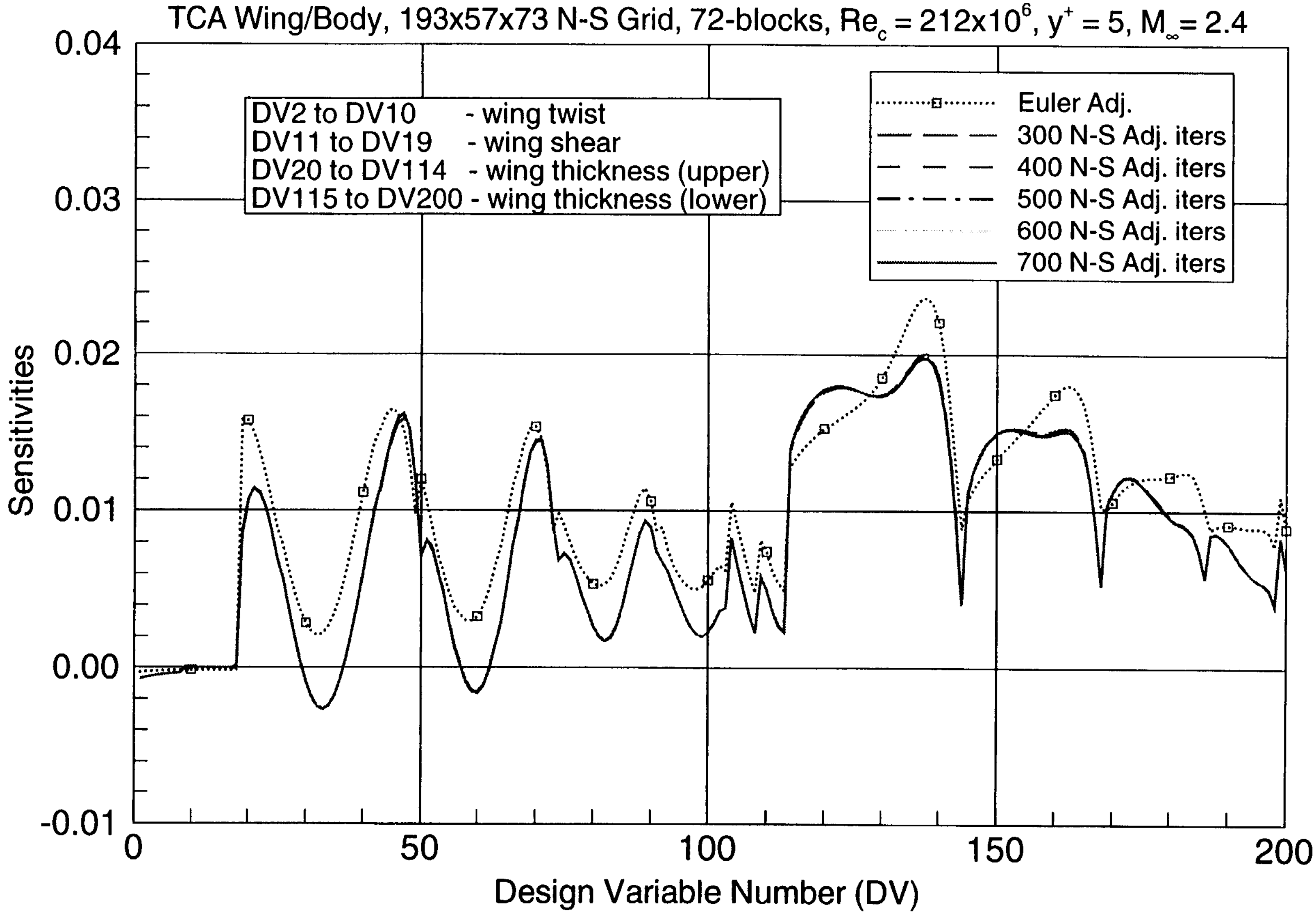

BOEING

Conclusions and Future Work

In conclusion, this study shows that ADIFOR and ADJIFOR-processed codes provide accurate analytical sensitivities that can be used for aerodynamic shape optimizations. The power of ADJIFOR adjoint combined with the parallel processing for design cycle time reduction has been successfully demonstrated. Using this technology, the TCA baseline wing/body performance was increased by nearly by 5%. Navier-Stokes adjoint sensitivities using the ADJIFOR-processed CFL3D can be successfully used for viscous design optimization with fast turn-around time. Full configuration viscous design using the Navier-Stokes ADJIFOR adjoint sensitivities is possible for fairly large grid sizes. Work towards this goal is in progress.

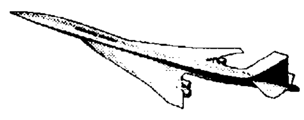

Conclusions and Future Work

High Speed Aerodynamics, Long Beach

- ADIFOR-processed codes provide accurate sensitivities
- The W/B design technology demonstrator using CFL3D Euler ADIFOR gradients improved TCA (L/D) by 5%
- Parallel processing enables design cycle time reduction
- Parallel processing eliminates ADIFOR memory limitations and ADJIFOR disc space issues
- CFL3D Navier-Stokes ADJIFOR gradients have been rapidly and successfully computed
- Navier-Stokes designs for TCA wing/body and wing/body/nacelle/diverter are underway

BOEING

Technology Development for a Multipoint Optimization Process for an HSCT

Robert Narducci, James Hager, Eric Unger, Geojoe Kuruvila,
P. Sundaram, Peter Hartwich, Grant Martin,
Raul Mendoza, Alan Arslan, Shreekant Agrawal

The Boeing Company, Phantom Works - Long Beach

High Speed Research Airframe Review
Anaheim, California
February 8-11, 1999

BOEING

Introduction

Previous non-linear aerodynamic optimization work has focused mainly on the most important leg of the HSCT mission, the supersonic cruise. The benefits of this single-point optimization has not yet been fully realized and it is possible that with further work the goals of the HSR program may be met. However, consideration of the supersonic cruise performance may not be adequate to obtain a truly optimized HSCT since the airplane flies through diverse flowfields to accomplish each leg of its mission

Much of the technology development in 1998 has been to increase the fidelity of the analysis model, increase the number of degrees-of-freedom of the design, and reduce the cost of optimization. While these elements oppose each other, they are critical for a practical and successful multipoint optimization process.

This paper begins by assessing the progress of nonlinear aerodynamic shape optimization towards meeting program goals set for the Technology Concept Airplane (TCA). This section establishes that program goals have not been met and that steps towards reaching these goals may be made through a multipoint approach. The next section defines two approaches for multipoint optimization. The first involves a series of single-point optimizations where the OML is defined by supersonic cruise considerations, and flap schedules are determined in subsequent optimizations at off-design Mach numbers. The second approach involves concurrent assessments of the design performance at all critical Mach numbers.

The next section documents the optimization technology development in 1998. This includes enhancements to grid generation, configuration modeling, flow analysis, gradient calculations, and design variable definitions. Intermediate results that demonstrate these technologies conclude this paper.

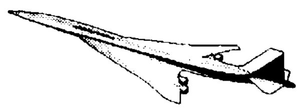

Outline

- Current Status of Aerodynamic Optimization
- Multipoint Optimization Processes
- Technology Developments in 1998
- Intermediate Results
- Conclusions

BOEING

Current Status - Supersonic

The objectives of this chart is to map out a feasible design space for the TCA at supersonic cruise and to determine where current variants of the TCA come to lie in this design space. The basic idea for designing this carpet plot is the assumption that the variation of drag with lift can be approximated by a parabola:

$$C_D = C_{D_0} + KE \times C_L^2 \tag{1}$$

Straightforward differentiation of this formula gives the relationship between $(L/D)_{max}$ as a function of minimum drag and shape factor KE. Minimum drag is primarily driven by skin friction, by volume, and by nacelle installation. Primarily the effects of twist, camber and thickness distributions of the wing and of the fuselage (without twist, of course) determine the shape factor KE; the smaller KE, the better the performance of the aircraft. The estimates for the upper and lower bounds for these two parameters are taken from Kulfan.[1] The maximum lift-to-drag ratio for the Concorde is provided to put current results in perspective.

The maximum lift-to-drag ratio for three configurations at supersonic cruise Mach number is indicated in the feasible design space. A linear optimization process produced the baseline TCA. The TCA Cycle2 and the NCV variants of the baseline TCA are the result of nonlinear design processes. Differences in the design processes and in the sets of constraints led to the different performance levels for the two nonlinear design variants of the TCA.

The three data points indicate that current designs emphasize reducing the shape factor, KE. Furthermore, assuming that Kulfan's estimates for the upper and lower bounds for minimum drag and shape factor KE are correct, it appears that the current design processes have come close to exhausting their capacity for further performance improvements through primarily optimizing thickness distributions, twist, and camber. On the other hand, minimum drag has suffered as a consequence of the optimization processes and is in danger of dropping below acceptable limits for $C_{D,o}$. These results suggest that future improvements to design optimization methods should be aimed at reducing installation drag and exploiting any beneficial thrust and trim effects.

Current Status - Supersonic

High Speed Aerodynamics, Long Beach

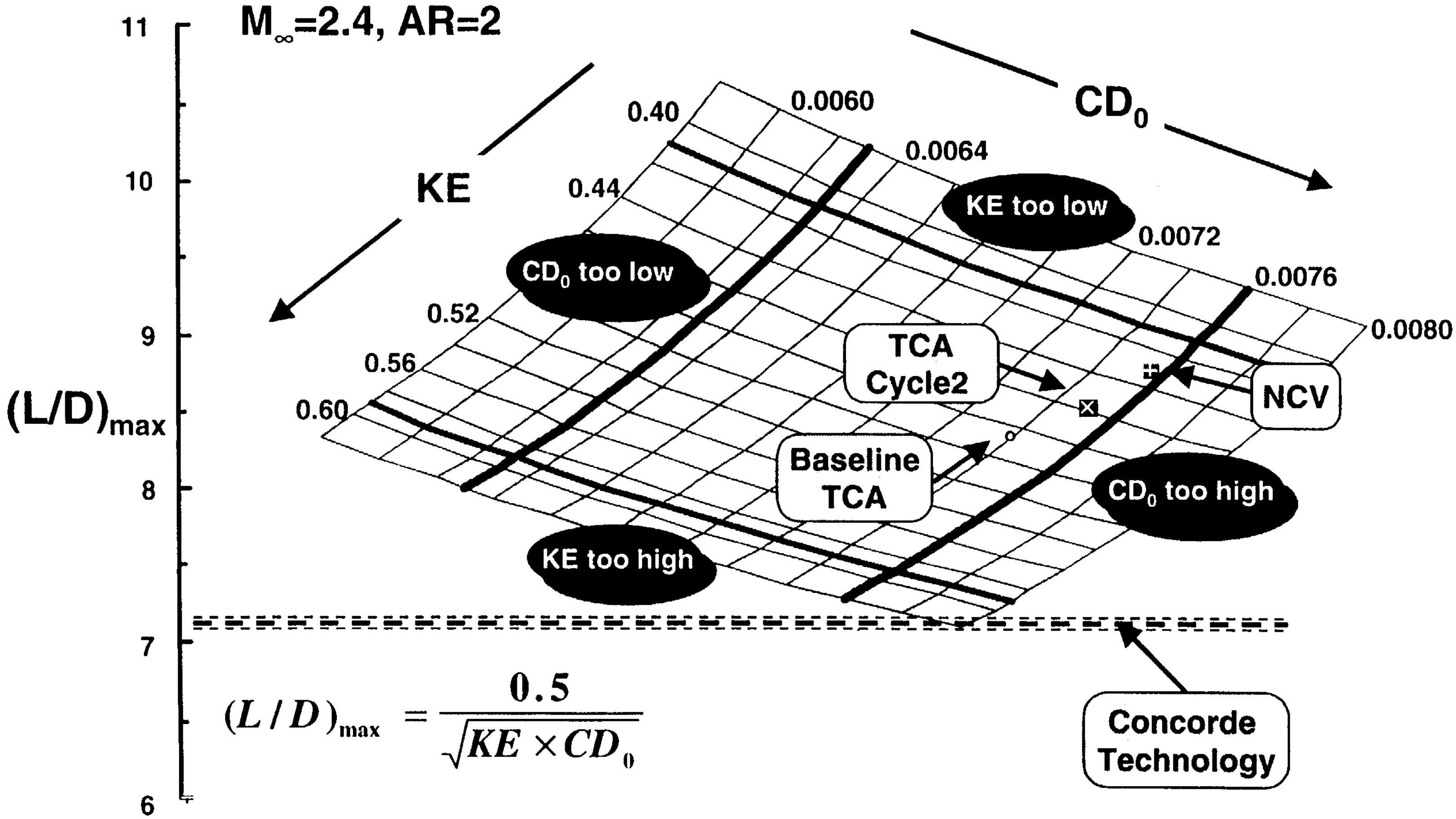

$$(L/D)_{max} = \frac{0.5}{\sqrt{KE \times CD_0}}$$

Current Status - Subsonic

This chart makes an attempt at quantifying the impact of flaps on the aerodynamic performance of a TCA wing/body configuration at transonic cruise Mach numbers. To this end, variations of a metric called suction parameter are plotted against lift coefficient. The six different curves pertain to a hypothetical case of minimum drag due to elliptic loading, a technical projection (=95 percent of ideal suction), the TCA without deployed transonic flaps, the TCA with the leading- and trailing-edge flaps set to achieve the performance maxima as determined in computational and experimental parametric studies, and the TCA with all-wing flaps (inboard and outboard) set for maximum performance as determined by a nonlinear flap schedule optimization method. The suction parameter is defined as

$$S = \left(C_D\big|_{suction=0} - C_D\big|_{actual} \right) \Big/ \left(C_D\big|_{suction=0} - C_D\big|_{elliptic} \right) \tag{2}$$

where

$$C_D\big|_{elliptic} = C_{D_0} + C_L^2 \big/ (\pi AR)$$

is the minimum drag due to elliptic load distribution, and

$$C_D\big|_{suction=0} = C_{D_0} + C_L^2 \big/ (C_L \tan^{-1}\alpha) = C_{D_0} + C_L^2 \big/ C_{L_\alpha}$$

is the drag in absence of any leading-edge thrust. As indicated in the chart, achieving maximum performance (i.e., S=1) requires the hypothetical case of

$$C_D\big|_{actual} = C_D\big|_{elliptic} .$$

The TCA without deployed flaps turns in the worst performance. While the flap settings as determined in the parametric studies yield better peak performances for $0.04<C_L<0.16$, the optimized flap schedule surpasses the performance of all alternate flap settings at the transonic cruise condition ($M_\infty=0.9$, $C_L=0.18$). As a matter of fact, the optimized flap schedule lets the TCA perform at 93 percent of the technical projection, which, in turn, maintains that 95 percent of the ideal suction can be realized. This means that while there might be still further improvement achieved through refined nonlinear optimization of the transonic flap schedule, the current optimization results are already quite close to the practical limit.

For completeness, let it be mentioned that the estimation of the suction parameter based on experimental values is rather sensitive to uncertainties in determining minimum drag. This explains why the peak performance of some of the TCA wing/body configurations with transonic flaps exceeds the projected value and in one case even appears to match ideal performance; the experimental minimum drag values are most likely too low for these configurations by a few counts of drag.

Current Status - Subsonic

High Speed Aerodynamics, Long Beach

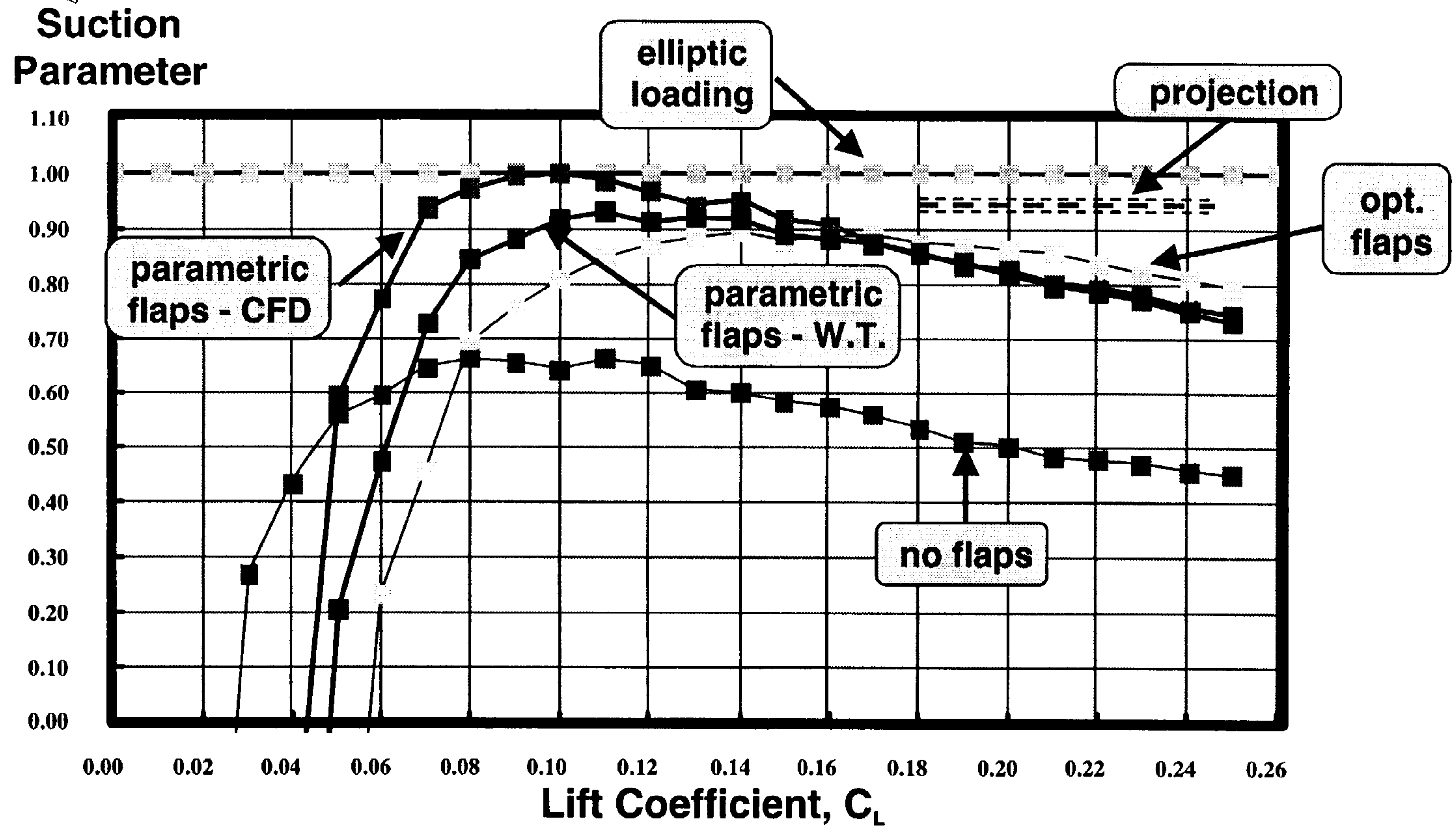

TCA Wing/Body Configuration with Flaps

M_∞=0.9, Data: 16-ft Transonic Wind Tunnel

BOEING

Multipoint Optimization Process

The multipoint optimization process shown below is an extension of the single-point methodologies used to perform the supersonic cruise optimization and the transonic flap optimization. The process can be thought to consist of 4 steps. The first two are start-up procedures; the third consists of optimization with *AEROSHOP*, and the fourth is an analysis of the results produced in step three. The first step involves careful consideration of the design objectives and the available resources. It involves defining design variables, constraints, and the evaluation model. The evaluation of a design includes elements such as the level of geometric complexity and the figure of merit (i.e., the objective function). Other considerations involved in step 1 include a decision of the preferred method for flow analysis and sensitivities, and the preferred computing platform.

The second step involves generating data and processes to be used in the optimization routine to accomplish the goals established in step 1. These include generating the baseline grid, defining grid perturbation procedures, compiling computer codes, and generating baseline data (skin friction, spillage, etc.).

The third step is the heart of the optimization problem; it is the execution of the AEROdynamic SHape OPtimization system (*AEROSHOP*). The system solves general optimization problems. Within the context of multipoint optimizations, *AEROSHOP* executes surface perturbation, grid generation, and CFD analysis codes for each point of the design conditions. The data is passed to a design evaluation module and a sensitivity evaluation model. This data is used by *AEROSHOP* to further improve the design. An optimized design is produced at the conclusion of this step. Optimizations may take advantage of shortcomings in the evaluation model or the flow solutions. Therefore, it is often necessary to perform the fourth step, a post-analysis of the design. This step involves generating plots of the optimization history, a refined CFD analysis, and communication to experts in other disciplines. Shortcomings are often addressed and the process is repeated.

Multipoint Design Process

High Speed Aerodynamics, Long Beach

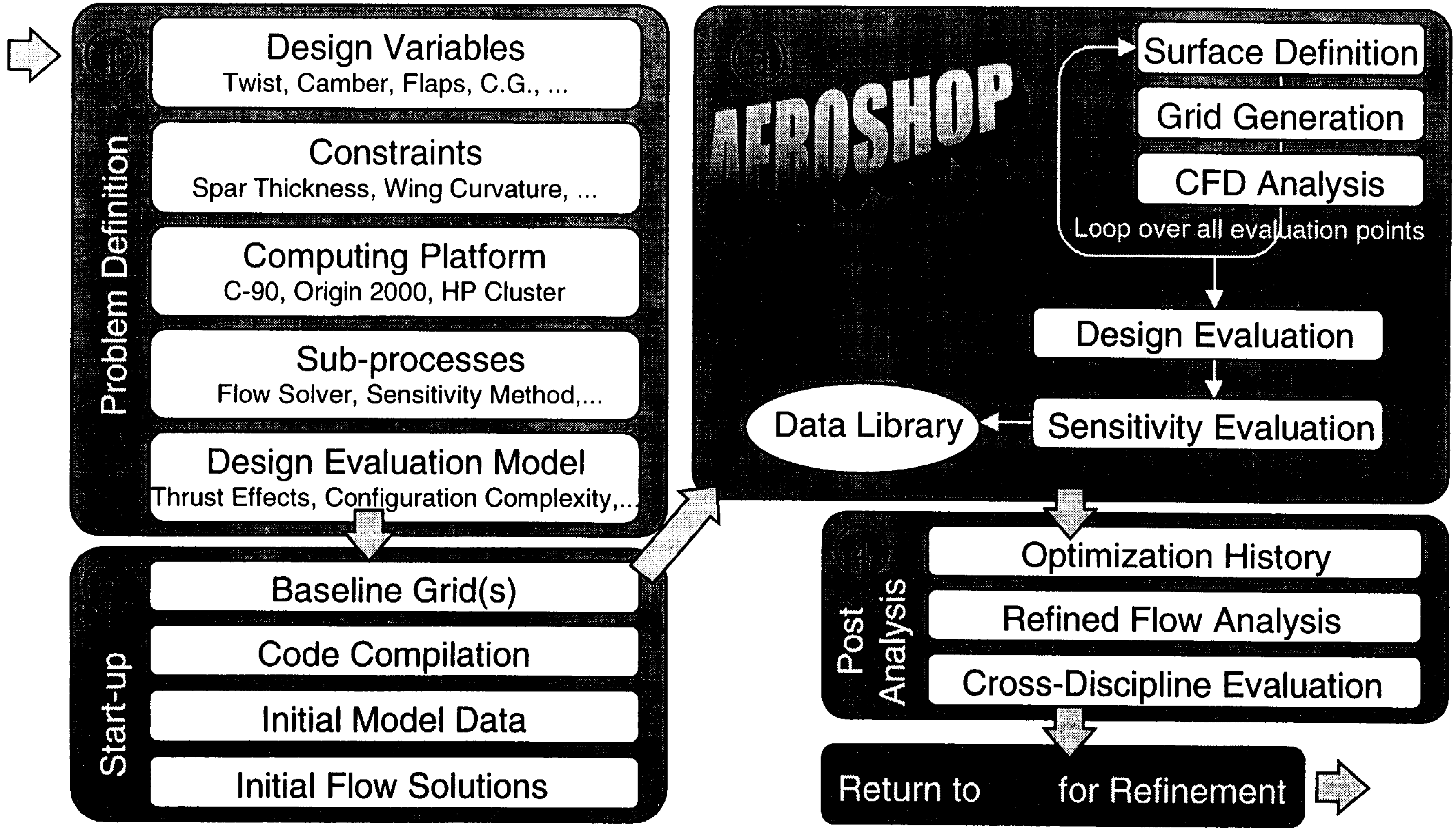

BOEING

Multipoint Strategies

Two strategies are currently implemented for multipoint design at Phantom Works. In the first, the optimization is performed in several steps. The first step involved optimization for supersonic cruise. Here, the OML is redefined in wing twist, thickness, camber, and shear, fuselage camber, area distribution and shape, and nacelle shape. The supersonic cruise optimization is followed by several independent, single-point flap optimizations at conditions away from the supersonic cruise point. In the second approach, the OML and flap settings are determined simultaneously for all relevant conditions with each condition having its own flap schedule. Flaps are retracted at the supersonic cruise condition.

The assumption in approach 1 is that performance levels away from the M_∞=2.4 are not heavily dependent on the geometric features that resulted from the supersonic cruise point optimization. The assumption implies that whatever drag penalty might be incurred, away from supersonic cruise, is small or can be regained with optimized flap deflections. The second approach removes the major assumption made in the first approach. Here, the optimization is carried out by integrating input from all relevant flight conditions. Conditions away from the supersonic cruise point can influence the wing and fuselage OML.

Multipoint Strategies

- Sequential Approach
  - Perform shape optimization at supersonic cruise point
  - Optimize flap schedule at other flight conditions
- Simultaneous Approach
  - Weight performance at several flight conditions for shape and flap optimization

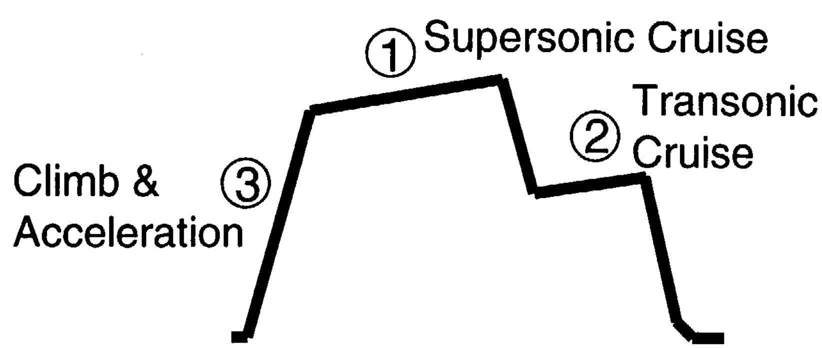

BOEING

AEROSHOP Framework

Multipoint optimization can be performed within the framework of the AEROdynamic SHape OPtimization (*AEROSHOP*) system. *AEROSHOP* is the preferred environment for shape optimization with nonlinear aerodynamic considerations at Boeing – Long Beach. It features a modular structure ideal for testing new technologies and runs on many platforms including the Cray C-90, J90, T3E, the SGI Origin 2000, and clusters of Hewlett Packard Workstations. In a top-level viewpoint, the design problem definition is input to the *AEROSHOP* core executable. The optimizer within the core is MDOPT, a Boeing proprietary version of NPSOL. When the optimizer needs to perform a search direction or a line search calculation, the core relinquishes control to *AEROSHOP* scripts. The scripts are batch files of UNIX commands designed to perform a function. Two scripts are needed; the first generates an evaluation of the design and the second returns the gradient of the evaluation with respect to each of the design variables. Here, an evaluation consists of the objective function and all constraints. At the end of a script's execution, control of the optimization is returned to the core. The scripts can be custom-built to incorporate well established, heritage technologies or new, state-of-the-art technologies. The modularity of the *AEROSHOP* scripts also allows for codes to take advantage of parallel environments.

The dependence of the gradient script to the evaluation script can be strong or weak. In a finite-difference approach, the connection between the two scripts is strong as the gradient script will execute the evaluation script many times to generate the data needed for the difference. In an adjoint approach, the dependence is weaker. The gradient script will call the evaluation script to solve the flowfield equations, but then will execute a new branch to solve adjoint-related codes.

AEROSHOP Framework

High Speed Aerodynamics, Long Beach

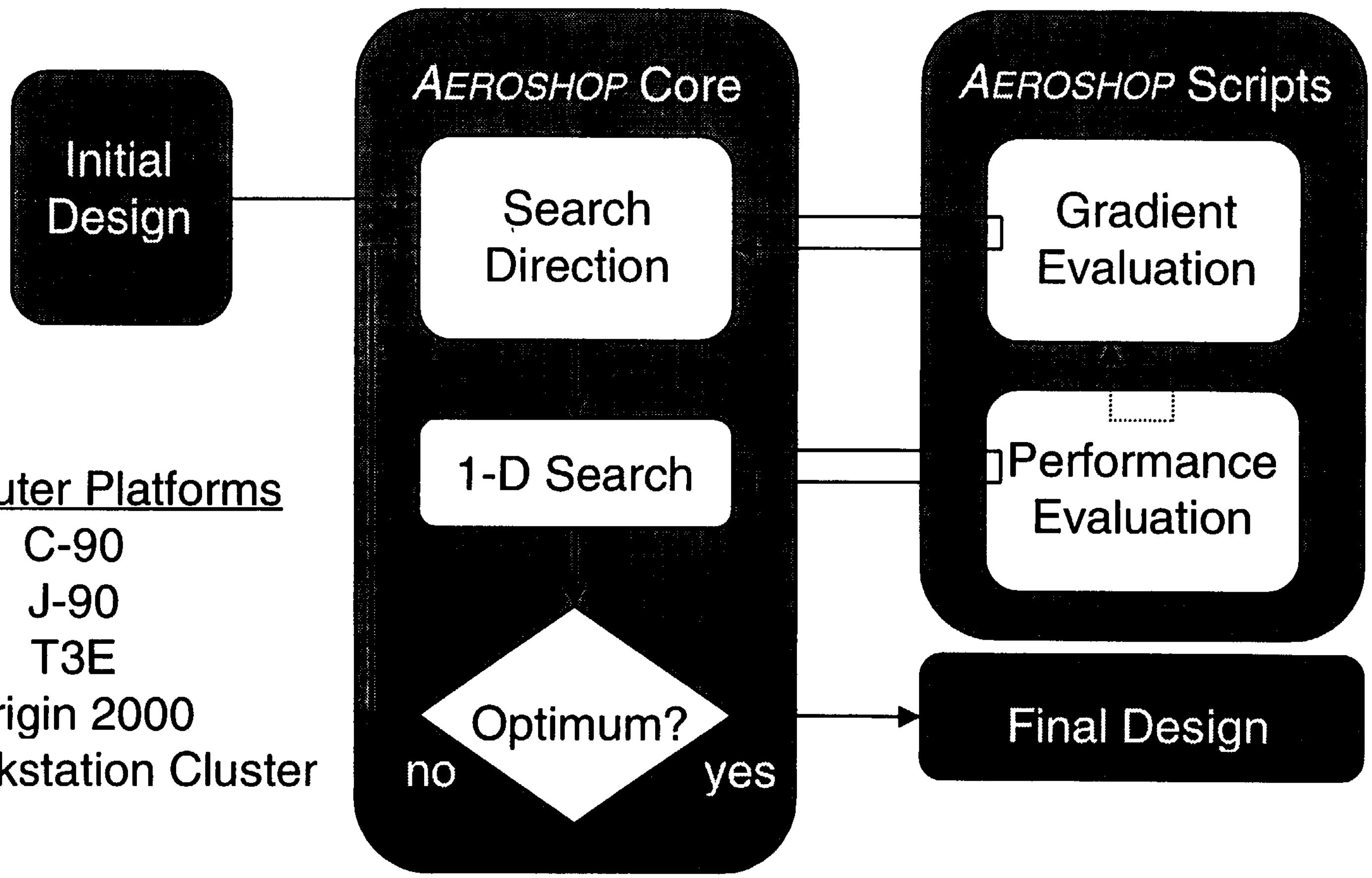

Computer Platforms

C-90

J-90

T3E

Origin 2000

HP Workstation Cluster

Configuration Modeling

The success of an optimization problem is strongly dependent on the analysis model, the objective function, and the constraints. The optimizer may exploit weaknesses in any of these pieces of the multipoint model. These elements, as applied to the TCA, are the next topics addressed.

The technology developed at Phantom Works is focused on solving a multipoint optimization problem of an HSCT similar to the layout of the Technology Concept Airplane (TCA). The major components under consideration are the wing (W), body (B), nacelles (N), diverters (D), canards (C), horizontal and vertical tails (E), and main wing flaps (F). Grid perturbation and CFD input files have been generated for full configuration optimization in addition to certain configurations containing subsets of the above mentioned components. These sub-configurations include W/B, W/B/F, W/B/N/D, W/B/N/D/C, W/B/N/D/E, W/B/N/D/F, W/B/N/D/E/F, and W/B/N/D/C/F. When nacelles and diverters are included in the configuration, it is not possible to deflect the inboard and middle trailing-edge flaps. When the W/B/F configuration is considered, additional details are provided to model the gap between the wing and the flaps at the trailing edge. Configurations may differ among evaluation points. This allows flaps to be deflected at low speed, transonic, and low supersonic conditions, while being retracted at the supersonic cruise condition.

Configuration Modeling

- Configurations may include different components at each design point
- Available component combinations include:
  - W/B
  - W/B/N/D
  - W/B/N/D/E
  - W/B/N/D/C
  - W/B/N/D/C/E
  - W/B/F
  - W/B/N/D/F*
  - W/B/N/D/E/F*
  - W/B/N/D/C/F*
  - W/B/N/D/C/E/F*

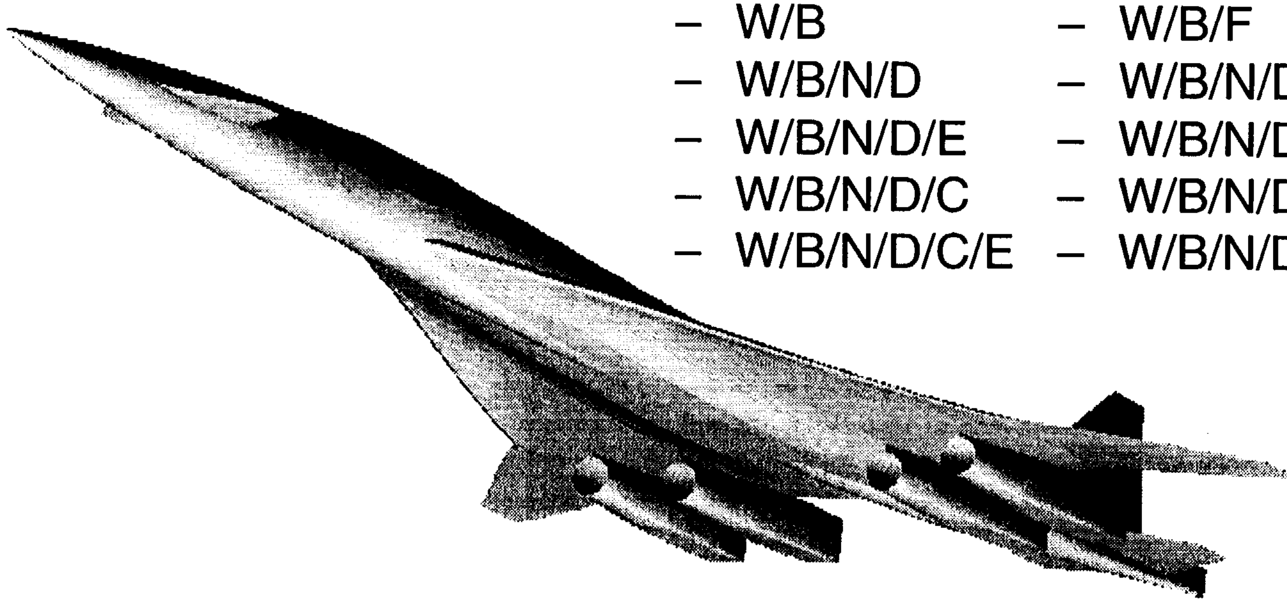

* Does not include inboard & middle trailing-edge flaps

The Objective Function

The objective function is the heart of any optimization problem. An improperly constructed objective function will inevitably lead to a non-optimum design. In aircraft design the formulation of the objective function is a complex task. Ultimately, one would like to present a design that features the lowest purchase and operating costs while satisfying all the mission requirements. Modeling cost is not well established for any aircraft much less for an airplane like the HSCT. Thus, we base our objective function on historical data that seems to indicate that the cost of an aircraft is proportional to its take-off gross weight (TOGW). In a single discipline optimization, modeling the TOGW is impossible since all the elements contributing to its evaluation are simply not available. In aerodynamic shape optimization, the best that can be done is to assume the TOGW is proportional to the fuel consumption and thus proportional to the thrust. It is on this premise that we base the objective function on a weighted sum of the thrust evaluated at key points along the mission profile,

$$f = \sum_i \omega_i C_{T_i} \,. \tag{1}$$

The weights associated with each element of the mission and which elements to include in the evaluation of (1) is an area of little understanding. It seems natural to exploit the Technology Integration team's analysis of the TCA mission profile that suggests the dominant legs of the mission are the supersonic cruise (M_∞=2.4, C_L=0.1), the transonic cruise (M_∞=0.9, C_L=0.18), and the supersonic acceleration (M_∞=1.1, C_L=0.15). The weights associated with these segments are 1, 0.3, and 0.15, respectively.

The thrust is computed according to the free-body diagram shown in the figure below. The net thrust is comprised of the engine thrust, C_T, the nacelle-inlet ram drag, C_{Dram}, and aerodynamic drag, C_{Daero}. The engine thrust acts at and along the centroid of the CA reference-nacelle nozzle, and the magnitude is the same for all nacelles. (The CA reference nacelle is the one in the IGES file that the CA community uses. It does not have an inlet spike or true nozzle.) The engine thrust is calculated to balance the forces in the drag direction. The ram-drag acts at the centroid of the CA reference-nacelle inlet in the drag direction, and is a constant. The components of the aerodynamic drag include pressure, viscous, spillage, and excressence drag and are assumed to act at the aerodynamic center. Engine thrust, ram drag, and aerodynamic drag are included when evaluating trim conditions

The Objective Function

- The objective function is a weighted sum of the aerodynamic performance at each design point

$$P=\omega_1 P_1+\omega_2 P_2+\ldots+\omega_n P_n$$

where ω_i are the weighting factors and P_i is typically C_D, D/L, or C_T

- Thrust is computed to balance drag

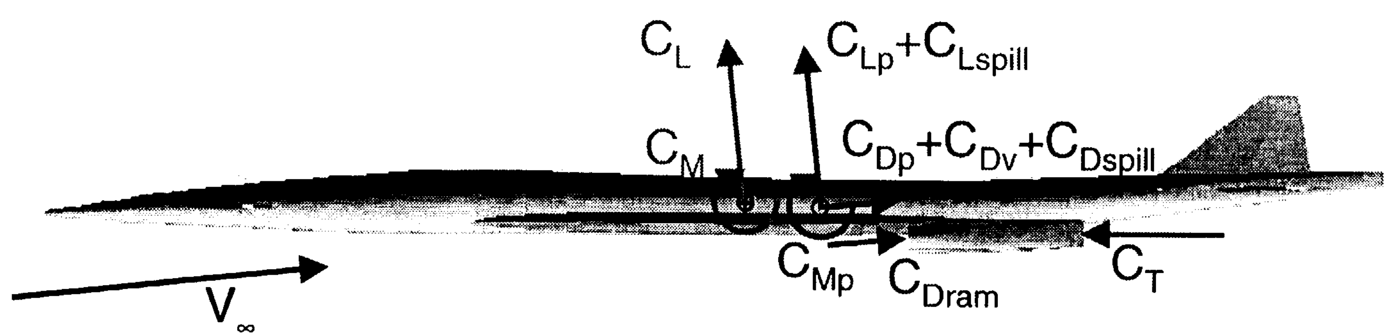

Constraints

The constraint package used during the single-point optimization for Cycle 2 has been relatively unmodified. Constraints that may be enforced for a multipoint design include those indicated in the figure below, though it is unlikely that inlet flow quality will be exercised. Geometric constraints with a dependence on the flow condition, such as the in-flight deck incidence, will be enforced at the supersonic cruise condition, and may be relaxed at other conditions.

Constraints

High Speed Aerodynamics, Long Beach

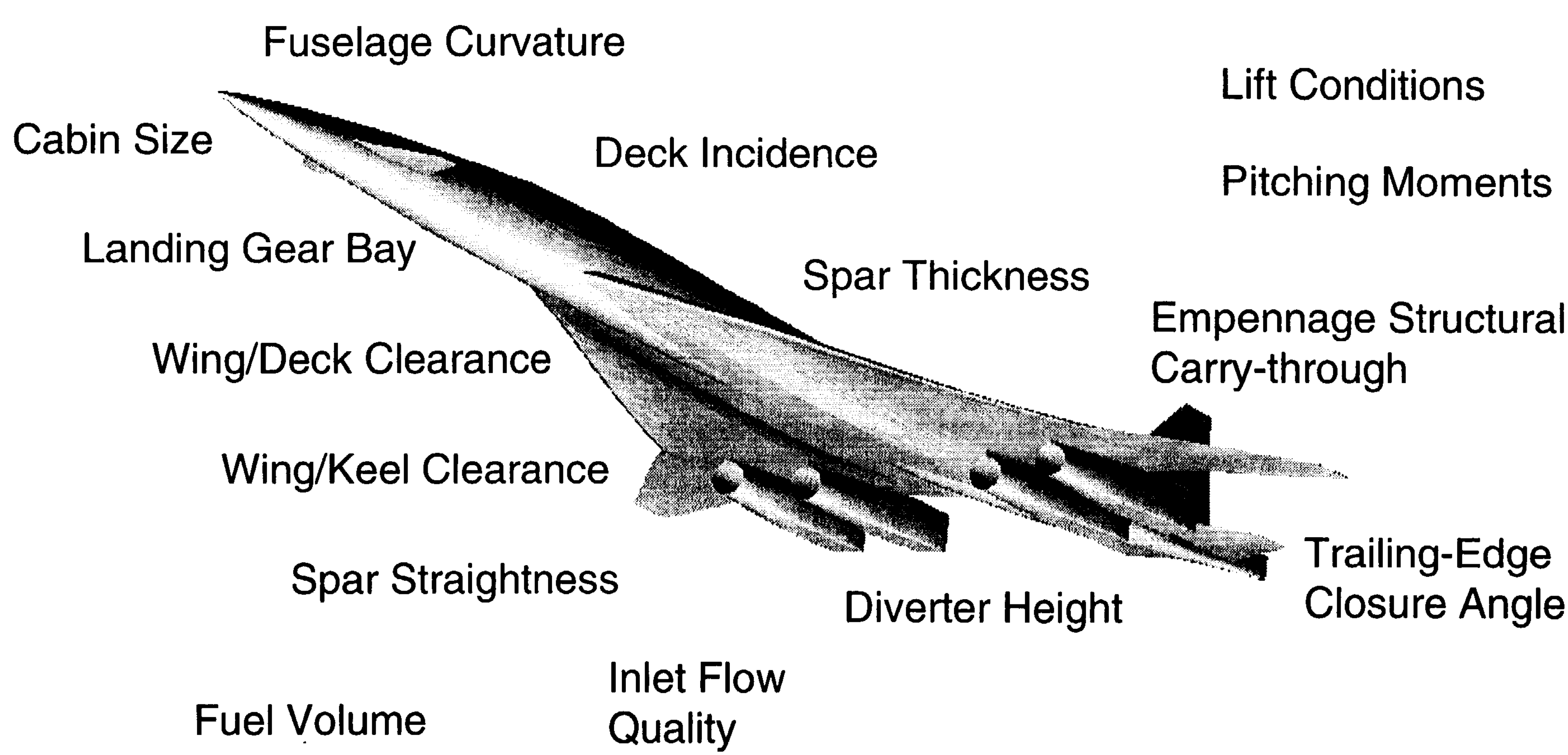

Design Variables

Most design variables are formulated as shape function perturbations to an underlying geometry. Shape functions can allow for a smooth progression from the initial geometry to an optimized shape, though when many shape functions are used in a single optimization it often becomes necessary for a post-optimization smoothing procedure. Shape functions have an advantage over NURBS-based design by reducing the number of design variables required to define an optimized shape. Formulating the design variables as perturbations assumes that the initial design is good and the optimum shape is close. Perturbations offer the advantage that large changes to the design are not possible. This avoids wild designs that are often undesirable, difficult to grid, and hard to analyze. Design variables which are applied as absolute values (i.e., are not perturbations) include the angle-of-attack, flap deflections, and canard and empennage incidences.

Changes to the configuration can occur on the wing, fuselage, and nacelles. The wing can change in twist, camber, thickness, shear, and flap deflection. The fuselage can change in camber, cross-sectional area, and cross-sectional shape.

Design Variables

High Speed Aerodynamics, Long Beach

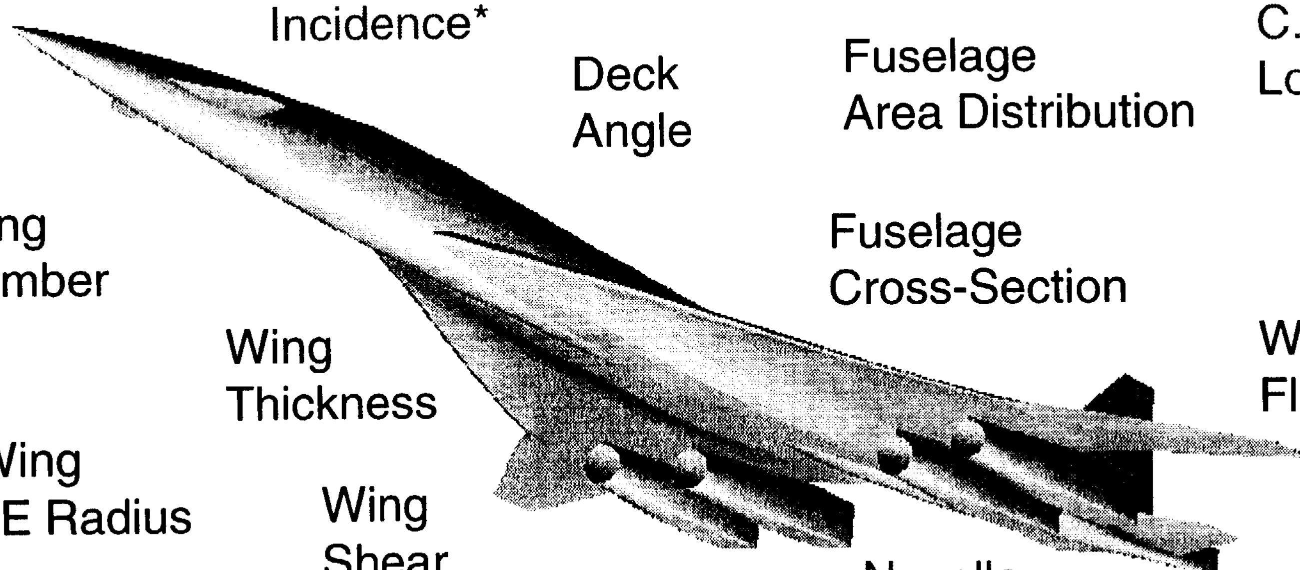

Fuselage Camber

Canard Incidence*

Deck Angle

Fuselage Area Distribution

C.G. Location*

Wing Camber

Fuselage Cross-Section

Wing Thickness

Wing LE/TE Flaps

Wing Twist

Wing LE Radius

Wing Shear

Empennage Incidence*

Nacelle OML*

Inlet Alignment*

Nozzle Alignment*

Angle-of-Attack

Nacelle Alignment*

*New in 1998

BOEING

Nacelle/Diverter Shaping Capability

Design variables applied to the nacelles preserve the internal cross-sectional area, but allow the outer mold line to change in thickness and camber. The inlet, nozzle or entire nacelle may change in pitch and yaw. Variations to the empennage are limited to pitch. The canard can change in pitch and dihedral. Changes in horizontal and vertical placement of the canard and empennage are restricted due to its adverse impact on other disciplines. Shown below are the programmed degrees-of-freedom for changes to the nacelle shape.

Nacelle/Diverter Shaping Capability

High Speed Aerodynamics, Long Beach

Shearing Capability

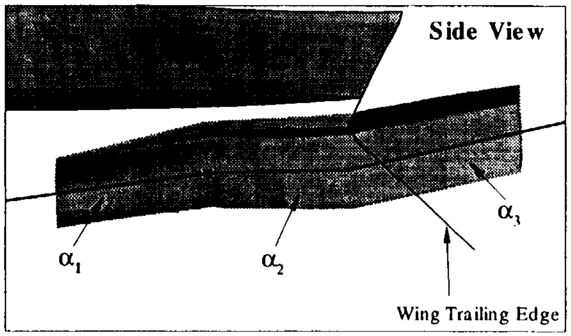

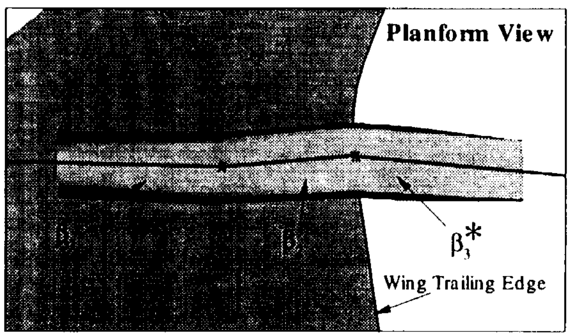

α_i= Shear in pitch variable for segment i
β_i= Shear in yaw variable for segment i

---

* Complete nacelle/diverter yaw variable

Outer Surface Design

TCA Nacelle Geometry Modification Procedure from a Discrete Surface

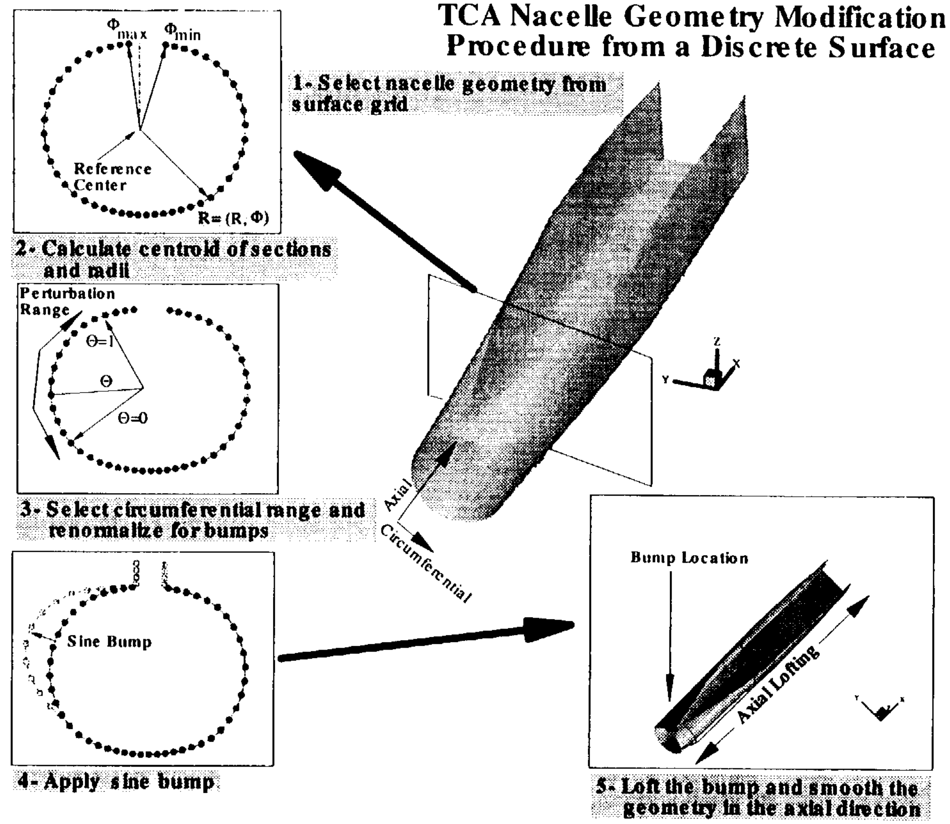

W/B/N/D Geometry/Grid Generation

A top-level diagram of the geometry and grid generation in *AEROSHOP* is shown below. Presented in its basic form, the geometry generation module takes baseline geometry and input design variables and then perturbs the W/B surface. Next, the nacelles are rolled and pitched to follow the lower surface of the wing (assuming a W/B/N/D configuration is being optimized). The final geometry step is the generation of a new diverter between the new wing and the translated and rotated nacelles.

The grid generation module uses the current defining geometry and creates a CFD surface grid on the W/B using the QGRID code. This surface grid is then passed to either CSCMDO or FlexMesh to create a multiblock W/B surface and to perturb the multiblock volume grid. Again, if only a W/B configuration is being optimized, the volume is single block, and the nacelle/diverter work is unnecessary.

W/B/N/D Geometry/Grid Generation

High Speed Aerodynamics, Long Beach

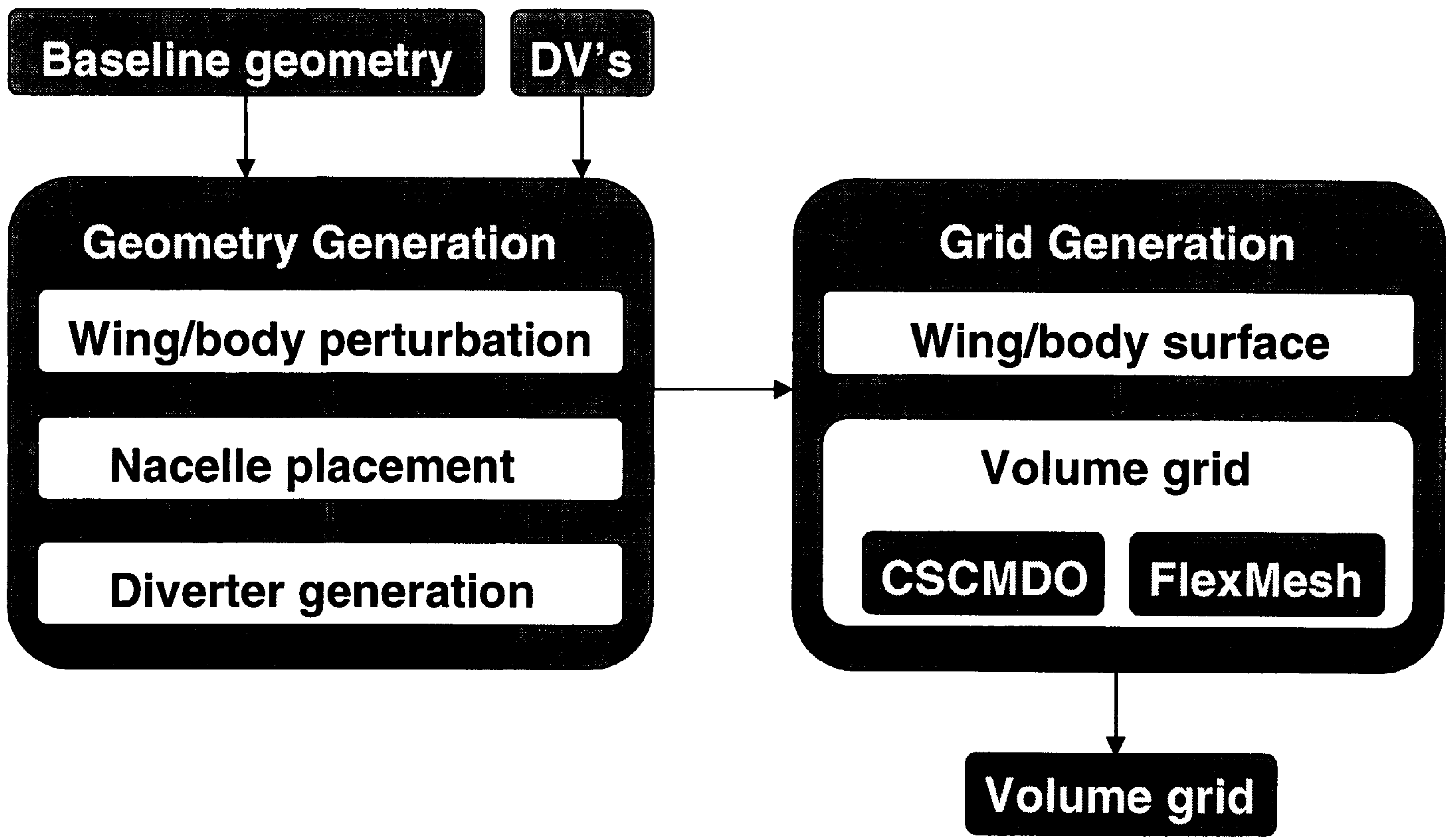

BOEING

Canard and Empennage Integration

A top-level diagram of the system that integrates/perturbs the canard and empennage grid blocks to an existing W/B/N/D configuration is shown. The first step in this process is to integrate the new canard to the current configuration. The canard can be modified in both pitch and dihedral and the system maintains the relative position of the canard on the fuselage. The new canard surface grid, along with a baseline W/B/N/D/C grid and the current configuration's W/B/N/D grid are given to CSCMDO to produce a new W/B/N/D/C surface and volume grids.

The next step in this process is similar to the canard module with the integration of the vertical and horizontal tail surfaces to the fuselege aftbody. Once again, the system maintains the relative position of the tails to the fuselage. These new empennage surfaces along with the baseline W/B/N/D/C/E grid and the previously created current W/B/N/D/C grid are again given to CSCMDO to produce a new W/B/N/D/C/E surface and volume grids for analysis.

Canard and Empennage Integration

High Speed Aerodynamics, Long Beach

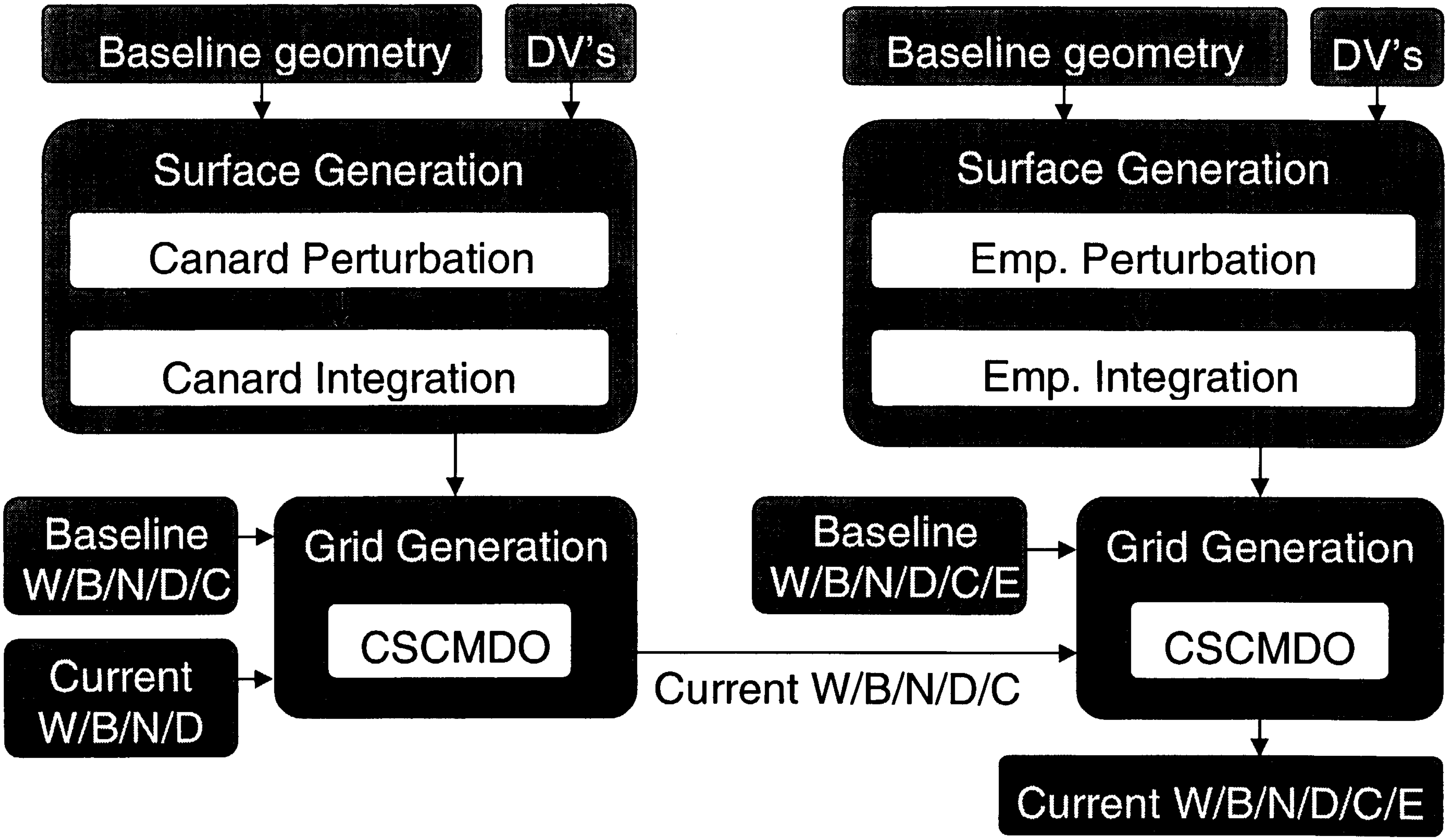

BOEING

Full Configuration Grid

The figure below shows the CFD surface grid for the W/B/N/D/C/E configuration with every-other point removed for clearity. Also shown are detailed views for the canard and empennage regions.

Full Configuration Design Grid

High Speed Aerodynamics, Long Beach

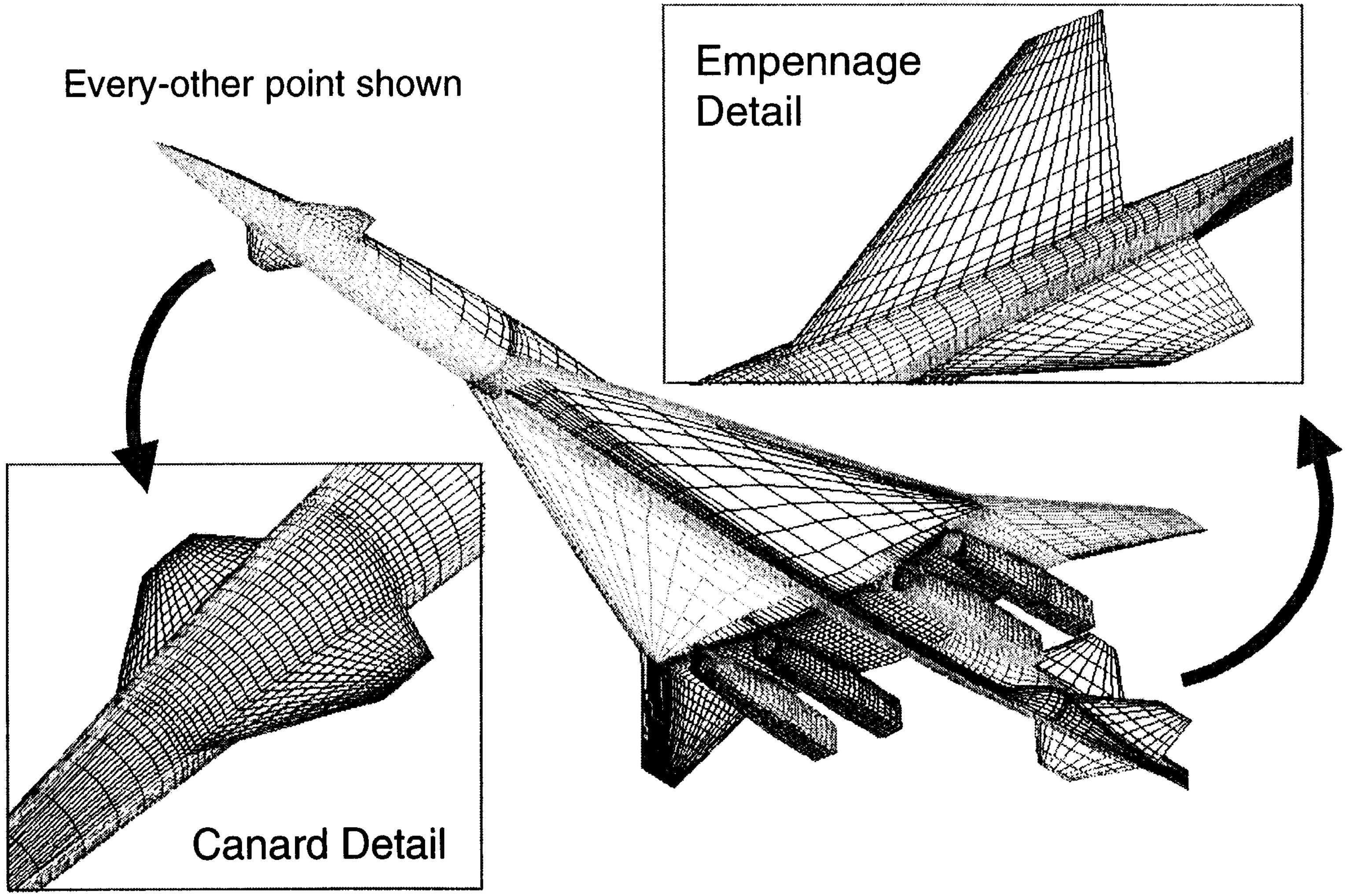

BOEING

Flow Analysis

The *AEROSHOP* system is connected to two different flow solvers at this time. The first of these is NASA Langley's well known CFL3D. This code was selected due to its ability to work on both point-matched and patched multiblock grids. CFL3D will work on both serial and parallel platforms providing *AEROSHOP* with even more flexibility. The code has been differentiated with ADIFOR in both the forward and reverse modes to provide flow sensitivities to *AEROSHOP* (in addition to a finite-difference option). In addition to these design-oriented enhancements, CFL3D now has a wall-function method to provide Navier-Stokes results on coarser meshes more suitable to the design environment.

The second solver that has been connected to *AEROSHOP* is the TLNS3D code, also from NASA Langley. Implementation of this code was delayed due to its previous inability to work with patched-multiblock grids (a handicap that has recently been lifted). TLNS3D also functions on serial and parallel platforms, thus offering the same flexibilty as CFL3D. The code offers very fast and generally more robust solutions than CFL3D, but it has not been processed through ADIFOR for sensitivities. There is however, a very efficient hand-differenced adjoint code developed for TLNS3D that has been used extensively in *AEROSHOP* for Euler-based optimzation.

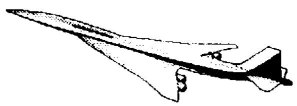

Flow Analysis for Optimization

- CFL3D
  - Operates in serial or parallel
  - Handles multiblock grids
  - Wall functions
  - Differentiated with ADIFOR (forward & reverse)
- TLNS3D
  - Operates in serial or parallel
  - Handles multiblock grids
  - Fast convergence
  - Hand-differentiated to obtain the adjoint

BOEING

Gradient Calculations

Automatic Differentiation

This chart shows a three-step process to obtain analytic gradients using automatic differentiated FORTRAN codes. The design variables are passed through surface and volume grid generation tools to produce a grid suitable for analysis. The differentiated CFL3D code operates on the grid to produce a flow solution and an adjoint solution. The next step involves generating grid sensitivities. These establish how the grids change with perturbations in the design variables. The flow, adjoint, and grid sensitivitives are passed along to the next step that produces the sensitivities of aerodynamic quantities with respect to design variables.

TLNS3D-Adjoint Gradients

High Speed Aerodynamics, Long Beach

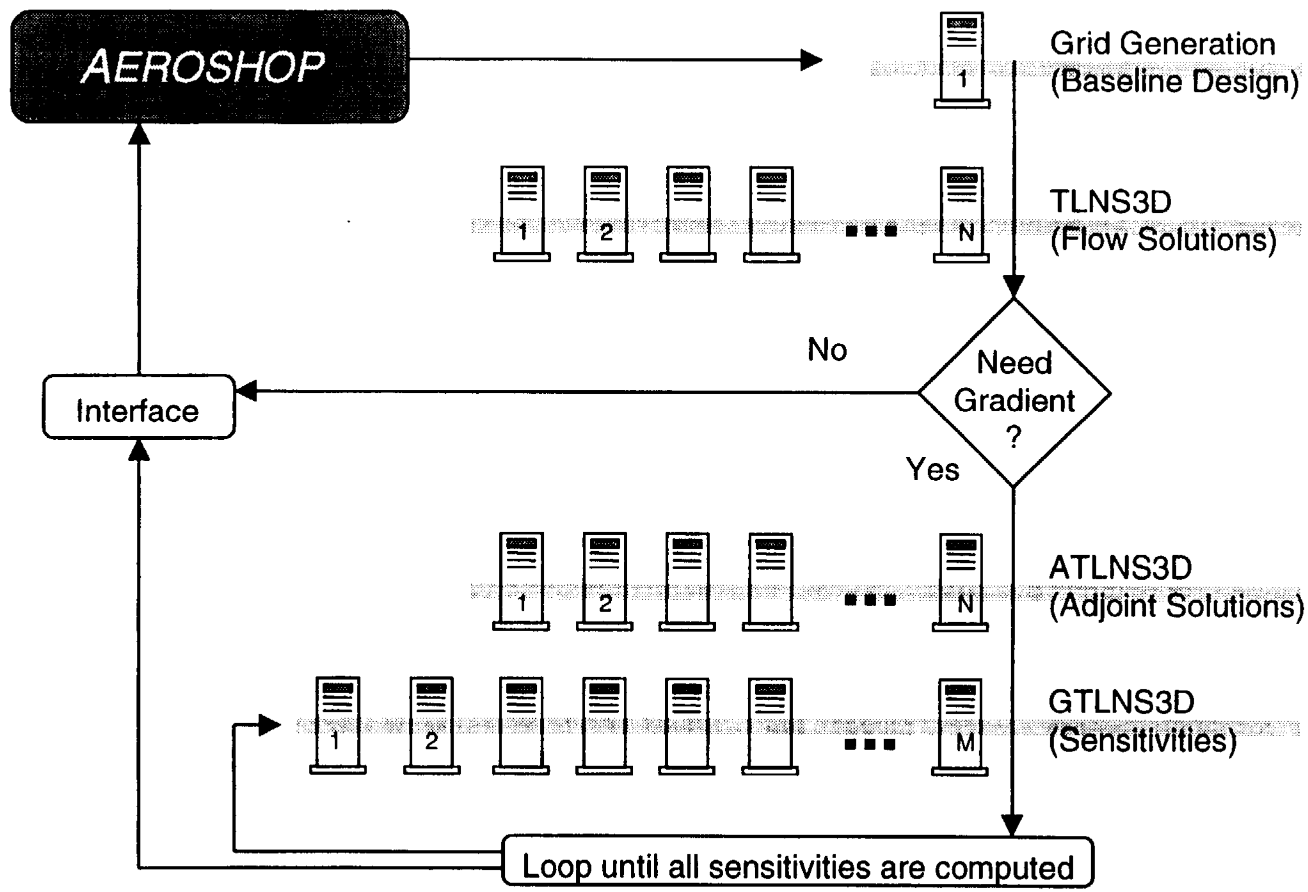

Gradient Calculations

TLNS3D-Adjoint

The adjoint method provides a means to compute sensitivities in an efficient and accurate manner. Details of the method can be found in many papers such as Reuther et al.[2] and Kuruvila et al.[3] In essence, the method requires two solutions for a gradient of an aerodynamic quantity with respect to all the design variables: the flow solution and the adjoint solution. For typical optimizations, two adjoint solutions are required for gradients of lift and drag. In addition to the flow and adjoint solutions, the TLNS3D-Adjoint formulation requires gradients of the grid with respect to the design variables. This can be computed by finite-difference or analytically. Finite-difference grid sensitivities are easy to compute, but can be inaccurate if a poor step size is chosen. Analytic sensitivities are not dependent on the step size, but can be difficult to obtain. The ADIFOR tool is ideal for obtaining analytic grid sensitivities.

Depicted below is the implementation of the TLNS3D-Adjoint system with the *AEROSHOP* framework for a single-point design. *AEROSHOP* relinquishes control to a script that drives TLNS3D-Adjoint when sensitivities are required. This script first generates a baseline grid. Next it computes a flow solution using TLNS3D. In a parallel environment, TLNS3D can run on a user-defined number of processors, typically between 10 and 30. The next step involves obtaining solutions for the adjoint equations. This step is repeated for each aerodynamic quantity required (*i.e.*, C_L, C_D, and C_M). The adjoint problem is similar in size to the flow problem and thus can be run on the same number of processors as was used to compute the flow solution. The next step involves obtaining the grid sensitivities. In the "production" version of *AEROSHOP*, the grid generator is applied to each perturbation of the design variables for a finite-difference estimation of the grid sensitivities. On a serial machine, this process is done sequentially and is the time dominating step in the optimization for problems involving large numbers of design variables. On a parallel machine, the grid sensitivities are done in blocks of *m* number of design variables. For efficient use of the computer, the number of processors used here should be close in value to the number used to compute the adjoint and flow solutions. The final step is the calculation of the sensitivities. For multipoint optimization, each step is repeated over the number of evaluation points.

Automatic Differentiation

High Speed Aerodynamics, Long Beach

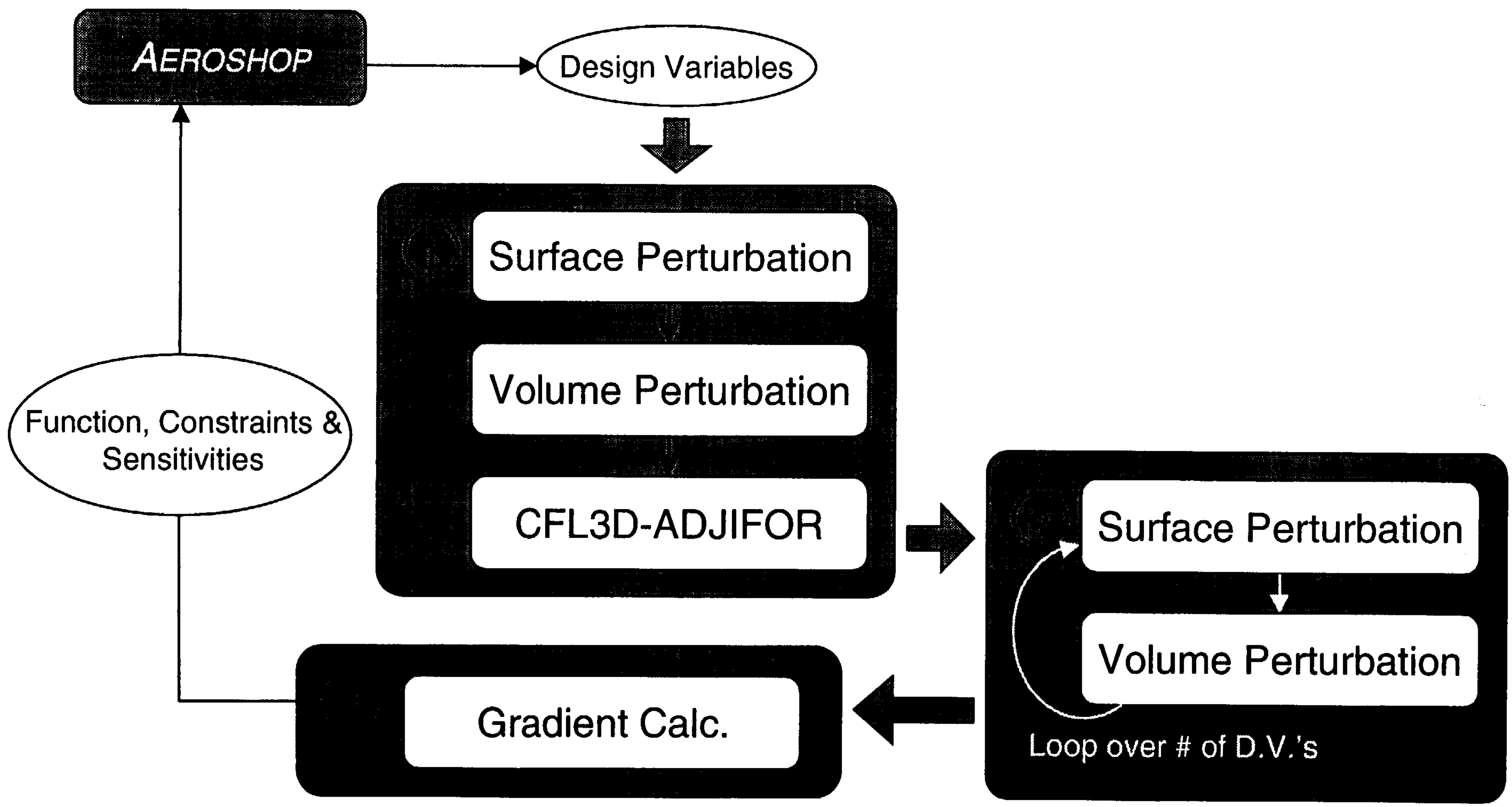

BOEING

Intermediate Results

Optimization with Analytic Derivatives

A head-to-head comparison of the analytic derivative methods, CFL3D-ADIFOR and TLNS3D-Adjoint, was performed using a W/B optimization of the TCA. The objective of the exercise was to compare the methods in accuracy, usability, and potential for growth. The optimization problem was set up identically in both cases; each started from the same configuration (TCA), used 401 design variables, and was formulated to minimize D/L at M_∞=2.4 for a given lift condition. The problem was constrained with the set of constraints used during Cycle 2 optimization. Sensitivities of the constraints, in both cases, were obtained using the ADIFORed processed constraint package.

Differences in the optimization were limited to the sensitivity method for aerodynamic quantities and the flow solver of performance evaluations. The ADIFOR optimization used CFL3D and the hand-differentiated adjoint used TLNS3D, thus making the analysis consistent with the sensitivity method.

The final results of the optimization are plotted on the polar below. The accuracy of the gradients produced by the methods seems to be comparable as both optimizations produced substantial improvements in the design. The CFL3D-ADIFOR procedure produced sensitivities in less wall clock time since it was able to make use of the parallel environment on the NAS Origin 2000. At the time of the optimizations, TLNS3D-Adjoint was restricted to serial computers and significant time was required to obtain grid sensitivities. The TLNS3D-Adjoint optimization has the advantage of running on a single platform and operated in a relatively hands-off manner. The line searches for the CFL3D-ADIFOR optimization was performed on the Cray C-90. This process required file transfers and thus was prone to human errors. Work is underway to eliminate the dependency on the C-90. Both methods have proven to be viable candidates for future optimizations.

Current State of TCA W/B Design

High Speed Aerodynamics, Long Beach

- Two optimizations were performed using analytic derivatives of the objective function and constraints
  - Case 1 computed flow sensitivities with ADIFORed-CFL3D
  - Case 2 computed flow sensitivites with TLNS3D-Adjoint
- Constraint sensitivities were computed with ADIFOR-based code
- Optimizations used 401 design variables and 55 constraints

CFL3D Euler Solutions
Computed on the Design Grid, M_∞=2.4

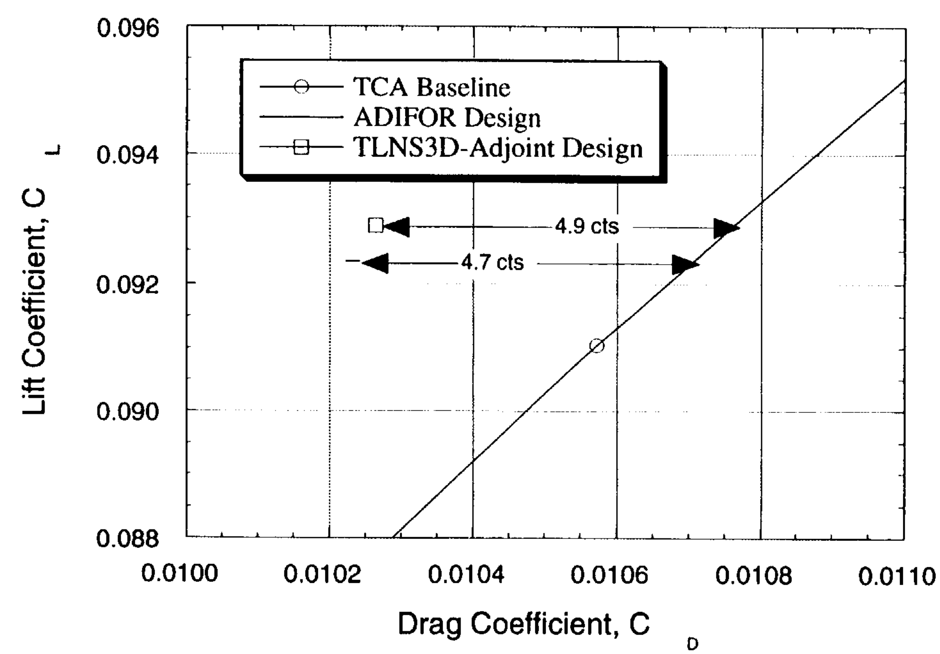

BOEING

Intermediate Results

Current State of W/B/N/D Optimization

This figure documents the impact of the technology developments at Phantom Works to W/B/N/D optimization. The process to obtain the Cycle 2 design was limited to configurations gridded with a single block, and gradients provided by finite-difference approximations. These limitations forced the optimization process to superimpose a baseline nacelle pressure field to the current design's W/B solution and run multiple optimizations with limited number of design variables. Navier-Stokes analyses showed that this process produced an improvement of 3.9 counts, though Euler solutions on the course design grid showed only a 3.5 count improvement.

The removal of the restriction to configurations griddable with a single-block grid provided the first major benefit to the *AEROSHOP* optimization process. This technology was demonstrated in a multipoint environment to simultaneously reduce the supersonic and transonic cruise point drag. At the supersonic condition, the W/B/N/D configuration was modeled while the transonic configuration was limited to W/B/F. The exercise produced a total improvement of 5.7 dragcounts at the supersonic condition as predicted by Euler analyses.

The development of the TLNS3D-Adjoint system benefited the optimization process in two ways. First, the flow sensitivities were computed with greater accuracy and second, they are computed with greater speed. The first implementation of the TLNS3D-Adjoint system was limited to optimizations involving single-block grids and thus the test case was restricted to the W/B configuration. Here, the latest geometry (from the W/B/N/D multipoint optimization) was used as the initial geometry with the nacelle removed. The nacelles were reinstalled after the optimization. The optimization effort further reduced the W/B/N/D Euler drag by 0.9 counts. The reduction can be attributed to greater accuracy in the gradients and the larger degree-of-freedom resulting from the hundreds of design variables used in the optimization.

The final point shown on the figure documents the benefit of two technologies; the nacelle kinking capability, and the extension of the TLNS3D-Adjoint system to configurations gridded with multiple blocks. The optimization exercised the nacelle shaping optimization that included inlet, nozzle, and the entire nacelle alignment in pitch and yaw. Optimization including the nacelle shape was not available at the time of this optimization. The technologies resulted in a 7.3 count improvement in Euler drag over the TCA Baseline configuration.

Current State of TCA W/B/N/D Design

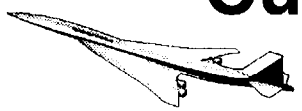

High Speed Aerodynamics, Long Beach

- Phase 1: W/B with nacelle effects; cruise-point design (Cycle 2)
- Phase 2: W/B/N/D multipoint design
- Phase 3: W/B design with adjoint gradients (hundreds of dv's; nacelles installed after optimization
- Phase 4: W/B/N/D adjoint cruise design including nacelle shearing

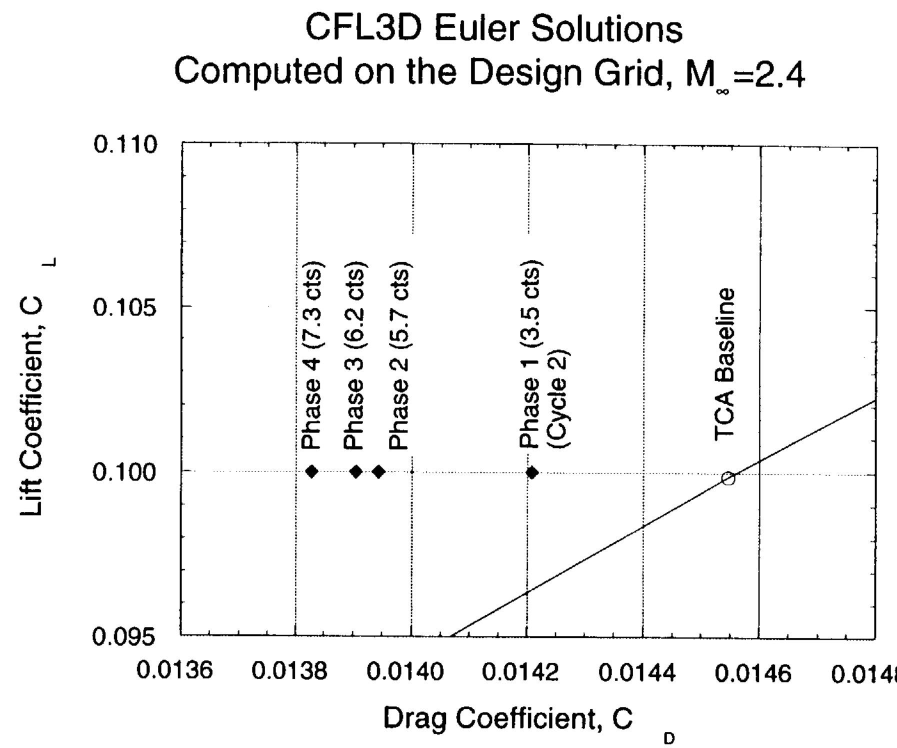

BOEING

Intermediate Results

Trim Conditions, x_{CG} variation

A parametric study was performed to evaluate the trim drag benefit of the TCA W/B/N/D/E configuration with thrust as a function of the axial CG location, x_{CG}. Trim drag is the difference in drag between the trimmed configuration and the configuration with no lift on the horizontal tail. Moving the CG aft reduces angle-of-attack, increases the tail incidence (i_H), and reduces the thrust and trim drag (C_{Dtrim}). At the aft-most CG location, the trim-drag benefit is 1.3 counts. This is close to the 1.0 count that the TI team has bookkept.

Effect of CG Location on Trim

High Speed Aerodynamics, Long Beach

Baseline TCA W/B/N/D/E with Thrust, CFL3D Euler, $M_\infty=2.4$

$Re_c=212\text{x}10^6$ ($C_{Dv}=45.63$ cts.), $C_{L,\ w/Thrust}=0.1$, $C_{D,\ Ram}=267.1$ cts., $Z_{CG}=218.0$ in.

Moving the CG aft:

- Reduces angle-of-attack
- Increases tail incidence
- Reduces required thrust
- Increases trim-drag benefit

Trim drag:

- $\Delta C_{D,\ Trim} = C_{D,\ Trim} - C_{D,\ no\ H\text{-}tail\ lift}$
- At the aft-most CG location:
  - CFD predicts 1.3 cts.
  - TI Team book-keeps 1.0 ct.

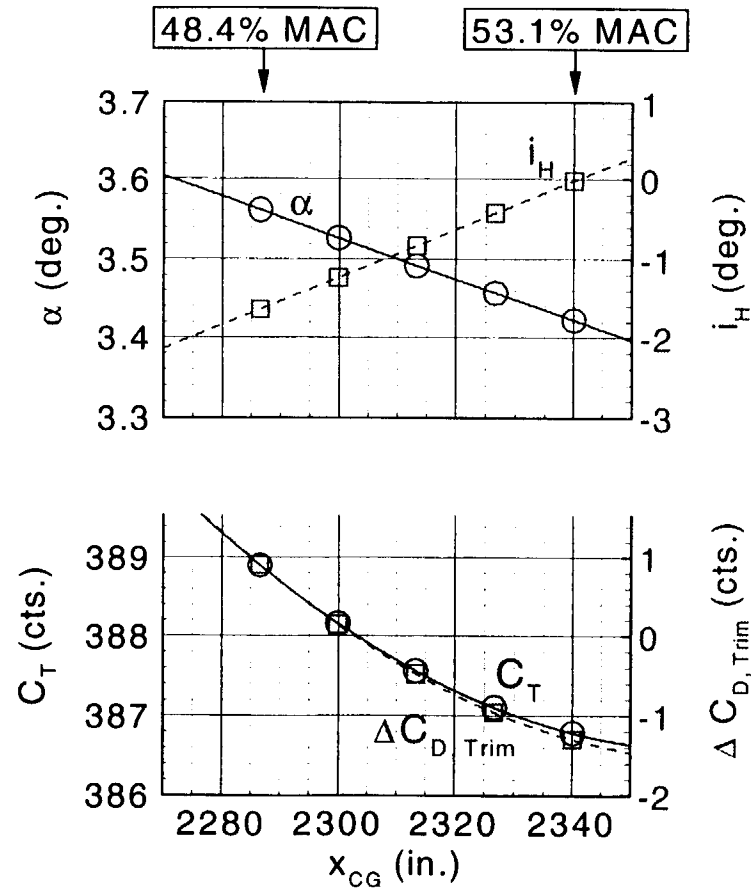

Intermediate Results

Trim Conditions, θ_T variation

A parametric study was performed to evaluate the trim drag benefit of the TCA W/B/N/D/E configuration with thrust as a function of the thrust-vector pitch angle, θ_T. For this study, θ_T is the same for the inboard and outboard engines and is independent of the nozzle angle. The baseline thrust-vector pitch angles are θ_T, inboard = -3.11° and θ_T, outboard = -2.15° for an average θ_T = -2.9°. Pitching the thrust-vector up reduces θ_T and i_H, and increases C_{Dtrim}. The minimum-thrust condition is near $\theta_T = 0.8°$.

Effect of Thrust-Vector Angle on Trim

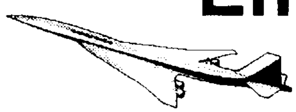

High Speed Aerodynamics, Long Beach

Baseline TCA W/B/N/D/E with Thrust, CFL3D Euler, M_∞=2.4
Re_c=212x10^6 (C_{Dv}=45.63 cts.), $C_{L,\ w/Thrust}$=0.1, $C_{D,\ Ram}$=267.1 cts., Z_{CG}=218.0 in.

Thrust Angle, θ_T:

- Pitch angle of thrust vector
- Opposite of exhaust angle
- Minimum thrust at $\theta_T \approx 1°$

Increasing θ_T:

- Reducing angle-of-attack
- Reducing tail incidence
- Reduces trim-drag benefit

Trim drag

- $\Delta C_{D,\ Trim} = C_{D,\ Trim} - C_{D,\ no\ H\text{-}tail\ lift}$

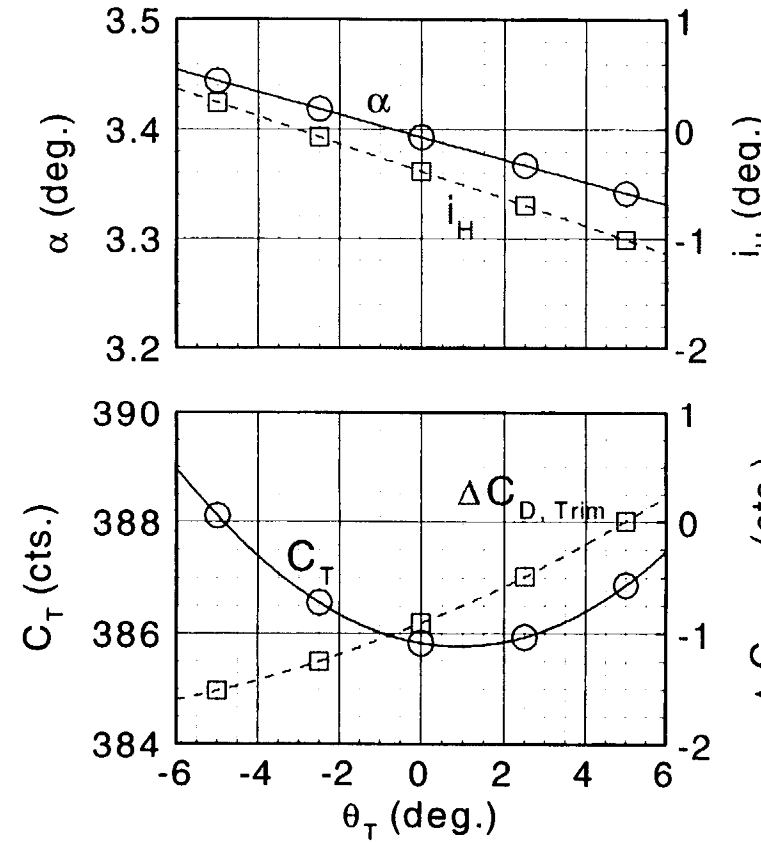

BOEING

Intermediate Results

Sequential Multipoint Optimization

The sequential procedure for multipoint design (outlined in an earlier section) has been applied to four supersonic cruise point designs. Three of these designs correspond to the Cycle 2 configurations produced by NASA Ames, BCAG, and Phantom Works. The fourth is a configuration representing the latest design from Phantom Works (Cycle 3). In this procedure, the OML is frozen with the exception of leading- and trailing-edge flaps. The optimization is done as a single-point design at M_∞=0.6, 0.9 and 1.1. The results of the optimizations are shown below as drag decrements with respect to the TCA baseline configuration with all flaps retracted. This exercise demonstrates that off-design Mach number performance is not seriously compromised as a result of supersonic cruise point design. This method, however, does not measure the benefits of a simultaneous multipoint design approach.

Sequential Multipoint Results

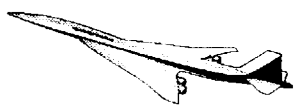

High Speed Aerodynamics, Long Beach

Drag Reduction Relative to TCA Baseline with no Flaps
Results Based on CFL3D Euler Analysies on the Design Grid

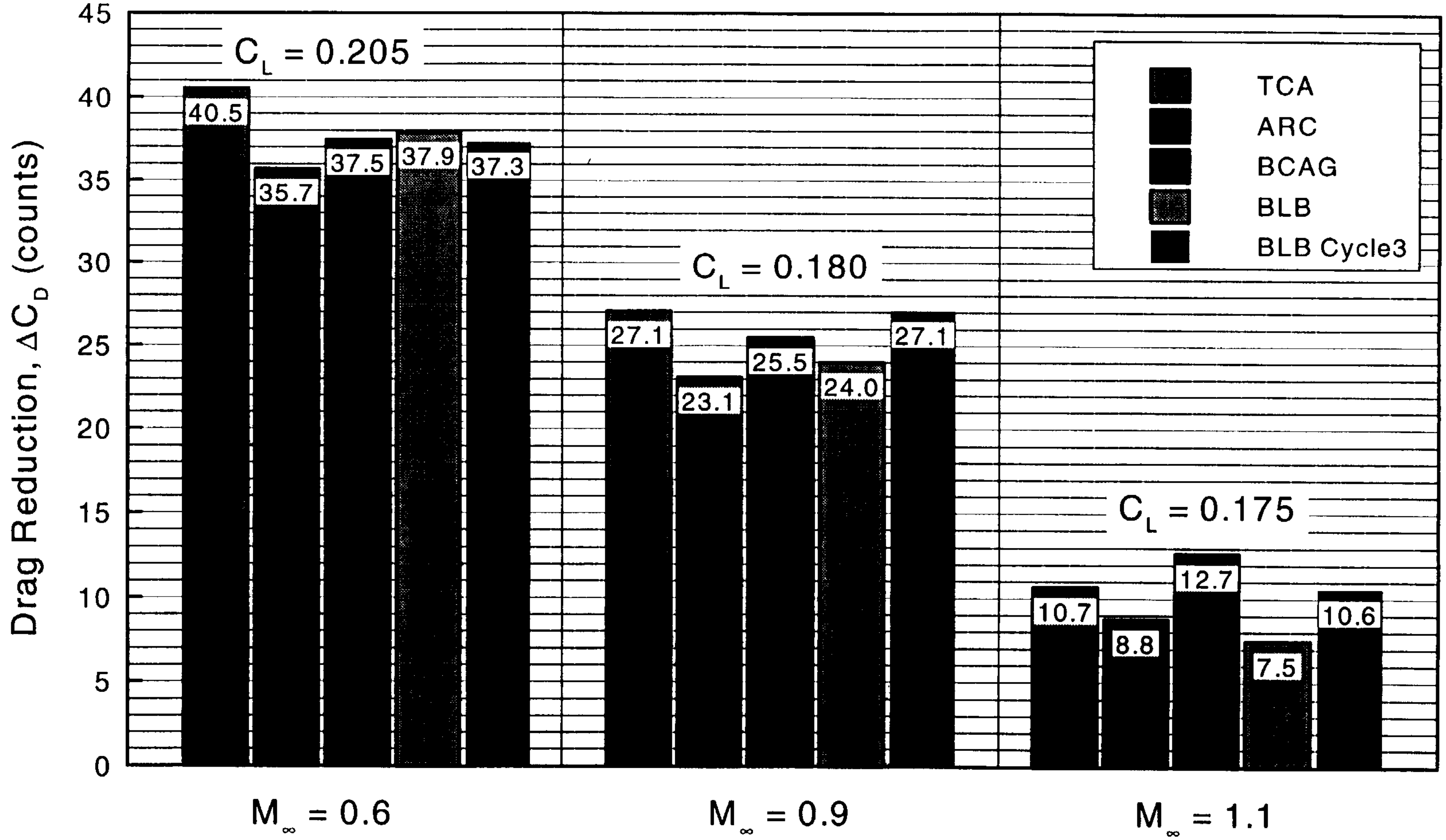

BOEING

Intermediate Results

Leading-edge Radius and Flap Optimization

One area of potential benefit to the overall performance of the TCA is the optimization of the leading edge. During take-off, climb, and transonic cruise, a blunt leading edge can benefit the performance by keeping the flow attached. At the supersonic cruise condition, a sharp leading edge is preferred to reduce wave drag. The purpose of this exercise is to optimize the leading edge for optimum performance.

In the first attempt, a single-point optimization was performed at the transonic cruise condition (M_∞=0.9, C_L=0.18). Here the transonic performance could be improved by modifying the thickness and camber of the leading edge or by deflecting the leading-edge flaps. Trailing-edge flaps and the angle-of-attack were other variables in the design problem to assist in maintaining the lift constraint. The result of the optimization was an increase in thickness of the leading edge near the break, and a droop in leading edge over the inboard section of the wing. The part-span inboard flap was deflected to 15°. This led to a 2.5 count reduction in drag at the design condition, but a significant 1 count increase at the supersonic cruise condition.

The second attempt repeated the optimization in a multipoint setting. Here, an objective function based on the drag at the supersonic and transonic cruise condition was constructed,

$$f = C_D\big|_{M_\infty=2.4, C_L=0.09} + 0.3C_D\big|_{M_\infty=0.9, C_L=0.18} \qquad (2)$$

This function, evaluated for the baseline TCA and the configuration obtained from the single-point optimization, is 86.6 and 86.9, respectively. The function after multipoint optimization was reduced to 86.2 with a small reduction in supersonic cruise drag (~0.1 count) and ¾ count reduction in transonic cruise drag. The reduction in the objective function is small because the configuration changes occur only at the leading edge (10% of the chord) and because each configuration has optimized flaps at the transonic condition (flaps are retracted at M_∞=2.4).

This result demonstrates the requirement of a simultaneous multipoint approach to improve the transonic performance without compromising the supersonic performance.

Leading-Edge Radius and Flap Optimization

High Speed Aerodynamics, Long Beach

Objective

- Improve transonic cruise performance with nonlinear aerodynamic optimization using leading-edge shape functions and flap settings

Approach

- Define leading-edge shape functions covering first 10% of the chord

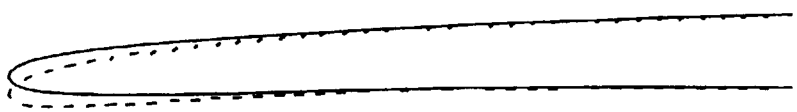

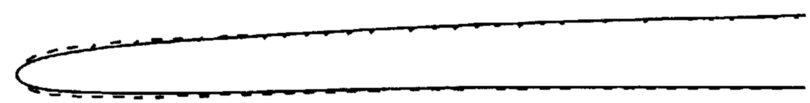

- Perform single-point optimization at $M_\infty = 0.9$
- Perform dual-point optimization at $M_\infty = 2.4$ and 0.9

$$F = C_{Dp,M=2.4} + 0.3C_{Dp,M=0.9}$$

- Optimizations performed in the distributed *AEROSHOP* environment with TLNS3D-Adjoint derivatives

Leading-Edge Optimization

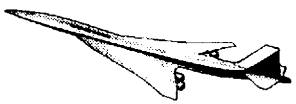

High Speed Aerodynamics, Long Beach

Drag Polars of TCA W/B Configurations Resulting from Single & Multipoint Optimizations

Analyses Performed with TLNS3D on the Design Level Grid

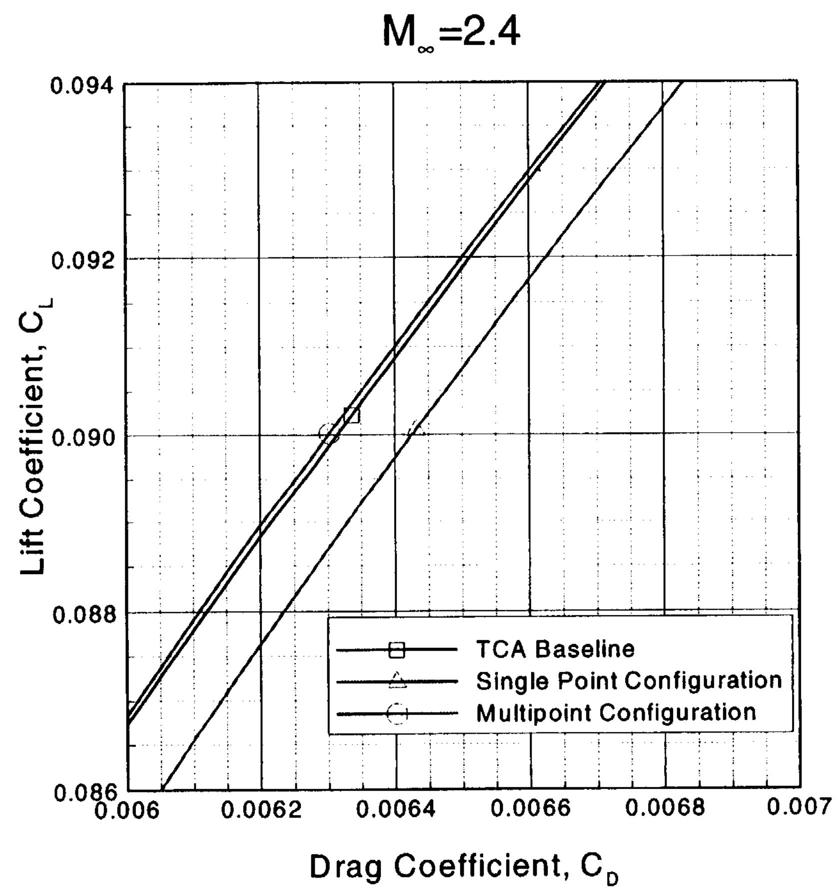

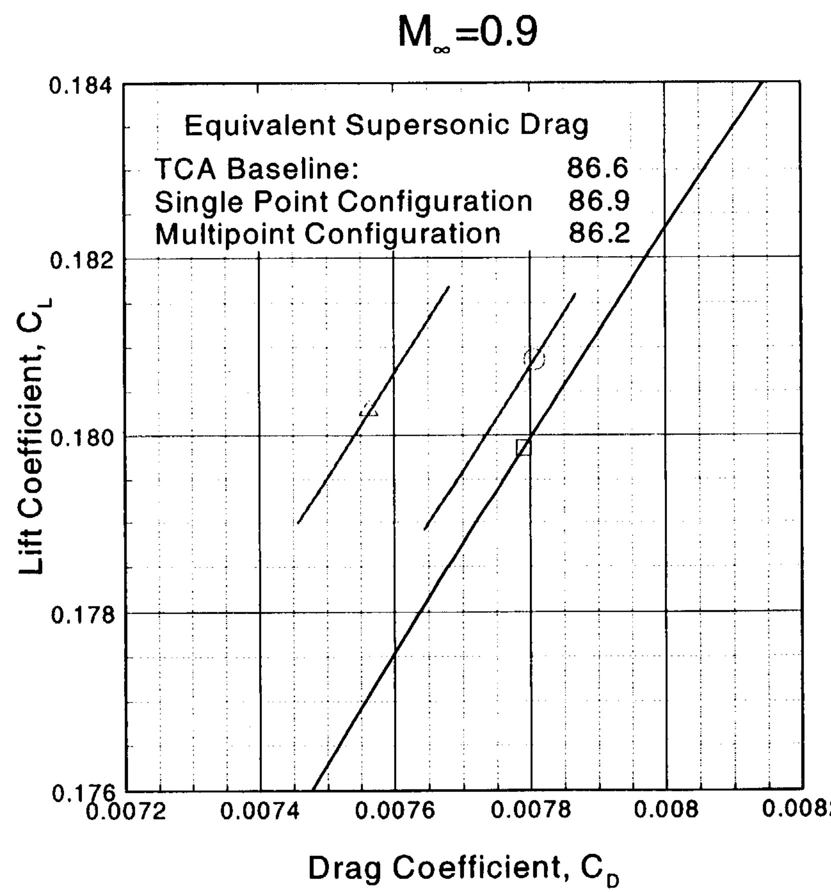

BOEING

Conclusions

This paper documents the need for further nonlinear aerodynamic shape optimization to meet the performance expectations of the HSR program. The optimization may be done as a single point of multipoint process. Multipoint optimization is a more general optimization and may produce a better overall design. Single-point optimization is cheaper, but does not offer any promises on performance away from the design condition. Multipoint optimization is costly and thus motivated the development of certain technologies to increase model fidelity and degrees-of-freedom while decreasing the cost of optimization.

The technologies developed at Phantom Works have focused on meeting these goals. Model fidelity has increased with the extention of grid perturbation tools to multiblock grids. Increases in degrees-of-freedom and the reduction of optimization costs have been accomplished with the development of TLNS3D-Adjoint and the portability of *AEROSHOP* to parallel environments. Sensitivity accuracy and quick turn-around time have been improved with sensitivities obtained through ADIFOR.

These technologies have been demonstrated in several applications to deliver tangible improvements to the TCA configuration.

Conclusions

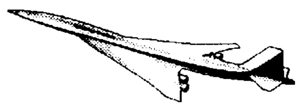

High Speed Aerodynamics, Long Beach

- Multipoint optimization processes have been defined
- Technologies have been enhanced with a focus toward meeting the requirements to do multipoint optimization
  - Full configuration grid perturbation (W/B/N/D/C/E/F)
  - Accurate and efficient gradients (hundreds of DV's)
  - Thrust effects modeling
  - Nacelle shaping
- Technologies have been demonstrated in several applications building up to full configuration multipoint design

BOEING

References

1. Kulfan, Robert, *Configuration Aerodynamics Metrics Update*, HSR Aerodynamics Performance Workshop Proceeding, February 25-28, 1997.

2. Reuther, J., Jameson, A., Farmer, J., Martinelli, L., Saunders, D., *Aerodynamic Shape Optimization of Complex Aircraft Configurations via an Adjoint Formulation*, 34th Aerospace Sciences Meeting & Exhibit, Paper No. AIAA 96-0094, 1996.

3. Kuruvila, G., Sundaram, P., Hager, J.O., *Aerodynamic Sensitivities Using Three Methods*, HSR Airframe Technical Review Proceeding, February 9-13, 1998.

Accounting for Laminar Run & Trip Drag in Supersonic Cruise Performance Testing

Aga M. Goodsell
Robert A. Kennelly
NASA Ames Research Center

February 11, 1999

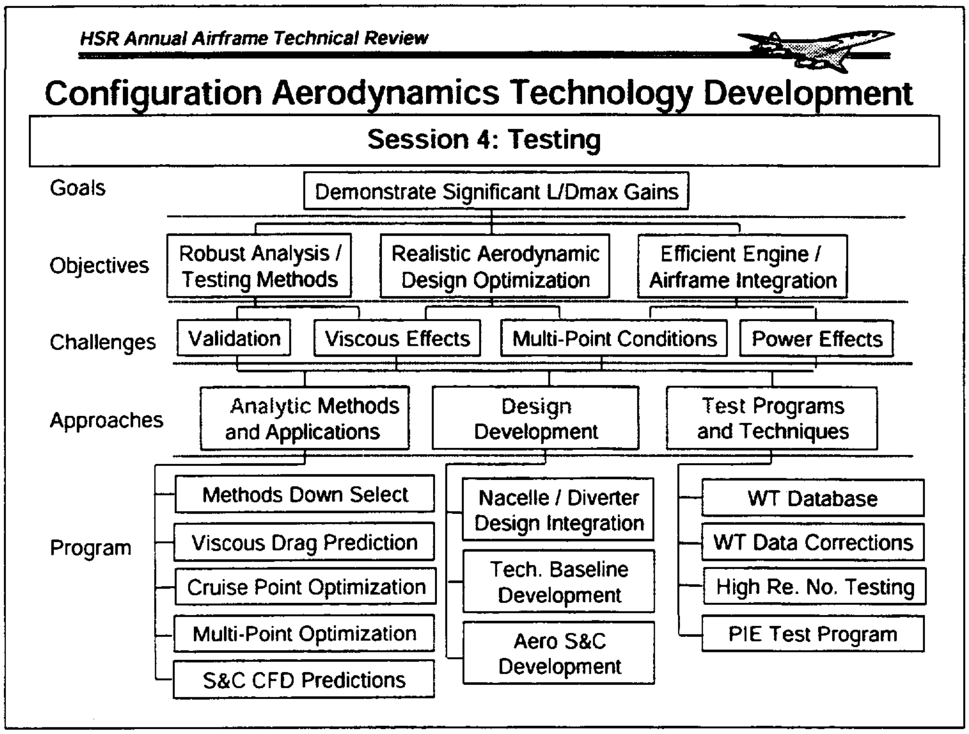

This work was done to support the the WT Database and WT Data Corrections programs under the Test Program and Techniques approach for the Configuration Aerodynamics Technology Development.

Background

High Speed Research Program seeks to achieve
new levels of precision and accuracy
in supersonic performance testing

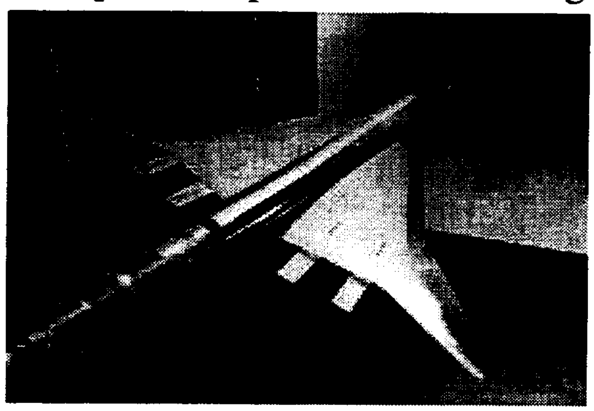

AMGoodsell/RAKennelly Slide 3

Background:

One of the goals of the High Speed Research Program is to achieve new levels of precision and accuracy, particularly in supersonic performance testing.

The picture shown below is that of the 1.675% Baseline TCA Model 2b. This is our baseline performance model which has been tested numerous times in the past couple of years.

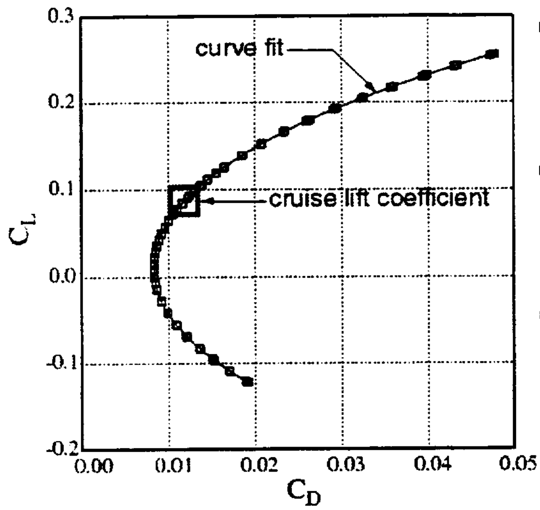

- Repeat measurements of C_L & C_D to reduce statistical uncertainty
- Least-squares polynomial fit used to represent data
- Primarily interested in drag at cruise lift coefficient

AMGoodsell/RAKennelly

Slide 4

Background (continued):

As part of the goal to obtain increased precision and accuracy, it is important to reduce the statistical uncertainty in the wind tunnel data. This is achieved by taking between 3-6 repeat measurements of lift and drag over a range of angles-of-attack.

The plot on the left shows an example of a drag polar for the 1.675% Baseline TCA Model. The squares are the actual lift and drag measurements. The data are represented by fitting a least-squares polynomial curve through the points.

However, we are primarily interested in determining the drag at cruise lift conditions.

Motivation

- Why do we care so much about drag?

  1 drag count (0.0001) ~ 6,000 lb. take-off weight

- Ultimate program goal is to measure drag to within ±0.5 count with 80% confidence

Motivation:

Why do we care so much about this cruise drag?

The reason is that, at supersonic cruise, each drag count costs approximately 6000 lb in take-off weight, which is equivalent to about 30 passengers. Therefore, there is a significant economic incentive to both know what the drag is and to try to reduce it.

The ultimate goal of the Configuration Aerodynamics Test Team is to obtain drag to within +/- 0.5 counts with 80% confidence at supersonic cruise.

HSR Annual Airframe Technical Review

Sub-scale Modeling Issues

- Cannot directly simulate flight conditions
  - Flight Re = 209 million; boundary layer transition near LE
  - Wind Tunnel Re = 6.4 million; transition is delayed
- Mixed laminar/turbulent skin friction is too low

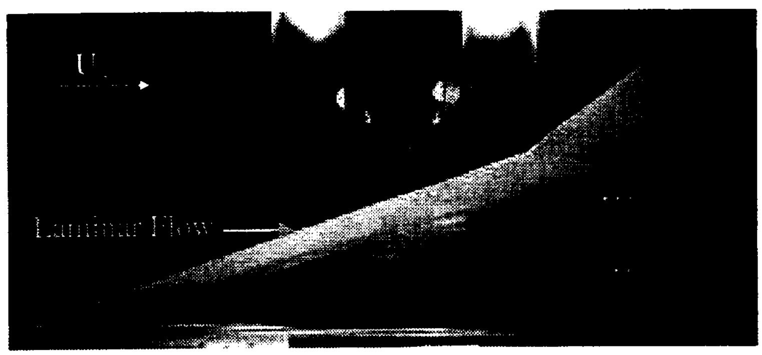

AMGoodsell/RAKennelly

Slide 6

Sub-scale Modeling Issues:

Part of the difficulty with wind tunnel testing is that we cannot directly simulate flight conditions.

For example, at flight, the Reynolds number for the TCA configuration is 209 million. At this Reynolds number, the boundary layer transition from laminar to turbulent flow is near the leading edge over most of the wing. On the other hand, a much lower Reynolds number is attained in the wind tunnel. The Reynolds number for the 1.675% TCA Model in the NASA Langley UPWT is equal to 6.4 million. For this low Reynolds number condition, the boundary layer transition is delayed over most of the wing. This is demonstrated in the flow visualization image below, which shows the extent of laminar flow on the model.

As a result of the mixed laminar/turbulent flow, the skin friction is lower than that for a flow which is fully-turbulent from the leading edge.

Forcing Early Transition

- Standard approach is to add roughness near wing leading edge
- This does not completely solve the problem
  - Transition may not move all the way forward, *especially in supersonic flow*
  - Roughness can create additional drag
- Analysis of wind tunnel drag data requires accounting for laminar run & trip drag

Forcing Early Transition:

The standard experimental approach to solve this problem is to add roughness (e.g., grit, glass beads, epoxy dots) near the leading edge of the wing in order to induce early transition.

However, this does not always resolve the difficulty. First of all, the transition line may not move all the way forward to the trip location, especially in supersonic flow. Second, applying roughness to the model can create additional drag.

Therefore, it is important that the analysis of the wind tunnel data takes into account all of the laminar run which exists behind the leading edge and any additional trip drag that occurs.

Not a New Problem

- Braslow (Langley, 1960s)
  - Advocated extrapolating to zero trip height
- Daugherty (Ames, 1970s)
  - Observed constant drag for a range of trip sizes
- Vaucheret (France, 1960s)
  - Applied laminar run correction
  - Corrected drag was constant for small trips

In all cases, prompt transition was obtained for sufficiently large roughness

AMGoodsell/RAKennelly

Slide 8

Not a New Problem:

The whole issue involved with tripping the flow and correcting the wind tunnel data is not a new problem in wind tunnel testing.

Braslow worked at NASA Langley in the 1960s to develop a method to estimate trip drag. He advocated using an extrapolation technique. This method extrapolates a curve through the drag data as a function of trip height in order to estimate the drag for zero trip height. This technique will be further examined in Slide 11.

Daugherty conducted a series of wind tunnel tests at NASA Ames in the 1970s on the XB-70 model. He observed constant drag over a range of trip sizes. Some of his results are presented on the next slide.

Vaucheret conducted tests on a delta wing/body model in France during the 1960s. Based on sublimation images, he observed some laminar flow on the model. Therefore, he first applied a laminar run correction to his drag data. Once he made the correction, he found that the drag was constant for small trips. Some data from his work are shown in Slide 10.

In all cases, it is believed that all of the researchers used airfoil sections with sharp leading edges which produced gentle pressure gradients. Therefore, they were able to obtain prompt transition for sufficiently large roughness sizes.

Jim Daugherty—XB-70 Test

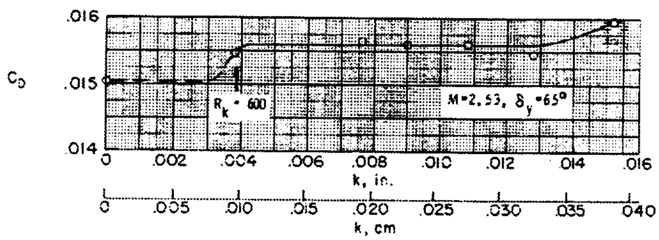

Daugherty, et al. (Ames)

- M = 2.53, Re = $4(10^6)$/ft, sharp LE sections
- Transition observed at or near the grit strip
- Drag "plateau" observed; zero trip drag for k up to about 0.013 in

AMGoodsell/RAKennelly Slide 9

Jim Daugherty—XB-70 Test:

For further information, please refer to the following references:

James C. Daugherty, "Wind-Tunnel/Flight Correlation Study of Aerodynamic Characteristics of a Large Flexible Supersonic Cruise Airplane (XB-70-1), I—Wind-Tunnel Tests of a 0.03-Scale Model at Mach Numbers from 0.6 to 2.53," NASA Technical Paper 1514, November 1979.

Henry H. Arnaiz, John B. Peterson, Jr., and James C. Daugherty, " Wind-Tunnel/Flight Correlation Study of Aerodynamic Characteristics of a Large Flexible Supersonic Cruise Airplane (XB-70-1), II—A Comparison Between Characteristics Predicted from Wind-Tunnel Measurements and Those Measured in Flight," NASA Technical Paper 1516, 1979.

HSR Annual Airframe Technical Review

Xavier Vaucheret

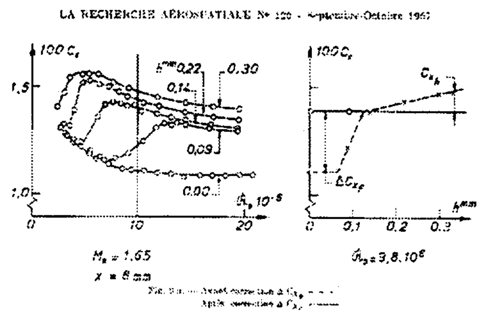

- M = 1.65, Re = 9.8(10^6)/m, $\alpha = 0°$, symmetrical sections
- Trip consisted of a single row of glass beads
- Drag "plateau" found after correcting for laminar flow

AMGoodsell/RAKennelly

Slide 10

Xavier Vaucheret:

For more details of Vaucheret's work and results for Mach 2.34, please refer to the following reference:

Xavier Vauchert, "Artificial Initiation of the Supersonic Transition," Translation of "Declenchement Artificiel de la Transition en Supersonique," La Recherche Aerospatiale, No. 120, pp. 25–32, 1967, NASA TT F-11, 558.

HSR Annual Airframe Technical Review

Drag vs. Trip Height

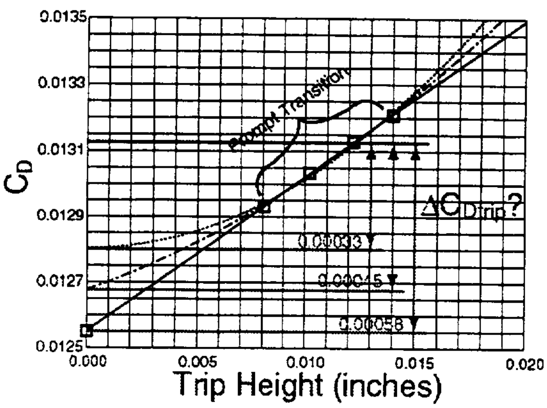

Analysis per Braslow:

- Plot drag vs. trip height
- Various methods used to extrapolate to zero trip height
- Trip drag is difference between measured & extrapolated values
- Unacceptably large range of corrections obtained

How do we resolve this uncertainty?

AMGoodsell/RAKennelly

Slide 11

Drag vs Trip Height:

The Configuration Aerodynamics Test Team attempted to follow Braslow's approach in their initial analysis of the wind tunnel data. The first step is to plot the drag as a function of trip height for those values where prompt transition is believed to occur. This is shown in the plot on the left. Then, a curve is extrapolated through the drag data to zero trip height. The trip drag is computed as the difference between the measured drag and the extrapolated drag.

For this data, it is not clear which extrapolation technique is the correct one to use. If a quadratic extrapolation is made, the trip drag is equal to 3.3 counts. On the other hand, if a linear extrapolation is applied, then the trip drag becomes 5.8 counts. The difference between these two methods—2.5 counts—is unacceptably large.

At this point, it was important to determine a way to resolve this uncertainty in the trip drag.

HSR Annual Airframe Technical Review

Test #1679

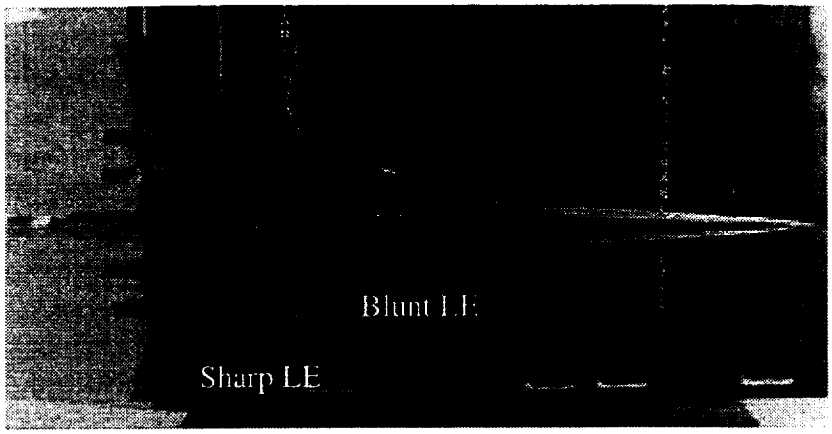

- Test conducted at Langley UPWT in Jan. 1997
- Collaborators included Mina Cappuccio (Ames) and Kevin Mejia (BCAG)

AMGoodsell/RAKennelly — Slide 12

<u>Test #1679:</u>

In order to resolve the uncertainty in estimating trip drag, a more careful examination of the results from Test #1679 was undertaken. This test was the first entry of the 1.675% Baseline TCA Model 2b in the Unitary Pressure Wind Tunnel Test Section #2 at NASA Langley Research Center. The other collaborators involved in this wind tunnel test were Mina Cappucio and Kevin Mejia.

It is important to note that the inboard section of this model has a blunt leading edge, whereas the outboard section has a sharp leading edge. The pressure distribution around the blunt leading edge is different from that around the sharp leading edge. The pressure distribution in the outboard section with the sharp leading edge is more similar to that obtained in the previous historical tests.

HSR Annual Airframe Technical Review

W/B Trip Drag Study

- Trip height on wing varied from k = 0.006” to 0.017”
- Trips were epoxy disks with diameter 0.050”, applied 0.6” from LE
- Each trip configuration was carefully applied and measured for uniformity
- Measure forces & moments at Ma = 2.4
- Obtain series of sublimation images at cruise (α = 3.5°) until stable pattern emerges

AMGoodsell/RAKennelly　　Slide 13

W/B Trip Drag Study:

In Test #1679, a trip drag study was conducted on the wing/body configuration. The trip height was varied from 0.006 inches to 0.017 inches. The trips were epoxy disks with a constant diameter equal to 0.050 inches. The disks were applied at 0.6 inches from the wing leading edge. The picture in the upper right corner shows an example of the trip disks on the model near the leading-edge break.

Each trip configuration was carefully applied and measured in order to maintain uniformity. For each trip configuration, forces and moments were measured at the supersonic cruise Mach number, which is equal to 2.4. In addition, a series of sublimation images at the cruise angle-of-attack were obtained until a stable pattern emerged in the sublimation material.

Sublimation Process

- Model is positioned with wings vertical
- Cameras are mounted on each side of test section
- Upper & lower surfaces of wing are sprayed with sublimation material
- Pictures are taken at 30 sec intervals
- Allows a complete record of the development of the transition front

AMGoodsell/RAKennelly

Slide 14

Sublimation Process:

To obtain the sublimation images, the model is rotated 90° so that the wings are vertical.

Cameras are mounted on each side of the test section to capture the upper and lower surfaces of one wing at the same time.

The upper and lower surfaces of the wing are sprayed with the sublimation material, which is a mixture of fluorene in Genesolv.

The test section is closed and the tunnel is brought up to the supersonic cruise condition.

Then, pictures are take every 30 seconds until a stable pattern emerges and most of the material has sublimed.

This allows a complete record of the development of the transition location.

Sublimation Reveals Transition

Elapsed time 5 minutes

8 minutes

11 minutes

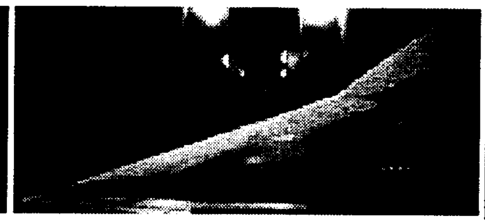

13 minutes

Sublimation Reveals Transition:

This slide gives examples of sublimation images for the free transition configuration at four different times.

The transition location is apparent in these images because the material sublimes more rapidly in areas of turbulent flow.

After 5 minutes, the initial development of the transition location appears. As more time elapses, the transition location becomes more evident. The last two images demonstrate that the transition location remains stable with time.

HSR Annual Airframe Technical Review

Locating Transition

Transition location was measured as a percentage
of local chord from the digitized images

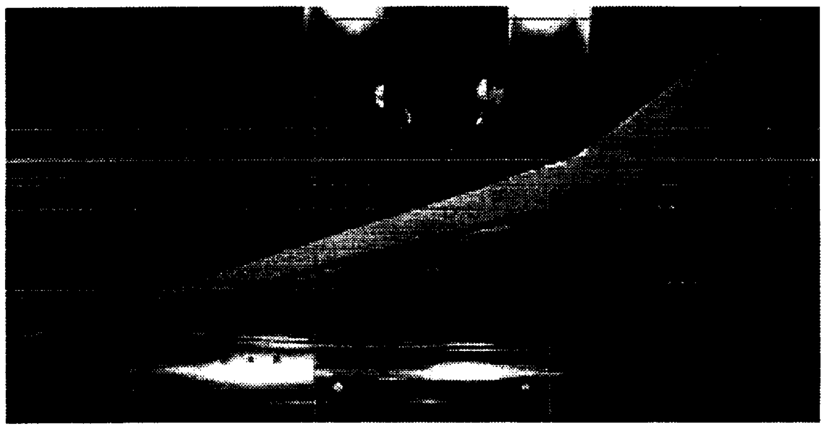

AMGoodsell/RAKennelly

Slide 16

<u>Locating Transition:</u>

The sublimation images are digitized and read into a software program like Adobe Illustrator to help locate the transition line on the model for each trip configuration.

First, the transition location is drawn on the wing, shown as a thick purple line in the picture above. Next, the green guidelines are used to measure the transition location as a percentage of the local chord for various spanwise stations.

This procedure is followed for all of the different trip height configurations.

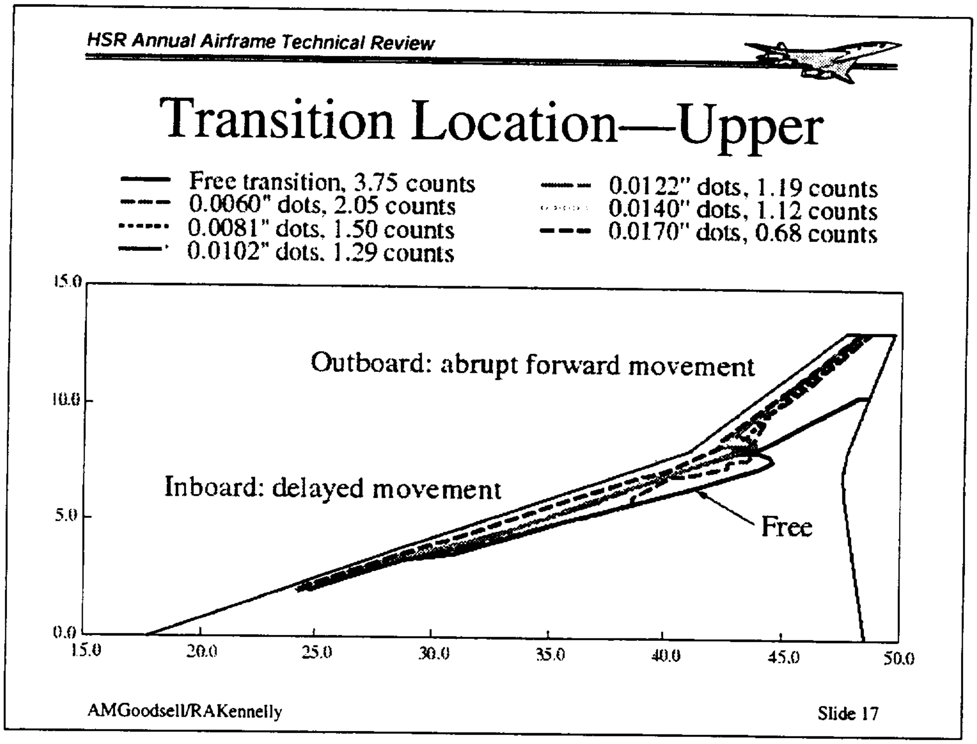

Transition Location—Upper:

This viewgraph gives a summary of the transition location for all of the dot heights tested on the upper surface. The thick black line represents the location of the free transition line. Note that transition is significantly delayed over most of the wing without any trip disks applied to the wing.

In the outboard section, which has sharp leading-edge airfoil sections, there is an abrupt forward movement of the transition location with any application of the epoxy disks, even for the smallest disk height. For disk heights of 0.010 inches and greater, the transition moves forward to the disk location.

On the other hand, the inboard section behaves differently. The blunt leading edge makes it difficult to trip the flow and transition is delayed for all disk heights. In fact, for the smallest disk height, the transition location is not changed from that for free transition, except in the region near the leading-edge break in the planform. Prompt transition is not attained for any of the trip configurations, even with the largest trip height of 0.017 inches.

The dissimilar behavior of the transition line in the inboard and outboard sections may be due to differences in the pressure gradient and boundary layer development between the two sections.

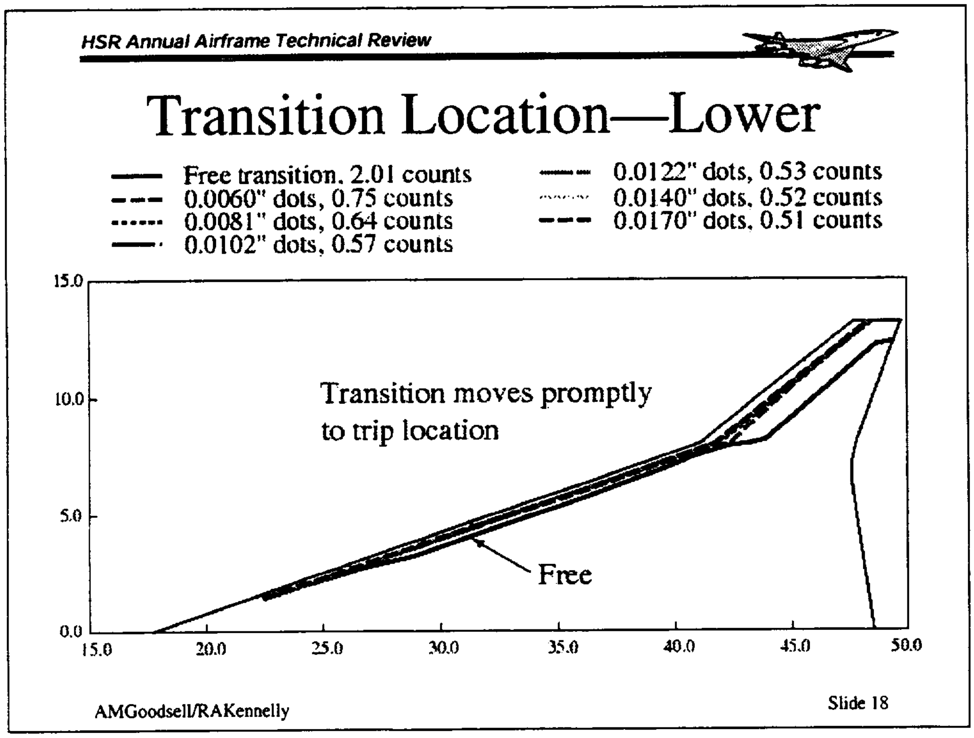

Transition Location—Lower:

The summary of the transition locations for the different trip heights on the lower surface of the wing is shown here.

The outboard section of the lower surface behaves similarly to that of the upper surface.

However, the transition location in the inboard section displays different behavior than on the upper surface. First of all, the free transition location is closer to the leading edge than observed on the upper surface. Furthermore, the application of most disk heights moves the transition forward to the trip location.

Methodology

- Laminar run correction
  - Compressible flat-plate skin friction code developed
  - Compute C_F for both mixed laminar/turbulent and fully-turbulent flow from LE
  - Difference between these is the laminar run correction, ΔC_{Dlam}

Once corrected, the data provided guidance for extrapolating to zero trip height, resolving the uncertainty in ΔC_{Dtrip}

AMGoodsell/RAKennelly Slide 19

Methodology:

Once it became evident that a significant amount of laminar flow existed, particularly on the inboard, upper, wing surface, it was clear that the wind tunnel data needed to be corrected for laminar run before the data could be analyzed for trip drag.

In order to make this laminar run correction, co-author Robert Kennelly wrote a FORTRAN code that estimates the skin friction for a compressible flow over a flat plate. This code was then used to compute the skin friction for a mixed laminar/turbulent flow using the measured transition locations and for a flow that is fully-turbulent from the leading edge. The difference between these two results is the laminar run correction.

Once the drag data was corrected and plotted against trip height, the proper extrapolation of the data to zero trip height became apparent, which resolves the uncertainty in the trip drag.

HSR Annual Airframe Technical Review

CDf: New Code, Old Method

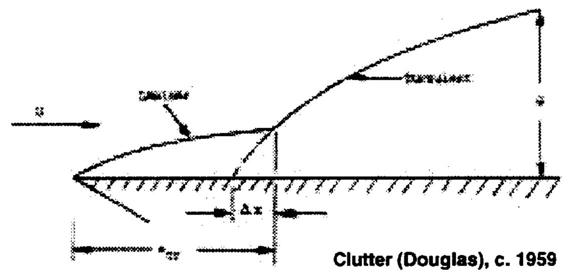

Clutter (Douglas), c. 1959

- Flat plate, compressible, several laminar and turbulent C_f methods
- Iteratively matches laminar & turbulent momentum thicknesses at a specified x-location
- Drag areas (D/q) are summed over all elements; normalized by Sref to yield C_D for configuration

AMGoodsell/RAKennelly

Slide 20

CDf: New Code, Old Method:

This FORTRAN code has been run on a number of platforms and is available through Robert Kennelly at rakennelly@mail.arc.nasa.gov.

HSR Annual Airframe Technical Review

Drag vs. Trip Height

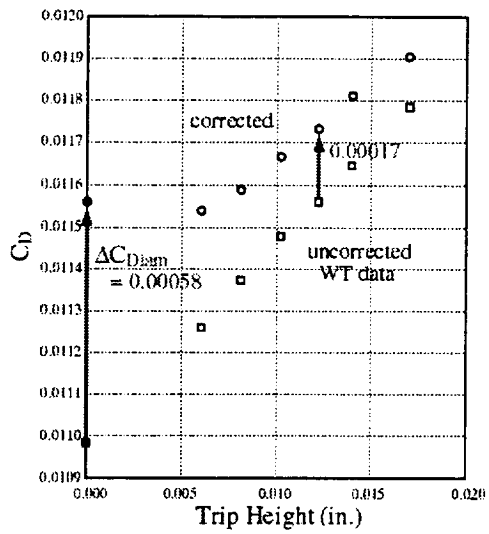

- Interpolated drag values at $\alpha = 3.5°$ are plotted against trip height
- Laminar run correction ΔC_{Dlam} is added to C_D for each trip height
- Corrected data points may be divided into two groups...

AMGoodsell/RAKennelly

Slide 21

Drag vs. Trip Height:

The reader will now be led through a step-by-step procedure for correcting the wind-tunnel data.

First, the drag data for α=3.5° is obtained by interpolating the 7th-order polynomial curves which represent the wind tunnel data. The drag data are plotted as a function of trip height for all values tested. The uncorrected drag data are shown as blue squares.

Next, the laminar run correction is added to the drag data for each disk height. The laminar run correction is largest for free transition and is equal to 5.8 counts. For a trip height of 0.012 inches, the laminar run correction is 1.7 counts. The corrected data are represented by the black circles.

The data, corrected for laminar run, fall into two regions that will be described further in the next slide.

HSR Annual Airframe Technical Review

Drag vs. Trip Height

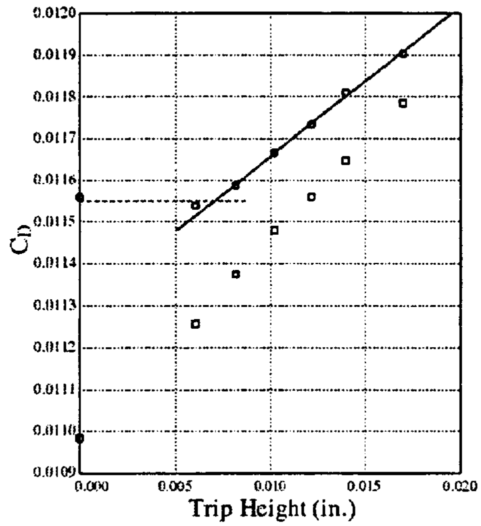

- Tentatively identify "drag plateau" formed by first two points
  - Some flattening of the curve expected
  - Consistent with Braslow's subsonic data & others' supersonic data
- Linear curve fits remaining data well
  - Drag proportional to disk frontal area (d • h)

AMGoodsell/RAKennelly

Slide 22

Drag vs. Trip Height:

First, a "drag plateau" is defined using data from the first two points—free transition and 0.006 inches. The plateau is only tentatively identified since drag data in between the two endpoints are not available from Test #1679. However, some flattening of the drag curve is expected as zero trip height is approached. In addition, the existence of a drag plateau is consistent with Braslow's analysis of earlier subsonic data and other researchers' supersonic data, including those of Daugherty and Vaucheret.

The remaining data varies linearly with trip height. For trip heights that are approximately equal to the boundary layer height or greater, the drag is expected to be proportional to the disk frontal area. Since the diameter remains constant in this study and only the height is varying, a linear variation of the drag with trip height is appropriate.

HSR Annual Airframe Technical Review

Final Drag vs. Trip Height

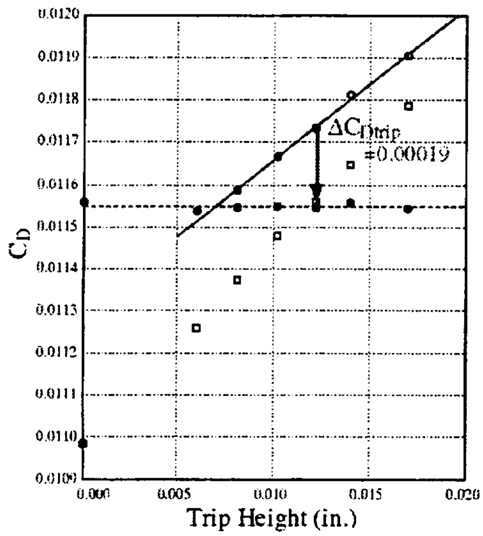

- Difference between linear fit and plateau is trip drag ΔC_{Dtrip}
- Trip drag is subtracted from data points
- Corrected drags are now consistent with plateau value
- For this configuration, plateau value is the fully-corrected cruise drag sought

AMGoodsell/RAKennelly

Slide 23

Final Drag vs. Trip Height:

The trip drag is computed by taking the difference between the linear fit of the data and the value of the drag plateau.

The trip drag is subtracted from each of the data points that lie above the plateau value. The trip drag for the disk height equal to 0.012 inches is 1.9 counts, which is close to the value of the laminar run correction for the same disk height.

The final corrected drag for all disk heights are represented by the solid black circles. All of the corrected drag data are now consistent with the value of the drag plateau.

Therefore, for this configuration at the cruise angle-of-attack, the plateau value is the fully-corrected cruise drag that the Configuration Aerodynamics Test Team has sought.

Comparison with CFD Results

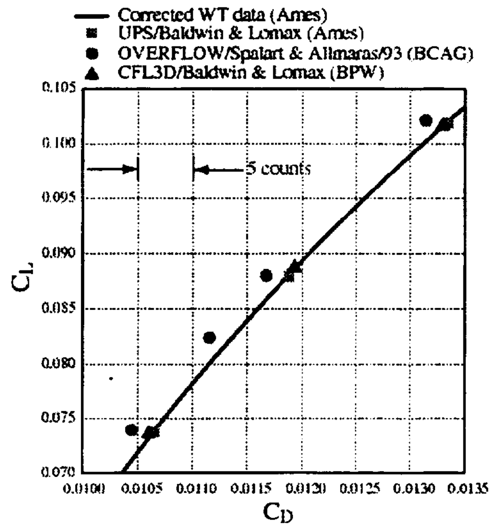

- Corrected WT data are in excellent agreement with UPS & CFL3D (Baldwin-Lomax)
- OVERFLOW results may be low because of anomalous Spalart-Allmaras behavior near leading edge

AMGoodsell/RAKennelly

Slide 24

Comparison with CFD Results:

In this slide, the final corrected wind tunnel data are compared to three different CFD solutions near the cruise angle-of-attack.

The corrected wind tunnel data are in excellent agreement with the lift and drag results from UPS (Scott Lawrence, NASA Ames Research Center) and CFL3D (Chih Fang Shieh, Boeing-Phantom Works, Long Beach). Both of these codes used the Baldwin-Lomax turbulence model.

On the other hand, the drag computed by OVERFLOW (Steve Chaney, Boeing Commercial Airplane Group, Seattle) is about two counts lower than the wind tunnel data. This is most likely due to the anomalous behavior of the Spalart-Allmaras turbulence model which exhibits a "laminar-flow effect" near the leading edge of the wing.

Nacelle Trip Drag Study

- Constant wing trip height: 0.012"
- Three nacelle trip heights (inside & out) tested: 0.008", 0.012", and 0.014"
- Note: large number of trip disks on nacelles (49% of wing total)
- Measure W/B/N/D forces & moments
- Sublimation images obtained at $\alpha = 3.5°$

Nacelle Trip Drag Study:

In addition to the wing/body trip drag study, a reduced trip drag study was conducted on the nacelles. For this nacelle study, the trip disk height on the wing was kept constant at 0.012 inches.

Three different trip heights were applied on the nacelles, both internally and externally, at 0.6 inches downstream from the leading edges of the nacelles. This results in a large number of disks on the nacelles—the total number of trip disks on the nacelles is about 49% of the total number on the wing.

Once again, the forces and moments were measured at the supersonic cruise Mach number, 2.4, and a series of sublimation images were obtained at the cruise angle-of-attack.

Nacelle Sublimation

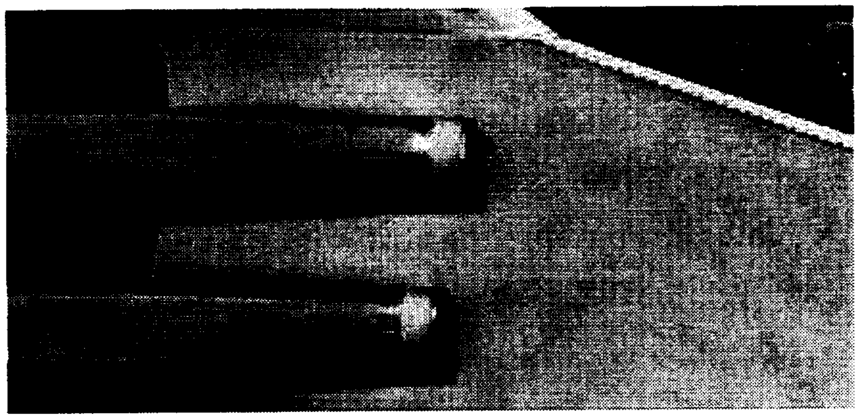

Poor visibility of transition location around nacelle perimeter requires estimate of laminar run correction

AMGoodsell/RAKennelly

Slide 26

Nacelle Sublimation:

This is an example of a sublimation image on the nacelles for a trip height of 0.014 inches. The nacelle transition location is not as easily discernible as the wing transition is in these images. In addition, only one of the four external surfaces of each nacelle is visible. Therefore, it is difficult to locate the transition line on the complete external surfaces of the nacelles due to poor visibility in the sublimation region and around the nacelles. As a result, the laminar run correction will assume that transition occurs at the trip location.

WBND Drag Corrections

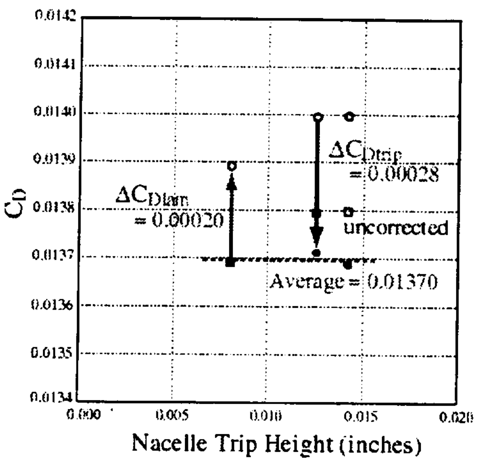

- Laminar run correction
  - –Wing: $\Delta C_{Dlam,w}$ taken from WB study (k = 0.012")
  - –Nacelles: assume transition at trip location (four exteriors) $\Delta C_{Dlam,n} = 0.000028$
  - –WT data reduction accounts for nacelle interiors
- Trip drag correction
  - –Wing: $\Delta C_{Dtrip,w}$ from WB study
  - –Nacelle: $\Delta C_{Dtrip,n}$ scaled from corresponding WB value
- Three final values agree

AMGoodsell/RAKennelly Slide 27

WBND Drag Corrections:

The plot on the left shows the drag coefficient for the W/B/N/D configuration at the cruise angle-of-attack as a function of the nacelle trip height. In addition, the complete laminar run and trip drag corrections for the W/B/N/D configuration are shown on this plot. Both the laminar run and trip drag corrections consist of a separate wing and a separate nacelle contribution.

The wing contribution to the laminar run correction is constant for all nacelle trip heights and is obtained from the wing/body study for a disk height equal to 0.012 inches. The laminar run contribution from the nacelles is based on the assumption that transition occurs at the trip location for all trip heights. Therefore, the nacelle laminar run contribution is also constant. This laminar run correction only takes into account the external surfaces of the nacelles because the internal skin friction, which includes the assumption of laminar flow between the leading edge and the trip location, is already removed from the wind tunnel data. The total laminar run correction (2.0 counts) is added to the drag data for each trip height.

Similar to the laminar run correction, the wing contribution to the trip drag is based on the value of the wing/body trip drag for a disk height of 0.012 inches. The nacelle contribution is computed by scaling the corresponding trip drag for the wing/body by 0.49, which accounts for both the internal and external dots. The combined trip drag value is subtracted from the drag for each disk height.

Once these corrections are applied, the final values agree with each other.

Comparison with CFD Results

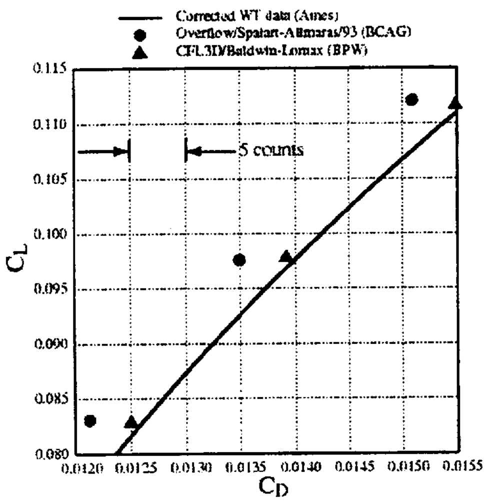

- Once again, corrected WT data agree well with CFL3D/B-L but differ from OVERFLOW/S-A by five counts
- The OVERFLOW/S-A results have not been examined for "laminar flow effect" at leading edges of nacelles

AMGoodsell/RAKennelly

Slide 28

Comparison with CFD results:

The plot on the left shows the drag polar including both final corrected wind tunnel and CFD data for the W/B/N/D configuration near the cruise condition. The comparison of the wind tunnel data for the W/B/N/D configuration to the lift and drag coefficients computed by CFL3D using the Baldwin-Lomax turbulence model show good agreement.

The OVERFLOW results with the Spalart-Allmaras turbulence model are about five drag counts lower than the corrected wind tunnel data. It is believed that this under prediction of the drag is, once again, due to the turbulence model, but the CFD solutions for the complete configuration have not been closely examined.

HSR Annual Airframe Technical Review

Work in Progress—
A Closer Look at the B'Layer

- Why is the *inboard*, upper surface so difficult to trip?
- Why do we see prompt transition on the *outboard* wing?
- Approach: Study boundary layers on flat plate and wing (CFD results provided by Scott Lawrence/Ames)

AMGoodsell/RAKennelly Slide 29

Work in Progress—A Closer Look at the Boundary Layer:

The authors are now going to switch directions from focusing on methodology to attempting to understand why a modified approach to trip drag is required. The main question that comes to mind is "why is the inboard, upper surface so difficult to trip?", whereas, prompt transition on the outboard wing is easy to obtain. Our initial approach to answering this question is to study the boundary layers on both flat plates and the baseline TCA wing using CFD results provided by Scott Lawrence at NASA Ames Research Center.

HSR Annual Airframe Technical Review

Laminar Boundary Layer Profile

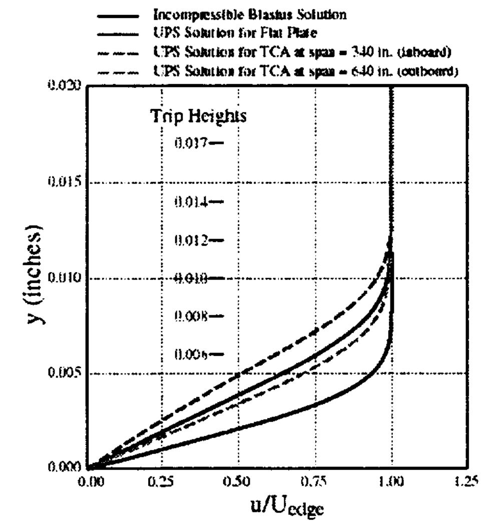

- Compressibility thickens boundary layer, requiring larger trip height
- Outboard: pressure gradient thins b'layer a small amount
- Inboard: b'layer *thicker* than flat plate—effect of attachment line boundary layer on blunt LE?

AMGoodsell/RAKennelly

Slide 30

<u>Laminar Boundary Layer Profiles:</u>

The plot on the left gives laminar boundary layer profiles computed by UPS at 0.6 inches downstream of the leading edge on a flat plate and on the baseline TCA wing at both an inboard and outboard section. The UPS solutions for the TCA were obtained at 3.6° angle-of-attack. Also shown on the plot, as a solid black line, is the incompressible Blasius solution for a flat plate. The heights of the trip disks applied to the wing in Test #1679 are indicated on the plot to show the disk heights relative to the boundary layer thickness.

The first observation in comparing the Blasius solution to the UPS solution for the flat plate is that compressibility thickens the boundary layer. This effect would require a larger disk height to trip the flow. Next, examining the differences in the boundary layer profile between the flat plate and TCA wing suggests that the gentle, favorable pressure gradient in the outboard section tends to slightly thin the boundary layer. This can be seen by comparing the solid, blue line with the dashed, green line. The opposite effect is observed for the inboard section where the boundary layer is thicker than on the flat plate (compare the dashed, red line to the solid, blue line). This may be a result of the attachment line boundary layer on the blunt leading edge. This increase in the boundary layer thickness implies that a larger trip height is required in the inboard section, but doesn't completely explain the why even the largest disk height does not cause prompt transition.

Mach & Re_y in Boundary Layer

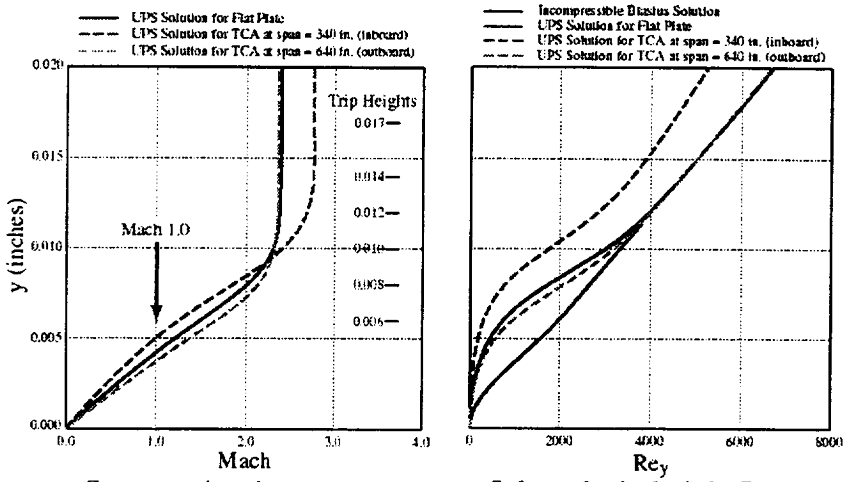

- Supersonic trips
- Inboard trip height Re very different from outboard

AMGoodsell/RAKennelly

Slide 31

Mach and Re_y in Boundary Layer:

The plot on the left gives the distribution of Mach number through the laminar boundary layers computed by UPS on a flat plate and the TCA wing. This plot shows that the flow at the top of all of the trip disks that were tested is supersonic.

The plot on the right provides the distribution of Reynolds number based on local flow properties with the length scale equal to the height off the surface. This Reynolds number is being examined because the value of the Reynolds number at the trip height, referred to Re_k, has been used by researchers in the past to predict the required trip height that will cause boundary layer transition. This plot shows that the value of the inboard trip height Reynolds number is lower than that of the flat plate and the outboard section. This further implies that a larger disk height is needed to trip the flow.

Summary

- Improved laminar run & trip drag corrections for supersonic cruise performance testing
  - Careful flow visualization revealed delayed transition, even for the largest disks
  - New code developed for laminar run corrections
  - Corrected data could be analyzed for trip drag
- Despite initial appearances, our data are consistent with (most) previous results
- Our approach extends prior work, taking into account the effects of blunt leading edges

Summary:

In summary, an improved laminar run and trip drag correction methodology for supersonic cruise performance testing was derived. This method required more careful analysis of the flow visualization images which revealed delayed transition particularly on the inboard upper surface, even for the largest trip disks. In addition, a new code was developed to estimate the laminar run correction. Once the data were corrected for laminar run, the correct approach to the analysis of the trip drag become evident.

Although the data originally appeared confusing, the corrected data are consistent with previous results. Furthermore, the modified approach, which was described in this presentation, extends prior historical work by taking into account the delayed transition caused by the blunt leading edges.

Follow-up "Grit Drag" Test in 4/99

- Repeat portions of Test #1679
- Investigate shorter trip disks to verify that a drag plateau exists
- Study Re & angle-of-attack effects
- Can we improve the present method?
  - Are there more efficient and/or effective trips?
    - Intentionally contaminate attachment line
    - Different trip configurations on outboard wing
  - Is it *really* necessary to trip the flow at all?

AMGoodsell/RAKennelly Slide 33

Follow-up Grit Drag Test in 4/99:

A follow-up grit drag test is planned for April 1999 at NASA Langley's UPWT Test Section #2. First, portions of Test #1679 will be repeated to confirm the general trends in the wing/body data which were observed during that test and reported in this presentation. Shorter trip disks will be tested on the wing and the resulting data will be examined to verify the existence of a drag plateau. In addition, some testing will be done to study the effects of varying Reynolds number and angle-of-attack on the wing transition location.

However, the main purpose of the follow-up test will be to try to improve the present method, which is time-consuming in both the testing and analysis aspects. First, more efficient and/or effect trip mechanisms will be examined. For the inboard section, intentionally contaminating the attachment line will be attempted. In the outboard region, different trip configurations will be tested. Second, it may be possible that for the baseline TCA configuration, it is not really necessary to trip the flow at all. If the free transition data corrected for laminar run provides the final answer, then testing without the application of trip disks is possible as long as other aerodynamic characteristics are not adversely affected.

NCV Flow Diagnostic Test Results (LaRC UPWT 1703)

Mina Cappuccio
NASA Ames Research Center

HSR Airframe Technical Review
Anaheim, CA
February 8-12, 1999

This test was done for Configuration Aerodynamics in support of WBS 4.3.1.1, Analysis and Testing Methods.

Configuration Aerodynamics Technology Development

Session 4: Testing

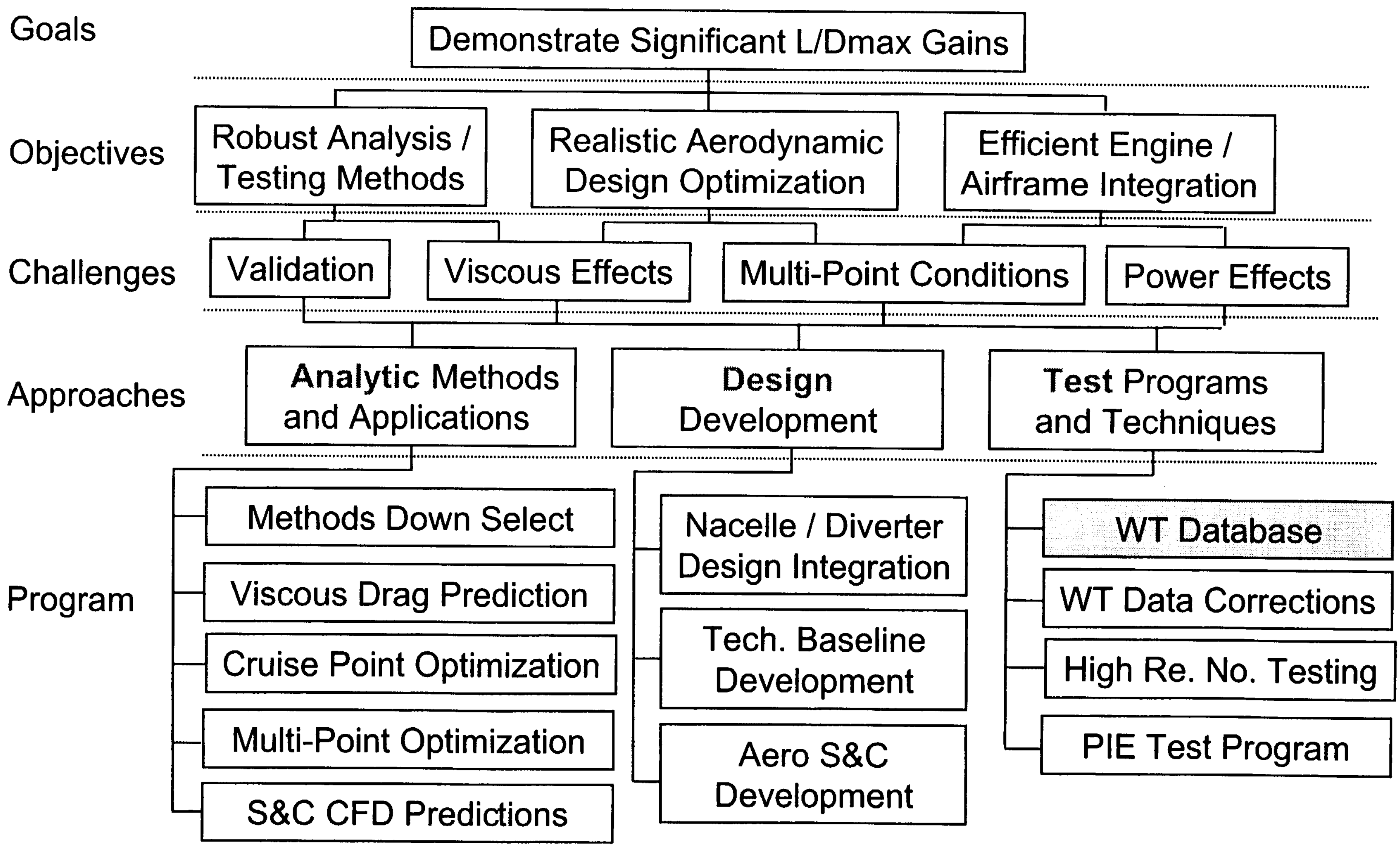

There were two objectives for this test. First, was to assess the reasons why there is approximately 1.5 drag counts (cts) discrepancy between measured and computed drag improvement of the Non-linear Cruise Validation (NCV) over the Technology Concept Airplane (TCA) wing body (WB) configurations. The Navier-Stokes (N-S) pre-test predictions from Boeing Commercial Airplane Group (BCAG) show 4.5 drag cts of improvement for NCV over TCA at a lift coefficient (CL) of 0.1 at Mach 2.4. The pre-test predictions from Boeing Phantom Works - Long Beach, BPW-LB, show 3.75 drag cts of improvement. BCAG used OVERFLOW and BPW-LB used CFL3D. The first test entry to validate the improvement was held at the NASA Langley Research Center (LaRC) UPWT, test number 1687. The experimental results showed that the drag improvement was only 2.6 cts, not accounting for laminar run and trip drag. This is approximately 1.5 cts less than predicted computationally. In addition to the low Reynolds Number (RN) test, there was a high RN test in the Boeing Supersonic Wind Tunnel (BSWT) of NCV and TCA. BSWT test 647 showed that the drag improvement of NCV over TCA was also 2.6 cts, but this did account for laminar run and trip drag. Every effort needed to be done to assess if the improvement measured in LaRC UPWT and BSWT was correct.

The second objective, once the first objective was met, was to assess the performance increment of NCV over TCA accounting for the associated laminar run and trip drag corrections in LaRC UPWT. We know that the configurations tested have laminar flow on portions of the wing and have trip drag due to the mechanisms used to force the flow to go from laminar to turbulent aft of the transition location.

Objectives

- Assess the reasons why there is ~1.5 ct discrepancy between measured and computed drag improvement of NCV over TCA
  - OVERFLOW: $\Delta CD = 4.5$ cts
  - CFL3D: $\Delta CD = 3.75$ cts
  - Test 1687: $\Delta CD = 2.6$cts

- Assess the performance increment of NCV over TCA with associated laminar run and trip drag corrections.

This is a photograph of the TCA WB configuration tested. The tripping mechanisms used on the wing upper and lower surfaces are 0.05-inch diameter epoxy discs spaced 0.2-inches apart, center to center, and are 0.012 inches high. They are placed o.6 inches aft of the leading edge in the streamwise direction on all wing surfaces. The same tripping mechanisms, of the same diameter and height, are also placed 1 inch aft of the nose, but spaced 0.1 inches apart.

The TCA WB shown here is the solid wing model known as TCA 2b. The TCA 2b model has been tested in the LaRC UPWT three (3) times in test section 2. It also was tested in BSWT as part of the high RN test of the NCV model and as part of an Internal Research and Development (IR&D) test.

TCA 2B WB

This is a photograph of the NCV WB configuration tested. The exact same trip configuration used on TCA 2b was used for the NCV model. This trip configuration is called the baseline trip configuration. Any other trip configuration is considered an alternate trip configuration. Alternate trip configurations were also applied to the NCV model to assess if it might be more effective to trip the flow and cause the drag improvement to increase. Alternate trip configurations were also used to assess the trip drag correction. A similar study of alternate trip was done very extensively on TCA 2b during test 1679.

NCV WB

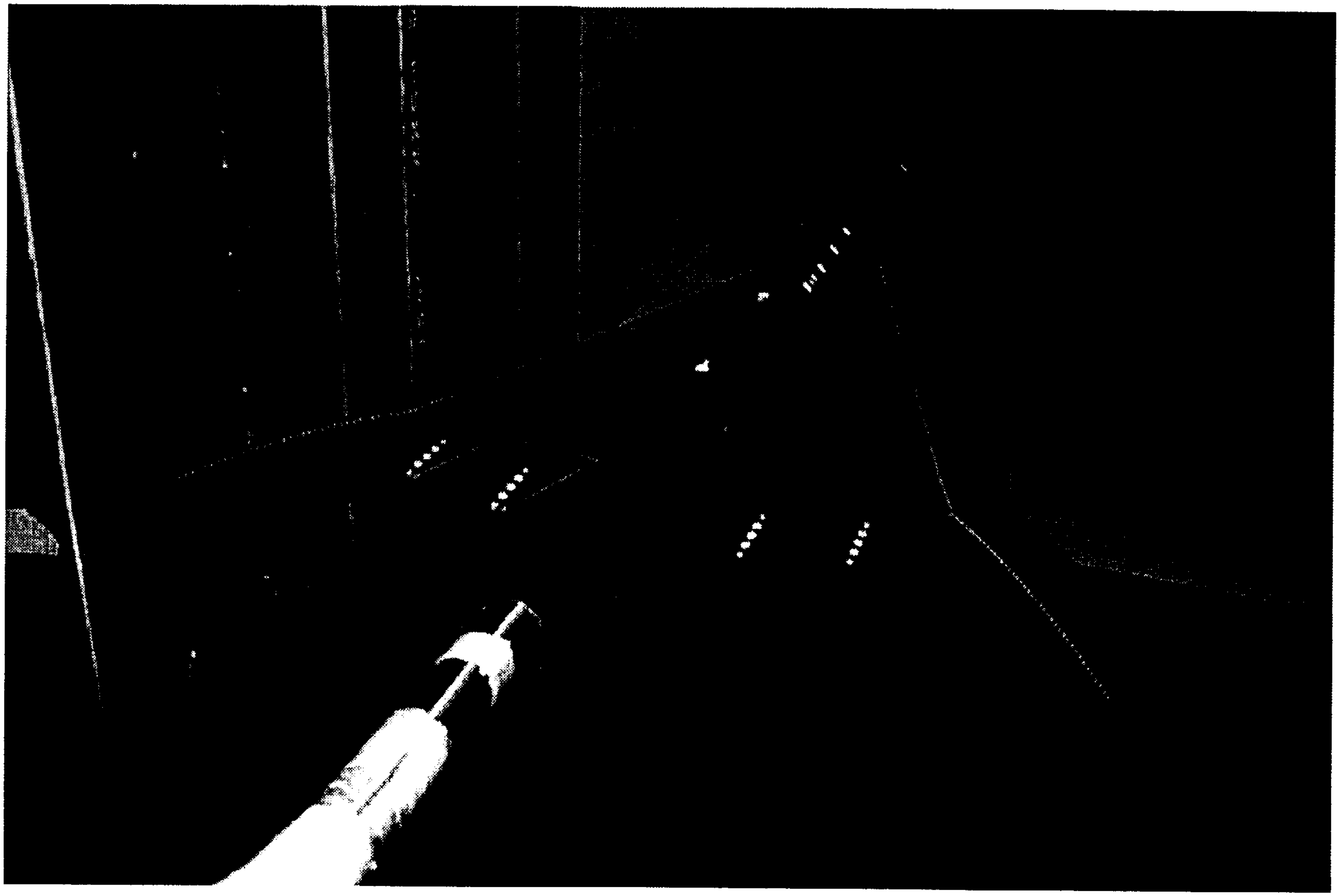

This is the drag polar from the BCAG OVERFLOW calculations showing 4.5 cts drag improvement of NCV over TCA WB at cruise CL of 0.1 at wind tunnel RN of 4 million/ft at Mach 2.4. The Spalart-Allmaras turbulence model was used in OVERFLOW for the N-S calculations.

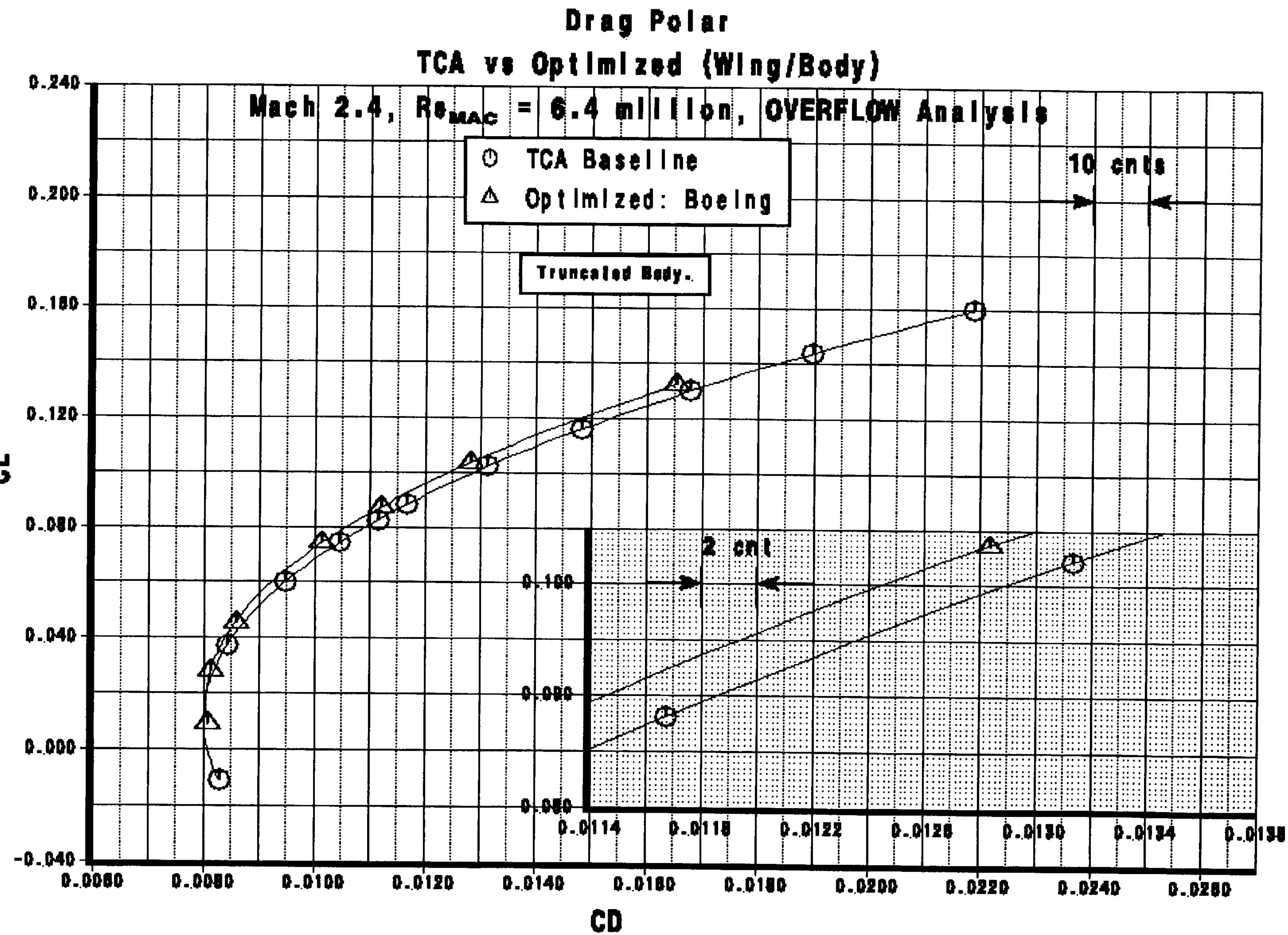
Drag Polar
TCA vs Optimized (Wing/Body)
Mach 2.4, Re_{MAC} = 6.4 million, OVERFLOW Analysis
TCA Baseline
Optimized: Boeing
Truncated Body.
10 cnts
2 cnt
CL
CD
0.240
0.200
0.160
0.120
0.080
0.040
0.000
-0.040
0.0060
0.0080
0.0100
0.0120
0.0140
0.0160
0.0180
0.0200
0.0220
0.0240
0.0260
0.100
0.080
0.060
0.0114
0.0118
0.0122
0.0126
0.0130
0.0134
0.0138

This is the drag polar of the BPW-LB CFL3D calculations showing 3.75 cts drag improvement of NCV over TCA WB as cruise CL of 0.1 at wind tunnel RN of 4million/ft. The Baldwin-Lomax turbulence model was used with CFL3D for the N-S calculations.

Drag Polars for the TCA and NCV Wing/Body

High Speed Aerodynamics, Long Beach

CFL3D Navier-Stokes, Truncated Fuselage, $M_\infty = 2.4$, $Re_c=6.36x10^6$

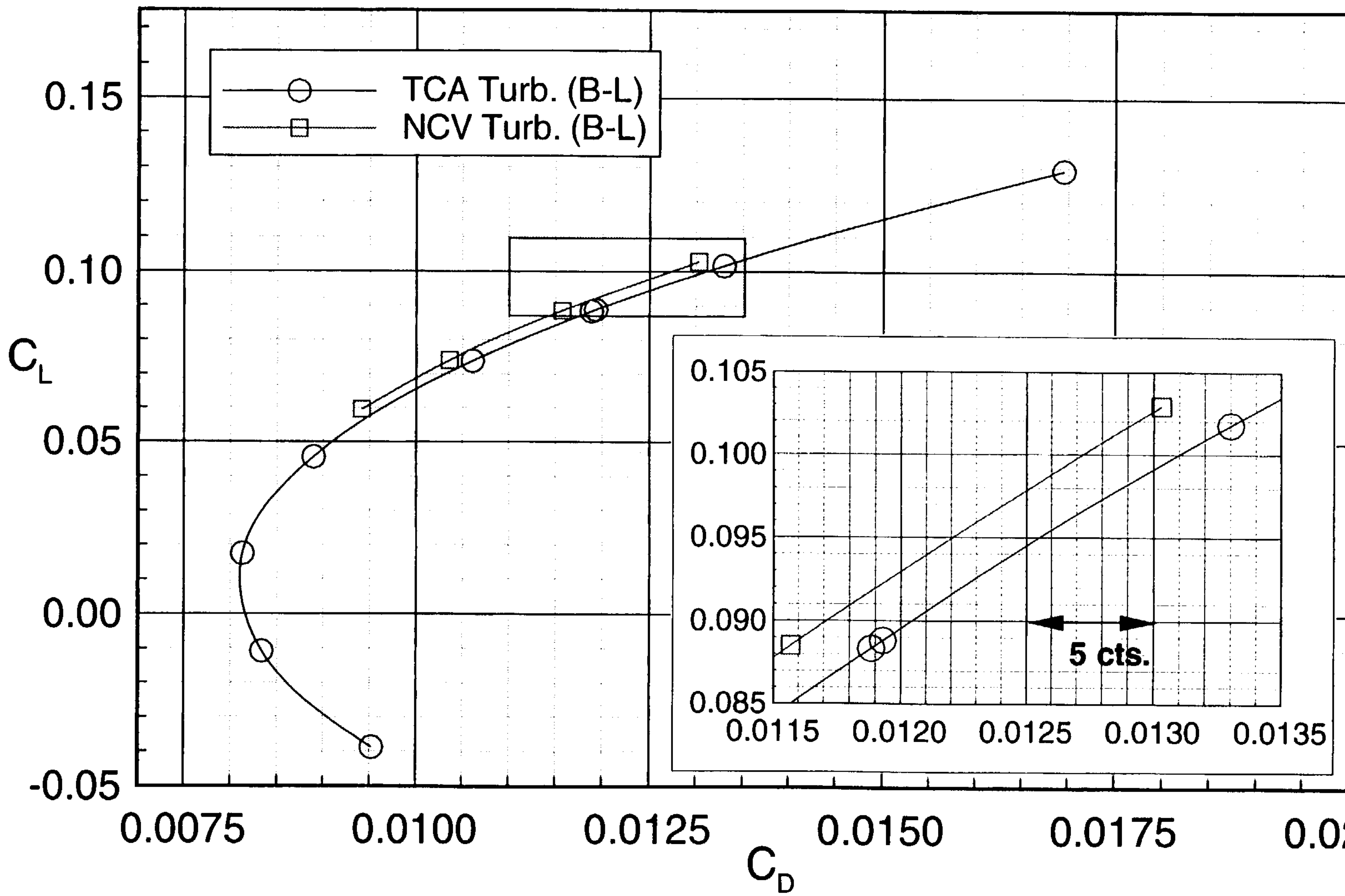

BOEING

This figure shows drag versus lift for NCV and TCA WB as measured during test 1687. The plot on the left is a close-up of the drag polars around minimum drag for the two configurations. The plot on the right is a close-up around cruise. The solid curve is for TCA and the dashed curve is for NCV. The curves represent the mean, using a 7^{th} order polynomial fit, through all runs within test 1687 of the same configuration. Test 1687 shows the drag improvement for NCV over TCA WB is only 2.6 cts. This is approximately 1.5 cts less than the calculated pre-test predictions.

SYMBOL	CONFIGURATION	MACH	RN	Q	DEWPT	TEST	RUN
————	TCA 2b WB	2.40	3.90	838.39	−13.36	1687	7−9
- - - - -	NCV WB	2.40	3.97	838.29	−15.05	1687	16−18,24−26,47−49

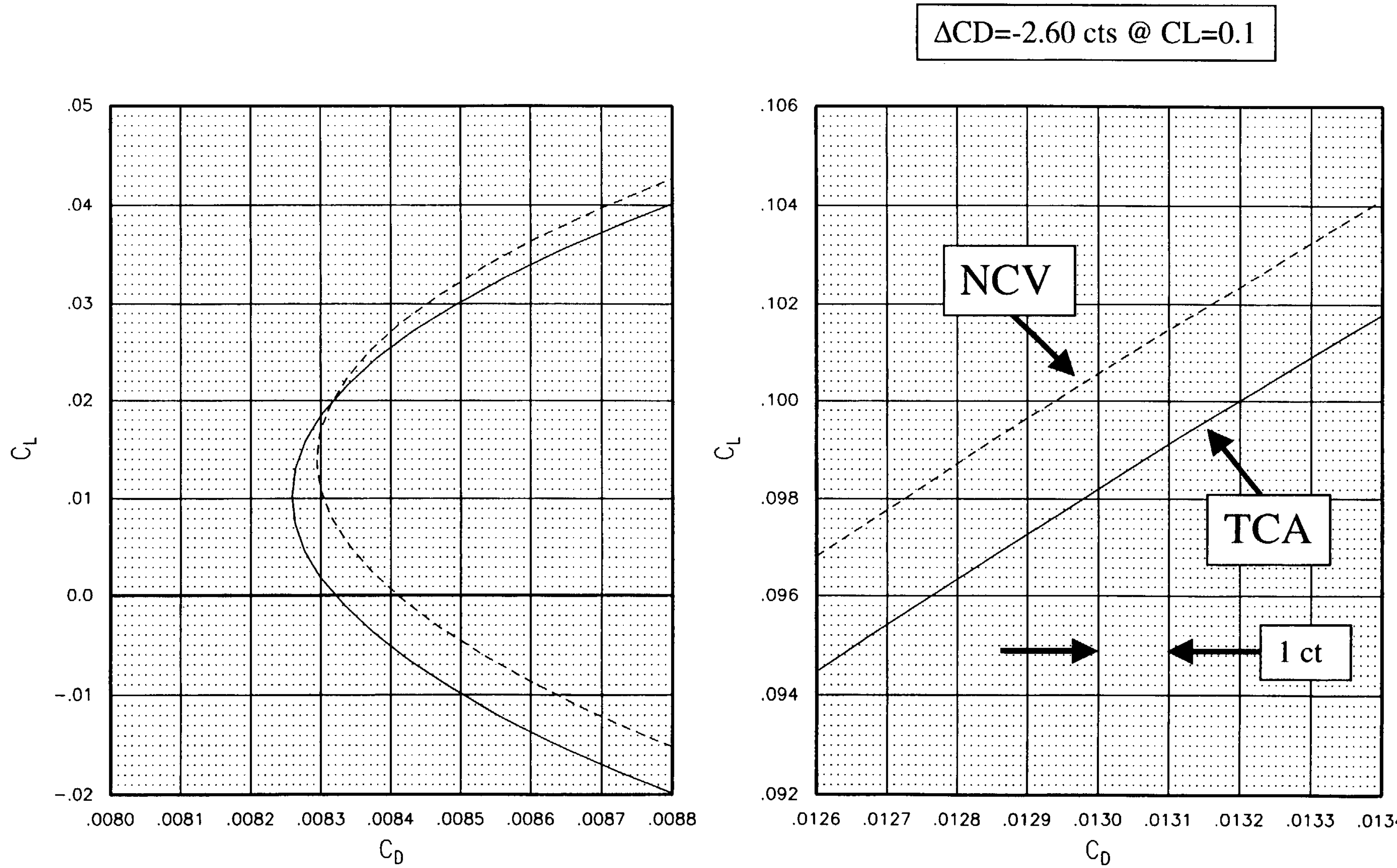

TCA vs NCV WB
Langley UPWT Test 1687

The approach taken to meet the objectives of the test is to measure forces and moments on both the TCA and NCV; get off body flow characteristics using Laser Vapor Screen (LVS) for both configurations; get TCA and NCV surface flow characteristics using UV oil and mini tufts; and test NCV with alternate trip configurations.

Approach

- WB Forces and Moments
- Off body flow characteristics using Laser Vapor Screen
- Surface flow characteristics using UV Oil and Mini Tufts
- Alternative trip configurations

Test procedures were carefully looked at and followed throughout the test to make sure the most accurate data possible was obtained to reduce errors that might have contributed to the measured drag improvement during test 1687. Angle of attack is one of the biggest influences on drag. An observation made during the test just prior to this one was that the adapter between the sting and strut needed to be replaced. The hardware set up produced an error in alpha that was not repeatable. In addition to installing a new adapter, brass buffers were added on the retaining area of the sting. The fit between hardware pieces uses a cylindrical fit. The buffers allow for the errors in alpha to be reduced when the system is under load.

Another component of angle of attack is the droop angle. This is the angle incurred by the weight of the model on the hardware support system. This angle gets measured for both the upright and inverted runs. The angle should be equal unless there is slop in the system or if the fit of the model on the balance is not perfect. For TCA, the upright is different from the inverted droop angle. The values of –2.92° upright and –2.54° inverted were consistent with previous tests. For NCV, the upright and inverted droop angles were the same. The value of –2.83° upright and inverted was different from test 1687. It is felt that the difference between tests is due to the hardware change. While for TCA, the difference between upright and inverted is tied up in the fit of the model on the balance.

An additional component of angle of attack is the balance to model misalignment angle. The model was designed such that the balance is installed in the model at a 2° angle down at the front of the balance. Models are rarely built such that this angle is met to within 0.001° accuracy. Test 1687 used the theoretical value for the balance to model misalignment angle. Test 1703 used the NASA Ames Research Center (ARC) QA measurements of –2.0061° for TCA and –2.0086° for NCV. What these new values ultimately effected was the computed stream angle correction. After test 1703 while QA'ing TCA and NCV, the balance to model misalignment angle was measured. There was a larger difference in the measurement of the TCA than for the NCV. The TCA LaRC QA measurement was smaller by 0.0166°. The NCV LaRC QA measurement was 0.002° smaller. These new measurements, if applied to the data, would not affect the data because the stream angle correction would compensate for the difference.

Another large influence to drag is the actual instrument used for measuring forces and moments. Balance UT65A was used for all HSR tests in the LaRC UPWT for TCA and NCV. The balance was monitored throughout the test. It showed shifts in normal, side, and axial force gages. Most of the shifts were within tolerances required by HSR. There was a time these shifts were outside of HSR tolerances and it was found that the UV oil damaged the moisture proofing on the gages. After this discovery, the balance was removed for the gages to be moisture proofed and for the rest of the test the balance was protected during the UV oil runs.

Another large correction to drag is the pressure acting on the balance by the cavity in the aftbody. The aftbody for the NCV configuration has an unusual shape due to the optimization process. The TCA aftbody cross section is circular. It was thought that the pressures across the aftbody shape might not be constant. Additional pressures were measured just behind the balance and just ahead of the fuselage exit at various radial locations.

Test Procedures

- Alpha
  - Adapter between sting and strut was replaced and added brass buffers on retaining area of sting.
  - Droop angle for upright and inverted runs were interrogated.
    - TCA 2b: upright = -2.92° and inverted = -2.54° (Consistent with other tests)
    - NCV: upright = inverted = -2.83° (Not consistent with previous test, but see item above)
  - Balance to model misalignment angle were updated to reflect ARC QA measurements.
    - TCA 2b = -2.0061° and NCV = -2.0086°
- Force/Moments
  - Balance UT65A showed shifts in NF, SF, and AF, but within HSR tolerances.
  - Balance needed to be protected during UV oil to protect moisture proofing on gages.
- Corrections
  - 6 chamber pressures in total. 4 just behind balance and 2 upstream of the fuselage exit.

The test was heavily supported on and off site. A large amount of flow visualization data was acquired. This required good documentation of the results. Images were acquired using Hasselblad and high resolution digital cameras. In addition to still images, standard and digital video cameras were used for moving images. The images, plots, data, and notes were posted on ADAPT daily. ADAPT is a secure website being used within the HSR community. No data was ever passed to others within HSR in a non-secure way.

The reason for posting all this information daily is so that others working on this test that couldn't be on site could participate during the test. Telecons were held daily between experimentalists and computational analysts. The team worked together to analyze the results and help make any changes necessary in the test plan.

When ever an interesting feature was detected that hadn't been looked at as part of the pre-test predictions, a computational solution or analysis was done to help the team assess what was observed.

This test could not have been successful as it was without the teamwork of NASA and Boeing personnel.

On and Off Site Support

- Images
  - Hasselblad and High Resolution Digital Cameras
  - Standard and Digital Video Cameras
- Images, plots, data, and notes were posted on ADAPT daily. Security held.
- Telecons with experimentalists and computational analysts daily.
- Fast turn around on CFD (C. F. Shieh) to correlate with flow visualization.
- Team Work: Gary Erickson (TE), Spencer Johnson & other UPWT technicians, Paul Bagby (photographer), Kevin Peterson, Kevin Keeley, and Raul Mendoza (Boeing), and Matt Kowalkowski (student).

The results from the test are presented as outlined for the rest of the presentation. First, the short and long term repeatability of the data will be shown. Second, the mini trip drag study that was done resulted in a laminar run and trip drag corrections to be made. Finally flow visualization images will be shown for the UV oil and LVS runs.

Outline of Results

- Short & Long Term Repeatability
- Laminar Run and Trip Drag Corrections
- UV Oil
- Laser Vapor Screen

This figure shows the short-term repeatability of the lift and pitching moment for TCA. These are mean curves through all the repeat runs for this configuration during the test. Short-term repeatability was very good for lift and pitching moment.

SYMBOL	CONFIGURATION	MACH	RN	Q	DEWPT	TEST	RUN
○	TCA 2b WB	2.40	3.98	838.03	−27.15	1703	56
○	TCA 2b WB	2.40	4.01	838.39	−26.99	1703	57
○	TCA 2b WB	2.40	4.00	838.33	−27.00	1703	58
———	TCA 2b WB	2.40	4.00	838.25	−27.05	1703	56−58

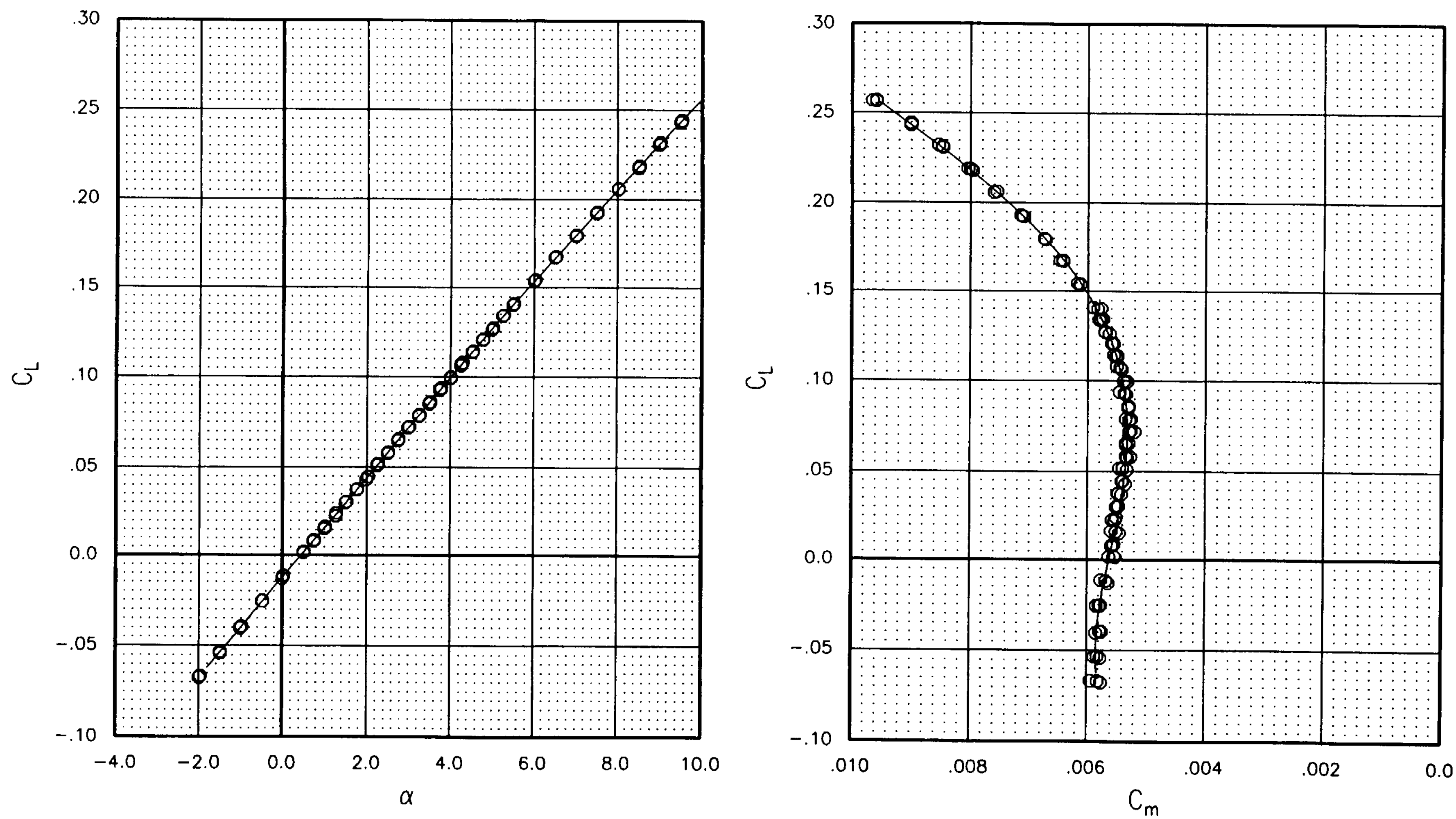

TCA 2b WB: Short Term Repeatability at M=2.4
Langley UPWT Test 1703

This figure shows the short-term repeatability of drag for TCA. A 7[th] order polynomial fit was put through the repeat runs to get a mean curve. The left plot shows a close-up around minimum drag. The right plot shows a close-up around the cruise point. The minimum to maximum range of drag at a CL of 0.1 shows a repeatability of less than ±0.5 cts. This is within the maximum tolerance required by HSR for supersonic cruise performance out of a wind tunnel test.

SYMBOL	CONFIGURATION	MACH	RN	Q	DEWPT	TEST	RUN
o	TCA 2b WB	2.40	3.98	838.03	−27.15	1703	56
o	TCA 2b WB	2.40	4.01	838.39	−26.99	1703	57
o	TCA 2b WB	2.40	4.00	838.33	−27.00	1703	58
———	TCA 2b WB	2.40	4.00	838.25	−27.05	1703	56−58

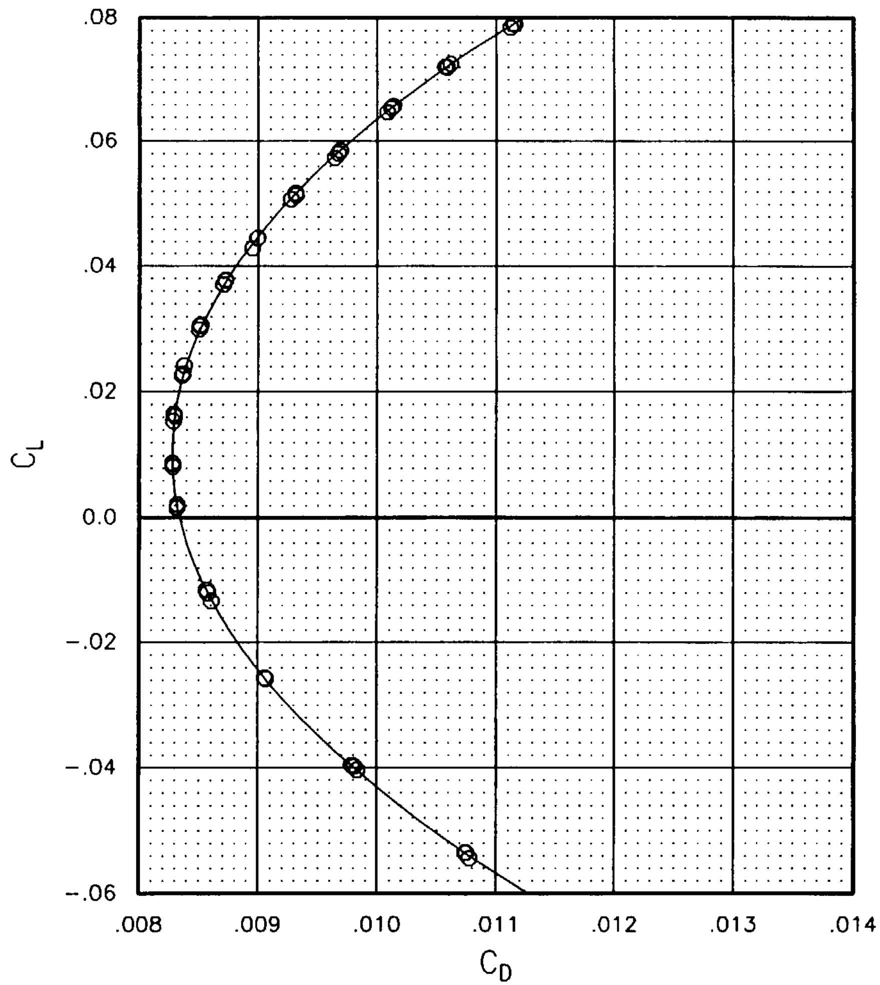

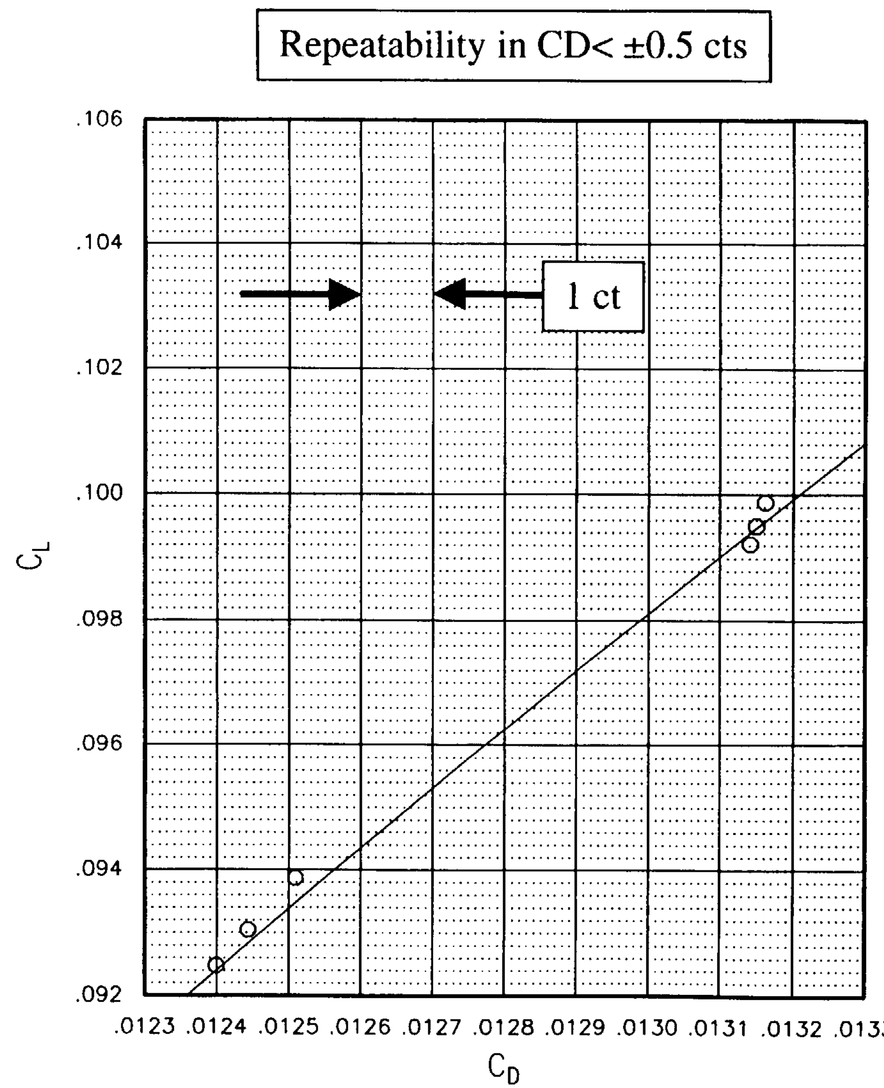

TCA 2b WB: Short Term Repeatability at M=2.4
Langley UPWT Test 1703

This figure shows the long-term repeatability of the lift and pitching moment for TCA. These are mean curves through all the repeat runs for this configuration during each test. Long-term repeatability was very good for lift and pitching moment between tests 1687 and 1703. It was slightly worse between tests 1703 and 1679. Test 1679 was the very first time the TCA-2b model was tested. The change in angle of attack between tests 1703 and previous tests at the CL of 0.1 is 0.0025° for test 1687 and 0.02° for test 1679.

SYMBOL	CONFIGURATION	MACH	RN	Q	DEWPT	TEST	RUN
———	TCA 2b WB	2.40	4.00	838.25	−27.05	1703	56−58
- - - - -	TCA 2b WB	2.40	3.90	838.39	−13.36	1687	7−9
— — —	TCA 2b WB	2.40	4.01	838.59	−33.03	1679	16−19,20−22,64−67

$\Delta\alpha$=0.0025° (1687)
$\Delta\alpha$=0.02° (1679)

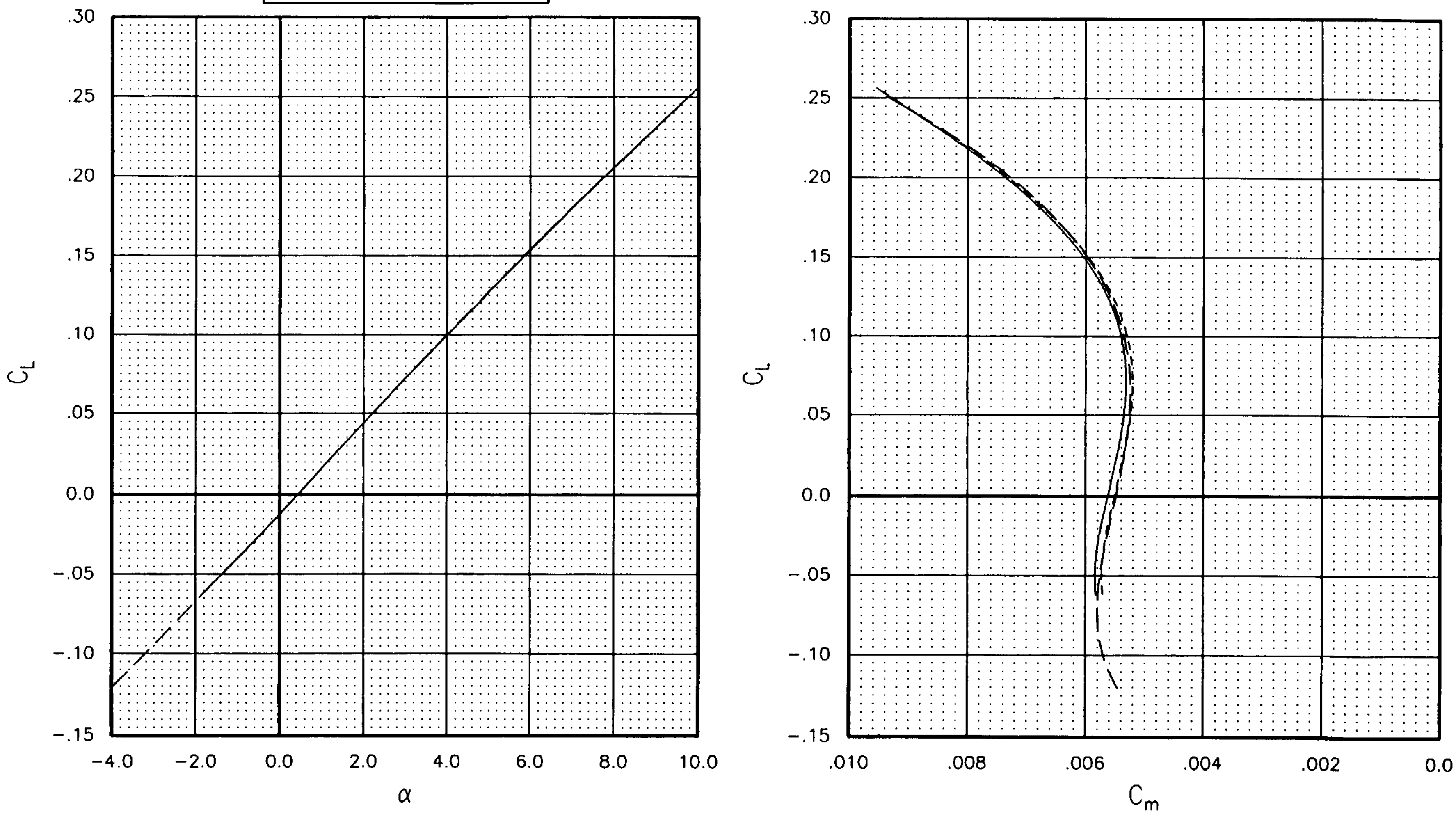

TCA WB: Long Term Repeatability with Mean Curve Through All Repeat Runs
Langley UPWT Test 1703 vs 1687 vs 1679

This figure shows the long-term repeatability of drag for TCA. These are mean curves through all the repeat runs for this configuration using a 7^{th} order polynomial fit through all the data during each test. The left plot shows a close-up around minimum drag. The right plot shows a close-up around the cruise point. Long term repeatability was very good for drag between tests 1687 and 1703. It was worse between tests 1703 and 1679. The change in drag between tests 1703 and previous tests at the CL of 0.1 is 0.1 cts less for test 1687 and 0.7 cts less for test 1679.

SYMBOL	CONFIGURATION	MACH	RN	Q	DEWPT	TEST	RUN
————	TCA 2b WB	2.40	4.00	838.25	−27.05	1703	56−58
- - - - - -	TCA 2b WB	2.40	3.90	838.39	−13.36	1687	7−9
— — —	TCA 2b WB	2.40	4.01	838.59	−33.03	1679	16−19,20−22,64−67

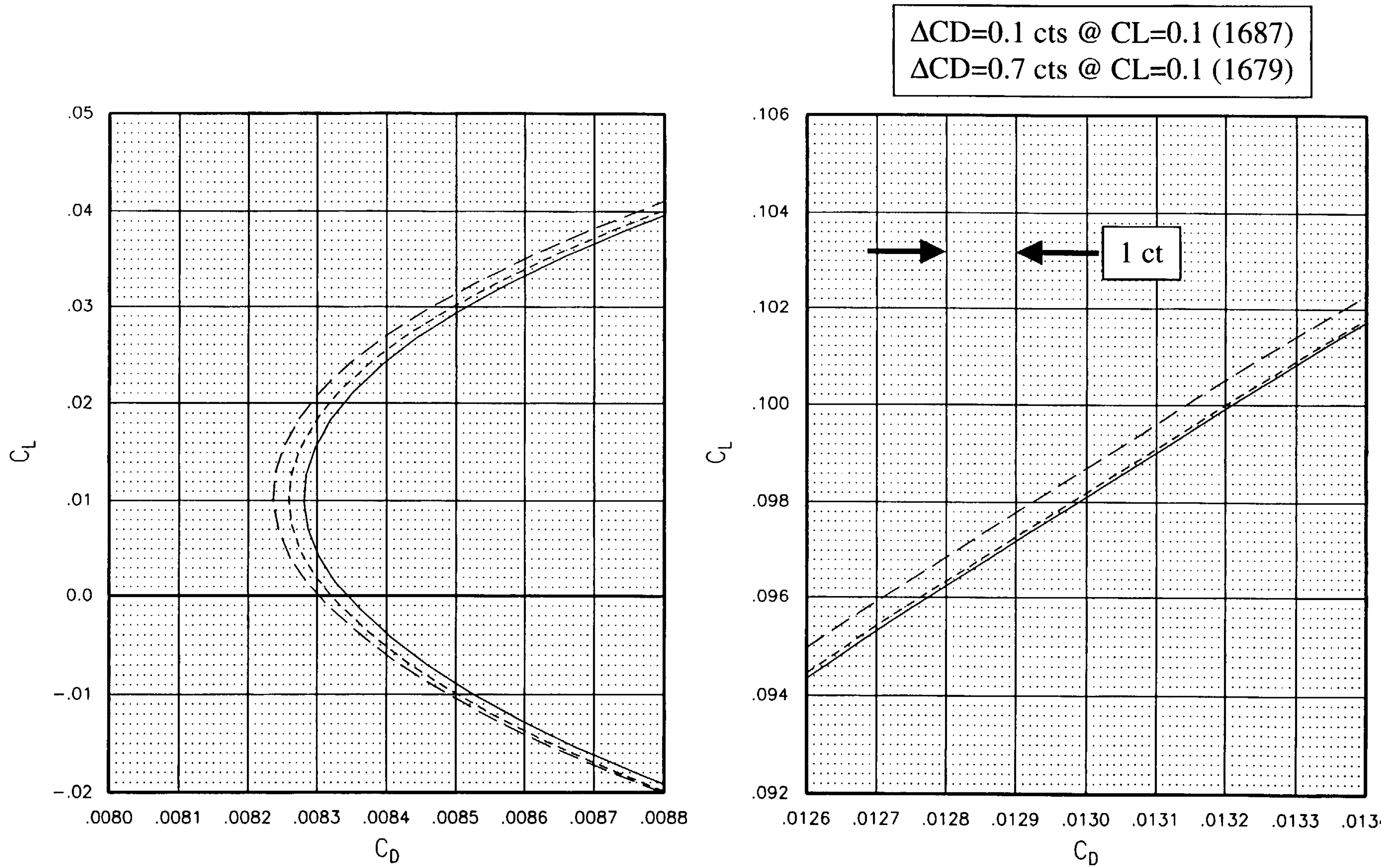

TCA WB: Long Term Repeatability with Mean Curve Through All Repeat Runs
Langley UPWT Test 1703 vs 1687 vs 1679

This figure shows the short-term repeatability of the lift and pitching moment for NCV. These are mean curves through all the repeat runs for this configuration during the test. Short-term repeatability was very good for lift and pitching moment.

SYMBOL	CONFIGURATION	MACH	RN	Q	DEWPT	TEST	RUN
○	NCV WB	2.40	4.01	838.56	−31.47	1703	9
○	NCV WB	2.40	3.99	838.09	−31.80	1703	10
○	NCV WB	2.40	3.99	838.15	−32.19	1703	11
——	NCV WB	2.40	4.00	838.27	−31.82	1703	9−11

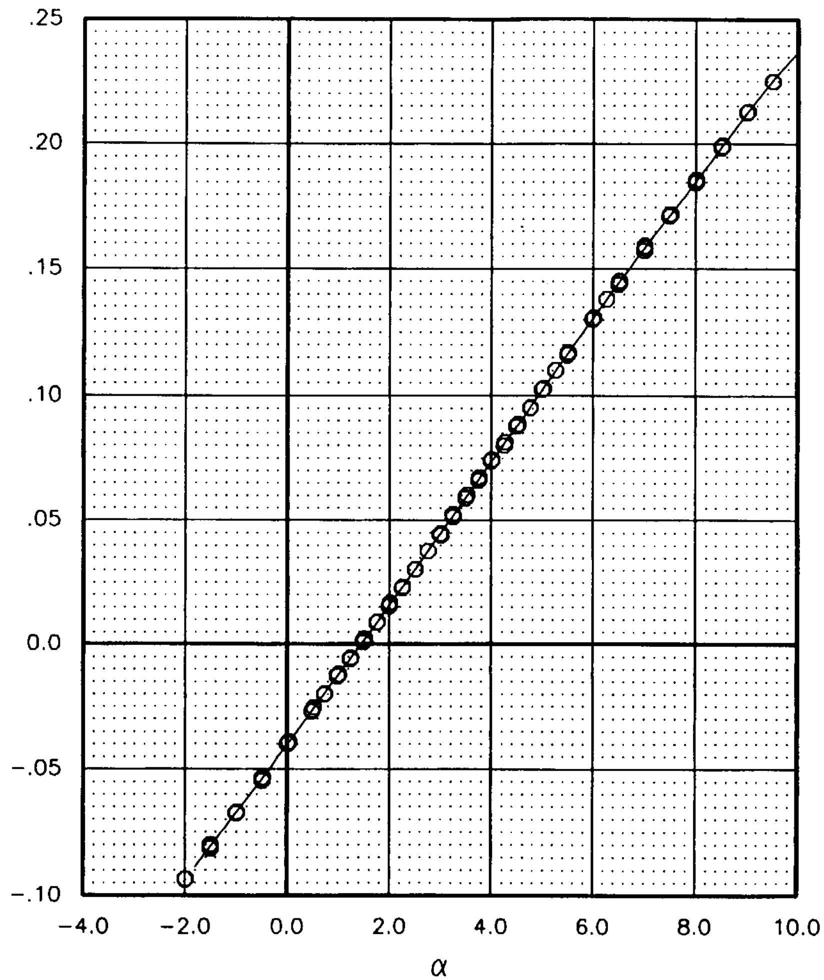

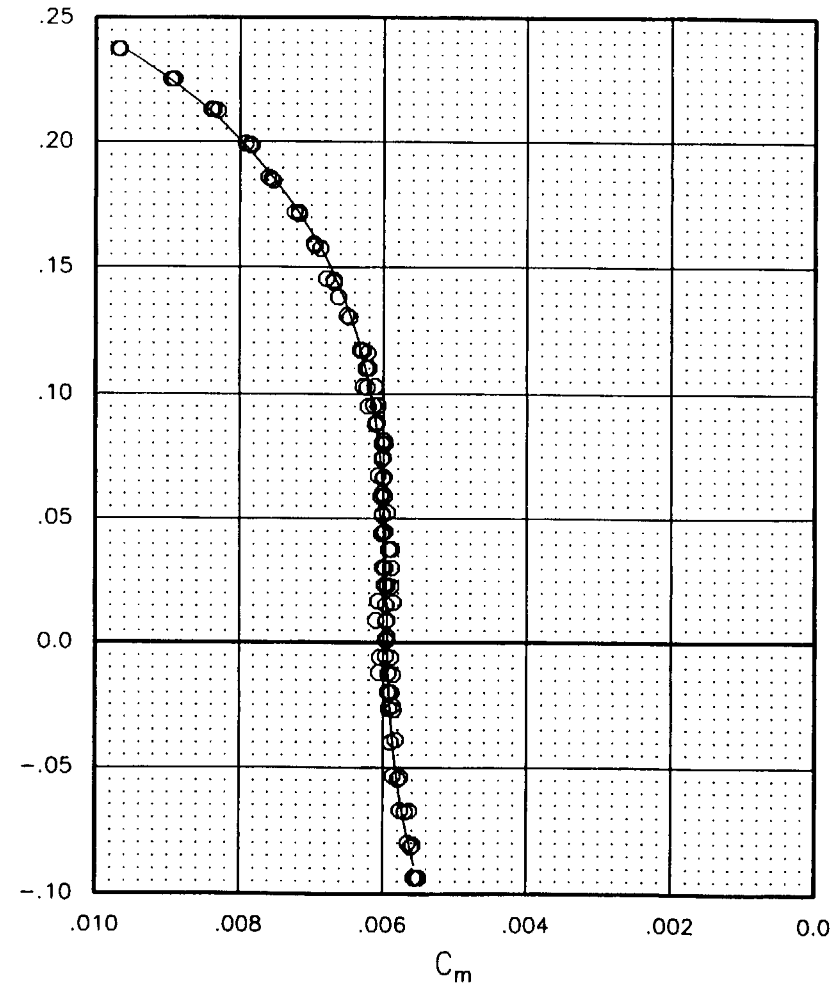

NCV WB: Short Term Repeatability at M=2.4
Langley UPWT Test 1703

This figure shows the short-term repeatability of drag for NCV. A 7^{th} order polynomial fit was put through the repeat runs to get a mean curve. The left plot shows a close-up around minimum drag. The right plot shows a close-up around the cruise point. The minimum to maximum range of drag at a CL of 0.1 shows a repeatability of less than ±0.25 cts. This is within the maximum tolerance required by HSR for supersonic cruise performance out of a wind tunnel test.

SYMBOL	CONFIGURATION	MACH	RN	Q	DEWPT	TEST	RUN
○	NCV WB	2.40	4.01	838.56	−31.47	1703	9
○	NCV WB	2.40	3.99	838.09	−31.80	1703	10
○	NCV WB	2.40	3.99	838.15	−32.19	1703	11
———	NCV WB	2.40	4.00	838.27	−31.82	1703	9−11

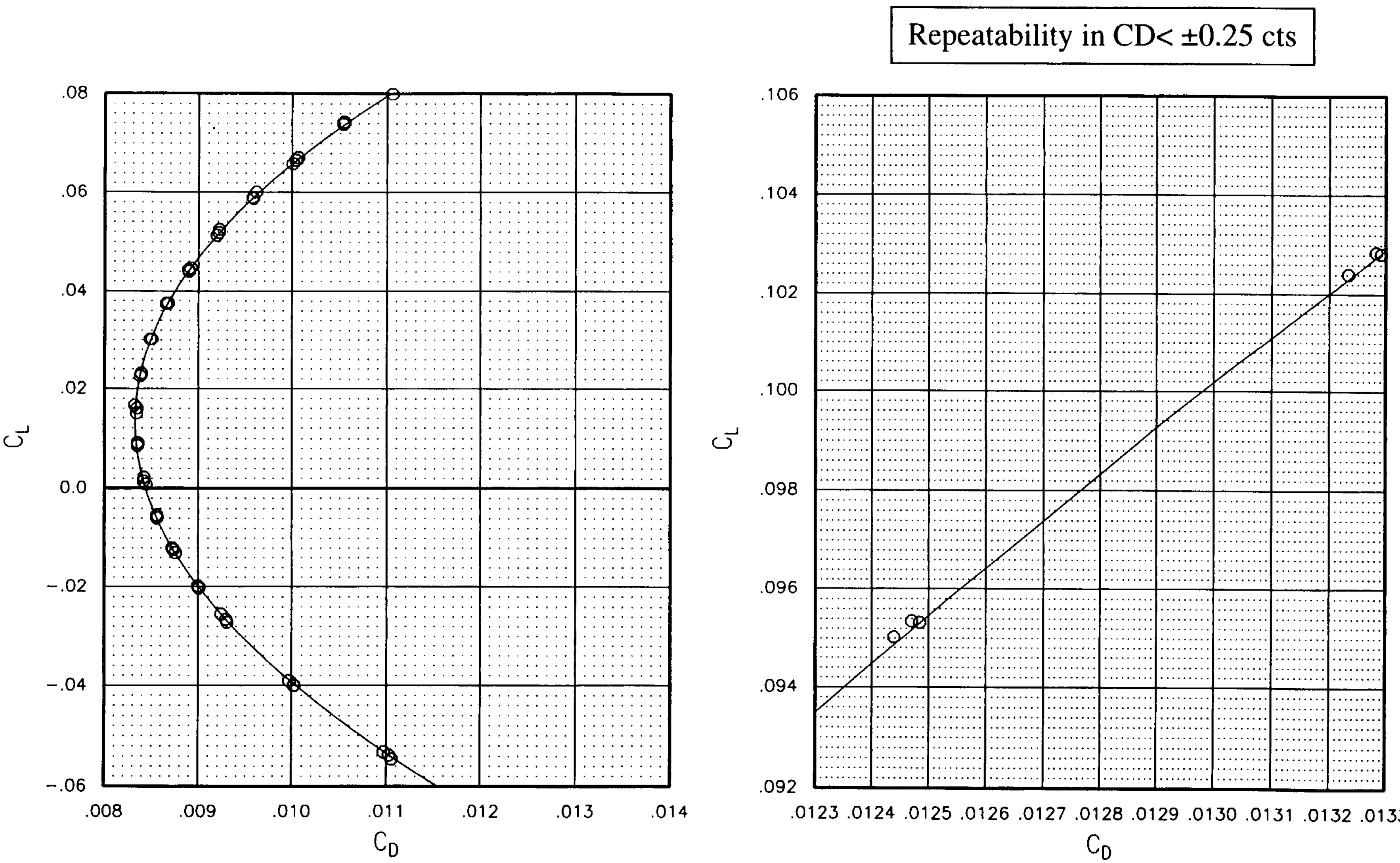

NCV WB: Short Term Repeatability at M=2.4
Langley UPWT Test 1703

This figure shows the long-term repeatability of the lift and pitching moment for NCV. These are mean curves through all the repeat runs for this configuration during each test. Long-term repeatability was very good for lift and pitching moment between tests 1687 and 1703. The change in angle of attack between tests 1703 and 1687 at the CL of 0.1 is 0.025° for test 1687.

SYMBOL	CONFIGURATION	MACH	RN	Q	DEWPT	TEST	RUN
———	NCV WB	2.40	4.00	838.27	−31.82	1703	9−11
- - - - -	NCV WB	2.40	3.97	838.29	−15.05	1687	16−18,24−26,47−49

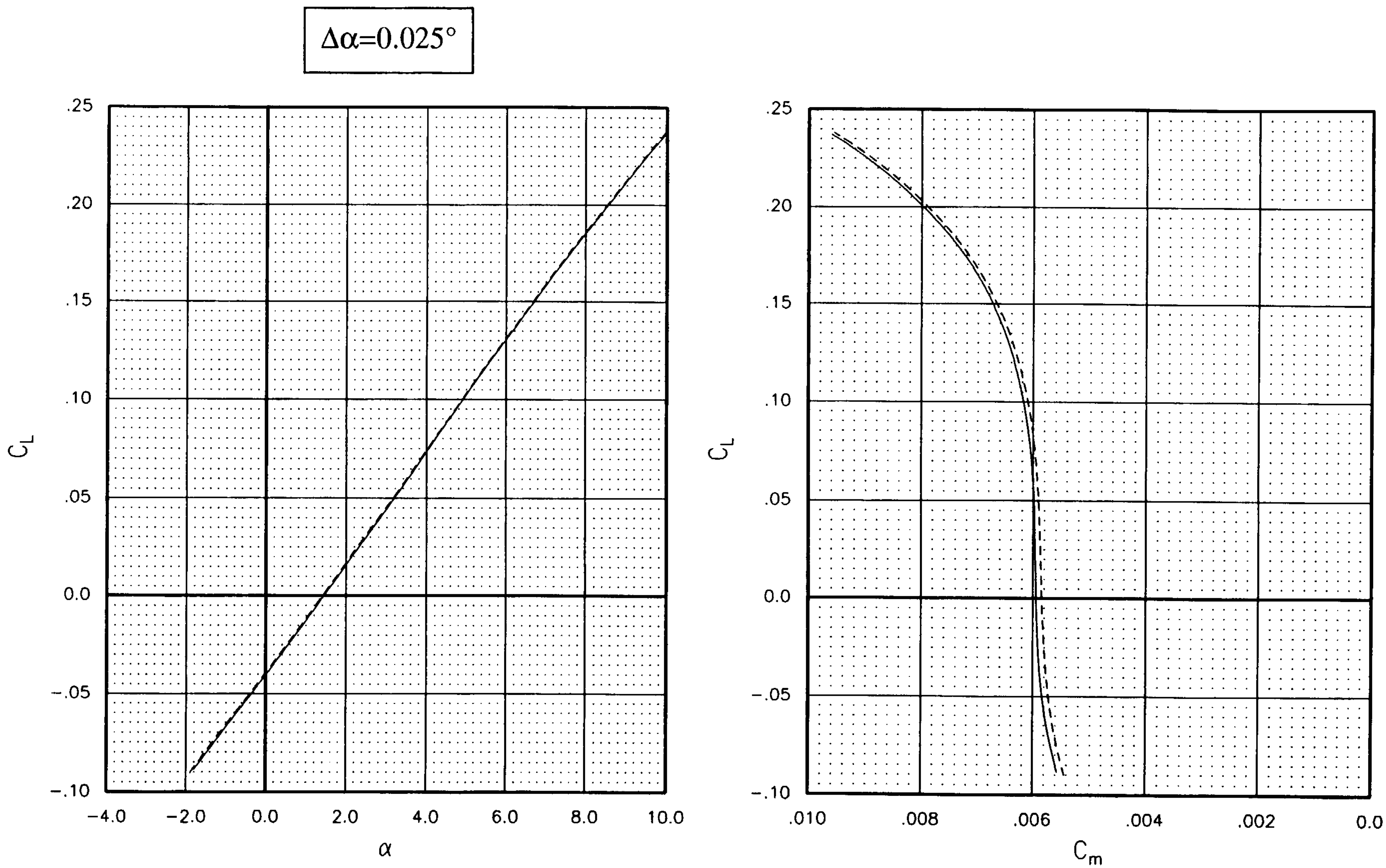

NCV WB: Long Term Repeatability with Mean Curve Through All Repeat Runs
Langley UPWT Test 1703 vs 1687

This figure shows the long-term repeatability of drag for NCV. These are mean curves through all the repeat runs for this configuration using a 7th order polynomial fit through all the data during each test. The left plot shows a close-up around minimum drag. The right plot shows a close-up around the cruise point. Long term repeatability was very good for drag between tests 1687 and 1703. The change in drag between tests 1703 and 1687 at the CL of 0.1 is 0.4 cts less for test 1687.

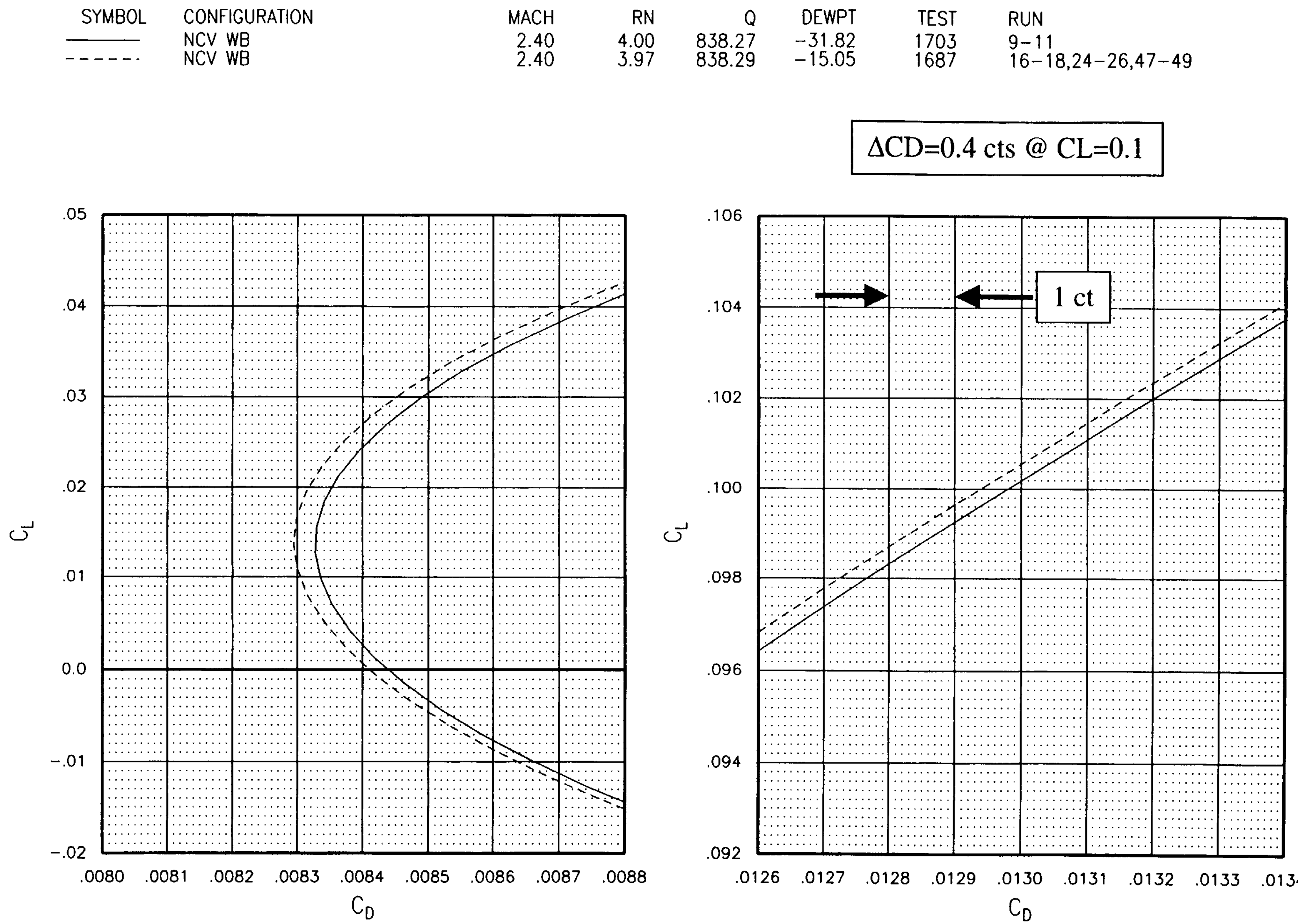

NCV WB: Long Term Repeatability with Mean Curve Through All Repeat Runs
Langley UPWT Test 1703 vs 1687

This figure shows the drag improvement for NCV over TCA for test 1703. NCV is 2.3 cts less than TCA. Recall test 1687 showed 2.6 cts improvement for NCV over TCA.

SYMBOL	CONFIGURATION	MACH	RN	Q	DEWPT	TEST	RUN
———	TCA 2b WB	2.40	4.00	838.25	−27.05	1703	56−58
- - - - -	NCV WB	2.40	4.00	838.27	−31.82	1703	9−11

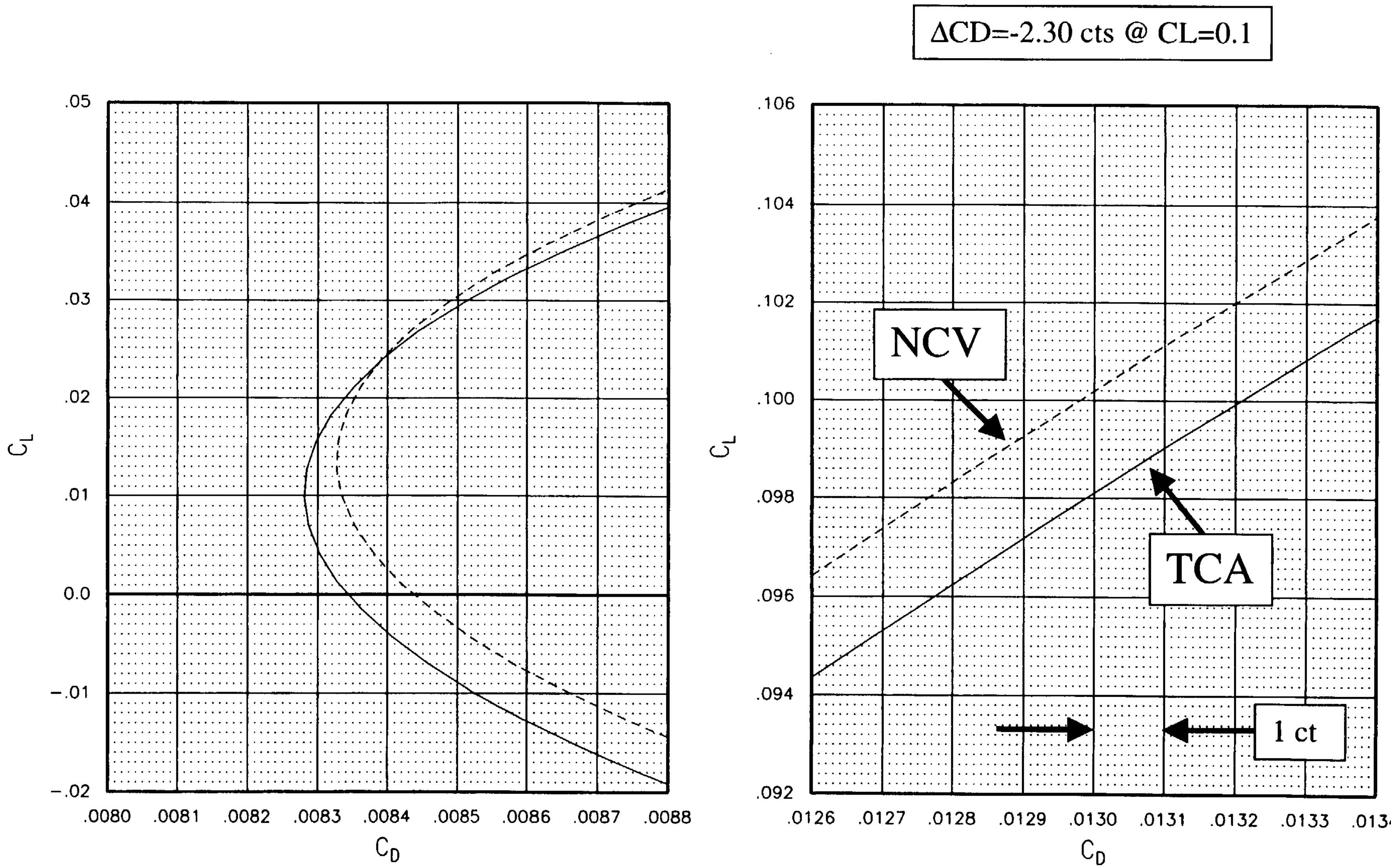

TCA vs NCV WB
Langley UPWT Test 1703

In an attempt to check if the tripping mechanisms used were the right ones for NCV, CFD pre-test calculations were done to assess the boundary layer thickness and the location of the baseline trip configuration with respect to the pressure distribution. The long dashed vertical lines are the trip discs located 0.6 inch aft of the leading edge in the streamwise direction. The dash-dot vertical lines represent the trip discs to be located at 1 inch aft of the leading edge. The top two plots are of the pressure distribution on the upper wing surface at two spanwise locations close to side of body. It was felt that the baseline location was not tripping the flow effectively because they were ahead of the pressure peak. The bottom two plots are of the boundary layer and displacement thickness. At 0.6 inch aft of the leading edge, the baseline trip discs were 0.012 inches high. This discs are taller than the boundary layer thickness. At 1 inch aft of the leading edge, it was felt that 0.015-inch high discs would be a good starting point to evaluate the trip effectiveness since this is the height of the boundary layer thickness. It was also evident that the trip configuration only needed to be replaced on the inboard upper wing surface. The baseline trip configuration was effective everywhere else.

C_p Distribution and Boundary Layer Thickness for NCV W/B

High Speed Aerodynamics, Long Beach

Wing Upper Surface

BL3D with CFL3D Euler C_p, $M_\infty = 2.4$, $Re_c = 6.36 \times 10^6$, $C_L = 0.089$

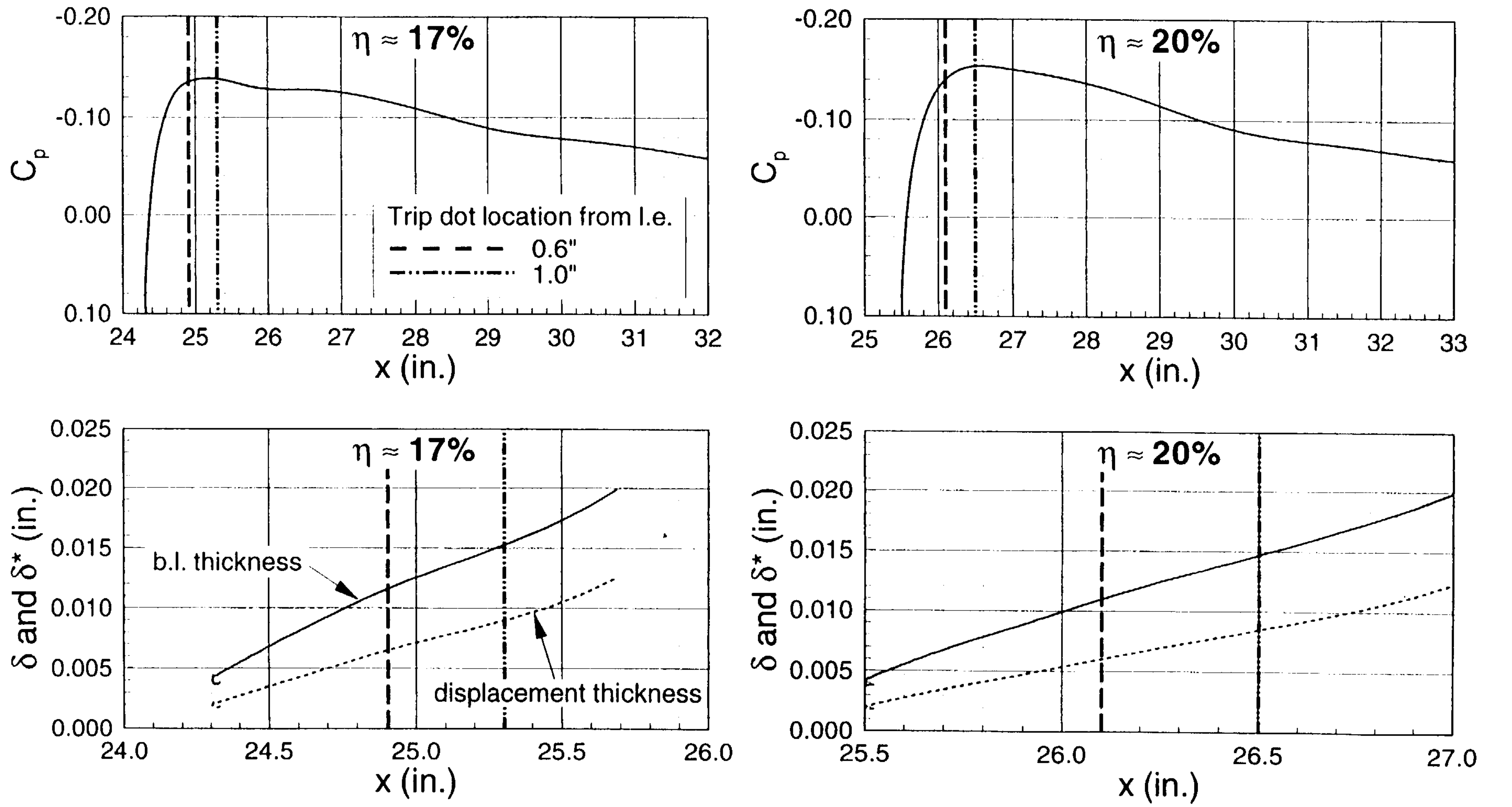

BOEING

In addition to the baseline trip configuration and 0.015-inch high discs located 1 inch aft of the leading edge, three other trip configurations were investigated as part of the mini trip drag study on the NCV model. The trip discs were totally removed from the upper and lower wing surfaces to get the data for free transition. The other trip heights investigated on the inboard upper wing surface were 0.012 and 0.016 inch high discs.

NCV Trip Drag Study

Trip Disk Height	Location
0	Upper and Lower Wing Surfaces
0.012”	X=0.6” on Upper and Lower Wing Surfaces
0.012”	X=1” on Inboard Upper Wing
0.015”	X=1” on Inboard Upper Wing
0.016”	X=1” on Inboard Upper Wing

The 0.016 inch high discs on the inboard upper wing surface were the most effective, but still did not force the flow to go turbulent just aft of the discs. There still was a small amount of laminar run past the disc location. The drag improvement of NCV over TCA using these discs on the NCV model increased the improvement only by 0.17 cts from the baseline trip configuration for a total drag improvement of 2.57 cts. This data is still not corrected for the laminar run and the trip drag.

SYMBOL	CONFIGURATION	MACH	RN	Q	DEWPT	TEST	RUN
———	TCA 2b WB	2.40	4.00	838.25	−27.05	1703	56−58
- - - - - -	NCV WB	2.40	3.99	838.11	−33.17	1703	47−49,65−71

ΔCD=-2.57 cts @ CL=0.1

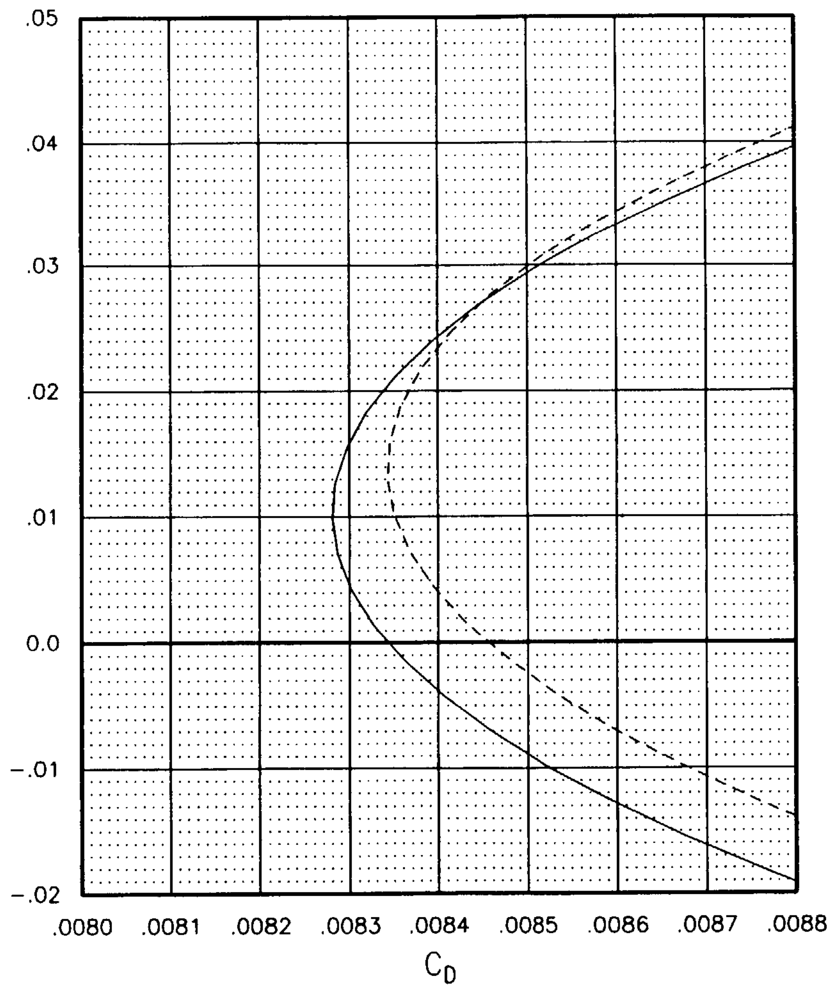

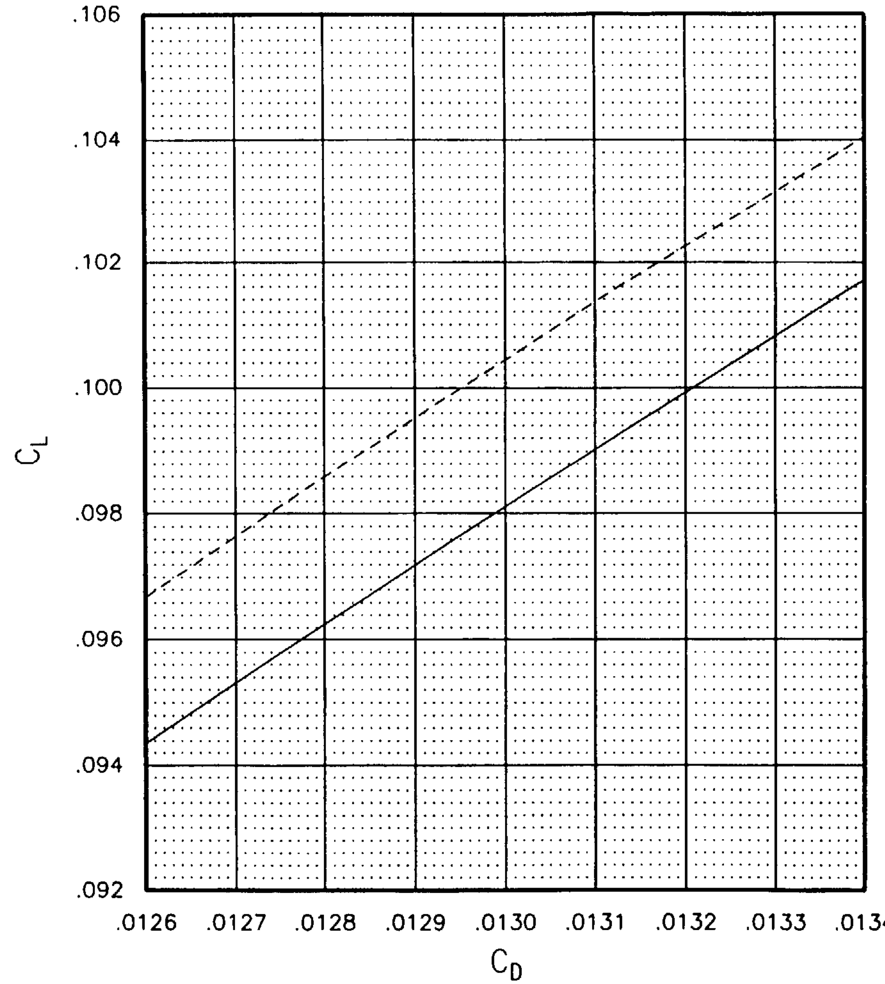

TCA k=0.012 @x=0.6 vs NCV WB k=0.016 @x=1
Langley UPWT Test 1703

To be able to make the laminar run correction, a series of images were taken during the sublimation flow visualization runs. Sublimation is a material that sublimes on the area of the wing that is turbulent. The material that remains represent s the areas of laminar run. These images are scanned and read into a program like Adobe Illustrator. The transition line is laid out on the image and points representing the line as a percentage of the wing chord are outputted. This data is used in a boundary layer code that was developed at NASA Ames Research center by Robert Kennelly. The code outputs the skin friction drag based on flat plate boundary layer theory on a fully turbulent and mixed laminar-turbulent wing flow. The difference between these outputs is the drag due to the laminar run that gets added to the total uncorrected drag.

I will be showing the images of some of the sublimation flow visualization runs on the NCV model. A trip drag study was done on TCA during test 1679. The results of the laminar run and trip drag analysis from the data acquired during test 1679 will be applied to the TCA data from this test.

This image is the transition line laid out for the free transition case on the upper wing surface of the NCV model. The points represent the transition line for the boundary layer code to compute the laminar run correction.

NCV Free Transition on Upper Wing

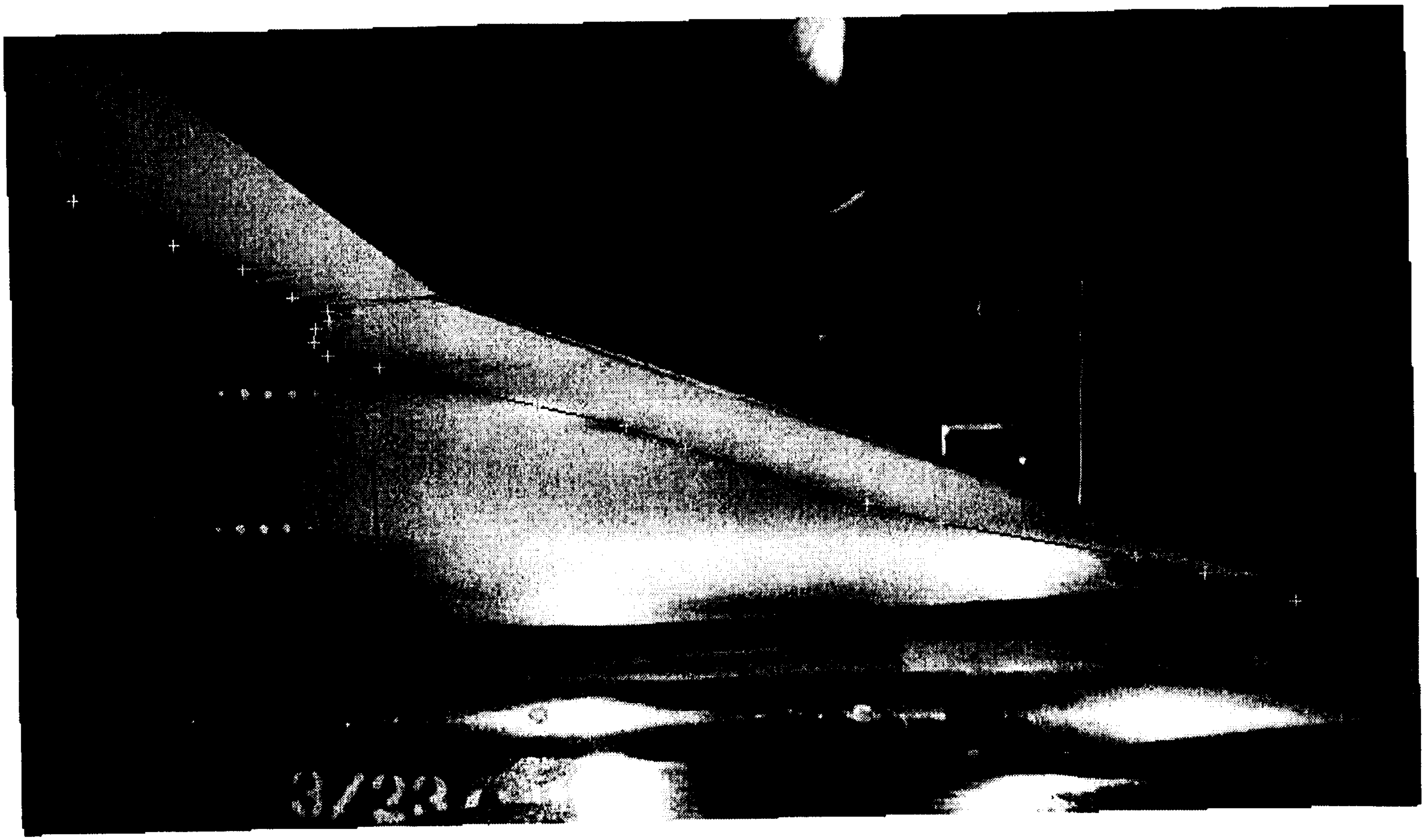

This image is from the sublimation run on the upper wing surface. The trip configuration here is 0.016-inch high discs located 1 inch aft of the leading edge inboard and 0.012 inch high discs located 0.6 inch aft of the leading edge outboard. To help determining the location of transition, two discs were removed on wither side of a disc to create a lone disc in regions of the wing. These lone discs help during a sublimation run to determine where transition occurs. A 15° turbulent wedge is created where the flow transitions from laminar to turbulent flow. These wedges can be seen readily wherever a lone disc exists. This helps the transition line to be laid out on the image on the wing surface. The transition line can sometimes be difficult to observe due to not being able to distinguish laminar from turbulent flow. The best attempt was made to lay out where turbulent flow starts.

NCV Transition for IB k=0.016/x=1 and OB k=0.012/x=0.6 on Upper Wing

This is a compilation chart of the transition line for each of the trip configurations tested for the upper wing surface. For each transition line, a corresponding laminar run correction is listed in the legend. An interesting observation is that the baseline trip was just as effective as the alternate trip location except for a small region of the wing near side of body. The difference between the baseline and the alternate trip laminar run is less than 0.2 cts.

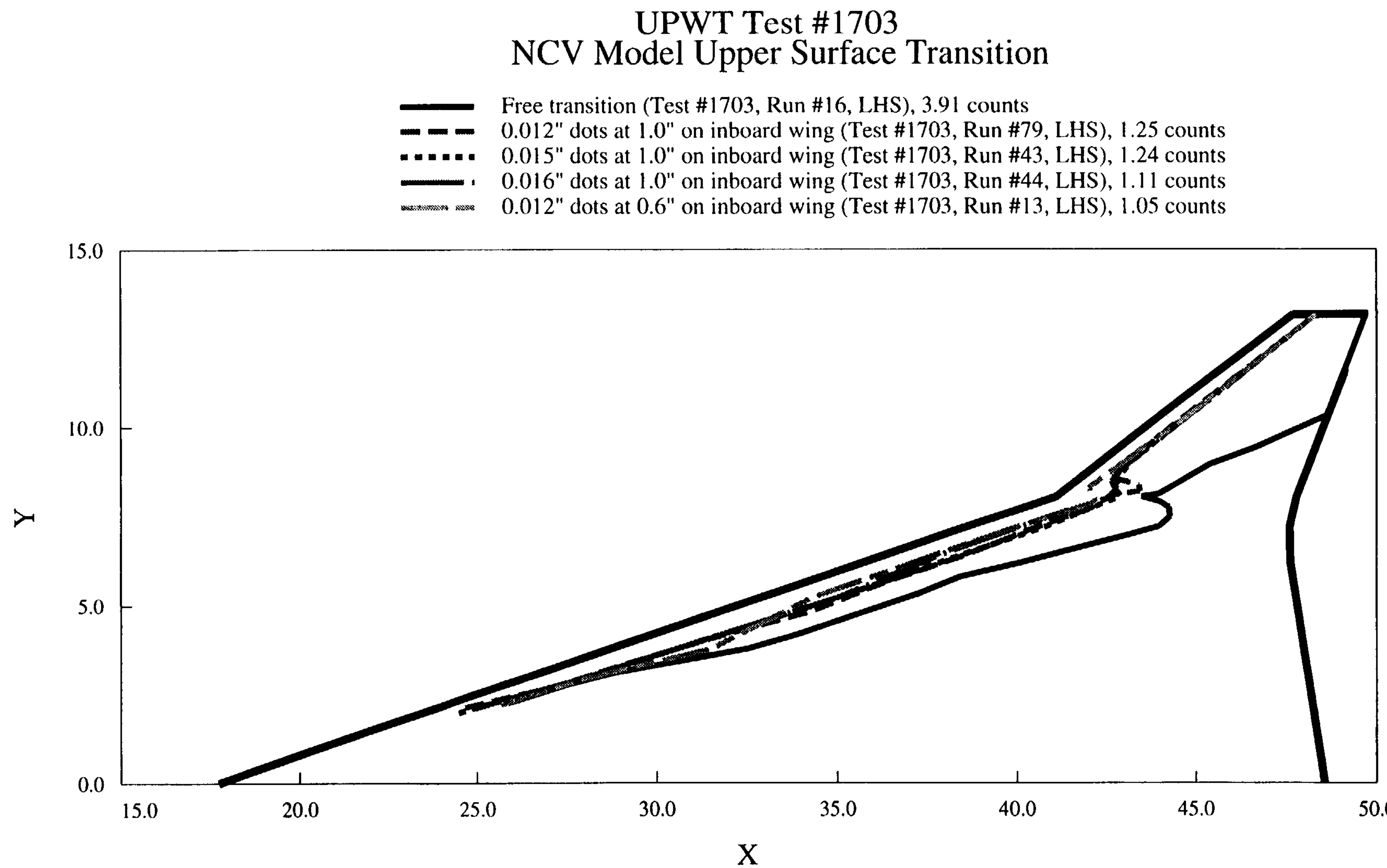

RAK/MC, 7/24/98

File name: ncv_upper.qpt Plot date: 12-Aug-98

Sublimation flow visualization runs were also done on the lower wing surface for the 2 trip configurations tested. This is an image of the transition line laid out for the free transition case.

NCV Free Transition on Lower Wing

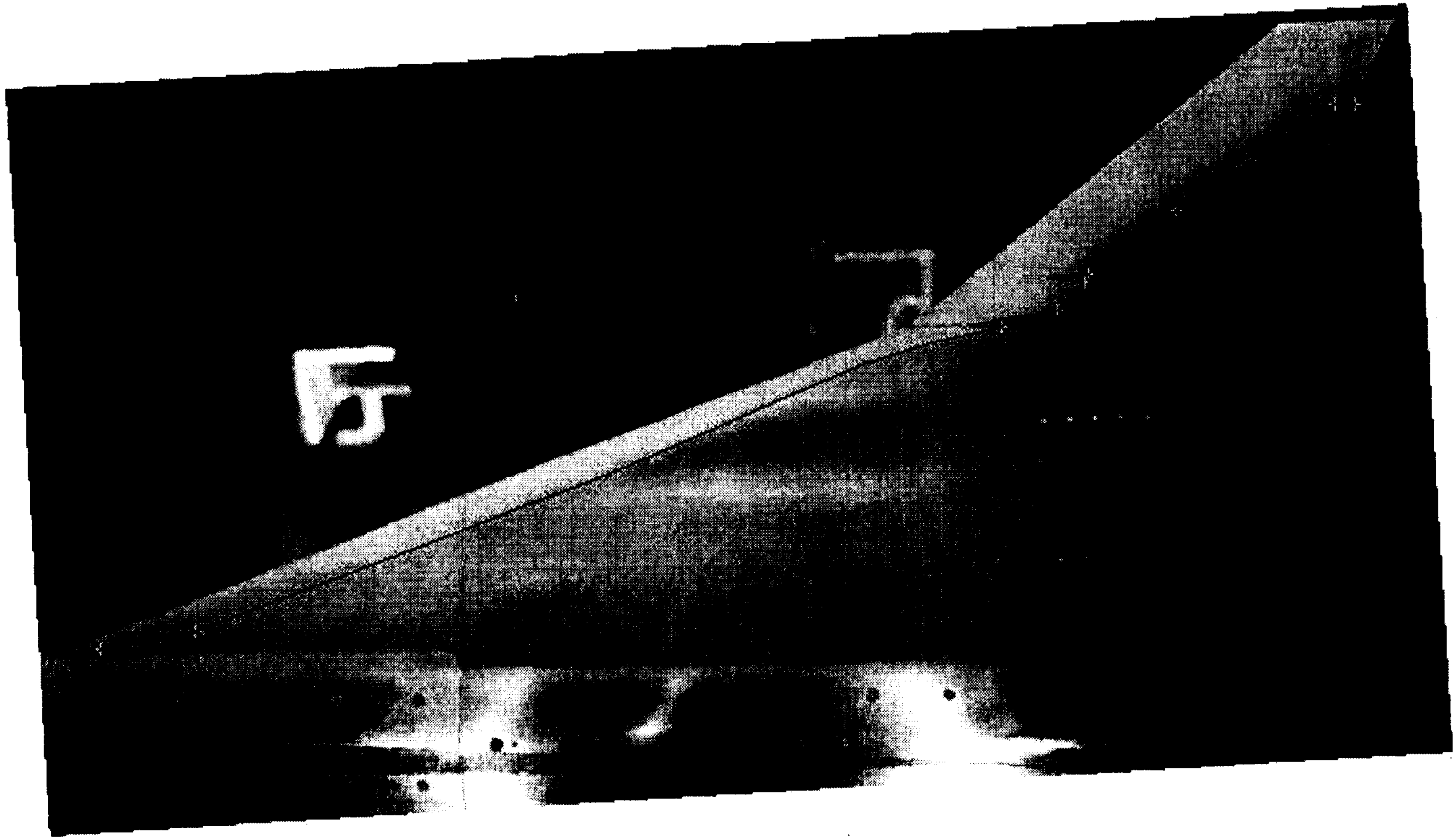

This is an image of the transition line laid out for the baseline trip configuration on the lower wing surface.

NCV Transition for k=0.012/x=0.6 on Lower Wing

This compilation chart show the difference between free transition and the baseline trip configuration. Note the amount of laminar run correction made for the lower wing surface for each configuration.

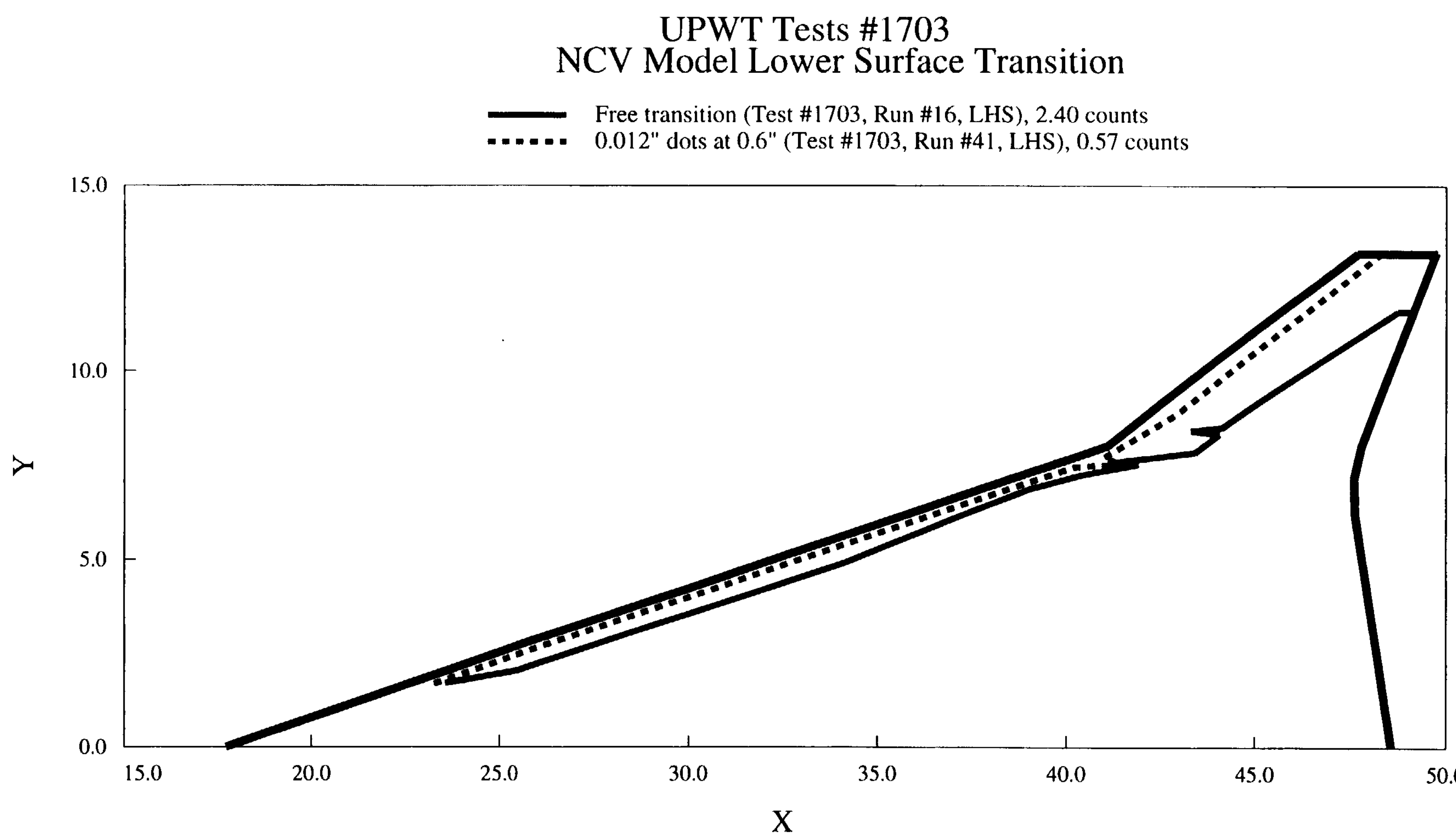

RAK/MC, 7/27/98

File name: ncv_tran_lower_1703.qpt   Plot date: 12-Aug-98

This plot shows the uncorrected and laminar run corrected drag at the lift coefficient the sublimation runs were acquired. The procedure on how trip drag is determined is described in the paper that proceeded this one by Aga Goodsell and Robert Kennelly. Due to this being a mini trip drag study, not enough trip configurations were tested to be able to determine where the drag plateau occurs. An estimation was made that the plateau occurs at zero trip height and that the rest of the data needed to cross the plateau at a trip height of 0.007 inches. These estimations came about from the trip drag study done on TCA during test 1679. A linear fit is put through the data for the configurations tested with trip discs. The difference between the linear fit and the plateau is the trip drag correction.

NCV WB Mini Trip Drag Study
@ CL=0.0875

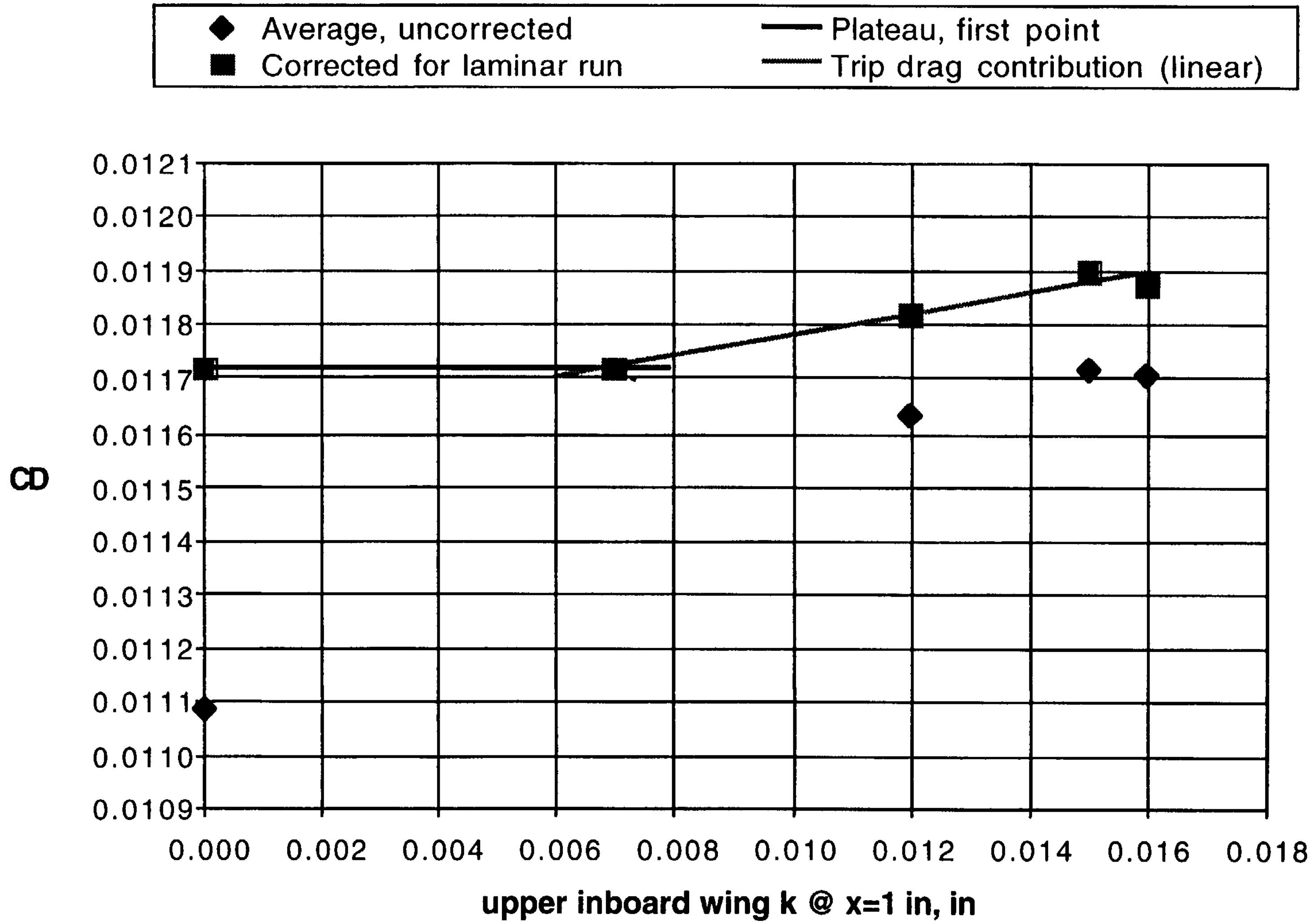

This plot shows the drag corrections made for laminar run and trip drag for each configuration tested. These corrections are applied to the whole drag polar. The laminar run correction is added, while the trip drag correction is subtracted.

NCV WB Mini Trip Drag Study @CL=0.0875
Laminar Run and Trip Drag Corrections

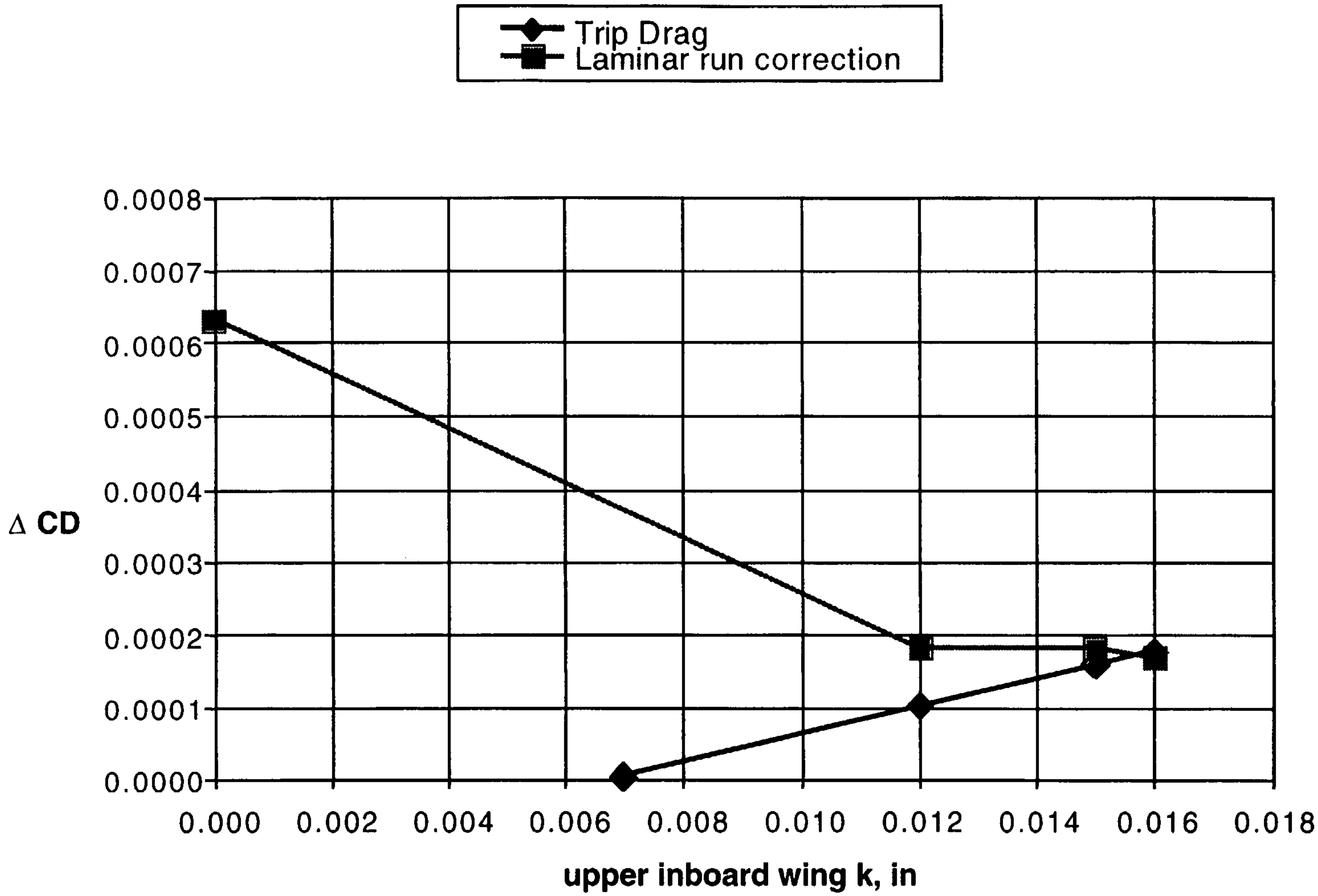

After making these corrections, the drag improvement of NCV over TCA only improved by 0.2 cts more than that determined using the uncorrected data. This applies to all tests and all trip configurations. For the baseline trip configuration the improvement of NCV over TCA is 2.8 cts. For test 1703, the improvement is 2.5 cts. The difference between the 2 tests is wrapped up in the long-term repeatability. For the alternate trip location and the highest height, the improvement is 2.8 cts. The difference between the baseline and the alternate trip configuration is wrapped up in the cumulative error in laminar run, trip drag, and data repeatability.

Laminar Run and Trip Drag Corrected Drag Improvement of NCV Over TCA

Trip Configuration	Uncorrected Drag Improvement	Corrected Drag Improvement
Test 1687 Baseline Trip	2.6	2.79
Test 1703 Baseline Trip	2.3	2.49
Test 1703 Trip Height=0.016” at X=1” on Inboard Upper Wing	2.57	2.8

This is a summary image of the UV oil run done on TCA at the supersonic cruise angle of attack. The upper most image is of the upper wing surface. Just under the upper wing is the lower wing image from the UV oil run. At the bottom left is side of body near the wing apex and on the right is looking at the forebody upper surface. Hasselblad cameras were mounted on both windows. This image makes up 2 runs. One run was with the model mounted wings vertically to get the upper surfaces. The second run was with the model mounted wings horizontally to get side of body. The images depicts the surface flow on the model. The flow is very clean without any separation.

TCA UV Oil at M=2.4 and Alpha=3.5°

Upper

Wing Trip=112
Nose Trip=112100105

Lower

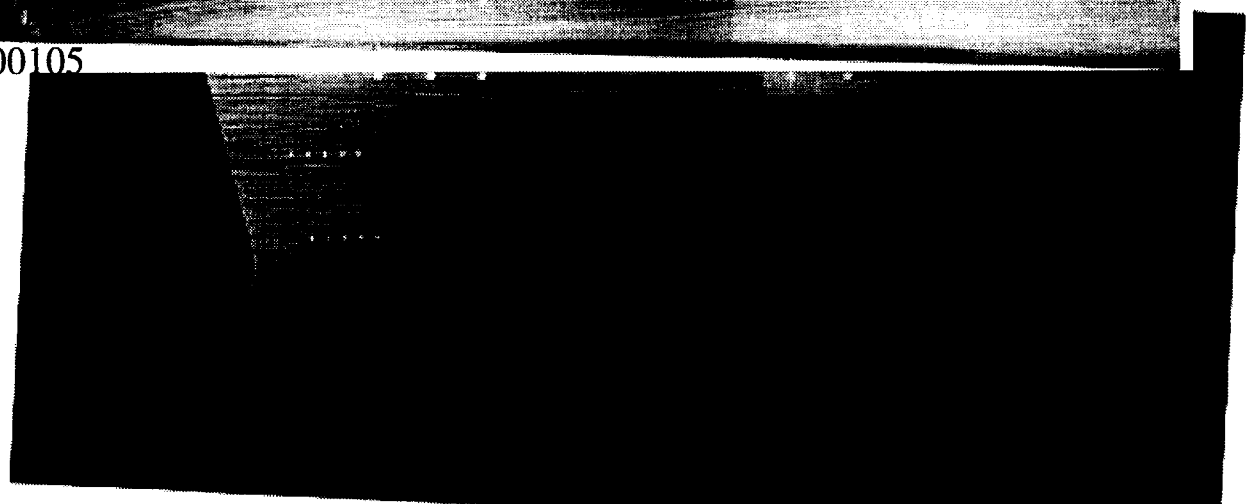

Side of Body

Forebody

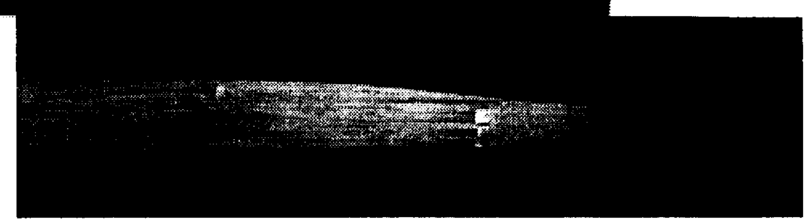

This is a compilation of images from UV oil runs on the NCV model at the supersonic cruise angle of attack. Here you will notice that the upper wing surface has some distinct features representing vortices. There seems to be two traces of the vortices on the wing. One goes streamwise over the inboard nacelle location and the other over the outboard nacelle location. The one that passes over the inboard nacelle location seems to be emanating from the wing body junction. The one that passes over the outboard nacelle location seems to come from the same region but moves span wise as it goes downstream. The vortices will be evident when the LVS images are seen.

The flow over the lower wing surface, side of body, and upper forebody look clean. There is no indication of separation in any of these regions.

NCV UV Oil at M=2.4 and Alpha= 4.5°

Upper

Wing Trip=112060205
Nose Trip=112100105

Lower

Side of Body

Forebody

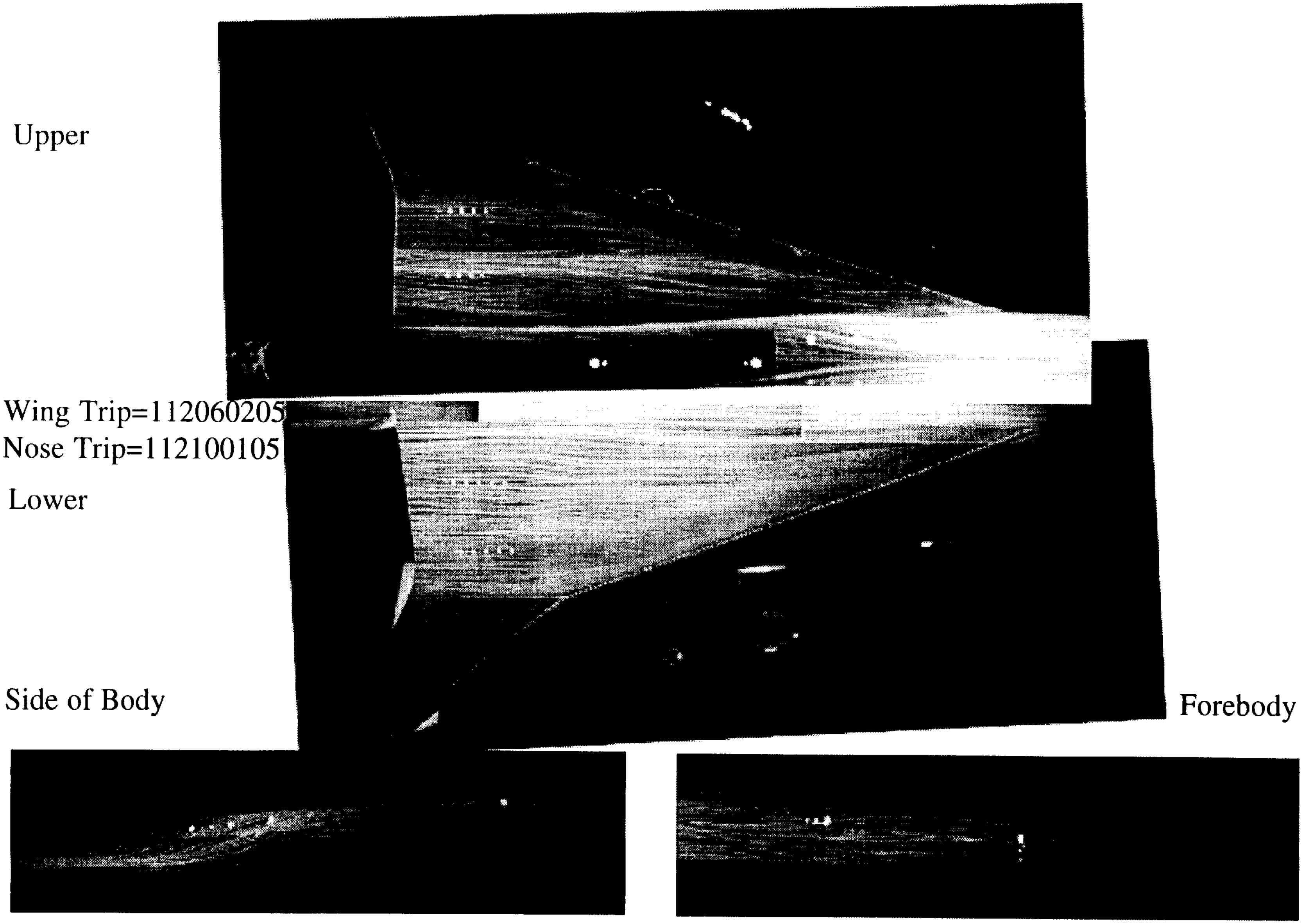

For every UV oil run, images for a maximum of three (3) angles of attack could be obtained. This figure shows the UV oil results for the cruise and two (2) higher angles of attack for the NCV model. The two (2) vortices that seem to pass over the upper wing surface become more evident at the higher angles of attack. They become stronger and cause flow separation on the wing surface.

NCV Wing UV Oil for Different Alphas

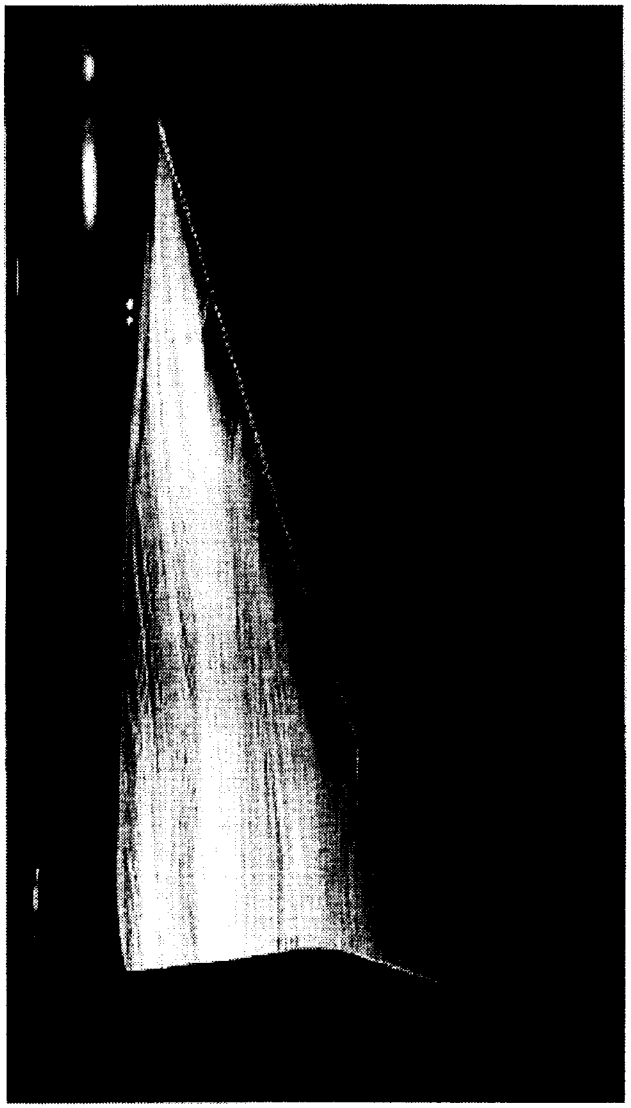

Alpha=4.5°

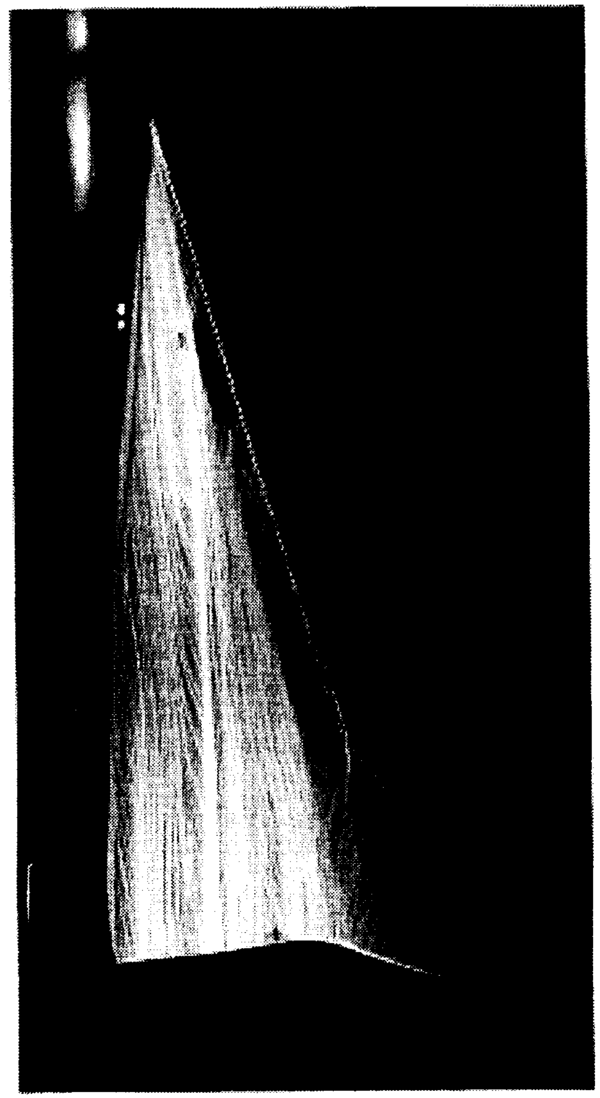

Alpha=6°

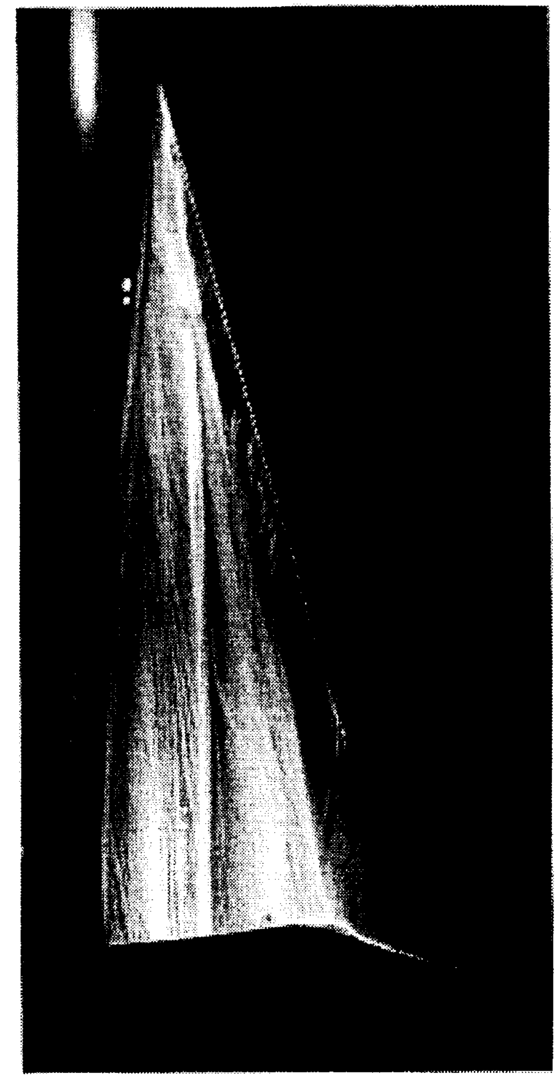

Alpha=8°

This figure show the UV oil results on the NCV model at the same three (3) angles of attack. The flow turns more and the attachment line moves as the angle of attack increases.

NCV Side of Body UV Oil for Different Alphas

Alpha=4.5°

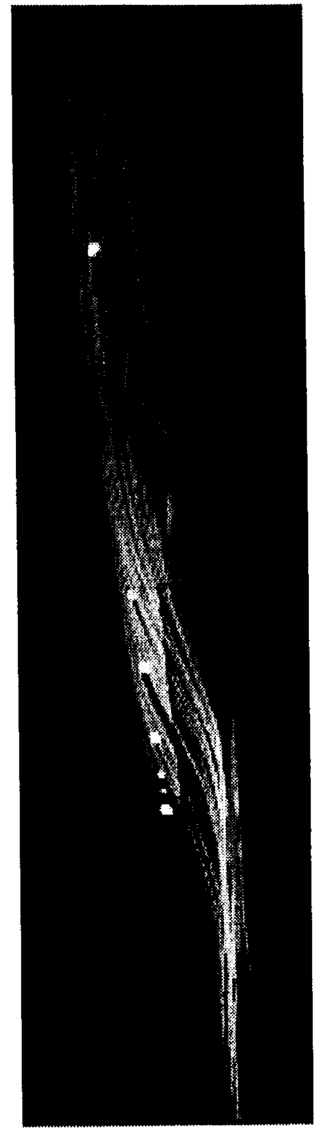

Alpha=6°

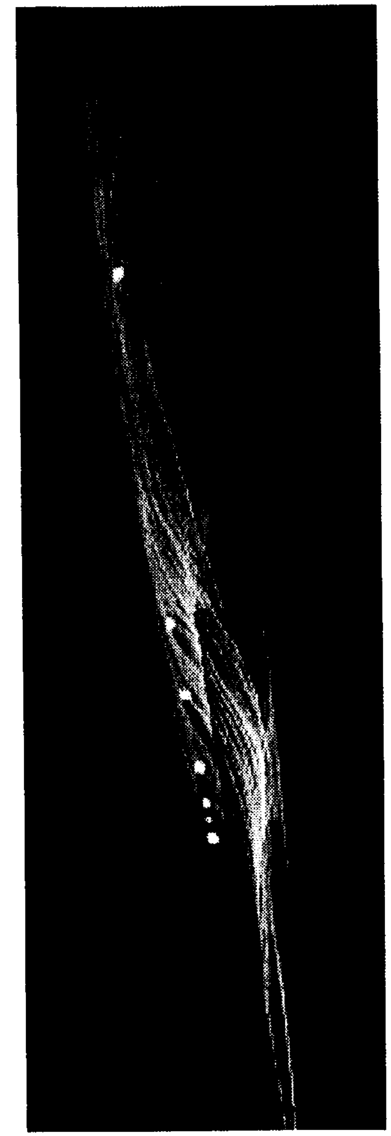

Alpha=8°

Post test, a comparison was made between the UV oil images and the CFD calculations that were done at NASA Ames Research Center by Scott Lawrence using UPS. The top figure compares the fully turbulent solution from UPS with the UV oil image. The bottom figure compares it with a fully laminar solution. It was determined from this that the original thought that the upper wing surface had laminar flow on it was incorrect. The flow is turbulent except ahead of the trip mechanisms and slightly behind.

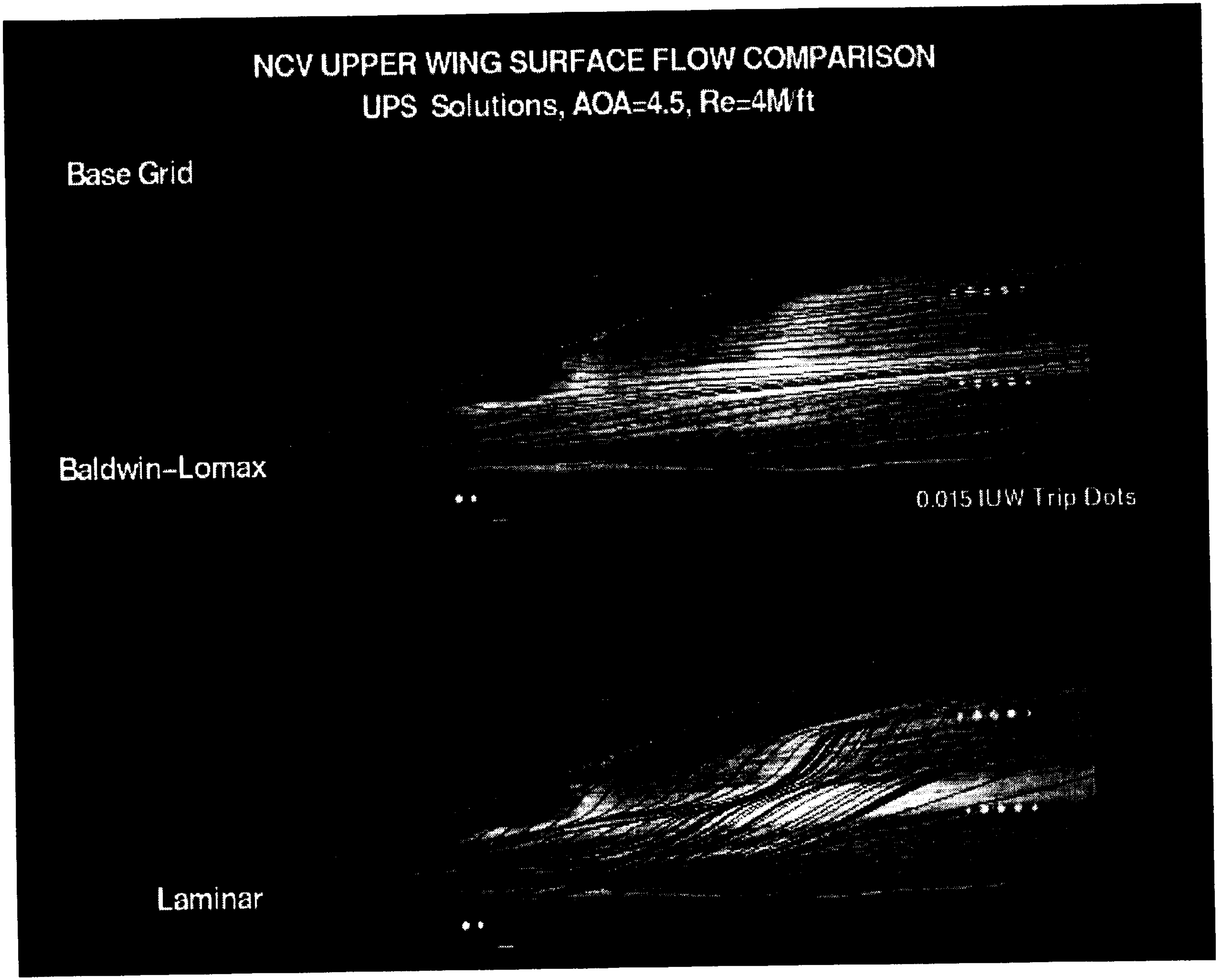
NCV UPPER WING SURFACE FLOW COMPARISON
UPS Solutions, AOA=4.5, Re=4M/ft
Base Grid
Baldwin–Lomax
0.015 IUW Trip Dots
Laminar

The UPS solution was also compared to the UV oil images for side of body. It was feared that the flow over the NCV forebody was laminar. It was hard to see during the sublimation runs. The top figure compares the fully laminar UPS solution with the UV oil image. The bottom two (2) figures compare fully turbulent UPS solutions with the UV oil image. The turbulence models being compared are Spalart-Allmaras and Baldwin-Lomax. The flow over the forebody is more like the fully turbulent UPS solutions.

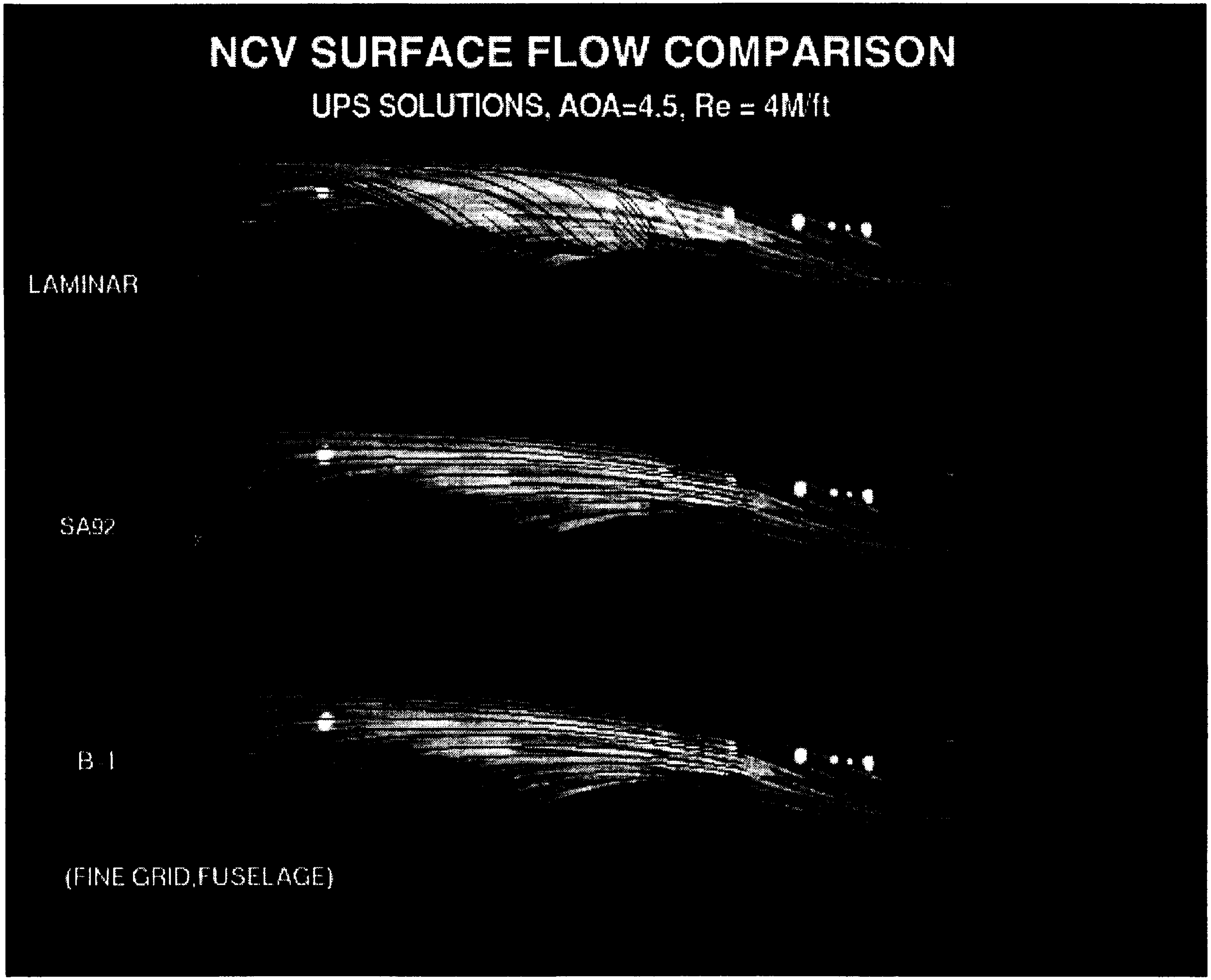
NCV SURFACE FLOW COMPARISON
UPS SOLUTIONS, AOA=4.5, Re = 4M/ft
LAMINAR
SA92
B-1
(FINE GRID,FUSELAGE)

This figure shows the set up used for the Laser Vapor Screen runs. The top left image shows the Spectra-Physics laser used. The right image shows a light box attached to the tunnel window. The model was translated axially so that the laser light sheet was at a different location on the model for tracking any shock and vortices. A Hasselblad camera was mounted in a housing to the tunnel ceiling and was remotely triggered in the control room to take the still image. A mini video camera was in a housing mounted to the hardware holding onto the model. The two (2) cameras can be seen in the bottom left image.

Laser Vapor Screen (LVS) Setup

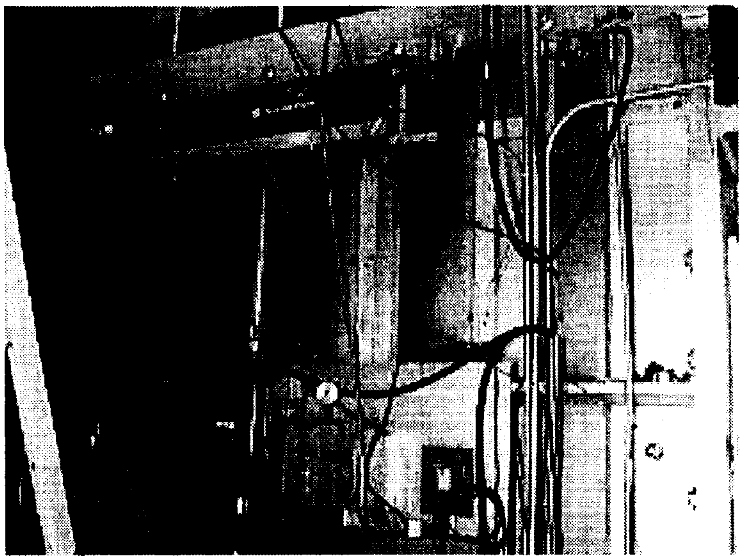

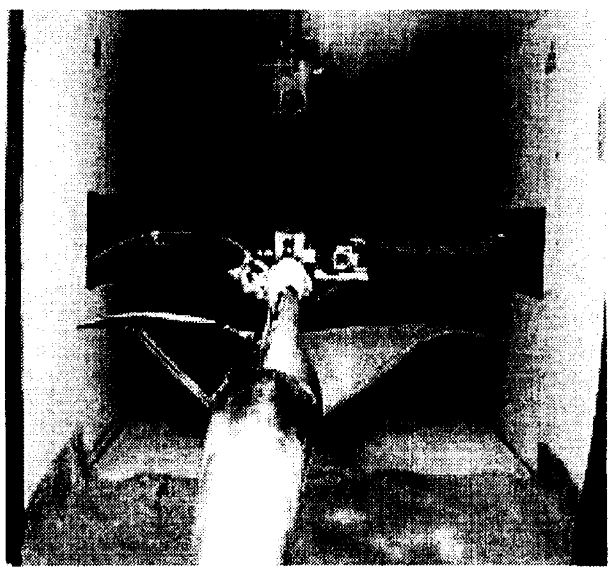

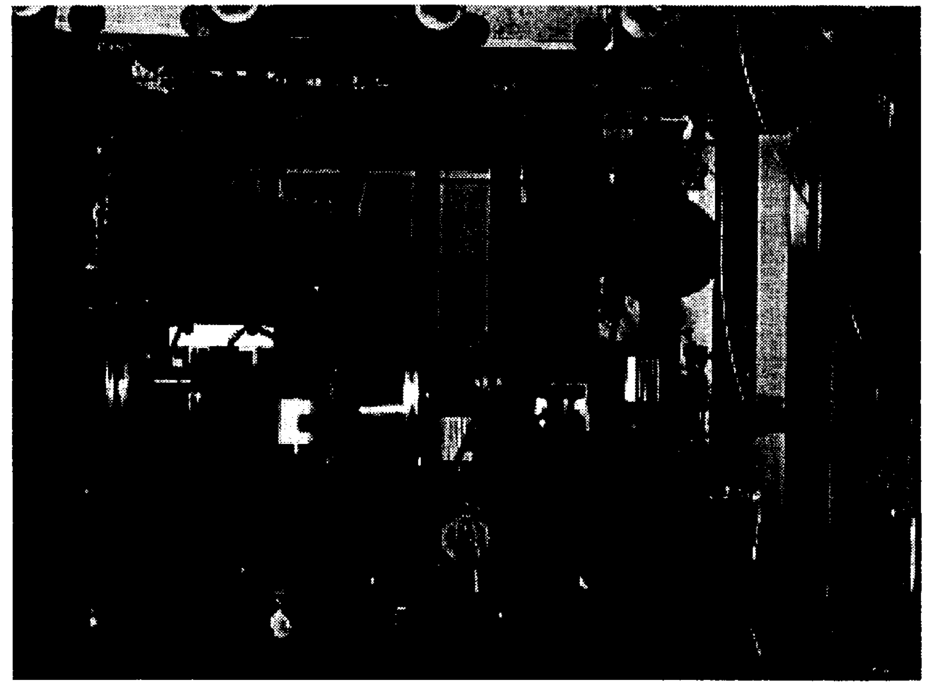

The model was painted black with reflective targets placed 4 inches apart from the aftbody forward. These targets were used to stop the axial movement of the model when the laser light sheet passed to take the still images. A video was recorded from the mini video camera signal of the entire LVS run. Any shocks and vortices were tracked for every angle of attack during the LVS run.

Model LVS Targets

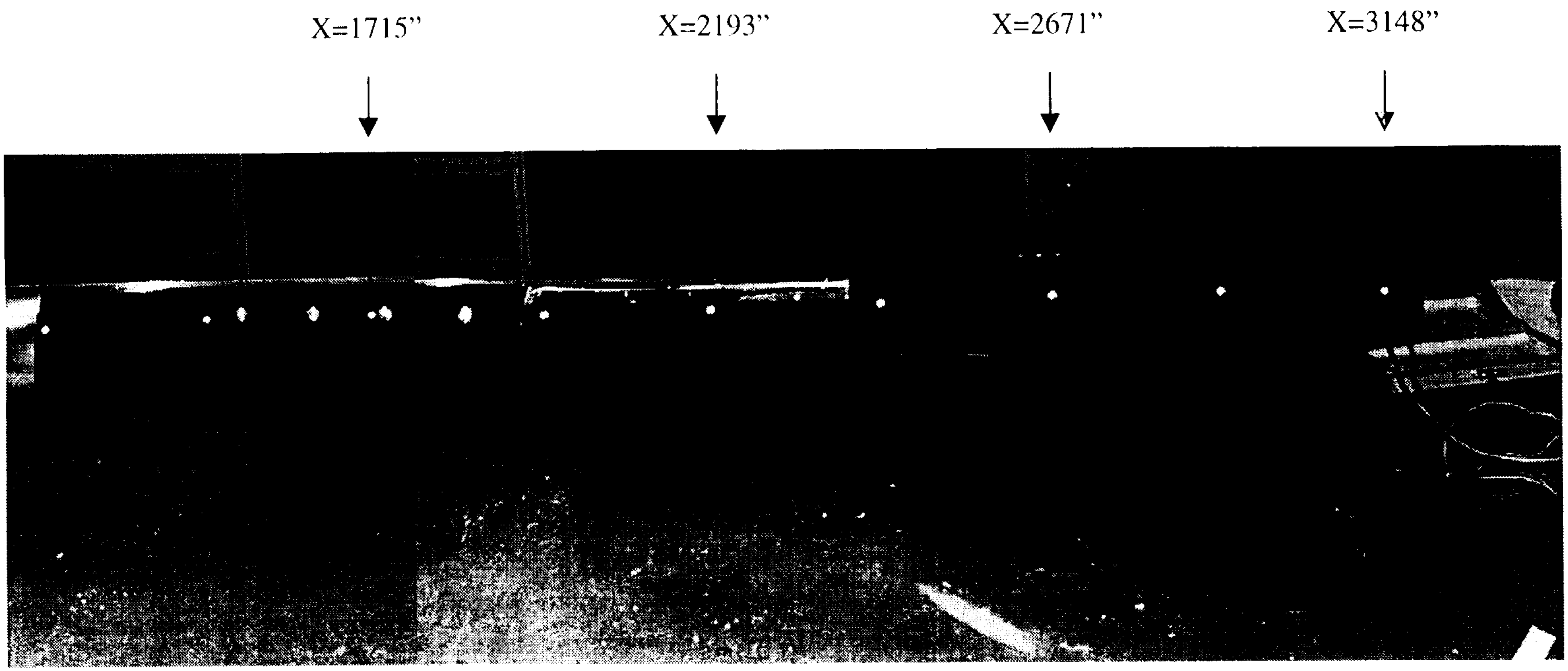

- Targets 4 inches Apart from Fuselage Base
- Left Hand Upper Side of Model Painted Flat Black

During the LVS run water was injected in the tunnel to create condensation to help better pick out shocks and vortices. This figure compares the LVS image between TCA and NCV at airplane station 2671 inches. The very dark area is the wing behind the light sheet. Above the light sheet close to the leading edge, a compression shock can be seen sitting on the wing. There is also a horseshoe vortex at side of body on the NCV model. It is hard to see it in this figure but the video clearly shows it. The TCA does not have a horseshoe vortex as strong as on the NCV as observed from the mini video camera.

LVS at X=2671" At Higher Alpha

TCA

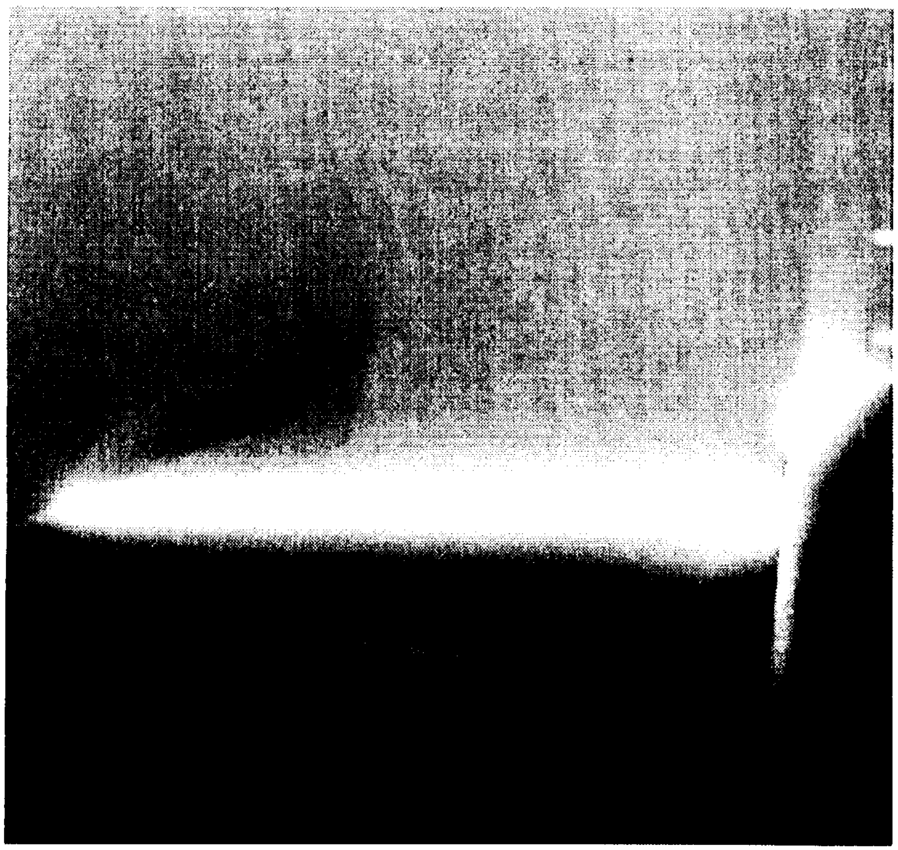

NCV

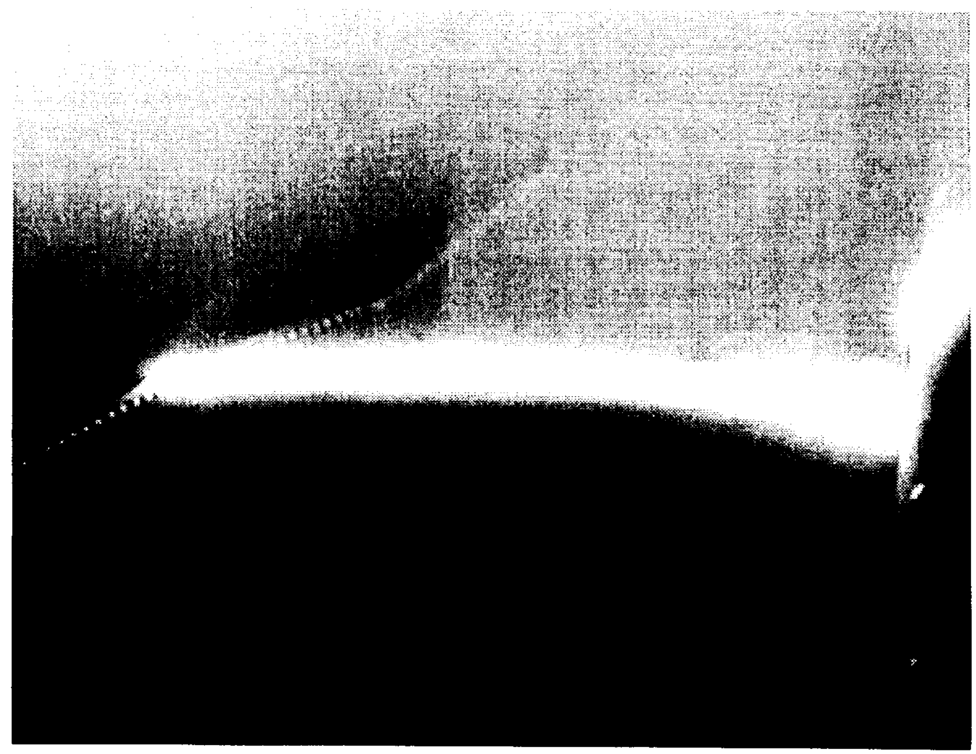

This figure compares the LVS run for TCA and NCV at the aftbody location, which is downstream of the wing trailing edge. This figure helps show that the NCV model has these two (2) vortices that pass over the upper wing surface. The NCV wake shows traces of two (2) vortices. The TCA wake is clean.

LVS at X=3148” and Cruise Alpha

TCA

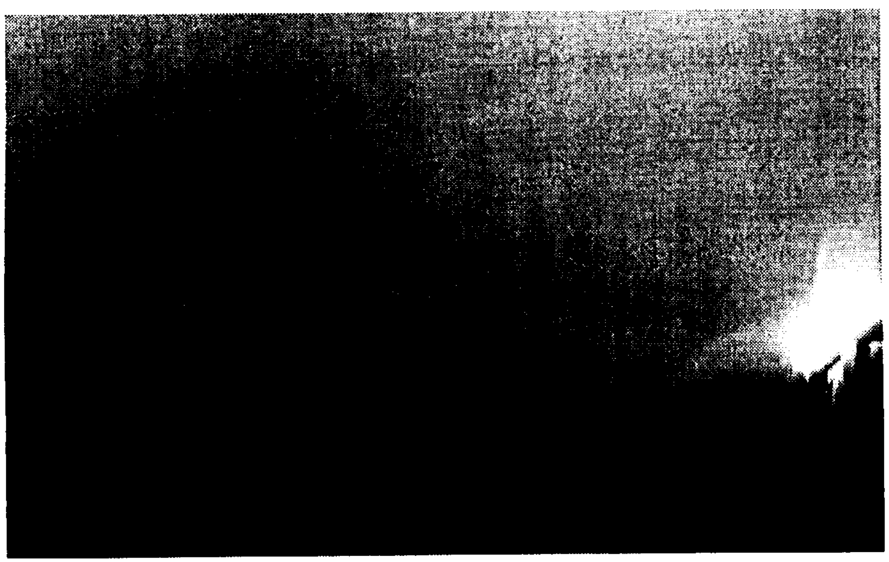

NCV

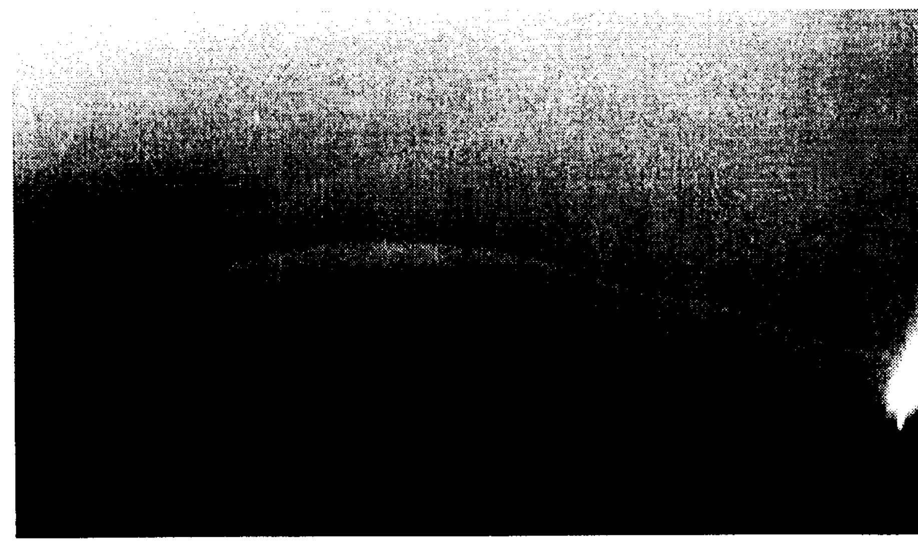

This figure compares TCA and NCV LVS results at an angle of attack of 1.5° above the cruise angle of attack for each configuration at airplane station 2671 inches. For TCA, the image is for 5°, and for NCV the image is for 6°. The dark spots above the light sheet for NCV are the horseshoe vortex and the vortex that passes over the inboard nacelle location. These cannot be seen for TCA.

LVS at X=2671” At Higher Alpha

TCA

NCV

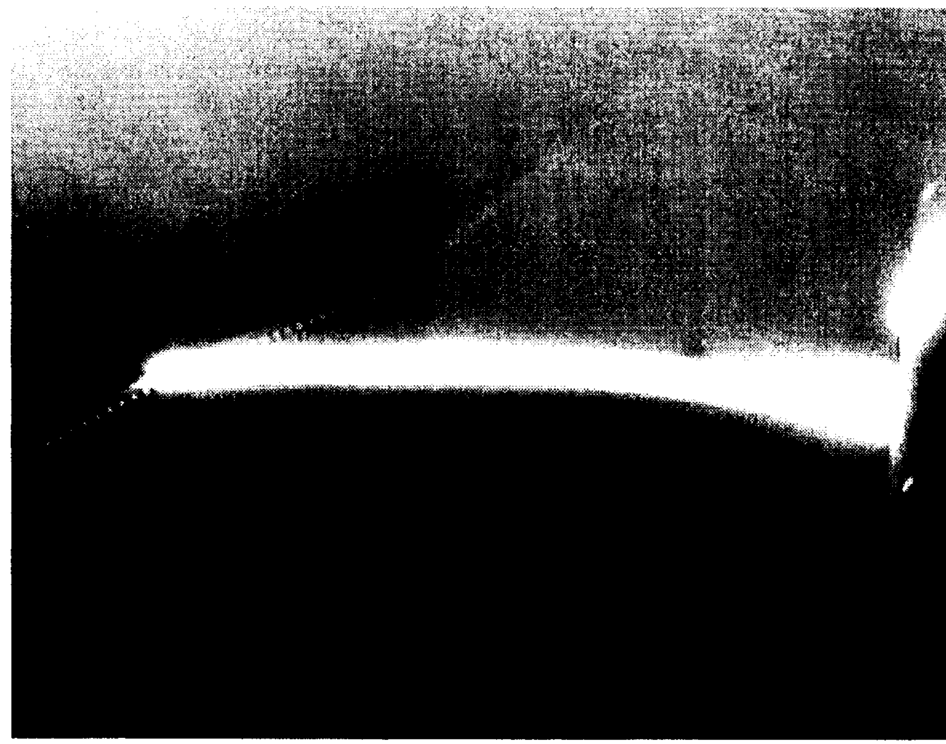

This figure shows the wake behind the wing trailing edge for TCA and NCV at 1.5° higher than the cruise angle of attack. The NCV wake clearly show three (3) vortices: a horseshoe vortex at side of body, a vortex that passes over the inboard nacelle location, and a vortex that passes over the outboard nacelle location. The TCA wake is just starting to show very weak vortices over the wing.

LVS at X=3148" at Higher Alpha

TCA

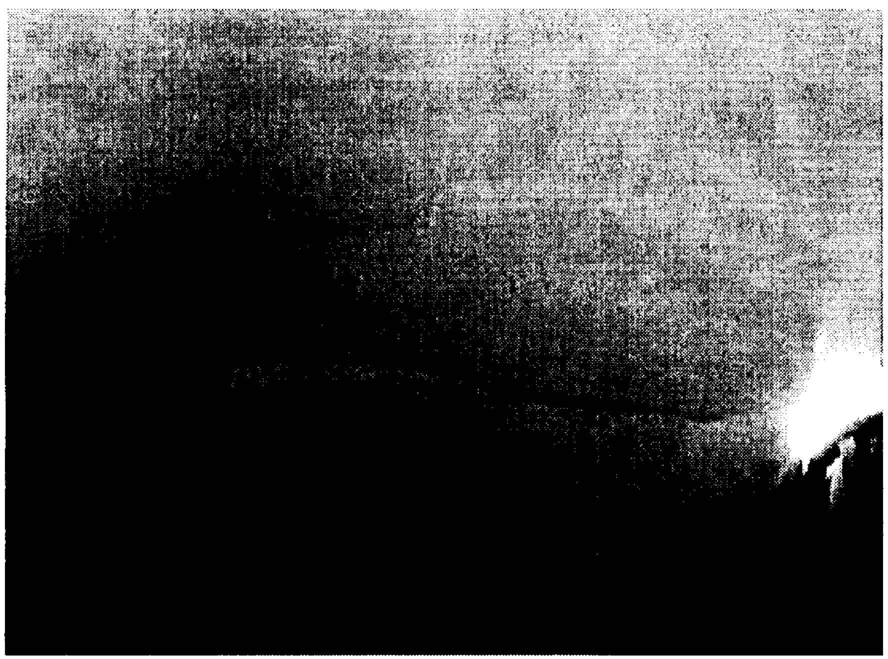

NCV

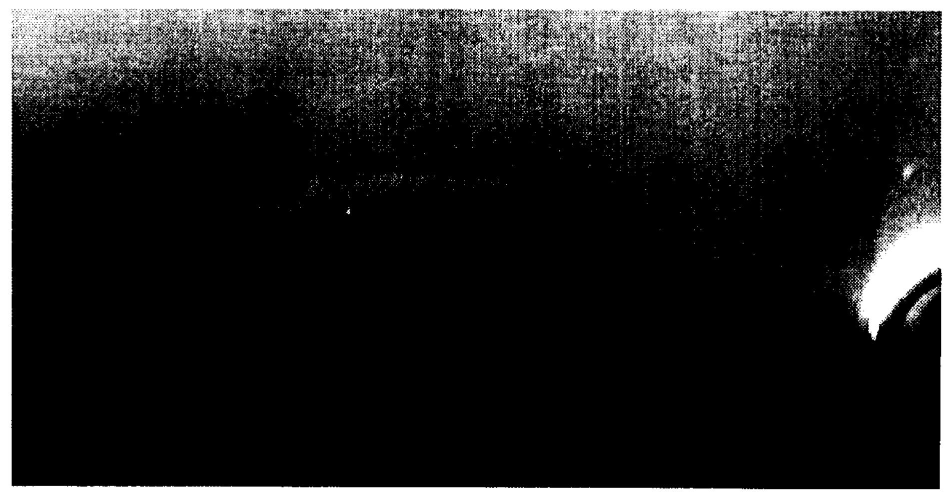

The forces and moments acquired on the NCV and TCA models are as good as can be with the angle of attack and balance instrumentation used during the test. Both the low and high RN tests did not measure the calculated drag improvement of NCV over TCA. Both tests show that NCV is approximately 2.8 cts better than TCA.

Both UV oil and LVS are good flow visualization tools for acquiring surface and off body flow characteristics. The two techniques go together well. LVS backs up what is seen in the UV oil images.

The only items that are needed to close-out the experimental portion of the NCV testing are to get surface pressure measurements, CFD solutions of as-measured (QA) geometry, and validate effect of balance bore angle measurements by LaRC on experimental results.

Conclusions

- Forces/Moments
  - Data is as good as can be with alpha and balance instrumentation.
  - Low and high RN tests did not measure calculated improvement of NCV over TCA.

- Flow Visualization
  - UV oil is very good indication of surface characteristics.
  - LVS is very informative for off body flow. It backed up what was seen in UV oil images.

- Needed for Close-Out
  - Pressure measurements
  - CFD of as-measured geometry.
  - LaRC QA of balance bore angle
    - TCA 2b = 1.9895° and NCV = 2.0066° and 0.007° nose right

Flowfield Studies for the TCA/NCV Configurations

Raul Mendoza, Chih Fang Shieh, and P. Sundaram

Configuration Aerodynamics
The Boeing Company
Phantom Works, Long Beach

High Speed Research Airframe Review
Anaheim, California
February 8-11, 1999

Outline

This paper will follow the standard outline shown here. First, an introduction will be given, and the objective of this work will be stated. Then, the approach will be described and some results presented. Finally, a summary and some conclusions will be offered.

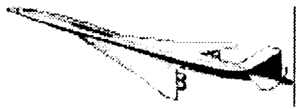

Outline

- Background
- Objective
- Approach
- Results
- Summary and conclusions

BOEING

Background

The Technology Concept Airplane (TCA) was developed using linear design and analysis methods. Ames Research Center (ARC), the Boeing Commercial Airplanes Group (BCAG), and Boeing Phantom Works (BPW) at Long Beach performed non-linear aerodynamic shape optimization to improve the supersonic cruise performance of the TCA. The three participating sites cross-checked the final designs using Euler and Navier-Stokes analyses of the wing/body (W/B) and wing/body/nacelle/diverter (W/B/N/D) configurations. The three optimized designs differed from each other, but all were shown to improve performance. Nevertheless, only the configuration that exhibited the best performance improvement over the TCA was selected for experimental validation and became known as the Non-linear Cruise point Validation (NCV) design.

However, wind-tunnel data did not match the predicted performance of the NCV W/B design. Navier-Stokes computations had shown an expected drag benefit for the NCV W/B configuration on the order of 4 to 4.5 counts over the TCA W/B at cruise conditions; but the improvement measured in the wind tunnel was on the order of only 2 to 2.5 counts. Even though the experimental drag reduction for the W/B/N/D configuration was also smaller than expected, the measured drag benefit associated with the addition of nacelles was considered to have matched the CFD predictions within the scatter of the data. Therefore, this paper will concentrate on the W/B configurations.

Background

- TCA designed with linear methods
- Three TCA Cycle 2 configurations developed though non-linear cruise-point optimization
- One optimized design selected for experimental validation: NCV
- Wind-tunnel data for W/B configurations did not show predicted performance gain of NCV over TCA
  - Predicted ΔC_D: 4 - 4.5 cts.
  - Measured ΔC_D: 2 - 2.5 cts.

BOEING

Background: Drag Polars for TCA and NCV W/B

This figure compares predicted and measured drag polars for the TCA and the NCV W/B configurations for cruise conditions at a wind-tunnel Reynolds number of $Re_c = 6.36 \times 10^6$. CFL3D Navier-Stokes computations with the Baldwin-Lomax turbulence model show an expected drag improvement for the NCV W/B configuration of about 3.7 counts over the TCA W/B. However, (uncorrected) experimental data obtained during Test 1703 at NASA Langley's Unitary Plan Wind Tunnel (UPWT) give a drag reduction of only 2.3 counts. The experimental curves shown in this plot and in subsequent figures were obtained by fitting a cubic spline though all the repeat runs.

Predicted and Measured Drag Polars for TCA and NCV W/B

High Speed Aerodynamics, Long Beach

CFL3D N-S (Baldwin-Lomax) vs. UPWT 1703

$M_\infty = 2.4$, $Re_c = 6.36\times10^6$

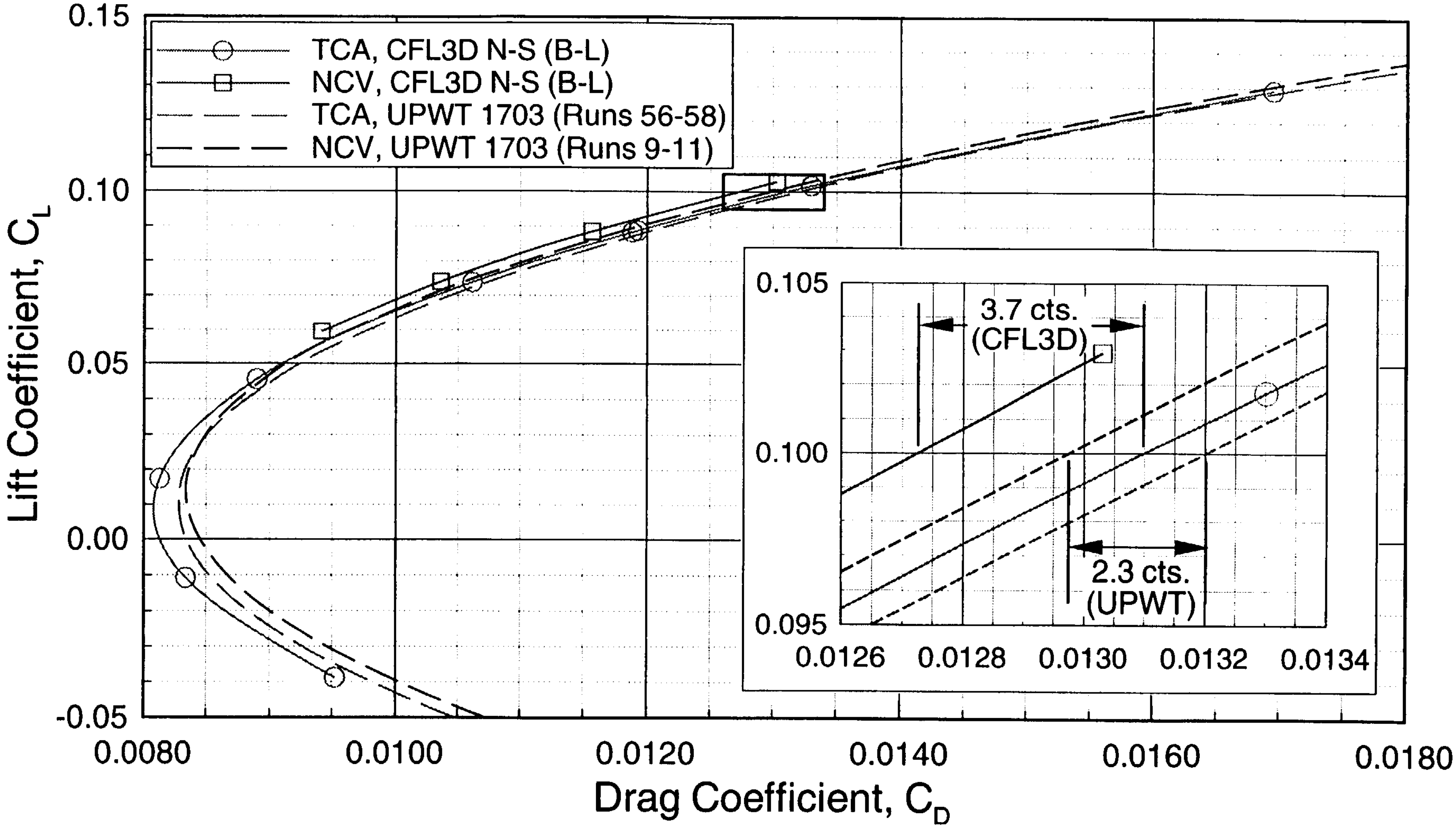

BOEING

Background: Drag Predictions at High Re

In order to eliminate trip drag uncertainties while minimizing the amount of laminar flow on the models, both the TCA and NCV configurations were tested in the Boeing Supersonic Wind Tunnel (BSWT) during a high Reynolds number entry (Test 647). For a Reynolds number of $Re_c = 22.27 \times 10^6$, CFL3D Navier-Stokes computations performed on a dense grid with more than 11 million points predicted a drag improvement of the NCV W/B over the TCA W/B of approximately 4.3 counts (as shown in the figure, the CFD data were extrapolated to a C_L of 0.1 using the local slope of the experimental curves). The drag improvement measured in the BSWT tunnel at these conditions, however, was only 2.8 counts. This is 1.5 counts less than the expected gain, based on uncorrected data.

Drag Predictions for TCA and NCV W/B Models at High Re

CFL3D N-S (Baldwin-Lomax) vs. BSWT 647 (Free Transition)

$M_\infty = 2.4$, $Re_c = 22.27\times10^6$, 185x481x129 C-O Grid (11.5×10^6 Points)

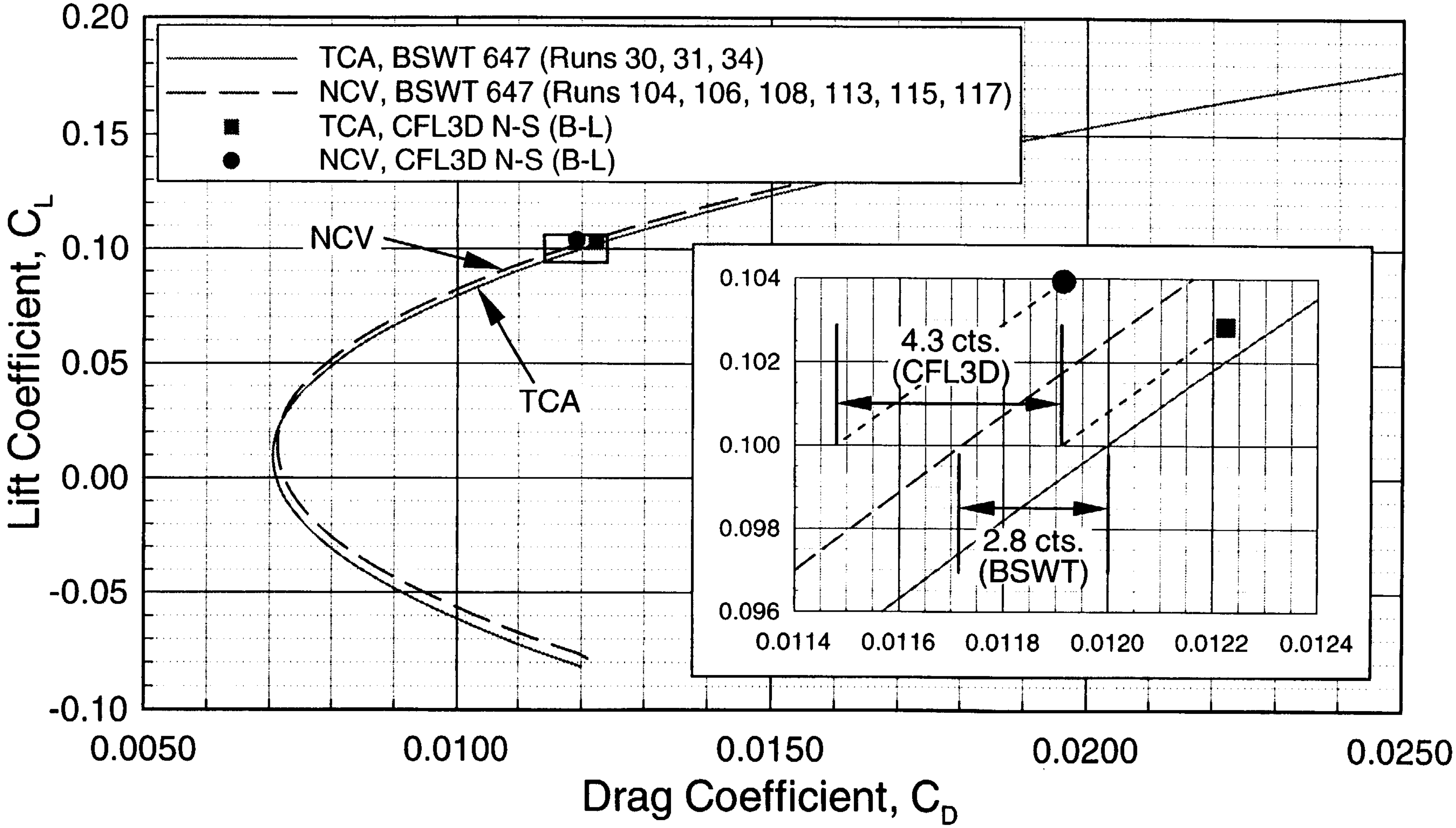

BOEING

Background: TCA-to-NCV Drag Reduction

As summarized in this bar chart, three different wind-tunnel tests failed to verify the predicted performance gain of the NCV over the TCA. For a unit Reynolds number of $4x10^6$/ft (or $Re_c = 6.36x10^6$, based on the mean aerodynamic chord of the 1.675%-scale models), OVERFLOW Spalart-Allmaras calculations (performed at BCAG) predict a 4.5-count drag reduction at the supersonic cruise condition ($M_\infty = 2.4$ and $C_L = 0.1$). CFL3D Baldwin-Lomax predictions (from BPW), on the other hand, show a drag reduction of 3.7 counts. This is 0.8 drag counts lower than the OVERFLOW prediction, but still considerably higher than the performance gains realized in the NASA Langley 4-ft Unitary Plan Wind Tunnel (UPWT) during two separate entries: Test 1687, 2.6 counts; and Test 1703, 2.3 counts. Also shown in this figure are predictions and wind-tunnel test results for a unit Reynolds number of $14x10^6$/ft (or $Re_c = 22.27x10^6$). For this condition, the drag reduction predicted by both OVERFLOW and CFL3D is approximately 4.3 counts at the cruise lift; yet, data from a test conducted at the Boeing Supersonic Wind Tunnel (BSWT Test 647) show an improvement of 2.8 counts. It should be noted that the experimental data presented in this chart have not been corrected for trip drag nor laminar run. The UPWT data were obtained with the HSR baseline trip configuration (0.012"-high trip disks located 0.6" downstream from the leading edge), while the BSWT data correspond to free-transition runs. Also, the CFD solutions were computed assuming fully turbulent flow on the rigid, theoretical configurations. (However, the Spalart-Allmaras turbulence model in the OVERFLOW code has a built-in transition model that simulates laminar flow with reduced skin friction immediately downstream of the attachment line at low Reynolds numbers.)

NCV Drag Reduction relative to TCA for W/B Configurations

High Speed Aerodynamics, Long Beach

CFD vs. Experiment

$M_\infty = 2.4$, $C_L = 0.1$ (1.675%-scale models)

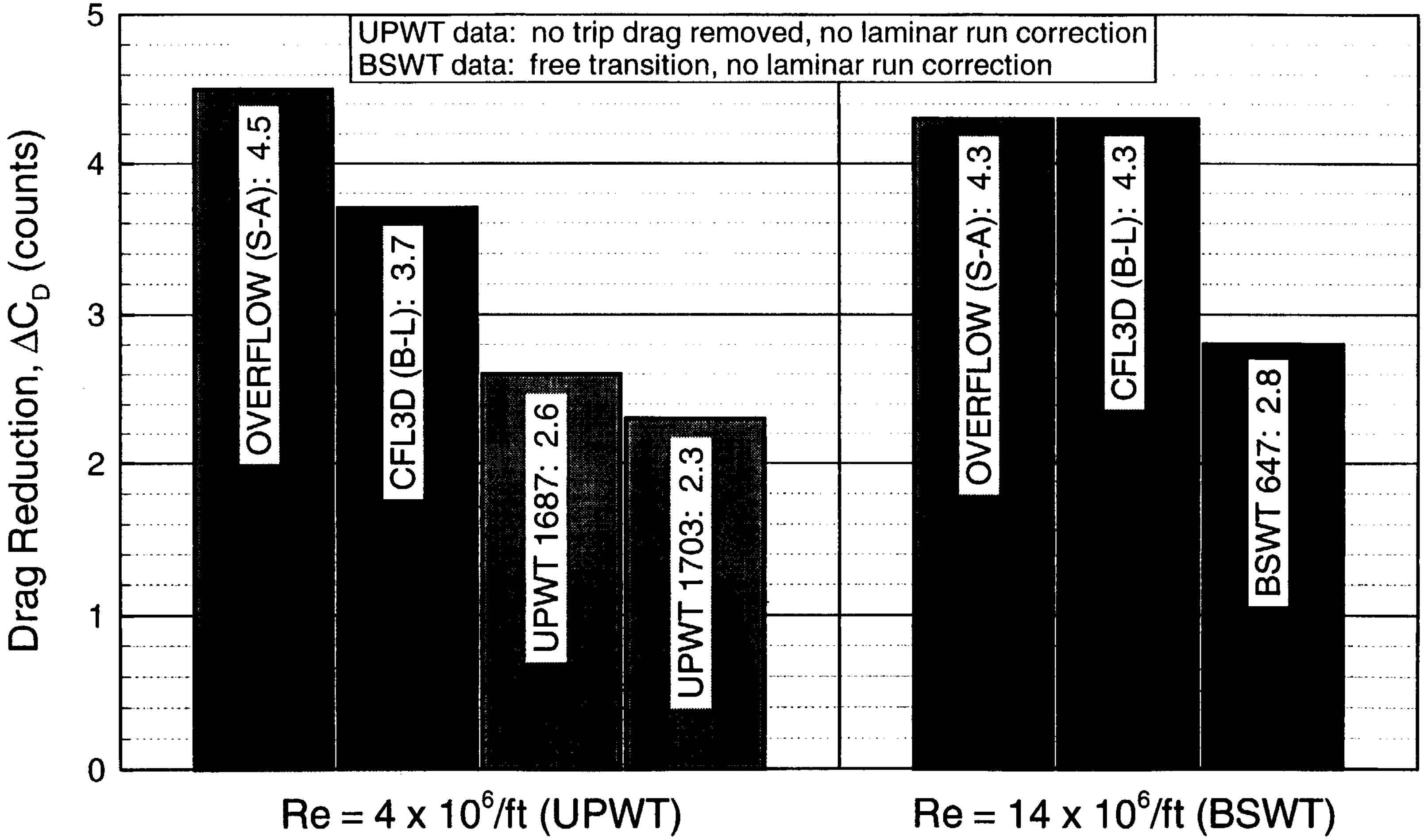

Objective

The objective of several Computational Fluid Dynamics (CFD) studies performed at BPW over the past few months was to identify and analyze potential factors that may have contributed to the discrepancies between the predicted and the measured performance improvement of the NCV W/B model.

Objective

High Speed Aerodynamics, Long Beach

- Analyze factors that may have contributed to discrepancies between the predicted and the measured aerodynamic performance of the NCV model

BOEING

Approach

Various hypotheses regarding the NCV performance shortfall have been suggested. In order to test some of these hypotheses, several CFD activities were performed at Boeing Phantom Works: flow analysis and flow visualization of the TCA and NCV W/B configurations, grid density effects on Navier-Stokes solutions, analysis of the as-built NCV geometry to quantify the effects of model fidelity, aeroelastic assessment of the TCA wind-tunnel model, boundary-layer stability analysis, and mixed laminar/turbulent flow computations to estimate laminar run corrections and trip drag.

Approach

- TCA/NCV flow analyses and flow visualization
- Grid density effects on CFL3D Navier-Stokes results
- Effects of model fabrication imprecision on NCV
- Effects of aeroelastic deformation on TCA
- Boundary layer stability analysis
- Mixed laminar/turbulent flow analyses
  - Laminar run corrections
  - Trip drag

BOEING

TCA/NCV Flow Analyses and Flow Visualization (CFD vs. Wind-Tunnel)

Surface Particle Traces on the TCA and NCV Fuselage

During the 2nd HSR Configuration Aerodynamics Testing Workshop, it was suggested that the wind-tunnel flow over the forward section of the NCV fuselage might not be fully turbulent as assumed in most Navier-Stokes computations. To try to answer this question, several CFL3D fully turbulent and fully laminar flow solutions were obtained. This figure compares surface particle traces on the TCA and NCV fuselage forbodies. With fully turbulent flow (Baldwin-Lomax), the patterns on the NCV are similar to those on the TCA. However, with fully laminar flow, the NCV shows an additional attachment line and a larger separation line than the TCA.

It was argued that there could be a problem with laminar flow separation affecting the NCV forebody in the wind tunnel. However, comparisons of CFD surface particle traces with flow visualization results (ultra violet oil and colored oil) from the NCV flow diagnostics test (UPWT 1703) indicated that the flow on the NCV forebody appeared to be, in fact, fully turbulent and did not trigger any massive laminar flow separation that could cause an increase in the NCV drag.

Surface Particle Traces on the TCA and NCV Fuselage

High Speed Aerodynamics, Long Beach

CFL3D N–S, $M_{\infty} = 2.4$, $Re_c = 6.36 \times 10^6$, $C_L = 0.089$

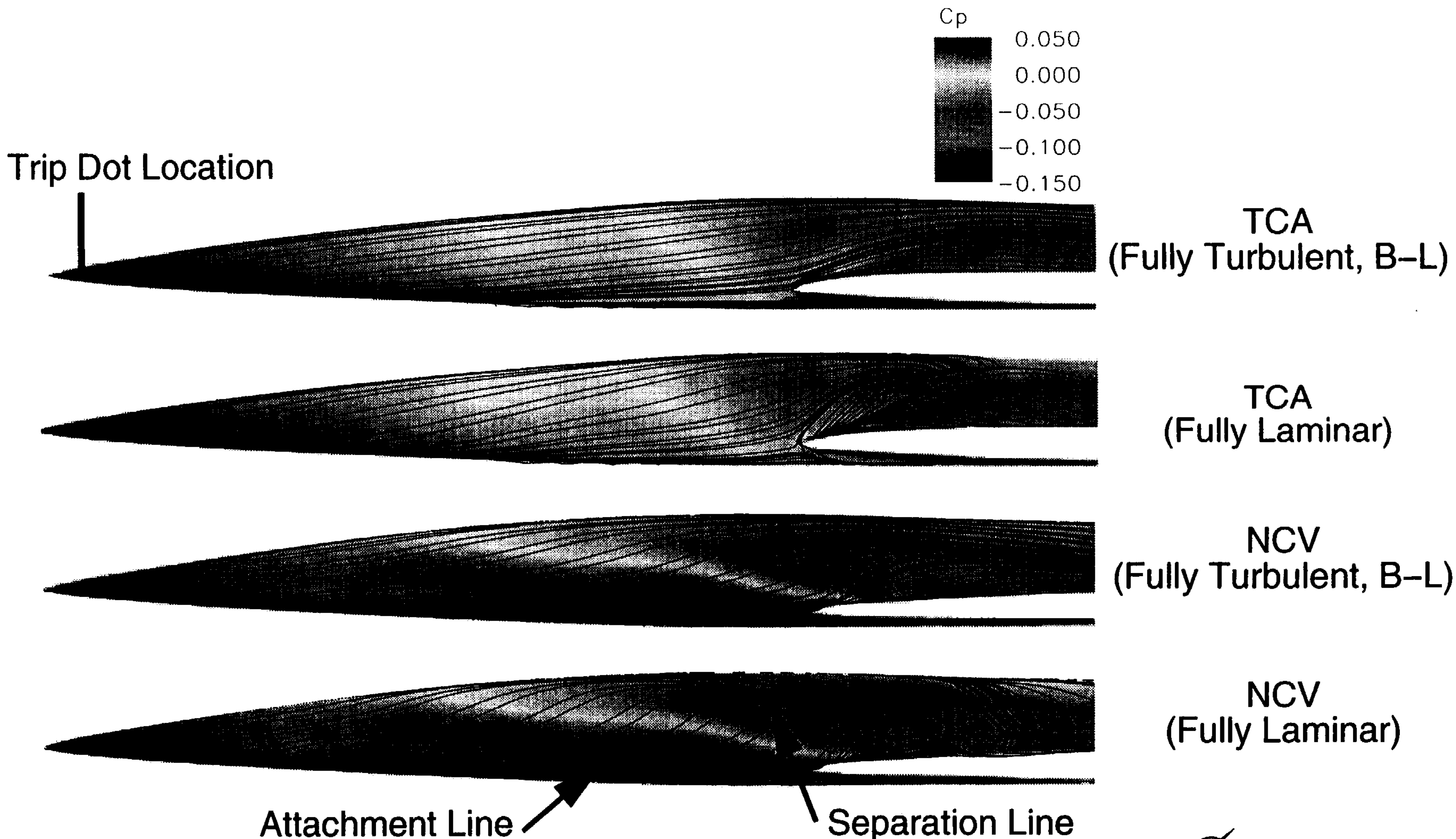

BOEING

CFS

NCV Crossflow Velocity Vectors

The Laser Vapor Screen (LVS) visualization technique that was employed during the NCV flow diagnostics test to visualize off-body flow detected a series of vortices on the NCV model. Of particular interest was a large vortex that originated near the wing apex and traveled downstream along the wing/body junction. This vortex was stronger at high angles-of-attack, but it was present even at an angle of 4.5°, which is near the design condition for the NCV configuration. The turbulent CFL3D solution indicates that the vortex does exist at these conditions, as illustrated in this figure by the crossflow velocity vectors at fuselage station FS2100. Also shown in the figure are off-body particle traces that point to the wing apex as the origin of the vortex. The computational results indicated that this vortex is indeed enhanced after FS1500, as detected in the experiment. Neither the wind-tunnel LVS results nor the CFL3D solutions showed any evidence of this vortex pattern forming on the TCA model at the design conditions.

NCV Crossflow Velocity Vectors

High Speed Aerodynamics, Long Beach

CFL3D N–S (B–L), Fully Turbulent, M_∞=2.4, C_L=0.089, Re_c =6.36 x 10^6

Fuselage Stations

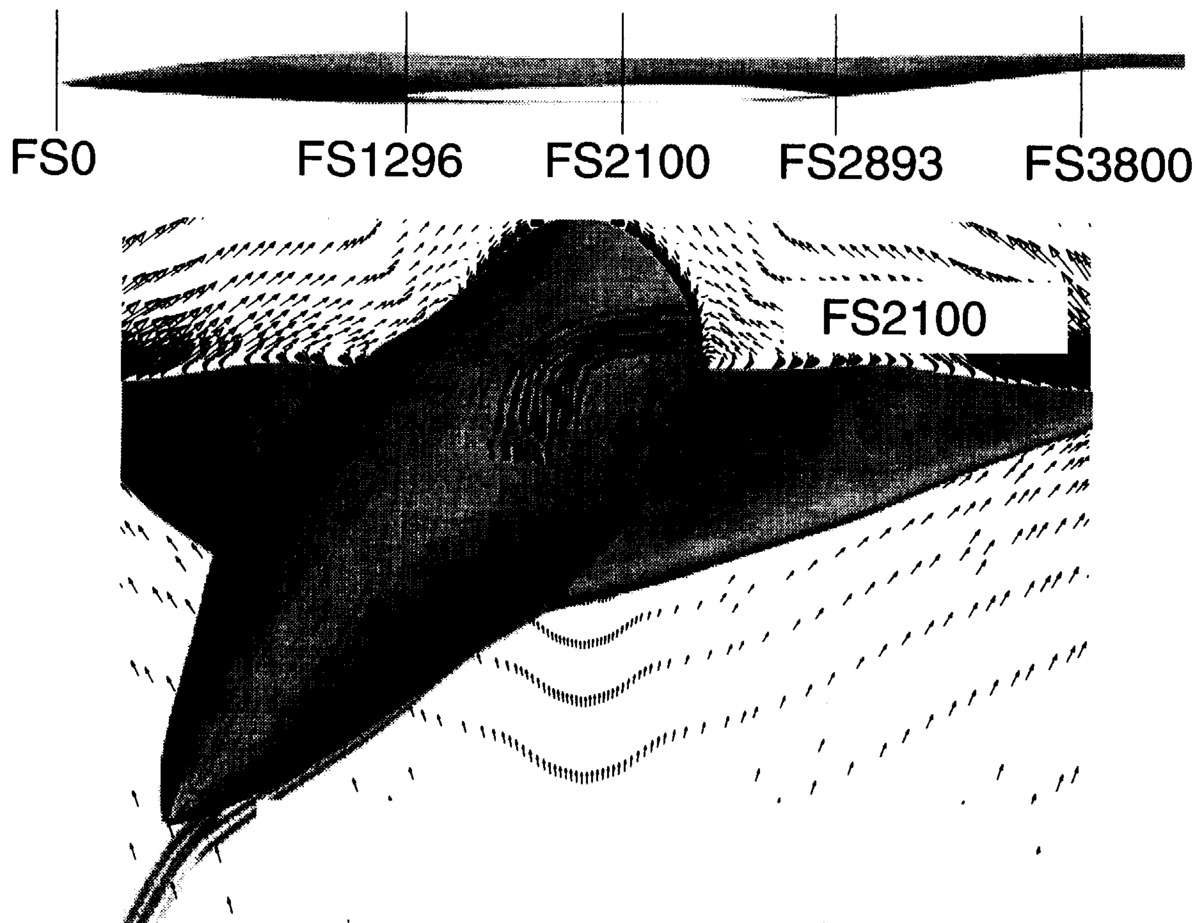

BOEING

TCA and NCV Pressure Distributions

Computed off-surface pressure contours for the TCA and NCV wing/body configurations are shown in this figure. At FS1500, the NCV results show a stronger flow compression than the TCA as the flow moves upward from the wing surface in the wing/body junction region. At FS2100, a spanwise-compression wave is observed near 33% semi-span. During UPWT Test 1703, a standing shock was clearly observed on the NCV inboard upper wing surface instead of the compression predicted by CFL3D at the cruise angle-of-attack. It is plausible that the presence of this shock could increase the drag of the NCV model in the wind tunnel, adversely impacting the NCV performance improvement. On the other hand, only a very weak shock was detected during the Laser Vapor Screen (LVS) runs on the TCA wing near cruise conditions.

In order to resolve the shock wave issue, and perhaps be able to capture the strength of the detected vortices more accurately, a grid refinement study was performed next for both the TCA and the NCV W/B configurations.

TCA and NCV Pressure Distributions

High Speed Aerodynamics, Long Beach

CFL3D N–S (B–L), Fully Turbulent, M_∞=2.4, C_L=0.089, Re_c =6.36 x 10^6

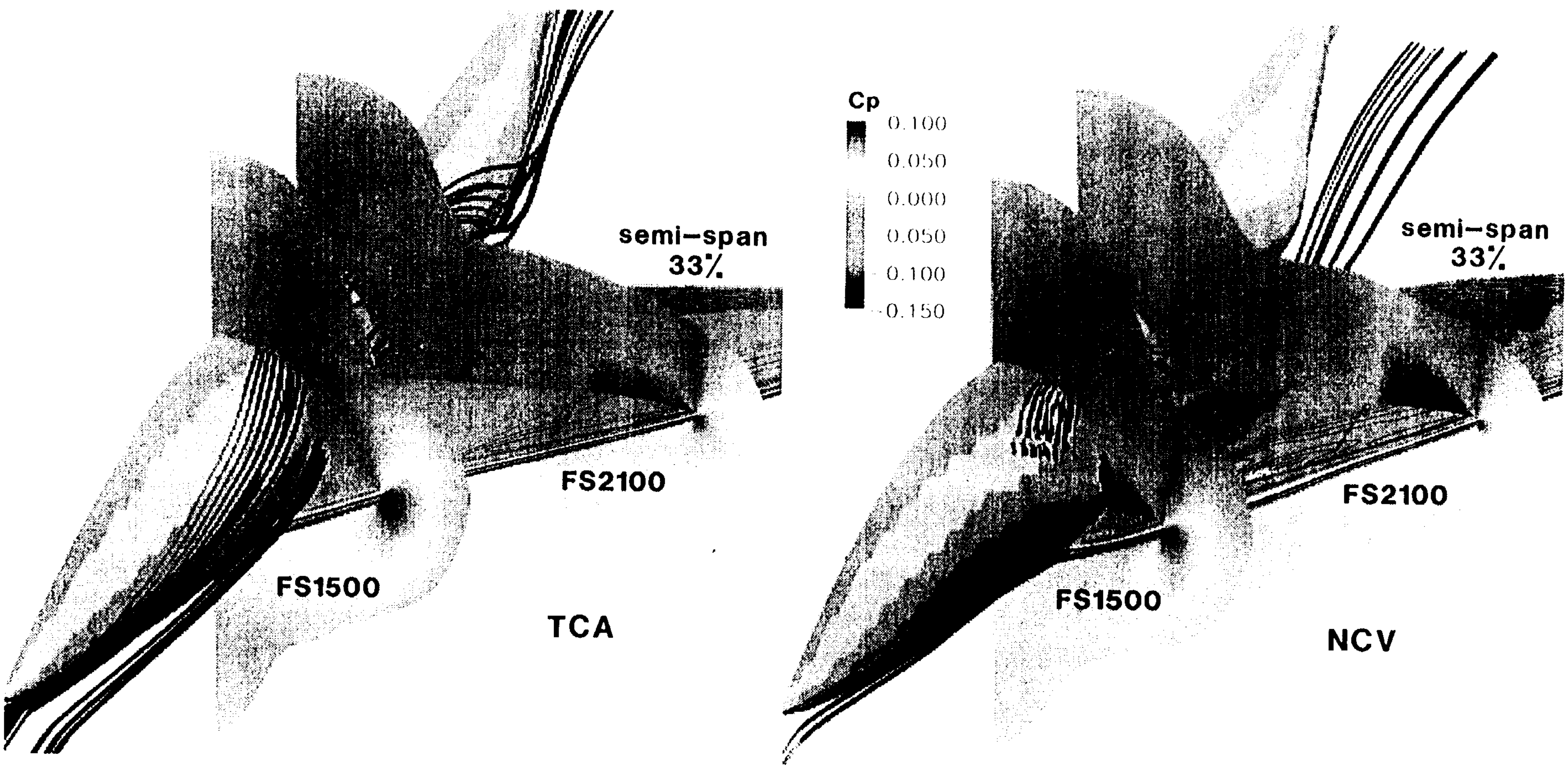

CFS **BOEING**

Grid Density Effects on CFL3D N-S Solutions

BOEING

Grid Density Effects on N-S Solutions

To investigate the effect of grid density on drag predictions, refined grids were generated, and new CFL3D Navier-Stokes (Baldwin-Lomax) solutions were computed for both the TCA and NCV W/B configurations. The new grids had eight times the number of points as the original grids: the number of grid points was doubled in each of the three computational coordinates compared to the original grids. Thus, the total number of grid points increased from 1.5 million to 11.5 million. Care was taken to ensure that the grid points inside the boundary layer were also doubled, while maintaining the original y^+ values next to the surface. The surface grids were refined using a linear interpolation of the original grids. Thus, the surface representation of the refined grids retained the same fidelity as the original grids.

In this figure, the original drag predictions are compared with the refined-grid Navier-Stokes results for the TCA and NCV W/B configurations. It can be seen that the refined-grid predictions fall almost on top of the corresponding original-grid polar, and therefore do not significantly change the predicted drag increment between the TCA and NCV configurations (3.3 counts at $C_L = 0.09$, $M_\infty = 2.4$ and $Re_c = 6.36 \times 10^6$).

Effect of Grid Density on Drag Predictions for TCA and NCV W/B

High Speed Aerodynamics, Long Beach

CFL3D Navier-Stokes (Baldwin-Lomax)

$M_\infty = 2.4$, $Re_c = 6.36 \times 10^6$

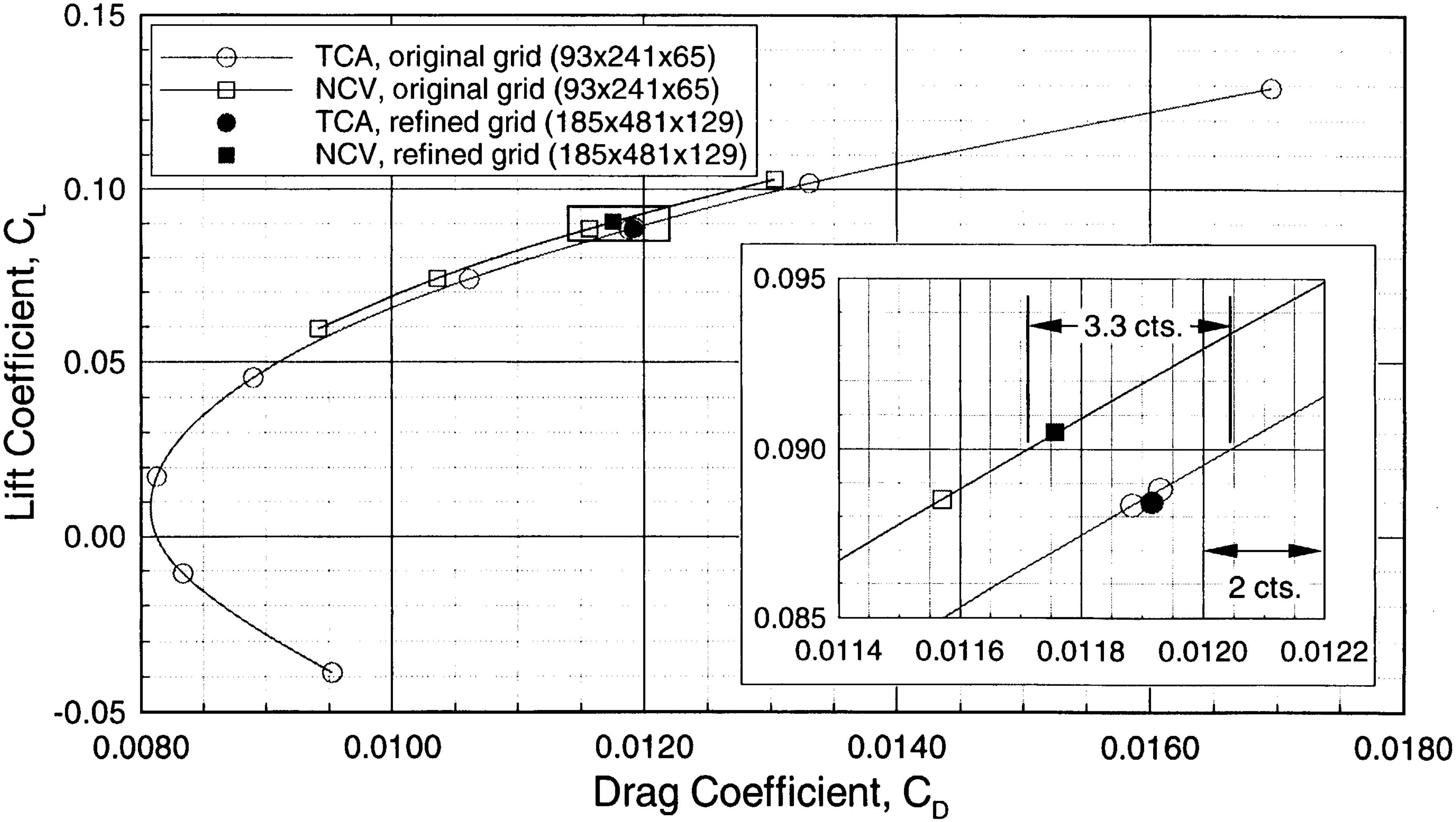

BOEING

Model Fabrication Imprecision Effects (NCV)

BOEING

Model Fabrication Imprecision Effects (NCV)

The impact of model fidelity on drag predictions was also examined. Detailed measurements of the NCV wind-tunnel model were used to create new computational grids. Noticeable differences between the theoretical NCV definition and the Quality Assurance (QA) measured geometry were observed, especially on the outboard wing panel. To assess the impact of these imprecisions, CFL3D Navier-Stokes computations for the as-built geometry were performed and compared to the original drag predictions for $M_\infty = 2.4$ and $Re_c = 6.36 \times 10^6$. The figure shows that the drag of the NCV QA geometry is 0.7 counts higher than the drag of the NCV as-designed model at cruise. The calculations were performed separately on each half of the model, and the two sets of results were then added together. So, the contribution from the right half of the QA model to the total drag increment is about 0.4 counts, while the contribution from the left half is approximately 0.3 counts. Most of the drag increase is due to an increase in pressure drag, as the viscous drag of the as-built model is nearly the same as that of the as-designed configuration.

A similar analysis of the TCA as-built model will be performed later when that the QA geometry becomes available.

Effect of Fabrication Imprecision on Performance of NCV W/B

High Speed Aerodynamics, Long Beach

CFL3D N-S (Baldwin-Lomax)

$M_\infty = 2.4$, $Re_c = 6.36\times10^6$, 93 x 241 x 65 C-O Grid

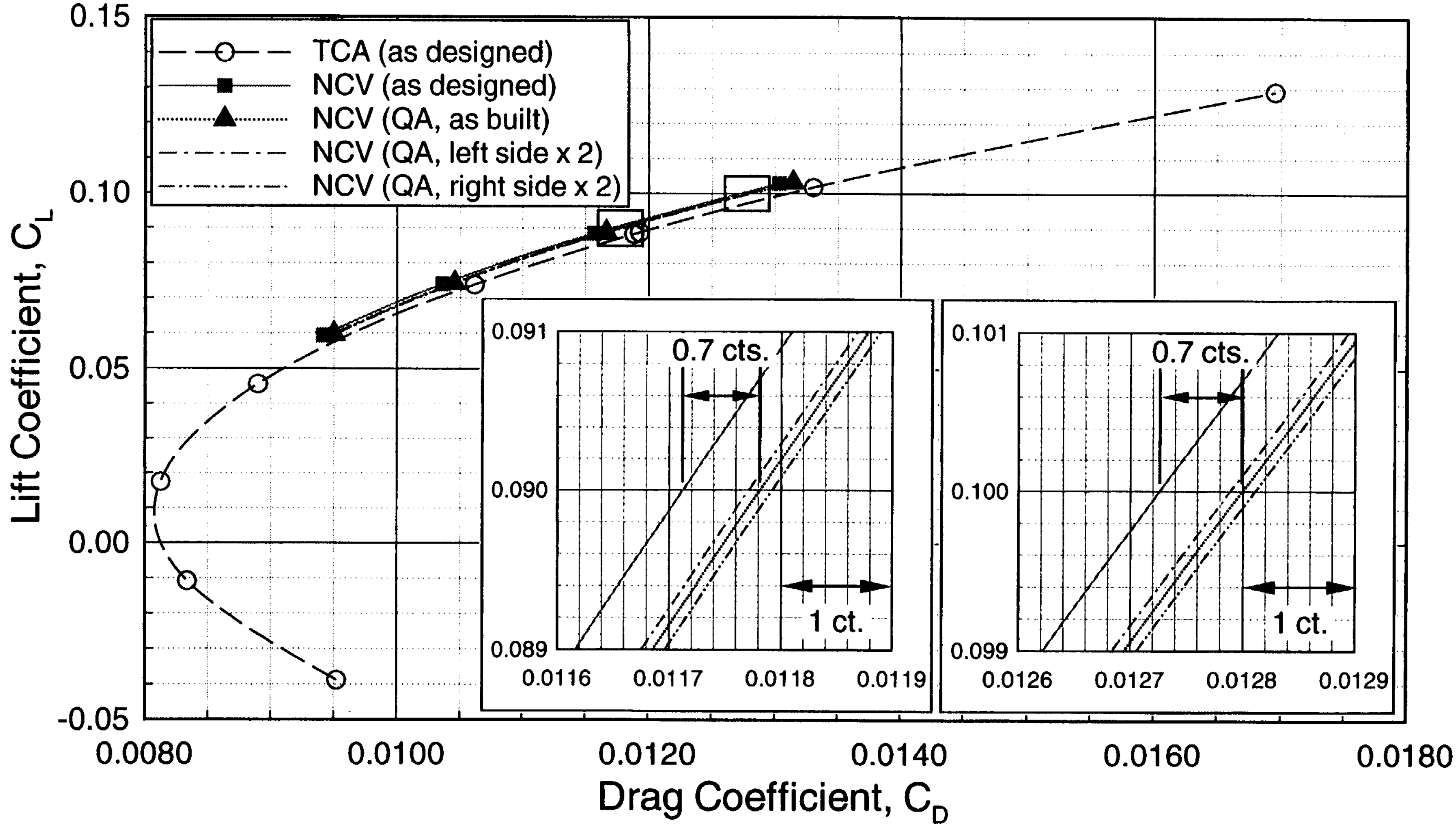

BOEING

Fabrication Imprecision Effects: C_P Distributions

This figure shows that the C_P distributions of the NCV theoretical and QA models are fairly similar. The most significant difference between the surface pressures of these two models is the presence of a suction peak on the lower surface of the NCV QA geometry near the leading edge of the right inboard wing (red dashed curve).

Pressure Distributions for the NCV W/B Model

High Speed Aerodynamics, Long Beach

CFL3D Navier-Stokes (Baldwin-Lomax)

$M_\infty = 2.4$, $C_L = 0.089$, $Re_c = 6.36 \times 10^6$

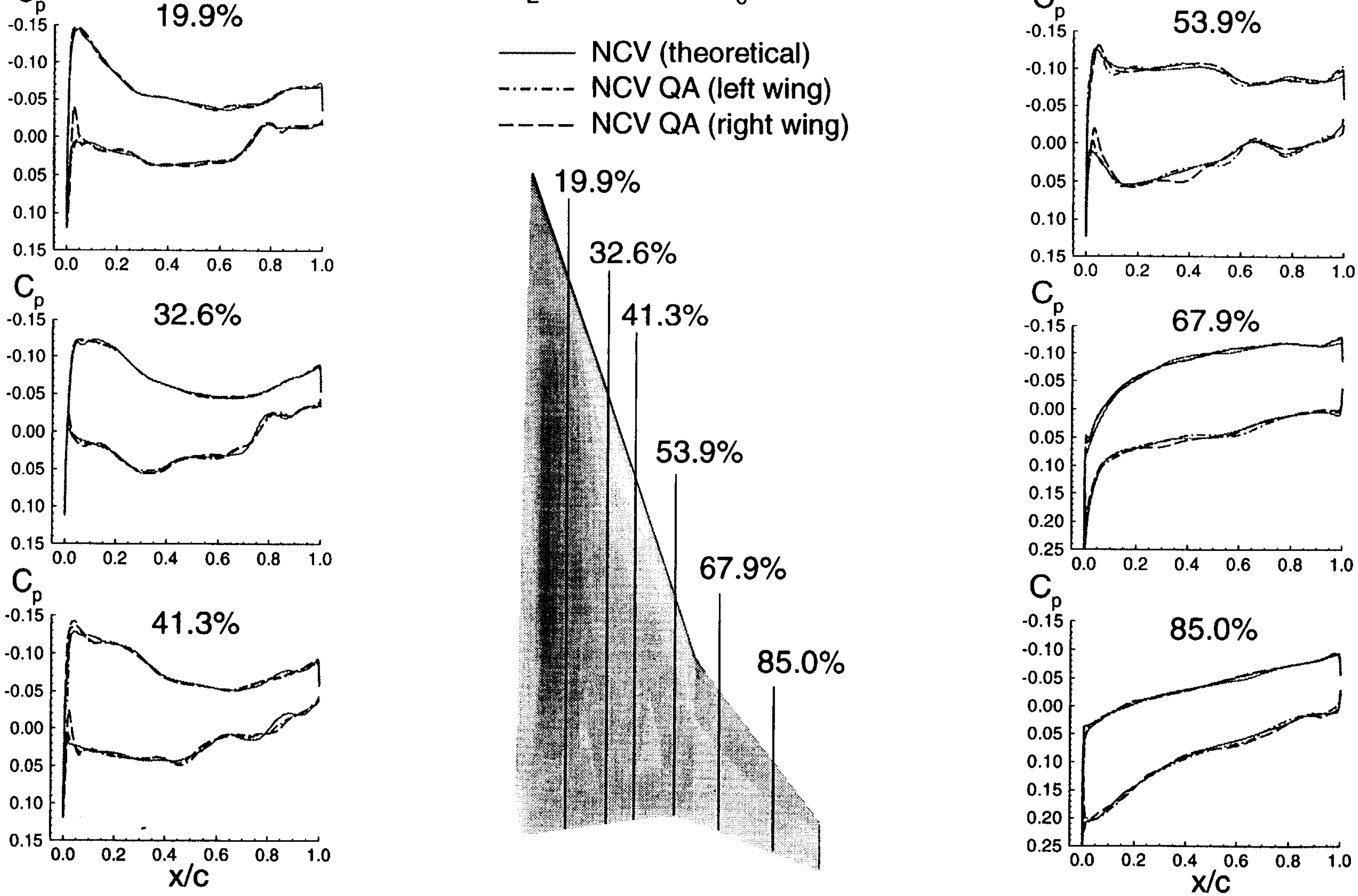

Fabrication Imprecision Effects: TCA-to-NCV Drag Reduction

This bar chart shows the impact of model fidelity on the CFD solutions for the NCV W/B. It can be seen that after NCV model imprecision effects are taken into account, the predicted NCV drag improvement over the TCA decreases from 3.3 to 2.6 counts at $M_\infty = 2.4$, $Re_c = 6.36 \times 10^6$, and $C_L = 0.09$ (this is approximately the lift coefficient generated by the W/B configurations at their respective cruise angle-of-attack). The NCV drag reduction measured during UPWT Test 1703 with the baseline trip configuration (k = 0.012” @ x = 0.6” from the leading edge), also shown in this figure, is 2.1 counts for these conditions. Therefore, once the CFL3D predictions account for NCV QA effects, the discrepancy between CFD and wind tunnel reduces from 1.2 to only 0.5 counts. As stated before, the TCA as-built model is yet to be analyzed to determine the exact impact of model imprecision on the CFD predictions.

NCV Drag Reduction relative to TCA for W/B Configurations

High Speed Aerodynamics, Long Beach

CFD (CFL3D N-S, B-L) vs. Experiment (UPWT 1703, k = 0.012" at x = 0.6")

$M_\infty = 2.4$, $Re_c = 6.36 \times 10^6$, $C_L = 0.09$

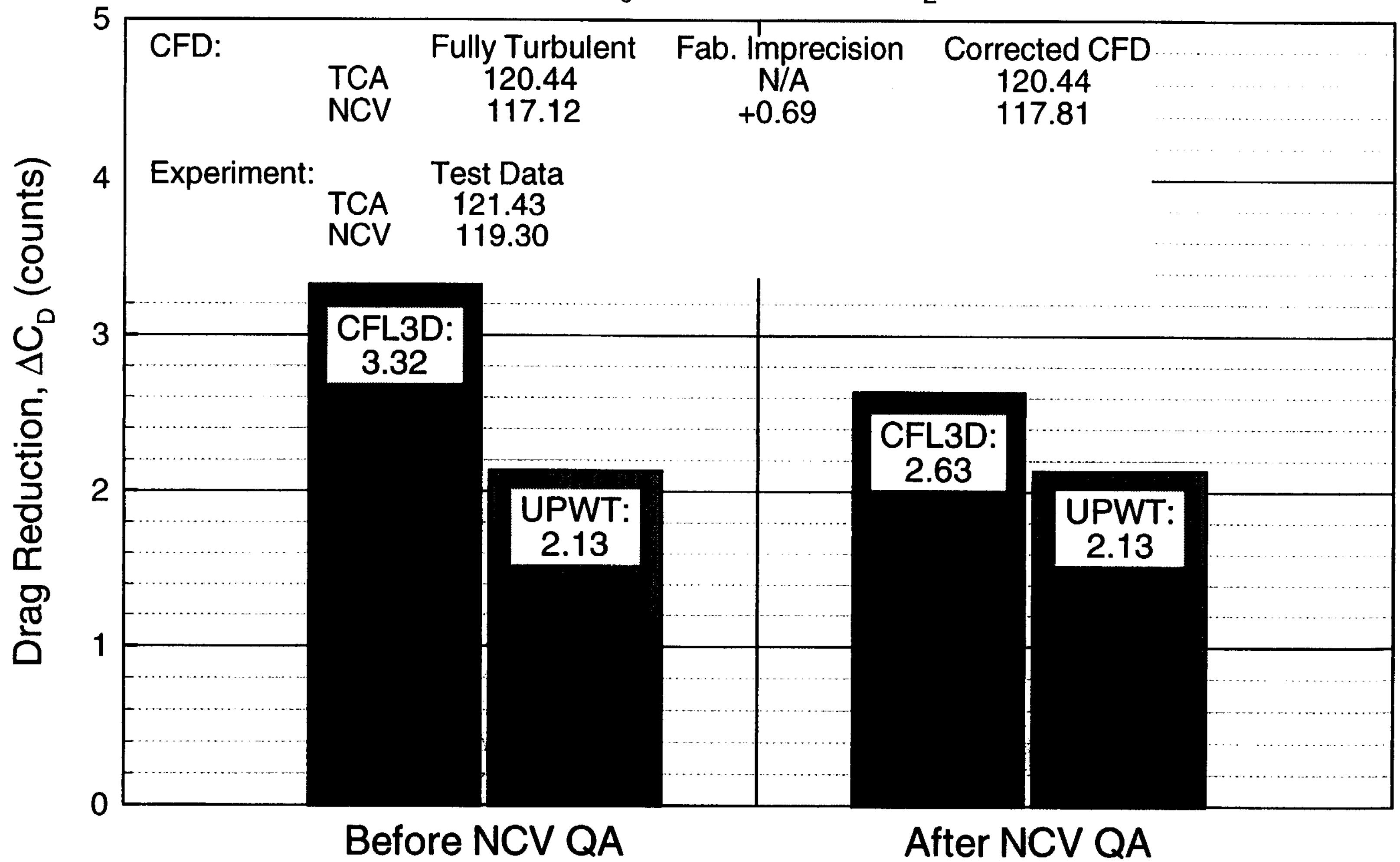

BOEING

Aeroelastic Deformation Effects (TCA)

BOEING

Aeroelastic Deformation Effects (TCA)

While a model undergoes deformation in the wind-tunnel due to aerodynamic loads, most CFD analyses assume a rigid configuration. So, in order to investigate the effects of static aeroelasticity on model performance, the deformations of the TCA Model 2a W/B/N/D configuration were measured at several angles-of-attack in the Unitary Plan Wind Tunnel (Test 1671) at $M_\infty = 2.4$ and $Re_c = 6.36 \times 10^6$. The deformations (vertical wing displacement and wing twist) measured for each of these angles-of-attack were then lofted onto the baseline TCA OML, and CFL3D Navier-Stokes analyses were performed on each of the deformed geometries. Changes in wing camber and deformation of the fuselage were assumed to be negligible.

The next four charts show the effects of aeroelastic deformation on the performance of the TCA W/B/N/D configuration. Wind-tunnel data are compared with Navier-Stokes results for the deformed configurations as well as computations for the rigid model.

The agreement between the predicted lift coefficient and test data improves when model deflections are included in the computations, as the outboard wing unloads reducing the overall lift. Due to the unloading of the outboard wing, there is a nose-up pitching moment. As a result, the agreement between the computed and the measured pitching moments improves significantly when the aeroelastic deformation of the wind-tunnel model is taken into account. However, the drag polar shows that the impact of aeroelasticity on the aerodynamic performance of the model is negligible, since there is no significant change in drag at a given lift coefficient. The unloading of the outboard wing is evident in the pressure cuts shown ($\eta = 67.9\%$ and $\eta = 85.0\%$, for instance).

Effect of Deformation on TCA Model 2a W/B/N/D

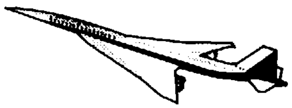

High Speed Aerodynamics, Long Beach

CFL3D N-S (B-L) Solutions and Wind-Tunnel Data
$M_\infty=2.4$, $Re_c=6.36\times10^6$

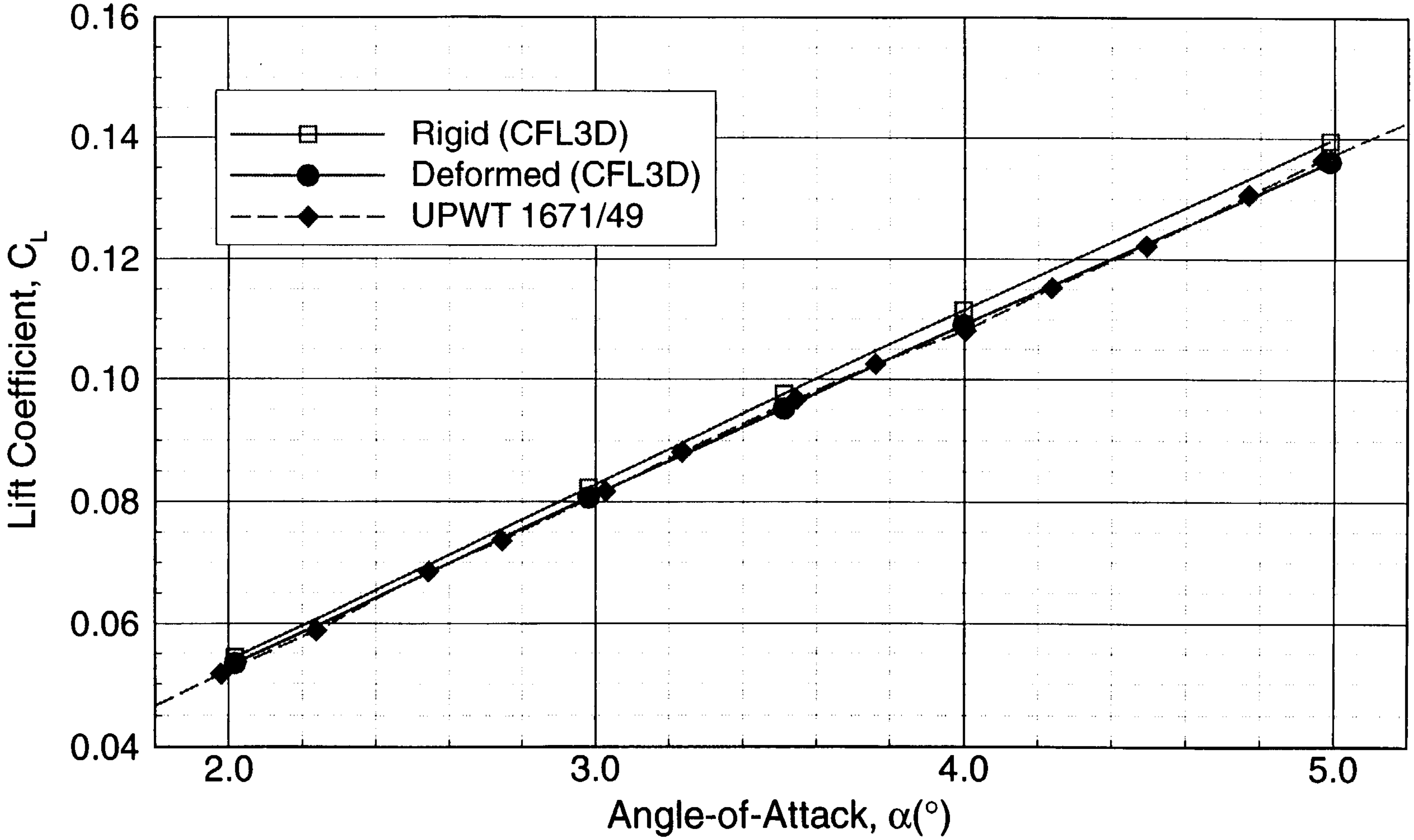

Effect of Deformation on TCA Model 2a W/B/N/D

High Speed Aerodynamics, Long Beach

CFL3D N-S (B-L) Solutions and Wind-Tunnel Data

$M_\infty = 2.4$, $Re_c = 6.36 \times 10^6$

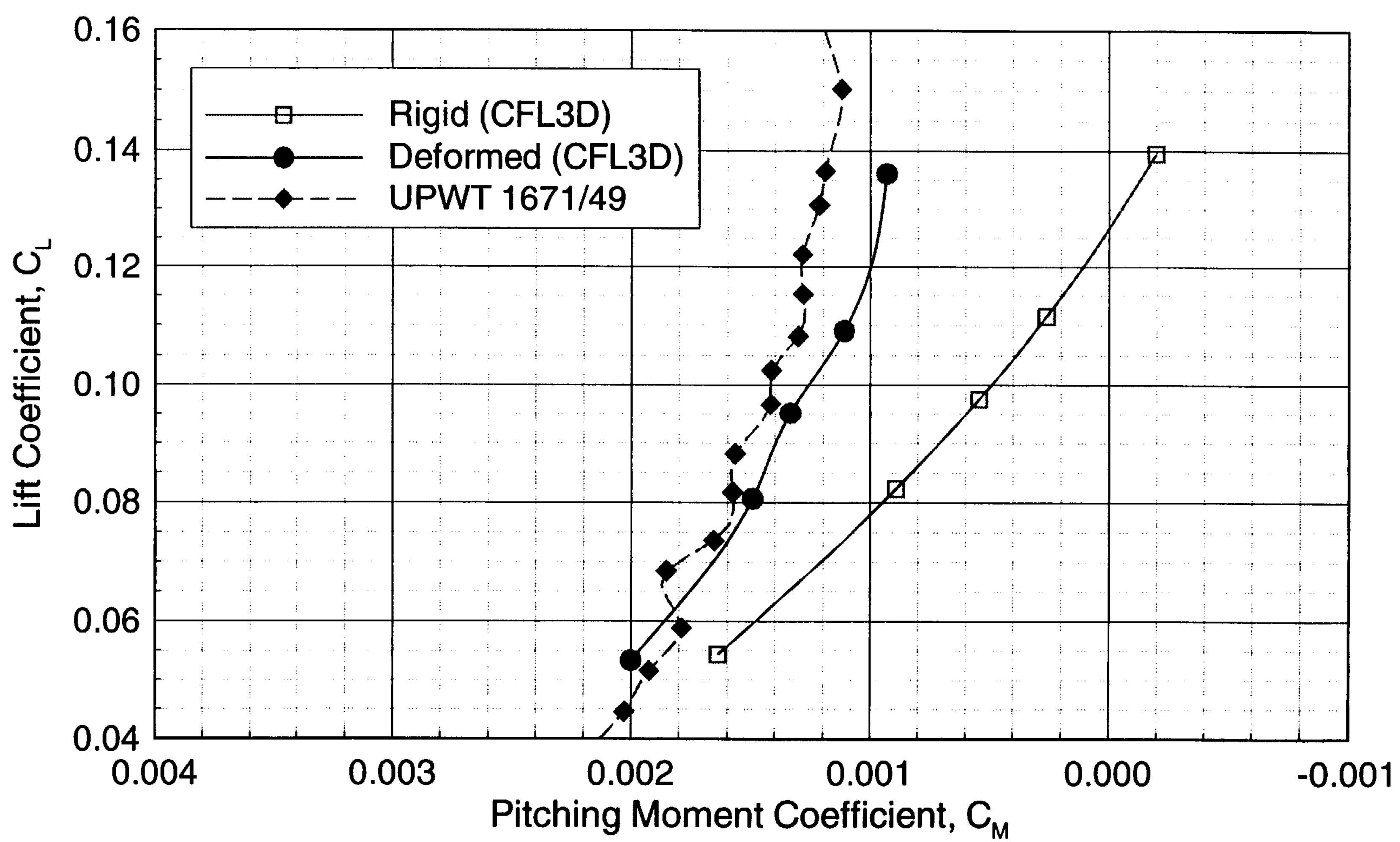

Effect of Deformation on TCA Model 2a W/B/N/D

High Speed Aerodynamics, Long Beach

CFL3D N-S (B-L) Solutions and Wind-Tunnel Data

$M_{\infty}=2.4$, $Re_{c}=6.36\mathrm{x}10^{6}$

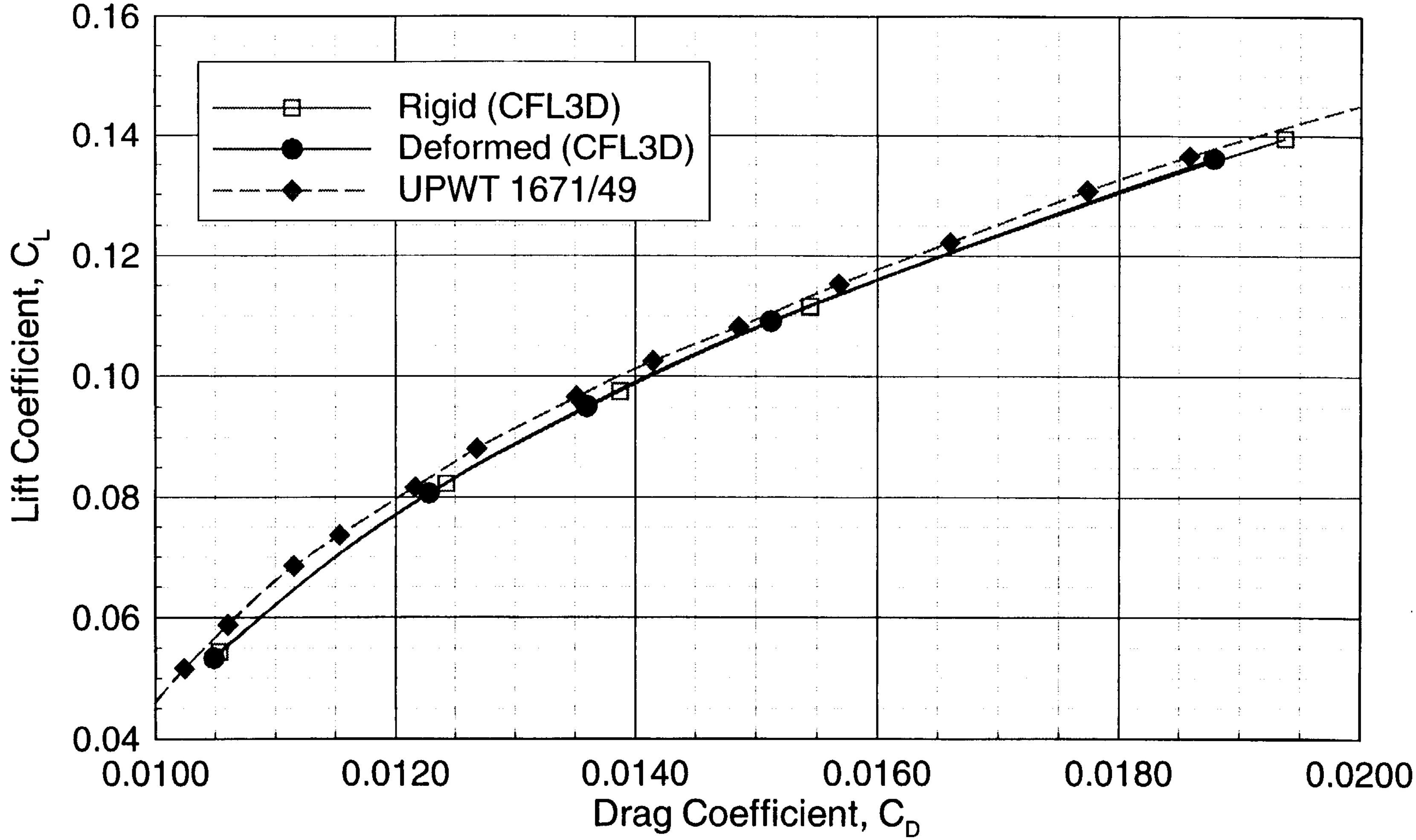

BOEING

Effect of Deformation on TCA Model 2a W/B/N/D

High Speed Aerodynamics, Long Beach

CFL3D N-S (B-L) Solutions and Wind-Tunnel Data
$M_\infty = 2.4$, $Re_c = 6.36\text{x}10^6$, $\alpha = 3.5°$ ($C_L \approx 0.1$)

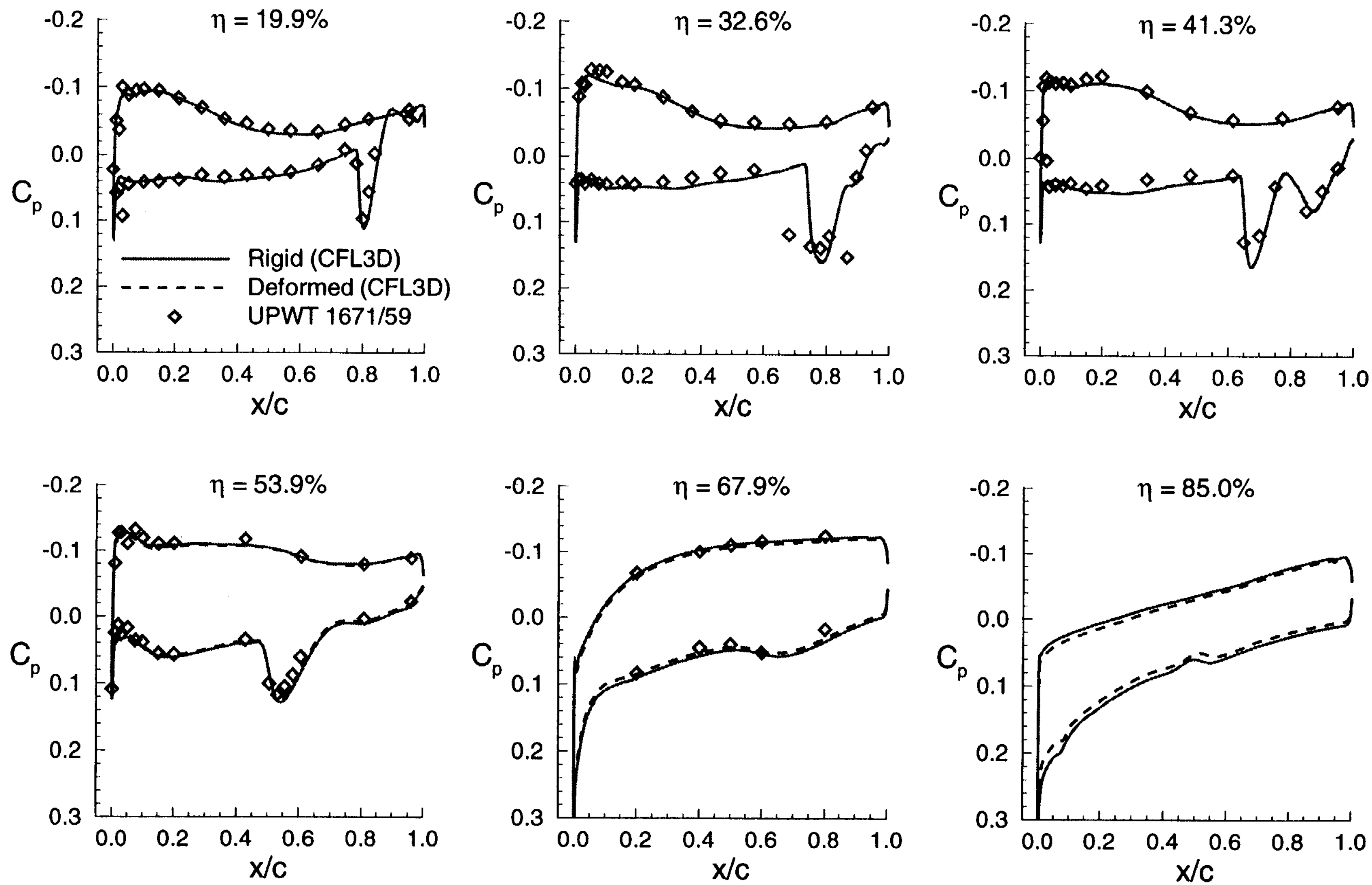

BOEING

Boundary Layer Stability Analysis

BOEING

Boundary Layer Stability Analysis

While most CFD predictions assume fully turbulent flow, in reality a model in a wind-tunnel entry may have a considerable run of laminar flow before the boundary layer transitions to a turbulent state (depending on the Reynolds number, among other factors). It has been suggested that the flow transition location on the TCA wing has been different than the transition location on the NCV wing, and that these differences may have contributed to the performance shortfall of the NCV in the wind tunnel. Trip dots have often been used throughout the HSR program to try to fix the transition location. However, this method of tripping the flow introduces uncertainties associated with trip drag, and the boundary layer does not always transition at the desired location. Even though testing in high Reynolds number facilities, such as Boeing's BSWT tunnel, reduces the amount of laminar flow on the models without the use of boundary layer trips, there is still a laminar flow correction that needs to be applied to the data.

The first step in correcting the test data for a proper comparison to CFD results is to determine the transition location of the flow. For this purpose and in order to obtain some insights into the characteristics of the boundary layer, estimates of the extent of laminar flow on the TCA and NCV wings were obtained through boundary layer stability analyses. The predictions were based on linear stability theory and the envelope method, in which the flow is assumed to become transitional if the calculated amplification rate of the disturbances reaches a value of e^N, where N is in the range of 8 to 9. The linear stability equations were solved using eMalik3d, a compressible code for laminar flow over general swept wings. Even though eMalik3d is a 3-D code, it does have limitations such as the parallel-flow assumption, which dictates that the mean flow cannot change abruptly in the streamwise or crossflow directions. The boundary layer profiles required by eMalik3d were generated from CFL3D N-S laminar flow solutions. The computations were performed at $M_\infty = 2.4$, $Re_c = 6.36 \times 10^6$, and $C_L = 0.09$.

Boundary Layer Stability Analysis

- CFL3D
  - N-S laminar boundary-layer profiles
- eMalik3d
  - Linear stability
  - Compressible flows
  - General swept wings
  - Parallel-flow assumption
- Envelope (e^N) method
  - Transition @ $N = 8$ or 9

BOEING

BL Stability Analysis: N Factors

The next two figures show the growth of the amplification factor, N, on the upper surface of the TCA and NCV wings at three representative semi-span stations (30%, 40%, and 50%) for frequencies ranging from 0 to 2,000 Hz. In general, the N factors on the NCV model are predicted to grow faster than the N factors on the TCA, except near the wing break (η = 50%, for instance) where the opposite is true. The baseline trip dot location (0.6" from the wing leading edge) is also marked in these figures. It can be seen that at this location the N factors on the TCA wing have a value of less than 4. The N factors on the NCV wing at the same location are only slightly higher.

Boundary Layer Stability Analysis for the TCA W/B Configuration

High Speed Aerodynamics, Long Beach

Amplification Factors on Wing Upper Surface

eMalik3d with CFL3D N-S, $M_\infty = 2.4$, $Re_c = 6.36 \times 10^6$, $C_L = 0.09$

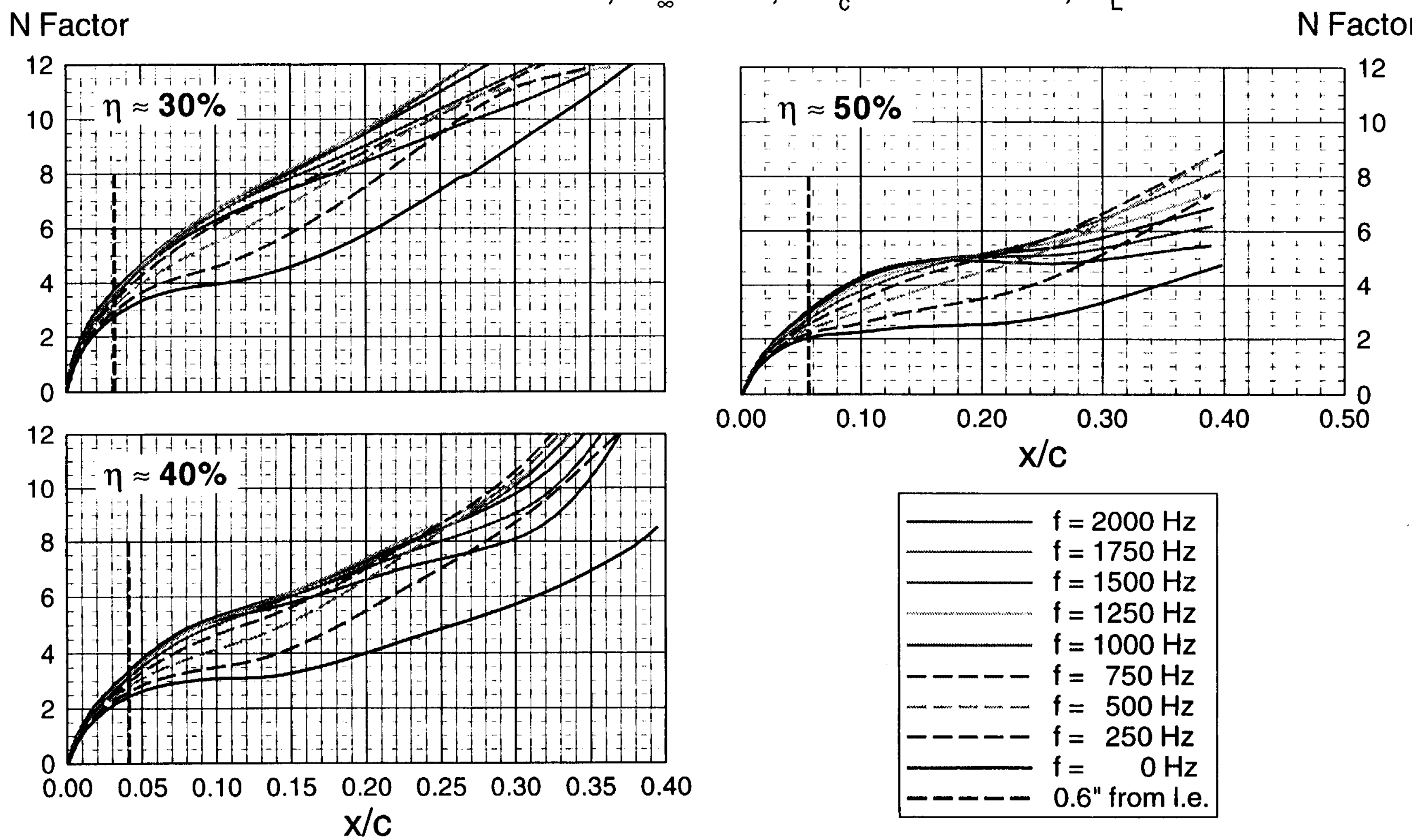

Boundary Layer Stability Analysis for the NCV W/B Configuration

High Speed Aerodynamics, Long Beach

Amplification Factors on Wing Upper Surface

eMalik3d with CFL3D N-S, $M_\infty = 2.4$, $Re_c = 6.36 \times 10^6$, $C_L = 0.09$

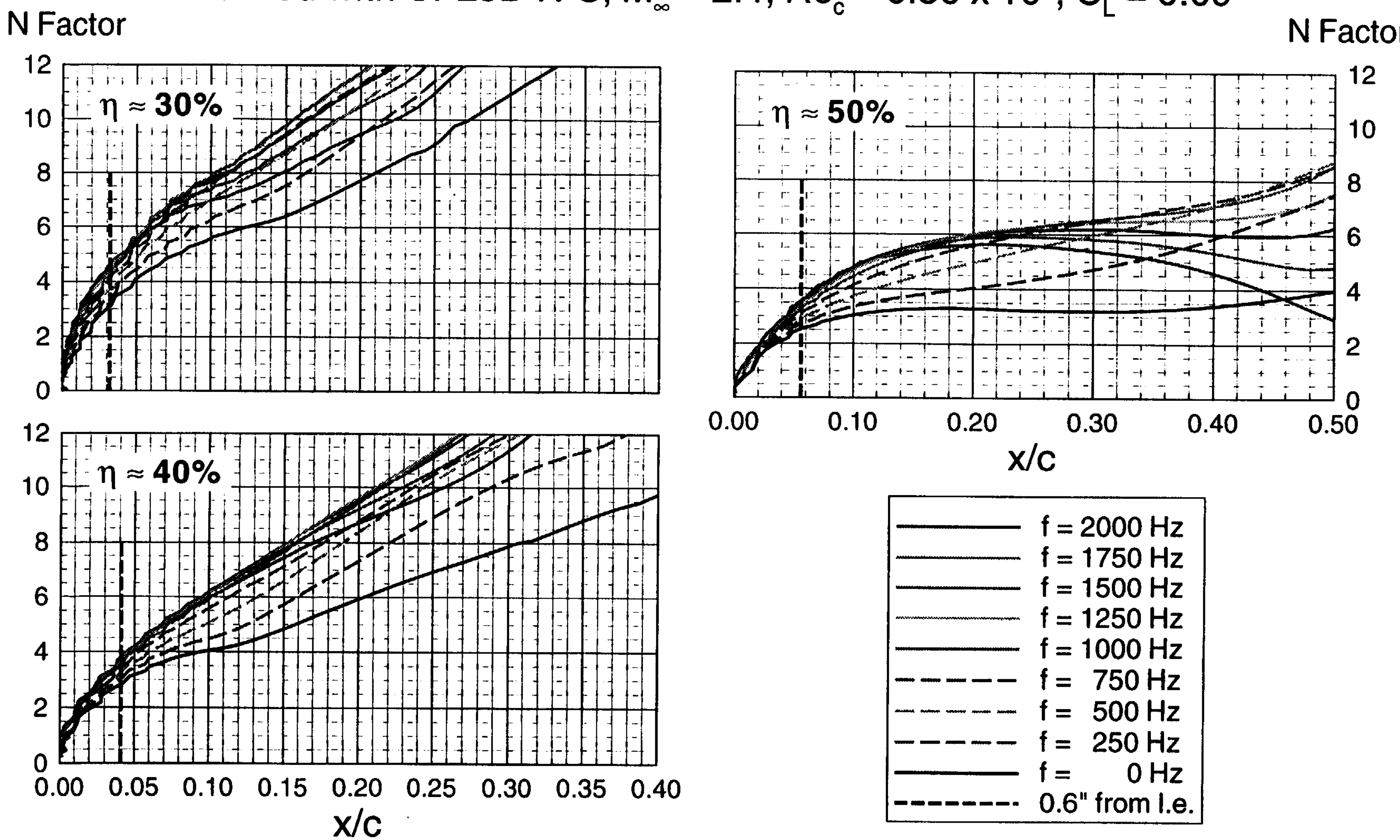

BL Stability Analysis: Transition Locations

The next two figures show a comparison of the predicted and the measured transition locations for the TCA and NCV wing upper surface. The experimental free-transition locations for the TCA and the NCV were determined by NASA Ames researchers from sublimation images obtained during UPWT Test 1679 and UPWT Test 1703, respectively. No trip dots were placed on the wings for these particular runs. Two sets of data from eMalik3d are presented in each figure, showing the locations on the wing surface where the amplification factor has reached values of 8 and 9.

It can be seen that the agreement between the stability analysis predictions and the experimentally-determined transition locations is quite good for the TCA model on the mid-wing region ($30\% \leq \eta \leq 55\%$). However, in the area close to the wing/body junction ($\eta \leq 25\%$), eMalik3d predicts the transition location on the TCA wing to occur considerably further downstream than measured in the wind tunnel. There are several factors that may contribute to the disagreement. First, the computational grid is skewed in the wing/body junction region, and this can reduce the accuracy of the mean-flow profiles used in the stability analysis. Also, the Navier-Stokes mean-flow profiles near the wing/body junction vary considerably not only in the streamwise but also in the spanwise direction, and this violates the parallel-flow assumption in the eMalik3d linear stability code. Furthermore, in the wind tunnel, the flow on the wing is contaminated by the turbulent wedge that is generated from the wing/body junction, but this is not modeled by the fully laminar CFL3D solutions. Consequently, the true profiles in this area are expected to differ from those obtained from the Navier-Stokes computations, in which the flow is assumed to be completely laminar.

The stability calculations on the NCV wing also correlate well with experiment, including the area near the wing/body junction. However, the good agreement observed between analysis and experiment in this region may be considered somewhat fortuitous, since some of the assumptions in the eMalik3d linear stability code are violated in this region of highly three-dimensional flow.

Boundary Layer Transition Location for the TCA W/B Configuration

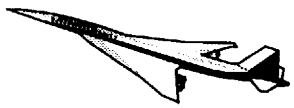

High Speed Aerodynamics, Long Beach

Stability Analysis vs. Experimental Measurements

$M_\infty = 2.4$, $Re_c = 6.36 \times 10^6$, $C_L = 0.09$

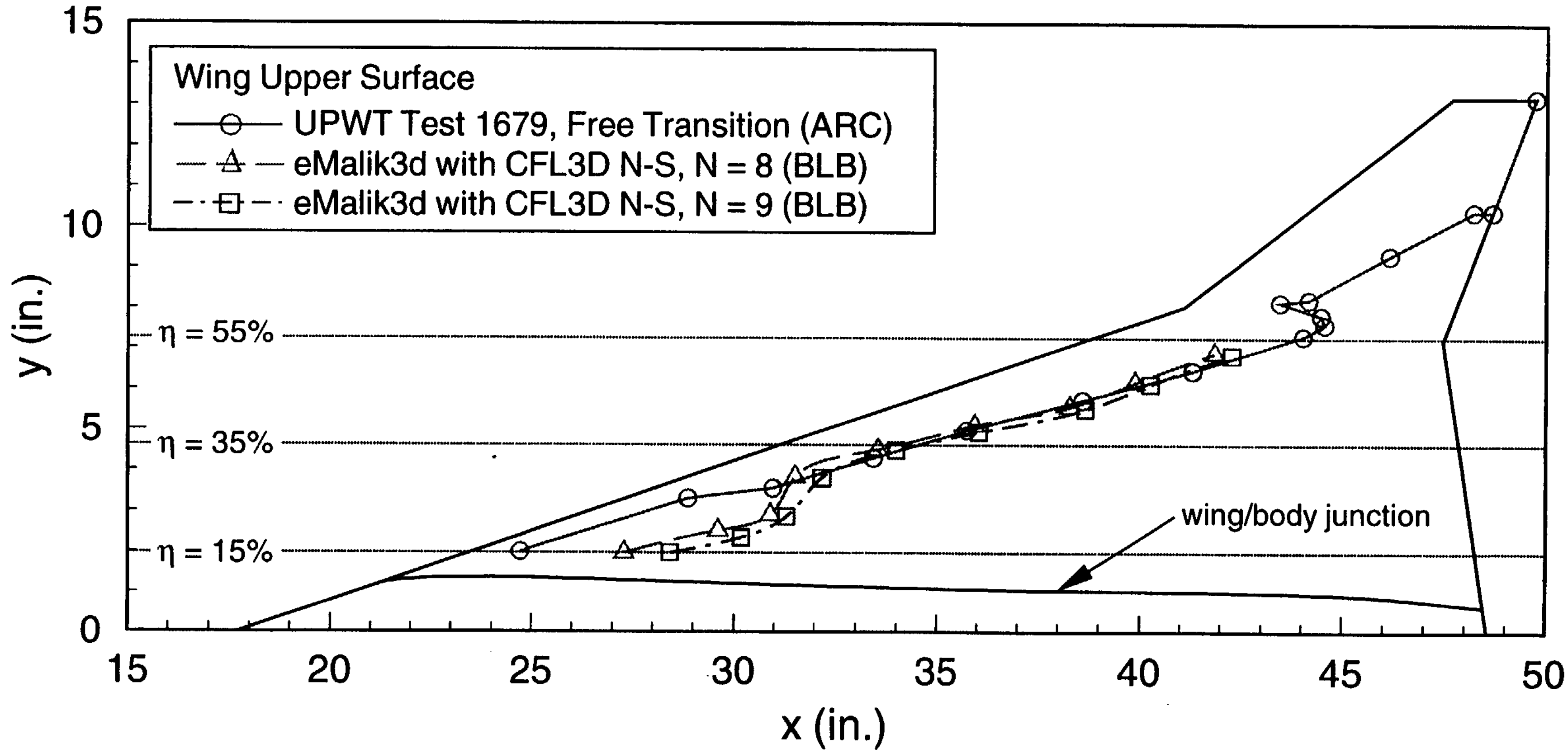

Boundary Layer Transition Location for the NCV W/B Configuration

High Speed Aerodynamics, Long Beach

Stability Analysis vs. Experimental Measurements

$M_\infty = 2.4$, $Re_c = 6.36 \times 10^6$, $C_L = 0.09$

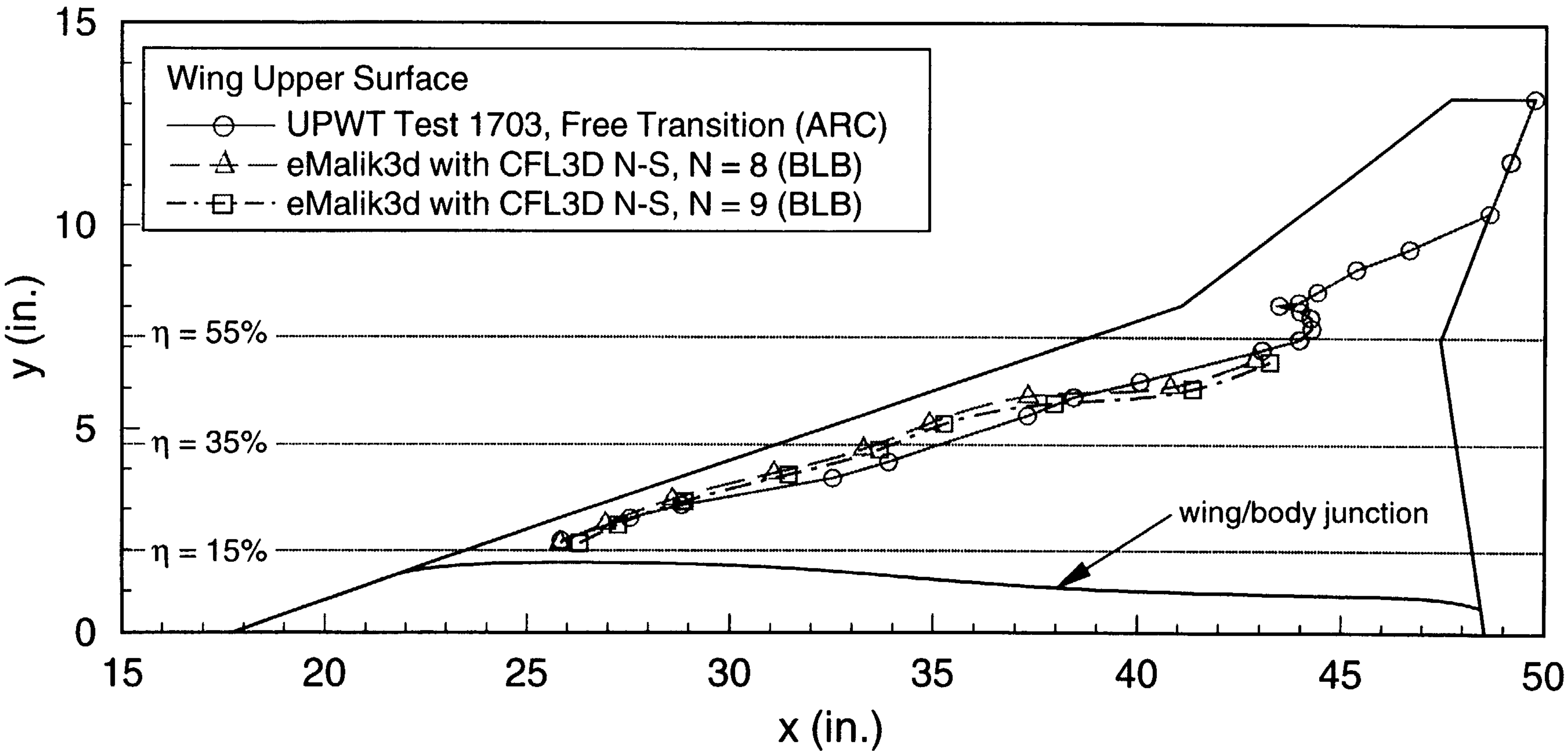

BL Stability Analysis: Transition Locations

The next two figures compare transition locations for both models on the same plot. The sublimation data shown in the first figure indicate that the experimental boundary layer transition locations for the TCA and NCV configurations are rather similar everywhere on the wing upper surface, including the area close to the wing/body junction. This was not expected, since the models (and, therefore, the flows) are quite different from each other. The linear stability results, on the other hand, show some differences between the predicted transition locations for the two models, with the most significant differences occurring close to the wing/body junction, as seen in the next figure.

Experimental BL Transition Location for TCA and NCV W/B

High Speed Aerodynamics, Long Beach

Sublimation Testing, Free Transition (ARC)

$M_\infty = 2.4$, $Re_c = 6.36 \times 10^6$, $C_L \approx 0.09$

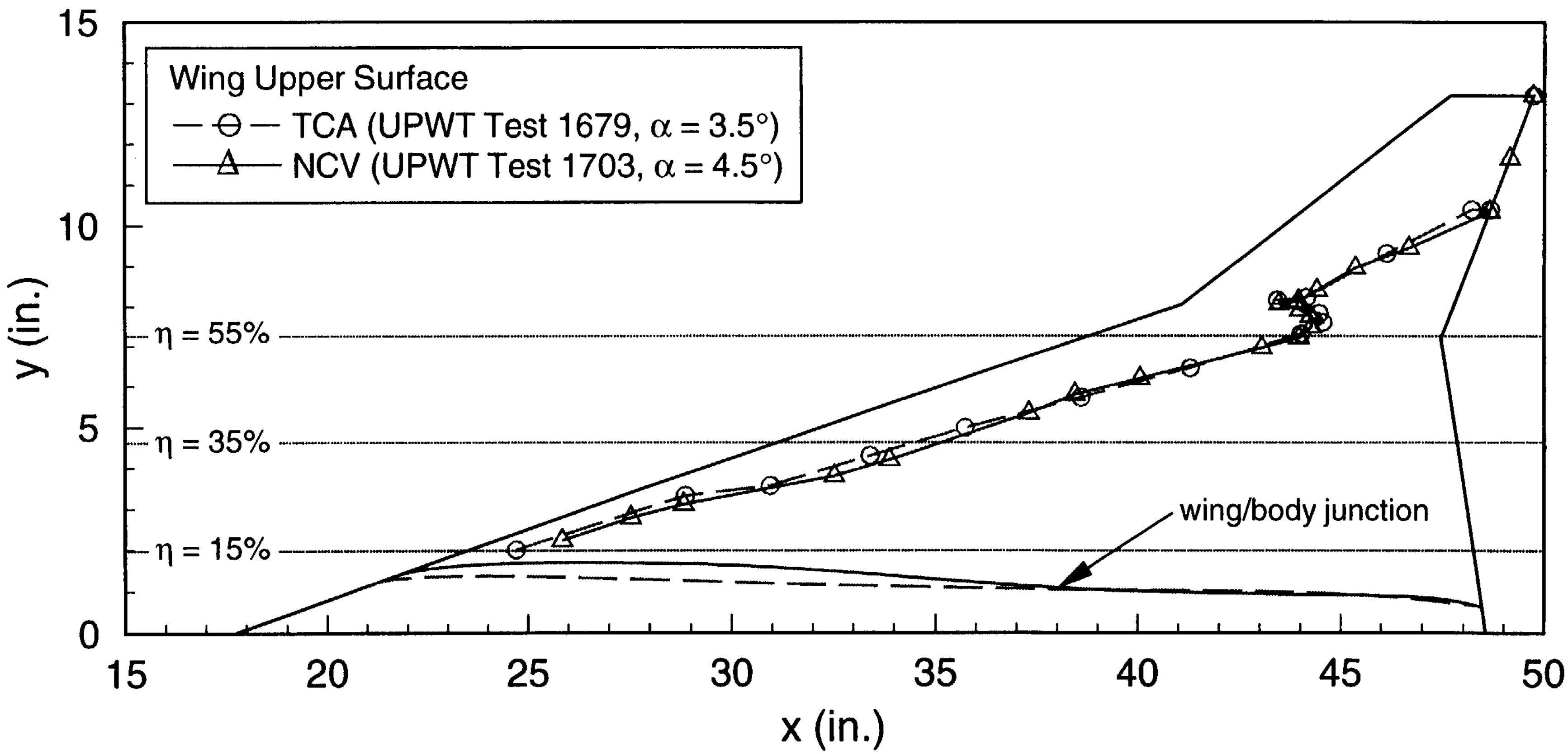

Predicted BL Transition Location for TCA and NCV W/B

High Speed Aerodynamics, Long Beach

eMalik3d with CFL3D N-S (Laminar)
$M_\infty = 2.4$, $Re_c = 6.36 \times 10^6$, $C_L = 0.09$

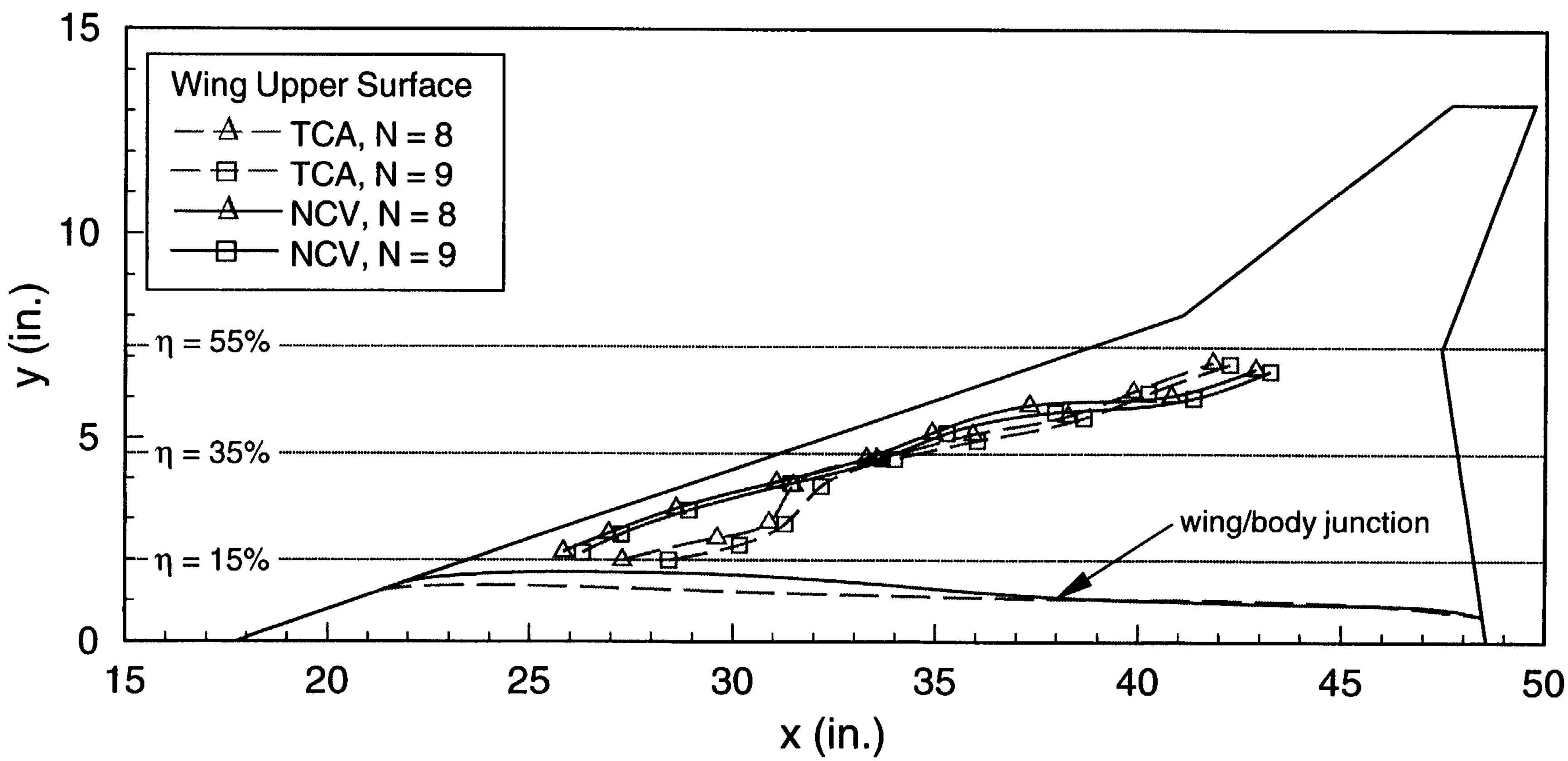

BOEING

BL Stability Analysis: C_P Distributions

The surface pressure associated with the laminar flow solutions used in the stability analyses do suggest that the flow on the inboard wing upper surface of the NCV should transition before the flow on the TCA. This figure shows the computed laminar pressure distributions for the TCA and NCV W/B configurations, along with wind-tunnel pressures measured during UPWT Test 1671 for the TCA Model 2a. The experimental pressures were obtained with 0.012"-high trip dots on the model. It can be seen that on the mid-span and outboard regions, the pressure distributions for both models are fairly similar. However, on the inboard region of the wing (η = 19.9%, for example), the TCA and NCV pressures are quite different. The NCV, for instance, displays a peaky distribution, with a stronger adverse pressure gradient close to the leading edge that could promote transition of the boundary layer. The TCA model, on the other hand, shows a milder pressure gradient. Thus, based exclusively on pressure distributions, it is reasonable to expect the flow on the inboard portion of the NCV wing to transition sooner than the flow on the TCA model (as predicted by the eMalik3d code, which assumes parallel flow and does not take into account factors such as freestream turbulence, flow contamination from the fuselage, or wall roughness).

Pressure Distributions for the TCA and NCV W/B Models

High Speed Aerodynamics, Long Beach

UPWT Test 1671 and CFL3D Navier-Stokes

$M_\infty = 2.4$, $C_L \approx 0.09$, $Re_c = 6.36 \times 10^6$

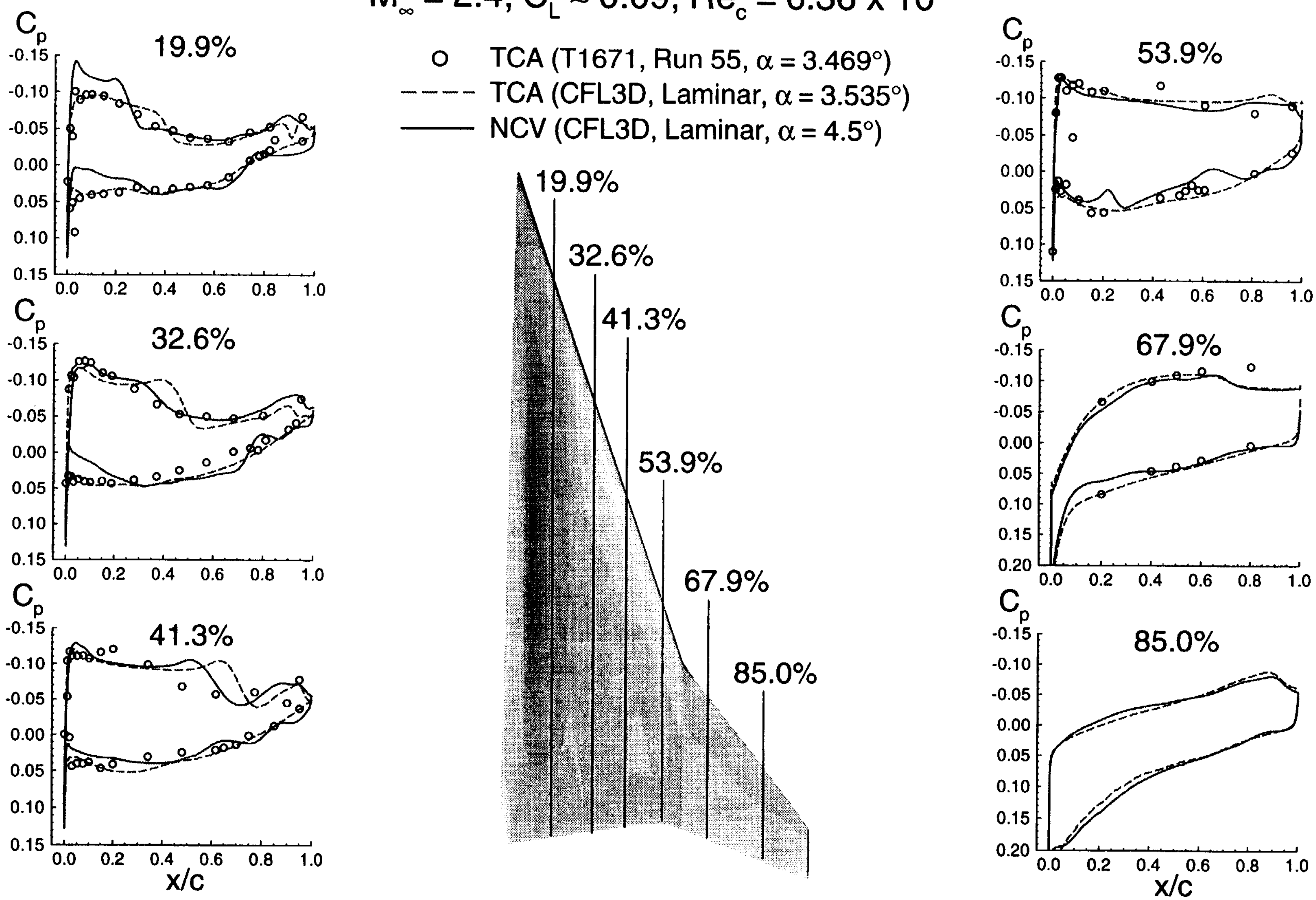

BOEING

Mixed Laminar/Turbulent Flow Analyses (Laminar Run and Trip Drag Corrections)

BOEING

Laminar Run Correction

Once the boundaries of laminar flow have been defined (based on stability analysis or sublimation photographs), an estimate of the laminar run corrections can be obtained. The first step in this process would be to compute the fully turbulent drag, $C_{D\ tur}$, of a model using CFD Navier-Stokes solutions (equivalent flat-plate estimates for skin friction can also be used). Next, drag predictions for mixed laminar/turbulent flows, $C_{D\ mix}$, are obtained using the predicted or measured transition locations. An estimate of the laminar-flow drag correction, $C_{D\ cor}$, can then be obtained by subtracting the combined laminar/turbulent-flow drag predictions from the computed fully turbulent flow drag values. Note that if skin-friction estimates from flat-plate theory are used instead of N-S solutions, any pressure drag contribution is assumed to be negligible.

In the figure, CFL3D results are shown for the TCA W/B configuration near the design condition. In this case, experimentally-determined transition locations from UPWT Test 1679 were used to perform the combined laminar/turbulent flow analyses. The laminar run corrections are seen to vary from 5.5 counts (for free-transition runs) to 1.9 counts (for runs with 0.014"-high trip dots).

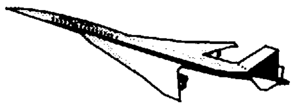

Laminar Run Correction

High Speed Aerodynamics, Long Beach

- Compute fully-turbulent drag, $C_{D\,tur}$, from CFD or flat-plate theory
- Compute mixed laminar/turbulent drag, $C_{D\,mix}$, using predicted (stability analysis) or measured (sublimation images) transition locations
- Laminar run correction: $C_{D\,cor} = C_{D\,tur} - C_{D\,mix}$

Laminar Run Corrections for TCA W/B
CFL3D N-S, $M_\infty = 2.4$, $Re_c = 6.36 \times 10^6$, $C_L = 0.089$
(Transition locations determined by NASA Ames from UPWT Test 1679)

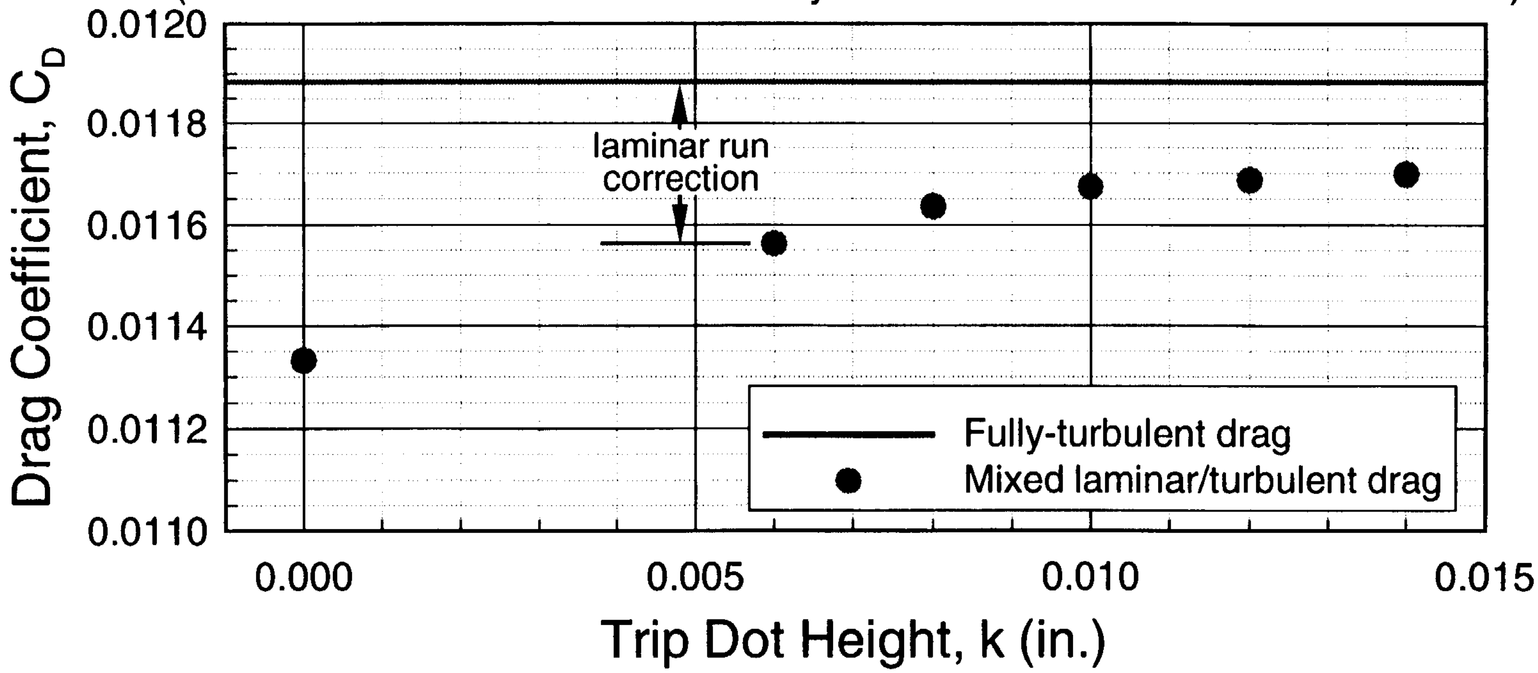

BOEING

Laminar Run Correction for TCA and NCV W/B

This figure shows CFL3D-based results from BPW along with the flat-plate estimates from NASA Ames. In general, the laminar-flow drag corrections obtained from CFD are approximately 0.2 counts higher than the flat-plate estimates for both the TCA and NCV configurations (except for the free-transition case where this pattern reverses). The transition locations used to perform the combined laminar/turbulent flow computations were defined by NASA Ames personnel from sublimation testing with different trip dot heights. The trip dots on the TCA wing were located 0.6 in. from the leading edge (UPWT Test 1679), while the NCV results presented here correspond to test runs for which the dots on this configuration were placed 1.0 in. downstream of the leading edge (UPWT Test 1703). A laminar run correction for the NCV with the baseline trip configuration (k = 0.012" @ 0.6" from the leading edge) was also obtained (1.96 cts.), even though it is not shown in the figure. The corresponding laminar flow correction for the TCA was found to be almost identical (1.97 cts.), as seen in the figure.

Laminar Run Correction for TCA and NCV W/B

High Speed Aerodynamics, Long Beach

Transition Locations Determined by NASA Ames from UPWT Tests 1679 and 1703
$M_\infty = 2.4,\ Re_c = 6.36 \times 10^6,\ C_L \approx 0.089$

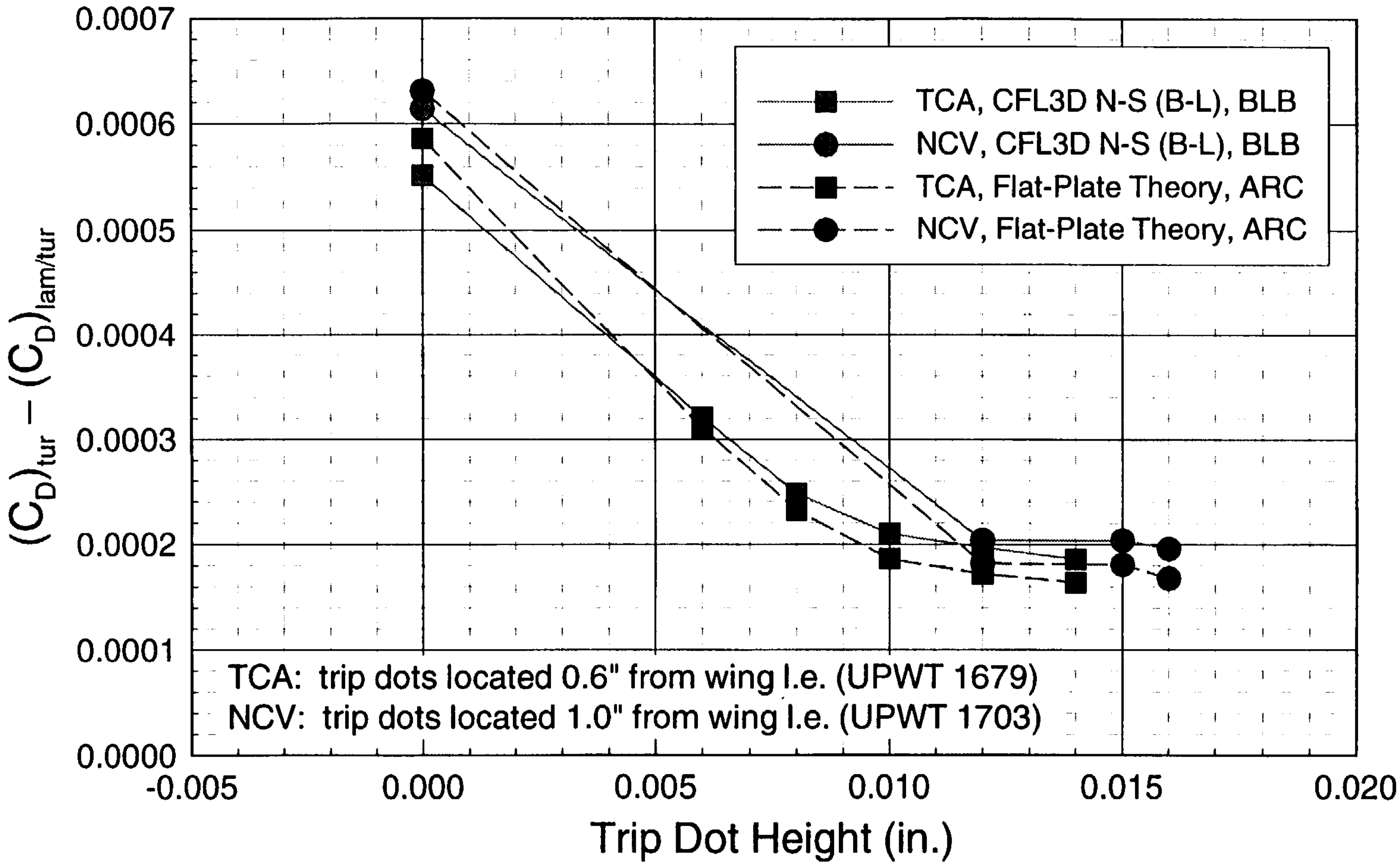

BOEING

Free-Transition Data Corrected for Laminar Flow

This chart illustrates the process for correcting free-transition data for laminar run in order to make a consistent comparison between the CFD fully turbulent drag predictions, $C_{D\,tur}$, and wind-tunnel measurements. The approach is to add the predicted laminar-flow drag correction, $C_{D\,cor}$, to the free-transition test data, $C_{D\,mix}$, as shown in this table. Since the wind-tunnel data are free-transition data, there are no trip drag corrections to apply. Once the laminar run adjustment is made, the experimental drag of the TCA W/B (from UPWT Test 1679) is seen to agree with the CFD-predicted fully turbulent drag coefficient to within 0.1 count near cruise conditions (all the C_D values shown in this table have been interpolated to a lift coefficient of 0.09). However, the agreement is not as good for the NCV model: CFL3D results for the theoretical configuration underpredict the corrected wind-tunnel drag (from UPWT Test 1703) by almost 2 counts. Before correcting the experimental data, the measured NCV drag improvement over the TCA was 2.03 counts. After applying laminar run corrections to both models, the NCV improvement reduces to only 1.41 counts, since the NCV correction is 0.62 counts greater than the TCA correction. As stated before, the CFL3D-predicted performance improvement for the NCV W/B at this lift coefficient is 3.32 counts, so that the difference between the CFD predictions (for the as-designed models) and the corrected experimental data becomes 1.91 counts.

The computed laminar flow corrections are influenced, of course, by the definition of the transition line, which was derived from the wind-tunnel data. Also, the extent of laminar flow is likely to vary with lift. Therefore, strictly speaking, the laminar flow corrections shown here would only apply in the immediate vicinity of the given lift coefficient.

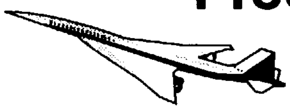

Free-Transition Data Corrected for Laminar Flow

High Speed Aerodynamics, Long Beach

Laminar run corrections obtained from CFL3D N-S solutions
(transition locations based on wind-tunnel data)
$M_\infty = 2.4$, $Re_c = 6.36\text{x}10^6$, $C_L = 0.09$

		$C_{D\,tur}$		$C_{D\,mix}$		$C_{D\,cor}$
TCA	CFL3D N-S (B-L)	120.44	–	114.92	=	5.52
	UPWT Test 1679	120.50	=	114.98	+	5.52
NCV	CFL3D N-S (B-L)	117.12	–	110.98	=	6.14
	UPWT Test 1703	119.09	=	112.95	+	6.14

	C_D, TCA		C_D, NCV		Drag Reduction
Wind-Tunnel Test	120.50	–	119.09	=	**1.41**
CFL3D N-S (B-L)	120.44	–	117.12	=	**3.32**
Test – CFD	0.06		1.97		**-1.91**

All drag values given in counts

Laminar Run Corrections: TCA-to-NCV Drag Reduction

The data presented in the previous slide is repeated in this figure, which shows a bar chart comparing CFD predictions with wind-tunnel measurements. The predicted NCV drag improvement is seen to decrease by 0.69 counts after NCV fabrication imprecision effects are accounted for in the CFL3D solutions (as explained earlier). The measured NCV drag improvement over the TCA, on the other hand, decreases by 0.62 counts (from 2.03 to 1.41 cts.) after the free-transition test data are adjusted for laminar run. As a result, the difference between the CFD-predicted and the measured performance improvement for the NCV W/B over the TCA W/B is still about the same, after corrections have been applied. Note that the experimental free-transition TCA-to-NCV drag reduction was computed using data from two separate tests: UPWT 1679 (TCA) and UPWT 1703 (NCV), since the NCV model was not tested during Test 1679 and free-transition data for the TCA model was not acquired during Test 1703.

NCV Drag Reduction relative to TCA for W/B Configurations

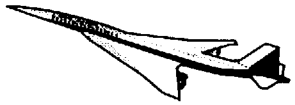

High Speed Aerodynamics, Long Beach

CFD (CFL3D N-S, B-L) vs. Experiment (UPWT 1679 & 1703, free transition)

$M_\infty = 2.4$, $Re_c = 6.36 \times 10^6$, $C_L = 0.09$

CFD:	Fully Turbulent	Fab. Imprecision	Corrected CFD
TCA	120.44	N/A	120.44
NCV	117.12	+0.69	117.81

Experiment:	Test Data	Lam. Run	Trip Drag	Corrected Data
TCA (UPWT 1679)	114.98	+5.52	0	120.50
NCV (UPWT 1703)	112.95	+6.14	0	119.09

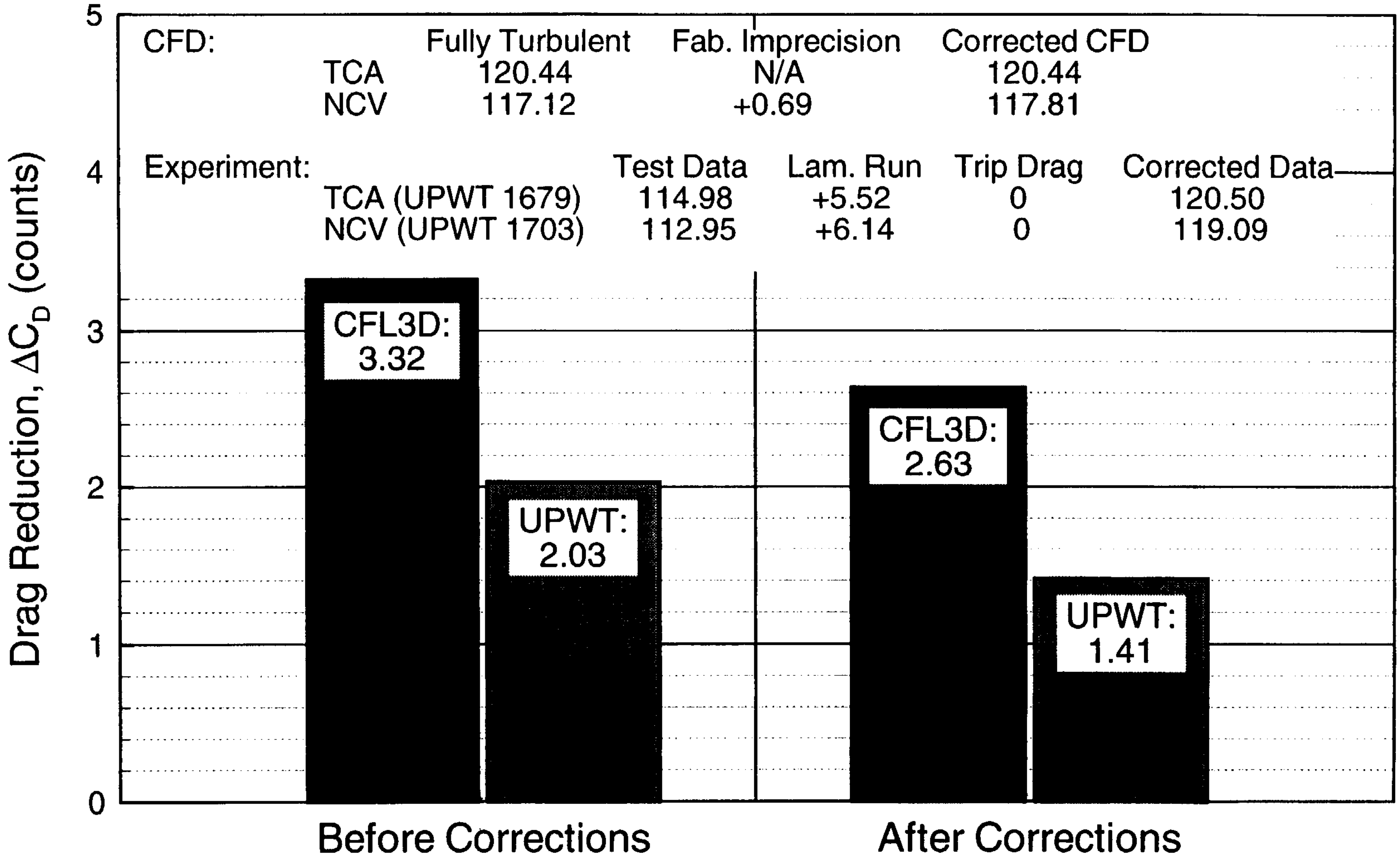

BOEING

Trip Drag

The laminar run corrections computed in the previous section can now be used to estimate the trip drag associated with different trip dot heights. First, the computed laminar-flow drag corrections, $C_{D\ cor}$, are added to the corresponding wind-tunnel drag values, $C_{D\ w\text{-}t}$, for different trip-dot heights. Since the free-transition drag corrected for laminar run requires no further corrections, this is the experimental fully turbulent drag (which is assumed to be the "true" drag of the model). The trip drag for each dot height, k, can now be estimated as the difference between the trips-on data corrected for laminar run and the free-transition data that has been adjusted for laminar flow, as illustrated in the figure. Shown here are trip drag corrections for the TCA W/B, as obtained from CFL3D computations with transition locations defined from UPWT 1679 data at cruise conditions.

Trip Drag

- Laminar run corrections applied to wind-tunnel data for each dot height, k:

  $C_{D\,tur} = C_{D\,w\text{-}t} + C_{D\,cor}$
- Corrected free-transition data, $C_{D\,tur}(k=0)$, assumed to be "true" drag of model
- Trip drag: $C_{D\,trip} = C_{D\,tur}(k>0) - C_{D\,tur}(k=0)$

Trip Drag for the TCA W/B
CFL3D N-S, $M_\infty = 2.4$, $Re_c = 6.36\text{x}10^6$, $C_L = 0.09$
(Transition locations determined by NASA Ames from UPWT Test 1679)

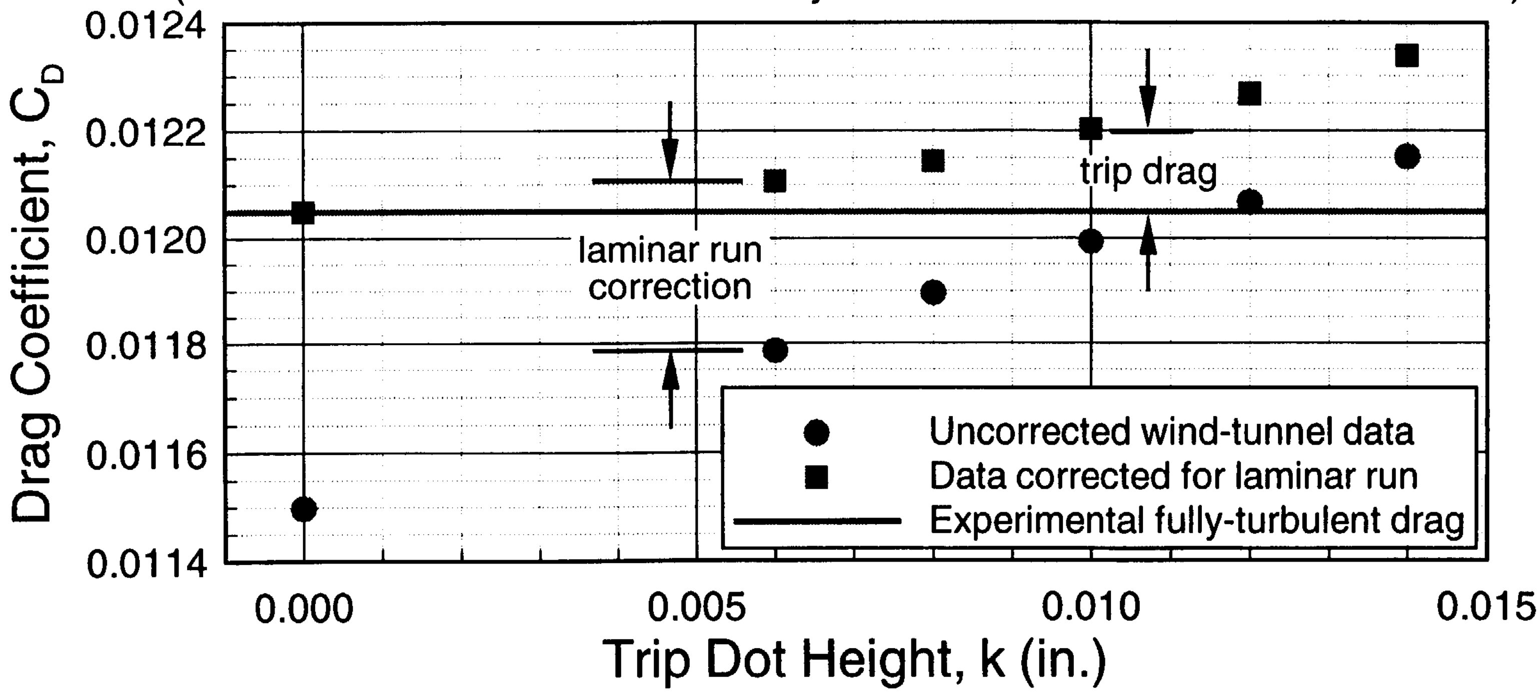

Trip Drag for TCA and NCV W/B

The TCA and NCV trip drag for different dot heights is shown in this figure. Both, CFD results and flat-plate estimates are presented. It can be seen that the CFL3D trip drag computations are about 0.3 to 0.6 counts higher than the flat-plate estimates. For a typical trip dot height of 0.012", the trip drag estimates for the TCA and NCV configurations are approximately 2.2 and 1.6 counts, respectively (based on the laminar-flow correction from the CFL3D solutions). Note that the trip dots on the TCA model are located 0.6" from the wing leading edge, whereas the dots on the NCV wing are 1" downstream of the leading edge. Previous trip drag estimates obtained using techniques such as the variable trip height and the variable Reynolds number methods were as high as 5 counts.

Trip Drag for TCA and NCV W/B

High Speed Aerodynamics, Long Beach

Transition locations determined by NASA Ames from UPWT Tests 1679 and 1703
$M_\infty = 2.4$, $Re_c = 6.36 \times 10^6$, $C_L \approx 0.089$

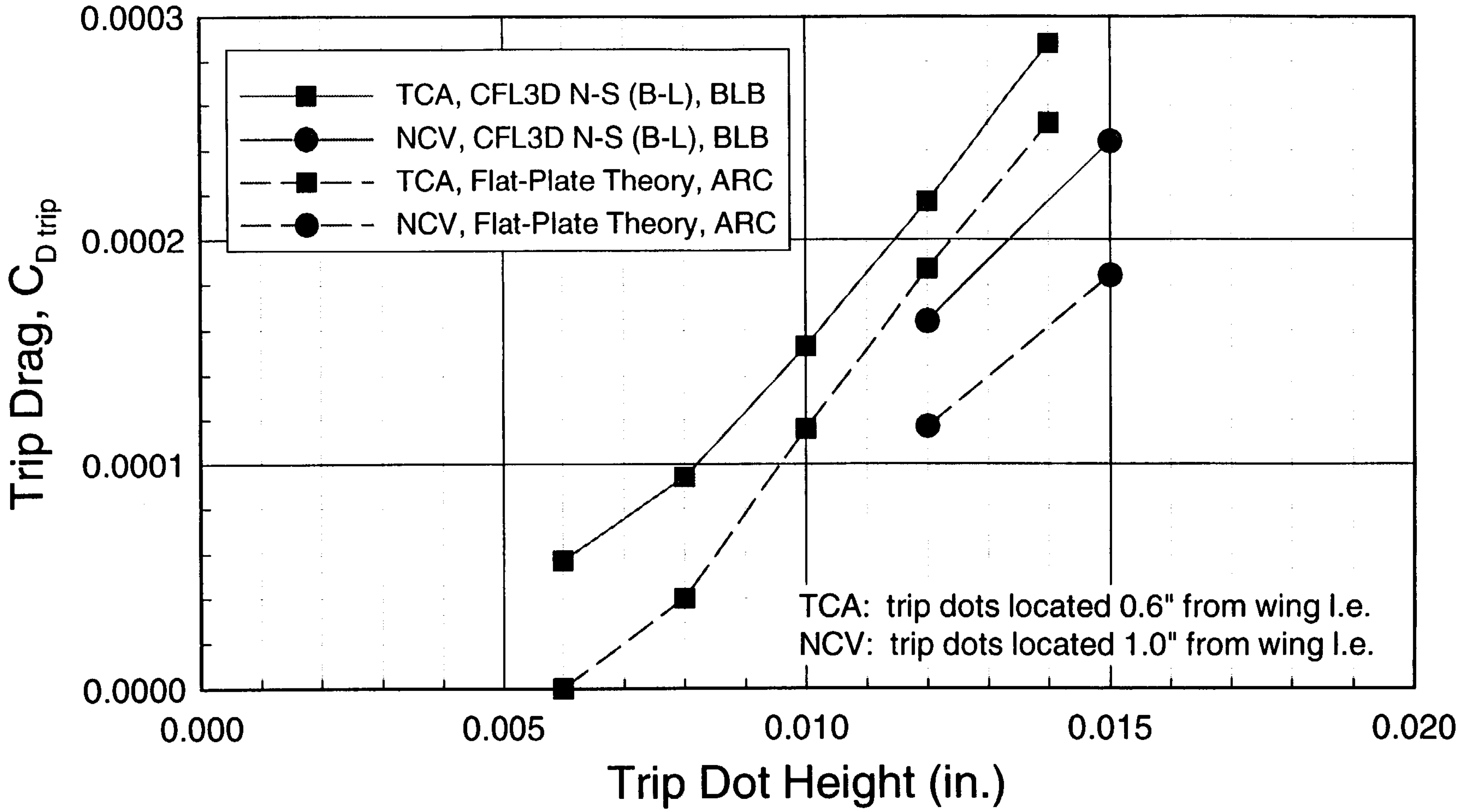

Data Corrections: TCA-to-NCV Drag Reduction (UPWT 1703)

This bar chart shows the predicted and measured NCV drag improvement over the TCA before and after corrections have been applied to the data. The experimental drag values presented in this figure were obtained from the NCV flow diagnostics test (UPWT 1703) with the baseline trip configuration (k = 0.012" @ x = 0.6" from the leading edge) on both models. The details on how the corrected data were obtained are also given in the figure. At the given conditions ($M_\infty = 2.4$, $Re_c = 6.36 \times 10^6$, and $C_L = 0.09$), for instance, it can be seen that the laminar run correction is about 2 counts for both models. Similarly, the trip drag for both the TCA and NCV W/B configurations with k = 0.012" is approximately 2.2 counts. Therefore, since the corrections for the NCV data are about the same as the corrections applied to the TCA data, the change in the measured NCV drag improvement before and after corrections is negligible (only 0.03 drag cts., from 2.13 to 2.16 cts.). However, because the CFD-predicted improvement decreases by 0.7 when the NCV as-built model is analyzed, the difference between CFD predictions and wind-tunnel measurements now becomes only 0.5 counts (in terms of TCA-to-NCV drag reduction).

Recall that the wind-tunnel data corrections for the TCA were derived using data from UPWT Test 1679, while the corrections for the NCV data were obtained from UPWT Test 1703. However, as long as the conditions remain the same, it is assumed that data corrections derived from one test can be applied to data from another test.

NCV Drag Reduction relative to TCA for W/B Configurations

High Speed Aerodynamics, Long Beach

CFD (CFL3D N-S, B-L) vs. Experiment (UPWT 1703, k = 0.012" at x = 0.6")

$M_\infty = 2.4$, $Re_c = 6.36 \times 10^6$, $C_L = 0.09$

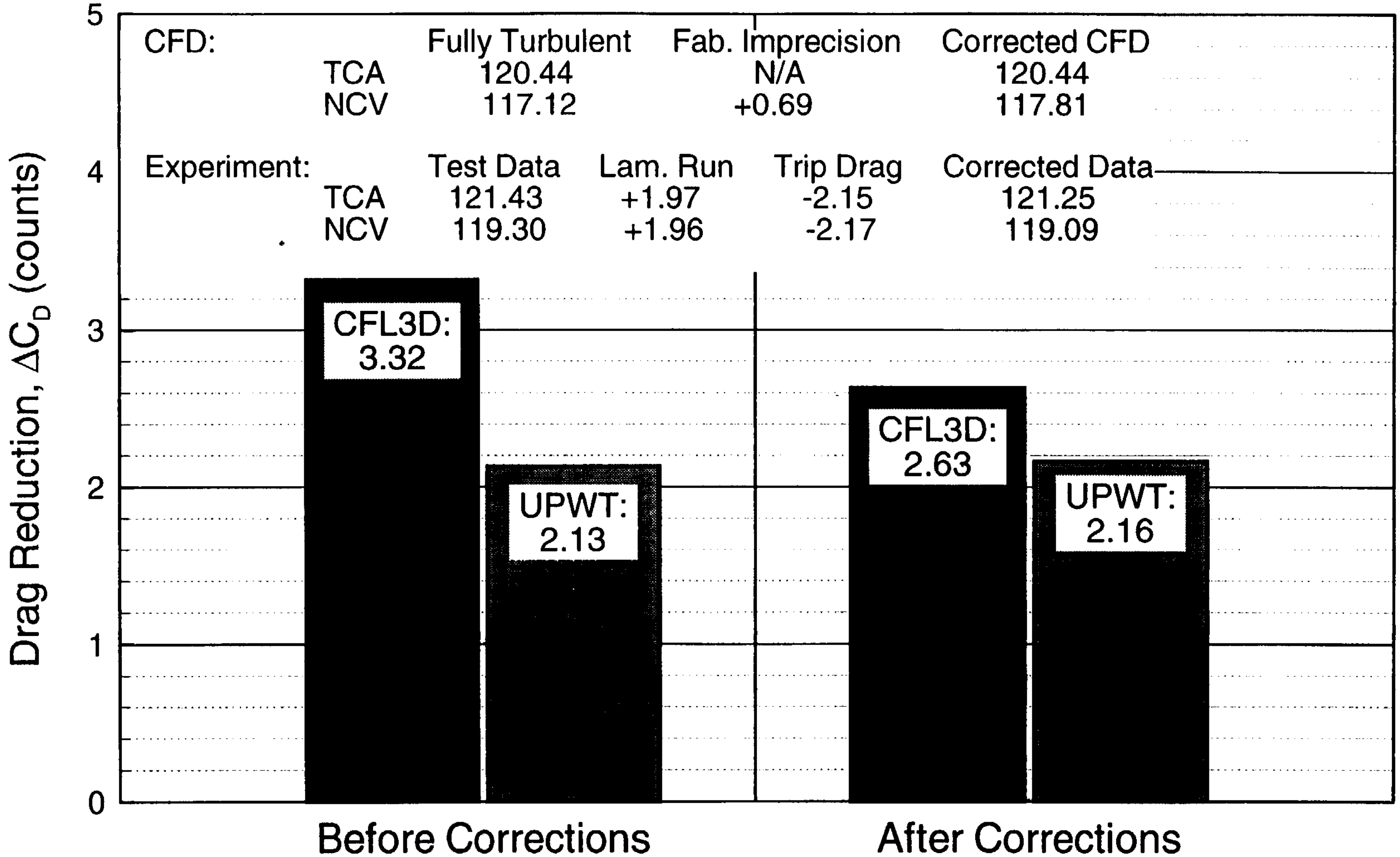

CFD:		Fully Turbulent	Fab. Imprecision	Corrected CFD
	TCA	120.44	N/A	120.44
	NCV	117.12	+0.69	117.81

Experiment:		Test Data	Lam. Run	Trip Drag	Corrected Data
	TCA	121.43	+1.97	-2.15	121.25
	NCV	119.30	+1.96	-2.17	119.09

BOEING

Data Corrections: TCA-to-NCV Drag Reduction (UPWT 1687)

Experimental data from UPTW Test 1687 with the baseline trip configuration are presented in this chart. Since the conditions are the same as for the previous set of data (UPWT 1703), the data corrections are assumed to be the same. Hence, again, the measured NCV drag improvement is essentially the same before and after corrections are applied. However, the NCV drag improvement observed during this wind-tunnel test is 0.34 counts higher than the improvement measured during UPWT Test 1703. Therefore, the agreement between the CFL3D-predicted improvement (corrected for NCV model imprecisions) and data from UPTW Test 1687 reduces to just over 0.1 drag counts.

NCV Drag Reduction relative to TCA for W/B Configurations

High Speed Aerodynamics, Long Beach

CFD (CFL3D N-S, B-L) vs. Experiment (UPWT 1687, k = 0.012" at x = 0.6")

$M_\infty = 2.4$, $Re_c = 6.36 \times 10^6$, $C_L = 0.09$

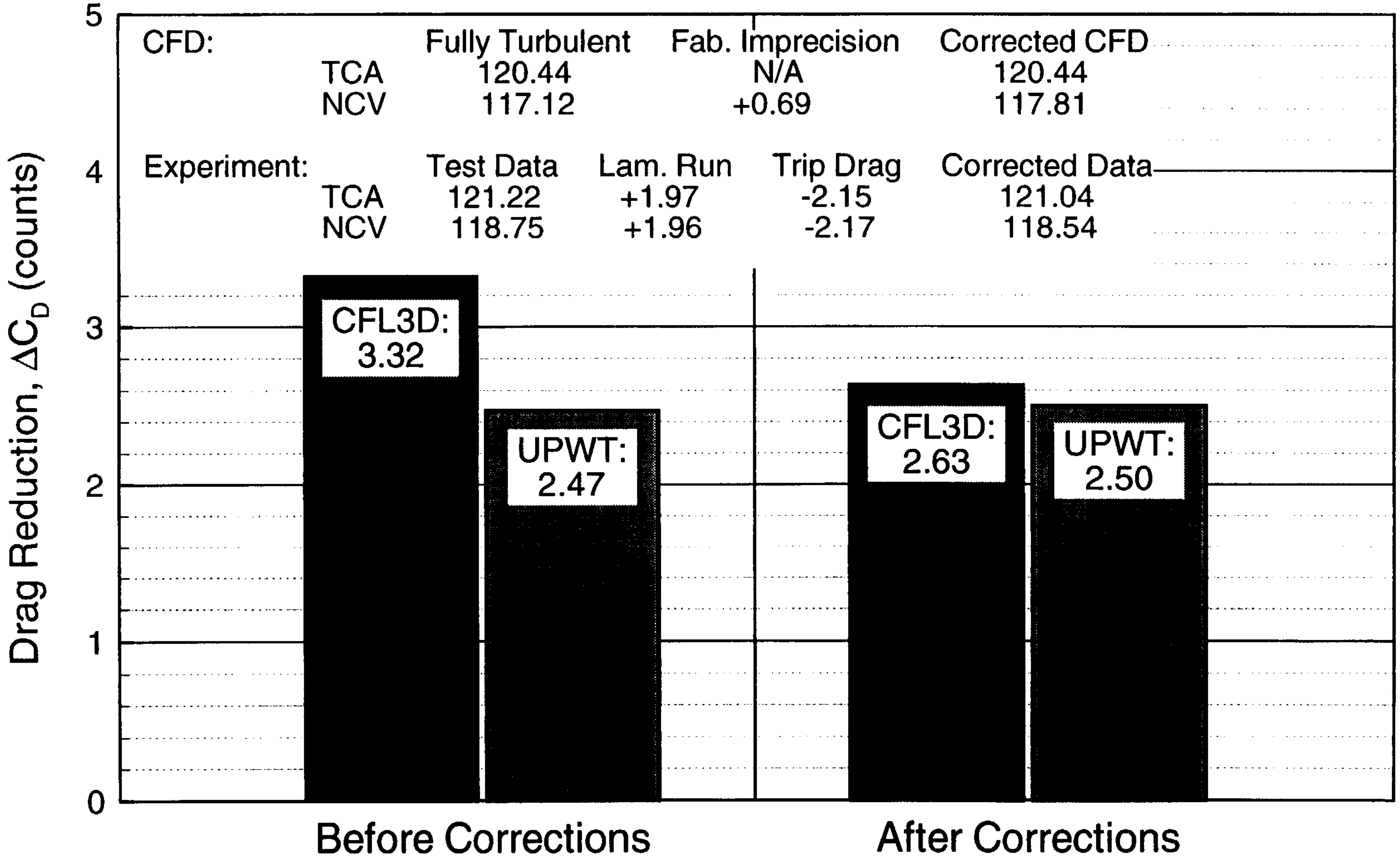

BOEING

Summary and Conclusions

While a single definite reason for the NCV performance shortfall was not found, several factors have been identified as possible culprits and others have been ruled out.

Factors that have been found to have no impact on the discrepancies between the predicted and the measured performance improvement of the NCV W/B over the TCA W/B are the following:

• Laminar flow separation on the NCV forebody: On-body flow visualization data obtained from ultraviolet oil flow during the NCV diagnostics entry in the UPWT (Test 1703) confirmed that the flow over the NCV forebody is fully turbulent (as modeled in most CFD simulations), ruling out the possibility that laminar-flow separation in this region could contribute to the NCV performance shortfall.

• Grid density effects on CFD solutions: The effect of grid density on the CFD drag predictions for both models was investigated by increasing the number of points in the computational grid from 1.5 million to 11.5 million. The refined-grid Navier-Stokes solutions performed at $Re_c = 6.36 \times 10^6$ did not significantly change the original predictions at $Re_c = 6.36 \times 10^6$.

• Aeroelastic effects on drag: Results from Navier-Stokes analyses of the TCA W/B/N/D model with aeroelastic deformations indicate that static aeroelasticity affects lift and pitching moment, but it does not have a significant impact on the drag polar of the TCA configuration.

Summary and Conclusions

- Definite cause of TCA-to-NCV performance shortfall not found
- Ruled out
  - Laminar separation on NCV forebody
  - Grid density effects on CFD solutions
  - Static aeroelastic effects on drag at wind-tunnel conditions

Summary and Conclusions (Cont'd)

Factors that have been found to contribute to changing either the predicted or measured TCA-to-NCV drag improvement are the following:

• Model fabrication imprecision: The impact of model fidelity on drag predictions was examined by performing Navier-Stokes analyses of the NCV QA model. It was found that the predicted drag of the as-built geometry is approximately 0.7 counts higher than the drag of the as-designed W/B configuration at cruise. The TCA as-built model will have to be analyzed in order to assess the full impact of model fidelity on the CFD predictions.

• Laminar flow and trip drag corrections: After free-transition test data from UPWT 1679 (TCA) and UPWT 1703 (NCV) were adjusted for laminar flow, the corrected NCV W/B drag improvement over the TCA W/B actually reduced by approximately 0.6 counts. When laminar and trip drag corrections are applied to trips-on experimental data (UPWT 1703 and also UPWT 1687), the measured NCV performance improvement before and after corrections does not change significantly. However, the agreement between the predicted NCV-to-TCA drag reduction and wind-tunnel data improves significantly when trips-on data are used instead of free-transition data. When data from UPWT Test 1703 are used, the agreement between CFD and experiment is within 0.5 count; if data from UPWT Test 1687 are used, the difference between CFD predictions and wind-tunnel data is just over 0.1 count.

• Shock on the NCV wing upper surface: Off-body flow visualization data obtained from laser vapor screen testing on the NCV, detected the presence of a shock on the upper surface of the wing at the cruise conditions. CFD computations, however, apparently failed to capture the shock. It is possible that this shock could adversely affect the NCV performance.

Summary and Conclusions (Cont'd)

- Partial contributors
  - Model fabrication imprecision
    - NCV QA has 0.7 cts. more drag than theoretical design
    - TCA QA must be analyzed to assess full impact
  - Laminar flow and trip drag
    - Laminar run corrections applied to free-transition data decrease measured TCA-to-NCV drag improvement by 0.6 cts.
    - For baseline HSR trip configuration (k = 0.012” @ x = 0.6”), laminar run and trip drag corrections do not change measured improvement significantly
  - Shock on NCV wing upper surface
    - Observed in wind tunnel
    - Not predicted by CFD

Summary and Conclusions (Cont'd)

Two important unresolved issues remain:

- Uncertainty of wind-tunnel measurements: It has been suggested that the uncertainty in wind-tunnel measurements is as big as 2 or even 2.5 counts. If this were the case, the wind-tunnel drag uncertainty band would be large enough to include the CFD predictions. But an extensive test techniques program to reduce such a large uncertainty would need to be conducted.

- Accuracy of CFD predictions: The accuracy of the CFD computations has not been quantified. Perhaps the CFD tools used in the HSR program cannot accurately predict wind-tunnel flows over configurations like the TCA or NCV. In this case, a test program for validation/calibration of CFD tools would be appropriate.

Summary and Conclusions (Cont'd)

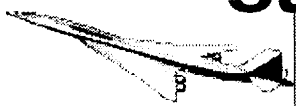

High Speed Aerodynamics, Long Beach

- Unresolved issues
  - Uncertainty of wind-tunnel measurements
  - Accuracy of CFD predictions

BOEING

SUPERSONIC AFTBODY CLOSURE WIND-TUNNEL TESTING, DATA ANALYSIS, AND COMPUTATIONAL RESULTS

Jerry Allen, LaRC
Grant Martin, BPW
Paul Kubiatko, BPW

Configuration Aerodynamics

HSR Airframe Technical Review
Anaheim, California
February 8-11, 1999

Supersonic Aftbody Closure Wind-Tunnel Testing, Data Analysis, and Computational Results

This paper reports on the model, test, and results from the Langley Supersonic Aftbody Closure wind tunnel test. Each of the authors prepared a specific section of the paper. Jerry Allen from Langley prepared the opening section describing the test and model. Grant Martin from Boeing Phantom Works prepared the section on the performance results. Paul Kubiatko, also from Boeing Phantom Works, prepared the section on the stability and control results. Each author presented his section during the oral presentation of the paper.

Configuration Aerodynamics Technology Development

This presentation was the fourth paper in the Testing Session (Session 4) held on Thursday, February 11, 1999. The work included in this paper supports the three activities that are shaded in this chart.

Configuration Aerodynamics Technology Development

Session 4: Testing Session

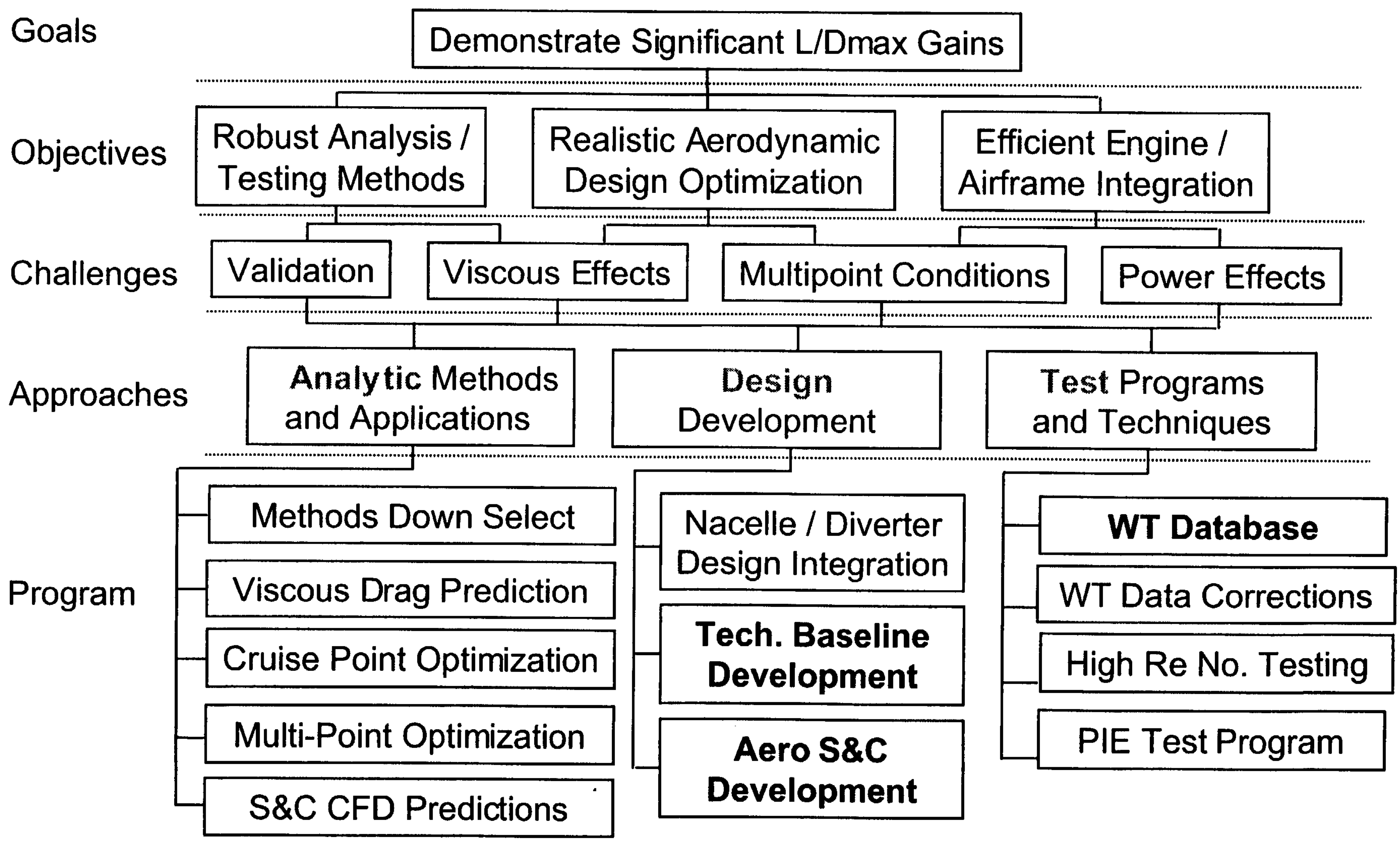

Presentation Outline

Project Background:

This project is an experimental evaluation of the 1.5% Technology Concept Aircraft (TCA) aftbody closure model (Model 23) in the Langley Unitary Plan Wind Tunnel. The baseline TCA design is the result of a multidisciplinary, multipoint optimization process and was developed using linear design and analysis methods, supplemented with Euler and Navier-Stokes numerical methods. After a thorough design review, it was decided to use an upswept blade attached to the forebody as the mounting system. Structural concerns dictated that a wingtip support system would not be feasible. Only the aftbody part of the model is metric. The metric break was chosen to be at the fuselage station where prior aft-sting supported models had been truncated. Model 23 is thus a modified version of Model 20. The wing strongback, flap parts, and nacelles from Model 20 were used, whereas new aftbodies, a common forebody, and some new tails were fabricated. Microcraft of Hampton was tasked with the design and fabrication of the new hardware.

Presentation Outline:

The presentation will follow the outline as shown in this bullet chart. The project objectives, model geometry and test highlights will be presented first. This will be followed by a summary of the performance results of the test, which will include comparisons with CFD and flow viz. The third section will be an analysis of the stability and control results. A summary will be given at the end of each data analysis section.

Presentation Outline

- Objectives
- Test support
- Model geometry
- Test highlights
- Performance results
  - Data analysis, data vs. CFD, & flow viz
- Performance summary
- Stability & Control results
  - Longitudinal/directional characteristics
- Stability & Control summary

Test Objectives

The six objectives of this test listed in this figure can be grouped into the following four areas: 1) determine the drag characteristics and trim drag increments of the various aftbodies, 2) validate the aftbody stability levels and tail control effectiveness, 3) provide a database for CFD code validation and correlation with other models, and 4) establish and validate the aftbody closure test technique at supersonic speeds.

Test Objectives

Acquire experimental data for several aftbody configurations to:

- Determine drag characteristics
- Determine trim drag increments
- Validate aftbody longitudinal and directional stability levels
- Validate tail control effectiveness
- Provide database for CFD code validation and correlation with other models
- Establish and validate aftbody closure test techniques at supersonic speeds

Test Support

NASA Langley served as the lead aero organization for this test, and was provided on-site support by Boeing-Phantom Works (BPW) and Boeing-Seattle (BCAG). Jerry Allen served as focal point for NASA Langley and was on-site for the 7.5-week duration of the test. Support from Boeing was provided by David Blake (BPW), Paul Kubiatko (BPW), Grant Martin (BPW), Christine Titzer (BCAG), Greg Stanislaw (BCAG), and Servando Flores (BCAG). David Tuttle of NASA Langley served as the lead test engineer throughout the test. The UPWT technicians listed in this figure made model changes and kept the tunnel running.

Test Support

- Researchers:
  - LaRC: Jerry Allen
  - BCAG: Chris Titzer, Greg Stanislaw, Servando Flores
  - BPW: David Blake, Paul Kubiatko, Grant Martin
- Test Engineer: David Tuttle
- Data Analyst: David Shaw
- Technicians: Bob Edwards, Ricky Hall, Billy Graham, Joseph Moore, Dan Pritchard

Comparison of Aftbody Configurations

This figure shows comparison drawings of the three aftbody configurations used in this test – flared, baseline closed and modified closed. Also indicated are which parts were new for this test and which came from the preexisting sting-mounted model (Model 20). Basically, all three configurations used the same forebody, wing section, and nacelles, but had separate aftbody transition sections and metric aftbodies. The flared configuration used the existing tails from Model 20, whereas the closed configurations needed new tails to match their aftbody shapes. All three configurations used the same internal balance to measure force and moment data. There were actually two models of the baseline aftbody. In addition to the force and moment model, a separate pressure-instrumented model was built. This model had 47 pressure taps located at 12 longitudinal stations on the aftbody to measure detailed pressure distributions on this configuration.

Comparison of Aftbody Configurations

New forebody, existing wing center section and nacelles

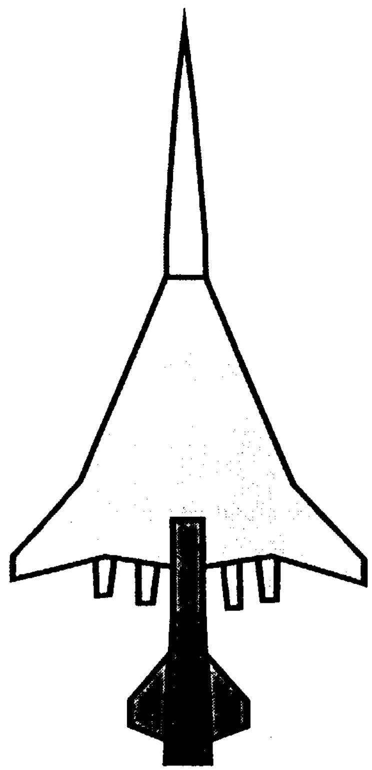

Flared Aftbody (without dummy sting)

- New aftbody
- New transition section
- Model 20 tails

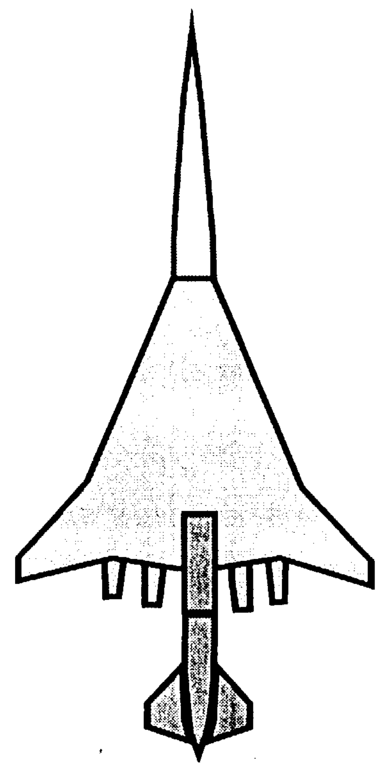

Baseline TCA

- New aftbody
- New transition section
- New tails

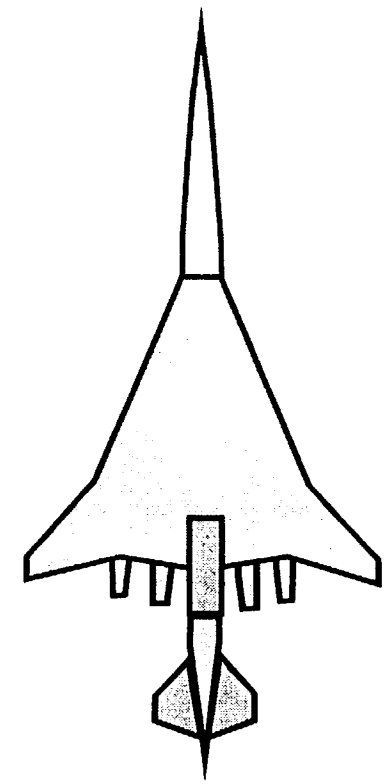

Modified Baseline TCA

- New aftbody
- Baseline transition section
- Baseline horizontal tails
- New vertical tail

Model Installation in UPWT

A side view drawing of the UPWT test setup of the flared aftbody configuration is shown in this figure. The items outlined in red are part of the permanent model support equipment in the test section. This figure shows the forward blade attachment sting that was used for all aftbody configurations to support the model throughout this test. For some of the flared aftbody runs a dummy sting (not shown in this figure) was used to simulate the aft-sting mounted Model 20 setup.

1.5% TCA Aftbody Closure Model Installation in UPWT

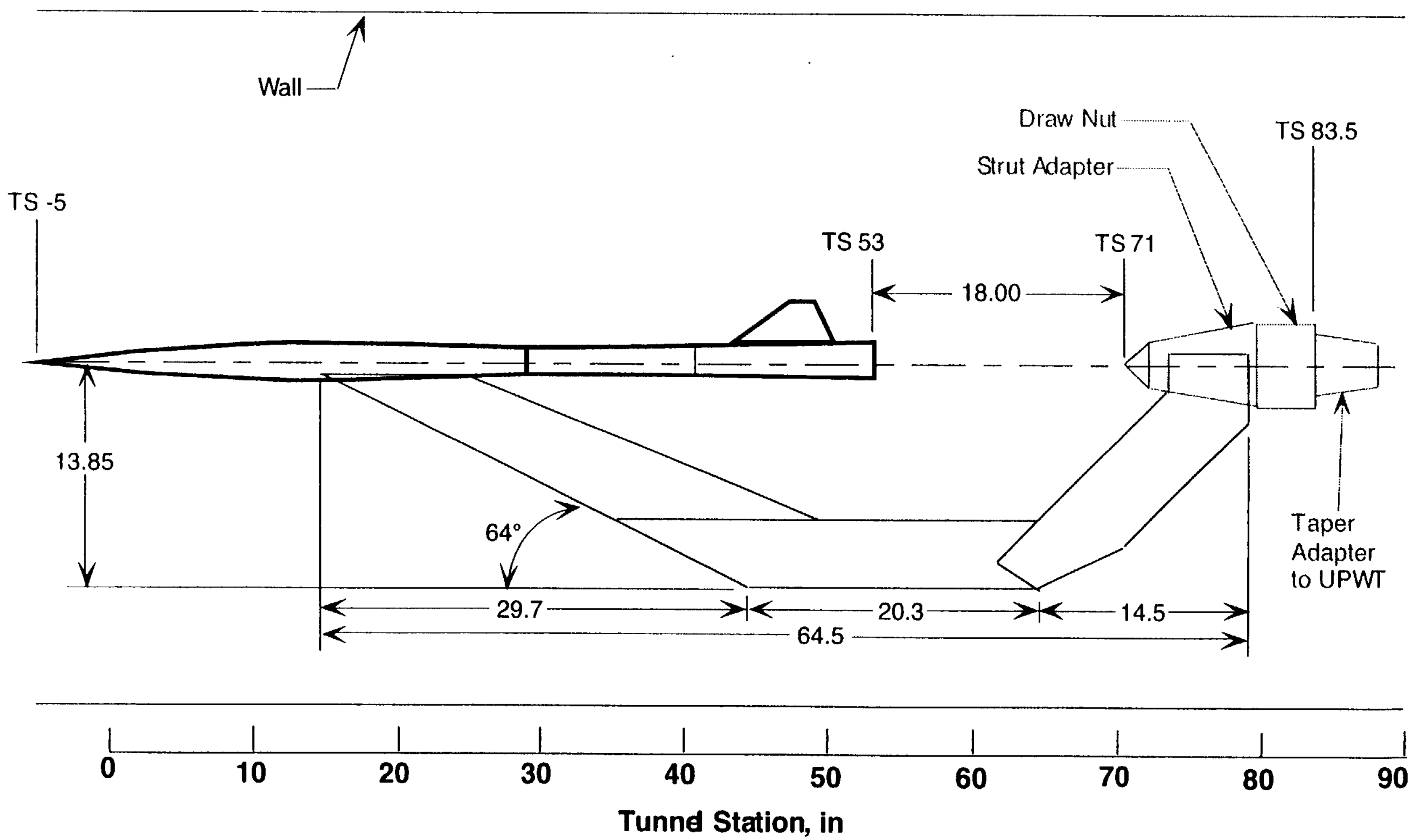

Flared Aftbody Configuration in UPWT

A side-view photograph of the flared aftbody configuration with dummy sting attached is shown in this figure. The front end of the dummy sting is located inside the base cavity but does not make contact with the model so that the aftbody balance measurements would not be compromised. As shown in this figure, the dummy sting is held in place by attachment of its downstream end to the permanent model support equipment of the tunnel.

Flared Aftbody Configuration in UPWT

Dummy Sting for Flared Aftbody

For some runs the model was placed at sideslip angles by rotating it about the attachment point to the blade sting on the forebody part of the model. Because it did not rotate with the model, the dummy sting could be used only at zero sideslip angle. This figure shows photographs of the flared aftbody configuration with and without the dummy sting attached. Note the pressure tube running along the dummy sting into the base cavity of the model. For the majority of the test this was the only method used to measure the pressures inside the cavity. Thus base cavity pressures were not measured on runs where the dummy sting was not used. This deficiency was addressed toward the end of the test, as will be discussed in a later figure.

Dummy Sting for Flared Aftbody

sting on

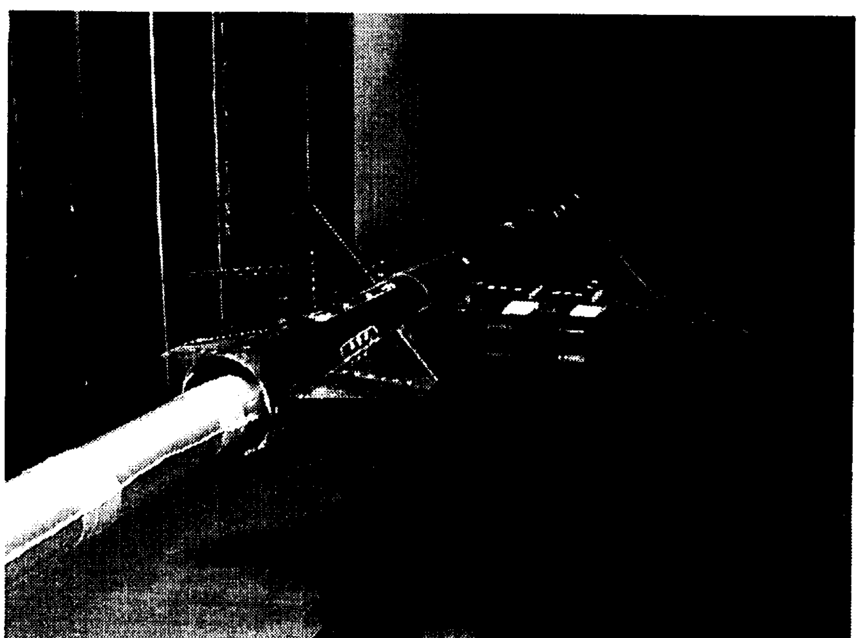

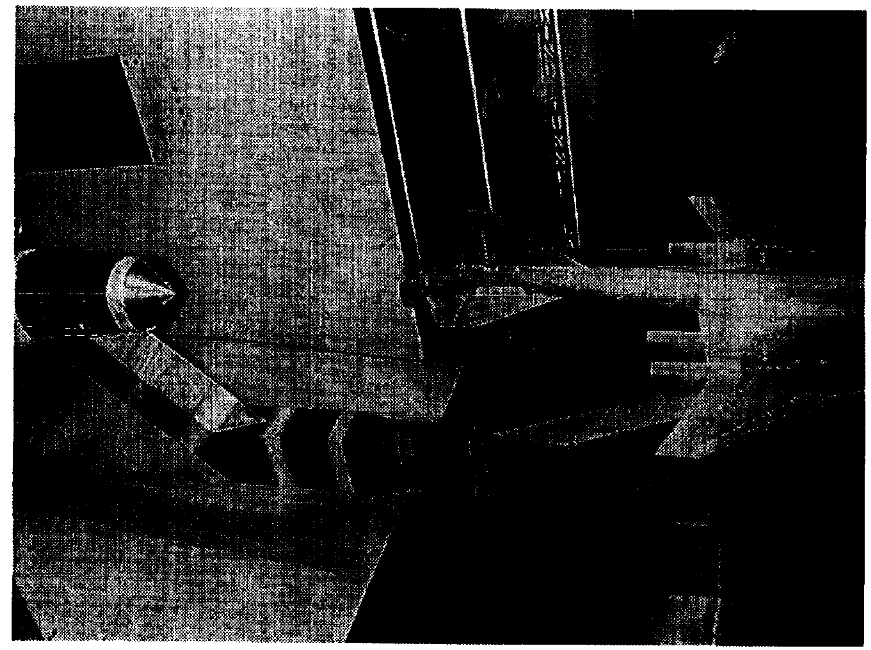

sting off

Baseline Closed Tail

A photo of the baseline closed aftbody is shown in this figure. Since the closed configurations had no base cavity, there was never any need to use the dummy sting with these configurations. This figure also highlights the metric break which isolated the aftbodies from the rest of the configuration. The white area seen in the gap at the metric break is a very thin piece of Teflon tape that was inserted in groves that were cut in the facing surfaces. This tape was designed to inhibit airflow into the metric break area while not fouling the balance measurements. This tape was used on all configurations for force and moment runs.

Baseline Closed Tail

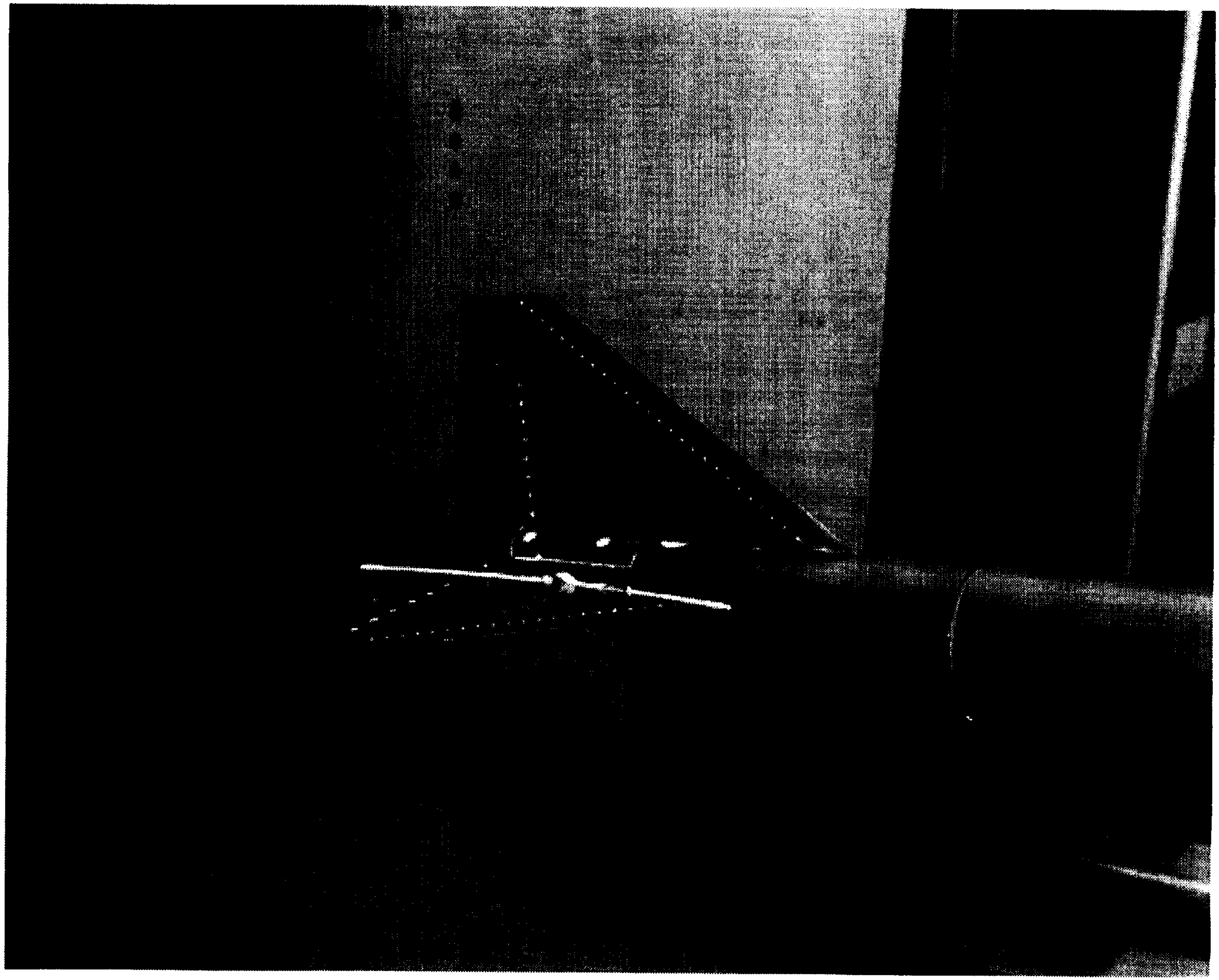

Comparison of Aftbodies

Side-by-side photographs of the three aftbody configurations are shown in this figure in both top and side views. No tails are attached on either aftbody; however, the modified aftbody is in its tails-off running configuration - a vertical-tail-off block is attached and the horizontal tail mounting holes have been filled. The basic purpose of the modified aftbody was to provide larger flat surfaces on the sides of the aftbody to prevent unporting of the horizontal tails. The differences in the two closed aftbodies seems small from the top view of the aftbodies in this figure, but is clearly seen in the side view.

Comparison of Aftbodies

Top View

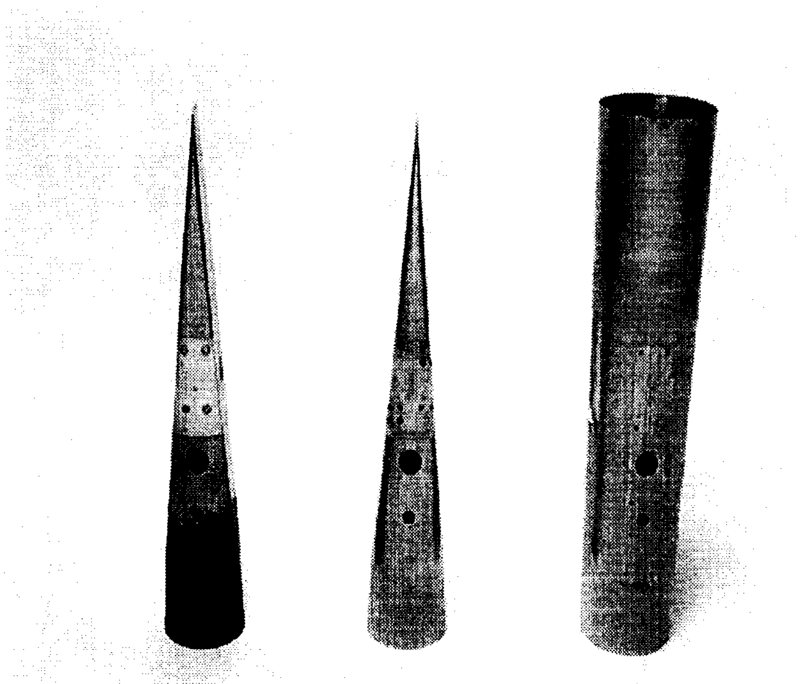

Modified Baseline Flared

Side View

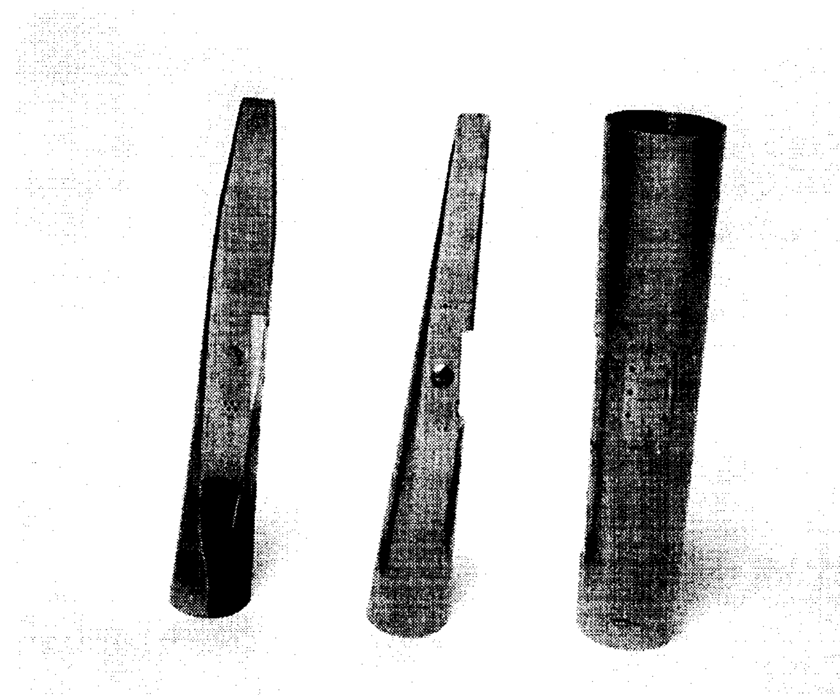

Modified Baseline Flared

Comparison of Baseline and Modified Aftbodies

The unporting of the horizontal tails on the two closed aftbodies is illustrated in the drawings in this figure, where the tails are shown at +4 deg. incidence. The top-view drawings at the bottom of this figure show the gap that is created between the tail root chord and the baseline aftbody fuselage. The size of this gap increases with tail incidence angle due to the curvature of the aftbody. The gap is been to be virtually eliminated for the modified aftbody due to the larger flat surface on the fuselage.

Comparison of Baseline and Modified Aftbody

Horizontal Tail δ_{HT}=4° (2° FRP)

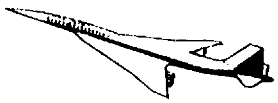

High Speed Aerodynamics, Long Beach

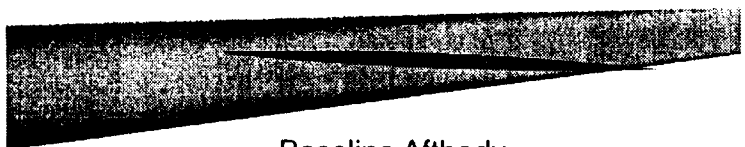

Baseline Aftbody

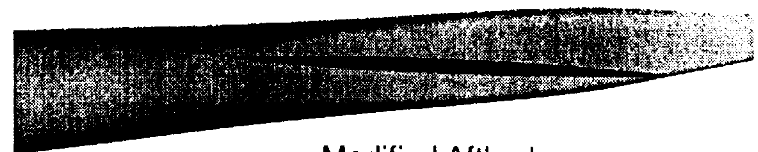

Modified Aftbody

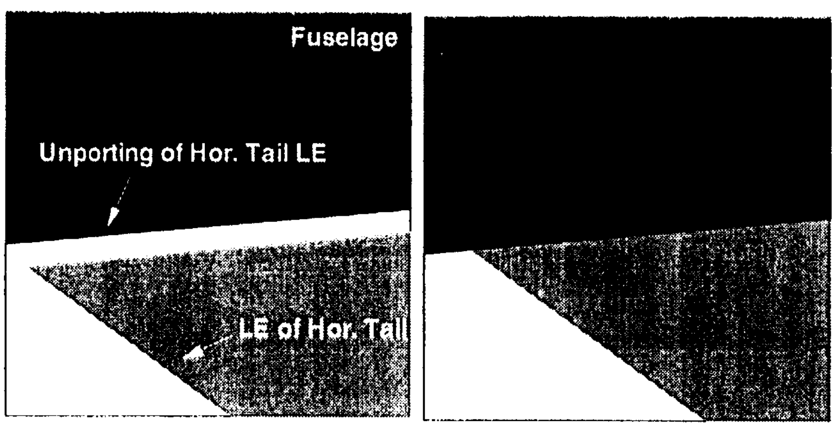

Baseline

Modified

Top View of Hor. Tail LE (zoomed)

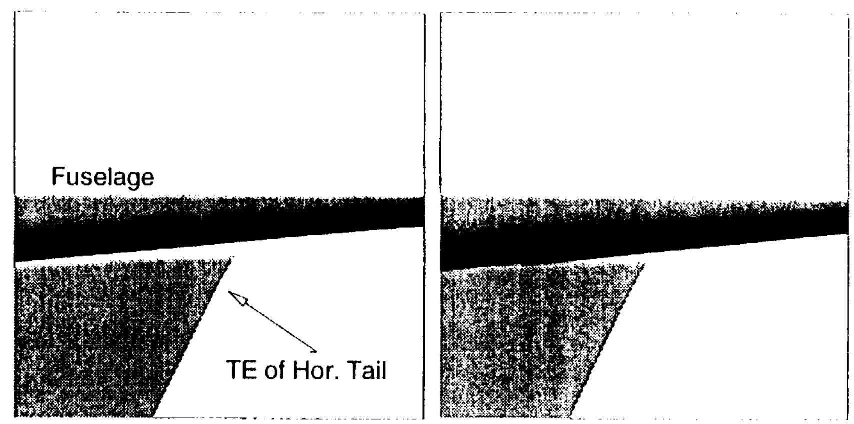

Baseline

Modified

Top View of Hor. Tail TE

BOEING

Aftbody Streamwise Sections

This figure shows longitudinal cuts at the centerline of both the flared and closed aftbodies to show how the balance was attached to the metric and non-metric parts of the model. Note that the drawing is not to scale downstream of the metric break (the base cavity on the flared aftbody is much deeper than it appears here). There are three distinct internal cavities on this model on which pressures could act. One is from the nose of the model to the upstream face of the balance mounting block. The second is in the metric break region. And the third is in the base cavity region (flared aftbody only). The first cavity lies entirely in the nonmetric part of the configuration; therefore the pressures in this cavity have no effect on the balance measurements. Pressures on the later two cavities, however, act on the metric aftbody and therefore have to be accounted for when correcting the measured drag. In this test the pressure in the metric-break cavity was measured for all runs; however, the base cavity pressures on the flared aftbody were measured initially only when the dummy sting was used. This created an issue that had to be resolved to get accurate drag data on the flared aftbody. This issue was addressed by having several runs at the end of the test that were dedicated to measuring the base cavity pressures without the dummy sting. This was done as shown in the next figure.

Aftbody Streamwise Sections

Flared Aftbody

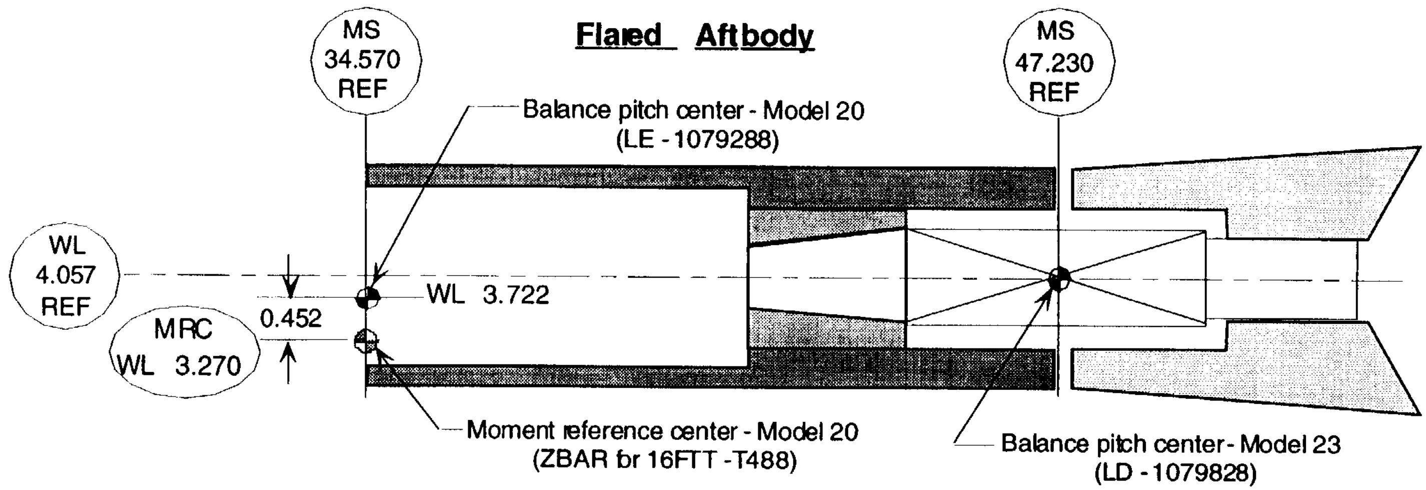

TCA and Modified Aftbodies

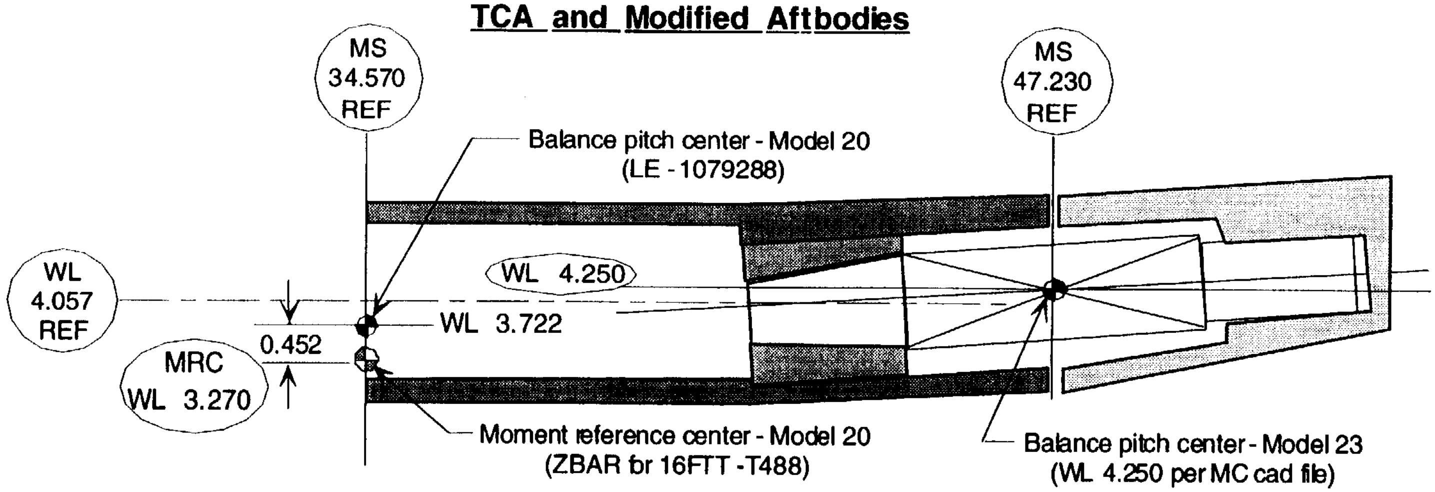

Measuring Base Cavity Pressures without Sting

This figure shows a rear view of the flared aftbody configuration for the dedicated base pressure runs. Four pressure tubes were run down the outside of the fuselage to the base of the model and routed into the base cavity. Since these tubes bridge the metric gap, valid balance data were not recorded for these runs. Base cavity pressures were thus measured without the dummy sting being present.

Measuring Base Cavity Pressures without Sting

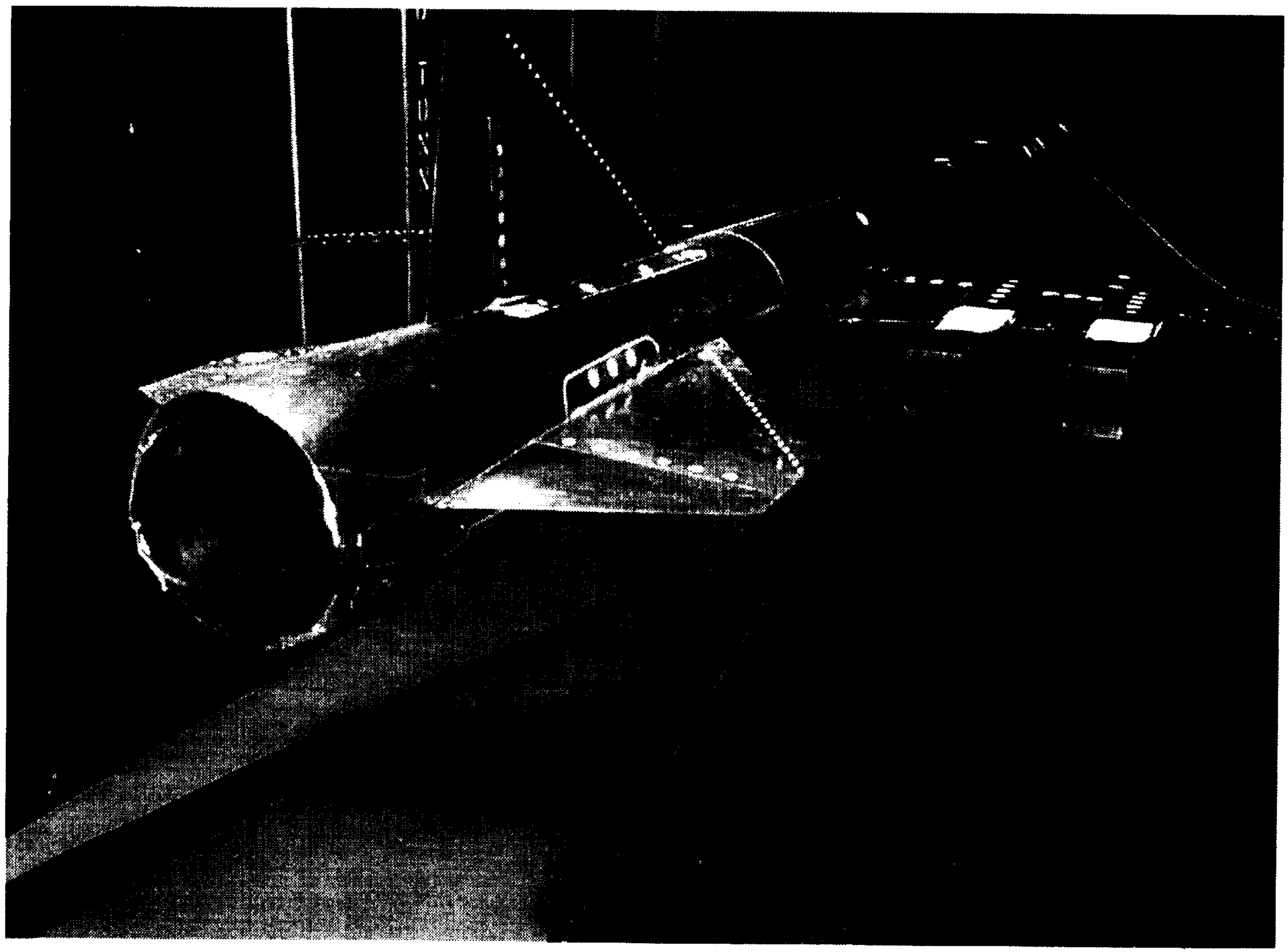

Internal Cavity Pressures

A plot of the measured pressures in the internal cavities of the flared aftbody at zero sideslip angle are shown in this figure. The pressures in the balance (metric break) cavity are near freestream static pressure, and thus have little effect on the measured drag. The pressures in the base cavity, however, are about 50% lower than freestream static. The corrections needed for these pressures had a large effect on the final drag data. In addition, this figure shows that there were small but measurable effects of the dummy sting on the base cavity pressures. The most ideal way of obtaining accurate drag on the flared aftbody configuration without the dummy sting, therefore, would be to measure base cavity pressures simultaneously with the balance measurements for all test conditions. Modifications to the model have been made to do this and will be incorporated into the upcoming test on this model at the 16-FT Transonic Tunnel at Langley.

Internal Cavity Pressures

$\beta = 0$

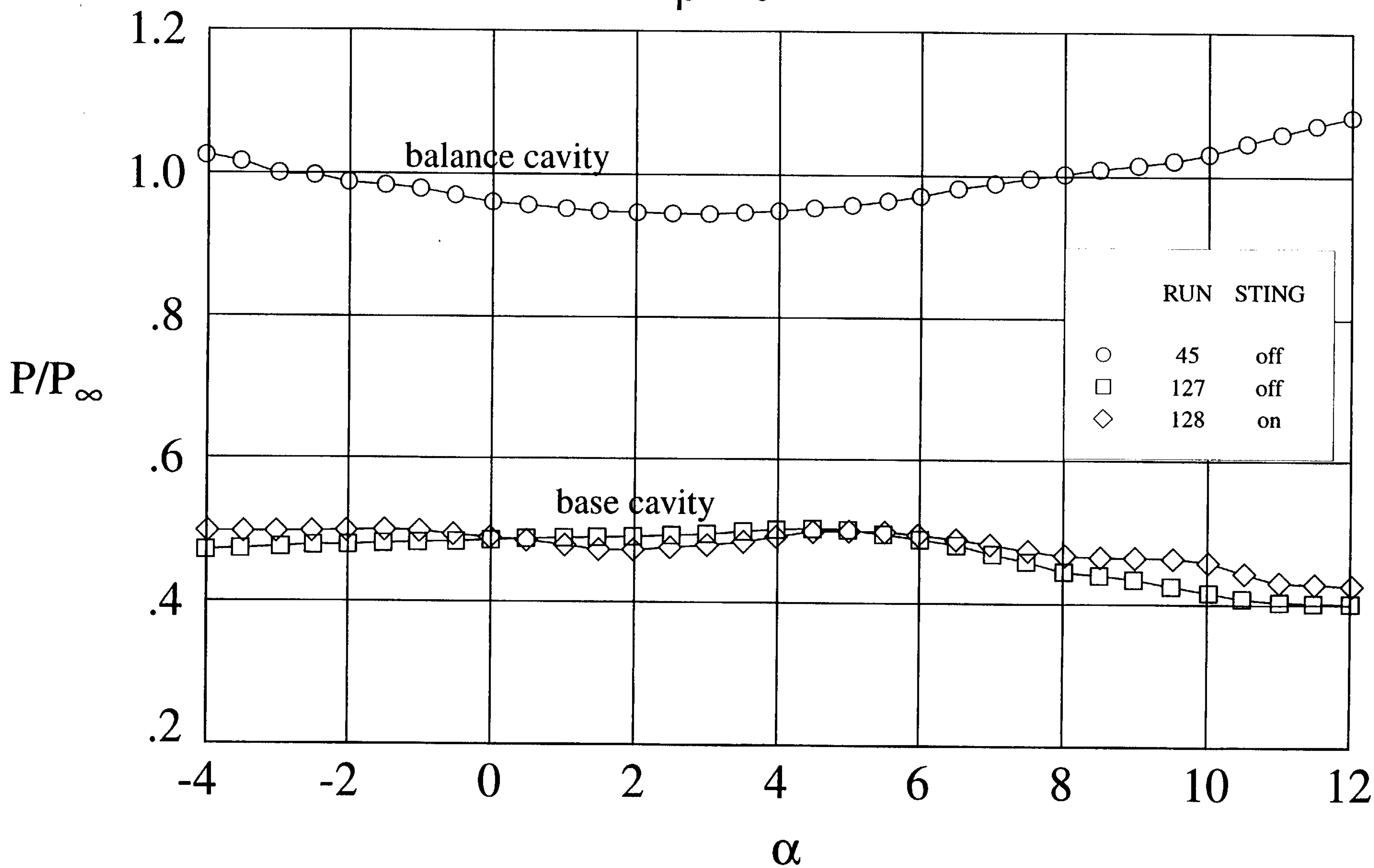

Test Highlights

A summary of the test conditions are listed in this figure. The test was conducted in June of 1998 in the high Mach number test section of the Langley Unitary Plan Wind tunnel, and covered a duration of about 7.5 weeks of one-shift operation. All data were taken at a Mach number of 2.4 and a Reynolds number of 4 million per foot. A total of 104 runs were made, and the figure shows the run breakdown for each configuration Most of the data were aftbody force and moment runs, which were all pitch sweeps at angles of attack up to 12 deg, at sideslip angles of 0, 3, and 6 deg. A few runs were made on a pressure instrumented version of the baseline closed aftbody. Also, some limited UV and colored oil runs were made.

Test Highlights

Tunnel: LaRC UPWT TS# 2

Dates: May 4 - June 24, 1998 (7.5 weeks)

Mach Number: 2.4

Reynolds Number: 4 million per foot

Aftbodies: Flared (41 Runs)
Baseline closed (38 Runs)
Modified closed (20 Runs)
Pressure-instrumented (5 Runs)

Data: Aftbody force and moment
Aftbody pressures
Flow viz (UV and colored oil)

Runs: 104, all pitch sweeps to $\alpha = 12°$
for $\beta=0°, \pm3°, +6°$

Performance Results

The performance portion of this report will be presented in the order listed above.

Performance Results

- Repeatability
  - Baseline aftbody (W/B, W/B/N/D/V/H configs.)
- Force & moment
  - Baseline aftbody
  - Modified aftbody
  - Flared aftbody
- Aftbody closure effects
- Trim drag
- Pressure data
- Test data comparisons with CFD

Short-Term Repeatability

1.5% TCA Model 23, Baseline Aftbody, W/B Configuration

Langley UPWT Test 1707, M_{∞}=2.4, Re=4x10^6/ft

The following charts document the repeatability of the 1.5% TCA Model 23 with the baseline aftbody. Lift versus angle-of-attack and drag versus angle-of-attack are presented. Throughout the range of angles-of-attack, the lift is repeatable within ±0.0001. The drag is generally repeatable within ±0.2 counts at a given angle-of-attack. Near the cruise condition, the drag repeatability improves to within ±0.1 count, which is equivalent to 2.5% of the total drag on the aftbody.

Short-Term Lift Repeatability

1.5% TCA Model 23, Baseline Aftbody on W/B Configuration

Langley UPWT Test 1707, M_∞=2.4, Re=4x10^6/ft (forces measured on aftbody)

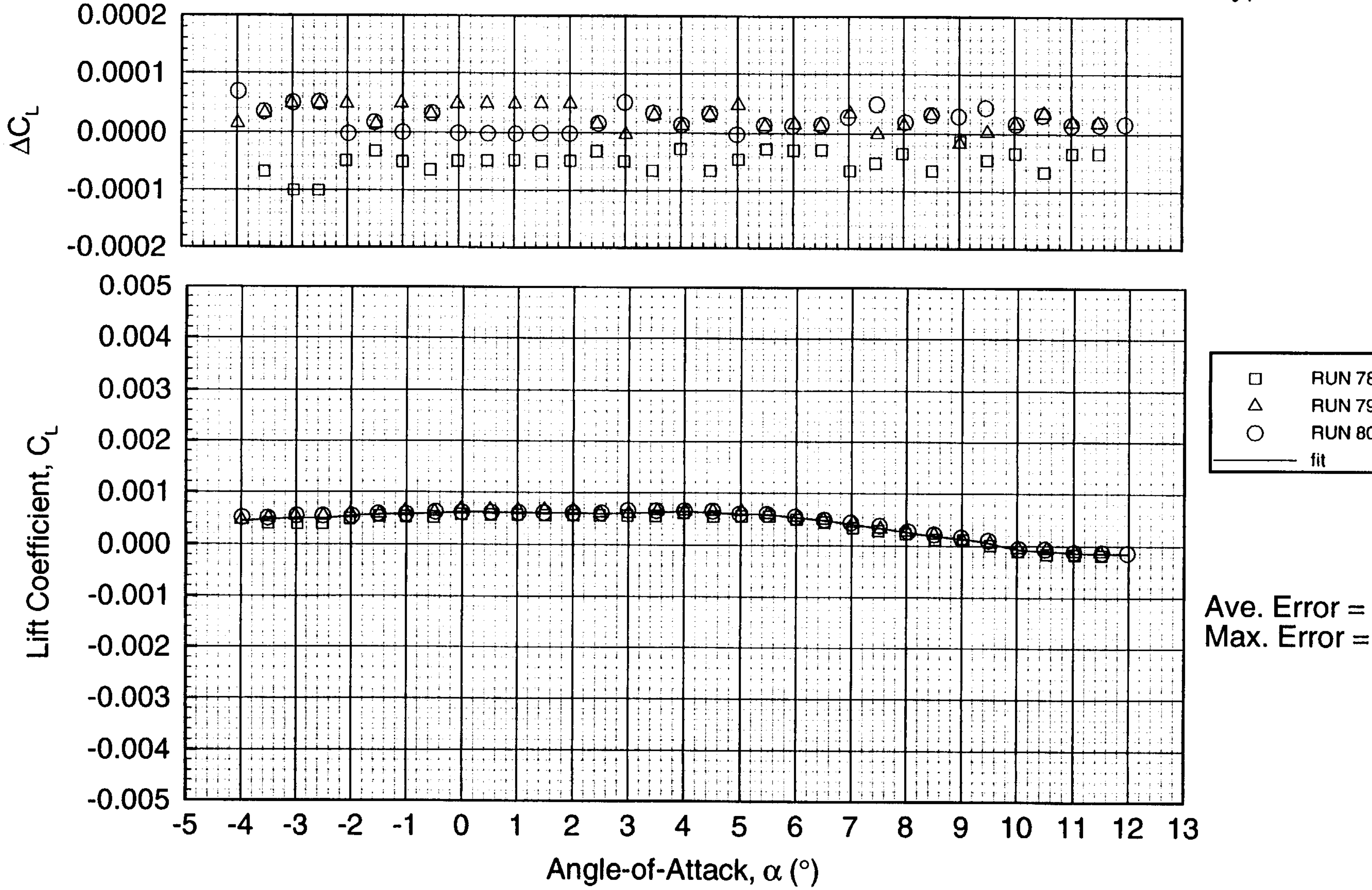

Ave. Error = 3.3×10^{-5}
Max. Error = 1.0×10^{-4}

Short-Term Drag Repeatability

1.5% TCA Model 23, Baseline Aftbody on W/B Configuration

Langley UPWT Test 1707, M_∞=2.4, Re=$4x10^6$/ft (forces measured on aftbody)

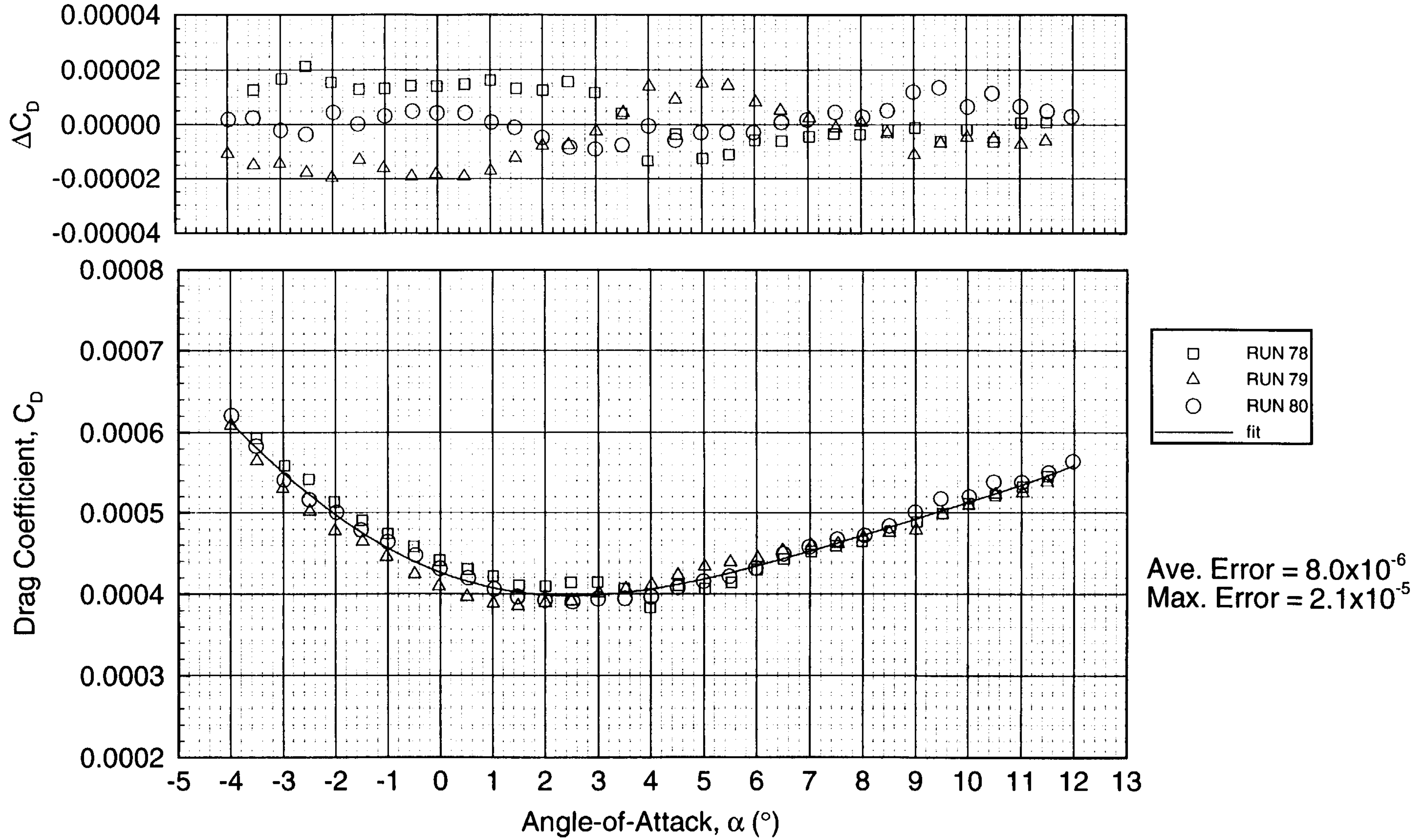

Short-Term Repeatability
1.5% TCA Model 23, Baseline Aftbody, W/B/N/D/V/H Configuration

Langley UPWT Test 1707, M_∞=2.4, Re=4x10^6/ft

The next set of figures show the short-term repeatability for the baseline aftbody with the W/B/N/D/V/H configuration (i_H=0°). Throughout the range of angles-of-attack, the lift is repeatable within ±0.0001. Excellent repeatability is seen in the aftbody drag throughout the alpha sweep. Near the cruise condition, the drag repeatability is ±0.10 count.

Short-Term Lift Repeatability

1.5% TCA Model 23, Baseline Aftbody on W/B/N/D/V/H Configuration (i_H=0°)
Langley UPWT Test 1707, M_∞=2.4, Re=4x10^6/ft (forces measured on aftbody)

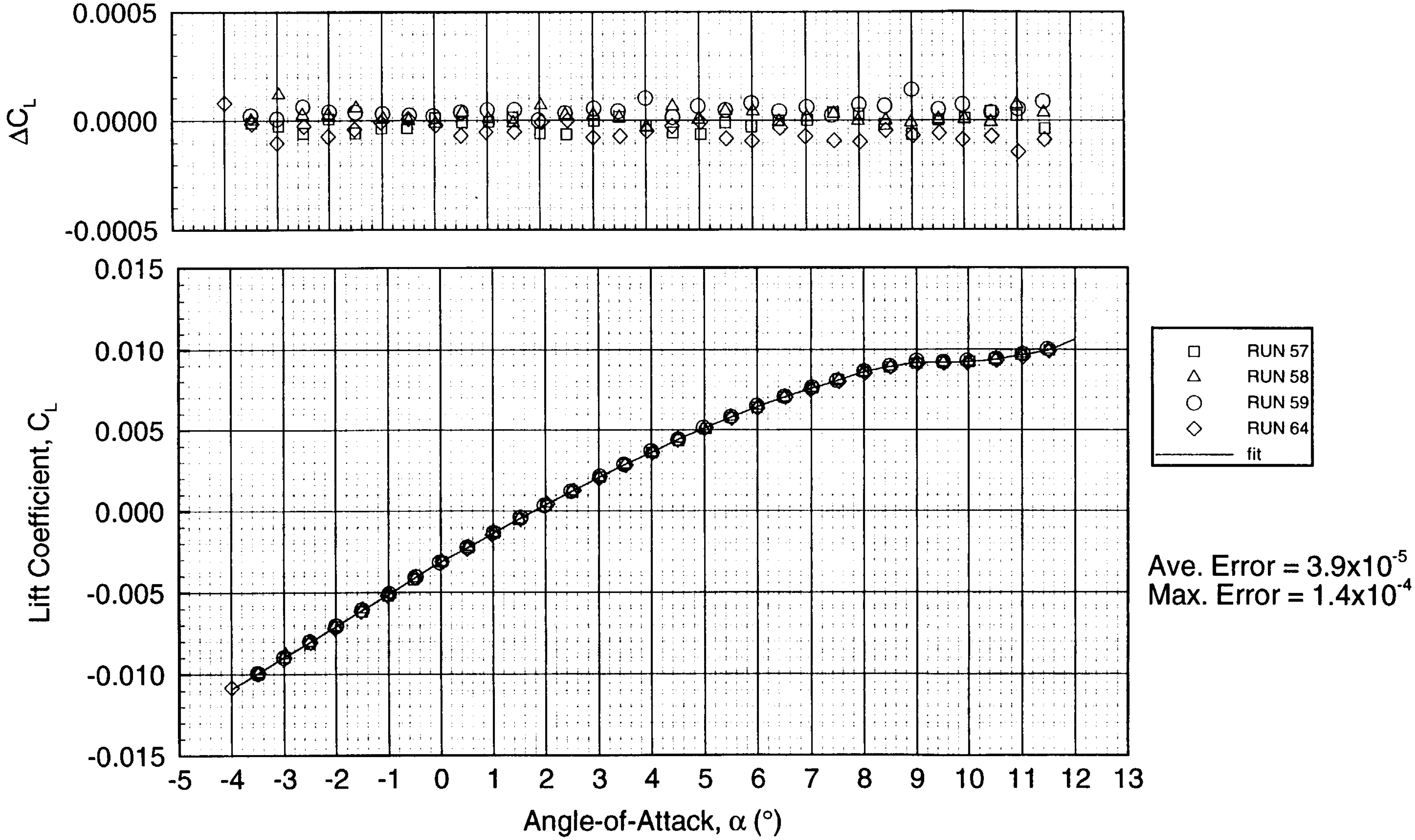

Short-Term Drag Repeatability

1.5% TCA Model 23, Baseline Aftbody on W/B/N/D/V/H Configuration (i_H=0°)
Langley UPWT Test 1707, M_∞=2.4, Re=4x10^6/ft (forces measured on aftbody)

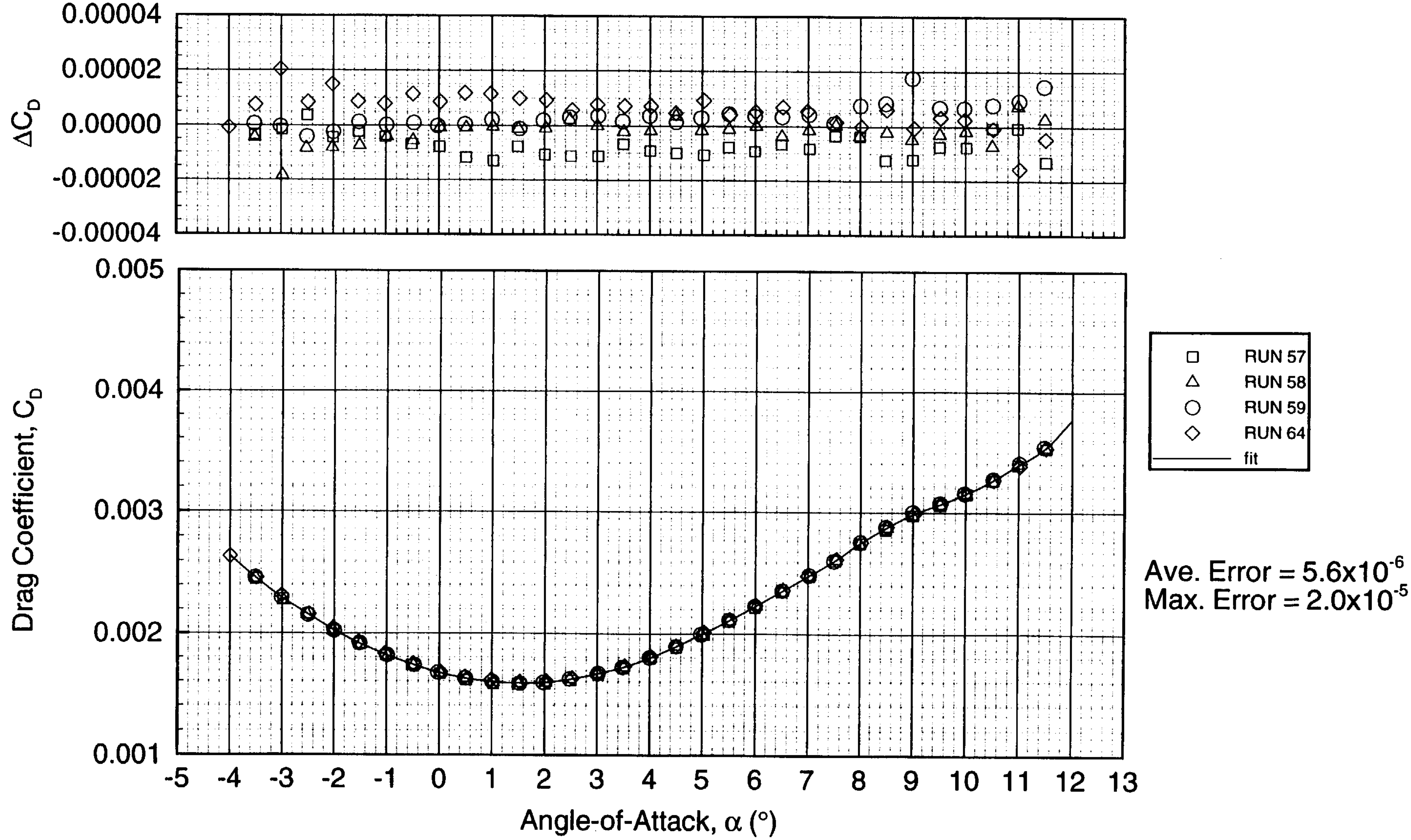

TCA Baseline Aftbody Lift
1.5% TCA Model 23

The next few charts present a build-up for the baseline aftbody. Six configurations are shown: W/B, W/B/N/D, W/B/N/D/V, W/B/N/D/H, W/B/V/H, and W/B/N/D/V/H. It is evident that without the horizontal stabilizers, the aftbody generates little or no lift. Adding nacelles to the W/B/E configuration increases the aftbody lift-curve slope, while adding the nacelles to the W/B configuration shows little sensitivity. The W/B/N/D/H configuration generates the most lift on the aftbody at $\alpha=3.5°$. The addition of the vertical stabilizer at $\alpha=3.5°$, reduces the C_L by 0.0002 and 0.0003 for the W/B/N/D and the W/B/N/D/H configurations, respectively.

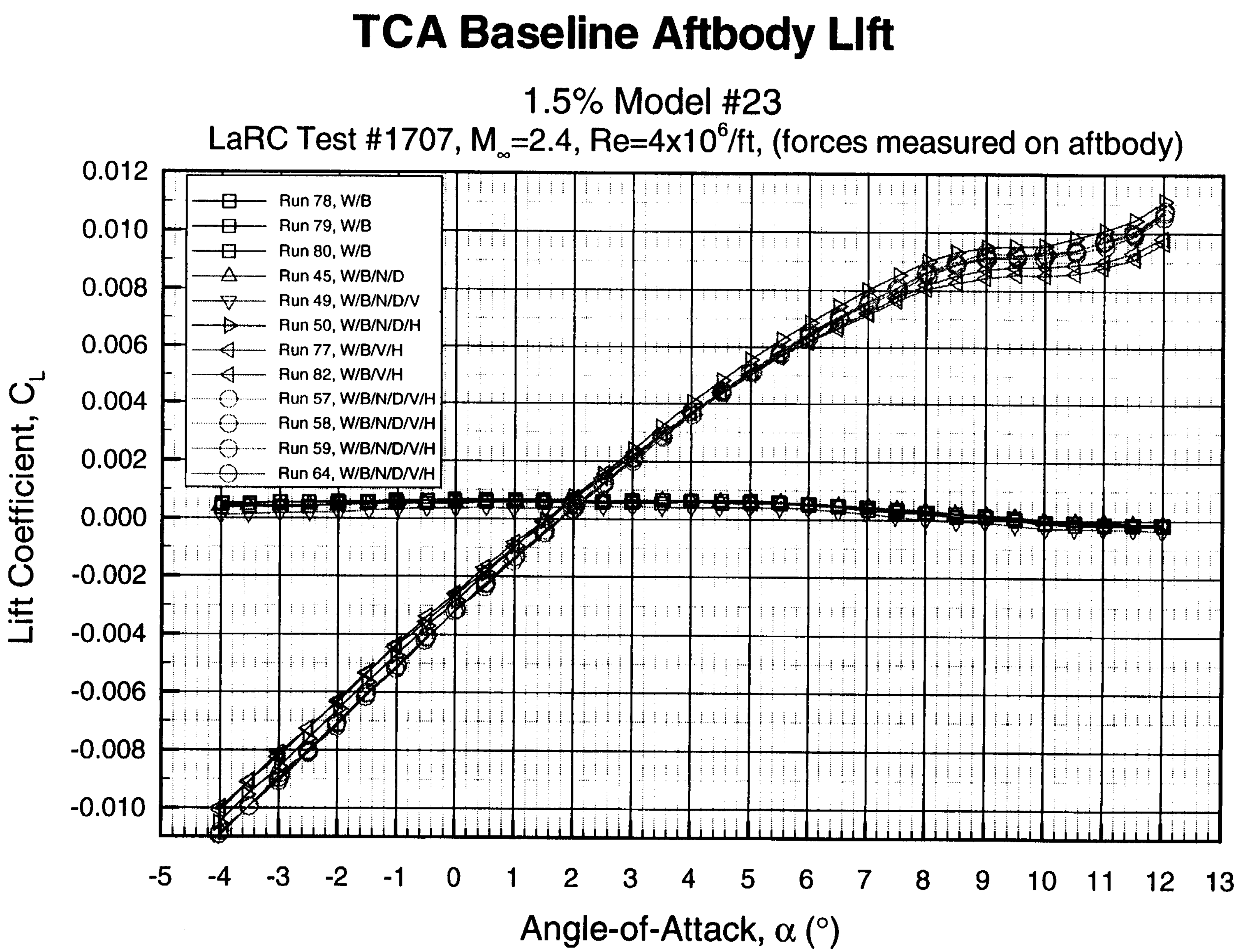

TCA Baseline Aftbody LIft
1.5% Model #23
LaRC Test #1707, M∞=2.4, Re=4x10^6/ft, (forces measured on aftbody)
Run 78, W/B
Run 79, W/B
Run 80, W/B
Run 45, W/B/N/D
Run 49, W/B/N/D/V
Run 50, W/B/N/D/H
Run 77, W/B/V/H
Run 82, W/B/V/H
Run 57, W/B/N/D/V/H
Run 58, W/B/N/D/V/H
Run 59, W/B/N/D/V/H
Run 64, W/B/N/D/V/H
Lift Coefficient, C_L
0.012
0.010
0.008
0.006
0.004
0.002
0.000
-0.002
-0.004
-0.006
-0.008
-0.010
-5
-4
-3
-2
-1
0
1
2
3
4
5
6
7
8
9
10
11
12
13
Angle-of-Attack, α (°)

TCA Baseline Aftbody Drag
1.5% TCA Model 23

The aftbody drag for the six baseline configurations tested are presented below. At α=3.5°, the aftbody drag for the W/B and W/B/N/D configurations are approximately 4.0 counts. Addition of the nacelles on the W/B/E increases drag by 0.7 counts at α=3.5°. The addition of the vertical stabilizer increases the drag by 4.2 and 4.4 counts for the W/B/N/D and W/B/N/D/H configurations, respectively. The horizontal stabilizers increase the aftbody drag by 8.6 and 8.8 counts for the W/B/N/D and W/B/N/D/V configurations, respectively. The minimum aftbody drag occurs at $\alpha\cong$1.5° for all the horizontal stab-on configurations. Although the test data has not been corrected for the trip drag, the correction is expected to be small compared to the total aftbody drag.

TCA Baseline Aftbody Drag

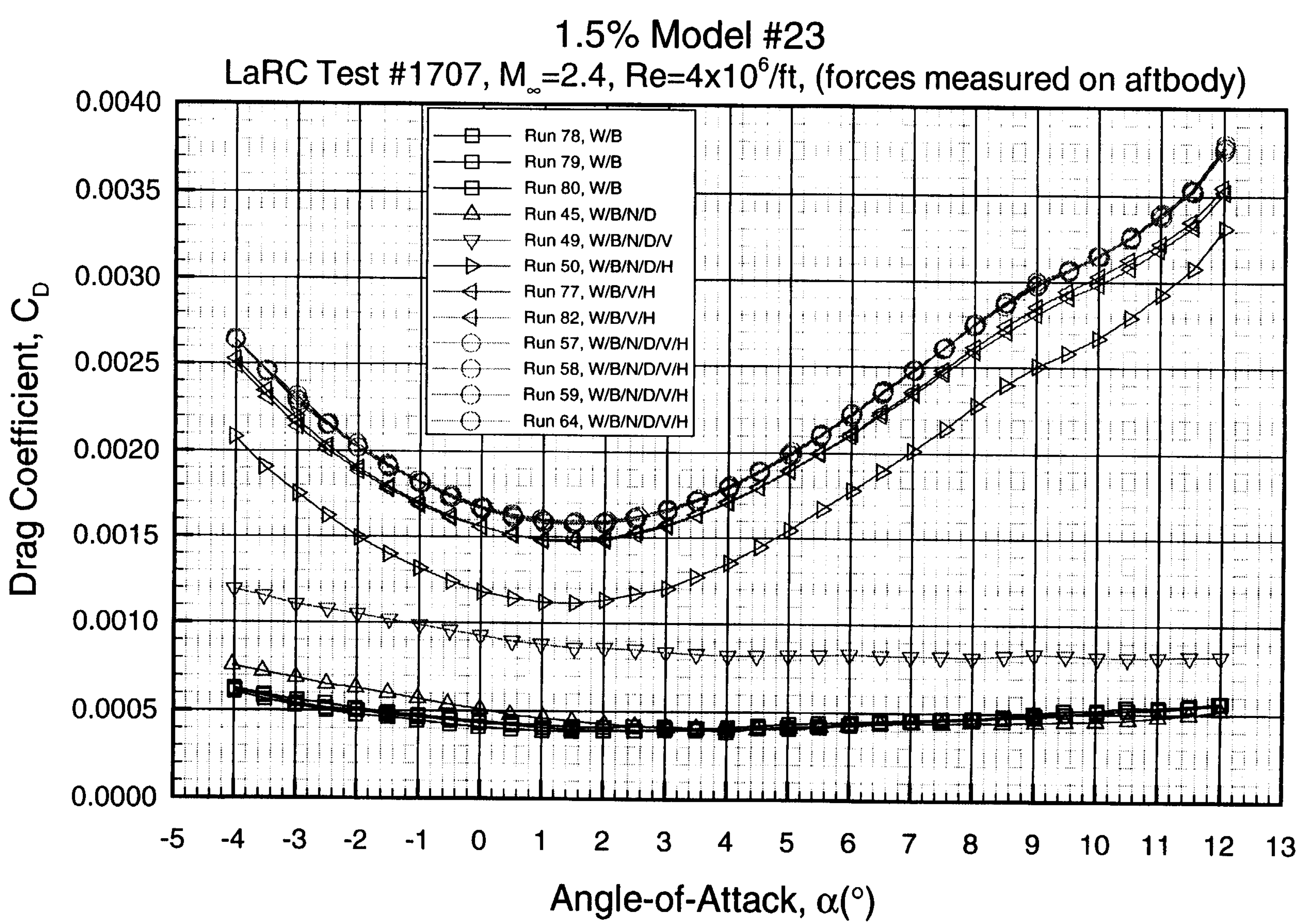

TCA Baseline Aftbody Pitching Moment
1.5% TCA Model 23

All configurations without the horizontal stabilizers have a small negative (nose-down) pitching moment, while the horizontal stab-on runs show a stable aftbody up to 9° angle-of-attack. The addition of the nacelles on the W/B/E decreases the C_M slope producing a slightly more stable aftbody. The vertical stabilizer increases the pitching moment for both the W/B/N/D and W/B/N/D/H configurations.

TCA Baseline Aftbody Pitching Moment

1.5% Model #23

LaRC Test #1707, M_∞=2.4, Re=4x10^6/ft, (forces measured on aftbody)

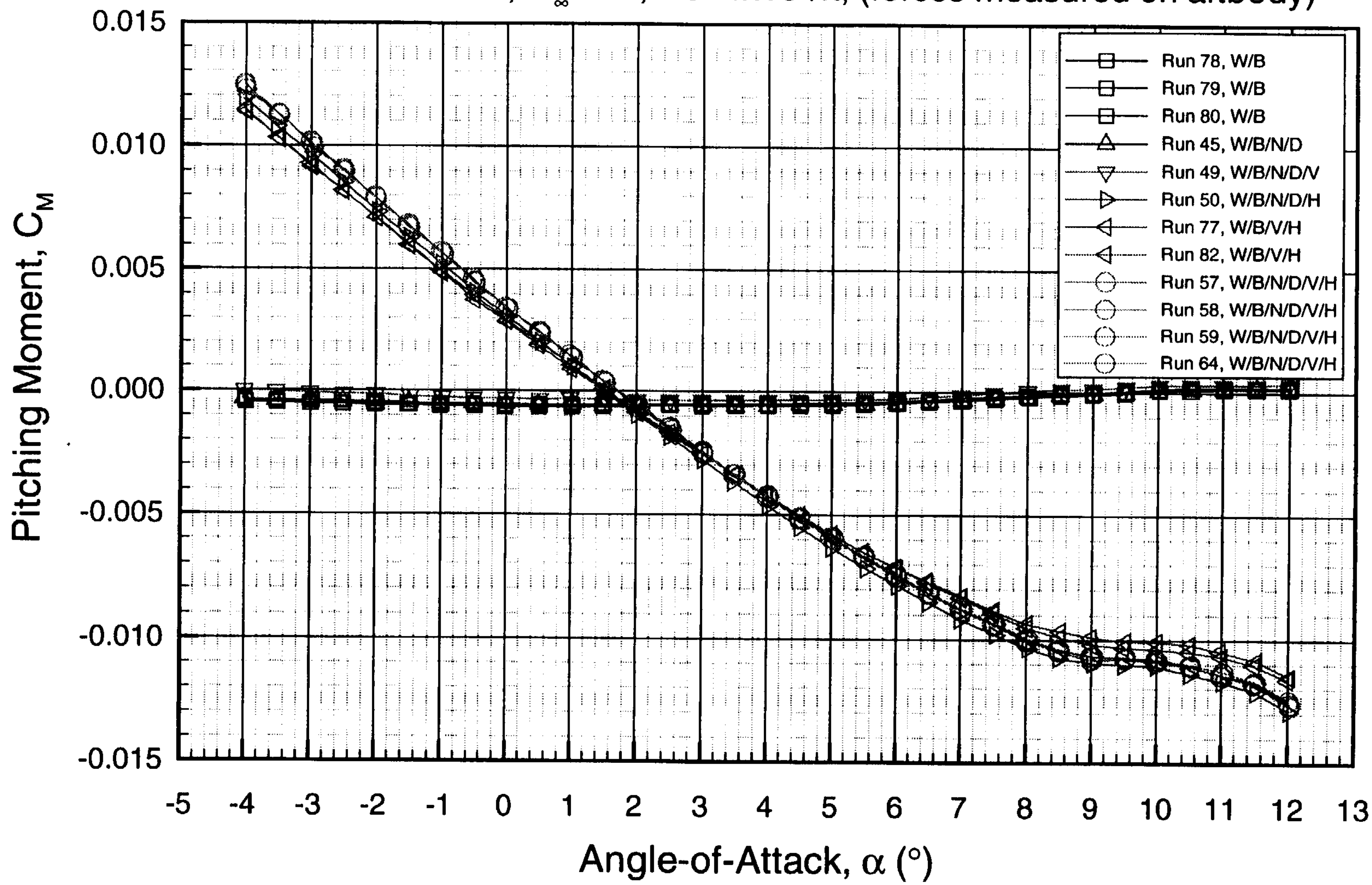

Comparison of Baseline and Flared Aftbody Lift
1.5% TCA Model 23, W/B/N/D/V/H Configuration, $i_H = 0°$

The baseline and flared abodes are compared in this section. The lift curve comparison is shown below. The flared aftbody has a higher lift coefficient throughout the angle-of-attack range.

Lift from the TCA Baseline and Flared Aftbodies

1.5% Model #23, W/B/N/D/E configuration, $i_H=0°$

LaRC Test #1707, $M_\infty=2.4$, $Re=4\times10^6/ft$, (forces measured on aftbody)

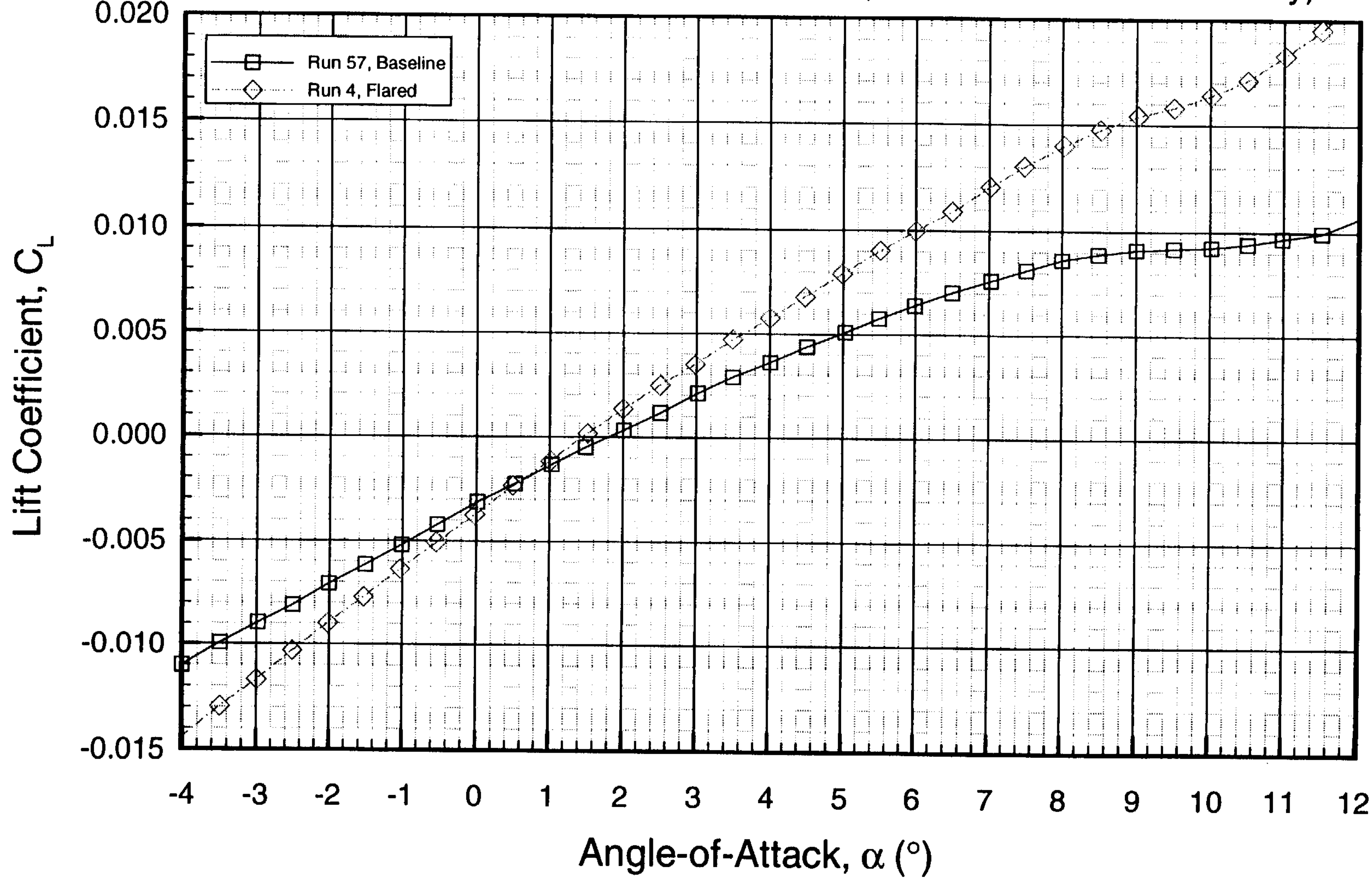

Comparison of Baseline and Flared Aftbody Drag
1.5% TCA Model 23, W/B/N/D/V/H Configuration $i_H = 0^\circ$

At α=3.5°, the flared aftbody drag is ~2 counts greater than the baseline. The difference increases with angle-of-attack.

Drag from the TCA Baseline and Flared Aftbodies

1.5% Model #23, W/B/N/D/E configuration, $i_H=0°$

LaRC Test #1707, $M_\infty=2.4$, $Re=4x10^6/ft$, (forces measured on aftbody)

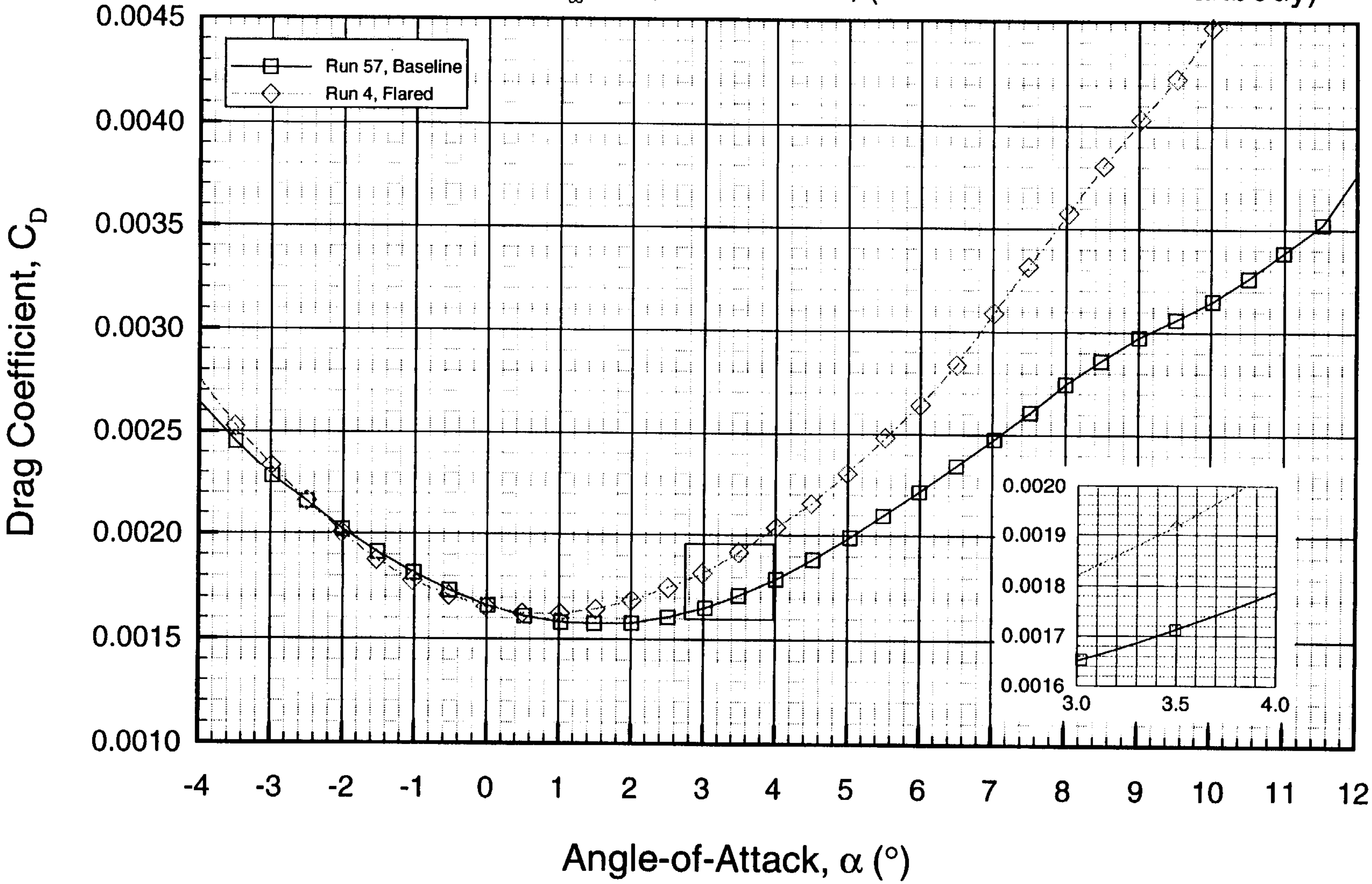

Comparison of Baseline and Flared Aftbody Pitching Moment
1.5% TCA Model 23, W/B/N/D/V/H Configuration $i_H = 0°$

The baseline aftbody shows a considerable reduction in longitudinal stability compared to the flared aftbody.

Pitching Moment from the TCA Baseline and Flared Aftbodies

1.5% Model #23, W/B/N/D/E configuration, $i_H=0°$

LaRC Test #1707, $M_\infty=2.4$, $Re=4x10^6/ft$, (forces measured on aftbody)

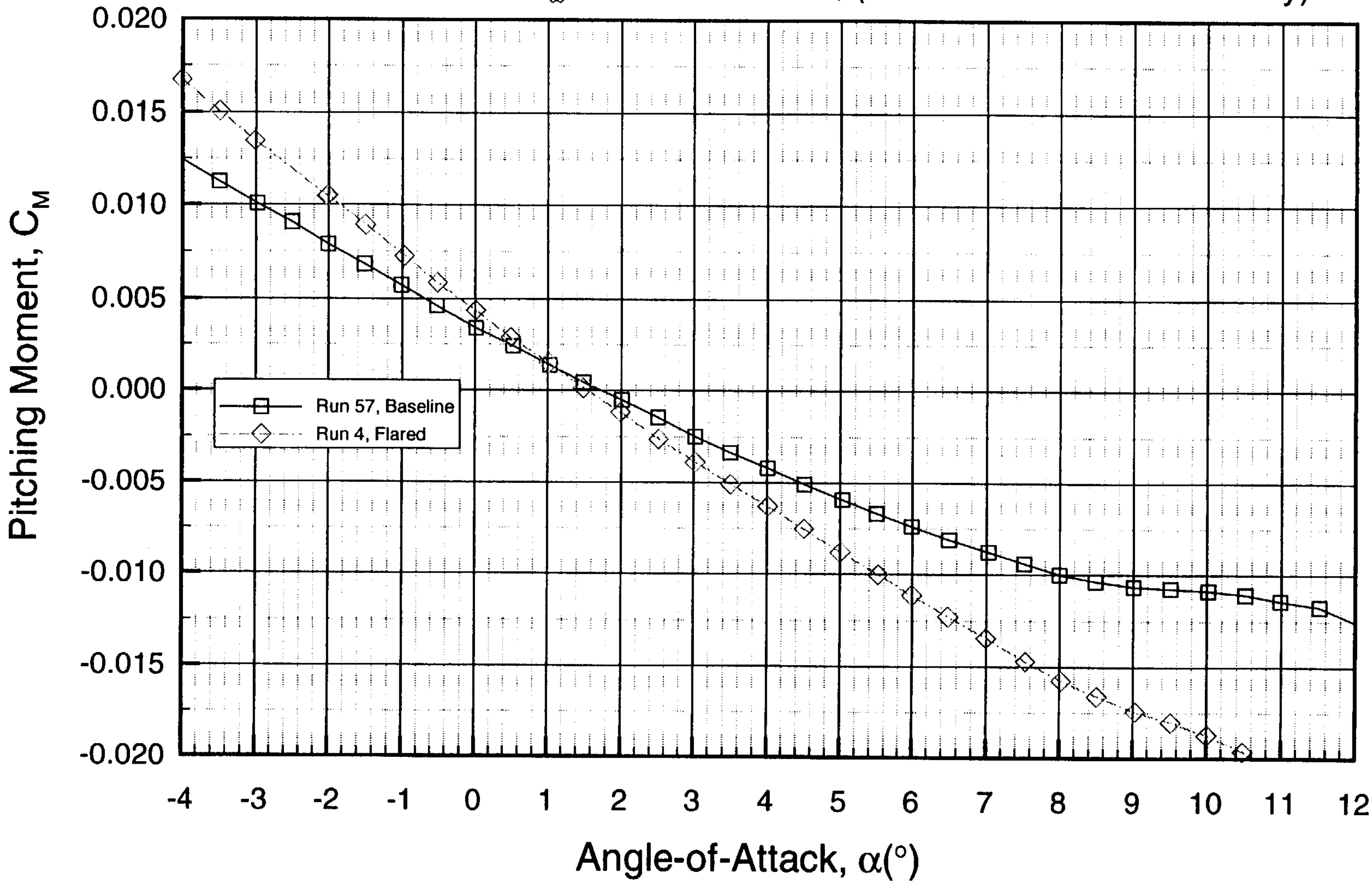

Aftbody Closure Effects
1.5% TCA Model, W/B/N/D/V/H Configuration $i_H = 0°$

This section presents the corrected and uncorrected lift curve, drag polar, and pitching moment for the 1.5% TCA Model. The uncorrected data was obtained from a previous sting-mounted test at the UPWT (Test 1677) using the flared aftbody geometry. Differences between the flared and baseline aftbodies were obtained (shown in the previous slides) and applied to the uncorrected data to obtain the corrected data. The aftbody closure effect on the lift curve is seen above. The lift-curve slope is reduced slightly. At $\alpha=3.5°$, the corrected drag is reduced ~2 counts. A C_{Dv} correction was made for the sting-mounted data since the data was obtained at $3x10^6$/ft. The increment due to aftbody geometry is shown to significantly reduce the longitudinal stability of the TCA configuration.

TCA Lift Coefficient Corrected for Aftbody Closure Effects

M_∞=2.4, 1.5% TCA Model, W/B/N/D/V/H configuration, i_H=0°

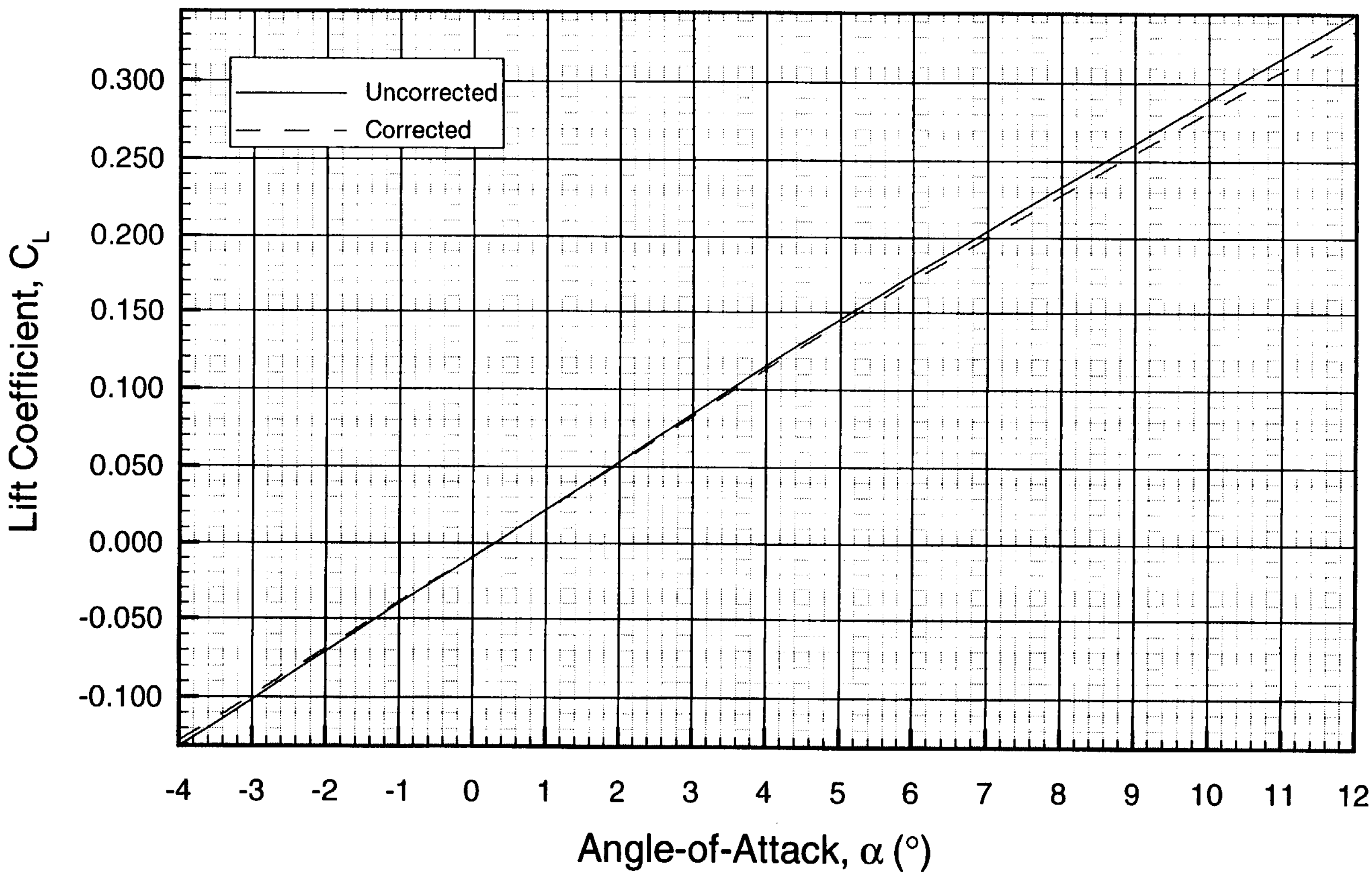

TCA Drag Coefficient Corrected for Aftbody Closure Effects

1.5% TCA Model, W/B/N/D/V/H configuration, $i_H=0°$

$M_\infty=2.4$, $Re=4 \times 10^6/ft$

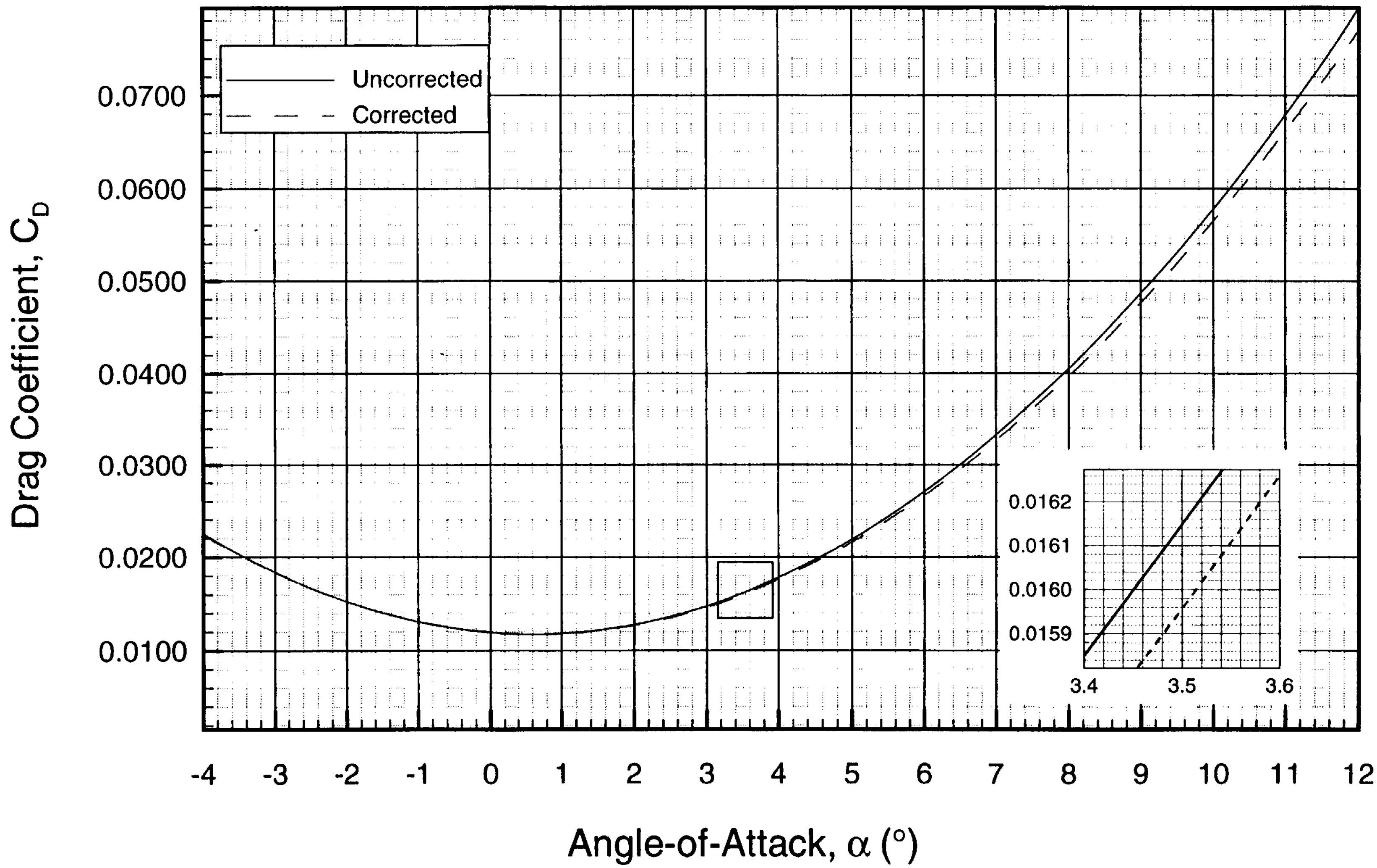

TCA Pitching Moment Coefficient Corrected for Aftbody Closure Effects

M_∞=2.4, 1.5% TCA Model, W/B/N/D/V/H configuration, i_H=0°

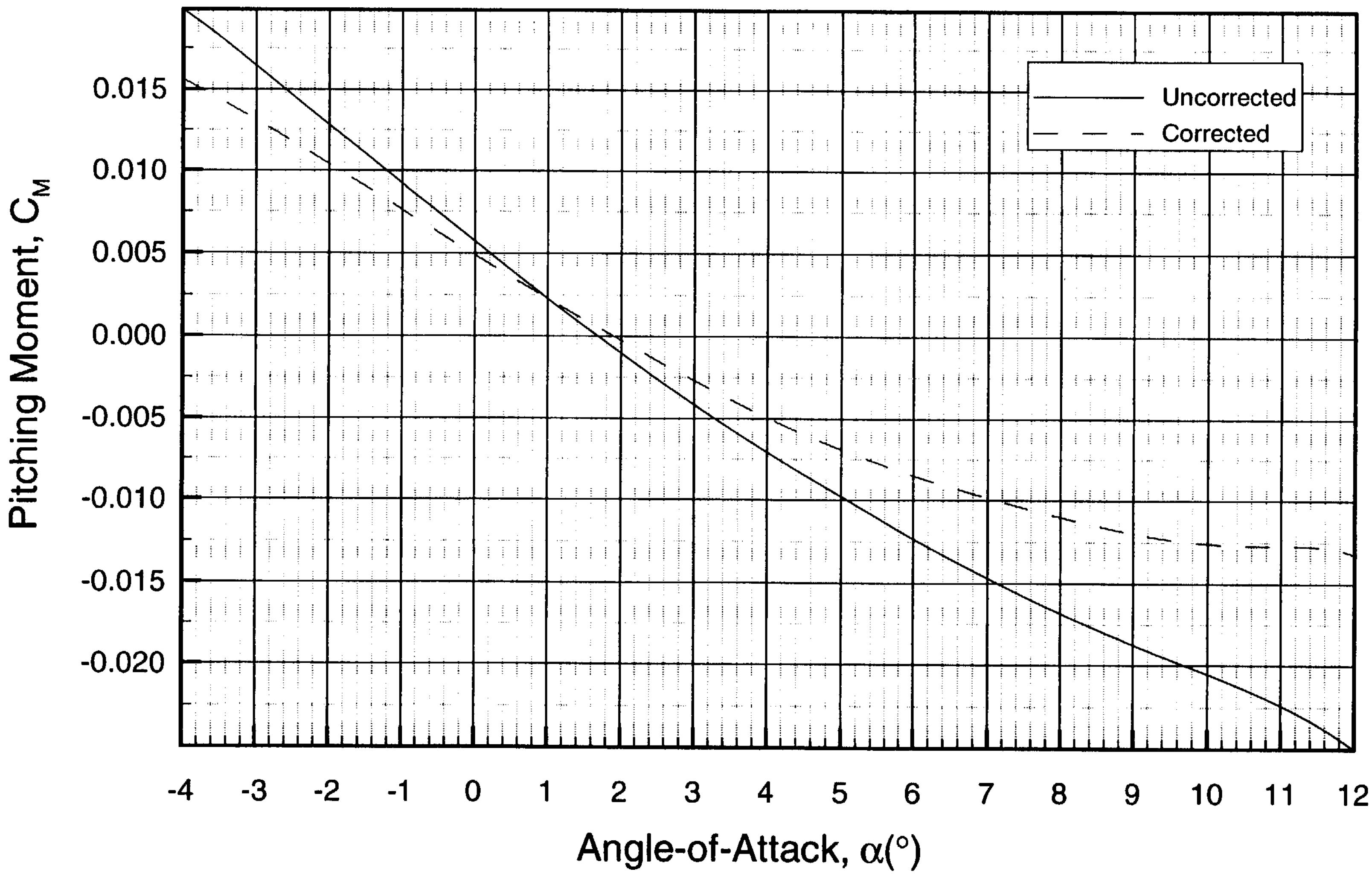

Aftbody Contribution to Full Aircraft Forces at 1.5% TCA Model 23, Baseline Aftbody on W/B/N/D/V/H Configuration $i_H = 0°$

The baseline aftbody drag and lift contribution to the full configuration is 10% and 3%, respectively. The full configuration forces were obtained from a previous sting-mounted test at the UPWT (Test 1677) with the aftbody closure effects obtained in Test 1707 corrected to the data.

Aftbody Contribution to Full Aircraft Forces (α=3.5°)

M_∞=2.4, β=0°, i_H=0°, Re=4x10^6/ft

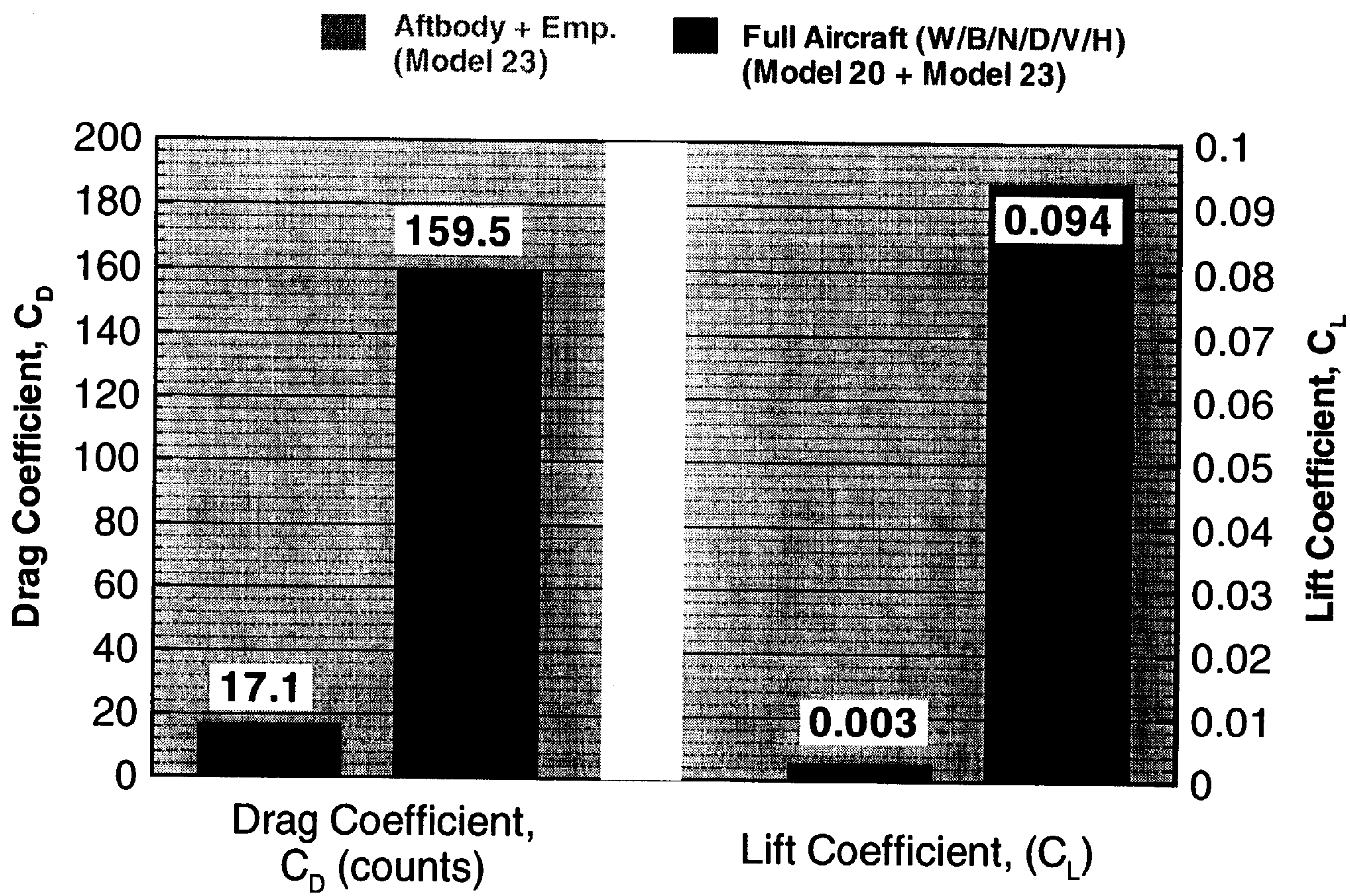

*** Trip drag not removed from test data**

Comparison of Baseline and Modified Aftbody Lift
1.5% TCA Model 23, W/B/N/D/V/H Configuration $i_H = 0°$

The baseline and modified afbodies are compared in this section. The lift curve comparison is shown below. The modified aftbody has a higher lift coefficient throughout the angle-of-attack range. At α=3.5°, the modified aftbody C_L is 0.0005 higher than the baseline aftbody.

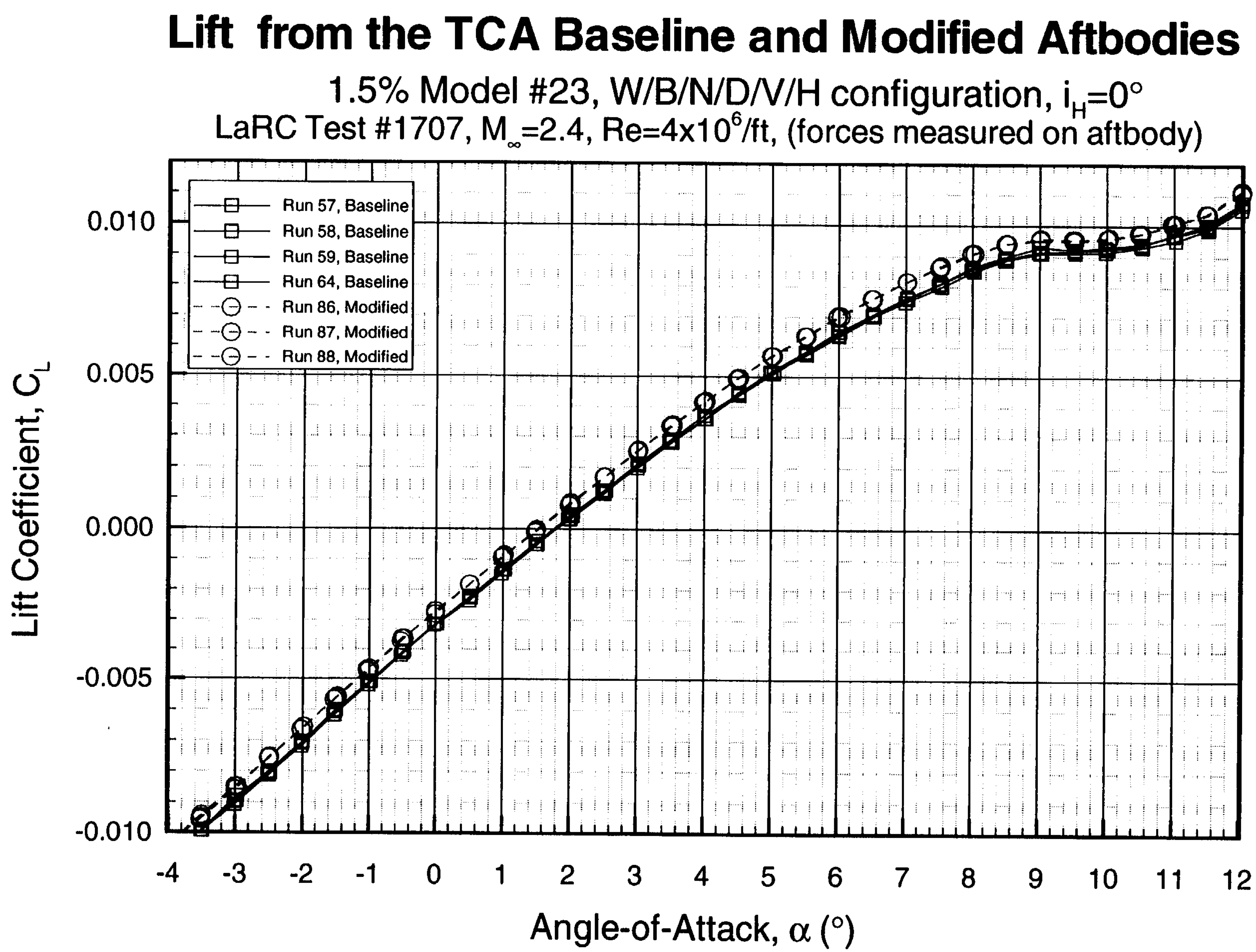

Lift from the TCA Baseline and Modified Aftbodies
1.5% Model #23, W/B/N/D/V/H configuration, i_H=0°
LaRC Test #1707, M_∞=2.4, Re=4x10^6/ft, (forces measured on aftbody)
Run 57, Baseline
Run 58, Baseline
Run 59, Baseline
Run 64, Baseline
Run 86, Modified
Run 87, Modified
Run 88, Modified
Lift Coefficient, C_L
0.010
0.005
0.000
-0.005
-0.010
-4
-3
-2
-1
0
1
2
3
4
5
6
7
8
9
10
11
12
Angle-of-Attack, α (°)

Comparison of Baseline and Modified Aftbody Drag
1.5% TCA Model 23, W/B/N/D/V/H Configuration $i_H = 0°$

At α=3.5°, the modified aftbody drag is 17.7 counts, 0.6 counts greater than the baseline. The modified aftbody has less drag from angle-of-attack –4° to 0.5, higher drag from 0.5° to 10°, and then similar

Drag from the TCA Baseline and Modified Aftbodies

1.5% Model #23, W/B/N/D/V/H configuration, $i_H=0°$

LaRC Test #1707, $M_\infty=2.4$, $Re=4x10^6$/ft, (forces measured on aftbody)

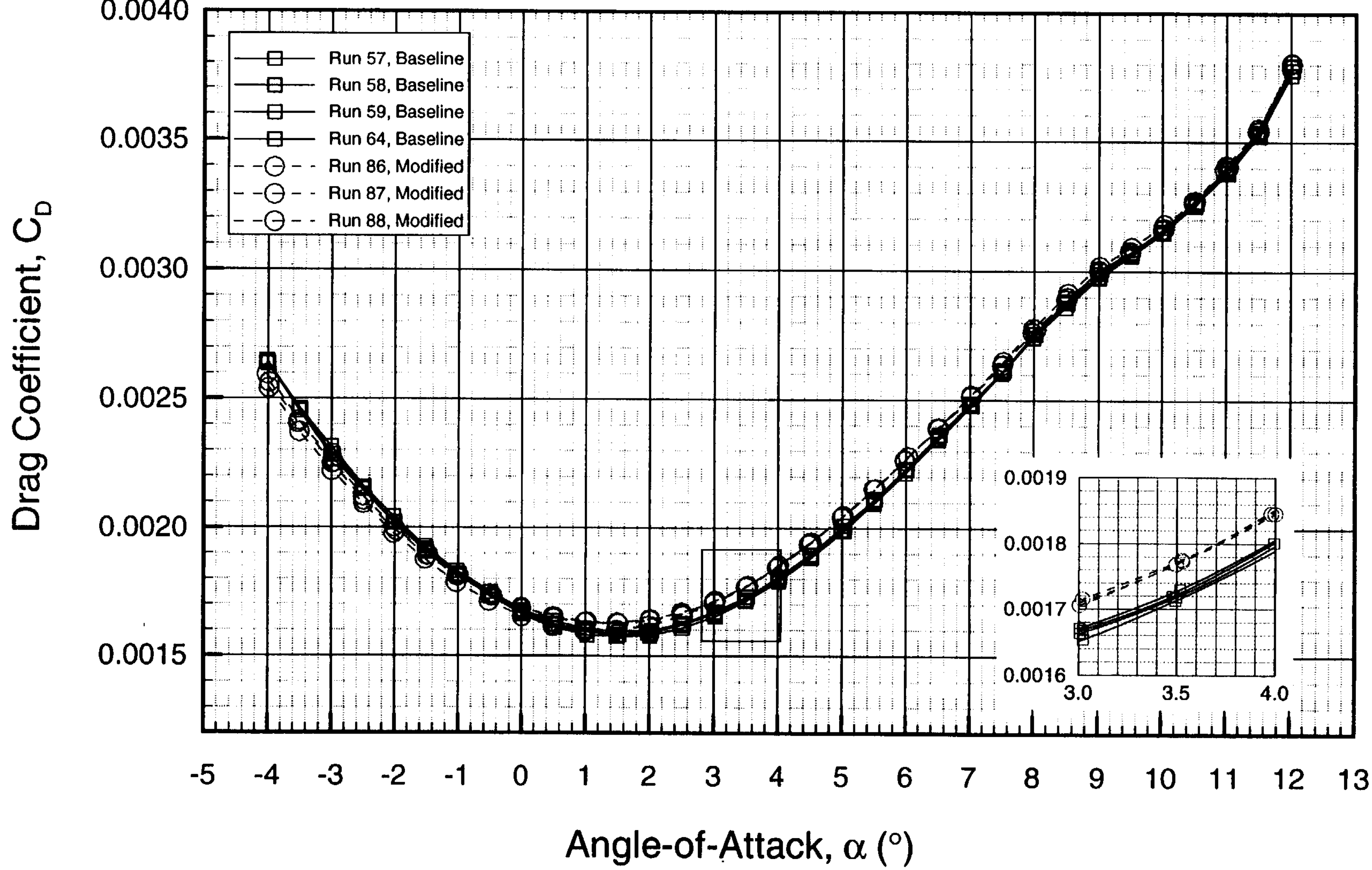

Comparison of Baseline and Modified Aftbody Pitching Moment
1.5% TCA Model 23, W/B/N/D/V/H Configuration $i_H = 0°$

The modified and baseline aftbodies have similar C_M slopes. The modified aftbody shows a more negative (nose-down) C_M.

Pitching Moment from the TCA Baseline and Modified Aftbodies

1.5% Model #23, W/B/N/D/V/H configuration, $i_H=0°$

LaRC Test #1707, $M_\infty=2.4$, $Re=4x10^6/ft$, (forces measured on aftbody)

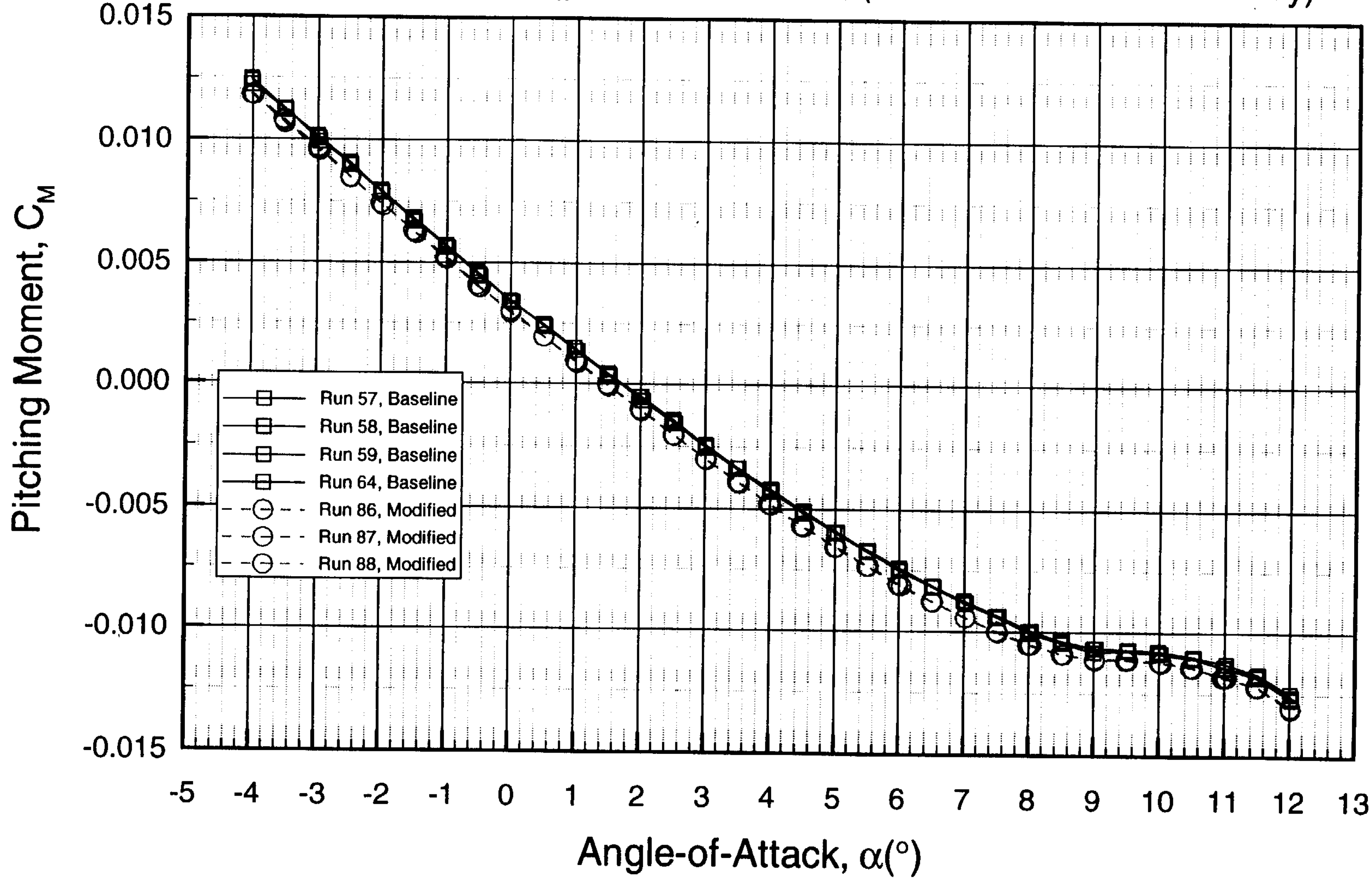

Trim Drag
1.5% TCA Model with Modified Aftbody
W/B/N/D/V/H Configuration $i_H = 0°$

Trim drag is the drag of the aircraft at $C_M=0$ minus the drag of the aircraft where the horizontal tail has zero lift. During Test 1707, trim drag studies were planned for both the baseline and modified aftbodies. The baseline aftbody trim study was dropped from the run schedule due to time limitations in the wind tunnel. The chart above shows the process of determining trim drag for the modified aftbody configuration. The full configuration force and moments were obtained from a previous sting-mounted test at the UPWT (Test 1677) using the flared aftbody geometry. Differences between the flared and modified aftbodies were obtained and applied to the existing data. The trim drag was determined to be –0.4 counts for the modified aftbody.

Trim Drag

M_∞=2.4, Re=4x10^6/ft, C_L=0.1

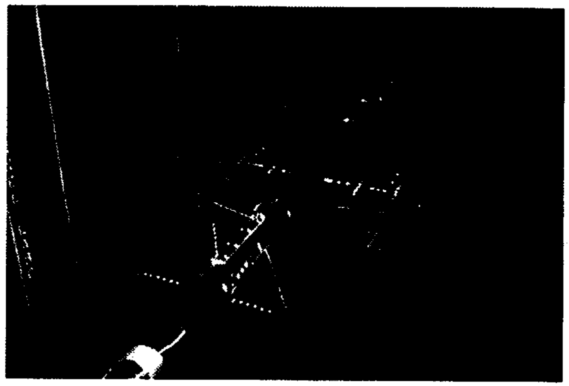

Model 20 (W/B/N/D/V/H forces)
-Flared aftbody
- sting mounted

Trim drag: $C_{D\,(C_M=0)} - C_{D\,i_H\,(C_L=0)}$

ΔC_D= -0.4 counts

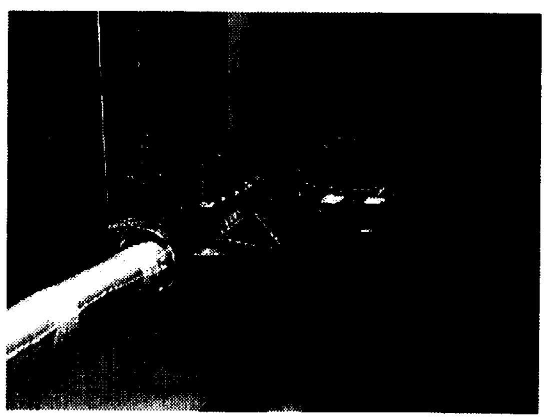

Model 23 (Flared aftbody forces)

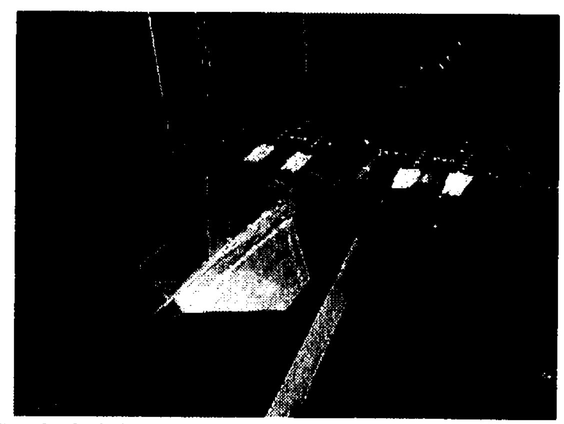

Model 23 (Modified aftbody forces)
i_H= 0°, ±2°

Flow Solver and Computational Grid

The nonlinear flow solver, CFL3D, was used in simulations of flows over the TCA configuration. A parallel version of CFL3D was used on the SGI Origin 2000. CFL3D uses an upwind Roe's flux-differencing scheme to solve either the Euler or Navier-Stokes equations on patched, structured, multi-block grids. A number of convergence accelerators are programmed in CFL3D to reduce CPU time. Here, grid sequencing and multigrid were actively used. The Baldwin-Lomax turbulence model was used in all the calculations.

Flow Solver & Computational Grid

- CFL3D
  - Baldwin-Lomax turbulence model
  - Parallel version
  - SGI Origin 2000

- TCA supersonic W/B/N/D/V/H grid
  - 21 blocks
  - 6.7 milion points
  - 1:1 and patched block boundaries
  - Strut not modeled in CFD

Comparison of CFL3D N-S and Test Data
1.5% TCA Model 23, Baseline Aftbody

Predicted and measured drag on the aftbody of the 1.5% Model 23 with the baseline aftbody at $\alpha=3.5°$ is shown above. From the CFL3D N-S solutions on the W/B, the aftbody drag is under-predicted by 0.6 cts. The predicted aftbody drag from the W/B/V/H and W/B/N/D/V/H solutions are in good agreement with the test data. Although the test data has not been corrected for the trip drag, the correction is expected to be small compared to the total aftbody drag. Note that the CFD results do not model the forward swept strut used to support the wind-tunnel model in the test. Also shown are the CFL3D N-S pressure distribution over the entire aircraft and a picture of the 1.5% TCA Model 23 in the UPWT test section.

Comparison of Predicted and Measured Aftbody Drag

1.5% TCA Model 23, Baseline Aftbody, W/B/N/D/V/H Configuration

M_∞=2.4, α=3.5°, β=0°, Re=4x10^6/ft

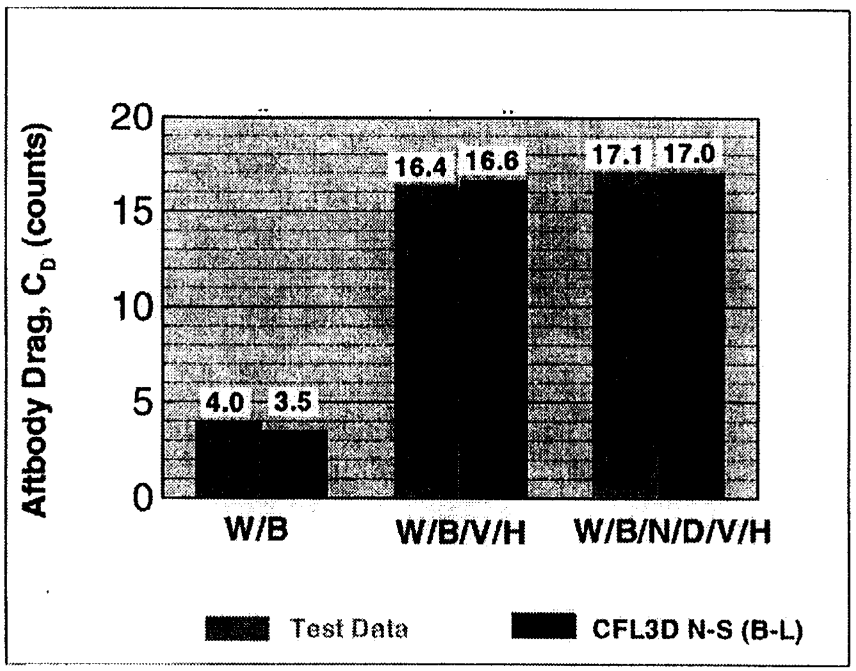

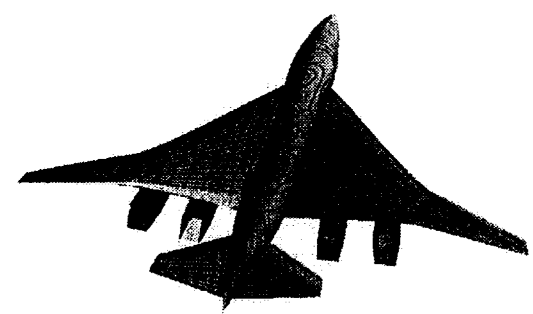

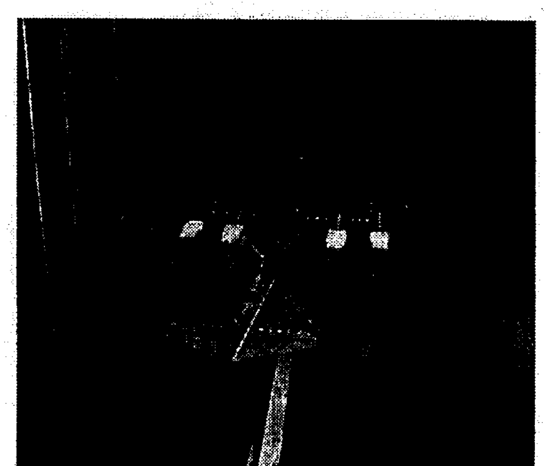

Comparison of CFL3D N-S and Test Data
1.5% TCA Model 23, Modified Aftbody

Predicted and measured drag on the modified aftbody for the 1.5% Model 23 at M_∞=2.4, α=3.5°, and Re=4×10^6/ft. CFL3D predicts 0.2 counts less aftbody drag than the wind tunnel test. Although the test data has not been corrected for the trip drag, the correction is expected to be small compared to the total aftbody drag. The CFD solutions do not model the forward swept strut used to support the wind-tunnel model in the test section. The CFL3D N-S pressure distribution and surface streamlines in the aftbody region are also shown. CFL3D N-S does not predict separation in the aftbody region. CFL3D N-S and test data show that the modified aftbody has ~0.5 counts more drag than the baseline aftbody.

Comparison of Predicted and Measured Aftbody Drag

1.5% TCA Model 23, Modified Aftbody, W/B/N/D/V/H Configuration

M_∞=2.4, α=3.5°, β=0°, Re=4x10^6/ft

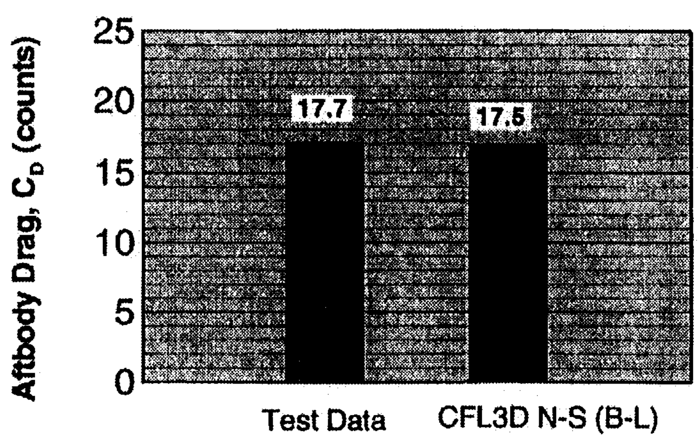

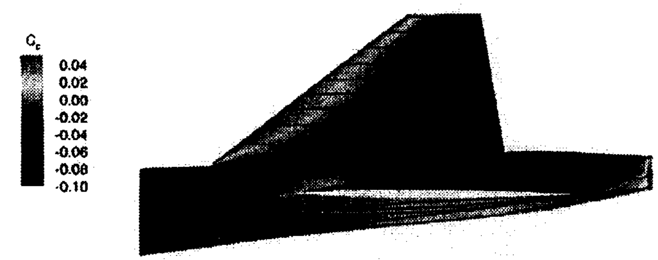

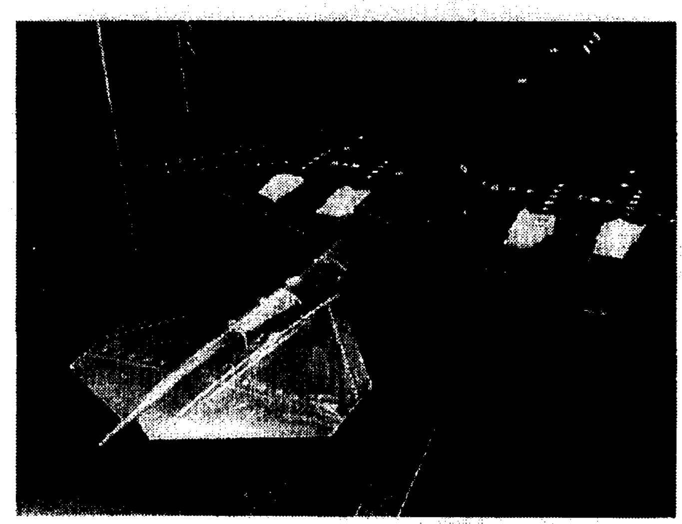

Comparison of CFL3D N-S and Test Data Pressure Distributions

1.5% TCA Model 23, Baseline Aftbody

Predicted and measured pressures are compared for the baseline aftbody The CFL3D N-S surface pressures agree well with the test data for WL 4.086, 4.586, 5.086, and the upper centerline station. The comparison is not as good for the lower centerline pressures starting at MS 54.

Pressure Distributions for the TCA Baseline Aftbody

UPWT Test #1707, W/B/N/D/V/H Configuration
$M_\infty=2.4$, $\alpha=3.53°$, $Re=4\times10^6$/ft

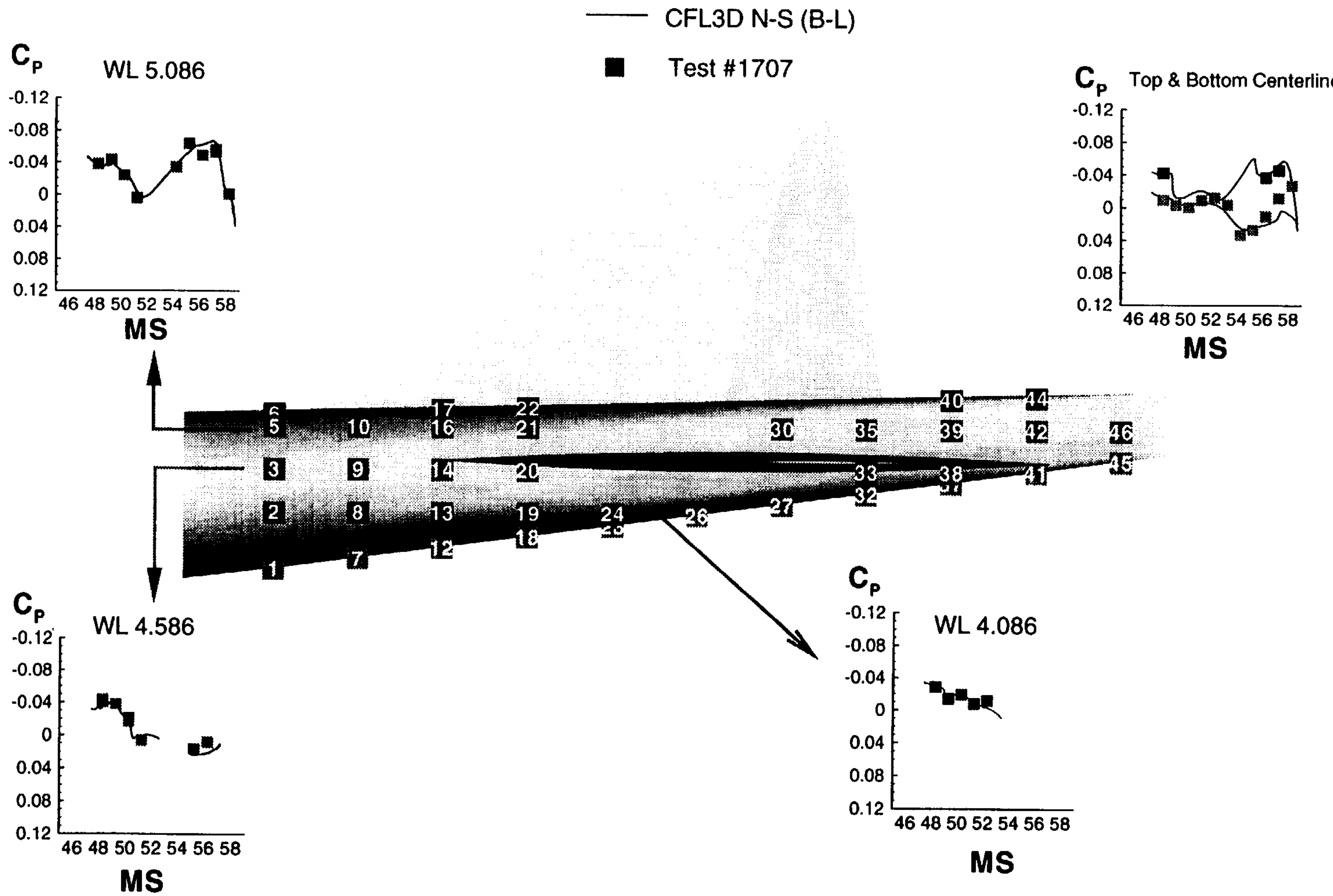

Comparison of CFL3D N-S and Test Data Surface Streamlines
1.5% TCA Model 23, Baseline Aftbody

CFL3D N-S surface streamlines and UV oil are compared in the above chart for the W/B/N/D/V/H configuration. Overall, there is good agreement between the computational and experimental surface flow visualization.

Particle Traces on the TCA Baseline Aftbody

1.5% TCA Model 23, W/B/N/D/V/H Configuration

M_∞=2.4, Re=4×10^6/ft, α=3.5°, i_H=0°

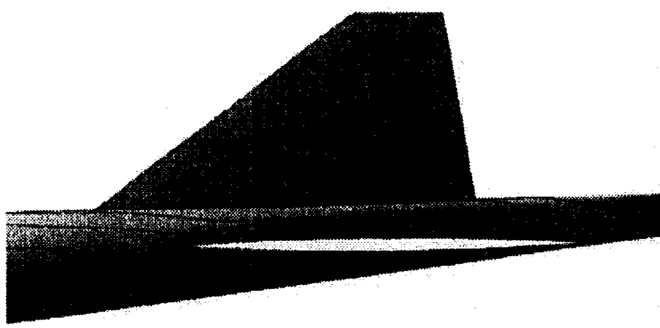

CFL3D N-S (B-L)

UV Oil

Summary of Performance Results

The test data exhibits excellent short-term repeatability. Overall, there was good agreement between the predicted CFL3D forces and the test data for the 1.5% TCA Model 23. This agreement is extremely important in order to validate the analysis tools used for the complex configurations. The trim drag was determined for the modified aftbody configuration. The modified aftbody allowed the horizontal tail to remain ported at higher tail incidence angles compared to the baseline aftbody. The UV oil images and CFL3D N-S surface streamlines showed no signs of separation on the aftbody. The wind-tunnel test established aftbody closure test techniques.

Summary of Performance Results

- Excellent short-term repeatability (± 0.2 counts)
- Aftbody closure effects at α=3.5°:

  ΔC_D= -2.1 counts, ΔC_L= -0.002, and ΔC_M = 0.02
- Good agreement between CFD and wind-tunnel for 1.5% TCA Model 23 baseline and modified aftbody drag on W/B/N/D/V/H config.
  - Baseline aftbody: WT C_D=17.1 cts.

    CFD C_D=17.0 cts.
  - Modified aftbody: WT C_D=17.7 cts.

    CFD C_D=17.5 cts.
- Modified aftbody allowed horizontal stab to remain ported at higher i_H compared to baseline

Summary of Performance Results (cont.)

- Both UV oil images and CFD results indicate attached flow on the aftbody near supersonic cruise
- Established aftbody closure test techniques at supersonic speeds

Stability and Control Test Objectives

This slide outlines the stability and control objectives of the aftbody closure test. First the longitudinal and directional stability levels of the flared and baseline closed aftbody will be determined so that an increment between the two can be derived. Similarly, the longitudinal and directional control effectiveness for the horizontal stabilizer, elevator, and rudder will be determined between the flared aftbody and the baseline closed aftbody so that an increment between the two can be derived.

These stability and control increments can be compared against those predicted by CFD codes, such as A502SC, to gage the ability of those codes to estimate aftbody closure effects. The aftbody increments determined from the test can also be used to correct the stability and control database obtained for the TCA configuration with the flared aftbody. This corrected database can then be used for development of a non-linear aerodynamic simulation of the TCA configuration.

Stability and Control Test Objectives

- **Validate Aftbody Longitudinal and Directional Stability Levels:**

  ΔCm_{α} , ΔCn_{β}

  (Δ = **Baseline Closed Aftbody - Flared Aftbody**)

- **Validate Control Effectiveness Levels:**

  ΔCm_{iH} ,$\Delta Cm_{\delta e}$,$\Delta Cn_{\delta r}$

  (Δ = **Baseline Closed Aftbody - Flared Aftbody**)

- **Provide Database for CFD Code Validation and Corrections to the TCA Aerodynamic Database:**

  $C_{x_{corrected}} = C_{x_{uncorrected}} + \Delta C_x$
  (where x is any force or moment variable)

Longitudinal Characteristics
Stability Comparison (ABB vs. ABF)

This slide shows the variation of horizontal tail-on, and horizontal tail-off pitching moment coefficient with angle-of-attack for the flared aftbody (ABF) and the baseline TCA closed aftbody (ABB) at Mach 2.4. The pitching moment data shown was measured for each aftbody but resolved to the wing reference point (50%MAC). The data shows that the ABB aftbody, with or without the horizontal tail, has less longitudinal stability (slope of curve is more positive) than the ABF aftbody. The reduction in longitudinal stability is more significant for the horizontal tail-on configuration than for the horizontal tail-off configuration indicating that this is primarily caused by the reduction in carry-over (buried) area of the horizontal tail for the ABB configuration.

Longitudinal Characteristics Stability Comparison (ABB vs. ABF)

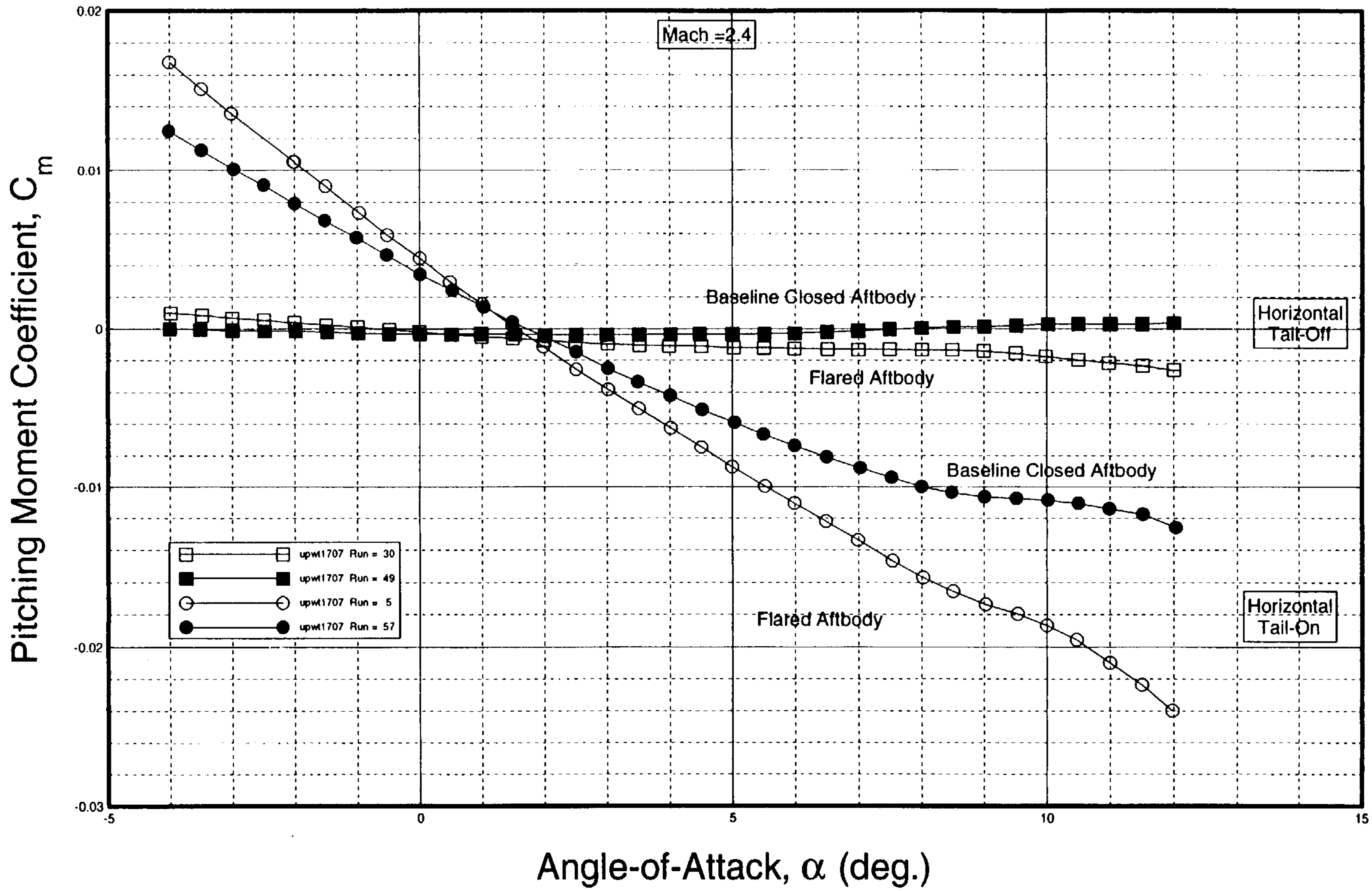

TCA Pitching Moment Coefficient Corrected for Aftbody Closure Effects

This figure shows the corrected and uncorrected pitching moment coefficient variation with angle-of-attack for the TCA configuration at Mach 2.4. The uncorrected data was obtained from a previous sting-mounted test at the UPWT (test #1677) using the flared aftbody geometry. Horizontal tail-on and off increments due to the difference between the flared and closed aftbody geometries were obtained from the previous slide and applied to the uncorrected data to obtain the corrected pitching moment curves shown here. The increment due to aftbody geometry is shown to significantly reduce the horizontal tail-on longitudinal stability of the TCA configuration.

TCA Pitching Moment Coefficient Corrected for Aftbody Closure Effects

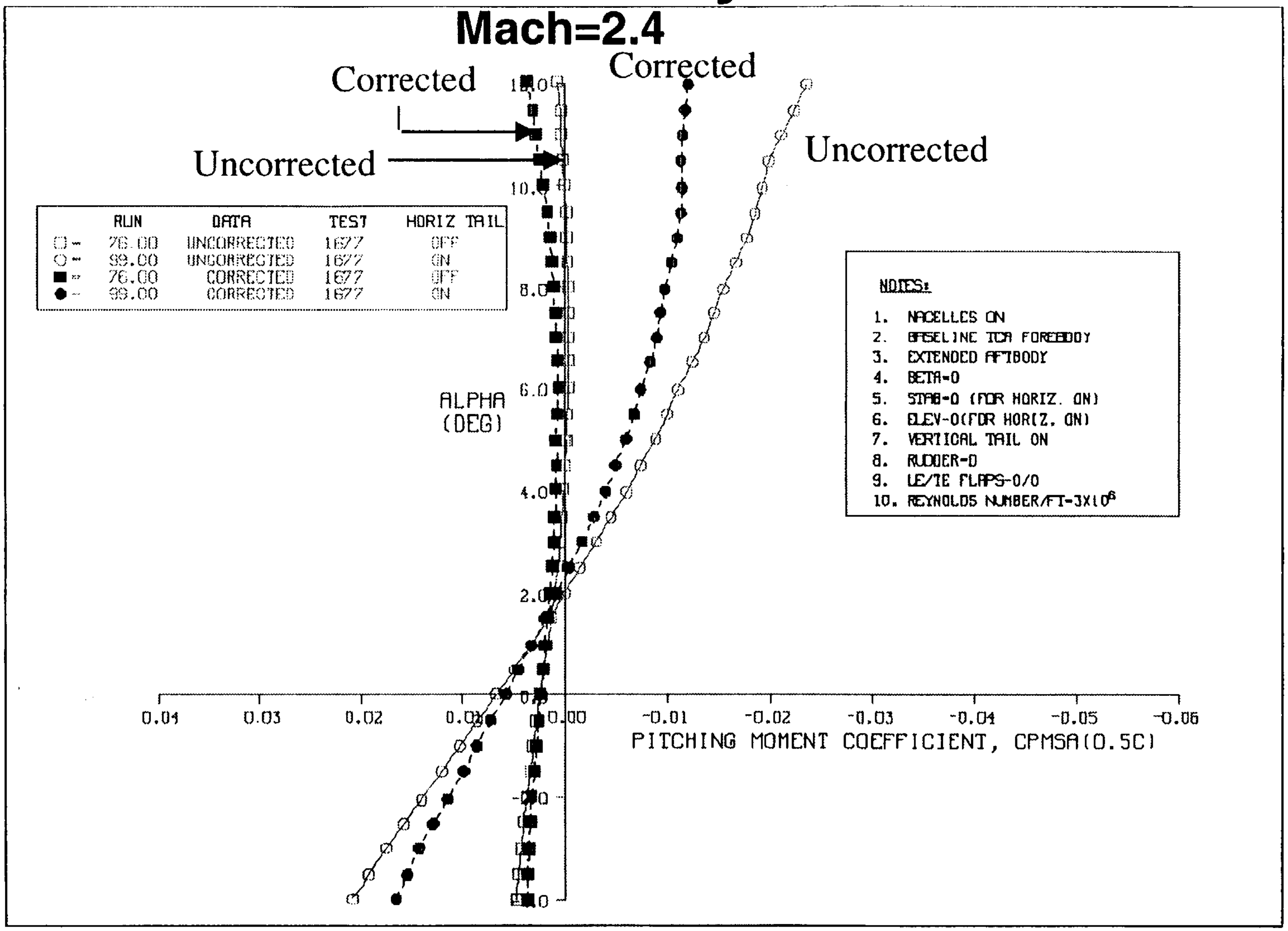

Tails-On Longitudinal Characteristics
Stabilizer Control Effectiveness
(ABB vs. ABF)

This slide shows the variation of pitching moment coefficient vith angle-of-attack and horizontal stabilizer deflection ,at Mach 2.4, for the ABB and ABF aftbody geometries. Horizontal stabilizer deflections tested include 0, +6, and -6 degrees. Stabilizer effectiveness (incremental pitching moment per degree of stabilizer deflection) is fairly constant with angle-of-attack for either aftbody geometry; however, the stabilizer effectivenes for the ABB configuration is reduced relative to the ABF configuration. Again, the primary reason for the effectiveness reduction is the smaller carry-over area of the ABB configuration. The stabilizer effectiveness for either aftbody geometry is shown to be fairly constant between positive and negative deflections.

Tails-On Longitudinal Characteristics Stabilizer Control Effectiveness (ABB vs. ABF)

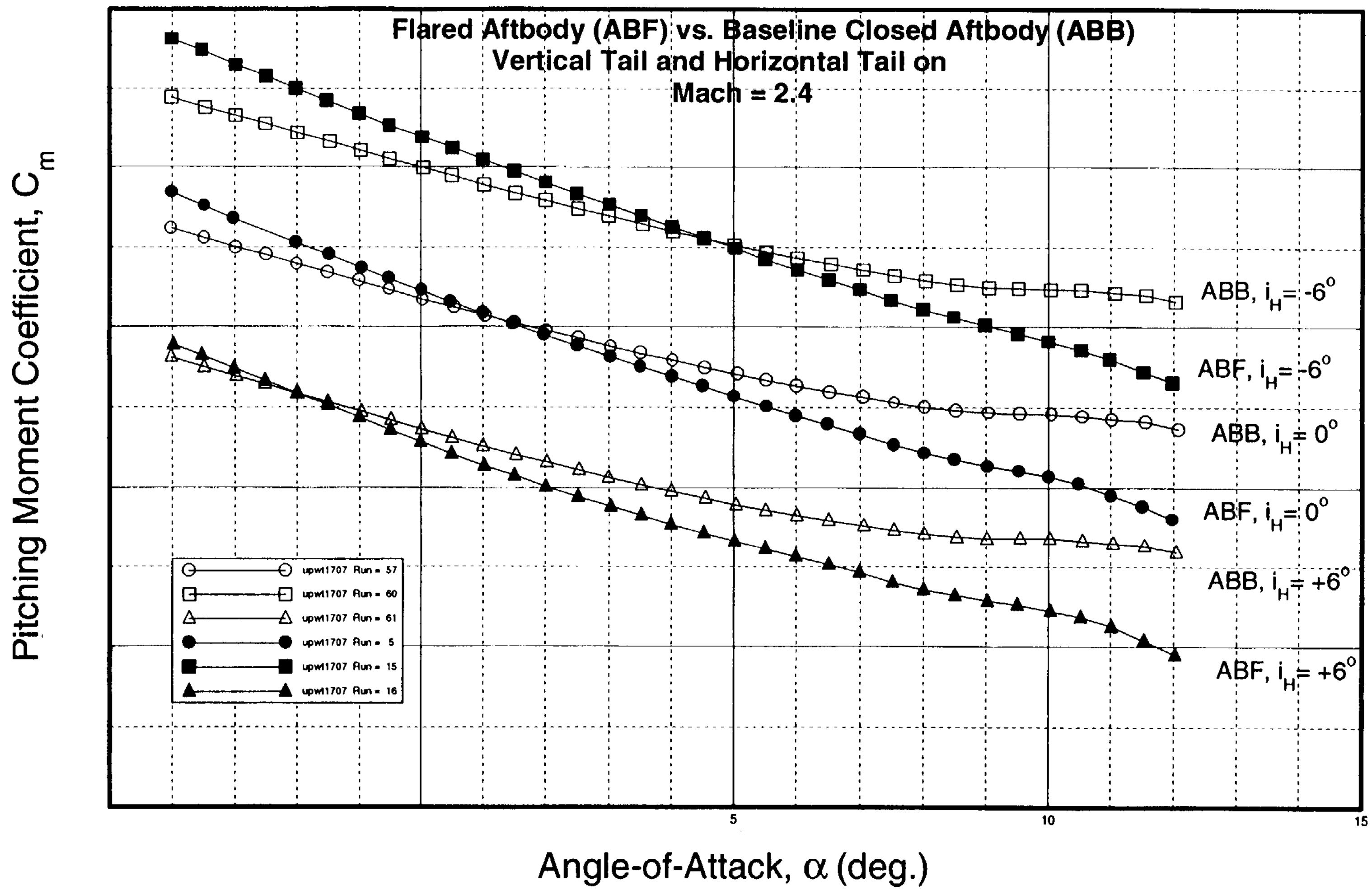

Tails-On Longitudinal Characteristics
Elevator Control Effectiveness
(ABB vs. ABF)

This slide shows the variation of pitching moment coefficient vith angle-of-attack and elevator deflection ,at Mach 2.4, for the ABB and ABF aftbody geometries. Elevator deflections tested include 0, +10, and +20 degrees. Elevator effectiveness (incremental pitching moment per degree of elevator deflection) is fairly constant with angle-of-attack for both aftbody geometries. Also, there is only a small difference in elevator effectiveness between the two aftbody geometries. This is in contrast to the stabilizer effectiveness comparison shown on the previous slide.

Tails-On Longitudinal Characteristics Elevator Control Effectiveness (ABB vs. ABF)

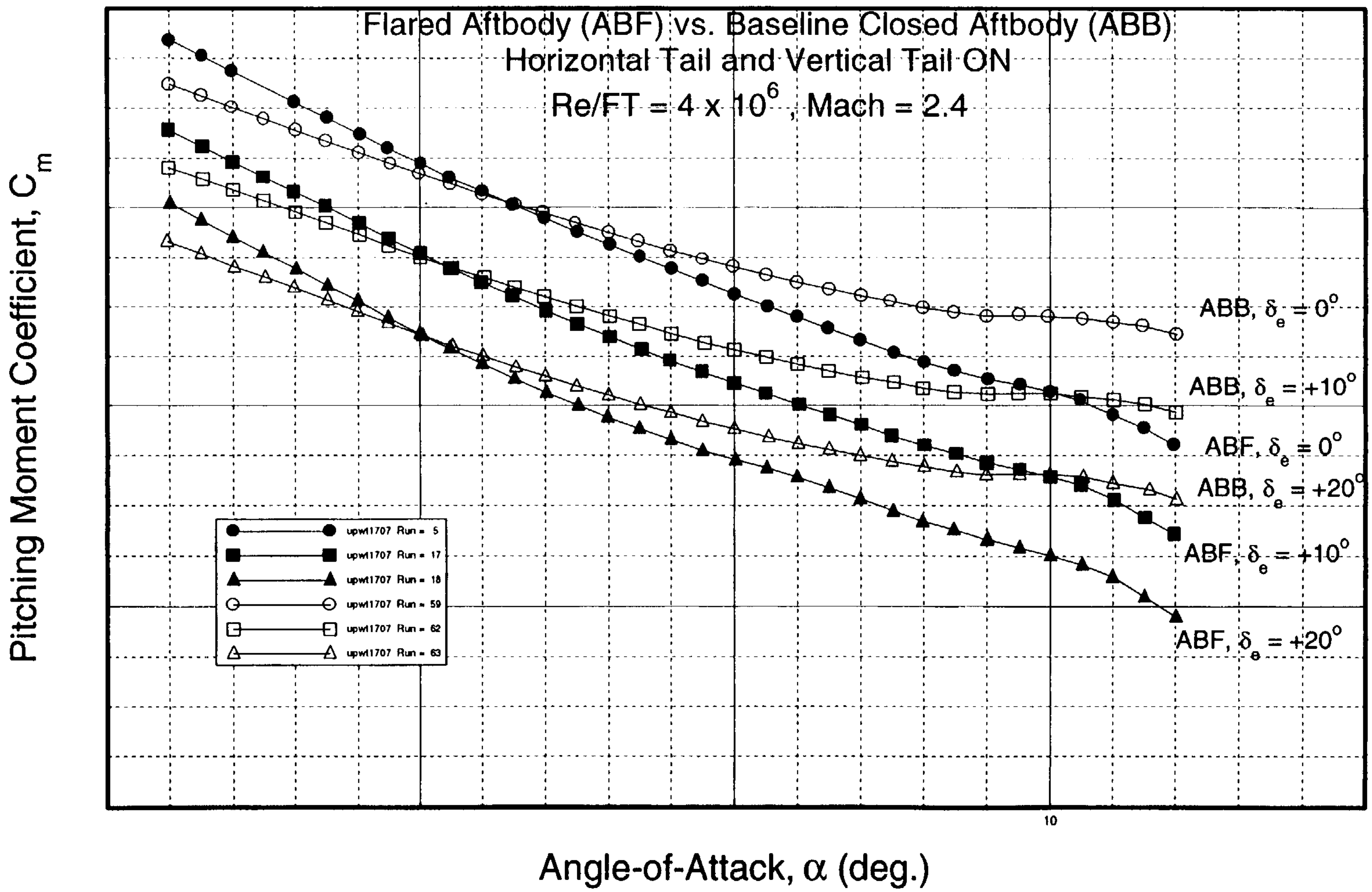

Longitudinal Characteristics
Stability and Control Derivatives
(ABB vs. ABF)

This slide summarizes the longitudinal stability and control derivative comparison between the flared and baseline closed aftbody geometries at a representative angle-of-attack of 3.5 degrees. The significant reduction in tail-on stability, the moderate reduction in stabilizer effectiveness, and the small reduction in elevator effectiveness are easily observed for the baseline closed aftbody when compared to the flared aftbody. Stabilizer effectiveness is shown to be symmetric between positive and negative deflections for both aftbodies. Also, elevator effectiveness remains constant up to +20 degrees of deflection for both aftbodies.

Longitudinal Characteristics Stability and Control Derivatives (ABB vs. ABF)

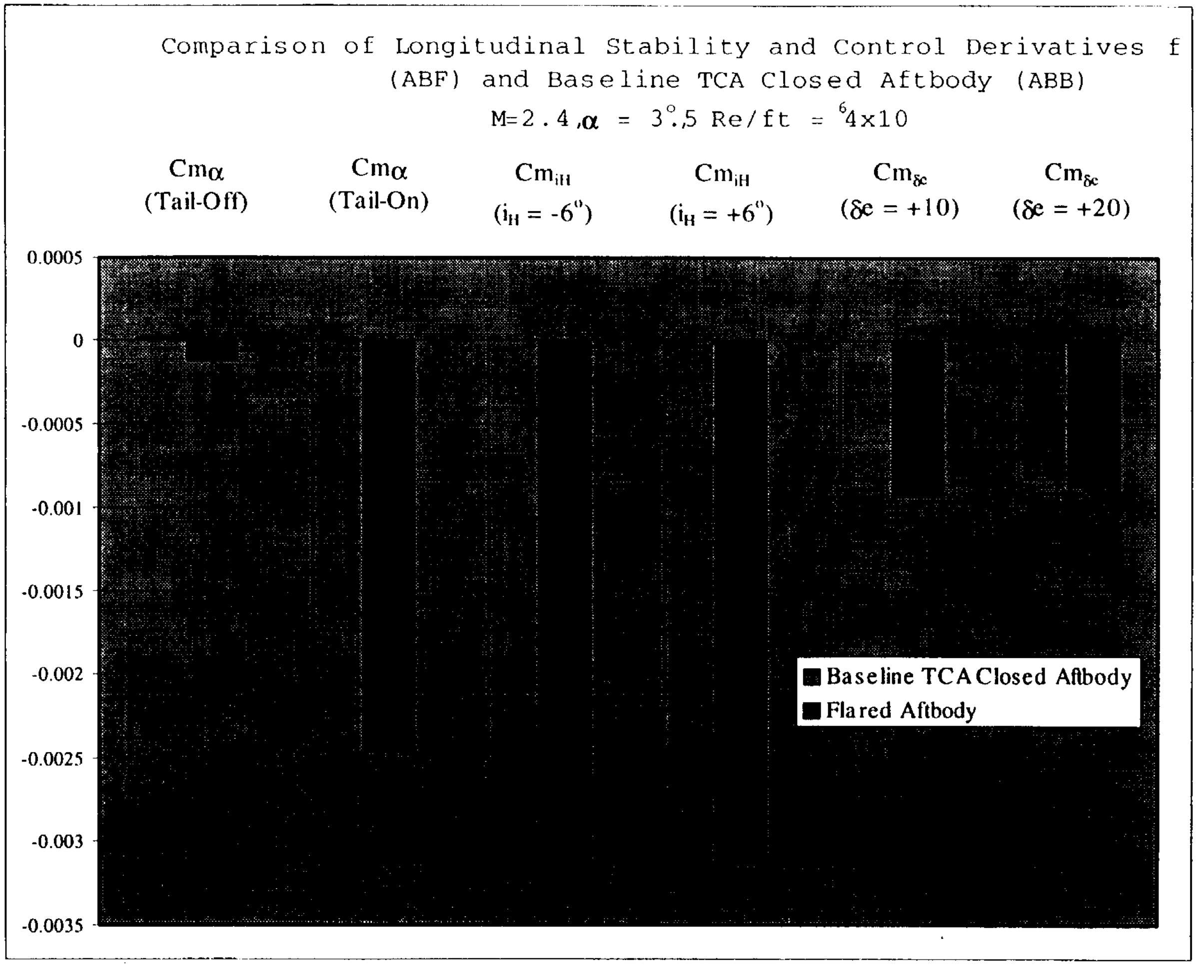

Tails-On Directional Characteristics
Stability Comparison (ABB vs. ABF)

This slide shows the variation of vertical tail-on yawing moment coefficient with angle-of-atttack for the ABB and ABF aftbody geometries at constant angles of sideslip of 0, +3, +6, and -3 degrees. The yawing moment data shown was measured for each aftbody but resolved to the wing reference point (50%MAC). Directional stability (variation of yawing moment with sideslip) can be determined by subtracting the yawing moment at $\beta=0$ from the yawing moment at any other β and dividing the resulting yawing moment by the β. The data shows that the ABB aftbody, has significantly less directional stability than the ABF aftbody. This reduction in directional stability for the ABB aftbody is the result of a reduction in both the aftbody side area, as well as, the reduction in vertical tail carry-over lift.

Tails-On Directional Characteristics Stability Comparison (ABB vs. ABF)

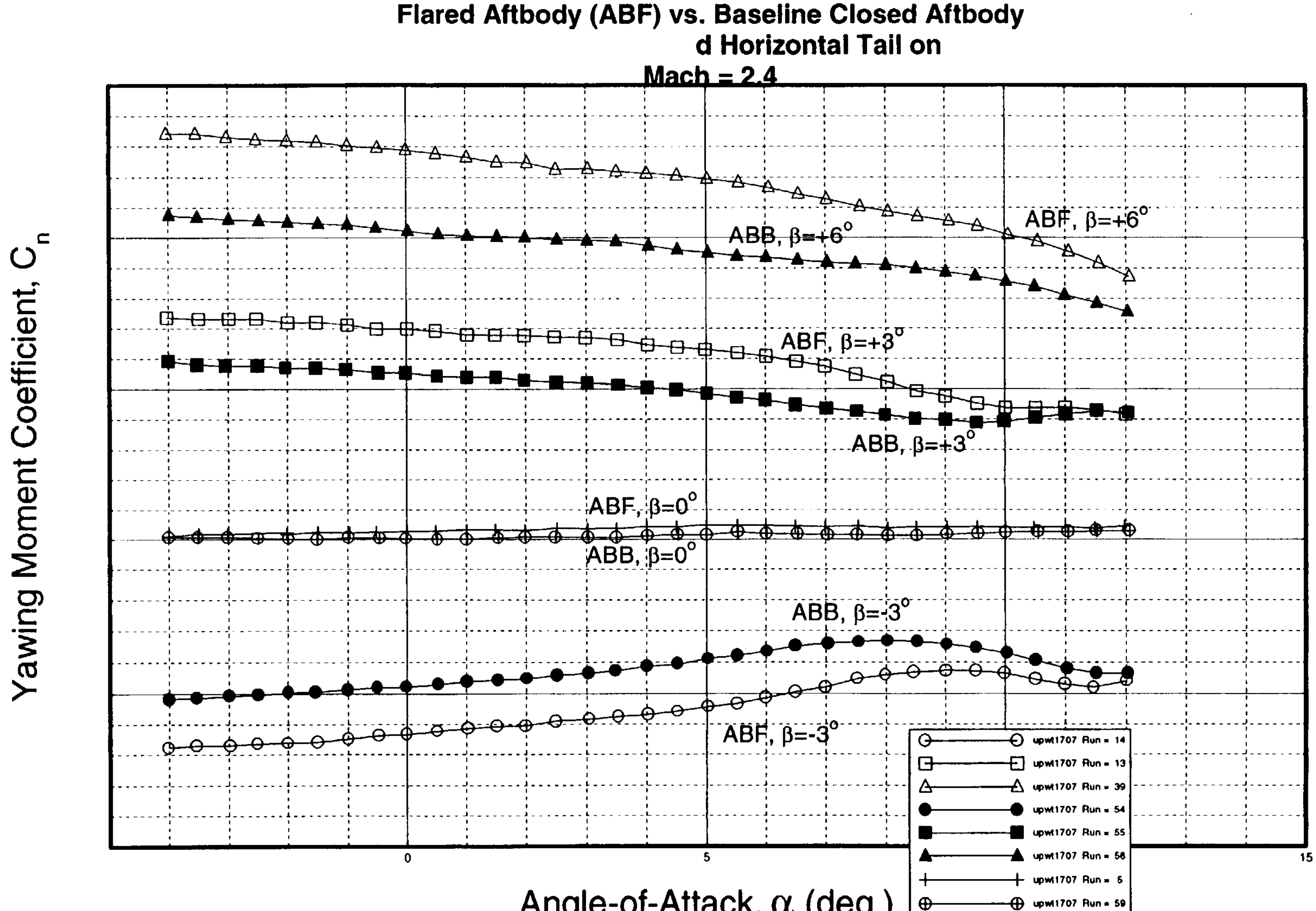

TCA Yawing Moment Coefficient Corrected for Aftbody Closure Effects

This figure shows the corrected and uncorrected yawing moment coefficient variation with angle-of-attack for the TCA configuration at Mach 2.4 and sideslip angle of +3 degrees. The uncorrected data was obtained from a previous sting-mounted test at the UPWT (test #1677) using the flared aftbody geometry. Vertical tail-on and off increments due to the difference between the flared and closed aftbody geometries were obtained from the UPWT-1707 test and applied to the uncorrected data to obtain the corrected yawing moment curves shown here. The increment due to aftbody geometry is shown to reduce both the vertical tail-on and vertical tail-off directional stability of the TCA configuration, although the reduction for the vertical tail-on is more significant.

TCA Yawing Moment Coefficient Corrected for Aftbody Closure Effects

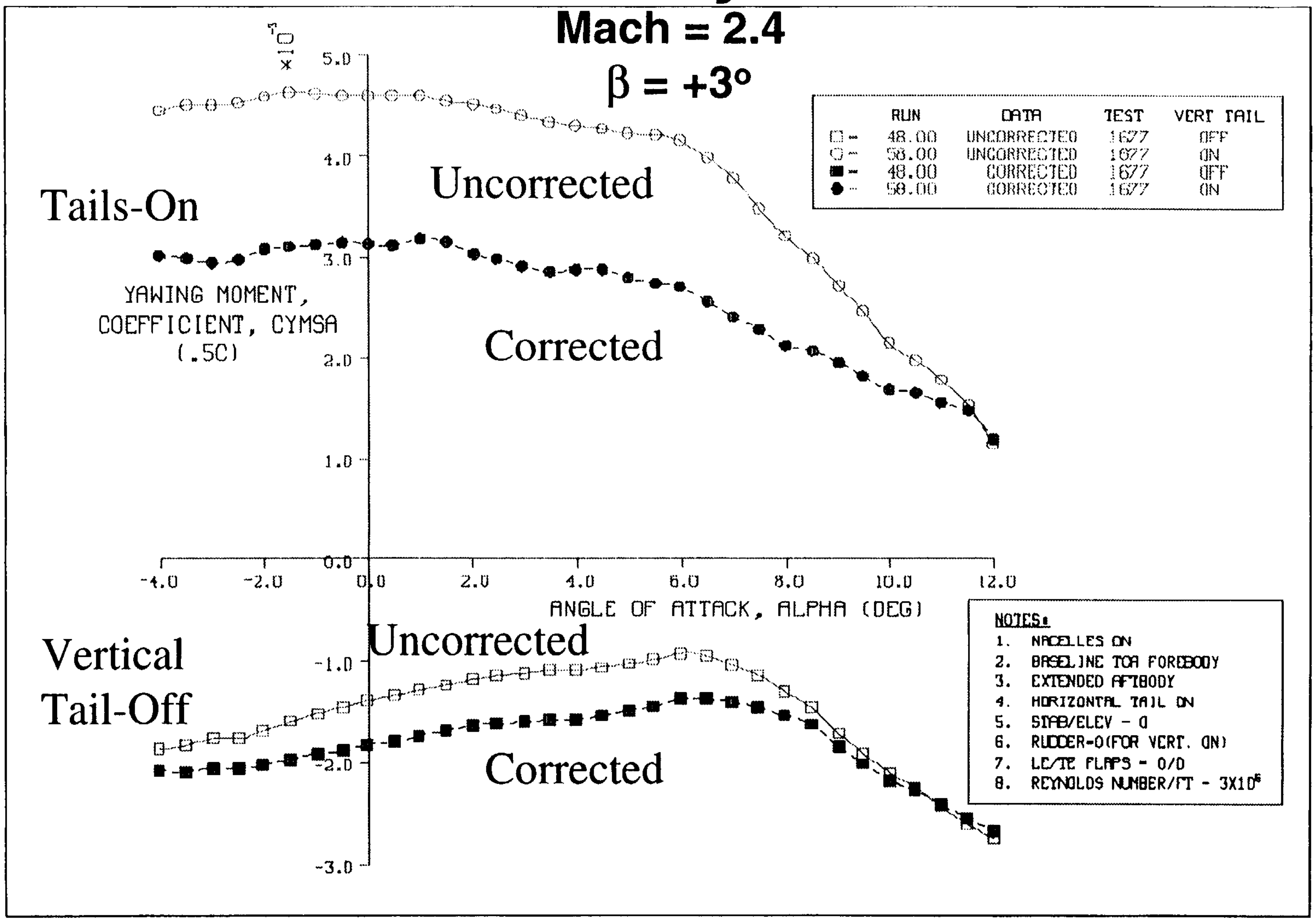

Tails-On Directional Characteristics Stability Derivative Comparison (ABB vs. ABF)

This slide summarizes the directional stability comparison between the ABB and ABF aftbody geometries at several sideslip angles and at a representative angle-of-attack of 3.5 degrees. The moderate reduction in directional stability of the ABB aftbody compared to the ABF aftbody is shown at each of the sideslip angles tested. Also shown is the relative asymetry in measured directional stability between the $\beta = +3$ and $\beta = -3$ degrees. This is believed to be caused by asymmetries associated with the model and tunnel sideflow which was not determined during the test.

Tails-On Directional Characteristics Stability Derivative Comparison (ABB vs. ABF)

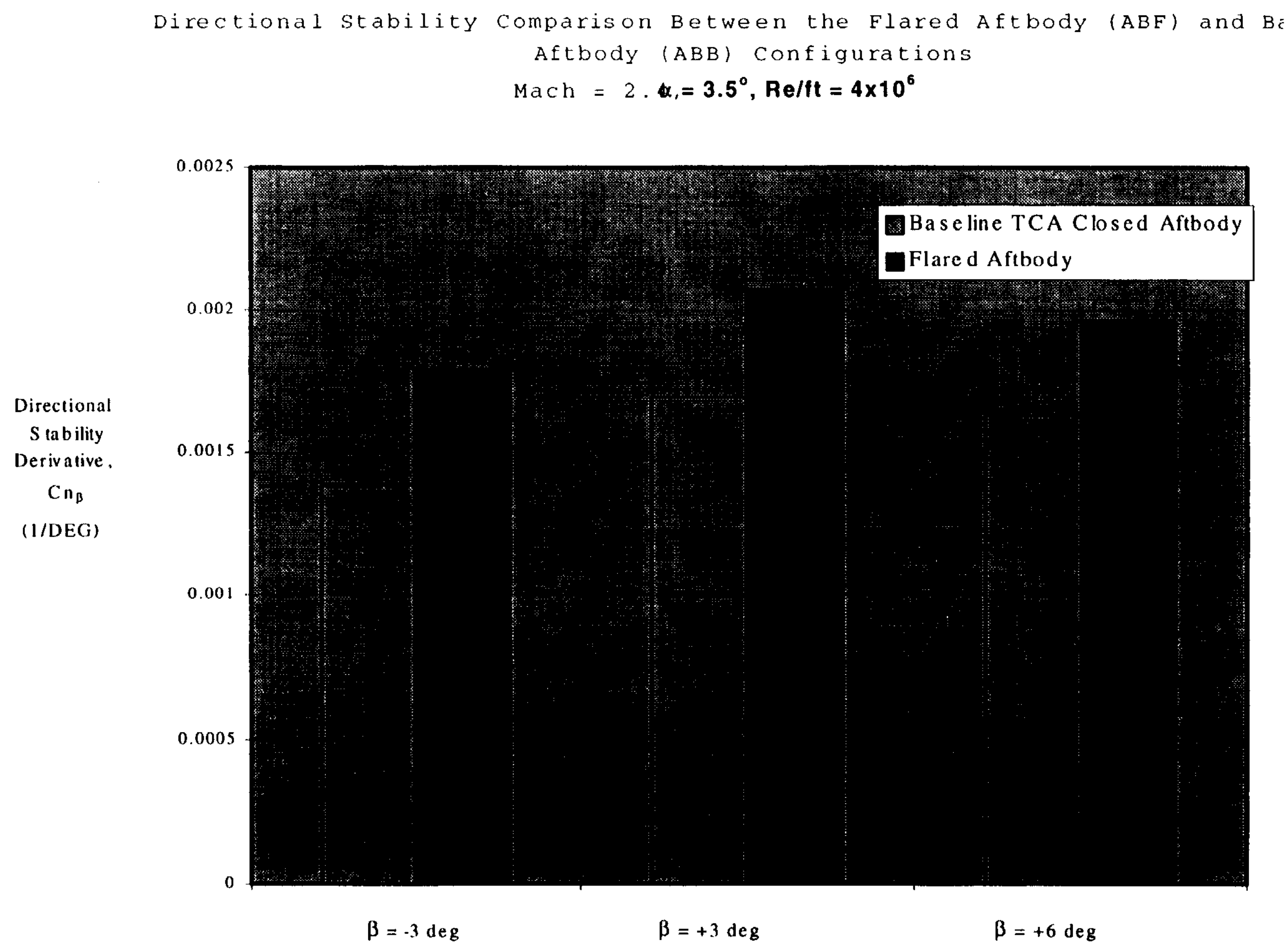

Tails-On Directional Characteristics
Rudder Control Effectiveness at β=0°
(ABB vs. ABF)

The slide below shows the variation of yawing moment coefficient with angle-of-attack and rudder deflection ,at Mach 2.4, for the ABB and ABF aftbody geometries at a constant β of 0 degrees. Rudder deflections tested include 0, +10, and +20 degrees. Rudder effectiveness (incremental yawing moment per degree of rudder deflection) is fairly constant with angle-of-attack for either aftbody geometry; however, the rudder effectivenes for the ABB configuration is reduced relative to the ABF configuration. Again, the primary reason for the effectiveness reduction is the smaller carry-over area of the ABB configuration. The effectiveness reduction is most dramatic at the +20 degree rudder deflection.

Tails-On Directional Characteristics Rudder Control Effectiveness at β=0° (ABB vs. ABF)

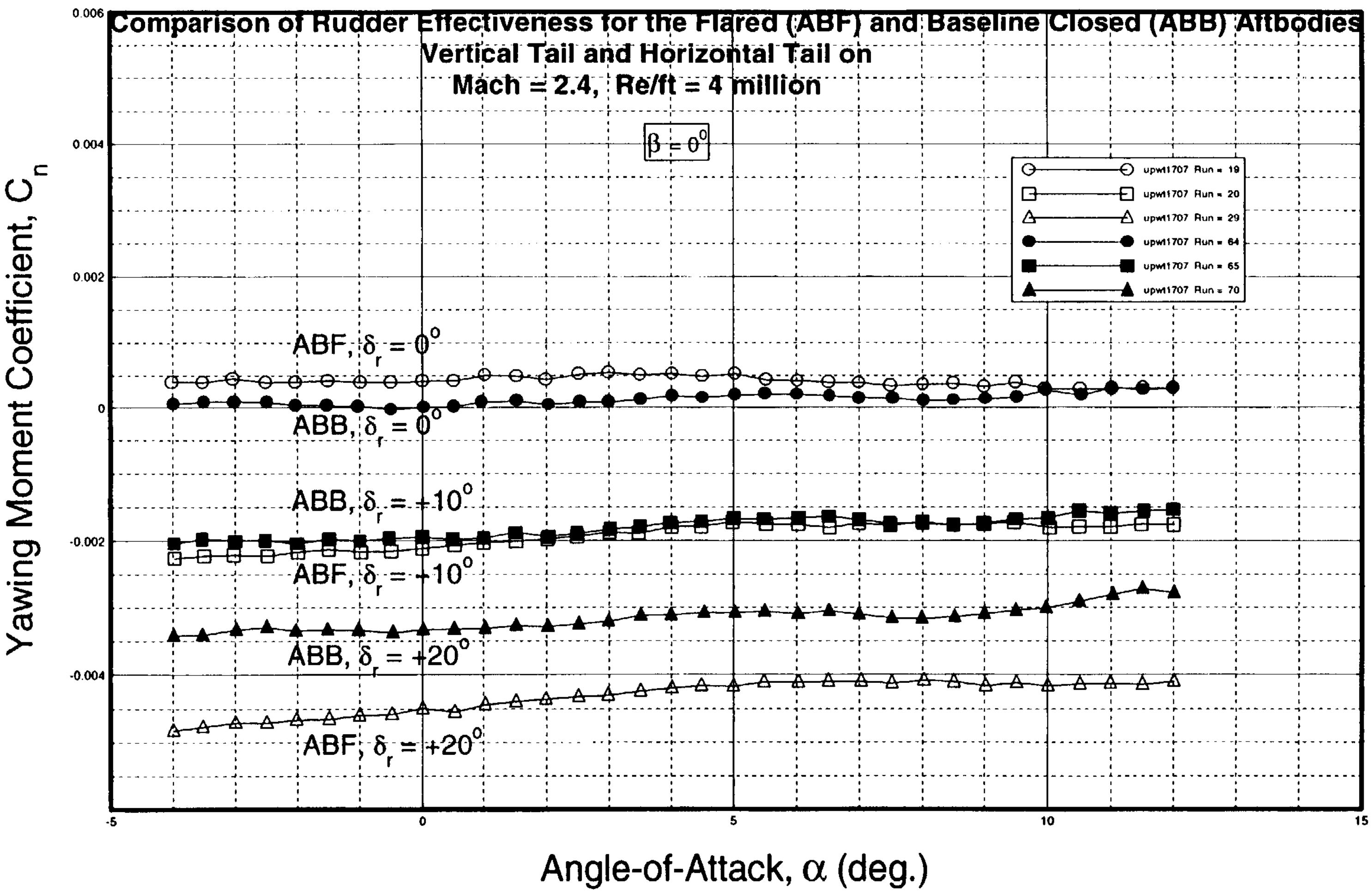

Tails-On Directional Characteristics
Rudder Control Effectiveness at β= -3°
(ABB vs. ABF)

The slide below shows the variation of yawing moment coefficient with angle-of-attack and rudder deflection ,at Mach 2.4, for the ABB and ABF aftbody geometries at a constant β of -3 degrees. For positive rudder deflections, a negative sideslip angle will result in an increased (more negative) yawing moment level due to positive directional stability. Rudder effectiveness for the ABF aftbody remained fairly constant when compared to the level at β = 0; however, rudder effectiveness of the ABB aftbody increased significantly but still remained below the level of the ABF aftbody.

Tails-On Directional Characteristics Rudder Control Effectiveness at β= -3° (ABB vs. ABF)

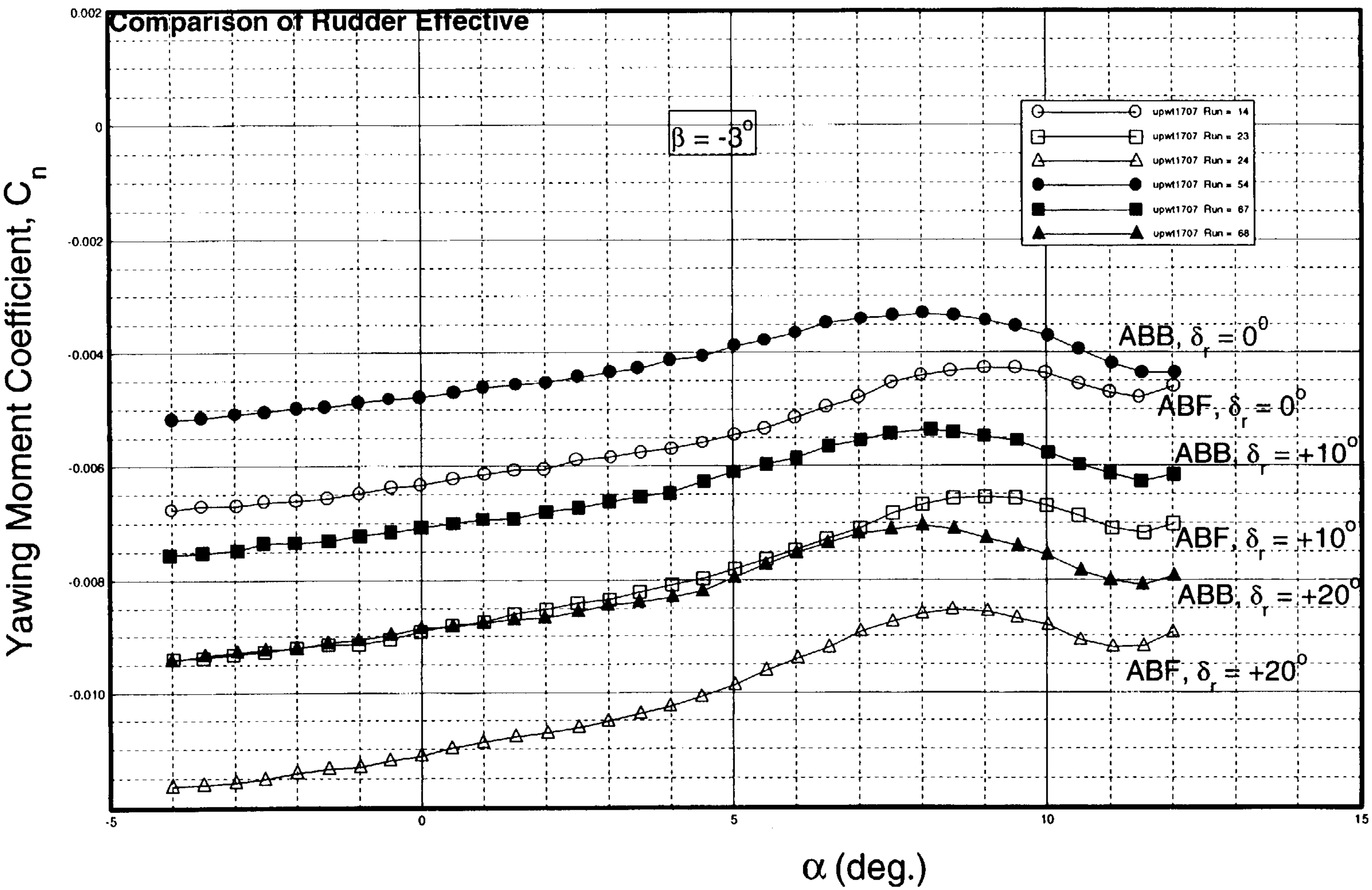

Tails-On Directional Characteristics
Rudder Control Effectiveness at β= +3°
(ABB vs. ABF)

The slide below shows the variation of yawing moment coefficient with angle-of-attack and rudder deflection ,at Mach 2.4, for the ABB and ABF aftbody geometries at a constant β of +3 degrees. For positive rudder deflections, a positive sideslip angle will result in a decrease (more positive) yawing moment level due to positive directional stability. Rudder effectiveness for both the ABF and ABB aftbodies remained fairly constant when compared to the level at β = 0except the +20 degree rudder deflection on the ABF aftbody which appears to have less effectiveness at β = +3 than at β = 0 degrees.

Tails-On Directional Characteristics Rudder Control Effectiveness at $\beta = +3^o$ (ABB vs. ABF)

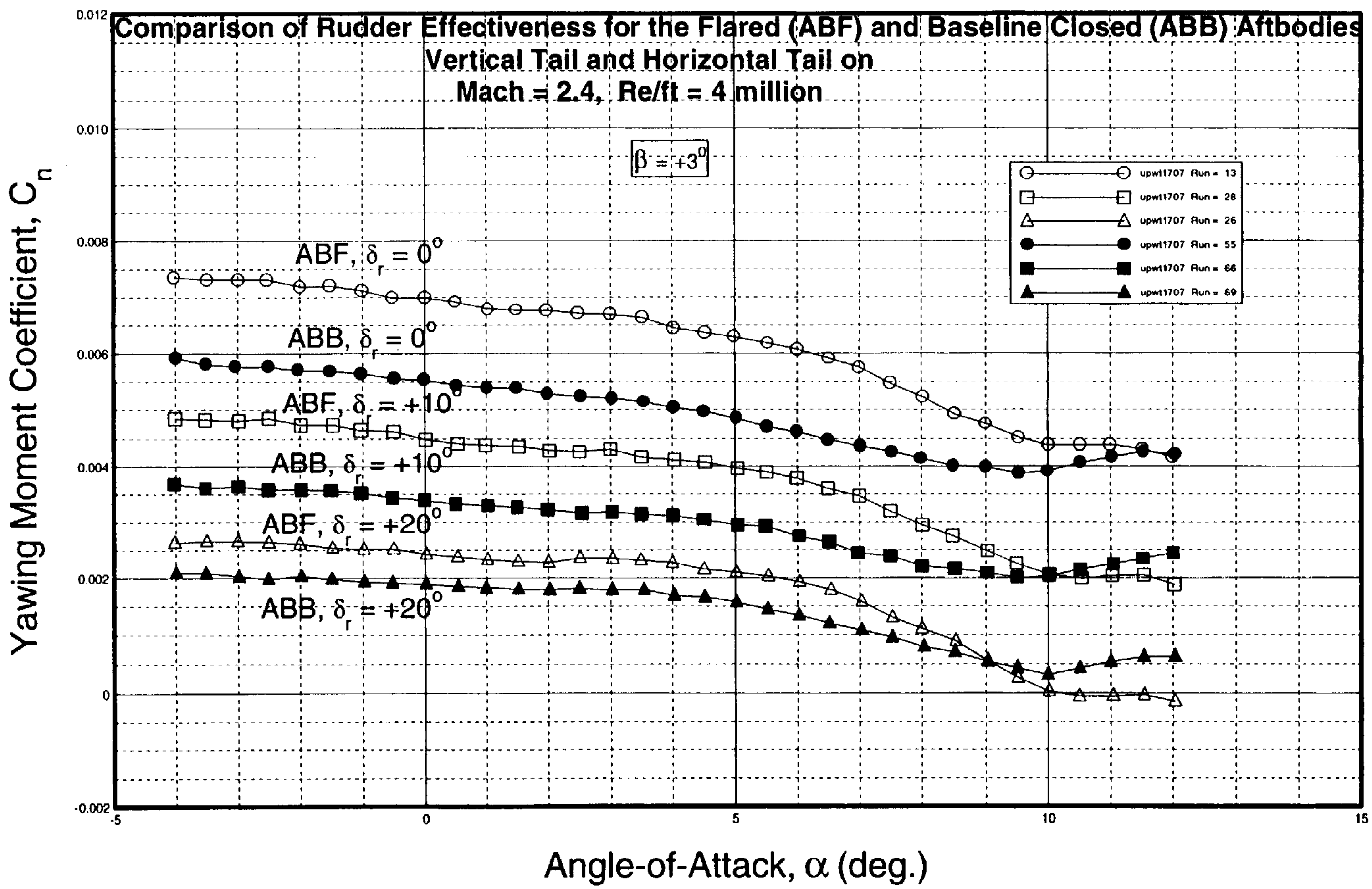

Tails-On Directional Characteristics
Rudder Control Derivative Comparison
(ABB vs. ABF)

This slide summarizes the rudder effectiveness comparison between the ABB and ABF aftbody geometries at several sideslip angles and at a representative angle-of-attack of 3.5 degrees. The significantly reduced rudder effectiveness of the ABB aftbody configuration at $\beta = 0$ degrees and the significant increase at $\beta = -3$ degrees are easily observed.

Tails-On Directional Characteristics Rudder Control Derivative Comparison (ABB vs. ABF)

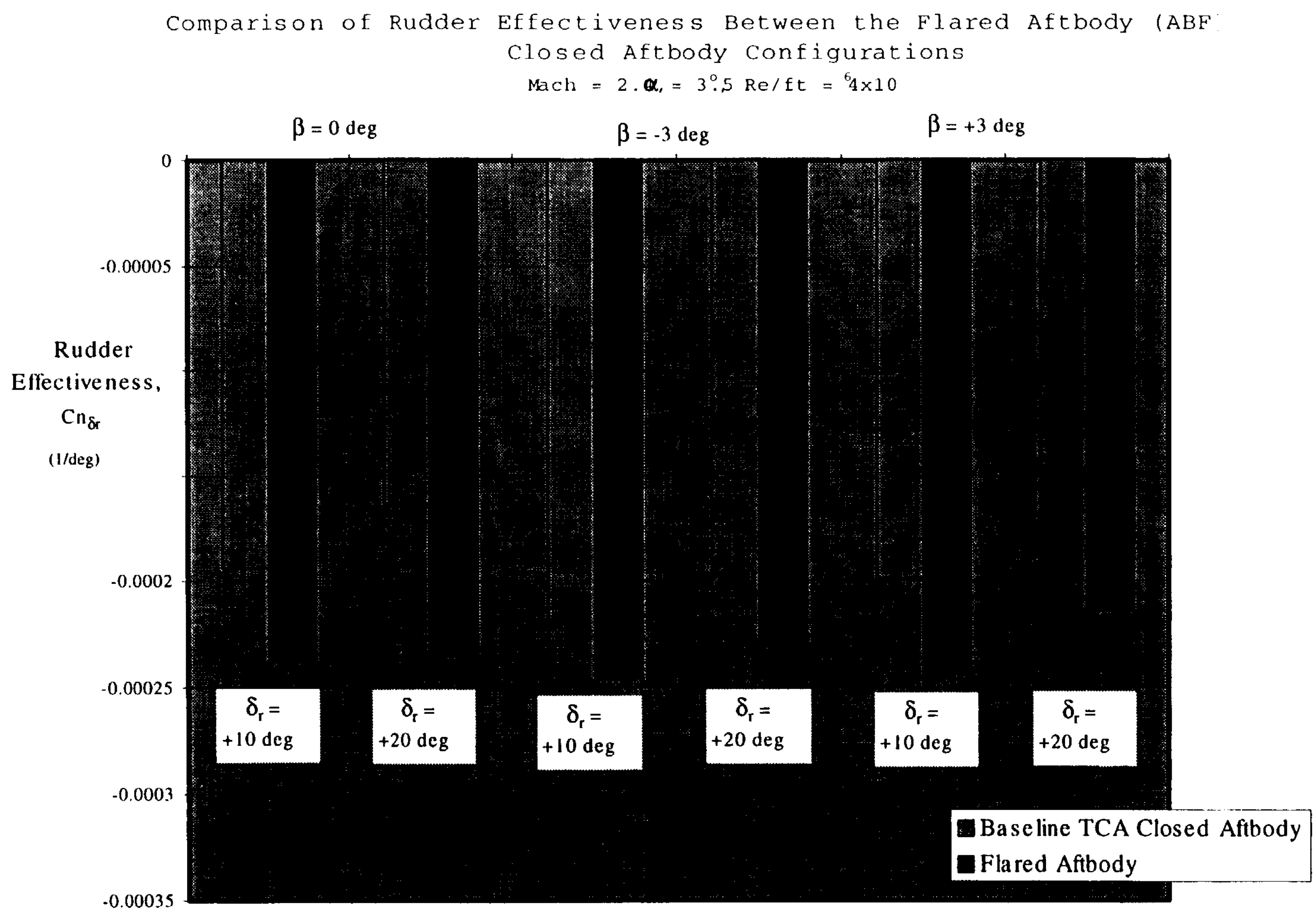

Stability and Control Summary of Results

In summary, significant differences in longitudinal and direction stability and control characteristics between the ABF and ABB aftbody geometries were measured. Correcting the experimental data obtained for the TCA configuration with the flared aftbody to the representative of the baseline TCA closed aftbody will result in a significant reduction in longitudinal stability, a moderate reduction in stabilizer effectiveness and directional stability, and a moderate to significant reduction in rudder effectiveness. These reductions in the stability and control effectiveness levels of the baseline TCA closed aftbody are attributed to the reduction in carry-over area.

Stability and Control Summary of Results

Comparing the S&C characteristics of the TCA closed aftbody to the TCA flared aftbody configuration:

- **Longitudinal stability**
  - Significant reduction in longitudinal stability (28%)
- **Longitudinal control effectiveness**
  - Moderate reduction in stabilizer effectiveness (16%)
  - Insignificant reduction in elevator effectiveness
- **Directional stability**
  - Moderate reduction in directional stability (20%)
- **Directional control effectiveness**
  - Moderate to significant reduction in rudder effectiveness (16-30%)

The reductions observed in the stability and control effectiveness levels of the baseline TCA closed aftbody are directly attributed to the reduction of carry-over area

Aft Body Closure - Predicted Strut Effects at M=2.4

John E. Lamar, NASA LaRC

Javier A. Garriz, ViGYAN,Inc.

HSR Annual Airframe Technical Review

Anaheim Marriott, Anaheim, CA

February 8-12, 1999

This paper reports the predicted M = 2.4 strut-interference effects on a closed aft body with empennage for the TCA baseline model. The strut mounting technique was needed in order to assess the impact of aft-end shaping, i.e. open for a sting or closed to better represent a flight vehicle. However, this technique can potentially lead to unanticipated effects that are measured on the aft body. Therefore, a set of computations were performed in order to examine the closed aft body with and without strut present, at both zero and non-zero angles of sideslip (AOS). The work was divided into a computational task performed by Javier A. Garrriz, using an inviscid (Euler) solver, and a monitoring/reporting task done by John E. Lamar. All this work was performed during FY98 at the NASA Langley Research Center.

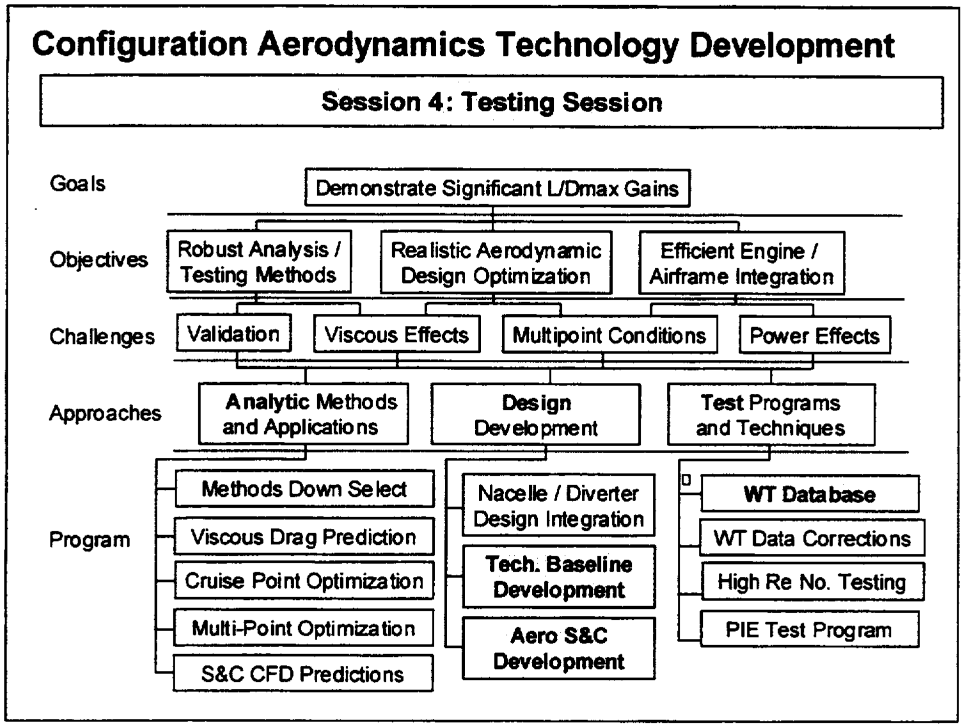

The work reported in this paper is associated with the highlighted boxes.

Outline

- CFD Objectives and Geometrical Modeling
- Supersonic Results
- Conclusions
- Recommendations

This presentation has four parts. The first deals with the objectives of the CFD study and details the geometrical modeling employed. The second part shows the resulting pressures and forces/moments obtained at M = 2.4 with the strut-off and -on. The last two parts summarize the paper with some conclusions and provides recommendations for further studies.

CFD Objectives and Geometrical Modeling

- Estimate strut interference on TCA airplane model at M=2.4, 0.6, 0.9 and 1.2 for AOA 4° and AOS of 0° and -3° using an Euler solver (USM3Dns in its inviscid mode)

- Complete airplane - tip to tip - and supersonic strut modeled

- Strut added to airplane at AOS of 0° and -3°

The general goal of this task is to be able to estimate the strut interference effects on the TCA airplane model at both transonic and supersonic speeds. To date only the M = 2.4 computations have been completed at an angle-of-attack (AOA) = 4 degrees and at AOS = 0 and -3 degrees. These have been made using the USM3Dns code in its Euler or inviscid mode. An overall description of the code follows:

USM3Dns is a tetrahedral-based Euler and Navier-Stokes flow solver. Spatial discretization is accomplished by a cell-centered finite-volume formulation using an accurate linear reconstruction scheme and upwind flux differencing. Time is advanced by an implicit backward-Euler time-stepping scheme. Flow turbulence effects are modeled by the Spalart-Allmaras one-equation model, which is coupled with a wall function to reduce the number of cells in the sublayer region of the boundary layer.

Since the study involved sideslip, it was necessary to model the entire configuration and not take advantage of symmetry. Even though this was not required at AOS = 0 degrees, for consistency full configuration modeling was maintained for all computational situations.

In addition, the supersonic strut was modeled, including the region where it abutted the lower surface of the model. All together about 1.3 million cells were used to model the complete airplane and strut combination.

During the computations, the model geometry was maintained at AOS = 0 degrees regardless of the onset flow. For AOS = -3 degrees the boundary conditions for the flow solution were changed on the model and the relative alignment angle (as viewed from the top) between the model and the strut was altered by moving the strut only the 3 degrees. This was done because the strut surface was represented by a fewer number of cells than the model.

Perspective Top View of TCA

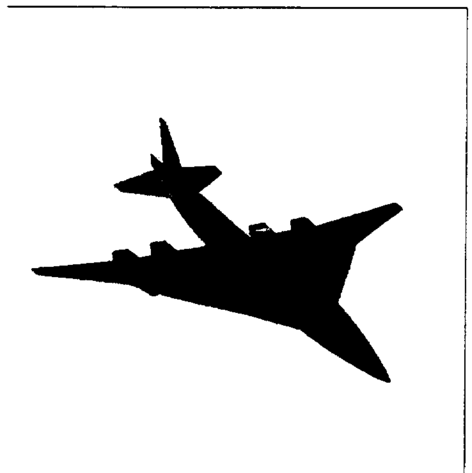

This figures shows a top view of the complete TCA aircraft model from a 3/4 front perspective. The different colors on the various parts of the model are only to assist in keeping track of the geometrical elements during the grid generation portion of this task.

Top View of TCA - UPWT Strut at AOS of 0°

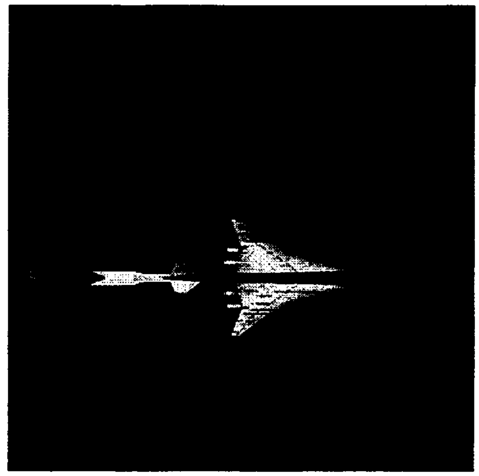

This figure shows the arrangement of the complete TCA model and the supersonic strut from a top view at an AOS = 0 degrees. Again the various colors shown on the different surfaces are only used to keep track of the geometrical elements during the grid creation process.

Side View of TCA - UPWT Strut at AOS of 0°

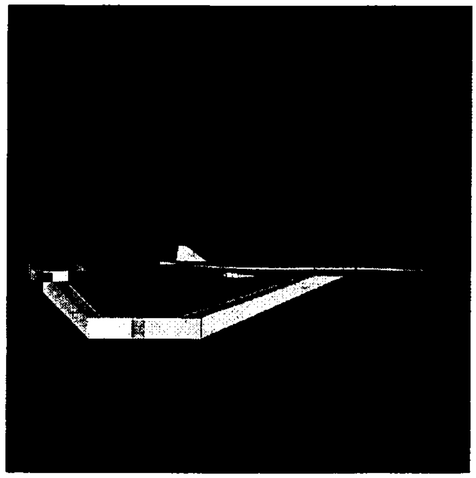

Side view of TCA model mounted atop the supersonic strut at AOS = 0 degrees.

Perspective View of TCA - UPWT Strut at AOS of 0°

This figure is a lower surface view from a 3/4 front perspective of the TCA model mounted atop the supersonic strut at AOS = 0 degrees. Some details of the strut system, both in terms of its cross sectional change with longitudinal distance and the face of the strut where attaches to the tunnel support system, can be seen here.

Alt. Perspective view of TCA - UPWT Strut at AOS of 0°

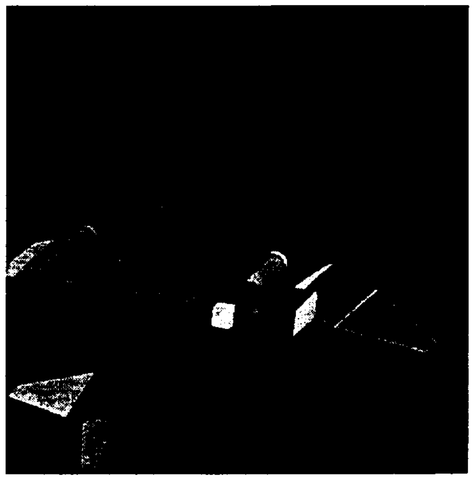

This figure is another lower surface view of the TCA model and supersonic strut system at AOS = 0 degrees, but this time looking forward from underneath the model and with a 3/4 rear perspective.

Top View of TCA - UPWT Strut at AOS of -3°

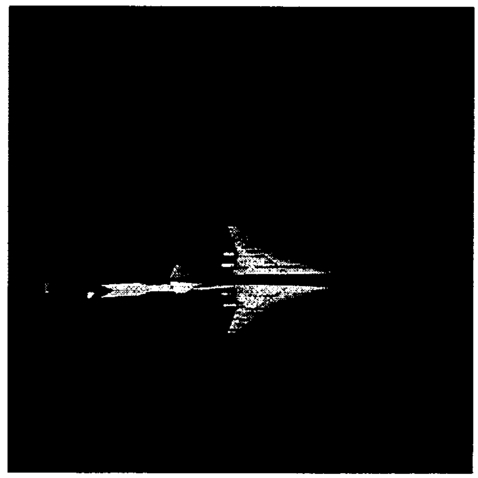

This figure shows the arrangement of the complete TCA model and the supersonic strut from a top view at an AOS = -3 degrees. Again the various colors shown on the different surfaces are only used to keep track of the geometrical elements during the grid creation process.

Perspective View TCA - UPWT Strut Juncture at AOS of -3°

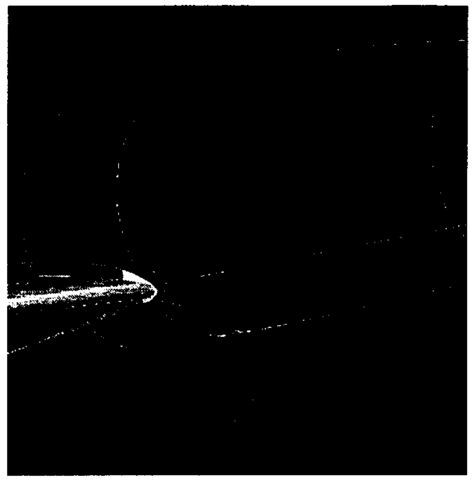

This figure is a lower surface view from a 3/4 front perspective of the juncture between the TCA model mounted and the supersonic strut at AOS = -3 degrees. Note that at the top of the strut leading-edge there is an air gap between the strut and the model which does occur because of the 3 degree misalignment. This gap was modeled.

Supersonic Results

- Surface Pressure Contours
- Forces/Moments
- Cross Sections and Pressures

The figures that follow present the M = 2.4 aerodynamic results for AOA = 4 degrees at AOS = 0 and -3 degrees with the strut-off and -on. These figures include eight surface pressure contours, four for the upper and four for the lower; the overall forces/moments for the entire configuration, as well as the forces/moments for the aft body alone; and cross-sectional plots of local pressures and associated wing/body geometry at fixed Fuselage Stations. The figure presentation follows this order.

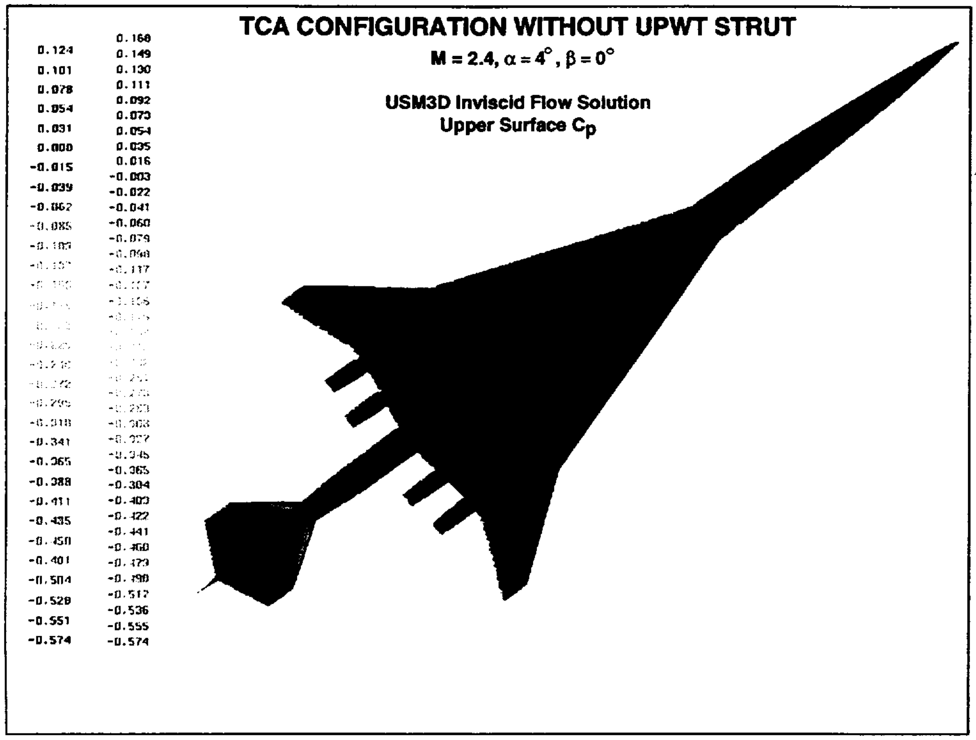

This figure shows the upper surface pressure coefficient contours for the TCA configuration **without** the supersonic strut at M = 2.4, AOA = 4 degrees, and AOS = 0 degrees. The most noticeable phenomenon is that even at AOS = 0 degrees the contours are **not exactly** symmetrical. This is due to the unstructured CFD code (USM3D) modeling the entire configuration and not taking advantage of geometrical symmetry. Consequently, one should expect small lateral side-force and moments at this attitude.

Along the inboard leading-edge and trailing aft over the outboard wing, a region of higher suction pressure is present.

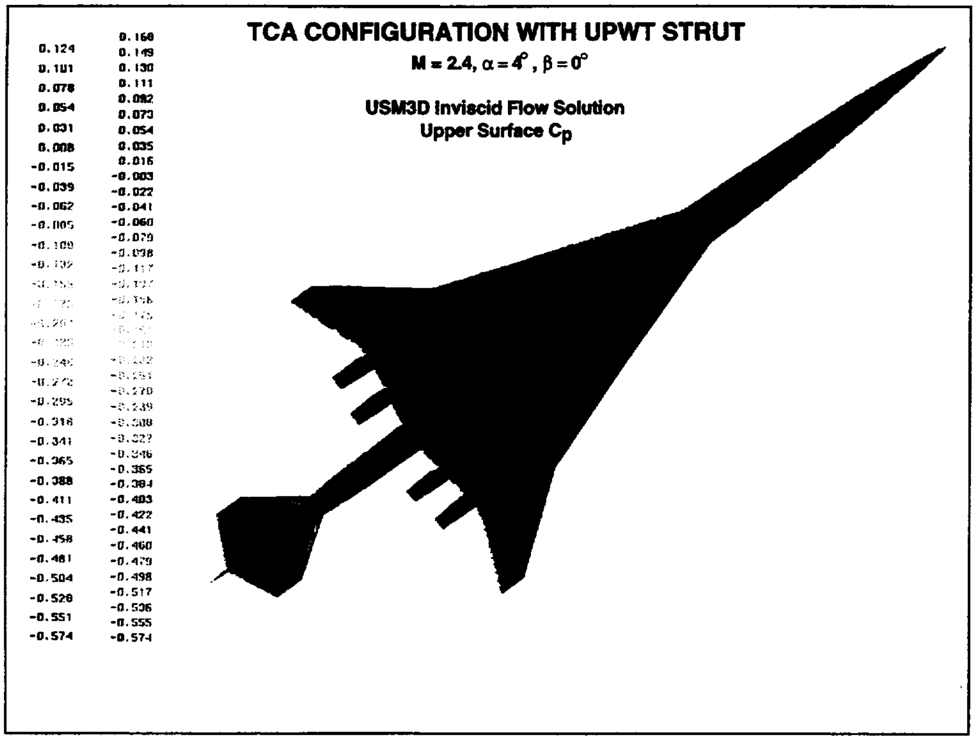

This figure shows the upper surface pressure coefficient contours for the TCA configuration **with** the supersonic strut at M = 2.4, AOA = 4 degrees, and AOS = 0 degrees. In comparison with the previous figure (strut-off), there are no striking differences seen on the upper surface associated with the strut, as would be expected under these conditions.

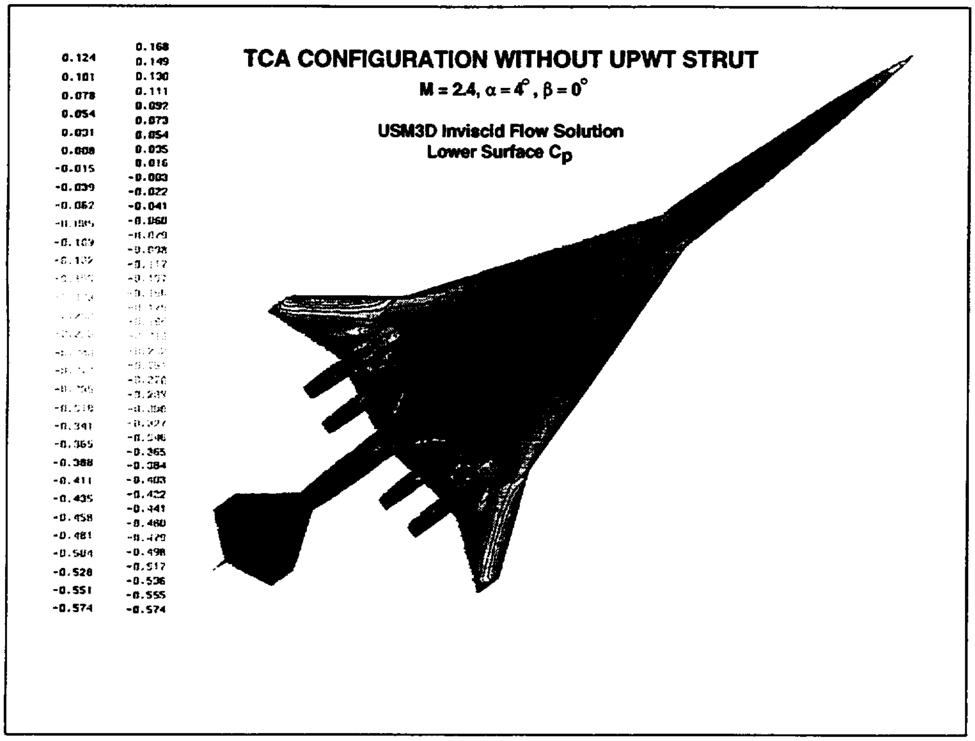

This figure shows the lower surface pressure coefficient contours for the TCA configuration **without** the supersonic strut at M = 2.4, AOA = 4 degrees, and AOS = 0 degrees. Just as for the upper surface, these contours are **not exactly** symmetrical even at AOS = 0 degrees. The most interesting features here are the shock-on-shock interactions between the nacelles, the relatively large suction values of pressure coefficient reached inboard of the inner nacelles, due to flow expansion, and the larger positive pressure coefficients near the outer-wing leading edge.

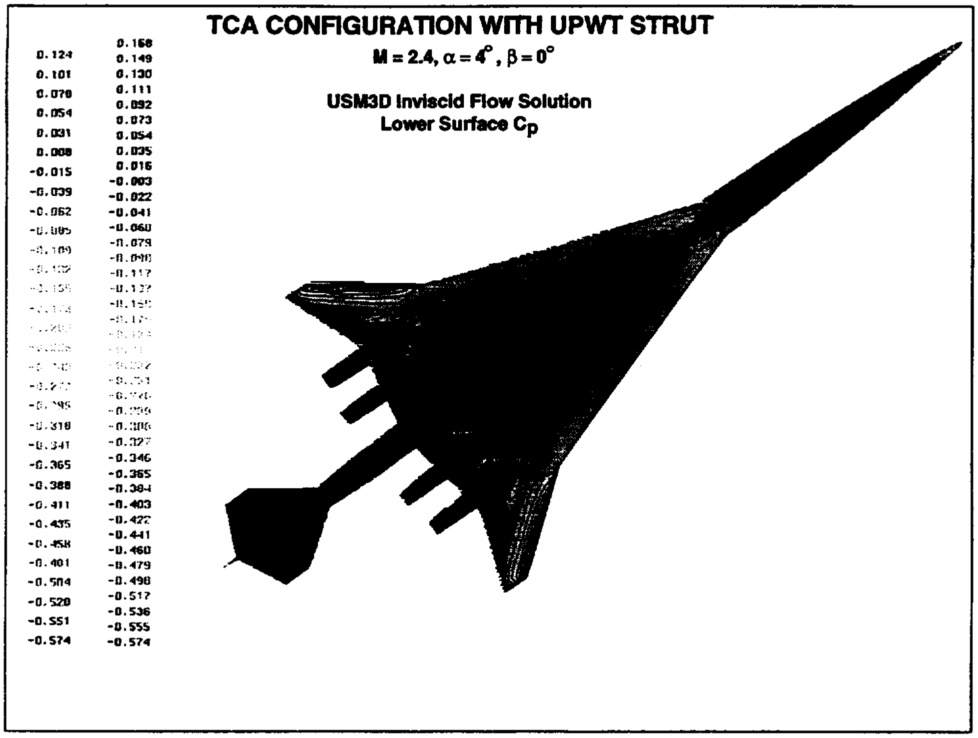

This figure shows the lower surface pressure coefficient contours for the TCA configuration **with** the supersonic strut at M = 2.4, AOA = 4 degrees, and AOS = 0 degrees. In comparison with the previous figure (strut-off), the nacelle shocks and outer-wing leading edge pressure coefficients appear the same. However, there are differences in the pressure coefficients in the streamwise region between the fuselage/wing juncture and the start of the wing outer panel. The presence of the strut is to cause this region of the wing (an inverted V-shape just inboard-and-downstream of the inboard leading-edges) to have a larger positive value than without the strut. Moreover, along the centerline and downstream of the wing/fuselage juncture -- where the strut footprint would be located (see figure 25) -- there is a region of higher suction pressure coefficient indicated on the model. This is unexpected result for a no-flow situation and therefore the integration of the pressure underneath the strut footprint is not performed. Another reason for omitting these force/moment contributions to the reported values is given on later on figure 21.

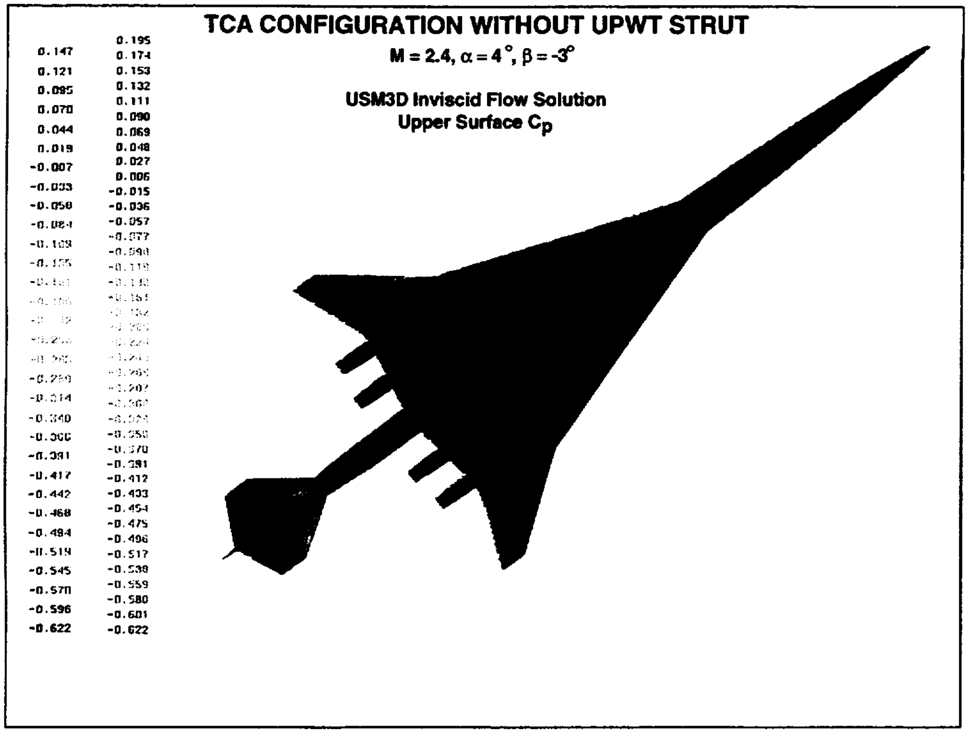

This figure shows the upper surface pressure coefficient contours for the TCA configuration **without** the supersonic strut at M = 2.4, AOA = 4 degrees, and AOS = -3 degrees. The effect of sideslip is clearly noted on the inboard wing where the higher suction region on the windward wing moves inboard and on the leeward wing moves outboard. Moreover, asymmetries are noted in local pressures over the entire length of the model, including higher suctions on the leeward portion of the horizontal tail.

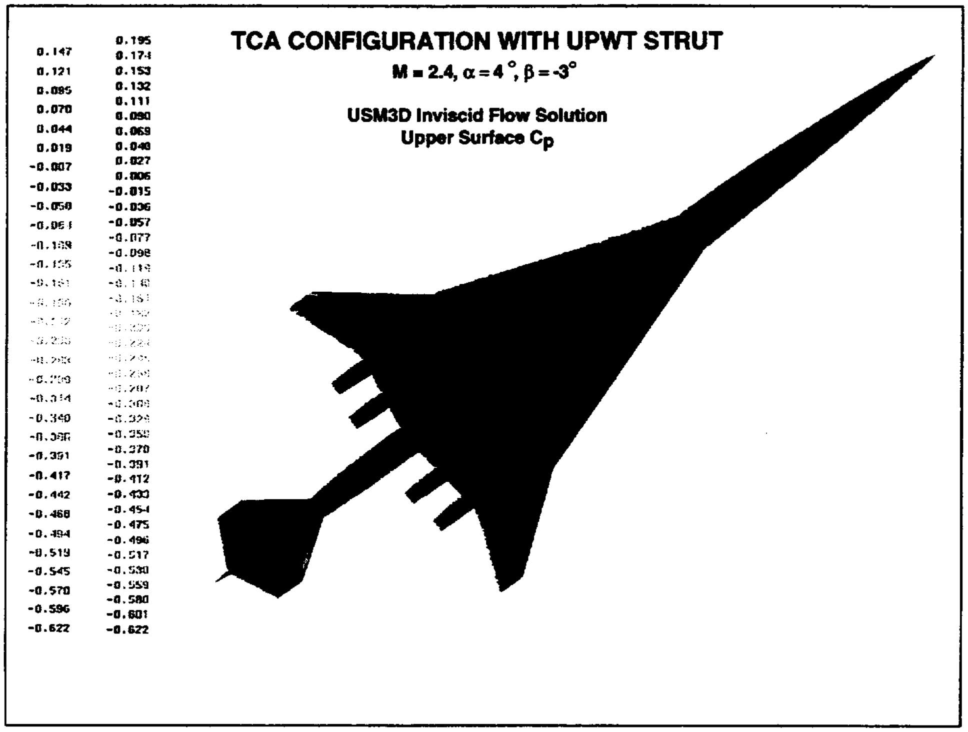

This figure shows the upper surface pressure coefficient contours for the TCA configuration **with** the supersonic strut at M = 2.4, AOA = 4 degrees, and AOS = -3 degrees. In comparison with the previous figure (strut-off), there are no striking differences seen on the upper surface associated with the strut, as would be expected under these conditions.

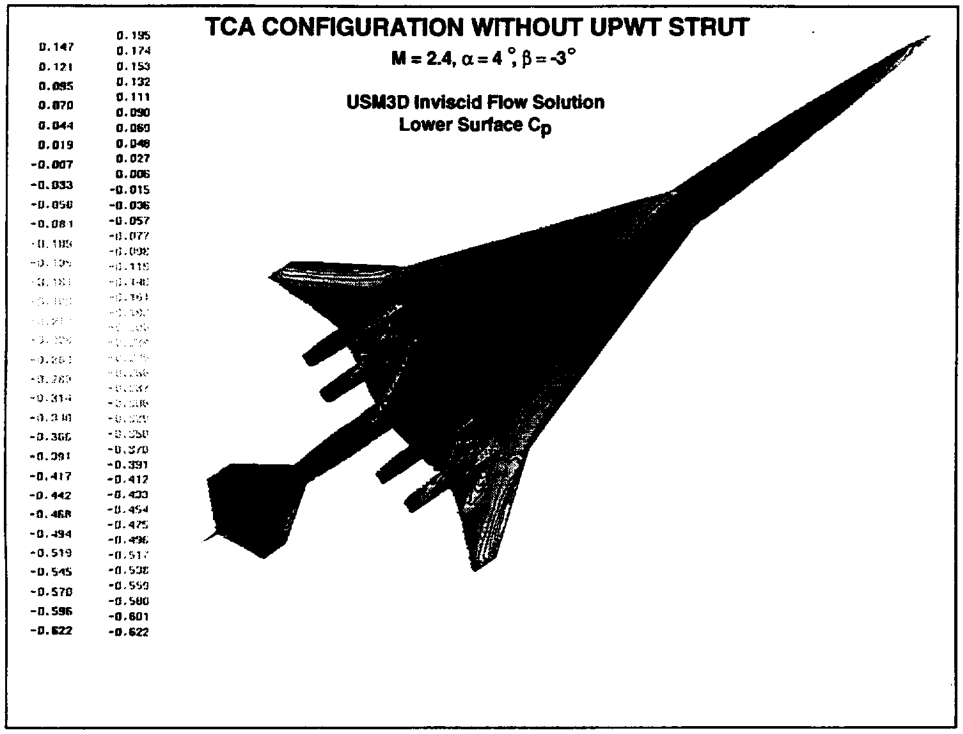

This figure shows the lower surface pressure coefficient contours for the TCA configuration **without** the supersonic strut at M = 2.4, AOA = 4 degrees, and AOS = -3 degrees. In comparison with figure 15 at AOS = 0 degree, the asymmetries associated with sideslip are present all along the configuration, but especially noticeable are the changes to the nacelle shocks and the pressures on the lifting surfaces.

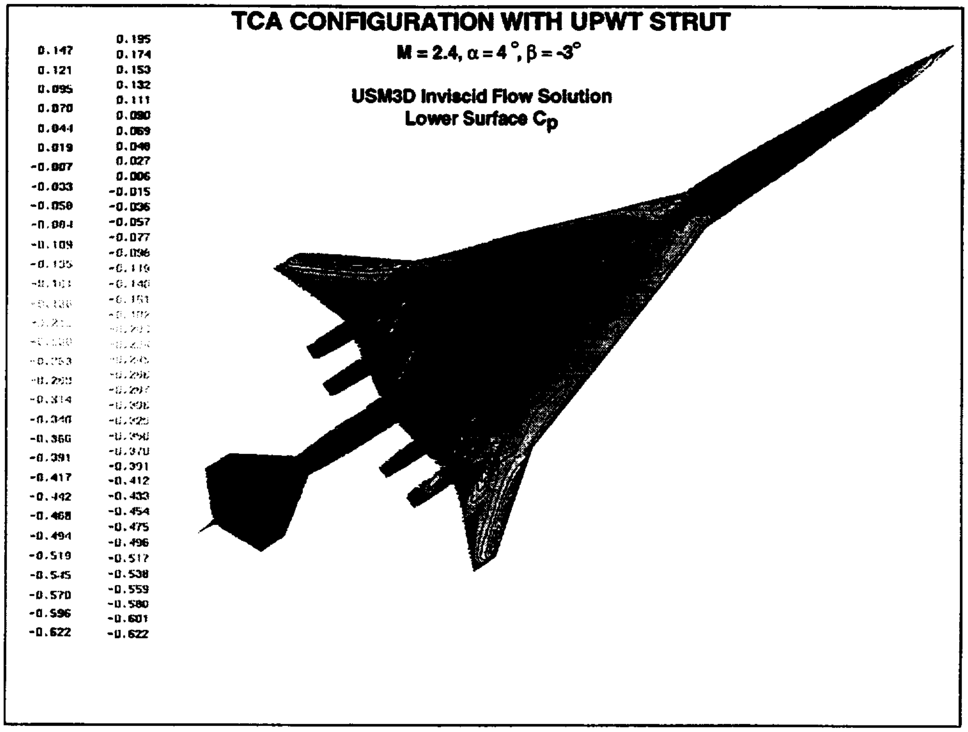

This figure shows the lower surface pressure coefficient contours for the TCA configuration **with** the supersonic strut at M = 2.4, AOA = 4 degrees, and AOS = -3 degrees. In comparison with figure 19 (strut-off), the nacelle shocks and outer-wing leading edge pressure coefficients appear the same. However, there are differences in the pressure coefficients in the streamwise region between the fuselage/wing juncture and the start of the wing outer panel. In particular, the inverted V-shape noted in figure 16 at AOS = 0 degrees is more-or-less retained at sideslip. Hence, the strut tends to have a mitigating effect on the pressures in its immediate vicinity.

TCA Total Force Coefficients
Estimated by Euler Solver (USM3D)

M = 2.4, AOA = 4°

AOS = 0°

	Normal	Axial	Side
• Without strut	0.11392	0.00104	0.00080
• With strut	0.11363	0.00145	-0.00003

AOS = 3°

	Normal	Axial	Side
• Without strut	0.11277	0.00097	0.00035
• With strut	0.11316	0.00147	0.01514

[Note that the forces/moments reported in figures 21 to 24 for the TCA airplane model do not contain those generated over the area associated with the strut footprint (see figure 25). This is done to keep the comparisons consistent with the minimum exposed model-surface-area, i.e. strut on.]

The strut effect on the normal- and side-force coefficients at both AOS of 0 and -3 degrees is seen to be small, and its effect on the axial force coefficient at either AOS value amounts to a “pressure drag” increase of about ~5xE-04 (~5 drag counts).

(Note that the side force coefficient should be zero at AOS = 0 degrees and it isn’t due to the unstructured grid modeling of the complete configuration.)

TCA Total Moment Coefficients
Estimated by Euler Solver (USM3D)

M = 2.4, AOA = 4°

AOS = 0°

	Pitch	Roll	Yaw
• Without strut	-0.21010	-0.00229	-0.00059
• With strut	0.00203	-0.00001	0.0

AOS = 3°

	Pitch	Roll	Yaw
• Without strut	-0.02056	-0.04442	0.09141
• With strut	0.00155	0.00157	-0.00302

At both AOS of 0 and -3 degrees the strut effect on the rolling- and yawing-moment coefficients is seen to be small*; however, there is a destabilizing effect on the pitching moment coefficient to the extent that it goes from stable to slightly unstable.

* Note they should be zero as should all lateral moments values at AOS = 0 degrees.

TCA Total and Aftbody Force Coefficients
Estimated by Euler Solver (USM3D)

M = 2.4, AOA = 4°, AOS = 0°

Total Configuration

	Normal	Axial	Side
• Without strut	0.11392	0.00104	0.00080
• With strut	0.11363	0.00145	-0.00003

Aftbody Only

	Normal	Axial	Side
• Without strut	0.00075	0.00028	0.00001
• With strut	0.00047	0.00032	-0.00003

The strut effect at AOS of 0 degrees on the total TCA configuration force coefficients are repeated from figure 21 for comparison with those for the aft body only. For both it is noted that the changes in aft body force coefficients mirror those of the total configuration. In particular, with the strut present there is less normal force and more axial force; moreover the increase in the latter or "pressure drag" amounts to about one-tenth (~5E-05 or ~0.5 drag counts) of the total increase (~5E-04 or ~5 drag counts).

TCA Total and Aftbody Moments Coefficients
Estimated by Euler Solver (USM3D)

M = 2.4, AOA = 4°, AOS = 0°

Total Configuration

	Pitch	Roll	Yaw
• Without strut	-0.21010	-0.00229	-0.00059
• With strut	0.00203	-0.00001	0.0

Aftbody Only

	Pitch	Roll	Yaw
• Without strut	-0.00079	0.0	0.0
• With strut	-0.00046	0.0	0.00002

The strut effect at AOS of 0 degrees on the total moments coefficients are repeated from figure 22 for comparison with those for the aft body only. The only consistent strut effect noted between the two sets of data is the slightly destabilizing effect on pitching moment coefficient. The other aft body moment coefficients should all be zero but are not due to the unstructured modeling of the complete configuration.

TCA Pertinent Locations

C_p Computation Stations

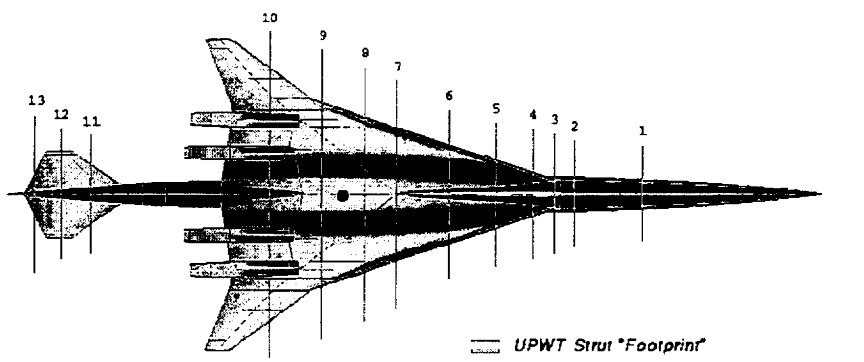

This figure shows the lower surface of the TCA airplane model, the footprint of the strut at AOS = 0 degrees, the moment reference point and the thirteen computational stations where the local pressure coefficients were computed. Not all thirteen locations of pressure data are presented, but enough of them are shown in order to provide understanding as to how the reported forces/moments are developed. Stations 2 to 7 bound the strut footprint on the model.

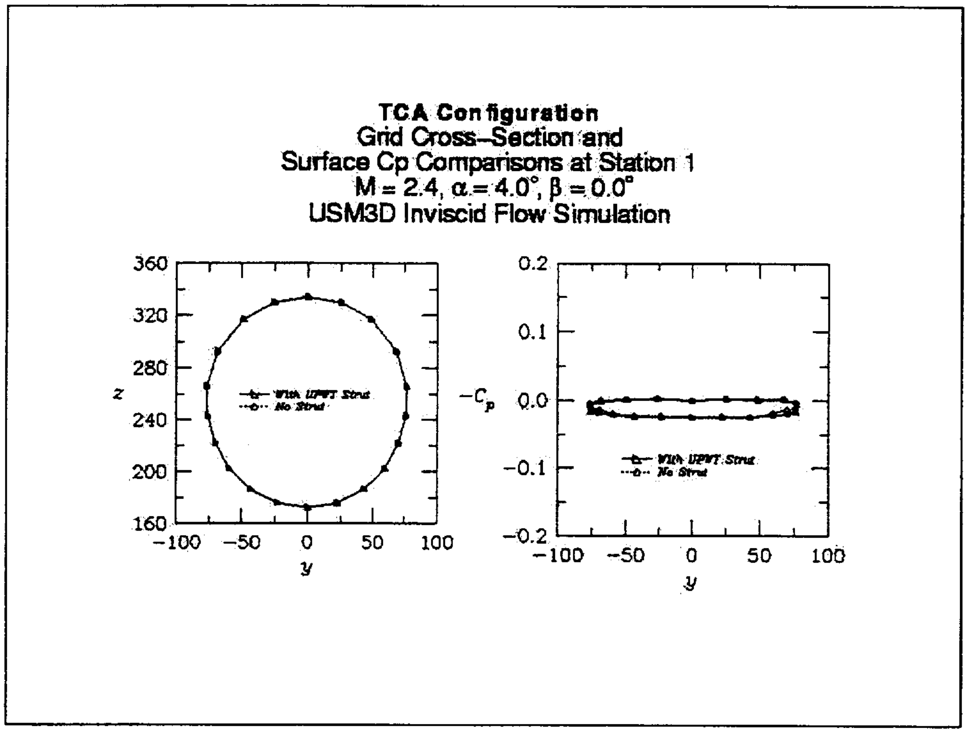

[Note for figures 26 to 37 that the view is looking upstream with the right hand side having the positive y values.]

This figure shows the grid cross-section and the USM3Dns inviscid solution for surface pressure coefficients at station 1, M = 2.4, AOA = 4 degrees and AOS = 0 degrees. This station was chosen because it is ahead of the strut, hence no effect is expected here and thus it can be used for validating the solutions. The pressure data show a negligible effect of the strut.

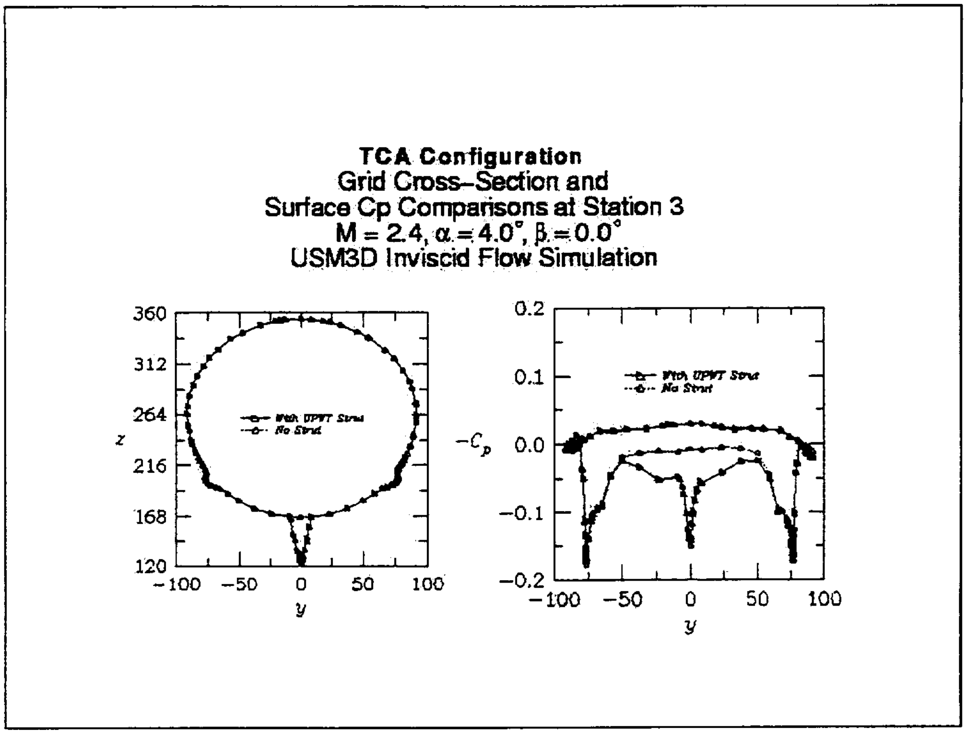

This figure shows the grid cross-section and the USM3Dns inviscid solution for surface pressure coefficients at station 3, M = 2.4, AOA = 4 degrees and AOS = 0 degrees. This is the first station on the strut and shows there to be more positive pressure on the lower surface with the strut present, hence more normal force. Since this station is ahead of the moment reference point, it will contribute a more nose-up moment and be destabilizing.

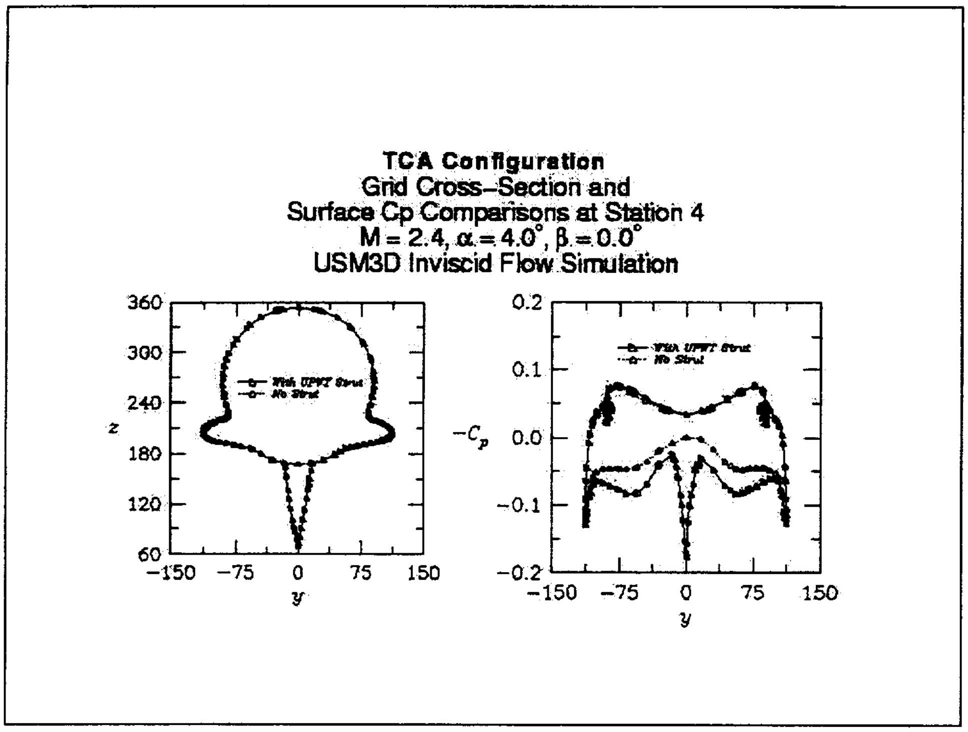

This figure shows the grid cross-section and the USM3Dns inviscid solution for surface pressure coefficients at station 4, M = 2.4, AOA = 4 degrees and AOS = 0 degrees. This station also shows there to be more positive pressure on the lower surface with the strut present, hence more normal force. Since this station is also ahead of the moment reference point, it will contribute a more nose-up moment and be destabilizing.

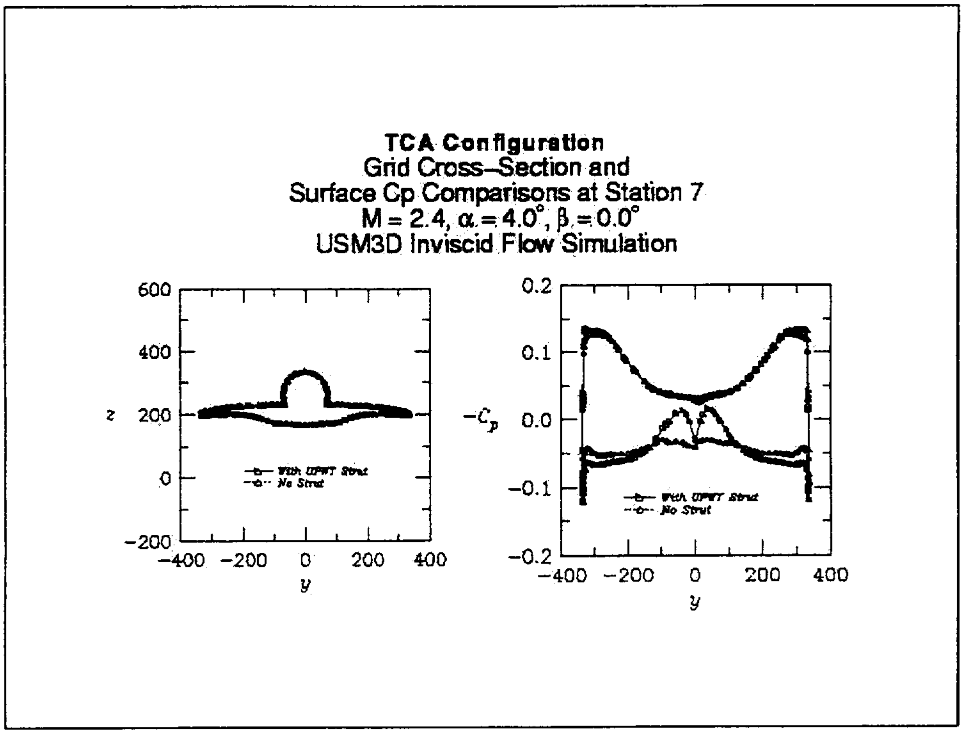

This figure shows the grid cross-section and the USM3Dns inviscid solution for surface pressure coefficients at station 7, M = 2.4, AOA = 4 degrees and AOS = 0 degrees. This station shows that with the strut present there are two suction pressure spikes on the lower surface near y = 0. However, the strut on pressures are more positive outboard of y = +/-140, hence the resulting normal force could be slightly less or the same-as the no-strut configuration. Since this station is still ahead of the moment reference point, the strut effect could be slightly stabilizing or produce no change.

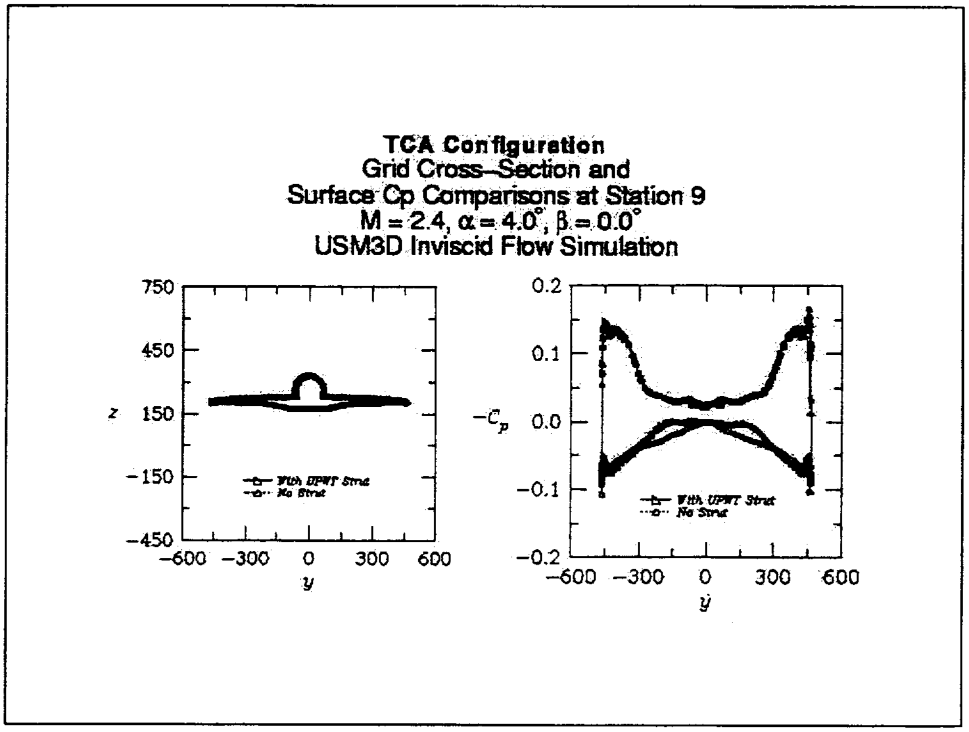

This figure shows the grid cross-section and the USM3Dns inviscid solution for surface pressure coefficients at station 9, M = 2.4, AOA = 4 degrees and AOS = 0 degrees. This station shows that with the strut present there is less positive pressure on the lower surface, hence less normal force. Since this station is behind the moment reference point, it will contribute a smaller nose-down moment and therefore be destabilizing.

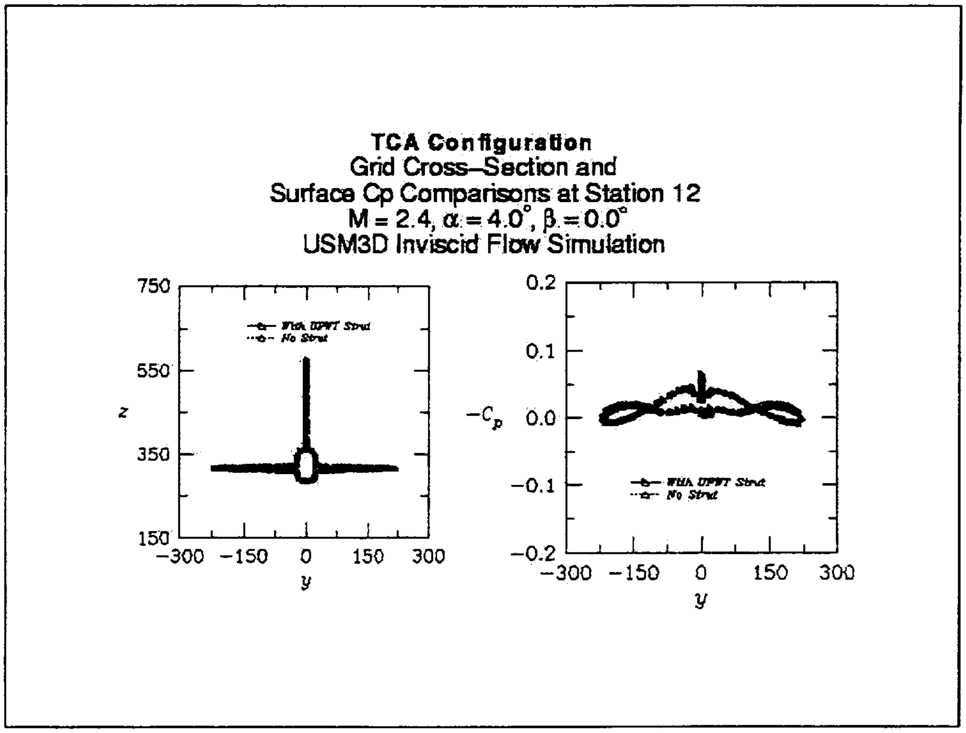

This figure shows the grid cross-section and the USM3Dns inviscid solution for surface pressure coefficients at station 12, M = 2.4, AOA = 4 degrees and AOS = 0 degrees. No discernable differences are noted in the pressure coefficients so no incremental contribution to the normal force or pitching moment from the strut is expected on the empennage.

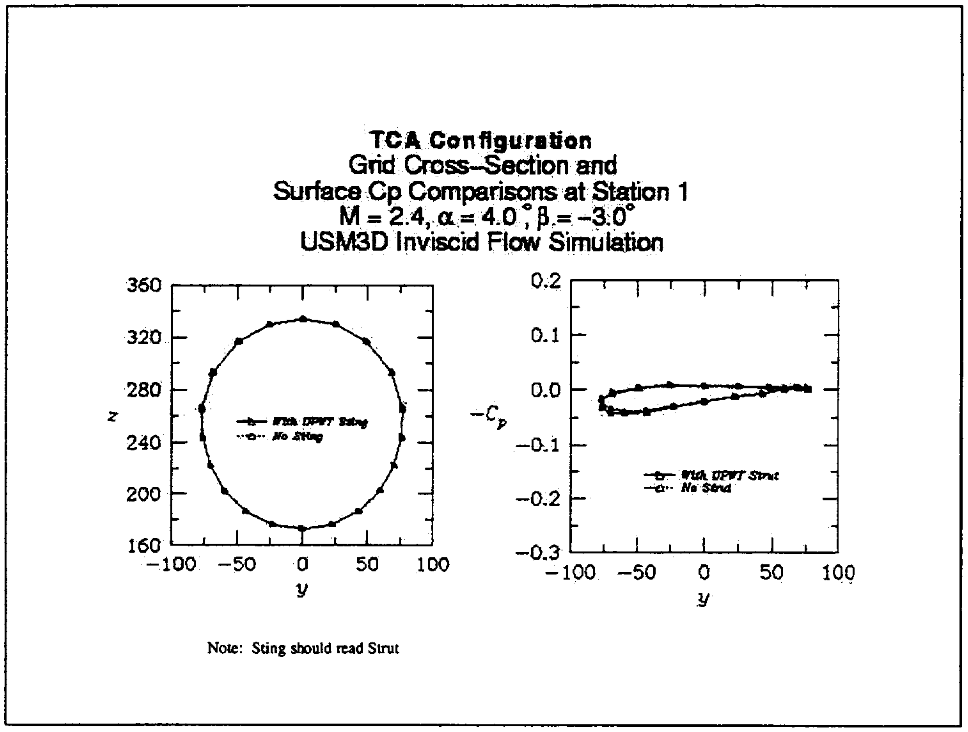

This figure shows the grid cross-section and the USM3Dns inviscid solution for surface pressure coefficients at station 1, M = 2.4, AOA = 4 degrees and AOS = -3 degrees. This station was chosen because it is ahead of the strut, hence no effect is expected here and thus it can be used for validating the solutions. The pressure data show a negligible effect of the strut.

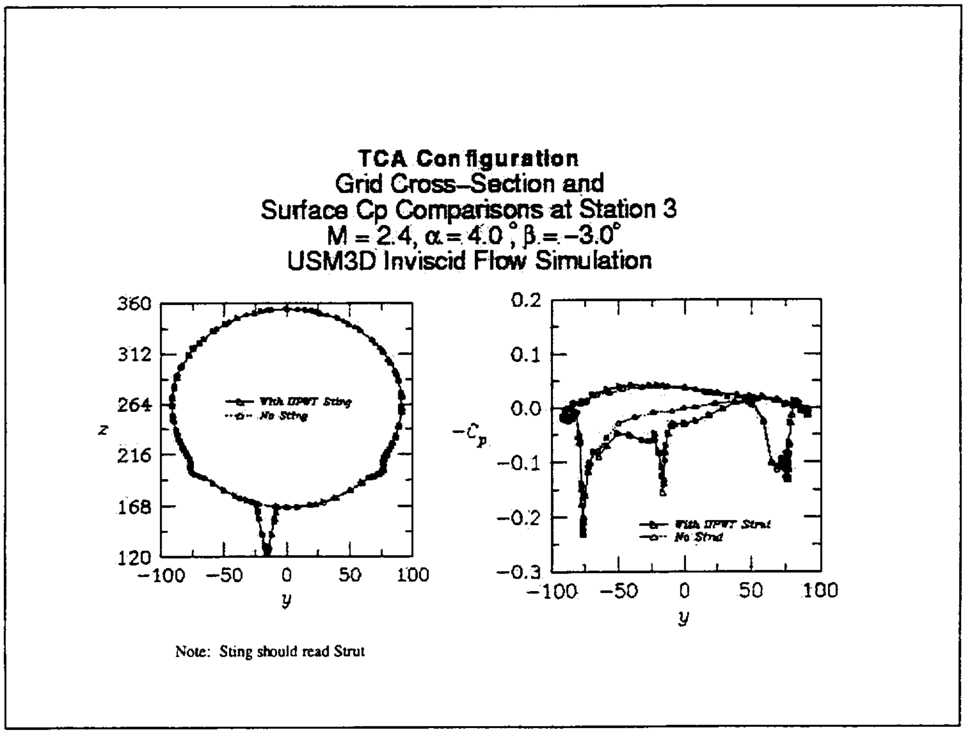

This figure shows the grid cross-section and the USM3Dns inviscid solution for surface pressure coefficients at station 3, M = 2.4, AOA = 4 degrees and AOS = -3 degrees. This is the first station on the strut and shows there to be more positive pressure on the lower surface with the strut present, hence more normal force. Since this station is ahead of the moment reference point, it will contribute a more nose-up moment and be destabilizing.

[Note that there will be small side force coefficient and rolling- and yawing-moment coefficient differences associated with the integration of the two different lateral, delta-pressure-coefficient distributions over the cross-sectional geometry for figures 33 to 37.]

TCA Configuration
Grid Cross-Section and
Surface Cp Comparisons at Station 4
M = 2.4, α = 4.0°, β = -3.0°
USM3D Inviscid Flow Simulation

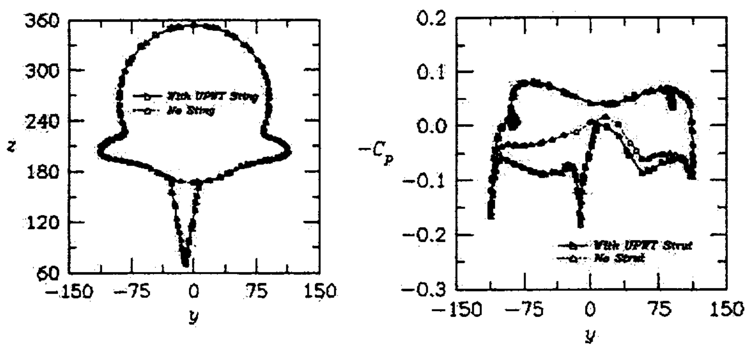

Note: Sting should read Strut

This figure shows the grid cross-section and the USM3Dns inviscid solution for surface pressure coefficients at station 4, M = 2.4, AOA = 4 degrees and AOS = -3 degrees. This station also shows there to be more positive pressure on the lower surface with the strut present, hence more normal force. Since this station is also ahead of the moment reference point, it will contribute a more nose-up moment and be destabilizing.

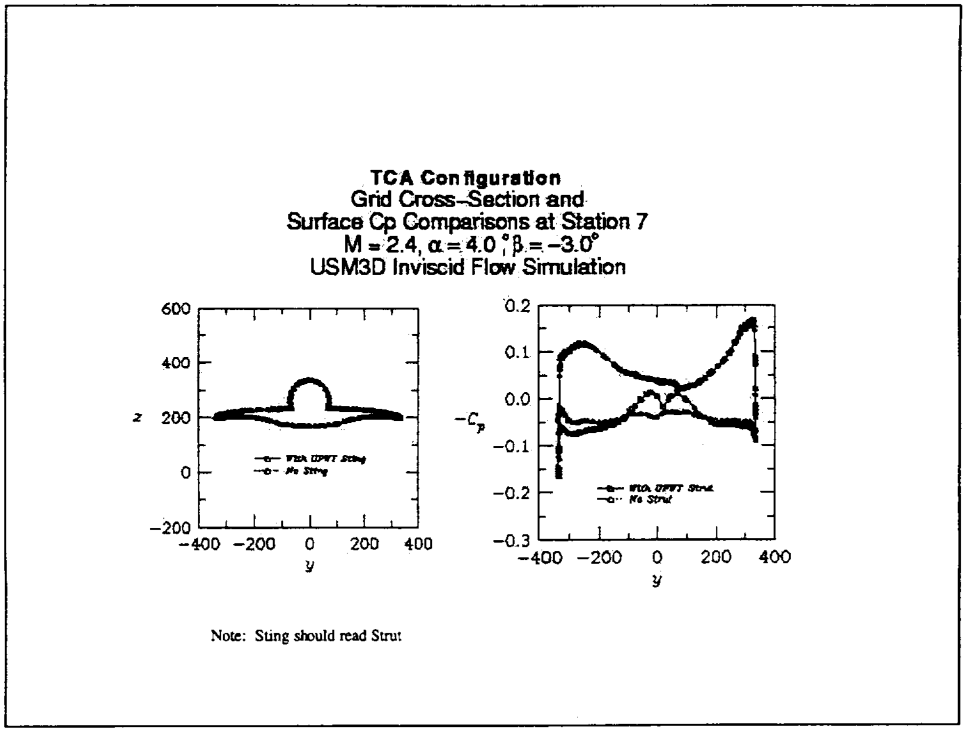

This figure shows the grid cross-section and the USM3Dns inviscid solution for surface pressure coefficients at station 7, M = 2.4, AOA = 4 degrees and AOS = -3 degrees. This station shows that with the strut present there are two suction pressure spikes on the lower surface near y = 0. However, the strut on pressures are more positive outboard of y = -100 and +150, hence the resulting normal force could be slightly less or the same-as the no-strut configuration. Since this station is still ahead of the moment reference point, the strut effect could be slightly stabilizing or produce no change.

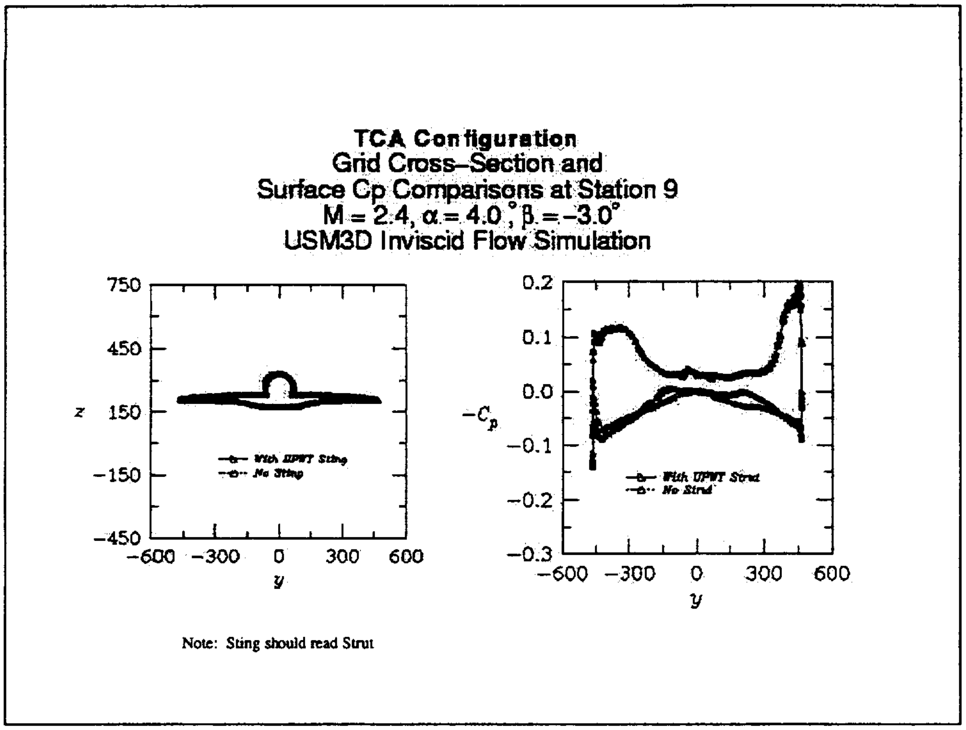

This figure shows the grid cross-section and the USM3Dns inviscid solution for surface pressure coefficients at station 9, M = 2.4, AOA = 4 degrees and AOS = -3 degrees. This station shows that with the strut present there is less positive pressure on the lower surface, hence less normal force. Since this station is behind the moment reference point, it will contribute a smaller nose-down moment and therefore be destabilizing.

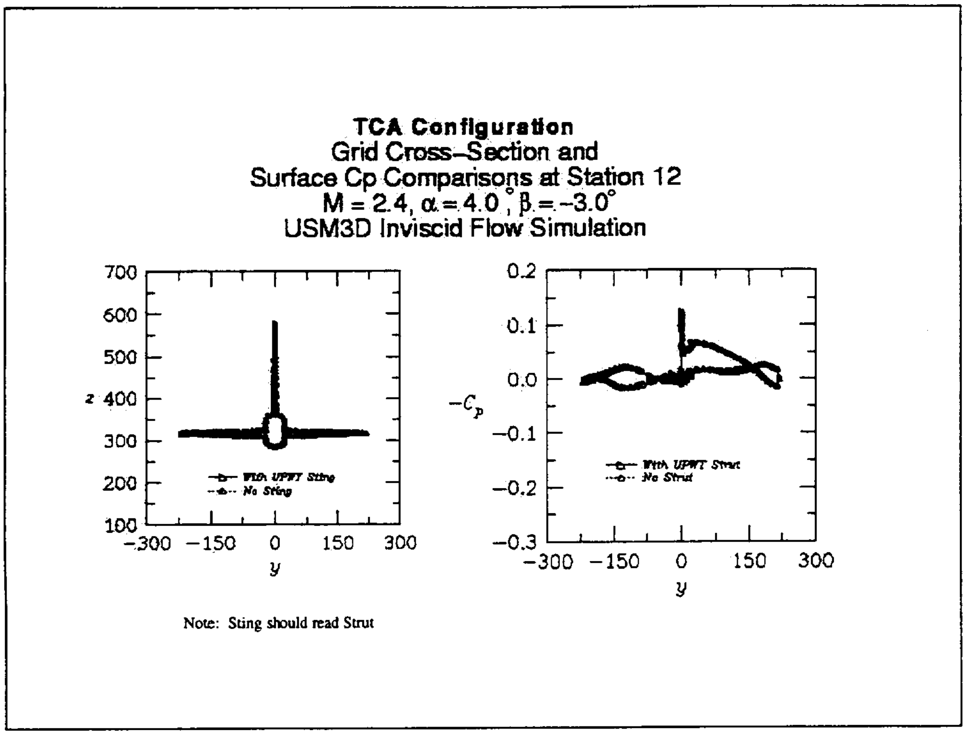

This figure shows the grid cross-section and the USM3Dns inviscid solution for surface pressure coefficients at station 12, M = 2.4, AOA = 4 degrees and AOS = -3 degrees. No discernable differences are noted in the pressure coefficients so no incremental contribution to the normal force or pitching moment from the strut is expected on the empennage.

Conclusions

Inviscid (Euler) strut effects at M=2.4 on the TCA configuration and aft body are:

- Negligible for normal force coefficient

- Increase pressure drag (axial force) coefficient

- Slightly pitch destabilizing

The USM3Dns code has been used in its inviscid (Euler) mode to provide solutions for the TCA model in free air and in the presence of a support strut at M = 2.4 at both Angles Of Sideslip (AOS) of 0 and -3 degrees. The strut effects on the TCA configuration and aft body were determined to be negligible on normal force, to increase the pressure drag by ~5 counts on the TCA configuration and ~0.5 counts on the aft body, and be slightly pitch destabilizing on both.

Recommendations

- Compare Euler and Navier-Stokes solutions over the TCA aft body for particle traces, Cp, and force/moment
- Do transonic solutions of ***transonic strut*** and compete airplane prior to testing in 16FTT in FY99

It is recommended that viscous (Navier-Stokes) solutions be generated for comparison with those shown herein. The resulting comparisons should include particle traces, pressure coefficients, and forces/moments over the aft body.

It is also recommended that prior to the transonic wind-tunnel testing of the TCA model in the 16FTT during Spring 1999, transonic solutions, of at least the Euler type, be available to provide understanding of the anticipated strut-interference effects. Since the transonic strut is shaped differently than the supersonic one, there is a need for some new geometric modeling to be completed in order for this task to be preformed.

BOEING

Thrust Drag Bookkeeping and The Calibration of Nacelles for Internal Drag

Eric Adamson

HSCT Configuration Aerodynamics

February 2, 1999

The task of developing an internal drag calibration process for HSCT nacelles falls under the category of wind tunnel corrections. For the most part, however, it has been funded out of the Propulsion Induced Effects (PIE) Program. This interesting funding arrangement makes sense because a HSCT nacelle calibration process is a critical requirement for any PIE testing. As the HSCT program has evolved, accurate experimental assessments of nacelle integration effects have become more critical, and nacelle internal geometries have become more complex. As a result, it was apparent that the program had outgrown the empirical nacelle internal skin friction corrections of the past. In the case of M=2.4 cruise point experimental evaluation, the cost and accuracy of CFD based corrections may be sufficient to meet the programs internal drag correction needs. For off-design evaluations, the nacelle internal geometry becomes more complex (ramps & plugs), the number of required CFD runs increase, and convergence time and uncertainty increase. All this adds up to a cost for CFD based corrections that is currently unacceptable. Consequently, the preferred approach taken by most major transport or fighter programs is to calibrate nacelles. Historically, nacelle calibration has been shown to be a reliable, accurate, and cost effective approach to determining nacelle internal forces. Unfortunately, because of several unique features in current HSCT geometries and the thrust-drag bookkeeping system, the program could not adopt "as-is" an existing calibration procedure from one of these programs.

Configuration Aerodynamics Technology Development

BOEING

High Speed Civil Transport

Program Selects Best Analysis / Design Optimization Methods

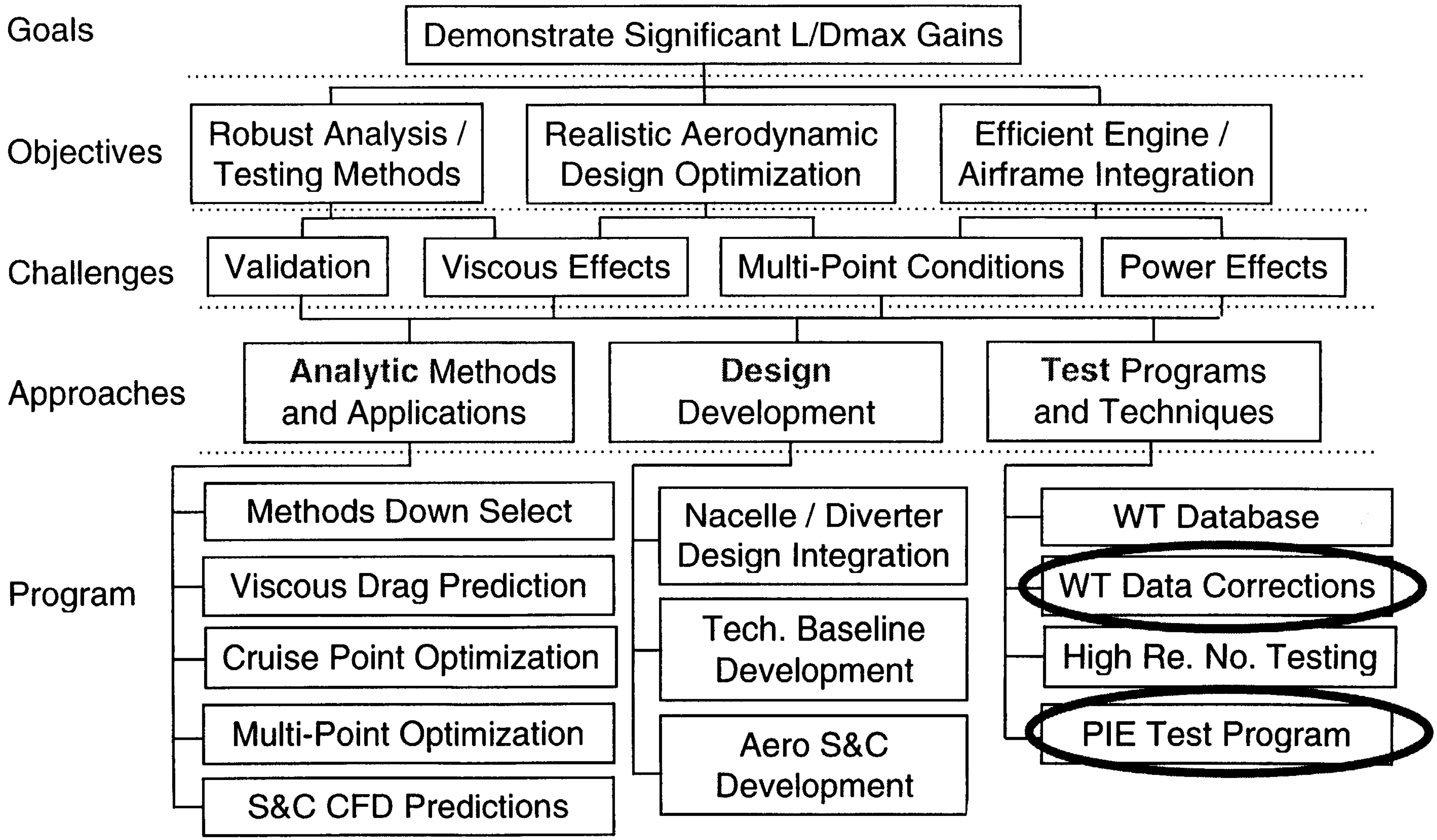

Outline

This report documents the results of two tests that were run in the Boeing Flight Simulation Chamber (FSC) to develop an HSCT specific calibration process. The report is divided into 6 parts. The first part is a review of thrust-drag accounting systems. The choice of how internal drag can be obtained is determined by the T-D system. The second part reviews the basic principles concerning how and why calibration works. The third and fourth part review results of the first HSCT calibration test. This test went a long way toward validating a HSCT methodology. The fifth and sixth parts review the results of the second calibration test. This test was intended to use some available hardware to refine the handling of Reynolds number effects and to explore the feasibility of calibrating with supersonic duct flow.

Outline

- Review of Thrust-Drag Bookkeeping Basic Principles
- Review of Nacelle Calibration Basic Principles
- Results From 1st HSCT Test/Calibration (Dec-Feb/IRAD)
- Conclusions/Recommendations (1st Entry)
- Results From 2nd HSCT Calibration (October/HSR)
- Conclusions/Recommendations (2nd Entry)

February 1999 HSR Airframe Technical Review

Before a HSCT specific internal drag calibration methodology can be developed, one must understand the HSCT definition of internal drag. Concurrent with this 1998 CA task was a Technology Integration (TI) Thrust-Drag (T-D) task. This task was chartered to review the existing documentation on the HSCT T-D bookkeeping system and compare that definition to the thrust and drag databases being generated with CFD and experiments. It also compared the HSCT T-D system to that of other commercial and military programs. The ultimate goal of the TI task was to figure out where there were mismatches between the WT & CFD databases being generated and the T-D system that would be used to develop airplane performance. Recommendations could then be made as to whether to change the types of tests being planned, the types of data these tests would generate, and/or how these data went into airplane performance.

This review indicated that there were some commonly held misconceptions as to what the definition of internal drag was and what it meant relative to aircraft performance. The understanding among many people was that internal drag was the sum of all nacelle internal forces and that to correct wind tunnel model or CFD model forces, one simply removes the forces predicted on the internal surfaces. While this may be a useful approximation for a select few scenarios, for most cases, it is a gross oversimplification. Internal drag is negative net thrust. Because the Propulsion group never runs installed propulsion systems, the actual definition is a complex arrangement negotiated by the T-D document. In the case of aircraft performance, it turns out that it is more important that thrust and drag are assessed consistantly than “accurately”. For example, if a T-D system lumps nacelle skin friction in with thrust, it decreases the thrust available per lb/fuel, but it also reduces the thrust required the same amount. If on the other hand neither staff includes nacelle skin friction, but calculates all other forces very accurately, a performance short fall will result.

Review of Thrust-Drag Basic Principles

<u>There are two common misconceptions about internal drag</u>

1) "Internal drag" is the summation all nacelle internal forces
2) "Drag" is entire model drag less the "internal drag"

<u>Reality:</u>

1) Internal drag is "Net Thrust" produced by a flow-thru nacelle
2) Internal drag may have no relation to internal forces
3) The definition of thrust and drag is a complex relation as defined by a Thrust-Drag bookkeeping system
4) In T-D, CONSISTENCY is more important than accuracy

A Thrust-Drag Bookkeeping System is a formal agreement between Aerodynamics and Propulsion staffs on how to handle 3 key questions: What is the control volume, what is the reference condition and how are off-reference conditions to be handled.

The control volume definition answers the questions: Where does drag end and thrust begin? How does it vary with external and internal conditions?

The reference system definition forms the baseline from which propulsion airframe interactions can be incremented. The fact is, airframe and propulsion control volumes interact. Variable geometry airframes and propulsion systems further complicate matters. Airframe effects entering the propulsion control volume change thrust, and effects within the propulsion control volume change lift and drag. The interactions are termed Propulsion Induced Effects (PIE). PIE effects must be incremented from a reference condition/geometry that is consistent between Aerodynamcs (Aero) and Propulsion staffs.

The off-reference PIE effects system clarifies who bookkeeps what. When an off-reference effect is produced, it often can be termed thrust or drag. The T-D system negotiates these ambiguities into a constant framework.

Review of Thrust-Drag Basic Principles

A Thrust-Drag Bookkeeping System is a formal agreement between Aerodynamics and Propulsion staffs on how to handle 3 key issues.

- **Control Volume:**
  - In general, where does Drag end and Thrust begin?
- **Reference System:**
  - What common configuration will be a baseline both Propulsion and Aero thrust and drag assessments?
- **Off-Reference PIE effects:**
  - For non-reference configuration, how will the resultant forces be handled.

February 1999 HSR Airframe Technical Review

In 1998, a comprehensive review of the HSCT Thrust-Drag Bookkeeping system was funded under the Technology Integration task. Because TI has the ultimate responsibility of incorporating the databases generated by each staff, it was natural that they should conduct such a review. The current T-D system has remained relatively unchanged since its first use on the old Boeing SST. The system has been reviewed twice since the SST. The first time was in 1991 in order to determine whether it was still acceptable for HSCT conceptual design studies. The second review was in 1995, when a downselect was required between the system used by Seattle HSCT and that used by Long Beach. The most recent review was meant to be more comprehensive. TI was to review the potential advantages and disadvantages of the current method and alternatives open for consideration. TI would make an assessment of how well current and future CFD and test databases would fit with current and alternate T-D systems. What TI found was that the current T-D system had issues with its control volume definition, reference system definition, and how PIE effects were handled. The conclusion was that the accurate determination of thrust in the current T-D system was expensive and error prone, that neither Aero or Propulsion are currently determining thrust accurately or consistently, and that Propulsion was ill equipped to change methodology in the short term.

Review of Thrust-Drag Basic Principles

TI Review of T-D status Found:

- The accurate determination of thrust in the current T-D system is expensive and error prone
- Propulsion is currently not accurately determining thrust
- Aero is currently not accurately determining thrust
- CFD solutions are not calculating thrust (internal drag)
- Aero and Propulsion are assessing thrust differently
- In the short term Propulsion cannot change methodology

The accompanying figure shows the current HSR control volume definition of thrust. This definition is a variation of what textbooks refer to as "intrinsic thrust". An accurate assessment of drag under this definition requires instrumentation to determine the integrated pressure, weight flow, and velocity at a location just upstream of the nacelle, at the nacelle highlight, and at the nacelle exit. In practice this would be costly, inaccurate, and problematic.

High Speed Civil Transport

Current T-D Control Volume

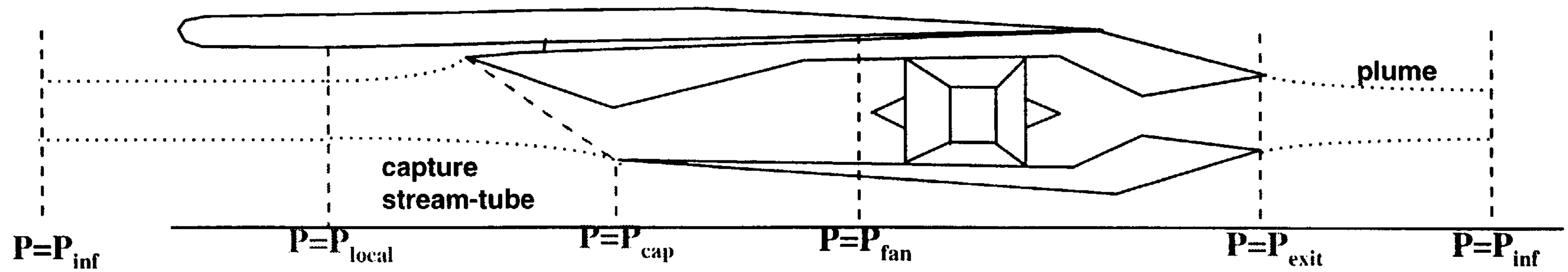

Current HSR Definition: Variation on *Intrinsic Thrust*:(unique to Industry)

Thrust =	$M_{dot}V_{exit} + A_{exit}(P_{exit} - P_{local})$	(Gross Thrust)
	$- [M_{dot}V_{cap} + A_{cap}(P_{cap} - P_{local}) - M_{dot}V_{local}]$	(Additive Drag)
	$- M_{dot}V_{local}$	(Local Ram)
	$- (P_{local} - P_{inf})(A_{cap} - A_{exit})$	(Pref correction)

An Accurate Experimental Assessment of Thrust is Problematic-Requires Flow Survey at 3 Locations

An example of the issues associated with the reference definition is shown in the following figure. The reference nacelle definition differs both from what Aero tests and what a real airplane sees over much of it's mission. As an example, the internal geometry is different for all three cases. For the reference nacelle, it is assumed that one flow enters the inlet and everything becomes thrust (so the internal geometry is irrelevant). The WT geometry in comparison, has a constant area flow-through duct. Finally, the flight article has the real geometry which has complex geometry throughout. Each of these geometries will have a different force in the lift direction. For the reference nacelle the force will be zero, the WT geometry will generate some force in the positive or negative lift direction, and the flight article might generate a large lift force in the positive direction. Is duct lift part of drag or thrust? Currently, Propulsion has no way to included lift in the engine deck and never runs an installed flow-thru nacelle so it can not be included in thrust. But Aero never runs the real geometry. The net result is that the Aero CFD solutions are generating a force that has no real home in the current T-D system.

The handling of off-reference PIE effects is further confused in the current system. All effects are broken down into installed versus isolated effects. This requires drag to be build up from 6 numbers: the flight conditions installed and isolated, the reference conditions installed and isolated, and the WT conditions installed and isolated. As one can see, the current system is hopelessly complicated.

Current T-D Reference System

BOEING
High Speed Civil Transport

Reference Nacelle Installation

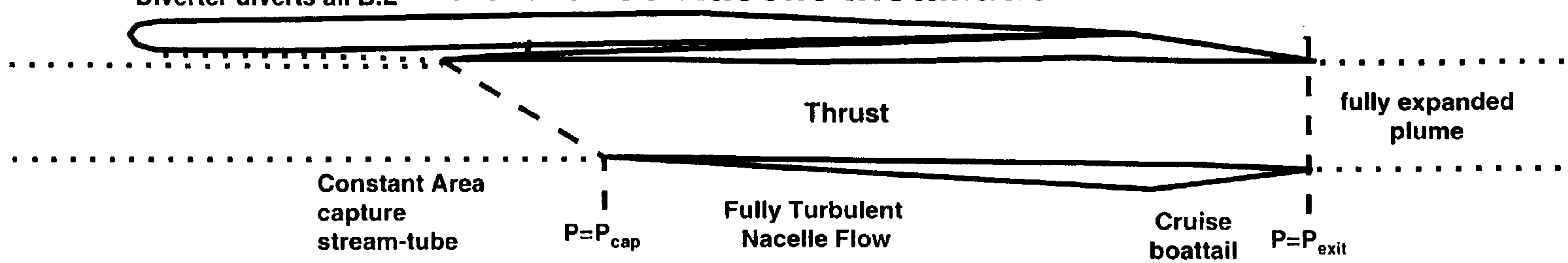

Nominal WT Conditions

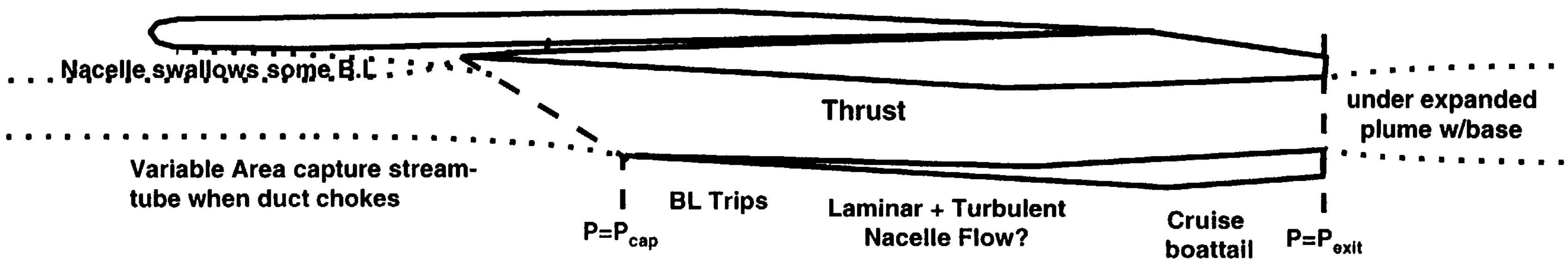

Nominal Flight Conditions

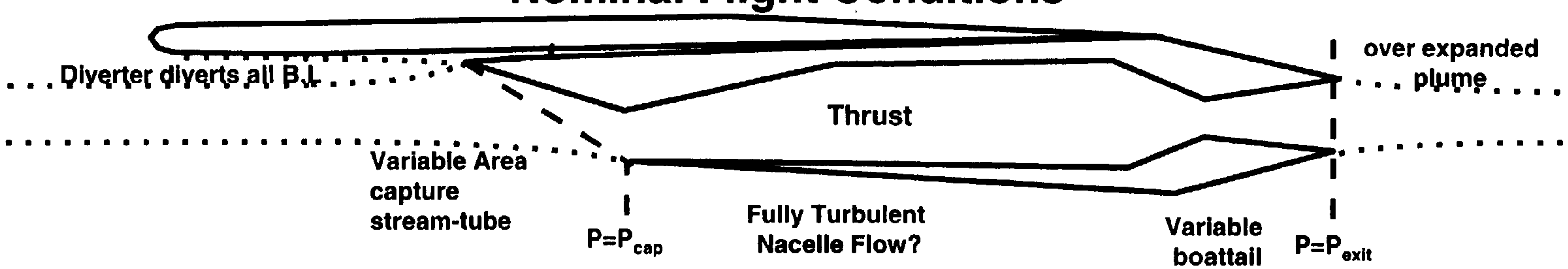

While the Technology Integration task was not directly related to the CA calibration methods task, it has been key to determining the direction of the calibration work. The T-D task indicated that there have been some major mismatches in the past on how Aero and Propulsion determine thrust and drag. These mismatches are not trivial and cannot be overcome without substantially more testing and analysis than is currently budgeted in the program management is prepared to spend. In short, , the study showed that it would be impractical to develop a calibration methodology that fully supports the current T-D system. As a result, a short term and a long term solution were proposed. Short term, Aero would incorporate into our drag model any forces that are a result of Aero/Propulsion mismatches. Aero could calculate thrust identical to Propulsion for our wind tunnel models and any forces above and beyond thrust are drag. This would solve the immediate problem of forces being double bookkept or systematically neglected. The long term solution proposed is to update the thrust drag bookkeeping system to something that could and would be supported by both experiment and CFD, and by Propulsion and Aero groups. The system that is proposed is "Net Standard Thrust" and is the industry standard. It is the recommended system by both AIAA and AGARD advisory groups. A nacelle internal drag calibration methodology can be readily adapted to this system. CFD codes can also be easily adapted to accommodate such a system.

Review of Thrust-Drag Basic Principles

<u>TI T-D status Review Recommendations:</u>

- Short term fix: Aero should calculate thrust like Propulsion (right or wrong), and assume all residual forces are drag.
- Long term fix: Adopt a new T-D system that Aero and Propulsion <u>can</u> and <u>will</u> follow

The TI task recommended a change to a new T-D system consisting of a different control volume, reference configuration, and division of PIE effects. The following figure illustrates the recommended control volume for the program in the future. Textbooks refer to this system as Net Standard Thrust. This system requires that the instrumentation to determine the integrated pressure, weight flow, and velocity only be at a single location. Ram drag is known from the exit weight flow and the freestream velocity.

The new reference configuration would be variable consisting of two or more configurations. As a minimum, there would be separate M=2.4 and M=.90 cruise references. These reference configurations would be chosen to match flight with the wind tunnel models as closely as possible.

Finally, the system of separating all PIE increments into isolated and installed effects would be discontinued.

Recommended Thrust Definition For Future Applications

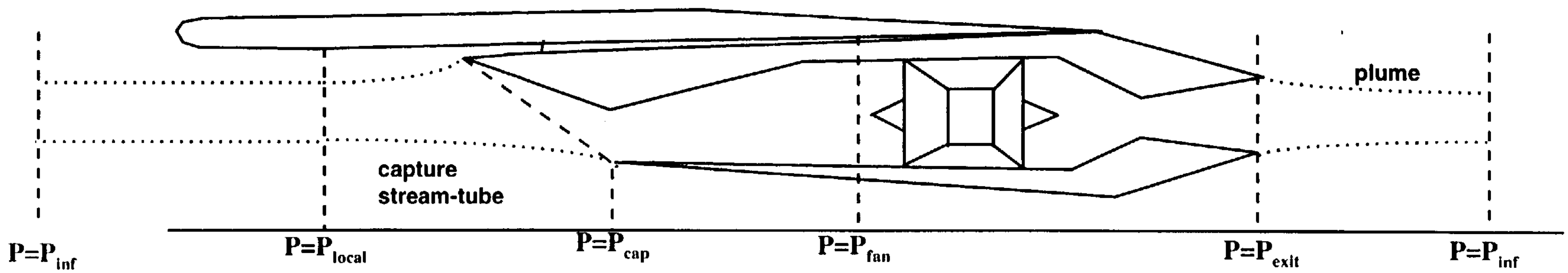

Proposed Definition : *Net Standard Thrust*: (Industry Standard)

$$\text{Thrust} = M_{dot} V_{exit} + A_{exit} (P_{exit} - P_{inf}) \quad \text{(Gross Thrust)}$$

$$- M_{dot} V_{inf} \quad \text{(Ram Drag)}$$

New T-D System Requires Accurate Momentum Measurements at 1 Location

General Internal Drag Objectives for HSCT Program

So why calibrate nacelles, and if it is such a good idea why haven't we done it before? The underlying assumption behind this work is that the program has reached the point where the accurate determination of internal drag is necessary and worth some expense. Historically HSCT nacelles were straight, constant area, circular ducts aligned with the local inlet flow. Most design work was focused exclusively at the M=2.4 cruise condition. For this scenario, an empirical skin friction analysis very closely approximates the real nacelle internal drag. However, over the last several years many things have changed. The internal ducts are rarely straight, often not aligned with the local flow, and off-design effects are considered important. At all conditions other than the M=2.4 condition, a ramp and exit plug must be included in the duct to simulate proper propulsion induced effects. As a result, empirical skin friction analysis is often not only inaccurate, but may bias results with respect to one technology or another.

Alternatives to empirical skin friction included CFD, direct force measurement, calculation from internal flow measurements, and calibration + internal flow measurements. Our recent experience with CFD has been mixed. We have had good results with CFD at the cruise condition but less so for transonic conditions. For a transonic WT test, we often want to know the installed internal drag over a broad range of angles of attack, for at four to eight Mach numbers, and for several configurations using the current state of the art, where the accuracy is debatable, the calendar time and cost for Navier-Stokes solutions have been prohibitivly high. There have been cases where 6 months of flow time were required for a matrix of solutions. CFD also has the problem of being run on the "desired" geometry/flow as opposed to WT geometry/flow. The actual model may not have the "desired" contour or smoothness and may have trips, partial laminar flow, and finite leading and trailing edge thickness. For some transonic conditions convergence may also be a problem. Direct force measurement (having a metric duct) is also an option. However, considering accuracy limitations caused by the limited size of HSCT nacelles and the potential cost of implementation, this is assumed to be an option of last resort. Calculation of internal forces from flow measurements is probably the most cost effective approach of the alternatives. However, historically uncalbrated flow measurements have yielded very poor accuracy. This leaves calibration as the most viable approach in terms of cost and accuracy.

General Internal Drag Objectives for HSCT Program

Transonic calibration has been has been the method of choice for internal corrections on most major programs for several reasons. It's cost is reasonable and it is quick. Bellmouths can cost less than $2,000. Test time can be as reasonable as $4000/geometry and take as little time as a single shift. Such a calibration covers the nacelle for all Machs/angle of attack. Most importantly, the results are consistant: They are consistent with the as-fabricated part and can be completely consistent with the thrust methodology and how Propulsion calibrates nozzles.

By comparison, even if a CFD post processor is modified to produce gross thrust forces per a T-D definition, there are still several obstacles. A comparable database in CFD might take 24 installed Navier-Stokes cases (4 alphas X 6 Mach numbers). With transonic convergence times running at 100hrs/run and $40/hr the cost for computer time alone might be as high as $96,000. Gridding and shepherding solutions through the queue could take months of flow time. Finally, the solution will not necessarily be consistent with the as-built geometry.

Why Calibrate Nacelles?

Transonic calibration has been has been the method of choice for internal corrections on most major programs

- Cheap
  - < $10K/config. (Estimates for transonic Overflow > $100K/config)
- Quick
  - < 2days/config. (Estimates for Overflow > 1 month)
  - CFD requires validation work & new post processor
- <u>Consistent</u>
  - Can use same methodology as Propulsion will for Thrust
  - Uses actual as built WT geometry

* Supersonic calibration is an unknown. May or may not offer improvement over CFD

The following figure illustrates how a "subsonic" calibration works. Pictured on the left is the mounting arrangement (above) and internal flow characteristics (below) of a nacelle in the wind tunnel. Pictured on the right is the mounting arrangement (above) and internal flow characteristics (below) of a nacelle in the FSC. The objective of a calibration is to correlate the nozzle exit gross thrust and weight flow characteristics with the nacelle internal flow. The nacelle exit flow (ie. exit Mach) is a function of both the upstream flow conditions and exit conditions (free stream Mach). It is not necessary to simulate the entire installed system to reproduce the same exit flow. All that is required is that the control volume just upstream and downstream of the exit is reproduced. The FSC does this by applying a pressure differential across the nacelle, thereby accelerating air though a converging bellmouth, through the nacelle, and out the nozzle exit. In this way only the subsonic flow in the duct aft of the inlet throat is simulated.

Calibration Basic Principles: Test Set Up For Subsonic Flow

Subsonic Duct WT Conditions

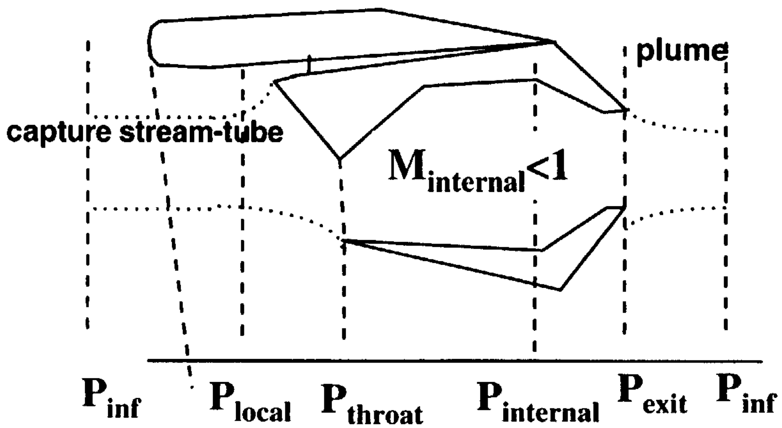

Subsonic Duct Calibration Conditions

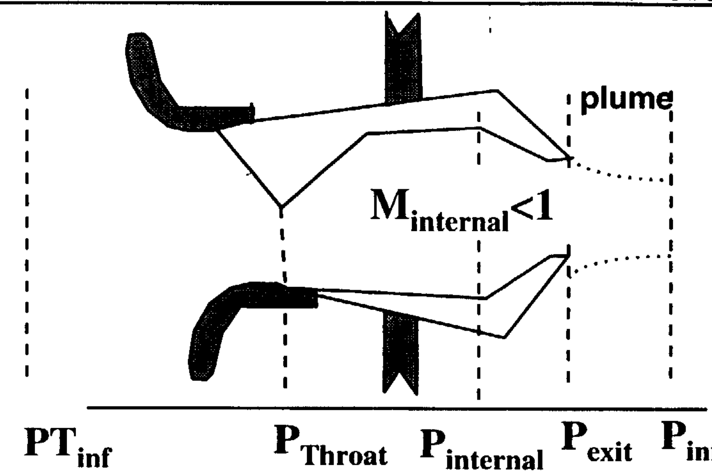

(WT flow simulated from P_{Throat} aft)

Range of Conditions

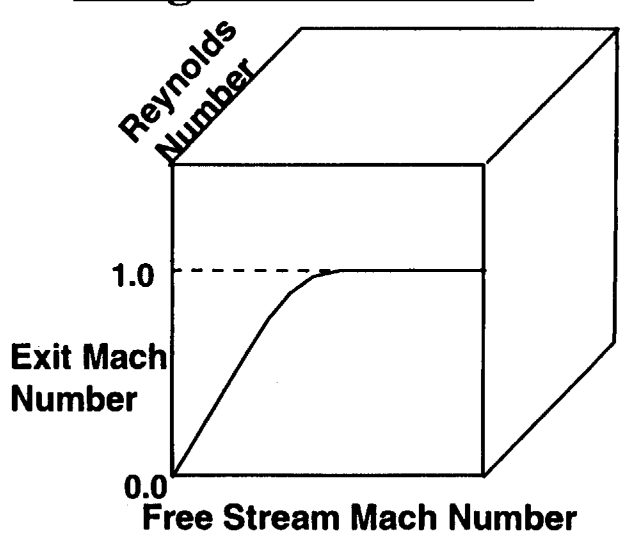

Range of Conditions

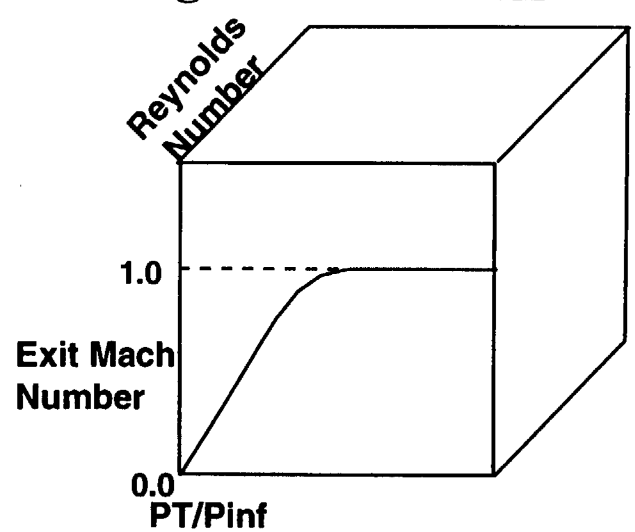

The following figure illustrates the nominal "plate mount" testing arrangement in the Boeing Flight Simulation Chamber. The FSC is a 4ft diameter by 12ft long chamber which provides the capability to calibrate a blown or flow-through nacelle over the Mach range from 0 to 1.4 at Reynolds numbers fairly consistent with an atmospheric WT system. At the forward end of the chamber is a dual force balance assembly consisting of a vertical model support structure supported on either side of the chamber by two 6 component balances. Each balance has a capacity of $\pm$ 100 lb. with a stated 2σ accuracy of $\pm$.1% of the applied load. An opening in the support frame midway between the balances allows the model to be mounted with the inlet open to room ambient pressure and the exhaust to be confined to the pressure enviroment of the chamber. The chamber is seal across the balance by a bellows. A pair of compensating bellows are incorporated to cancel out the large pressure force across the balance. This allows for smaller more accurate balances to be used. It also allows the balance to measure only the gross thrust produce by the test article. Two ejectors downstream of the chamber are used to maintain any desired chamber pressure from atmospheric down to 3 psi. Screens are installed in the chamber to break up the exhaust jet, prevent recirculation and entrainment and mix the flow before it exit through the low pressure Multiple Critical-flow Venturi (MCV) at the rear of the chamber. The MCV's provide an accurate reading of mass flow through the test article to a stated 2σ accuracy of $\pm$.08 % of the applied load. The tank minimum pressure limits the maximum attainable ideal Mach number of the system to 1.4.

Calibration Basic Principles: FSC Nominal Test Set Up

High Speed Civil Transport

Max Reynolds Number = 4.7million
Max Mach Number = 1.4

Momentum Flux In = 0
Mdot * $V_o = 0$ ($V_o = 0$)
A_o*(P_o-P_{inf}) = (canceled by compensating bellows)

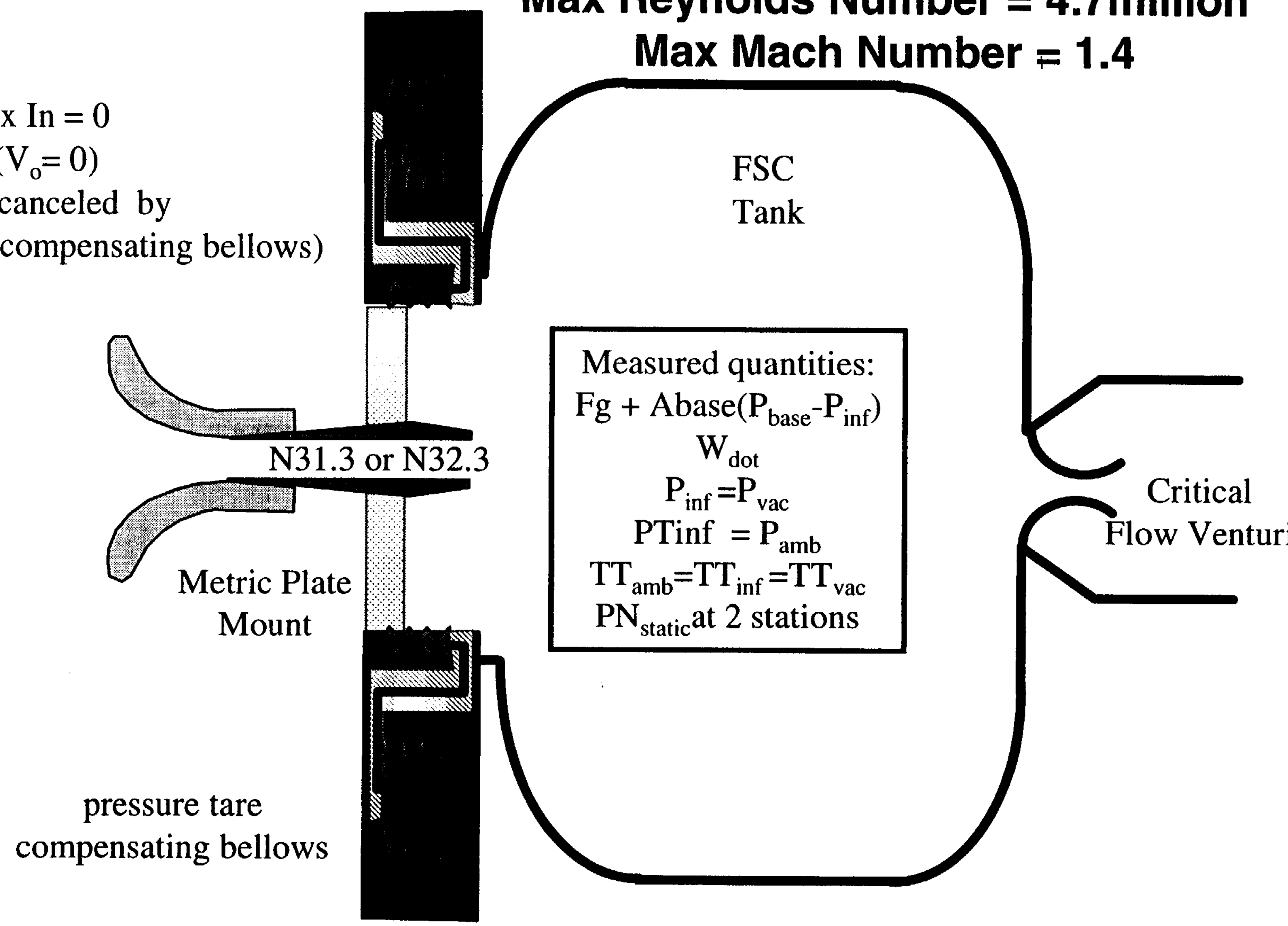

The following picture is of the HSCT 2-D nacelle N31 installed in the FSC in nominal the plate mount arrangement. Note the square bellmouth leading into the square nacelle nacelle inlet.

FSC Basic Principles: Nominal "Plate Mount" Test Set Up

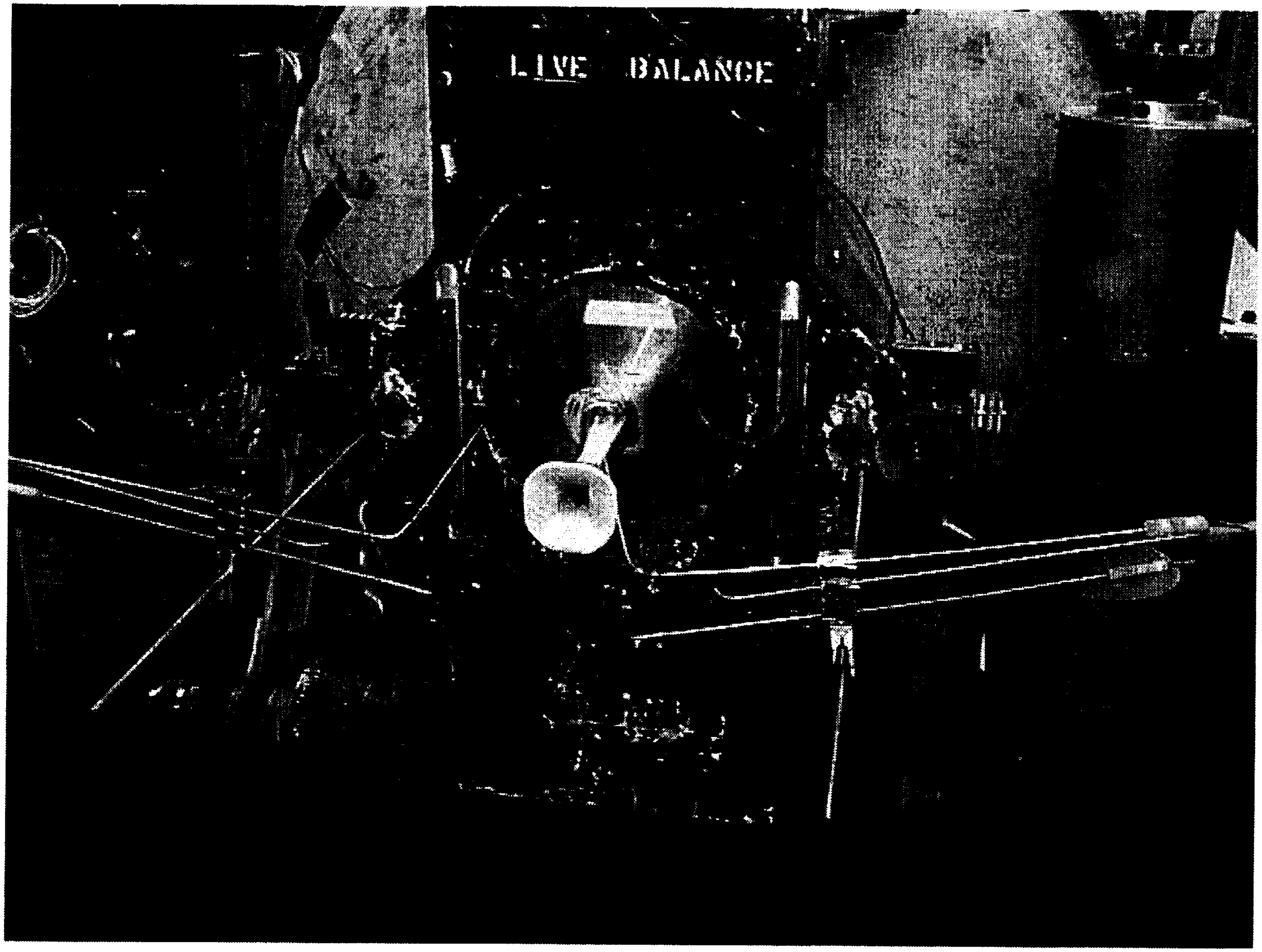

February 1999 HSR Airframe Technical Review

It is quite common to have some confusion about what the effect of inlet bellmouths should be. The FSC measures gross thrust by varying pressure ratio. In an ideal world, the bellmouth design would be so perfect so as to supply perfectly uniform flow with no boundary layer. Instrumentation is used to determine flow conditions in the duct. Now, suppose there were losses associated with the bellmouth. It is true that it would require a greater pressure differential to achieve the same gross thrust. But keep in mind, as a result the velocity in the duct must drop as well. This will show up in the duct instrumentation. The goal of calibration is to map the instrumentation reading to gross thrust, not facility pressure ratio.

BOEING High Speed Civil Transport

Use Of Bellmouths: How Do They Affect Calibration

Calibration maps instrumentation (PT, P, TT) to exit conditions (Weight flow, gross thrust)

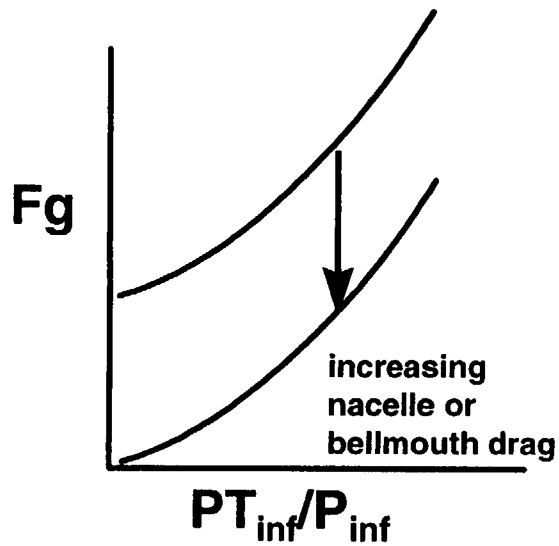

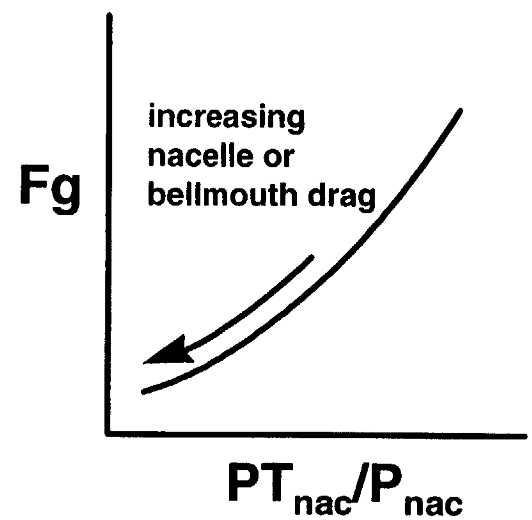

<u>Conclusions:</u>

- Not a requirement that bellmouth is zero drag
- However, a bellmouth that provides uniform laminar flow is ideal

While it is true that in theory, bellmouth losses should have a minimal effect on a calibration, it is good to know that historically Boeing's cubic bellmouth design has produced very near ideal flow. Pictured on the left is ratio of balance measured velocity versus the velocity of ideally (isentropic) expanded flow for a cubic calibration bellmouth/nozzle. The data were taken over 4 installations over 3 tests (1year). This cubic bellmouth's exit velocity is 99.5% of ideal. Pictured in the middle is the ratio of venturi measured weight flow versus the weight flow of ideally (isentropic) expanded flow. The fact that the weight flow is 99% of ideal indicates that there has been very little boundary layer growth. Pictured on the right is the internal drag of this bellmouth based on an HSCT Sref and mass flow. Over most of the regime, the losses are less than .3cts.

Use Of Bellmouths: How Do They Affect Calibration

Boeing "Cubic" bellmouth design has historically produced repeatable near uniform/laminar flow

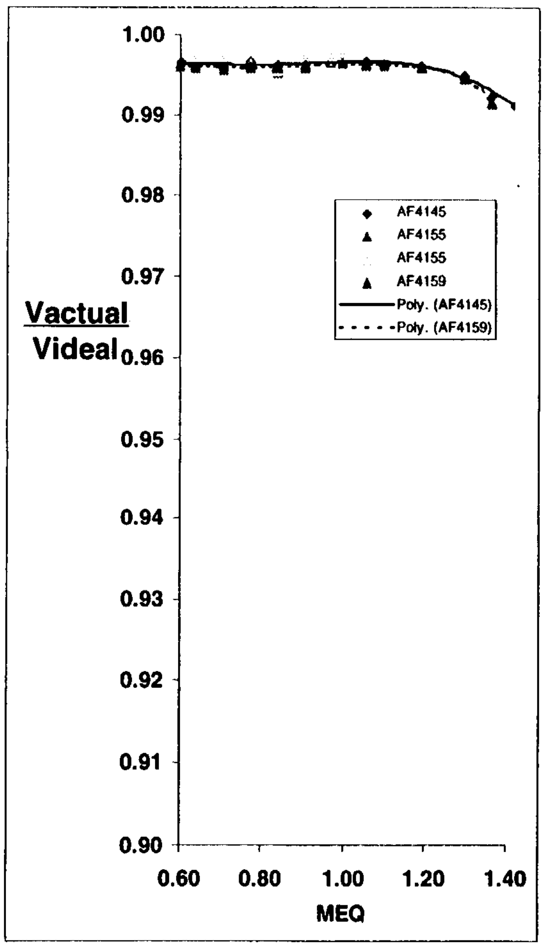

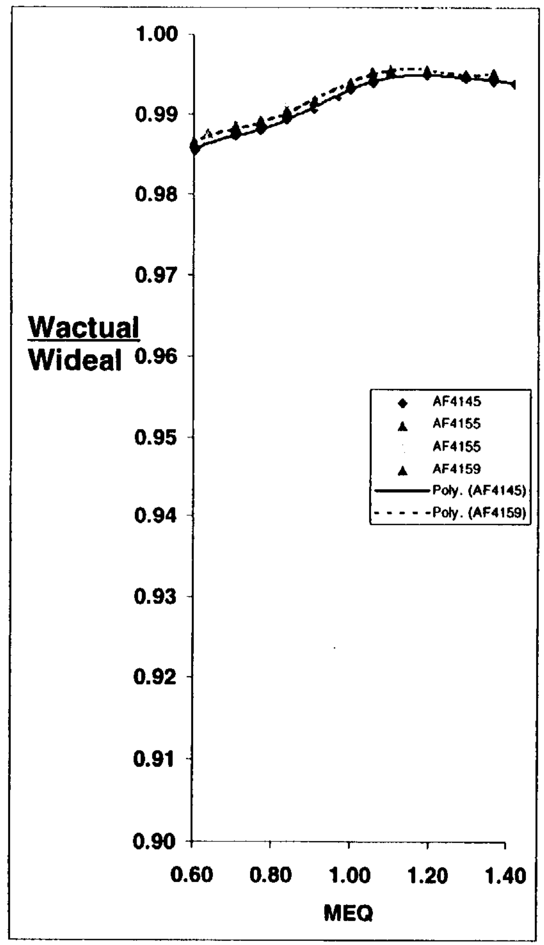

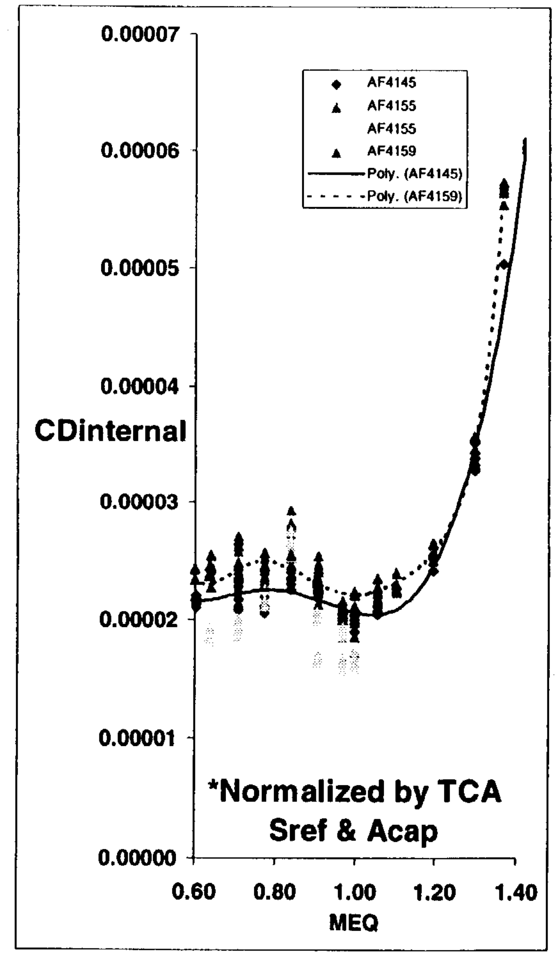

February 1999 HSR Airframe Technical Review

While nacelle calibration is common practice for most aircraft programs, there exist some very real challenges to adapting it to the HSCT program. HSCT nacelles are typically smaller because our models are sized by body length instead of wing span, and an HSCT is very long compared to a fighter or even a 747. Our thrust drag bookkeeping is unique. It is more consistent with preliminary design tools than experimental methods. Several facilities where we test at are not well matched in terms of Reynolds number and pressure ratio to available calibration facilities. The HSCT's inlet is mixed compression. As a result, the internal flow will be supersonic at the cruise condition. Lastly, an HSCT inlet is square. This presents a challenge of designing a bellmouth that can accelerate flow form M=0 to 1 while maintaining uniformity and laminar flow.

BOEING

High Speed Civil Transport

Challenges to HSCT Program Using Calibration to Improve Current T-D Situation

- Nacelles are small (Acap = 1sqin)
  - minimum room for instrumentation
  - High risk of instrumentation interference
  - Internal forces small <30% of most fighter or subsonic transport models
  - flow rate small <30% of most fighter or subsonic transport models
- HSCT Thrust-Drag bookkeeping system is unique
- Nominal Reynolds number in BSWT 2 X Nom. FSC Re.
- Supersonic duct flow calibration is not standard
- Nacelle inlets are square (bellmouth design?)

To address these challenges, two tests were conducted. The first test was a proof of concept calibration/wind tunnel test. The success of this test was a requirement for any follow on PIE testing. The goal of this test was to resolve if the T-D system, nacelle size, or facility cost/productivity would be an issue.

If this test was successful, a second test exploring long term repeatability, Reynolds number matching, and supersonic duct flow calibration techniques could be planned.

Two Tests Conducted to Resolve HSCT Calibration Challenges

BOEING

High Speed Civil Transport

<u>Test 1: IRAD FSC + BSWT (Must be success for HSR PIE test)</u>

- Resolve if Old T-D system is an obstacle
- Develop HSCT data reduction scheme
- Resolve if nacelle size is an obstacle
- Resolve if cost/productivity will be an issue

<u>Test 2: FSC (Desirable for reduction in long term costs)</u>

- Assess long term repeatability
- Explore Reynolds number matching
- Explore supersonic duct flow calibration technique

February 1999 HSR Airframe Technical Review

To have a focused methods development task, cost and accuracy goals were developed. In this way approaches that could not meet either the cost or accuracy requirement could be immediately abandoned.

The cost goals were based on comparisons with CFD, assuming Navier-Stokes could produce accurate WT matched forces on a flow-thru nacelle with a ramp and plug. If internal drag is to be known at our standard transonic Mach range, 24 runs (4 alphas at M=.9, .95, .98, 1.06, 1.2, 1.4) are required. At 100hrs/run and $40/hour that is $96k. Assuming engineering costs are $16K for 2 eng. months at $100/hour, the total cost would be $112K per geometry. Given some automation and realistic reductions in run time, the CFD cost should be able to be brought down by 50%-60%. Consequently, a reasonable goal for calibration costs appears to be <$45K

The calibration accuracy goals were derived from the WT workshop testing accuracy requirements. The total airplane requirement is ±1ct at M=2.4 and ±3ct transonically (and supersonic climb). Consequently, an acceptable level for each nacelle would translate to ±.1ct and ±.3ct repectively (note RSS error on 4 nacelles would be .2cts and .6cts respectively)

General Nacelle Calibration Objectives for HSCT Program

BOEING

High Speed Civil Transport

Cost:

- Calibration cost must be less \$30K/geometry
- Instrumentation cost must add less \$15K/nacelle
- Use of calibrated nacelles cannot significant reduce in-tunnel productivity

Accuracy:

- Calibration error (precision + bias) must be < $\pm$.1ct/nacelle for M=2.0-2.5
- Calibration error (precision + bias) must be < $\pm$.3ct/nacelle for M<2.0
- Data reduction process should be simple enough to be repeatable by any HSR researcher

February 1999 HSR Airframe Technical Review

The following chart provides the definition of accuracy, error, precision, and bias that will be used throughout this report.

Definition of Terms

- Accuracy - the closeness of agreement between a measured value and the truth.
- Error - the difference between the measured value and the true value.
- Precision - the random component of error.
  - Spot repeatability - samples within a data point
  - Short term repeatability - repeats within a test
  - Near term repeatability - repeat model builds within a test
  - Long term repeatability - repeat runs, different test
- Bias - the systematic component of error.

Error = Bias + Precision

Results Summary of First Test (February/IRAD)

Once set on the path of using Net Standard Thrust, the primary unknowns are the nozzle exit conditions. Any cost associated to assessing the local or hilight flow conditions become non-value added. The objective of the calibration work conducted in 1998 was to develop a methodology the would support both the existing and proposed definition of thrust without incurring the added costs that the current system mandates. In this way, interim performance numbers could be generated until the program formally changes the thrust definition.

If a calibration is done to generate net standard thrust, there is a way that the same data can support HSCT's intrinsic thrust definition. If all the inlet unknowns that are not required by net standard thrust are obtained directly from Propulsion, there can be no mismatch between Aero and Propulsion on the assessment of thrust. This hybrid solution may have a bias error relative to the "true" value of intrinsic thrust. However, this bias will have an offsetting drag increment that will result in the correct aircraft performance.

A calibration process can be applicable to either T-D system

Rewriting thrust relative to Pinf

$$\text{Thrust} = M_{dot}V_{exit} + A_{exit}(P_{exit} - P_{inf}) \quad \text{(Gross Thrust)}$$

$$- [M_{dot}V_{cap} + A_{cap}(P_{cap} - P_{local}) - M_{dot}V_{local}] \quad \text{(Additive Drag)}$$

$$- M_{dot}V_{local} \quad \text{(Local Ram)}$$

$$- A_{cap}(P_{local} - P_{inf}) \quad \text{(Pref correction)}$$

Terms from Calibration

Terms from Propulsion

Calibration Is Only to Map Gross Thrust and Weight Flow to Internal Instrumentation - All other Terms Are Analytical

February 1999 HSR Airframe Technical Review

How much information does the instrumentation have to provide in order to calculate drag. The following chart examines the instrumentation requirement based on 1-D flow.

Development of Calibration Process

How much instrumentation? To calculate internal drag, Fg and Wdot must be Known

Given $Me = 2.236\,[(Pe/PT)^{-2/7} - 1]^{(.5)}$

Then $Me = f\,(Pe/PT)$

Given $Ve = 49.02 * Me * TT^{(.5)} * (1 + 0.2 * Me^{2})^{(-.5)}$

Then $Ve = f\,(Pe/PT, TT)$

Given $Wdot = 0.91996 * PT * TT^{(-0.5)} * Ae * Cde * Me * (1 + 0.2 * Me^{2})^{(-3)}$

Given $Cde = f\,(Me, PT, TT)$

Then $Wdot = f\,(Pe/PT, PT, TT)$

Given $Fg = Wdot * Ve/g + Ae * (Pe - Pamb)$

Then $Fg = f\,(Pe/PT, PT, Pamb, TT)$

Conclusion: If Pe, PT, Pamb and TT are known, Fg and Wdot are also known

Goal of FSC is to calibrate measured values of Pe, PT, Pamb and TT to measured values of Fg and Wdot

For a long time propulsion staffs have known that it is not necessary to actually calculate exit gross thrust. In the first place, the calculation will invariably not agree with the test data (instrumentation bias, non-uniform flow, etc...). In the second place, actual thrust can more easily be approximated by some power series function of nozzle pressure ratio (PTnozzle/Pamb). This effectively makes static pressure instrumentation obsolete. The following chart illustrates that a function of NPR and direct calculation are one and the same.

Development of Calibration Process

Problem: It is difficult to instrument for Pe

Given $Mp = 2.236\,[(Pamb/PT)^{-2/7} - 1]^{(.5)}$

Then $Mp = f\,(Pamb/PT)$

Given $(Wdot)e = (Wdot)p$

Given $Wdot = 0.91996 * PT * TT^{(-0.5)} * Ap * Mp * (1 + 0.2 * Mp^{2})^{(-3)}$

Given $Ap = f\,(Mp, PT, TT)$

Then $Wdot = f\,(Pe/PT, PT, TT) = f\,(Pamb/PT, PT, TT)$

Therefore $Pe = f\,(Pamb/PT, PT, TT)$

Then $Wdot = f\,(Pamb/PT, PT, TT)$

Then $Fg = f\,(Pamb/PT, PT, TT)$

Conclusion: If PT, Pamb and TT are known, Fg and Wdot are also known (<u>and Pe is redundant</u>)

Static pressure instrumentation is far simpler to install in a small model than total pressure instrumentation. The following charts shows how, in theory, the static pressure at two stations provides as much information as the total pressure.

Development of Calibration Process

Problem: PT rakes add flow distortion

Define a upstream duct location, called a charging station, preferably where Acharge > Aexit

Given	$Mc = 2.236\,[(Pc/PT)^{-2/7} - 1]^{(.5)}$
Then	$Mc = f\,(Pc/PT)$
Given	$(Wdot)e = (Wdot)c$
Given	$Wdot = 0.91996 * PT * TT^{(-0.5)} * Ae * Cde * Me * (1 + 0.2 * Me^2)^{(-3)}$
	$= 0.91996 * PT * TT^{(-0.5)} * Ac * Cdc * Mc * (1 + 0.2 * Mc^2)^{(-3)}$
Given	$Cde = f\,(Me, PT, TT)$ and $Cdc = f\,(Mc, PT, TT)$
Then	$Wdot = f\,(Pe/PT, PT, TT) = f\,(Pc/PT, PT, TT)$
Therefore	$PT = f\,(Pe/Pc, Pc, TT)$
Then	$Wdot = f\,(Pe/Pc, Pc, TT))$
Then	$Fg = f\,(Pe/Pc, Pc, Pamb, TT)$

Conclusion: The static pressure at two stations, Pe and Pc, can substitute for knowing PT

Using the same logic that indicates knowledge of Pe is redundant if PTe is known, one can deduce that Pe is also redundant if Pc is known. The following chart is the derivation that in principle, a single nacelle static pressure along with the free stream static pressure (or total pressure) are enough to characterize the internal flow. There are two basic scenarios. The first is described here, where Ac < Ae and the duct is choked. In this situation the duct total pressure and a charging station pressure are offset but track almost one for one. Consequently Pc/Pamb can be substituted for PTe/Pamb. If Ac~Ae, and the duct is unchoked, Pc~Pamb, so Pc/Pamb~1 . For this scenario, the ratio of PTinf/Pc can be used instead. This is reasonable because if the duct is unchoked, PTinf > PTe (PTe includes duct viscous losses) and will track almost one for one.

Development of Calibration Process

Problem: It is difficult to instrument for Pe

Given $Mp = 2.236\,[(Pamb/PT)^{-2/7} - 1]^{(.5)}$

Then $Mp = f(Pamb/PT)$

Given $(Wdot)e = (Wdot)c = (Wdot)p$

Given $Wdot = 0.91996 * PT * TT^{(-0.5)} * Ap * Mp * (1 + 0.2 * Mp^{2})^{(-3)}$

Given $Ap = f(Mp, PT, TT)$

Then $Wdot = f(Pe/PT, PT, TT) = f(Pc/PT, PT, TT) = f(Pamb/PT, PT, TT)$

Therefore $PT = f(Pamb/Pc, Pamb, TT)$ and $Pe = f(Pamb/Pc, Pamb, TT)$

Then $Wdot = f(Pamb/Pc, Pamb, TT)$

Then $Fg = f(Pamb/Pc, Pamb, TT)$

Conclusion: If <u>only</u> Pc, Pamb and TT are known, Fg and Wdot are also known (<u>if</u> solution is unique)

The following figure illustrates the instrumentation suite selected for these tests. The preceding derivation indicates that a calibration can be accomplished by either static and total pressure instrumentation at a single station, static pressures at two stations, or static pressures at a single "charging station". Aside from fabrication costs (+2K/geometry), there doesn't seem to be any downsides to instrumented both the charging station and the exit for static pressure. Total pressure rakes, on the other hand, have a several issues. On nacelles of such small size, they are difficult and costly to install and tend to provide unsatisfactory readings of total pressure. This is because it is difficult to achieve high enough density in the rake while maintaining minimal rake induced distortion and blockage. In the end, the uncalibrated rake will never read the "true" average exit total pressure and will require a large calibration correction. The net result is that a rake seems to add less information than the uncertainty it creates. In the end, static instrumentation at two stations were selected because they provide the maximum data reduction possibilities (for little additional cost), and serve as an invaluable tool for duct flow validation/troubleshooting. The location of the charging station was just up stream of where the area growth of a plug would begin. The exit pressures were .1" upstream of the exit.

Development of Calibration Process for HSCT T-D system

High Speed Civil Transport

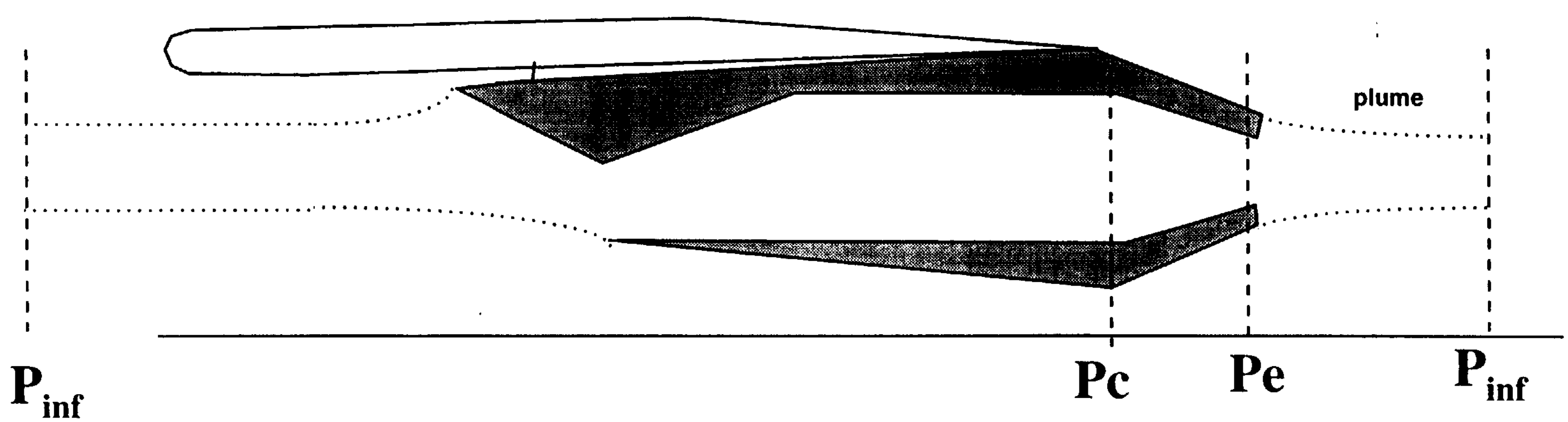

Selected "Rakeless" Instrumentation suite: static's at 2 stations

- Costly/Difficult to install rake in small model
- Difficult to get enough rake density 1 sqin duct
- Rake adds own uncertainty, PTexit/ PTrake < 93%

February 1999 HSR Airframe Technical Review

Developing a data reduction scheme for this test was challenging. While it would be desirable to strive for consistency between an HSCT methodology and that of another program, it is not obvious which program to select. It seems as if there is no shortage of parameters in use to normalize the calibration data. Some examples are

- Gross thrust coefficient: Cfg=Factual/Fideal or Cg= Factual/Fideal
- Velocity coefficient: CV=Vactual/Videal or Cv= Vactual/Vcalc
- Weight flow coefficient: Cw = Wactual/Wideal or Cw= Wactual/Wcalc
- Ideal thrust coefficient: CT=Fg/PTj/A*
- Vacuum thrust coefficient: Fs A/A*= Pe Ae(1-γ Me^2)/PTj/A*
- Stream thrust coefficient: (Fs A/A*)actual/(Fs A/A*)ideal

(Where "ideal" is defined by condition where Pe=Pamb, and "calc" is defined by 1-D flow equations)

The following chart reviews one of several methodologies used by St. Louis on fighter programs and the issues associated with applying them to an HSCT.

Development of Calibration Process

Military Group Process

Nacelle has total pressure rake PT, and exit pressure rake, PS

Thrust = Fg - Fram

$CW = Wdot_{actual}/Wdot_{rake\text{-}measured\text{-}calc}$

$= A0 + A1*(PTR/Pinf) + A2*(PTR/Pinf)^2 + A3*(PTR/Pinf)^3$

$CFG = Fg_{actual}/Fg_{rake\text{-}measured\text{-}calc}$

$= B0 + B1*(PTR/Pinf) + B2*(PTR/Pinf)^2 + B3*(PTR/Pinf)^3$

$Me = f(PT/PS)$
$Ve = f(Mc, TT)$
$Wdot_{ideal} = f(Me, PT, TT)$
$Fg_{Ideal} = Wdot_{Ideal}/g * Ve + Ae(PS - Pinf)$

$CDint = [CW\ Wdot_{Ideal}/g * Vinf]/Q/Sref$

$- [CFG\ Fg_{Ideal}]/Q/Sref$

HSCT Issues With This Process

- $Thrust = Fg - Fram_{local} - D_{add} - Dpref$
- Requires duct PT rake
- Requires exit static pressure
- Difficult to get an accurate reading of PT in a 1" model
- Rake adds own uncertainty, PTR-PTE > 7%
- Sparse rake may not fully capture Reynolds number variation

Advantages This Process

- In theory, does not require Reynolds number correction
- Captures any inlet shock PT losses

February 1999 HSR Airframe Technical Review

The following chart reviews one of several methodologies used by Seattle on transport programs and the issues associated with applying them to an HSCT.

Development of Calibration Process

Commercial Group Process

Nacelle has static pressures, PN, at 1 location

Thrust = Fg - Fram

$Wcorr = A0 + A1*(PT/PN) + A2*(PT/PN)^2 + A1*(PT/PN)^3$

$Wdot = Wcorr*(PT/14.696)/(TT/518.69)^{.5}$

$Mhi/(1+.2Mhi^2)^2 = Wcorr*1.68635/Ahi$

$VH/Vinf = Mhi/Minf * [(1+.2Minf^2)/(1+.2Mhi^2)]^{.5}$

$CV = Fg_{actual}/Fg_{ideal}$

$= B0 + B1*(VH/Vinf) + B2*(VH/Vinf)^2 + B1*(VH/Vinf)^3$

$CVNC = 1-(1-CV)(Re/ft\sim FSC/Re/ft\sim test)^{+.2}$

$CDint = (1-CVNC)Wdot/g * Vinf/Q/Sref$

HSCT Issues With This Process

- Thrust = Fg - $Fram_{local}$ - D_{add} - D_{Pref}
- Inlet shocks may make PTduct<PTinf
- For long ducts PTduct/PN not constant with Reynolds number (i.e. Re correction will be too large)
- For ducts where Ae<< Aduct, favorable pressure gradient may reduce Reynolds number effect

Advantages This Process

- Simplicity of application
- few curvefits reduce lack of fit error
- Requires only static pressures

February 1999 HSR Airframe Technical Review

Given that there are infinite variations of a data reduction scheme, which is best for an HSCT? For this test several methods where examined for assessing duct total pressure. The knowns in a calibration are weight flow, gross thrust, TT, and the static pressure and area at two stations. This implies that there are too few equations and too many knowns. Consequently, the total pressure can be solved for independently 5 ways.

1) Solve for PT at the charging station using static pressure and weight flow
2) Solve for PT at the charging station using static pressure, gross thrust and weight flow
3) Solve for PT at the exit station using static pressure and weight flow
4) Solve for PT at the exit station using static pressure, gross thrust and weight flow
5) Solve for PT at the either station using both static pressures and weight flow

Interestingly, each of these PT's will be different. There is also an infinite combinations of pressure ratios and functions that these resulting PT's can be correlated against.

A gross thrust coefficient was used to calibrate gross thrust. Coefficients based on measured gross thrust versus ideal (expanded to Pamb) and calculated (using ideal 2-D flow) gross thrust were looked at. Given there were 5 values of PT and two methods of gross thrust coefficient (Ideal & calculated), there were 10 ways to assess the thrust coefficient. As with the value of PT, there was also any number of variables to correlate to. In the end, all these methods are self consistent. They were derived from calibration weight flow and gross thrust values and will therefore produce these same values. When these numbers are subjected to wind tunnel data, the results diverge slightly. At M=.90, the scatter between methods was up to 2 counts. Ultimately, the "best" methodology is one that maintains consistency in form and process to what Propulsion must use to calibrate thrust (for wind tunnel and flight test). In that way "thrust", which is a defined value, will be by definition accurate.

Development of Calibration Process

- Dozens of data reduction schemes in use on other programs
- Examined 5+ methods for determining duct total pressure
- Examined 10+ methods for normalizing gross Thrust
- All methods are self consistent with calibration data
- Scatter among methods (applied to test) $\pm$1ct
- "Best method" is one that's most consistent with Propulsion

February 1999 HSR Airframe Technical Review

The following figure shows an example of the correlation curves for the 5 difference values of PT and 9 different values of gross thrust coefficient.

Development of Calibration Process

- Examined 5+ methods for determining duct total pressure
- Examined 10+ methods for normalizing gross Thrust

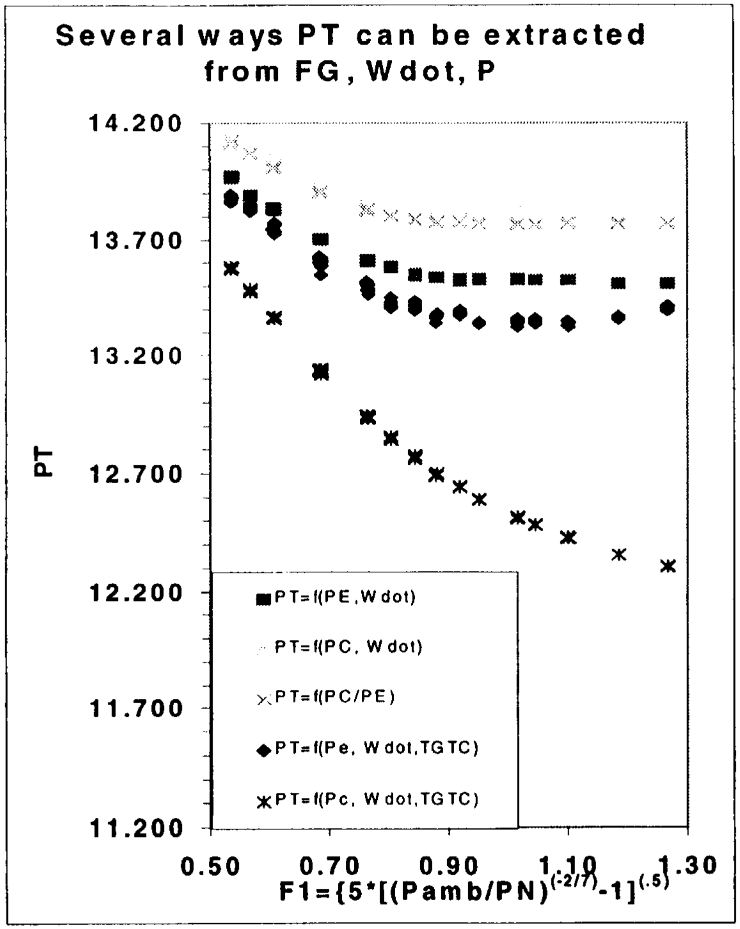

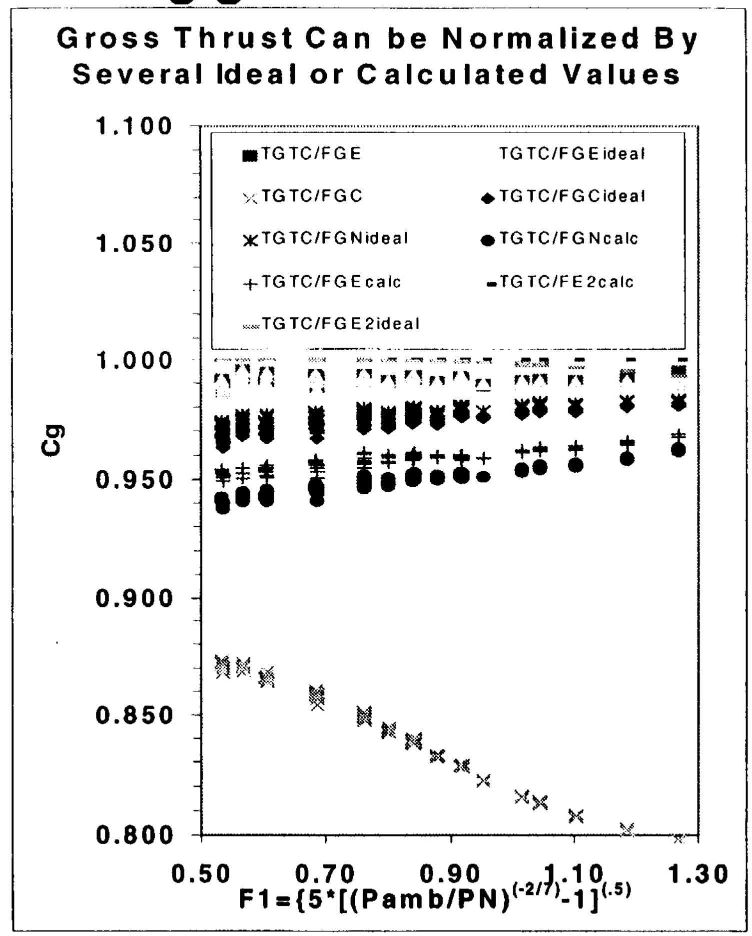

Given all these available methods, which one is recommended? While there is no clear distinction among the methods, it is reasonable to believe that getting a reliable reading of Pe where M~1 for most cases is considerably more difficult than Pc. Therefore, it is recommended the for the near term, PT be derived form Wdot and Pc, based only on Pc/Pamb. The issue of whether it is better to have gross thrust coefficients based on measured gross thrust versus ideal (expanded to Pamb) and calculated (using ideal 2-D flow) gross thrust is less clear. For the near term, Ideal gross thrust will be the preferred method because it is more consistent with Propulsions methodology. The following figure shows how the thrust coefficient will be incorporated into the data. It is worth noting that the gross thrust in this methodology is treated as a scalar quantity. This is because it is consistent with Propulsions current methodology.

Development of Calibration Process

Rewriting HSCT Thrust equations

$$\text{Thrust} = Fg - Fram_{local} - D_{add} - D_{Pref}$$

Introducing the following definitions:

$$Cg = Fg_{actual} / Fg_{calculated\ or\ ideal}$$

Resulting Definition Becomes:

$$\text{Thrust} = -CDint = Cg^{*}\, Fg_{calc/ideal} - Wdot_{calculated} * V_{local} - D_{add} - D_{Pref}$$

where

$V_{local} = f(M_{inf}, TT)$

$D_{add} = f(M_{inf}, TTinf, PTinf, Wdot_{actual})$

$Vc = f(Mc, TT)$

$Wdot_{caculated} = f(Mc, PTc, TT)$

$D_{Pref} = f(M_{inf}, TT)$

$Mc = f(PTc/Pc)$

$Fg_{calc/ideal} = Wdot_{calc} / g * V_{calc/ideal}$

$Cg = f(PN/Pamb)$

The following figure illustrates how the recommended process would be applied. PT is derived from Pc, and a function of Pc/Pamb. With Pc, PT, and TT, Wdot is calculated. Cg is also derived from the same function of Pc/Pamb. With PT and Pamb, FGideal is calculated. With Cg and FGideal, FG is calculated. With Wdot, PTinf , TT, and Pinf, Vlocal, Dadd, Dpref are calculated. Given Wdot, Sref, Q, FG, Vlocal, Dadd, and Dpref internal drag can be finally calculated.

Development of Calibration Process

Example of How Calibration Data is Used in WT Tunnel Corrections

Charging Station Total Pressure, PTC(from Wdot, PC, TT) is found from Pamb/PC

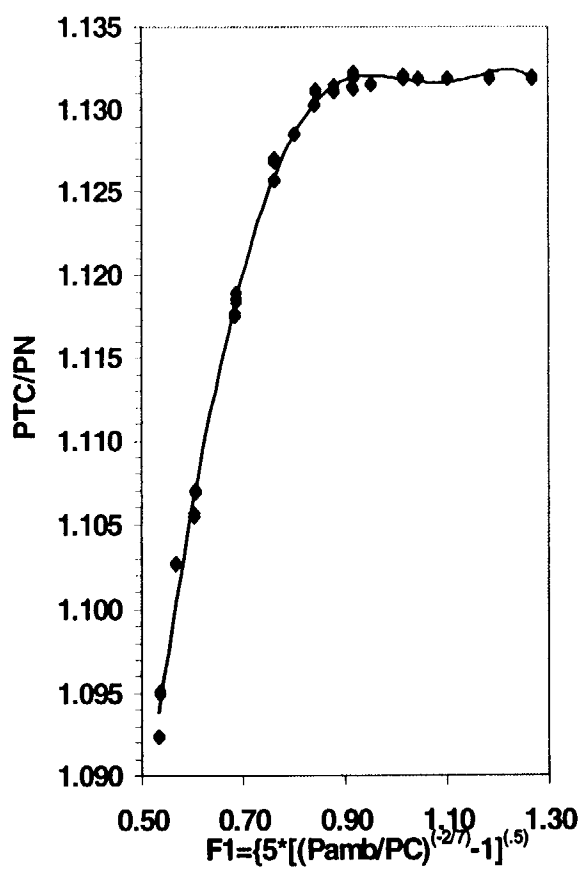

Gross Thust Coefficeint, PTC is found from Pamb/PC

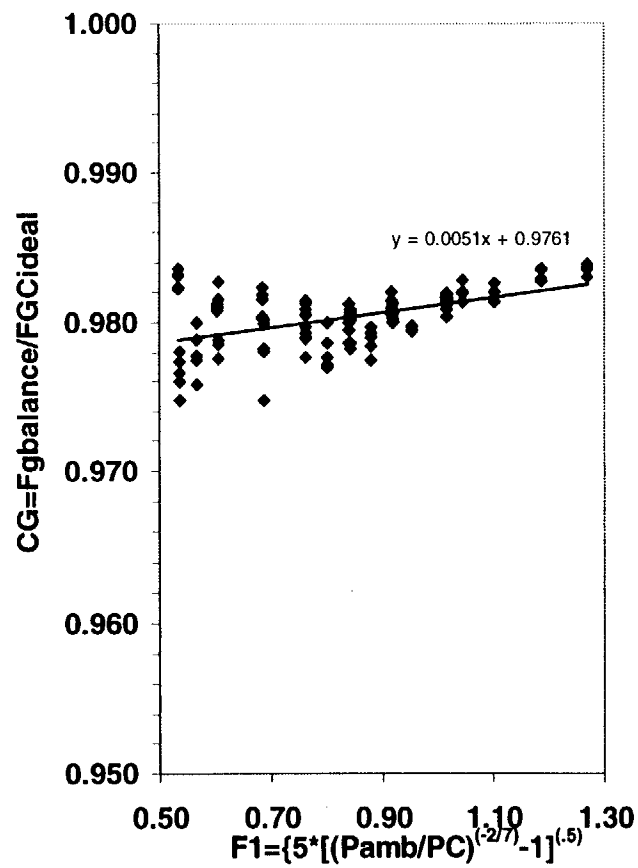

Step 1: Calculate PTC/PC from and Pamb/PN

Step 2: Calculate PTc from PTC/PC and PC

Step 3: Calculate Cg from Pamb/PC

Step 4: Calculate MC,VEideal from PC/PTC

Step 5: calculate Wdot

Step 6:Calculate Fgideal

Find 7: Calculate internal drag

February 1999 HSR Airframe Technical Review

One of the main objectives of the first test was to detirmine whether an HSCT model's small scale had exceeded the calibration facility's precision limits or whether the combination of repeatability and productivity would make the testing too costly. The short term force repeatability turned out to be less than $\pm$.04 cts. The balance checkloads were excellent, being within $\pm$.012 lbs (~.06cts) of the calibration standard. The short term repeatability of weight-flow was < $\pm$.03cts when converted to ram drag. The accuracy compared to the calibration standard is quoted to be (2 σ) $\pm$.08% (~.04cts).

Assessment of Facilities Force/Weight flow Measurement Repeatability/Accuracy for HSCT Type Nacelles

Force/Gross thrust:

- Short term force repeatability < $\pm$.04 cts
- Checkload within $\pm$.012 lbs (~.06cts)

Weight-flow/Ram Drag :

- Short term weight-flow repeatability < $\pm$.03cts
- Calibration accuracy (2 σ) $\pm$.08% (~.04cts)

The productivity was such that 2-3 installations/shift were possible (at $4k/shift). With the level of repeatability/accuracies seen in this test, there does not appear to be a big incentive to run multiple repeats within a test. Assuming new bellmouths are made ($3K), two nacelles are instrumented and calibrated ($4K), and total support from the Aero staff takes up 30 hours ($3K), the calibration cost run approximately $10K per geometry (less if multiple geometries are run). Nacelles were instrumented with 10 pressures at a cost of $2K/nacelle. Future tests will most likely only have 8. With the described data reduction methodology, the use of calibrated nacelles would not significantly reduce in-tunnel productivity because internal drag would be obtained with base drag data runs.

Assessment of Costs/Productivity for HSCT Applications

Costs:

- Calibration cost < $10K/geometry (no long-term repeats)
- Instrumentation cost < $2K/nacelle

Productivity:

- Over 3 shift test 6 Mach sweeps obtained
  - 2-3+ geometries can be calibrated per shift
- Use of calibrated nacelles would not significantly reduce in-tunnel productivity
- Internal drag obtained with base drag data

February 1999 HSR Airframe Technical Review

This chart shows the results of the BSWT spillage runs when the nacelle internal drag was corrected with the calibration data. 4 runs were made: Mach=0.90 and M=1.2 at ~8% and ~35% spillage. If Aero is assuming responsibility for all spillage effects above and beyond what Propulsion accounts for in additive drag, then spillage interference is the difference in nacelle increments between the ~8% and ~35% spillage cases. That number is shown in the right hand axis. At M=.9, CL=.24, spillage is worth ~8cts. At M=1.2, CL=.14, it is worth ~4.0cts. This result is consistent with past results from the 1995 ARC111-119 spillage test and recent OVERFLOW results.

2-D Inlet Spillage Increments Obtained in BCAG IRAD Test

BOEING

High Speed Civil Transport

- "Proof" of concept spillage test conducted in Dec' 1997
- Spillage increments consistent with Ames NAI test & Overflow results

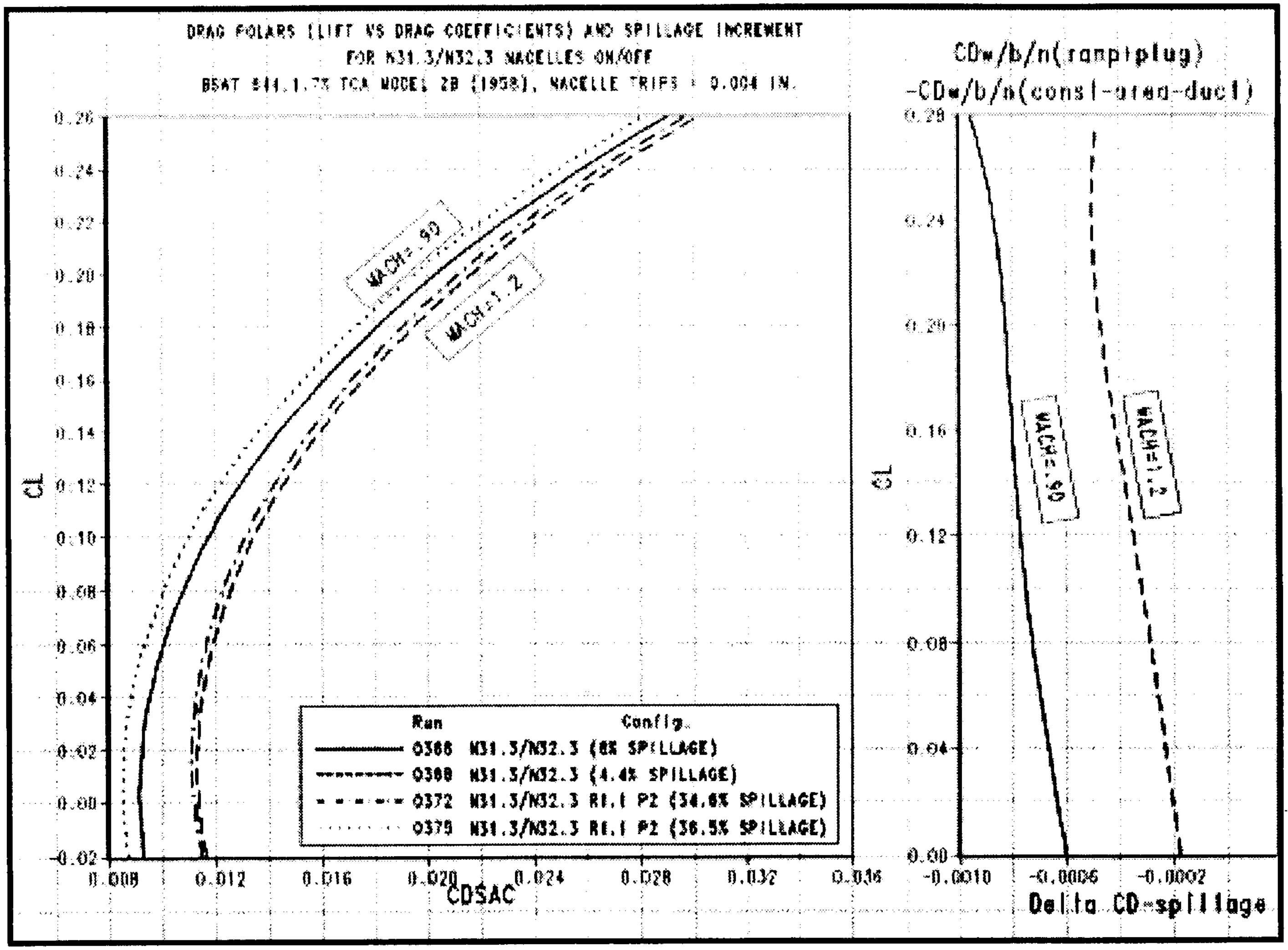

The first FSC test was a success in all respects. A "proof of concept" low cost PIE test was conducted, and the results were consistent with expectations. Several "rakeless" data reduction schemes were developed for old/new T-D systems so that despite the current small nacelles, repeatability/accuracy and costs (productivity) should meet requirements for HSCT applications. Despite the success of this test, follow-on improvements are always possible. It was therefore recommended that a future test should be conducted to assess long term repeatability, explore Reynolds number matching capability and supersonic duct flow. In addition, CFD and test should always be complementary. Therfore some CFD should be run on some of the calibration cases to assess uncertainty and evaluate the "best" data reduction scheme.

Conclusions After First FSC/BSWT Test

Summary:

- A "proof of concept" low cost PIE test was conducted
- Several "rakeless" data reduction schemes developed for old/new T-D system
- Despite nacelle size, repeatability/accuracy and costs (productivity) should meet requirements for HSCT applications

Recommendations

- Follow-on test should assess long term repeatability
- Follow-on test should explore Reynolds number matching capability and supersonic duct flow
- Follow-on CFD and uncertainty analysis is needed to "best" data reduction scheme

Results Summary of Second Test (October/HSR)

Scheduling issues required that the second test be broken down into two entries with another customer's test in between. The following table outlines the runs made in the first entry of two.

Run Log

Series	Runs	Configuration	RN	Mach	Comment	Result at end of series
11	227-237	2" CUBIC	nom	.6-1.4	repeat of facility check	Data Finally within historical trends
12	240-247	BM1, N31.3	nom	.6-1.4	repeat of test-to-test check	CDTC slightly higher than series 2
13	256-266	2" CUBIC, 7" STB	pt=14.7	.6-1.4	confirm no moment/installation tare	oposed to +-.02cts, and drag is higher by ~.5cts
14	267-274	2" CUBIC, 7" STB	PT=23	.6-1.4	confirm no moment/installation tare	down and CVN goes up only to the frre air level
Repeat of AF4145 configuration with STB mounted						
15	283-333	BM3.1, 7" STB, N31.3	4	.6-1.4	confirm no moment/installation tare	
16	283-333	BM3.1, 7" STB, N31.3	4	.6-1.4	confirm no moment/installation tare	
17	283-333	BM3.1, 7" STB, N31.3	4	.6-1.4	confirm no moment/installation tare	
18	283-333	BM3.1, 7" STB, N31.3	4	.6-1.4	confirm no moment/installation tare	Drag appears to go up with RN
Demonstrate Variable Rn M=2.4 pressure ratio concept						
19	339-341	BM7.1, 7" STB	7	2.4	Install alum. M=2.4 C-D bellmouth	CDV ~1, but the CVN are low at ~.97
20	342-385	BM3.1, 7" STB, N31.3	4	.8-1.4	repeat of N31.3 BM3.1	Repeat multiple RN capability
21	342-385	BM3.1, 7" STB, N31.3	4.5	.8-1.4	repeat of N31.3 BM3.1	Repeat multiple RN capability
22	342-385	BM3.1, 7" STB, N31.3	5.5	.8-1.4	repeat of N31.3 BM3.1	Repeat multiple RN capability
23	342-385	BM3.1, 7" STB, N31.3	7.2	.8-1.4	repeat of N31.3 BM3.1	much scatter and drag still goes up with RN
24	386-389	BM7, 7" STB	4,9,14	2.4	Install M=2.4 C-D bellmouth	indicate M=2.4
25	392-403	BM3.2, 7" STB	4.5	nom	repeat of N31.3 BM3.1	isolated belmouth
26	405-407	BM6	6,9,12	2.1	Install M=2.1 C-D bellmouth	indicate M=2.1
27	408-410	BM5	6,9,12	1.8	Install M=1.8 C-D bellmouth	indicate M=1.8
28	411-413	BM4	5,7,10	1.5	Install M=1.5 C-D bellmouth	indicate M=1.5
29	415-423	BM7, 7" STB	4,9,14	2.4	Install M=2.4 C-D bellmouth	indicate M=2.4
30	428-436	BM7.1, N31.3	4,9,14	2.4	Install alum. M=2.4 C-D bellmouth	drag
31	437-445	BM4, N31.3	4,9,14	1.5	Install M=1.5 C-D bellmouth	
32	446-462	BM3.2, 7" STB	4	.8-1.4		
33	446-462	BM3.2, 7" STB	4	.8-1.4		
34	446-462	BM3.2, 7" STB	4	.8-1.4		
35	446-462	BM3.2, 7" STB	4	.8-1.4		effects and yet drag on an isolated bellmout is almost
Set up to use MCV1 for mass flow measurement						
36	468-523	BM3.1, 7" STB, N31.3	4	.8-1.4	repeat of N31.3 BM3.1	
37	468-523	BM3.1, 7" STB, N31.3	4	.8-1.4	repeat of N31.3 BM3.1	
38	468-523	BM3.1, 7" STB, N31.3	4	.8-1.4	repeat of N31.3 BM3.1	
39	468-523	BM3.1, 7" STB, N31.3	4	.8-1.4	repeat of N31.3 BM3.1	drag is still increasing with Reynolds number
40	527-535	BM5, 7" STB, N31.3	4,9,14	1.8	Install M=1.8 C-D bellmouth	
41	536-544	BM6, 7" STB, N31.3	4,9,14	2.1	Install M=2.1 C-D bellmouth	
42	545-553	BM7, 7" STB, N31.3	4,9,14	2.4	Install M=2.4 C-D bellmouth	
43	554-562	BM7.1, 7" STB, N31.3	4,9,14	2.4	Install alum. M=2.4 C-D bellmouth	higher than skin friction.
44	566-601	BM3.1, 7" STB, N31.3 R1.1 P2	4	.8-1.4	repeat of N31.3 BM3.1	
45	566-601	BM3.1, 7" STB, N31.3 R1.1 P2	4	.8-1.4	repeat of N31.3 BM3.1	
46	566-601	BM3.1, 7" STB, N31.3 R1.1 P2	4	.8-1.4	repeat of N31.3 BM3.1	
47	566-601	BM3.1, 7" STB, N31.3 R1.1 P2	4	.8-1.4	repeat of N31.3 BM3.1	is basically insensitive to reynolds number
48	602-642	BM3.1, 7" STB, N31.3 trips off	4	.8-1.4	repeat of N31.3 BM3.1	
49	602-642	BM3.1, 7" STB, N31.3 trips off	4	.8-1.4	repeat of N31.3 BM3.1	
50	602-642	BM3.1, 7" STB, N31.3 trips off	4	.8-1.4	repeat of N31.3 BM3.1	
51	602-642	BM3.1, 7" STB, N31.3 trips off	4	.8-1.4	repeat of N31.3 BM3.1	that the trip on data, but it has less variability to RN.
		End of Entry 1				Total charged hours

This table outlines the runs made during the second entry of two.

Run Log

Series	Runs	Configuration	RN	Mach	Comment	Result at end of series
52	655-665	BM3.2 free air	nom	nom		is BAD
53	666-673	BM3.1, N31.3 free air	nom	nom	repeat of test-to-test check	data hi by .3cts, flow viz indicates stron recirculation b
54	678-685	BM1, N31.3 free air	nom	nom	repeat of test-to-test check	Agrees with series 12
55	688-695	BM3.2.1, N31.3 free air	nom	nom	modify adaptor to reduce recirculation	data looks better, but not yet back to plate mount level
56	696-700	BM3.2.2, N31.3 free air	nom	nom	modify adaptor to reduce recirculation	data looks still better, but not yet back to plate mount
57	701-709	BM3.2.2 free air	nom	nom	effects perf.	isolated bellmouth Matches original perf.
58	713-721	BM1, N31.3 R1.1 P2 TS2 free air	nom	nom	(TS2) free air	baseline nacelle with gaurenteed turbulant flow
59	722-731	BM1.1, N31.3 R1.1 P2 TS2 free air	nom	nom	(TS2) free air low mount tongue	
60	732-741	BM1.2, N31.3 R1.1 P2 TS2	nom	nom	(TS2) free air low mount and mid horiz	
61	751-787	BM3.2.2, STB, N31.3 R1.1 P2 TS2	4	.8-1.4	(TS2) STB	Find out if all super trip cases collapse
62	751-787	BM3.2.2, STB, N31.3 R1.1 P2 TS2	4.5	.8-1.4	(TS2) STB	
63	751-787	BM3.2.2, STB, N31.3 R1.1 P2 TS2	5.5	.8-1.4	(TS2) STB	
64	751-787	BM3.2.2, STB, N31.3 R1.1 P2 TS2	7.2	.8-1.4	(TS2) STB	
65	794-807	BM8, STB	14.7		1" cubic, free air	
66	810-813	BM7.0.1, STB, N31.3 R1.1 TS2	4,9,14	2.4	Run N31.3 R1 with BM7 bellmouth	Ramp broke off
67	815-817	BM7.0.1, STB, N31.3 R1.1 TS2	4,9,14	2.4	Run N31.3 R1 with BM7 bellmouth	wrong MCV code
68	818-820	BM7.0.1, STB, N31.3 R1.1 TS2	4,9,14	2.4	Run N31.3 R1 with BM7 bellmouth	run supersonic case with ramps
69	821	BM7.0.1, STB, N31.3 R1.1 TS2	4,9,14	2.4	Run N31.3 R1 with BM7 bellmouth	run supersonic case with ramps with "nickle" asymetri
70	823-825	BM6.0.1, STB, N31.3 R1.1 TS2	6,9,12	2.1	Run N31.3 R1 with BM6 bellmouth	run supersonic case with ramps
71	826-828	BM6.0.1, STB	6,9,12	2.1	isolated BM6 bellmouth	
72	829-832	BM7.0.1, STB	4,9,14	2.4	isolated BM7	
73	834-840	BM3.2.2, STB, N36 R1 N3 TS2	4	.8-1.4	(TS2) STB	
74	841-846	BM3.2.2, STB, N36 R1 N3 TS2	7	.8-1.4	(TS2) STB	
75	847-864	BM3.2.2, STB, N36 R1 N2 TS2	4	.8-1.4	(TS2) STB	
76	847-864	BM3.2.2, STB, N36 R1 N2 TS2	7	.8-1.4	(TS2) STB	
77	867-875	BM3.2.3, STB	4	.8-1.4	isolated BM3.2.3	modified bellmouth
	876	BM3.2.3, free air, flow viz	nom	0.95	isolated BM3.2.3	modified bellmouth, free air, flow viz
	877	BM3.2.2 free air, flow viz	nom	0.95	isolated BM3.2.2	modified bellmouth, free air, flow viz
	877	BM3.2 free air, flow viz	nom	0.95	isolated BM3.2	modified bellmouth, free air, flow viz
78	879-886	BM3.2.4 free air	nom	.8-1.4	isolated BM3.2.4	modified bellmouth, free air
	887	BM8, free air, flow viz	nom	0.95	isolated 1 inch cubic	flow viz
79	888-894	BM3.1.5 free air	nom	.8-1.4	isolated BM3.1.5	modified bellmouth, free air

In accordance with our objectives, the same model that was tested in the first test was re-tested in each of the second test's two entries. Long term force repeatability was under ±.16 cts. Long term weight-flow repeatability was under ±.07ct. It turns out that the random shifts in force correlated well with weight flow. Because drag is gross thrust minus ram drag, the net result is that the total variability on drag was less than ±.08cts.

Assessment of Long term repeatability for HSCT type nacelles

Force/Gross Thrust:

- Long term force repeatability < ±.16 cts

Weight-flow/Ram Drag :

- Long term weight-flow repeatability < ±.07ct

*Random Shifts in Force correlated well with Weight flow so uncertainty in Fnet < RSS(Fram + FG)

The following figure shows the short and long term repeatability of gross thrust in the left hand axis and of ram drag in the right hand axis.

Force Measurement Short/Long Term Repeatability
Weight Flow Short/Long Term Repeatability

BOEING

High Speed Civil Transport

Long Term Repeatability For N31.3
3 Entries + Different Belmouth Attachments
(Nominal Plate Mount Configuration)

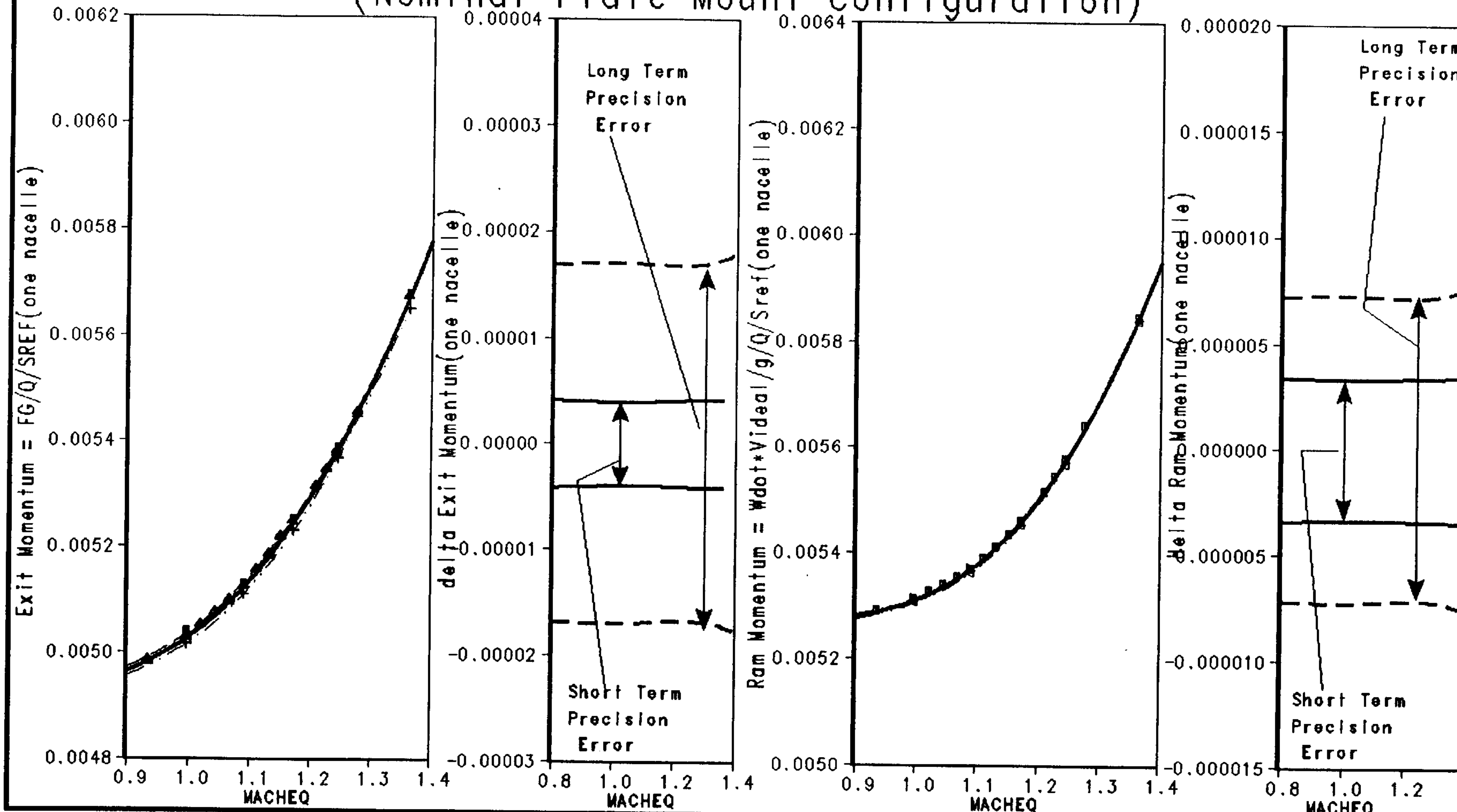

February 1999 HSR Airframe Technical Review

The BSWT test that was to use this calibration data was run at a Re=7million/ft. The calibration data was obtained at a Re~4million/ft. A reasonable question that is often posed is whether the Re=4million calibration data is still applicable at 7million, and what corrections should be applied. Having a mismatch between calibration Reynolds numbers and test is not unique to the HSCT program. Depending on the wind tunnel facility(High Reynolds number or atmospheric) and the calibration facility (FSC or Thrust stand) a Re mismatch of 2-4 times exists for most programs. Other programs have evolved two distinct approaches to handling this issue.

On commercial transports, nacelles are large and have a low length/diameter ratio (relative to an fighter). As a result $\delta^* <<$ duct diameter. Consequently, the nacelle internal static's pressure coefficient is relatively insensitive to changes in Reynolds number. Therefore if internal drag (1-Cv) is correlated to the nacelle pressure ratio (PTinf/PN), a correction must be applied to (1-Cv) for Reynolds number. A derivation of a first-order correction for axisysmetric and 2-D nacelles is described in the next two charts.

On fighter programs, the duct diameters are less and l/d is larger (~10). The net result is that δ^* is not small relative to the duct diameter so duct pressures are sensitive to changes in Reynolds number. Consequently, a drop in Reynolds number will show up in the average PT. The resultant change to the local Mach due to boundary layer growth must also show up in the the static pressures. So it follows that a calibration at a single Reynolds number has broad applicability without any corrections for Reynolds number.

So which is right for an HSCT? We have no reason to suspect that an HSCT should behave differently than a fighter model. But what if it doesn't and a correction is required? How would we go about developing such a correction? On an HSCT nacelle, skin friction changes by about .2cts per/nacelle going from 4-7million. The accuracy capability demonstrated in the first entry indicated that we should be able to resolve effects down to ±.08cts. In addition, the Boeing FSC has the hardware available (in the form of the "standard thrust body") to test at a wide range of Reynolds numbers. Therefore the easiest way to resolve the uncertainty is to run the test.

Do We Need to Calibrate At The Reynolds Number We Test?

- **The Reynolds Number Effect on Nacelles is small (.2ct/nacelle)**

- **Re correction could be unnecessary**
  - Changes in boundary layer should change Mach

- **If correction required, 1st order Re correction should work**
  - Re effects from CFD solutions have been consistent with a 1st order boundary layer growth
  - CFD has shown a uniform core flow (transonic, no plugs)

- **What if something other than 1st order needed**
  - Core flow may not be sufficiently uniform and Reynolds number dependent
  - δ^* is sufficiently large for HSCT ducts that H&W > δ^*
  - Trip effectiveness varies with Reynolds number
  - Plug nozzles have low velocity duct followed by rapid compression (favorable pressure gradient)

Solution: Test at Variable Reynolds Number In Entry 2

The following figure shows the derivation of the first order Reynolds number correction for a axisymmetric nacelle.

Analytical Correction Available to Match FSC Data to Test Facility

BOEING

High Speed Civil Transport

Derivation of Standard Reynolds Number Correction For Axisymmetric Nozzle

If
1. Core flow is sufficiently uniform
2. Boundary layer has axial symmetry
3. D >> δ^*

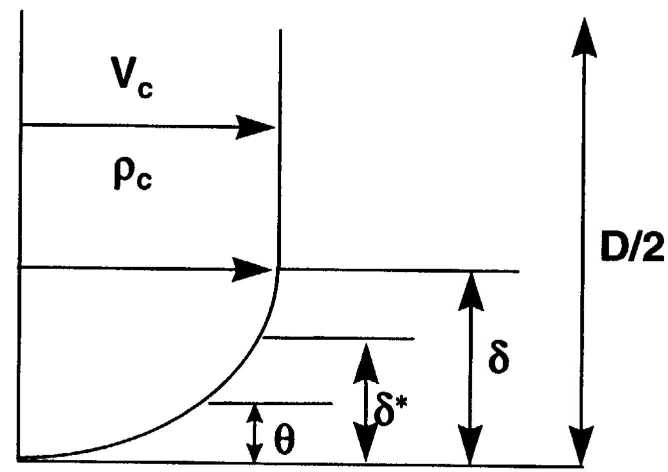

$$\frac{\dot{W}_{actual}}{\dot{W}_{ideal}} = Cd = \frac{\rho_c V_c \left(\frac{\pi D^2}{4} - \pi \delta^* D\right)}{\rho_c V_c \frac{\pi D^2}{4}} = 1 - \frac{4\delta^*}{D}$$

$$\frac{\dot{W}_{actual} V_{actual}}{\dot{W}_{actual} V_{ideal}} = Cv = \frac{\rho_c V_c^2 \left(\frac{\pi D^2}{4} - \pi \theta D\right)}{\rho_c V_c^2 \frac{\pi D^2}{4}} = 1 - \frac{4\theta}{D}$$

The relationship between δ^* and Reynolds number can be expressed by the equation:

$\delta^* = (\text{constant})\,(X)\,(Re_x)^{-.2}$

$\theta = (\text{constant})\,(X)\,(Re_x)^{-.2}$

$$\therefore \quad Cd_{test} = 1 - (1 - Cd_{FSC}) \left(\frac{RN/FT \sim FSC}{RN/FT \sim TEST}\right)^{+.2}$$

$$Cv_{test} = 1 - (1 - Cv_{FSC}) \left(\frac{RN/FT \sim FSC}{RN/FT \sim TEST}\right)^{+.2}$$

The following figure shows the derivation of the first order Reynolds number correction for a 2-D nacelle.

Analytical Correction Available to Match FSC Data to Test Facility

Derivation of Standard Reynolds Number Correction For 2-D Nozzle

If
1. Core flow is sufficiently uniform
2. Boundary layer has axial symmetry
3. H & W >> δ^*

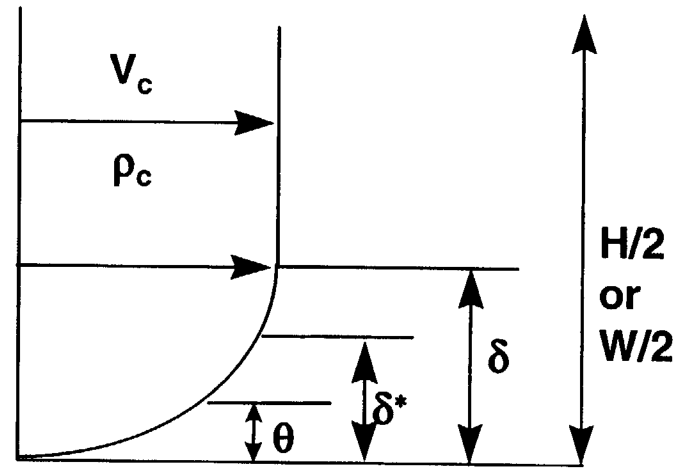

$$\frac{\dot{W}_{actual}}{\dot{W}_{ideal}} = Cd = \frac{\rho_c V_c [HW - 2\delta^*(H+W)]}{\rho_c V_c HW} = 1 - \frac{2\delta^*(H+W)}{HW}$$

$$\frac{\dot{W}_{actual} V_{actual}}{\dot{W}_{actual} V_{ideal}} = Cv = \frac{\rho_c V_c^2\,[HW - 2\theta(H+W)]}{\rho_c V_c^2\, HW} = 1 - \frac{2\theta(H+W)}{HW}$$

The relationship between δ^* and Reynolds number can be expressed by the equation:

$\delta^* = (\text{constant})\,(X)\,(Re_x)^{-.2}$

$\theta = (\text{constant})\,(X)\,(Re_x)^{-.2}$

$$\therefore \quad Cd_{test} = 1 - (1 - Cd_{FSC})\left(\frac{RN/FT \sim FSC}{RN/FT \sim TEST}\right)^{+.2}$$

$$Cv_{test} = 1 - (1 - Cv_{FSC})\left(\frac{RN/FT \sim FSC}{RN/FT \sim TEST}\right)^{+.2}$$

The following figure illustrates how Reynolds number matching can be achieved in the FSC. On a standard thrust stand or in the nominal FSC arrangement, either the upstream or downstream pressure is a variable, but never both. Consequently, the nozzle pressure ratio pressure is determined by a single pressure, and Reynolds number is a fallout. In the FSC, PT is fixed at atmospheric and the pressure ratio is varied by changing the downstream static pressure. On a thrust stand, it is PT that is the variable and the downstream static pressure that is fixed at atmospheric pressure. By attaching the "Standard Thrust Body" (STB) to the FSC upstream of the nacelle, uniform high pressure air can be supplied to the nacelle. In the STB mounting arrangement, both the upstream and downstream pressures can vary independently. The maximum pressure ratio is determined by a minimum tank pressure limit of 4psi and a maximum supply pressure of 300psi.

FSC Test Set Up For Variable PT/RE

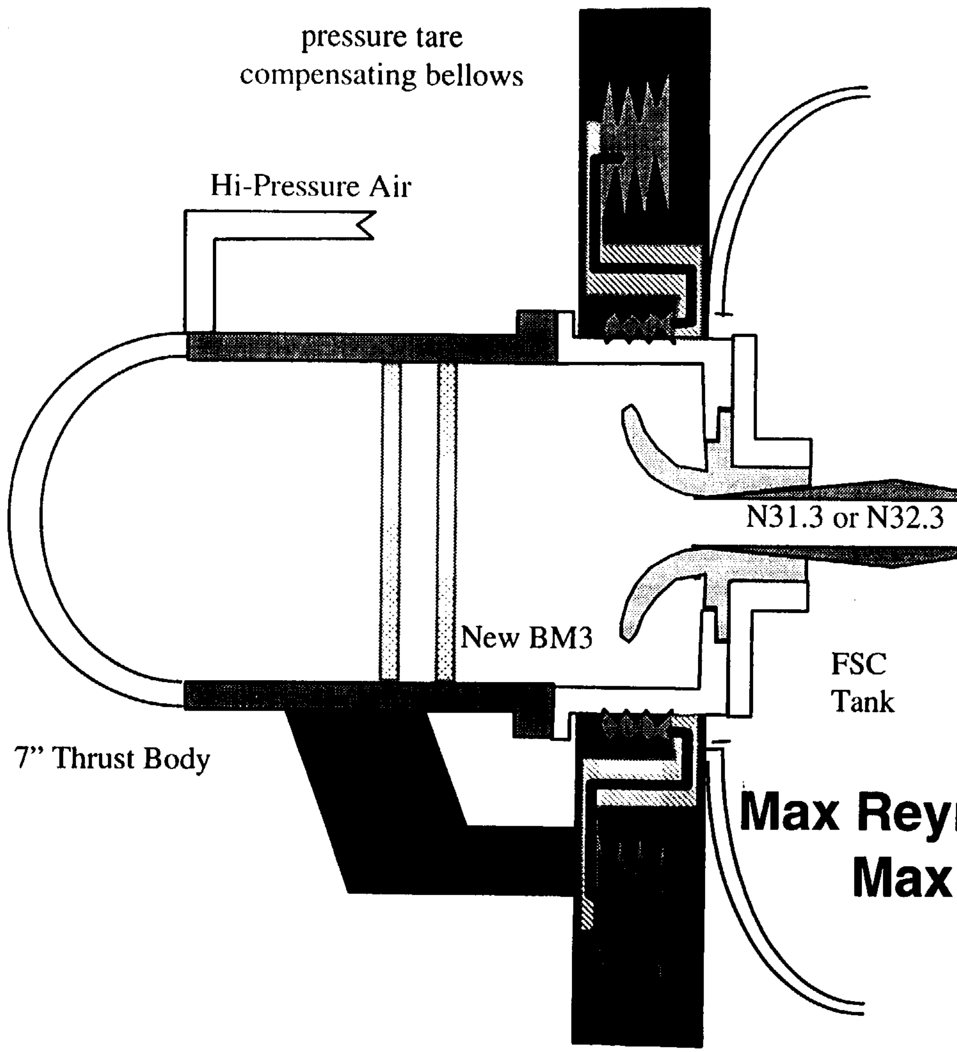

Measured quantities:
$Fg+A_{base}(P_{base}-P'_{inf})$
W_{dot}
$P_{inf}=P_{vac}$
$PT_{inf}=PT_{rake}$
$TT_{inf}=TT_{rake}=TT_{vac}$
PN_{static} at 2 stations

Max Reynolds Number =45 million
Max Mach Number = 2.4+

The following picture is of the STB installed on the FSC. Note the high pressure air lines entering the STB on forward right hand side. The line goes though 4 bellows assemblies, two of which are pictured (two can-like objects on right), to minimize the potential of a momentum tare.

BOEING

High Speed Civil Transport

FSC Test Set Up For Variable PT/RE

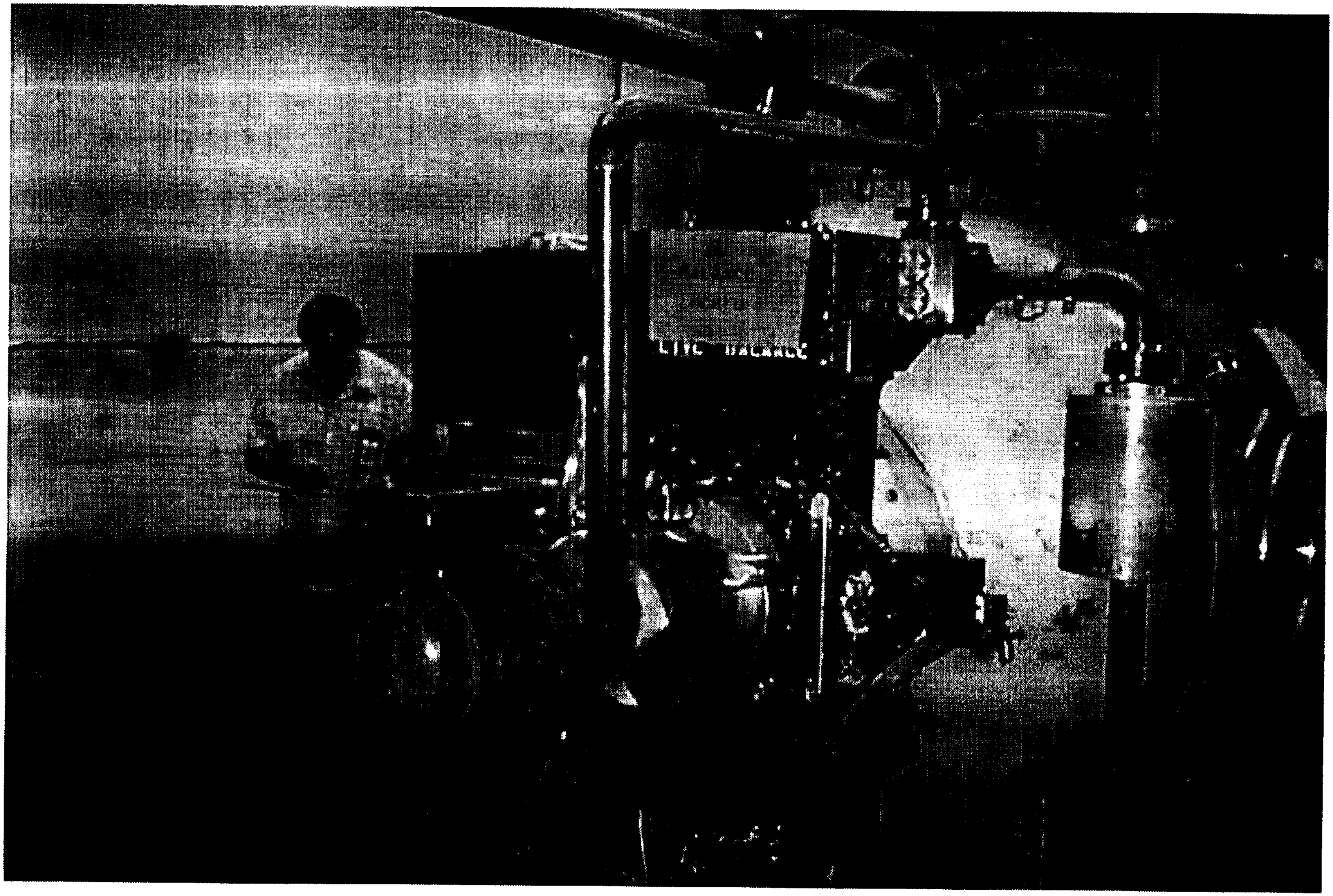

The following plot shows the operating envelope of Mach and Reynolds number with the STB installed. It is possible to expand the envelope with some re-engineering of the hardware to expand the minimum/maximum tank pressures or supply pressures.

FSC/STB Operational Envelope

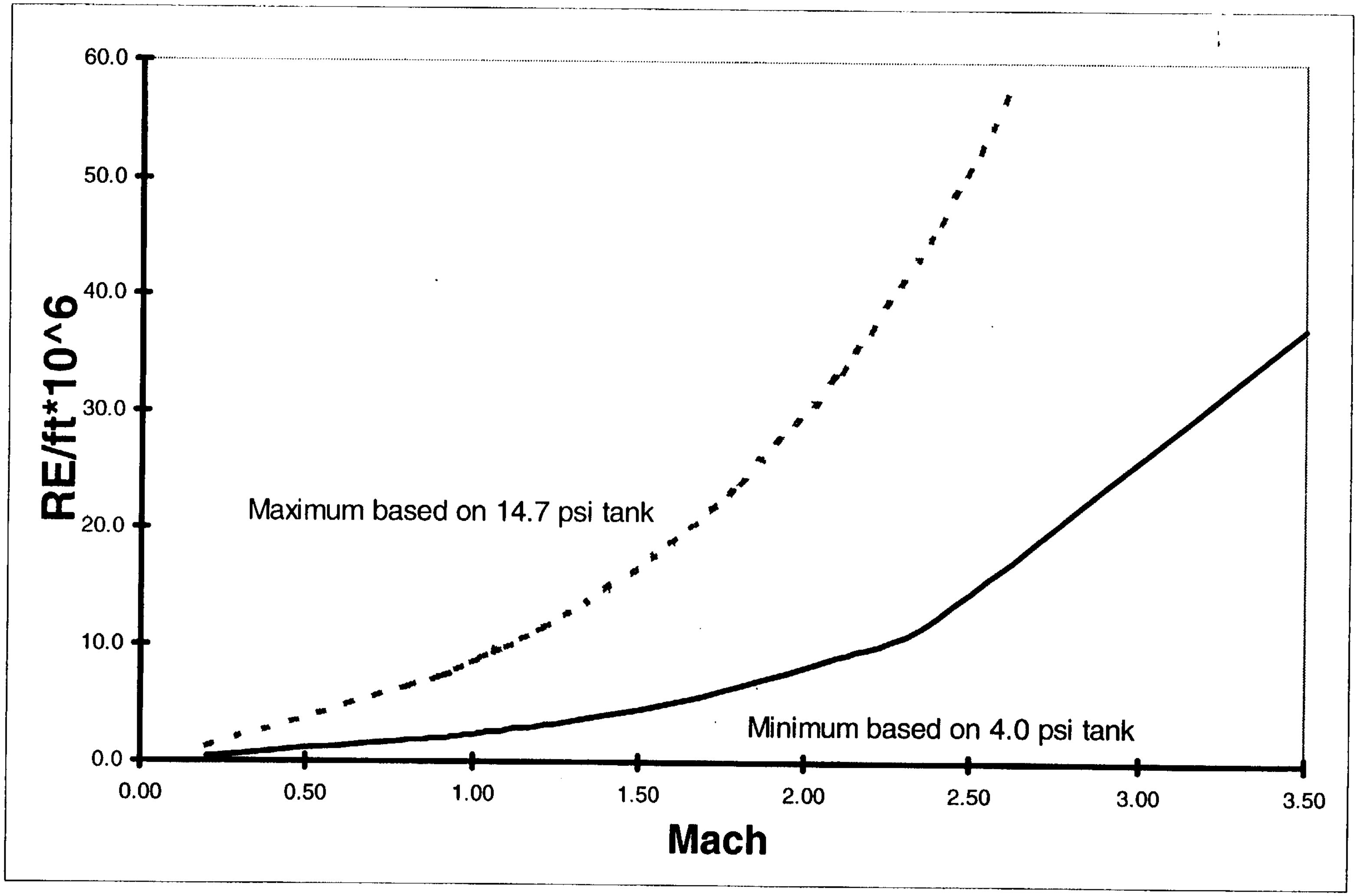

February 1999 HSR Airframe Technical Review

The following is a picture of the STB as viewed looking upstream. In the foreground is the instrumentation section that is placed between the STB and the test article. It consists of 4 PRT's to measure total temperature and 4 total pressure rakes of 8 probes a piece. Seen upstream of the rakes are a series of flow conditioning screens that insure the high pressure air supply is uniform.

FSC Basic Principles: Upstream Instrumentation For Variable PT/RE Test Rig

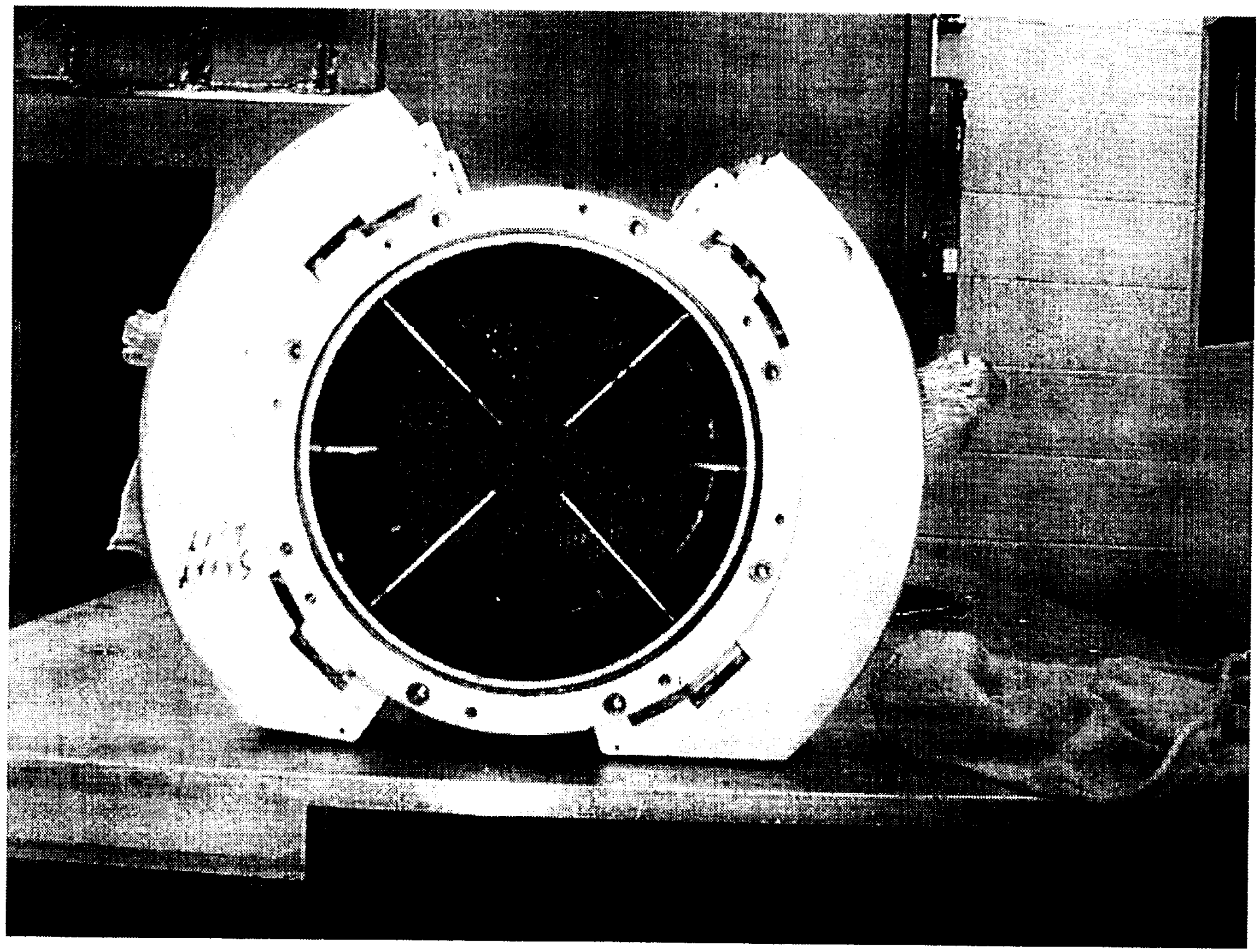

The results from using the STB were mixed. The good news is that , in general, the set up appeared to work. Comparison for the same nacelle between the plate mount and the STB indicate that the STB data fall within the long-term scatter of the plate mount data. To check for a bias with PT, the cubic calibration nozzle on the plate mount was compared with the cubic on the STB at two Reynolds numbers. The cubic calibration nozzles are designed to be insensitive to Reynolds number. At both Reynolds numbers the STB data fall within the long-term scatter of the plate mount data.

The bad news was that the use of the STB degraded the short term precision two fold. This was because it was almost impossible to set PT precisely and hold it constant for more than a few seconds. At the same time, the nacelle is unstable because it's throat is highly Reynolds number dependent. In addition to the precision penalty, productivity was also worse by a factor of two to three. This was because set up times are longer, setting PT was harder, and one naturally wants to run more Reynolds numbers if the STB is installed. The net result is that if only atmospheric data are all that is required, using the STB could increase the test time by a factor of 6 and offers no addtional benefits.

The other curious result was the assessment of Reynolds number effects. Several configurations were run at 4 Reynolds numbers. All runs always fell within the long term data scatter of plate mount data. However, the visable trend indicated that drag was either constant or went up with increasing Reynolds number. This is opposite of what CFD would predict. There are several potential explanations for these results. It could be just scatter, or it could be all the data are corrupted by the bellmouth design (discussed later), or it could be that there is some bias with PT we failed to diagnose, or it could be a real effect. Running the STB presents a real paradox. While the technique is necessary to simulate variable Reynolds Number, the reduced precision makes it harder to measure an effect.

Assess facilities ability to match Reynolds number (from 16ft to Polysonic)

Good News:

- Use of STB produces PT=Atmo data within the long-term scatter of the plate mount data

Bad News:

- Use of STB degrades precision by 2X (unstable system)
- No CFD data or calibration standard exist to rule out biases
- Use of STB degrades productivity by 2-3X
- All the Re variation runs were within the long-term scatter of the plate mount data. Measured trend could be same or opposite as CFD

Catch 22:

Technique necessary to simulate Reynolds Number is less likely to be able to measure effect.

February 1999 HSR Airframe Technical Review

The following figure illustrates how there is statistically no difference between platemount and STB mount data for nacelle N31.3.

BOEING

High Speed Civil Transport

Assess facilities ability to match Reynolds number (from 16ft to Polysonic)

Good News: At Same RE, STB Data Within Plate Mount Repeatability

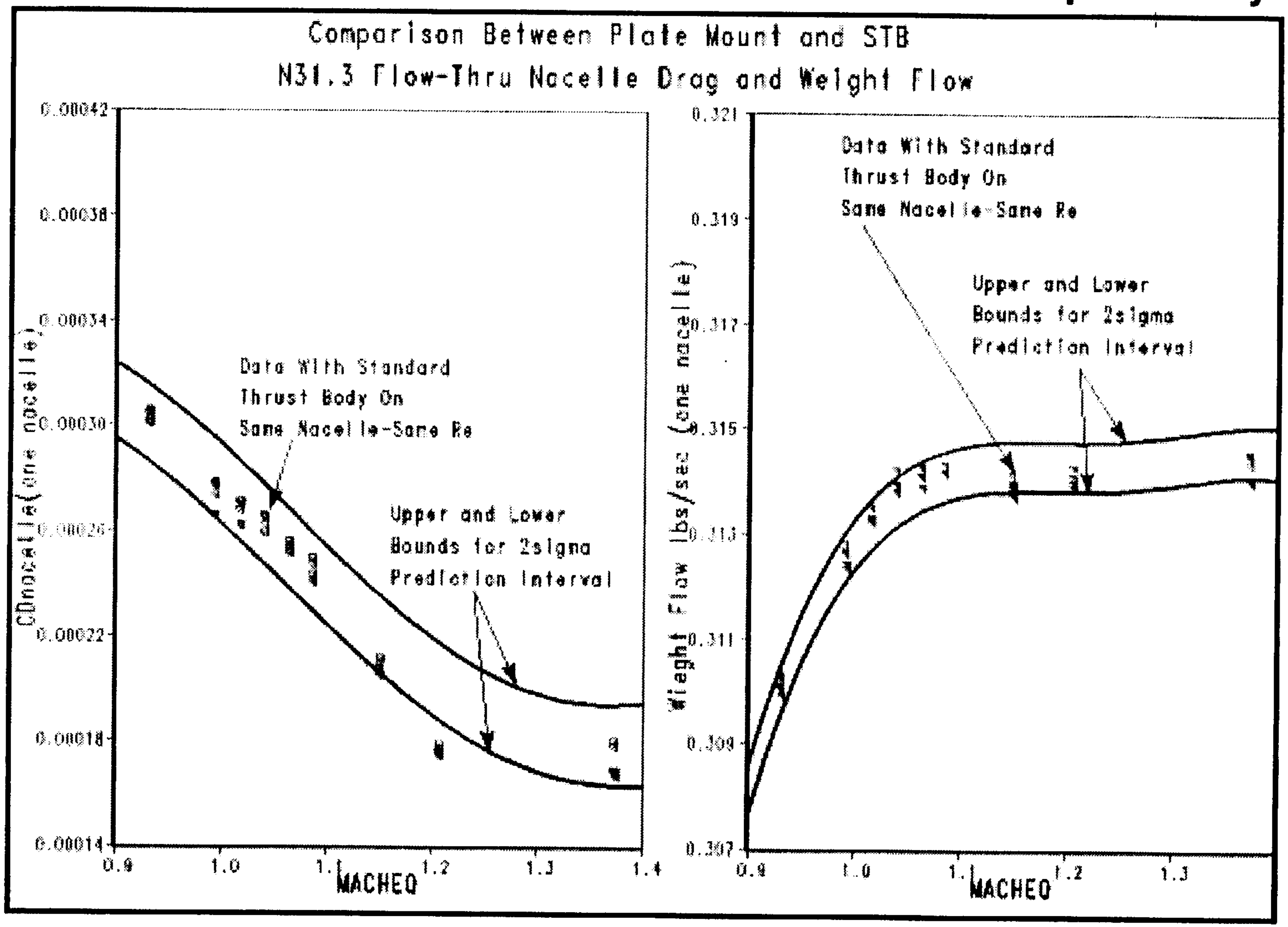

Data based on same instrumentation: MCV4 (aft tank venturi) and TTN (upstream TT)

A cubic calibration nozzle is designed to be insensitive to Reynolds number. Verification of the design has historically been done by comparing FSC data and Thrust Stand data. Within experimental precision limits, the two data sets have agreed despite a factor of two difference in Reynolds number (~4million vs ~7million) . To verify that the STB was not imparting a bias with PT setting, a 2" diameter cubic calibration nozzle was run at two PTs (14.7 & 23psi). The upper and lower bound of the data scatter for these two cases as well as a plate mount run are shown in the following figure. These data indicates that all data, regardless of mounting system or Reynolds number, produce the same results (within precision limits), and hence there is no system bias with PT. It should be noted that these data also illustrate the reduced precision of STB data.

Assess facilities ability to match Reynolds number (from 16ft to Polysonic)

BOEING
High Speed Civil Transport

Good News: At Same RE, STB Data Within Plate Mount Repeatability

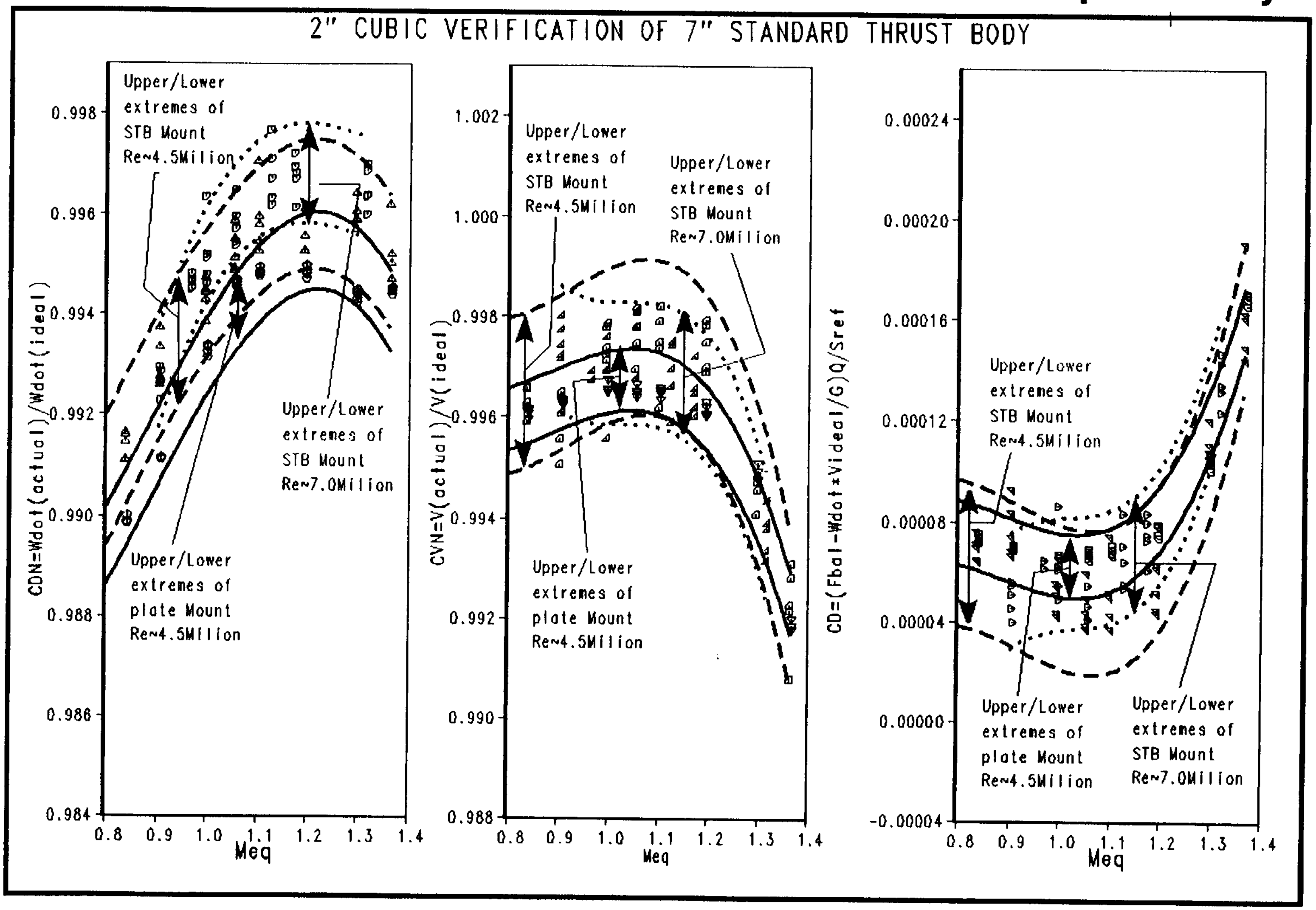

Data based on same instrumentation: MCV4 (aft tank venturi) and TTN (upstream TT)

The following figure shows the long term precision limits for the STB mount. Three installations on the STB are within the limits of the plate mount. These data would imply that the STB degrades the short term precision by a factor of two, but also that the effect on long term precision is negligible.

BOEING
High Speed Civil Transport

Assess facilities ability to match Reynolds number (from 16ft to Polysonic)

Good News: At Same RE, STB Data Within Plate Mount Repeatability

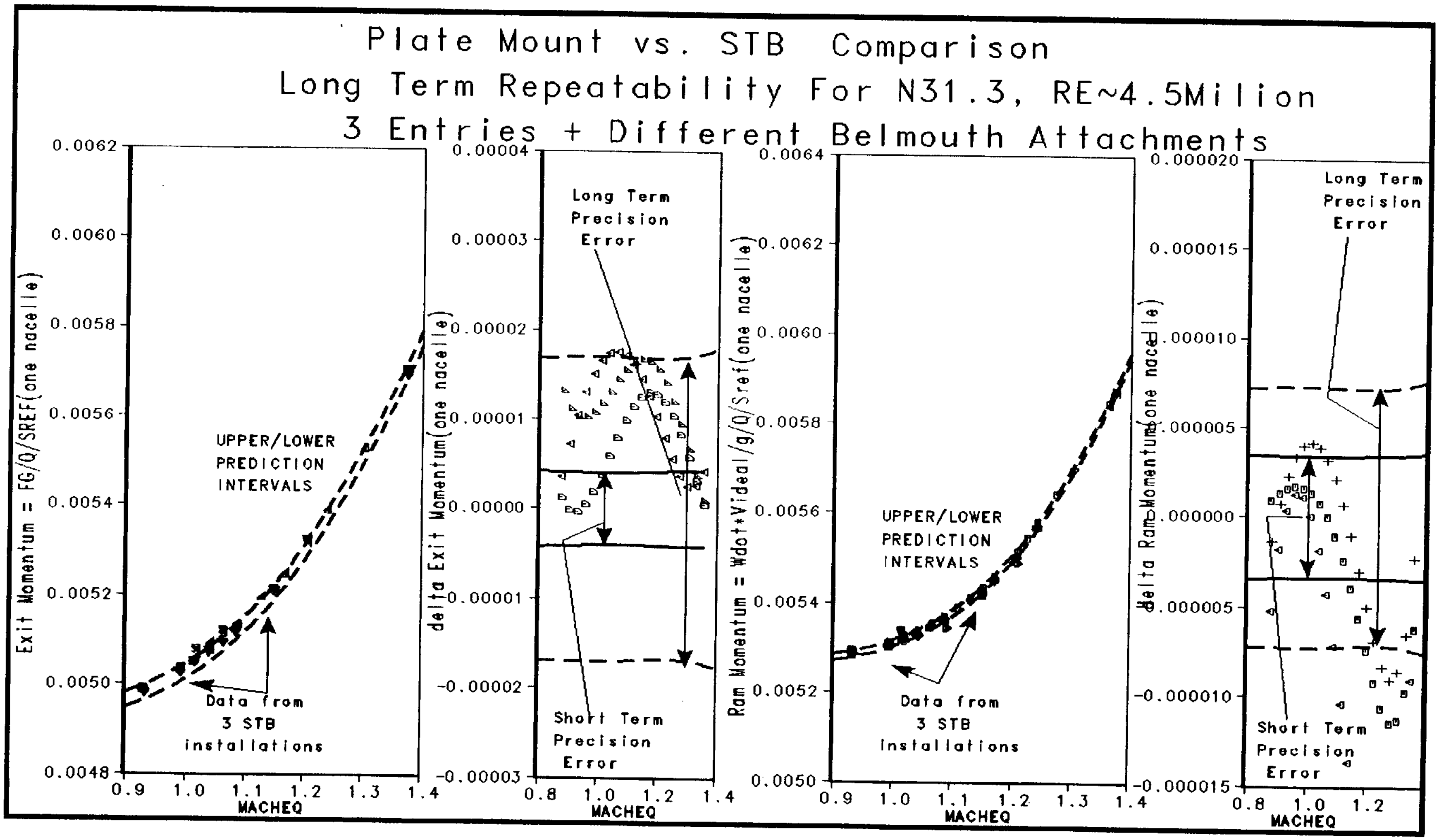

Data based on same instrumentation: MCV4 (aft tank venturi) and TTN (upstream TT)

There are two interesting issues with the STB data that may be contributing to the precision losses. The first is differences between the rake measured total temperatures from upstream of the nacelle, and the tank total measured at the tank exit. This is shown in the following left hand plot. The flow through the nacelle is believed to be adiabatic and for the plate mount/free air cases the instrumentation seems to substantiate this. When the STB is installed the data shows a 3 degree temperature drop from upsteam of the nacelle to downstream.

The second issue concerns the different readings of mass flow rate from the critical flow ventrui upstream of the STB/nacelle (MCV1), and the one downstream of the nacelle/tank (MCV4). The maximum scatter of MCV1 and MCV4 is shown in the following right hand plot. The reduction in short term precision seems to be caused by system instability. The complete system consists of 3 choked venturi's. The first is MCV1. Then there is a supply line that is approximately 5” diameter that runs ~12’ from MCV1 to the STB. For the Mach numbers of interest, the nacelle itself forms a choked venturi as its exit area fluctuates with Reynolds number based on upstream PT. Aft of the nacelle is the 4’ diameter, 12’ long settling chamber. At the exit of the chamber is MCV4, the primary measurement critical flow venturi. In practice, we found it very difficult to set and hold the supply line PT upstream of the STB for more than a few seconds. At the low mass flow rates of HSCT nacelles (.2lbs/sec), there was a lag between when PT was set and when it equalized at the rakes in the STB. This upstream PT is what would determine boundary layer characteristics through the nacelle and therefore the mass flow rate through the nacelle. There was also a lag between when the STB PT equalized and the when the tank ambient pressure would equalize. The tank pressure forms the PT for the MCV4 venturi. At any given moment, the system could conceivable see 3 different mass flow rates: MCV1 (upstream venturi), nacelle mass flow (felt by balance), and MCV4 (downstream venturi). Because the volume of air in the supply line between MCV1 and the STB is approximately 23 times less than that of the tank, it stands to reason that MCV1 should track the mass flow through the nacelle more closely and be less sensitive to supply pressure changes. However, MCV1 has never been as fully calibrated as MCV4 has for data accuracy.

Assess facilities ability to match Reynolds number (from 16ft to Polysonic)

STB's Reduced Precision is Caused By System Instability

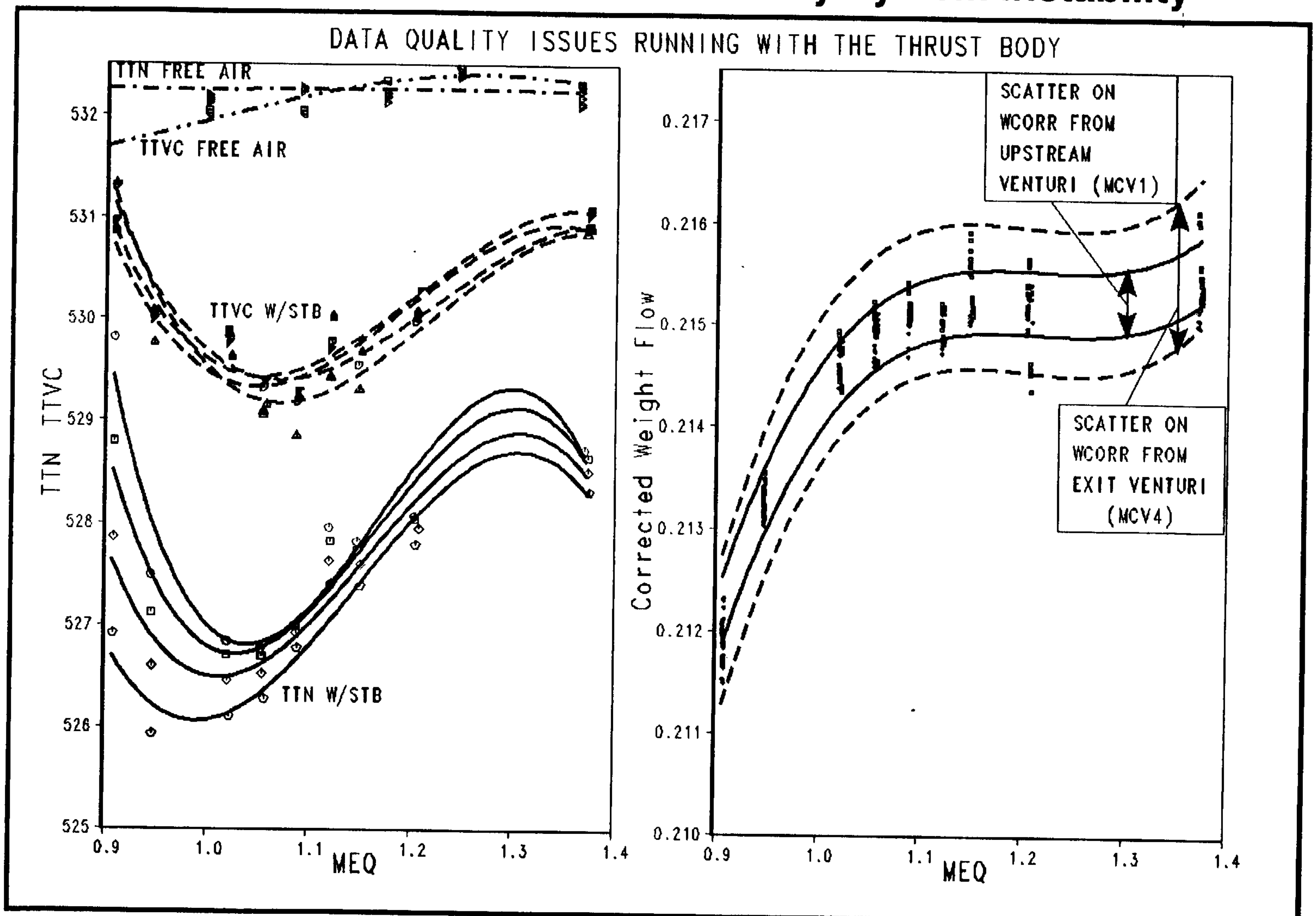

The following figure illustrates the difficulty in interpreting the Reynolds number trends from the STB. Taken at one level, this plot says that any variation in drag with Reynolds number is within the long term data scatter and is therefore meaningless. On another level, it is recognized that the Reynolds number variations are taken on a single installation over a very short period so it is the short term precision that should be viewed for comparison. If this second case is closer to reality, the data indicate the gross thrust per unit of weight flow actually increases as Reynolds number is decreased.

Assess facilities ability to match Reynolds number (from 16ft to Polysonic)

Bad News: At All RE, STB Data Within Plate Mount Repeatability

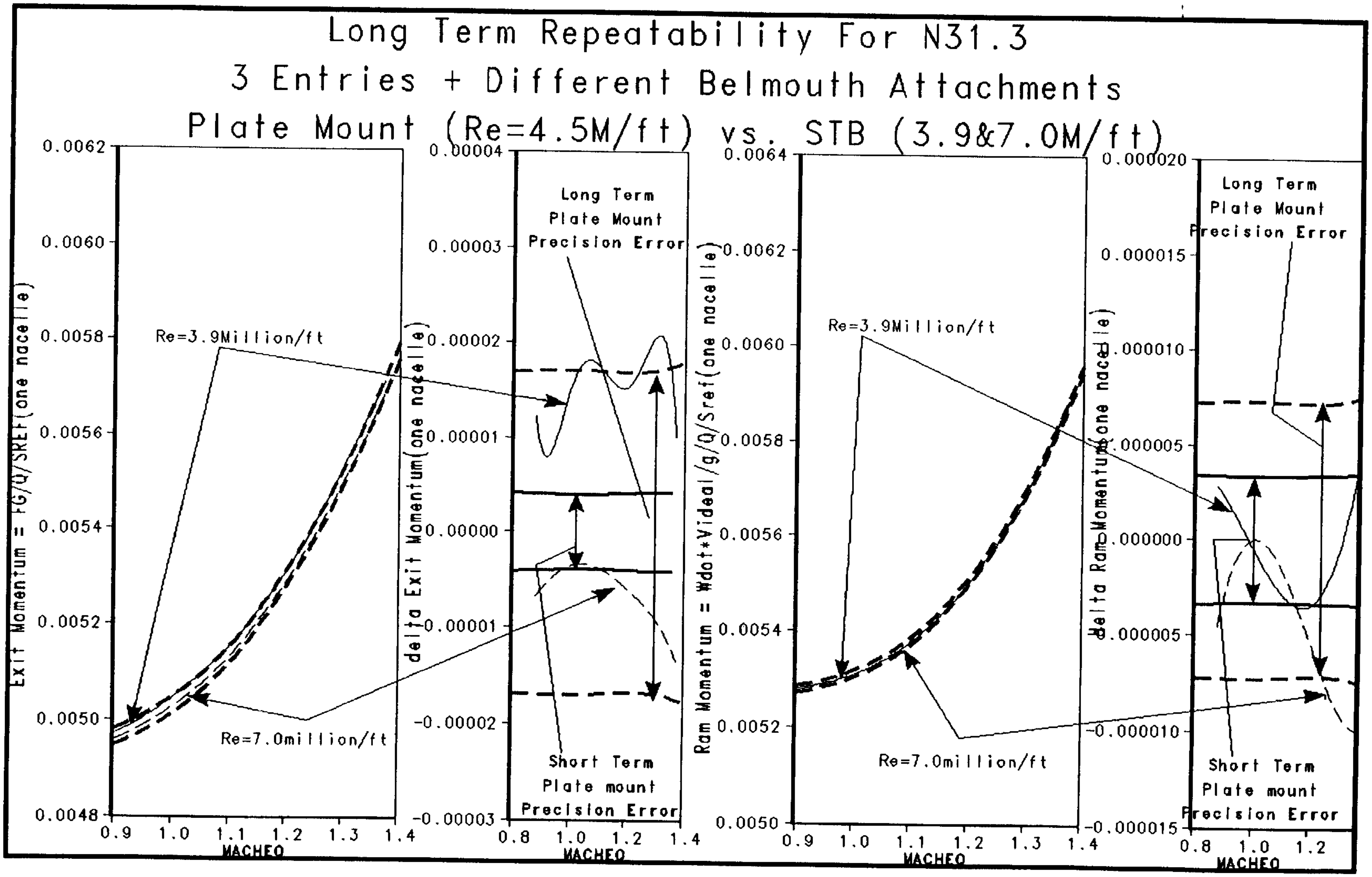

Depending on whether or not it is short or long term precision that is guiding the interpretation, a completely opposite trend with Reynolds number is indicated by the data. Shown in the left hand figure is the trend with Reynolds number extracted from a linear theory code (H349) and OVERFLOW NS. Both indicate that a Reynolds number increase form 4 to 7 million/ft will produce a drag reduction of .4cts per/pair (2 nacelles). If the STB Re variation data is just scatter, then it can be assumed that the nominal drag at 4 million corresponds to the plate mount data. This data can then be adjusted using the 1st order Reynolds number correction described previously. The resultant data also indicate that drag goes down by .4ct for a 4 to 7 million/ft Re change. On the other hand, if the STB data are good, then the trend actually is a drag increase of .4cts going from 4 to 7 million/ft.

If the STB data are not scatter, they could be caused by two effects. The first is a bias with PT. To change Reynolds number requires an increase in the upstream PT. If there is a systematic change in leak rate, pressure tare (through high pressure line), weight flow measurement or balance accuracy with change in PT, a misleading trend could be produced. All the checks available and the 2" cubic runs seem to rule out the possibility, but something could have been missed.

A second possibility is that the effects are real, but there is something going on in the calibration that is not going on in CFD. One such feature is the bellmouth design. This will be discussed later, but the bellmouth is imparting an unusually high drag bias to the data (relative to historical trends for cubics). If the bellmouth imparts "too" much distortion, adding boundary layer (by reducing Reynolds number) could actually reduce drag. The data in the next figure seems to support this theory.

Assess facilities ability to match Reynolds number (from 16ft to Polysonic)

BOEING
High Speed Civil Transport

Example of how precision error can result in misleading trend

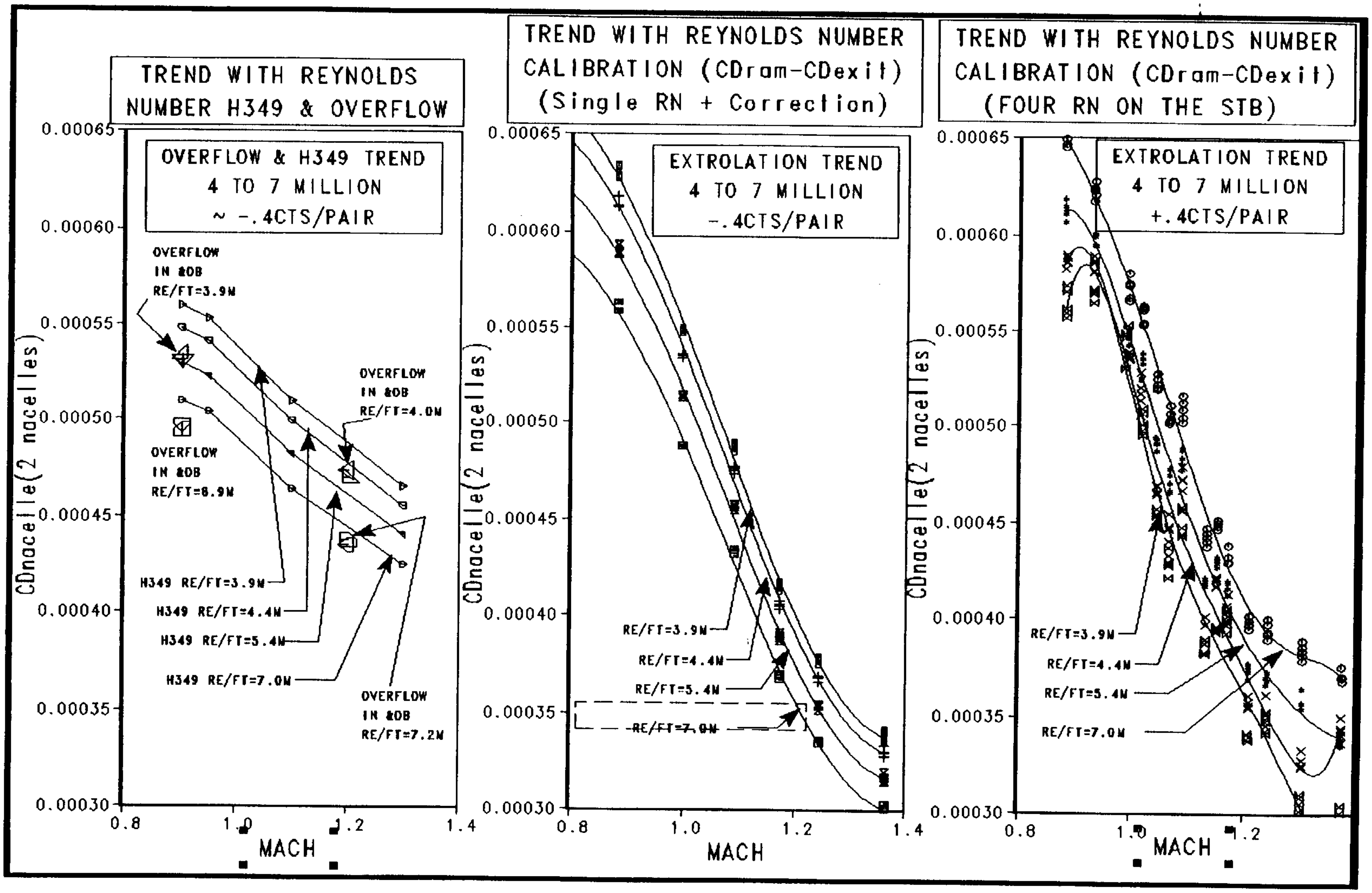

N31.3/N32.3 Flow Thru Nacelle Trip = .008"

February 1999 HSR Airframe Technical Review

There are two possible sources of thrust loss. There are PT losses in the boundary layer and flow non-uniformity in the core flow (pressure drag). Transonically, it is believed that the dominant effect for HSCT nacelles is boundary layer losses and that the core flow is fairly uniform. CFD solution have been consistant with this belief. It follows that a decrease in Reynolds number will result in a larger boundary layer, hence larger losses, with little effect on flow non-uniformity. To have a reverse trend with Reynolds number would require that the flow non-uniformity losses be greater than the boundary layer losses per unit of mass flow. Therefore, as more boundary layer fills the duct there would be less core flow, so the losses per unit of mass would actually be less.

The following figure provides some supporting data that this may actually be happening, and therefore the trend seen by the STB with Reynolds number might "real". Shown is a comparison between data from the same model with two different trip definitions. A large change in trip can dramatically change the boundary layer profile. In this way, a change in trip is very similar to a change in Reynolds number. Both configurations were run with the plate mount at a nominal Re=4 million/ft. Using this configuration, it can be said that these data have no hidden bias with respect to PT associated with the STB mount. One trip is the nominal trip or .008", .4" from the inlet. It was sized for BSWT at Re=7 million/ft, so it is probably under-tripped for the FSC. Consequently, the duct most likely has a substantial length of laminar flow. The second trip, designated the super trip, has #40 (.0165 in.) grit filling the space from the inlet leading edge all the way back to the nominal trip. There is no chance that this configuration has any laminar run. Moving left to right, the first chart shows that increased trip effectiveness reduces the weight flow (consistent with a large boundary layer). The second chart shows that supertrip is increasing thrust loss (Inlet thrust-exit thrust). Both charts are as one would expect. However, the third chart shows thrust loss as a function of inlet momentum. The supertrip case actually has less of a loss per/count of inlet momentum. The fourth chart shows exit momentum in counts versus inlet moment in counts. The fifth chart shows the same data as the fourth in lbs of thrust versus lbs of weight flow. These data clearly indicates this configuration has less reduced losses per lb of mass flow with increasing boundary layer. Therefore this configuration should show a reverse trend with Reynolds number when viewed by some variables.

Variable Trip Data Suggest That The Reverse RE Trend May Not Be Due to A STB Bias

BOEING
High Speed Civil Transport

Example of How Viscous Effects Can Actually Increase Thrust

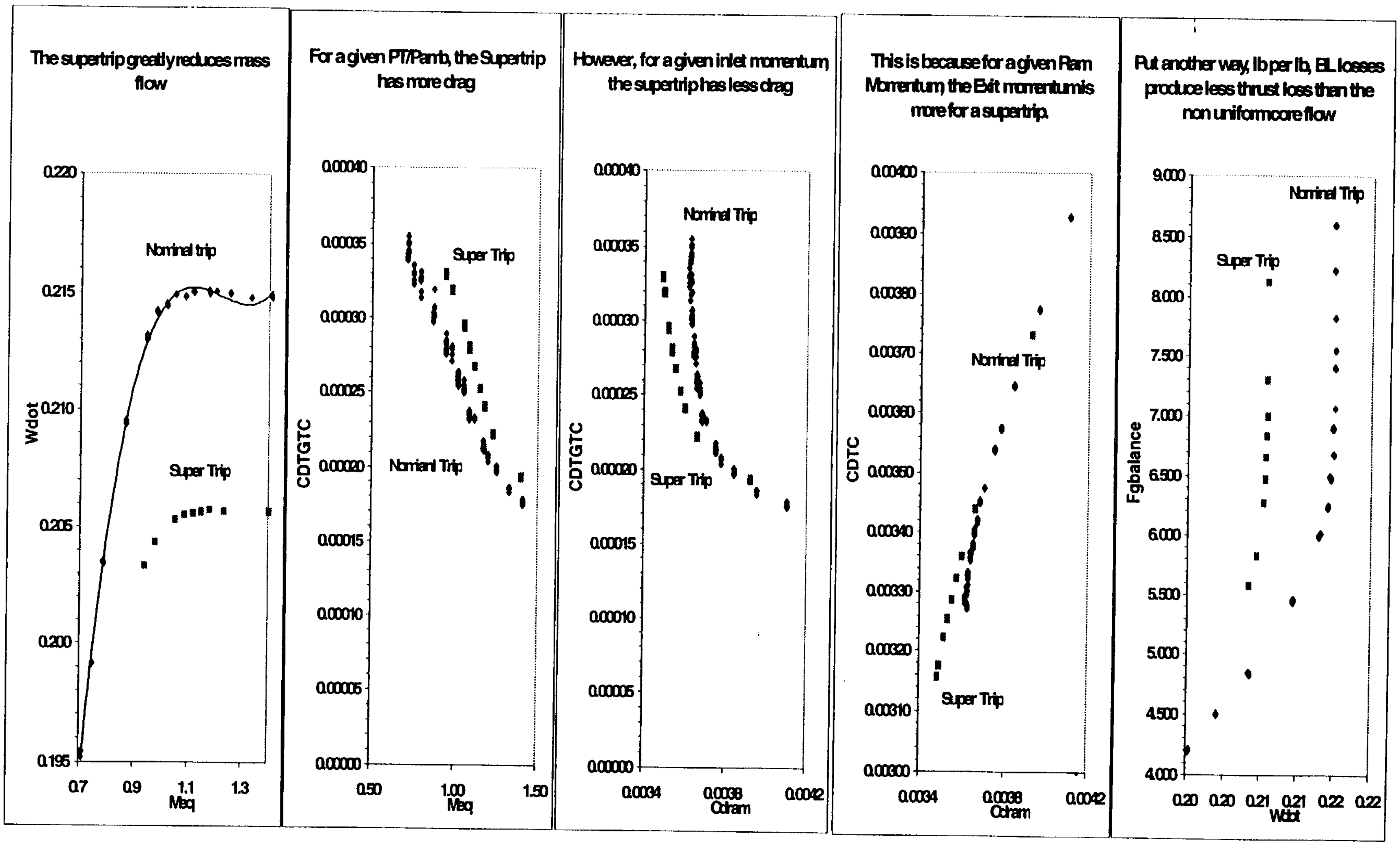

N31.3/N32.3 Flow Thru Nacelle Trip = .008"

One fortuitous feature of the mounting design to be used with the STB was the use of an adapter to hold the bellmouth. In the nominal plate mount arrangement, the nacelle is mounted to the plate and the bellmouth to the nacelle. This was how the nacelle was mounted in the first test. With this arrangement, there is no easy way to run an isolated bellmouth without making a new plate. When the STB is used, an adapter is mounted in the plate, the bellmouths are attached to the adapter, and the nacelle is mounted off the bellmouth. It is relatively easy to run an isolated bellmouth. When the trends with Reynolds number appeared, one diagnostic was to look at an isolated bellmouth. The following plots show the isolated bellmouth results.

Moving from left to right, the first plot shows the balance based velocity versus ideal, the second shows the venturi based weight flow versus ideal, and the last show the thrust loss. The first thing that was apparent for these results was that no one had imagined that such a bad bellmouth design was possible. Instead of getting >99% of ideal velocity and weightflow, this bellmouth was at 96% or worse. Instead of .8cts of drag it had up to 2.8cts. As mentioned earlier, past designs have been very successful. However those designs were all axisysmetric in nature. Other non-axisymmetric designs have been built (F-22, JSF), but those designs have not had their bellmouths tested isolated. It is possible that those bellmouths are also bad, but the fact was not obvious in the data. As mentioned earlier, it is possible to have a non-zero drag bellmouth that does not compromise the calibration. This requires that there is sufficient instrumentation in the duct that can pick up the bellmouth induced effects and not include them when they do not appear in a wind tunnel test. There was a concern that with the limited static pressures in the HSCT nacelles, they would be unable to distinguish bellmouth induced effects from the nominal duct effects. To assess this, an isolated bellmouth was run post-test in OVERFLOW NS.

Square Bellmouths: No One Imagined Such a Bad Design Was Possible

- Indications of high levels of distortion, possible turbulent flow
- Bellmouth has as much drag as an entire nacelle
- Internal instrumentation could never compensate >> distortion

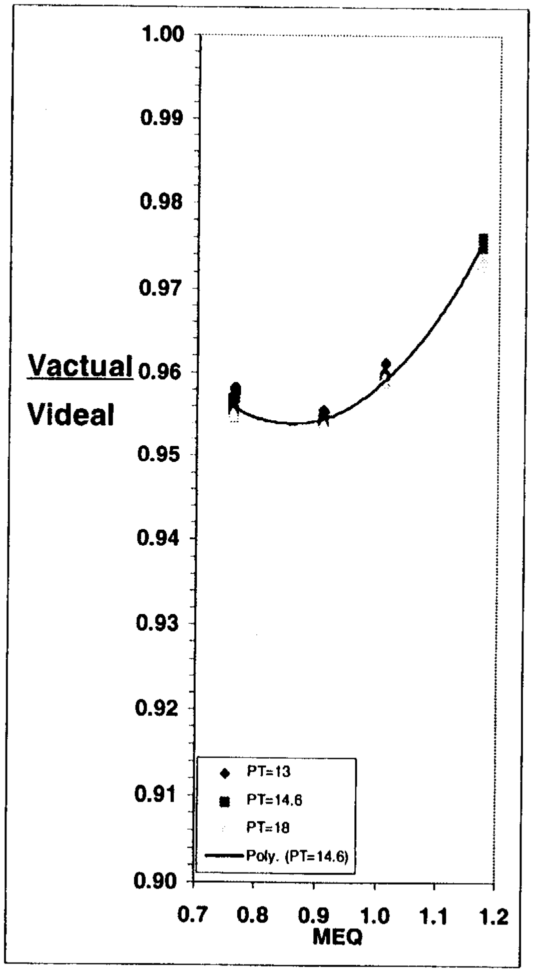

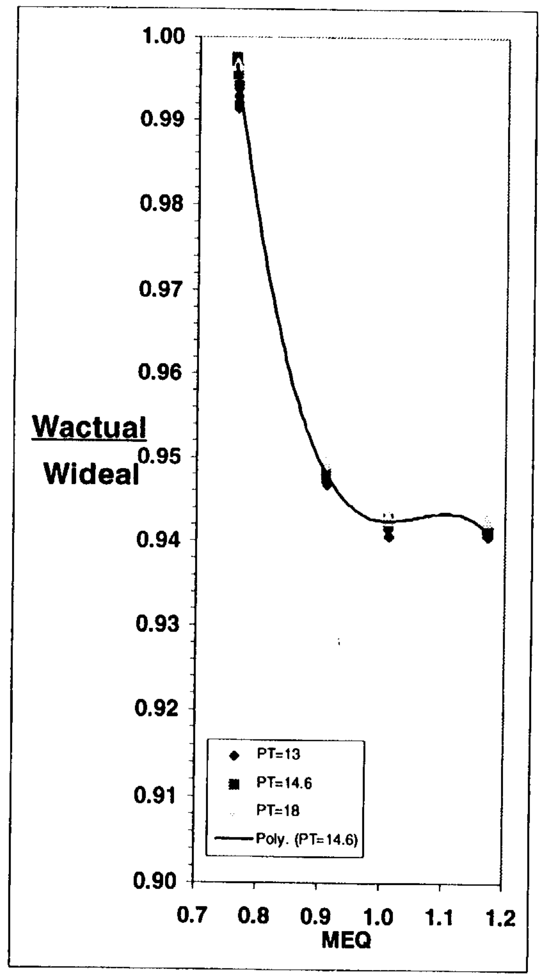

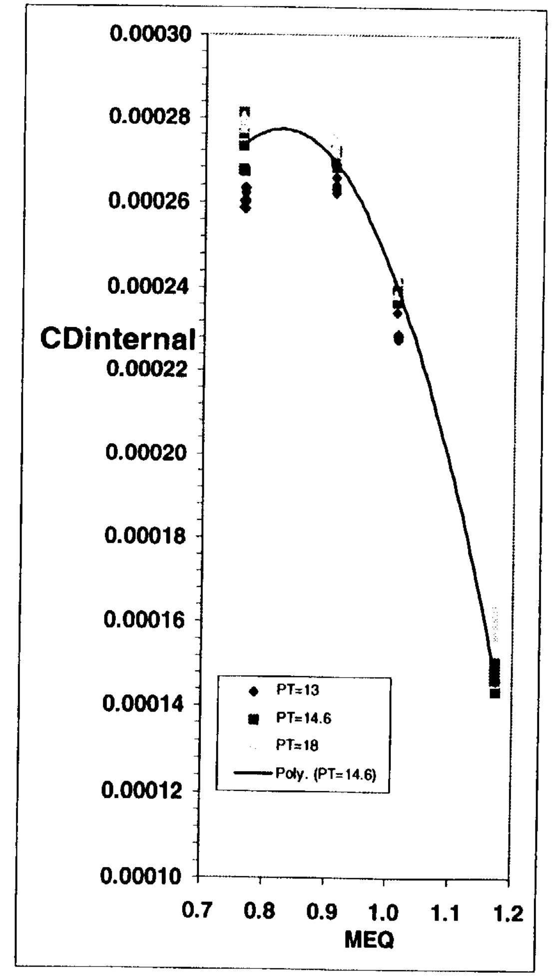

The following figure shows a post-test OVERFLOW solution at an equivalent Mach= 0.8. The PT contour plot indicates that there are no large PT losses so the drag of the bellmouth is associated primarily with distortion and not turbulent flow. The pressure and streamline data indicate that while the sidewalls are accelerating the flow uniformly, the three dimensional nature of the corners is producing a hyper acceleration. The result is a highly distorted flow that is substantially off ideal. Two other important facts are evident. First, the distortion is such that it will invariably propagate aft. The second is that the nacelle static pressures have little ability to compensate. This is because primary instrumentation at the charging station consists of only 4 nacelle static pressures located mid-wall on the four sides. The location and amount of instrumentation was selected based on transonic CFD solutions on the installed nacelle. These data indicated the duct static pressure profile to be very uniform. For such a scenario, a static pressure rake would be overkill. It would mostly cause more distortion than it would resolve.

For the calibration, instead of the bellmouth providing uniform flow at M=.8 and the pressures reading M=.8, CFD indicates the bellmouth is producing thrust more consistent with ideal flow at M=.75 with the pressures seeing M=.82. Clearly this has to introduce some bias into the system. With this much distortion it is possible that more gross thrust can be generated in the turbulent boundary layer than in the core flow. It is also possible that due to the boundary layer effects at the duct exit, the increased convergence makes the flow more uniform. In either case, this uncertainty makes it impossible to determine whether the reverse Reynolds number trends produced by the STB were the product of the bellmouth, data scatter, or some real effect.

BOEING
High Speed Civil Transport

Square Bellmouths: No One Imagined Such a Bad Design Was Possible

Bellmouth Inlet Surface Streamlines, Mach, Total Pressure
Bellmouth Exit Mach ~ 0.80

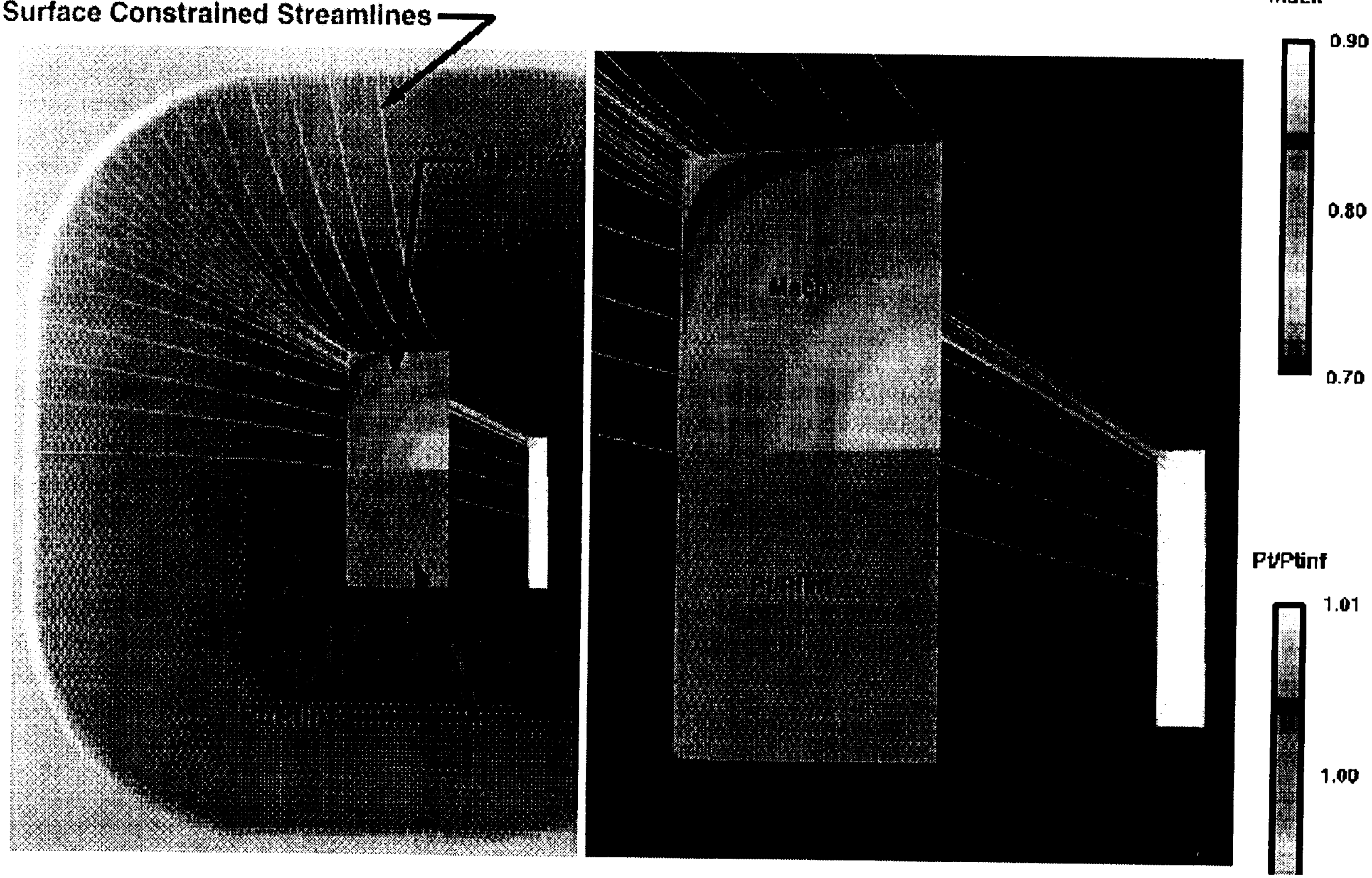

As mentioned earlier, subsonic transport programs apply Reynolds number corrections to calibration data where as fighter programs do not. Therefore, one of the principal objectives of this test was to verify whether some form of Reynolds correction would be required for an HSCT. With the resulting uncertainty in the STB data, the reverse trends, and the bellmouth issues, one might wonder if this entry got us any closer to knowing whether a Reynolds number correction is necessary for HSCT nacelles? The answer is yes. The main reason subsonic transports require a correction while fighters do not is that the instrumentation in a fighter flow-through nacelle tends to be sensitive to boundary layer changes.

The following charts show how trip effectiveness changes the static pressures inside an HSCT nacelle. Moving from left to right, the first chart shows the ratio of charging station static pressure to free stream static, the second shows the ratio of exit pressure static to free stream static, and the third shows the ratio of the two. For a nacelle where the boundary layer effects are small relative to the core flow, these three ratios should remain constant for the two trip definitions. If these ratios remained constant, a Reynolds number correction would be a requirement. There was a measurable change and because of this sensitivity, the static pressures become good indicators of changes in local Mach. This relation is shown in the last figure.

Nominal Plate Mount Data Should Be applicable Over Broad Re Range

BOEING

High Speed Civil Transport

Example of How Pressures Change With Trip/BL Profile

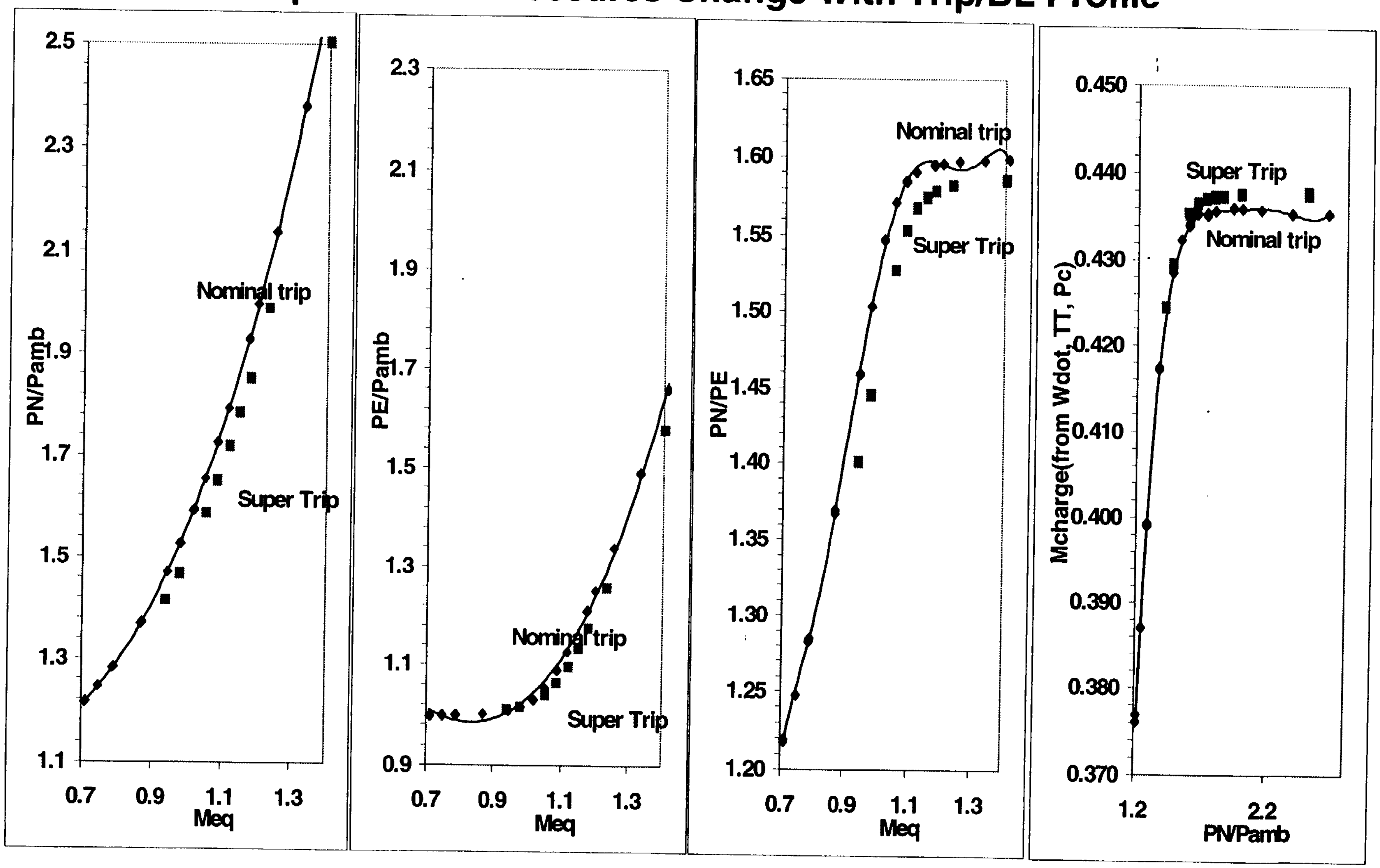

The following figure illustrates how a "supersonic" calibration works. Pictured on the left is the mounting arrangement (above) and internal flow characteristics (below) of a nacelle in the wind tunnel. Pictured on the right is the mounting arrangement (above) and internal flow characteristics (below) of a nacelle in the FSC. As with the subsonic calibration, the objective of a calibration is to correlate the nozzle exit gross thrust and weight flow characteristics with the nacelle internal flow. The nacelle exit flow (exit Mach) is a function of only the upstream flow conditions (Inlet local Mach). It is not necessary to simulate the entire installed system to reproduce the same exit flow. All that is required is that the control volume just upstream of the inlet is reproduced. If the effect of plume shape on gross thrust is also required, the static pressure downstream of the exit must also be reproduced. The FSC does this by applying a pressure differential across the nacelle, thereby accelerating air though a converging/ diverging bellmouth, followed by the nacelle, up to the nozzle exit. In this way entire nacelle internal flow aft of the inlet is simulated.

FSC Test Set Up For Supersonic Flow

Supersonic Duct WT Conditions

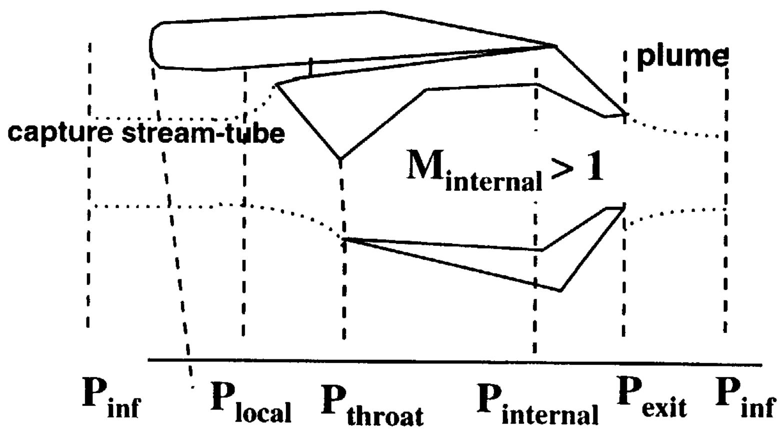

Supersonic Duct Calibration Conditions

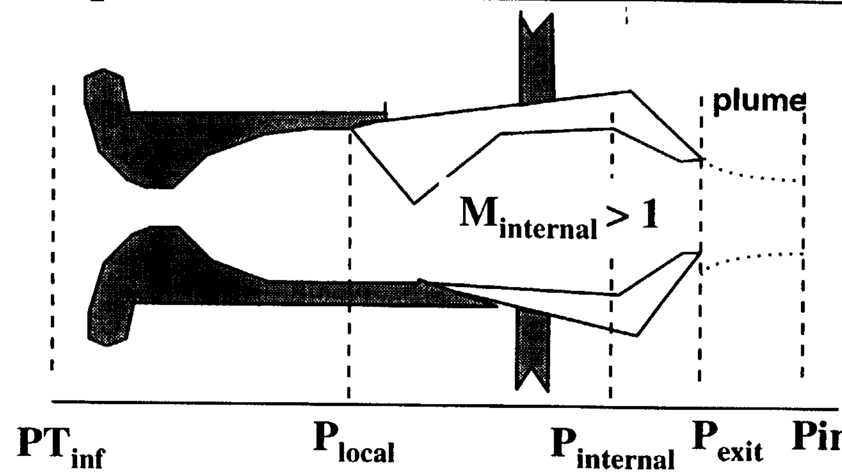

(WT flow simulated from P_{local} aft)

Range of Conditions

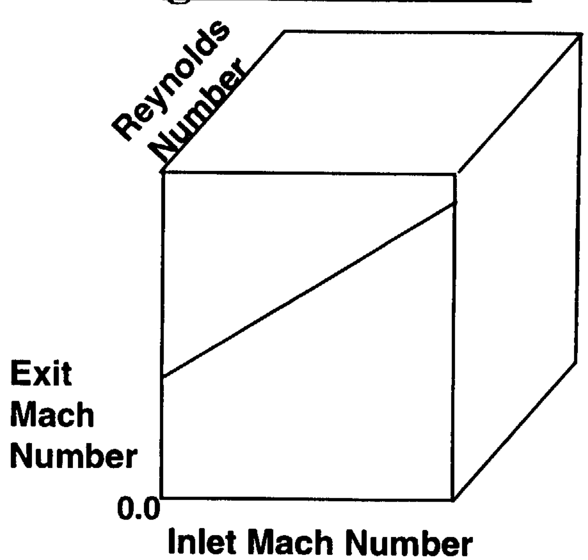

Range of Conditions

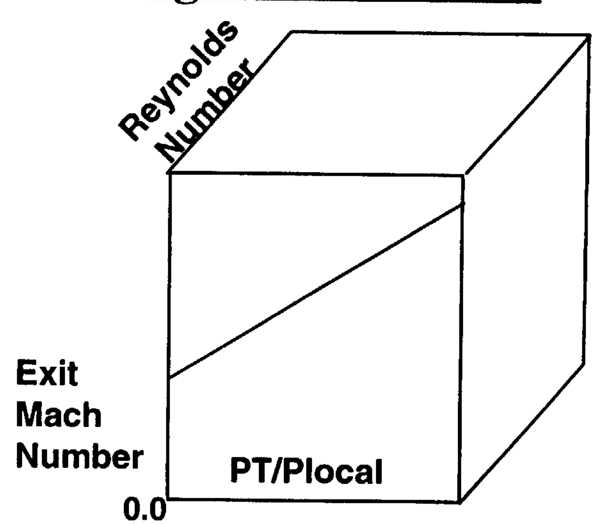

The following figure illustrates how supersonic flow is simulated in the FSC. The overall test setup is identical to the variable Reynolds number transonic set up. Again the STB is used. By replacing the converging bellmouth with a converging/diverging bellmouth, supersonic flow can be reproduced at the inlet highlight.

FSC Basic Principles: Test Set Up For Supersonic Flow

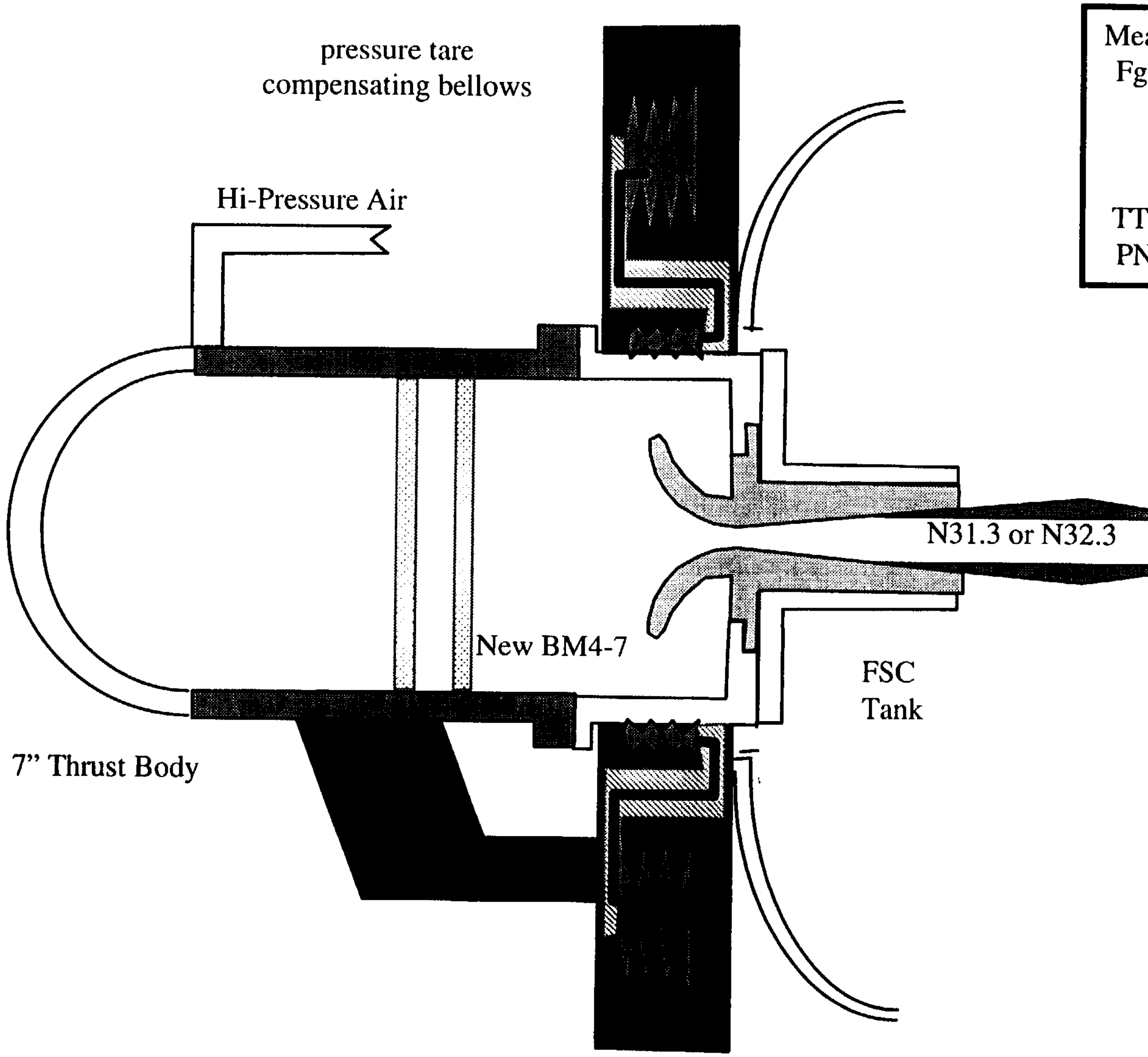

Measured quantities:
$Fg+A_{base}(P_{base}-P_{inf})$
W_{dot}
$P_{inf}=P_{vac}$
$PT_{inf}=PT_{rake}$
$TT_{inf}=TT_{rake}=TT_{vac}$
PN_{static} at 2 stations

February 1999 HSR Airframe Technical Review

On one level, this entry was a success for verifying that supersonic bellmouth design is possible and variable inlet Machs can be simulated. Inlet Machs of 1.6, 1.8, 2.1, and 2.4 were simulated at 3 Reynolds numbers a piece. Unfortunately, the same problems associated with the square bellmouth apply to the supersonic cases as well. The supersonic bellmouths were all tested isolated and showed the same high drag as the isolated subsonic. The supersonic bellmouths were fitted with static pressures just upstream of where the inlet face would be. These pressures were to be used in the data analysis to define the inlet Mach of the nacelle. What was found, as shown in the following figure, was that the wall static produced an indicated Mach very close to the ideal design Mach of each bellmouth. If the bellmouth was designed to supply M=2.4 flow, the statics indicated a mid-wall Mach of 2.399. However, the average Mach, as indicated from the manipulated balance data was substantially lower (maybe 2.25). This is a clear indication of the cornerflow distortion seen of the subsonic bellmouths propagating aft and it staying in the corners.

Assess Ability to Achieve M=2.4
Pressure Ratios and Supersonic duct Flow

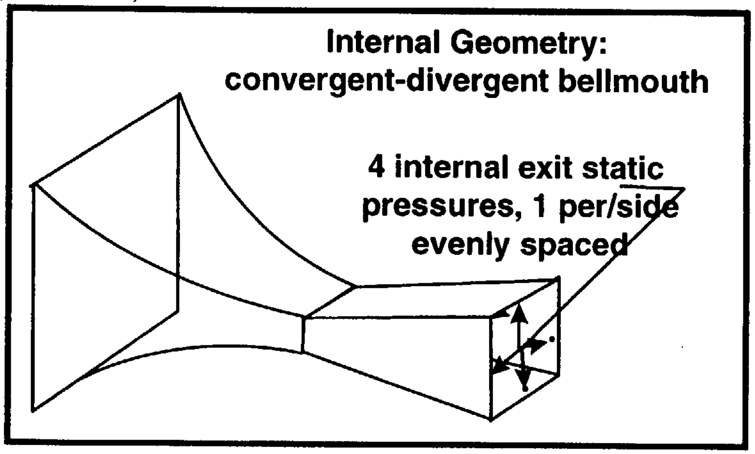

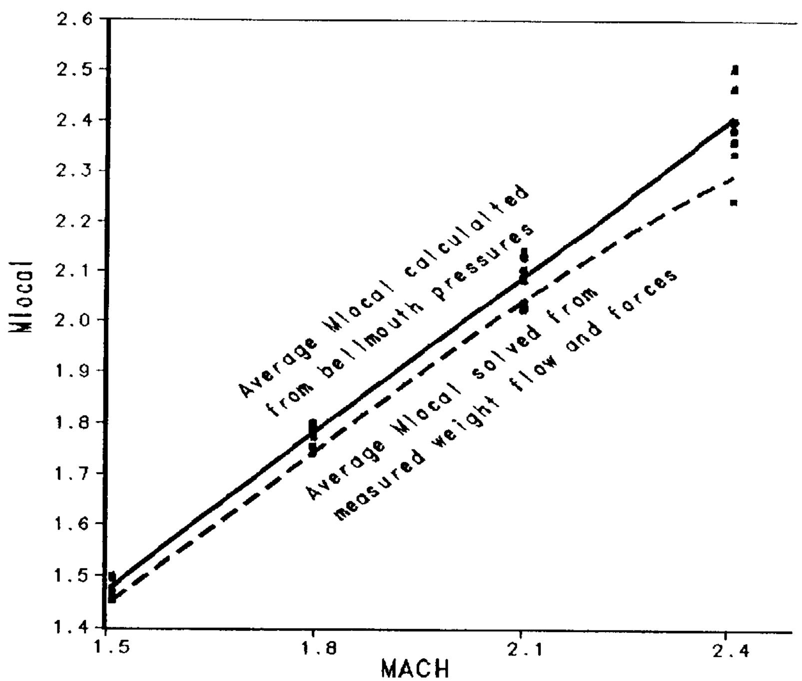

Achievements:

- 4 bellmouths run simulating Mlocal=1.5, 1.8, 2.1, 2.4
- 3 Reynolds numbers per/Mach

Issues:

- Static's indicate near ideal flow
- Balance & venturi data indicates large losses (2cts)
- No bellmouth static's in corners
- Only truncated data set run (Mlocal = Minf)
- Data also indicates constant CD vs. RN trend

Results Summary:

The second FSC test set had three goals: 1) Define long term repeatability, 2) Explore Reynolds number effects, and 3) Explore supersonic duct flow. The long term repeatability appears acceptable. The results of Reynolds number effects runs were inconclusive. The data from this test consistently showed a small reverse trend with Reynolds number. This effect could be real or it could be caused by random data scatter, a systematic bias for the STB mount with PT, or interactions with a bad bellmouth. Results from the 2"cubic nozzle appears to rule out bias, and plate mount runs with two trips implicate the bad bellmouth as a culprit. Unfortunately, there are insufficient data for a conclusive diagnosis. Productivity rates and precision limits on the STB mount indicate that the STB should be used only as a last result if no other way of correcting for Reynolds number effects is available. The two trip plate mount data indicated that the internal statics are responsive to changes in boundary layer profile. This implies that an HSCT calibration at a single Reynolds number (plate-mount) should have broad applicability across Reynolds numbers (similar to fighters).

The supersonic bellmouth work was also inconclusive. The data seemed to imply that the general experimental approach is feasible. Unfortunately, the distortion in the basic bellmouth compromised all the drag results. The basic bellmouth produced a vortex down the corners that is unrepresentative of wind tunnel conditions and cannot be picked up by simple internal instrumentation.

Recommendations

The first solution to most of these issues is to design a new bellmouth and verify the design in CFD before any new testing. Bellmouths are inexpensive <$2K, and it is believed round inlet bellmouths with short transition to the square inlet is all that is required to clean up the flow. The supersonic calibration should also be fixed with this new bellmouth design (<$4K). Based on these data, the recommendation for the PIE test is to calibrate nacelles using the plate mount method. Follow-on CFD and uncertainty analysis would be useful to determine "best" data reduction scheme.

BOEING

High Speed Civil Transport

Conclusions After Second FSC Test

Summary:

- STB feasibility was confirmed for Re matching, but results were inconclusive. Is it worth the effort?
- Square bellmouths are BAD. Effect is increased with Mach so all supersonic data were corrupted. New design necessary.

Recommendations

- New bellmouths should be round with short transition (<$2K)
- Redo supersonic calibration with new bellmouth design (<$4K)
- For PIE test, calibrate using plate mount data using 2 or more data reduction schemes
- Follow-on CFD and uncertainty analysis is needed to "best" data reduction scheme

This test was one of those tests when you find out that you did not even know what you did not know. In pretest discussions about risk, the bellmouth design was never considered a big issue. Now this appears to be the primary obstacle to accurate data. On the plus side, several successful CFD runs have already been made on low distortion bellmouths that fit our square inlet. Another lesson learned was to run the FSC with only one ejector. The FSC has two ejectors to suck down the tank. The low flow rates on our nacelles only require one to be run to achieve the appropriate tank pressures. In principle one or two ejectors should have no effect on data quality because the ejectors are downstream of the last MCV and no flow can propagate forward. In reality however, the extra ejector just pulses the entire test rig making accurate data acquisition difficult. The effect can be subtle, but it can reduce repeatability and impart biases to the balance load. In one case, in the beginning of the test, a faulty balance lead produced good data with low vibrations during checkloads and zeros, only to act up while the system is running with two ejectors.

Other lessons learned about the STB were that there is still an unresolved bias in TTN (upstream rakes) vs. TTVC (tank rake), and weight flow from upstream (MCV1) is twice as precise as from tank (MCV4). It is recommended that TTVC is the primary source of nacelle TT until the bias issue is resolved. It is also recommended that MCV4 remains the primary measurement of weight flow until more comparisons to MCV1 can be made.

Conclusions From HSCT FSC Entries

Lessons Learned

- Square bellmouths are BAD ! BAD! BAD!
- It is possible to make a bellmouth so bad that it effects calibration
- HSCT nacelles should always be run with only one ejector (reduce vibrations)
- There is an unresolved bias in TTN vs. TTVC with the STB
- When using the STB, weight flow from upstream (MCV1) is twice as precise as from tank (MCV4) but may introduce a bias

Lessons learned-continued

If one truly wants to understand Reynolds number effects, the STB still offers a unique capability. To fully utilize that capability requires confidence that all potential bias issues have been resolved. To that end an "HSCT" calibration standard with known Reynolds number characteristics could flush out bias issues between CFD and the FSC. Such a standard might consist of a 1in^2 cubic bellmouth followed by ~11" straight duct. The bellmouth/corner flow experience indicates you can never have enough internal instrumentation. Lastly, while the rakeless/single station data reduction scheme appears to work well, it remains unproven for all flow scenarios, and therfore, it is recommended that future designs continue to have static's at 2 stations.

Conclusions From HSCT FSC Entries

<u>Lessons Learned(continued)</u>

- A "HSCT" calibration standard could flush out bias issues between CFD and FSC
  - $1 in^2$ cubic bellmouth followed by ~11" straight duct
- Bellmouth/corner flow experience indicates you can never have enough internal instrumentation
- Rakeless/single station data reduction scheme remains unproven for all flow scenarios (keep static's at 2 stations)

REPORT DOCUMENTATION PAGE

Form Approved
OMB No. 07704-0188

1. AGENCY USE ONLY *(Leave blank)*	2. REPORT DATE	3. REPORT TYPE AND DATES COVERED
	December 1999	Conference Publication

4. TITLE AND SUBTITLE
1999 NASA High-Speed Research Program Aerodynamic Performance Workshop
Volume I—Configuration Aerodynamics

5. FUNDING NUMBERS
537-07-51-10

6. AUTHOR(S)
Edited by David E. Hahne

7. PERFORMING ORGANIZATION NAME(S) AND ADDRESS(ES)
NASA Langley Research Center
Hampton, VA 23681-2199

8. PERFORMING ORGANIZATION REPORT NUMBER
L-17911B

9. SPONSORING/MONITORING AGENCY NAME(S) AND ADDRESS(ES)
National Aeronautics and Space Administration
Washington, DC 20546-0001

10. SPONSORING/MONITORING AGENCY REPORT NUMBER
NASA/CP-1999-209704/VOL1/PT2

11. SUPPLEMENTARY NOTES

12a. DISTRIBUTION/AVAILABILITY STATEMENT
Unclassified–Unlimited
Subject Category 02 Distribution: Nonstandard
Availability: NASA CASI (301) 621-0390

12b. DISTRIBUTION CODE

13. ABSTRACT *(Maximum 200 words)*

NASA's High-Speed Research Program sponsored the 1999 Aerodynamic Performance Technical Review on February 8-12, 1999 in Anaheim, California. The review was designed to bring together NASA and industry High-Speed Civil Transport (HSCT) Aerodynamic Performance technology development participants in the areas of Configuration Aerodynamics (transonic and supersonic cruise drag prediction and minimization), High Lift, and Flight Controls. The review objectives were to (1) report the progress and status of HSCT aerodynamic performance technology development; (2) disseminate this technology within the appropriate technical communities; and (3) promote synergy among the scientists and engineers working on HSCT aerodynamics. In particular, single and midpoint optimized HSCT configurations, HSCT high-lift system performance predictions, and HSCT simulation results were presented, along with executive summaries for all the Aerodynamic Performance technology areas. The HSR Aerodynamic Performance Technical Review was held simultaneously with the annual review of the following airframe technology areas: Materials and Structures, Environmental Impact, Flight Deck, and Technology Integration. Thus, a fourth objective of the Review was to promote synergy between the Aerodynamic Performance technology area and the other technology areas of the HSR Program.

14. SUBJECT TERMS
High-speed research; High-Speed Civil Transport

15. NUMBER OF PAGES
775

16. PRICE CODE
A99

17. SECURITY CLASSIFICATION OF REPORT	18. SECURITY CLASSIFICATION OF THIS PAGE	19. SECURITY CLASSIFICATION OF ABSTRACT	20. LIMITATION OF ABSTRACT
Unclassified	Unclassified	Unclassified	UL

NSN 7540-01-280-5500

Standard Form 298 (Rev. 2-89)
Prescribed by ANSI Std. Z39-18
298-102